The Dissertation Committee for Matthew Thad LeBlanc certifies that this is the approved version of the following dissertation:

FIELD MEASUREMENT OF THE LINEAR AND NONLINEAR CONSTRAINED MODULI OF GRANULAR SOIL

COMMITTEE:

_____

Kenneth H. Stokoe II, Supervisor

_____

Robert B. Gilbert

_____

Ellen M. Rathje

_____

Loukas F. Kallivokas

_____

Clark R. Wilson

_____

Chadi Said El Mohtar

FIELD MEASUREMENT OF THE LINEAR AND NONLINEAR CONSTRAINED MODULI OF GRANULAR SOIL

by

Matthew Thad LeBlanc, B.S.C.E.; M.S.E.

Dissertation

Presented to the Faculty of the Graduate School
of The University of Texas at Austin
in Partial Fulfillment
of the Requirements
for the Degree of

Doctor of Philosophy

The University of Texas at Austin
August, 2013

DEDICATION

To my first civil engineering professor, who recognized my potential long before I did,
and started my journey into academia,

Dr. Bobby E. Price

ACKNOWLEDGEMENTS

No work of this magnitude can be accomplished without the assistance of so many other great individuals. First, I would like to express my gratitude to Col Greg Seely, Dr. Karen Henry, and the rest of the faculty at The United States Air Force Academy for the opportunity to enter a doctoral program and for their continued support and guidance. Additionally, my thanks to Dr. Richard Lee and the staff at Los Alamos National Laboratory for the financial support provided for the field experimentation portion of this program.

I would like to express my sincere gratitude to my supervising professor, Dr. Kenneth H. Stokoe, II, for his valuable guidance and encouragement throughout the course of my study. His enthusiasm and willingness to work around the demands required of a military-sponsored student are a credit to himself, The University of Texas at Austin, and the civil engineer profession as a whole. I would also like to give thanks to my committee members, Dr. Robert Gilbert, Dr. Ellen Rathje, Dr. Loukas Kallivokas, Dr. Clark Wilson, and Dr. Chadi El Mohtar, who gave me valuable comments and guidance.

Many thanks to the Geotechnical Engineering faculty, Dr. Roy Olson, Dr. Stephen Wright, Dr. Kenneth Stokoe, II, Dr. Robert Gilbert, Dr. Ellen Rathje, Dr. Jorge Zornberg, Dr. Fulvio Tonon, Dr. Chadi El Mohtar, and Dr. Brady Cox, for the education I have received both in and out of the classroom. Also, many thanks to the Geotechnical Engineering staff, Ms. Teresa Tice-Boggs, Ms. Chris Trevino, and Ms. Melinda Jakobovits, for their assistance with any administrative problems I had during this work. My sincerest appreciation is extended to Mr. Frank Wise for his technical assistance with instrumentation and to Mr. Federico Castro for his assistance with my laboratory work.

Sincere gratitude is expressed to current and former NEES staff at The University of Texas at Austin, Dr. Farn-Yuh Menq, Mr. Cecil Hoffpauir, Mr. Robert Kent, and Mr.

Curtis Mullins, who helped me arrange equipment scheduling and conduct the field experimentation part of this research program.

Also, I would like to thank my fellow graduate students and colleagues for their assistance, contributions, and comic relief throughout all stages of this research: Dr. Yin-Cheng Lin, Dr. Changyoung Kim, Dr. Rachelle Howell, Mr. Jung Su Lee, Mr. David Umberg, Mr. Clint Wood, Mr. Onur Kacar, and Ms. Julia Roberts.

I would like to specifically thank Capt Allen Branco for his friendship and assistance conducting the field experimentation portion of this program. His expertise was absolutely invaluable, and this dissertation would not have been possible without him. His remarkable level of competence and dedication are a credit to himself and the United States Air Force.

I would also like to express my deepest gratitude to my parents, my wife, and my children for their patience, encouragement, love, and support. Throughout the course of this work, they provided me with a constant reminder of what is truly important in life and where my priorities should lie. Each of them makes me a better person, and for this, I am eternally grateful.

Finally, I would like to thank the men and women of the Armed Forces of the United States of America for the blanket of freedom under which I have slept during the course of this research. Specifically, my deepest thanks to the United States Air Force Civil Engineer community, countless many of which have stood in my place during the course of this work and afforded me the opportunity to pursue such an endeavor as this research. I am particularly indebted to my brothers- and sisters-in-arms who have fought bravely to liberate an oppressed people and preserve the American way of life, yet will never again return to their homeland.

FIELD MEASUREMENT OF THE LINEAR AND NONLINEAR CONSTRAINED MODULI OF GRANULAR SOIL

Matthew Thad LeBlanc, Ph.D.
The University of Texas at Austin, 2013

Supervisor: Kenneth H. Stokoe, II

Traditional field seismic measurements have been performed for more than 50 years to determine the small-strain shear and constrained moduli of geotechnical materials under existing conditions. Field measurements to characterize the nonlinear response of the constrained modulus have received essentially no attention in the engineering community. This study was undertaken to characterize the in-situ response of the linear and nonlinear constrained moduli in one testing method. In this dissertation, a field method is presented which uses large shakers to impart vertical sinusoidal excitations directly above an embedded sensor array. This methodology essentially performs parametric studies on the constrained moduli of geotechnical materials in-situ over a wide range of axial strains.

In this study, embedded sensor arrays at two different locations were constructed. A staged loading sequence was used to determine the constrained compression wave velocities between sensors in the linear, i.e. small-strain, and nonlinear strain ranges. Constrained moduli were determined using the mass density of the soil and the constrained compression wave velocities. The axial strains generated between sensors were estimated using a displacement-based method. At both sensor arrays, the method successfully measured in the field: (1) the variation of the small-strain constrained compression wave velocity with increasing confining pressure and (2) the effect of axial strain on the constrained moduli of soil in various states of stress.

The field measurements indicate that, at lower levels of confining pressure, the constrained modulus increases slightly with increasing axial strain, but then decreases with increasing axial strain. However, in other cases, the constrained modulus increased with increasing axial strain and showed little or no tendency to reach a "peak" value. The nonlinear stress-strain behavior of the constrained modulus is quite complex and appears to be a function of several factors, including the amount of overconsolidation and cementation in the soil and the locations of the sensors in the array. Therefore, while the results of this study indicate that the proposed field method can be successfully used to investigate the constrained modulus, more work is required in this area to fully quantify the response of the constrained modulus in the nonlinear strain range.

TABLE OF CONTENTS

List of Tables

List of Figures

CHAPTER 1: INTRODUCTION

1.1 BACKGROUND

Characterization of the dynamic properties of soil is an important part of soil dynamics and geotechnical earthquake engineering problems and often serves as a basic first step in the solution of problems in these areas. Seismic measurements have been performed by traditional methods for more than 50 years to determine the small-strain shear and constrained moduli of geotechnical materials under in-situ existing conditions. It is well known that the stress-strain behavior in shear becomes nonlinear at even relatively small levels of shear strain, and more than 40 years ago, researchers proposed field curves for a variety of materials that show the nonlinear behavior of the shear modulus (e.g. Richart et al., 1970; Seed and Idriss, 1970; Hardin and Drnevich, 1972a and b). Therefore, the characterization effort for modeling the behavior of soil in shear generally involves determination of the response of the shear modulus to changes in shear strain amplitude, often by a combination of field and laboratory measurements.

Around the start of the 21st century, the research group at The University of Texas at Austin developed a field method to measure the linear and nonlinear dynamic shear moduli of soils over a range in strain levels (Phillips, 2000; Rathje et al., 2001; Stokoe et al., 2001; Axtell et al., 2002). This method utilizes a loading platen, usually a cast-in-place concrete footing, at or near the ground surface as the wave source and a sensor array embedded directly beneath the platen as receivers. Following the development of a new generation of vibroseis trucks (Stokoe et al., 2004), the methodology was refined by The University of Texas at Austin to perform parametric studies on the shear moduli of geotechnical materials in-situ over a wide range of strains (Stokoe et al., 2006; Park, 2010). This approach generally involves the following two major test phases.

1. To characterize linear and nonlinear shear moduli, steady-state excitation tests are performed in which a nees@UTexas vibroseis applies a horizontal sinusoidal excitation directly above an embedded sensor array of 3-D geophones. This excitation induces vertically-propagating, horizontally-polarized shear waves (or S_{VH} waves), and the response of the soil is measured by the sensors in the array. To limit the effects of the loading regimen on the underlying soil structure, a staged loading sequence is generally used in which the vibroseis applies static, vertical hold-down loads while simultaneously imparting progressively larger sinusoidal, horizontal load amplitudes. The shear modulus of the soil at each strain level induced by the vibroseis is calculated using the S_{VH}-wave velocity (V_{Svh}) determined from the interval travel times between adjacent embedded sensors.

2. In addition to these steady-state tests, a staged sequence of static vertical loads is applied to a precast concrete footing positioned over the sensor arrays. At each load stage, traditional small-strain, transient downhole and crosshole seismic tests are performed. The purposes of this test phase are: (1) to confirm that the steady-state excitation tests are measuring the S_{VH}-wave velocities at small strains and (2) to determine the variation of small-strain V_{Svh} with confining pressure.

Similar characterization of the linear and nonlinear response of the constrained modulus (M) has received essentially no attention in the civilian geotechnical engineering community. Primarily due to the complexities involved in the laboratory determination of the nonlinear constrained modulus, attempts to characterize the linear and nonlinear response of M have centered around field methods and have mainly been conducted in the military or seismological communities. These methods use strong ground motions generated either by controlled high-explosive detonations or earthquakes (Hadala, 1973; Beresnev and Wen, 1995; Beresnev et al., 2002). The concept of back-calculating in-situ linear and nonlinear dynamic properties of soil using earthquake records has been utilized

by several researchers during the past 20 years. In almost every case, the focus of the researchers has been on the nonlinear behavior of shear waves (e.g. Wen, 1994; Zeghal et al., 1995; Chang et al., 1996; Beresnev et al., 1998; Ghayamghamian and Kawakami, 2000; Kokusho et al., 2005). The focus on shear waves is partly due to the fact that documenting an earthquake with a sufficiently strong P-wave is rare (Beresnev and Wen, 1995). Due to the infrequency and unpredictability of these strong motion events, a need exists for an alternative field method to characterize the linear and nonlinear constrained moduli of soil.

1.2 RESEARCH OBJECTIVES

The vibroseis field method described above has been shown to be effective in characterizing the linear and nonlinear shear moduli of soils in-situ (Park, 2010), yet similar in-situ measurements of linear and nonlinear constrained moduli of soil have received little, if any, attention. The present research was undertaken to characterize the in-situ response of the linear and nonlinear constrained moduli. The two primary objectives of the proposed research program are as follows.

1. Investigate the feasibility of measuring linear and nonlinear constrained modulus using the generalized field methods developed by Stokoe et al. (2006) and Park (2010) for shear modulus. If the field method can be extended to constrained modulus, construction of normalized constrained modulus – log axial strain (M/M_{max} – log ε) curves can be developed over a range in confining pressures.

2. Determine how the small-strain P_v-wave velocity varies with confining pressure, and compare this behavior to the behavior of the small-strain S_{vh}-wave velocity with increasing confining pressure. These measurements also offer the possibility of investigating the in-situ stress state.

1.3 ORGANIZATION OF DISSERTATION

To address the two research objectives listed above, this dissertation is organized into nine chapters as follows.

In Chapter 1, the overall scope of the research program is introduced by discussing the need to evaluate linear and nonlinear constrained moduli in the field, the objectives of this research program, and the organization of this dissertation.

In Chapter 2, a review of previous studies which measured linear and nonlinear constrained moduli of soil in the field is presented. Additionally, the development and refinement of the vibroseis testing procedure used in this study is also discussed.

The instrumentation and equipment used in this study to measure the linear and nonlinear constrained and shear moduli in the field are discussed in Chapter 3. Technical information concerning the equipment is provided and the calibration of the measuring devices is discussed.

The methods used to reduce the data collected in this study are reviewed in Chapter 4, and example test data are shown. Determination of the wave velocities and estimation of the in-situ states of stress using wave velocities measured at small strains by the crosshole and downhole seismic tests are discussed. Additionally, example cases are provided which explain the process used to evaluate the dynamic moduli and the strains induced by the steady-state excitations from the vibroseis.

In Chapter 5, an initial suite of tests performed at a pre-existing embedded sensor array (Site 1) at Hornsby Bend, Texas, is discussed. These tests were performed primarily to refine the testing procedure and sensor layout for use in the evaluation of linear and nonlinear constrained moduli at a second site. The test program, site layout,

and the results of the linear and nonlinear testing are presented. Additionally, lessons learned from this initial suite of tests are provided.

In Chapter 6, the construction and installation of an embedded sensor array at a second site (Site 2) at Hornsby Bend, Texas, is discussed. The testing program at this site was more thorough than at Site 1, and the field set-up and test procedure are presented.

The results of the small-strain, downhole and crosshole seismic tests conducted in the linear range at Site 2 are presented in Chapter 7. The results of the downhole and crosshole tests are first presented separately, followed by a comparison of the wave velocities determined in both types of tests. The shear moduli in the linear range are compared with an empirical relationship for uncemented sand. The uncertainties and limitations associated with these types of tests are also discussed.

The results of the steady-state, sinusoidal excitation tests in the nonlinear range at Site 2 are presented in Chapter 8. The evaluation of the nonlinear constrained and shear moduli in the field are first presented separately. These results are then compared to previous determinations of constrained and shear moduli in the nonlinear range by other researchers. The uncertainties and limitations associated with the measurement of constrained and shear moduli in the nonlinear range are also provided.

In Chapter 9, the overall contents of this research program are summarized. Then, conclusions are made concerning the field measurement of the linear and nonlinear constrained modulus. Finally, a set of recommendations to further refine and improve the testing and analysis procedures is provided.

DISCLAIMER CLAUSE: The views expressed in this dissertation are those of the author and do not reflect the official policy or position of the United States Air Force, the Department of Defense, or the U.S. Government.

CHAPTER 2: BACKGROUND ON THE FIELD MEASUREMENTS OF LINEAR AND NONLINEAR CONSTRAINED MODULI OF SOIL

2.1 INTRODUCTION

Field seismic measurements have been performed for more than 50 years to determine the small-strain shear and constrained moduli of geotechnical materials under existing conditions. Although in-situ measurements of linear and nonlinear shear moduli have been studied, similar in-situ measurements of linear and nonlinear constrained moduli of soil have received little attention. The studies involving field measurements of constrained moduli can be grouped into two broad categories: (1) methods using strong ground motions generated either by controlled detonations or earthquakes (Hadala, 1973; Beresnev and Wen, 1995; Beresnev et al., 2002) or (2) methods using seismic devices which generate lower energy levels than detonations or earthquakes and are confined to a relatively localized area (Phillips, 2000; Rathje et al., 2001; Stokoe et al., 2001; Axtell et al., 2002; Stokoe et al., 2006; Kurtulus, 2006; Park, 2010). The previous studies on field measurements of linear and nonlinear constrained moduli are reviewed in this chapter.

2.2 STRONG GROUND MOTION FROM DETONATIONS OR EARTHQUAKES

In this section, field measurements of the linear and nonlinear constrained moduli of soil using strong ground motions generated by controlled detonations or earthquakes are reviewed.

2.2.1 Constitutive models based on controlled detonations (Hadala, 1973)

Since at least World War I, the United States government has conducted numerous tests using controlled detonations, generally for the purpose of understanding

the effects of blast waves on structures. These tests have used both conventional high-explosives (HE) and nuclear devices that have been detonated above, on, and below the ground surface. While the primary concern was on the improvement and fortification of military structures, these tests have also yielded significant information concerning soil response, i.e. nonlinear behavior, to large ground shock.

One such instance is described by Hadala (1973) while working with the U.S. Army Engineer Waterways Experiment Station (WES) to complete his PhD dissertation. Hadala identifies two primary regions which are generated after an above-ground detonation: (1) the superseismic region closest to ground zero (GZ), wherein the air blast propagates at a velocity faster than the soil's constrained compression wave (or P-wave) velocity and (2) the region further away from GZ where the air blast velocity decays to the point that it becomes slower than the P-wave velocity in the soil, and the ground shock effectively "outruns" the air blast. Hadala's primary focus was on the development of a computer code to model soil behavior in this outrunning-ground-shock region. While Hadala did not specifically set out to measure nonlinear constrained moduli of soils, he nonetheless was forced to address nonlinear soil behavior in the development of his constitutive model, and he presents compelling evidence for P-wave (and constrained modulus) nonlinearity.

Hadala (1973) created his code based on several detonations and test sites, but the primary event relating to constrained modulus nonlinearity occurred in April of 1952 at the Nevada Test Site (NTS) as part of OPERATION TUMBLER-SNAPPER. The first shot, named TUMBLER1, consisted of a 1.2-kton nuclear device which was air-dropped and detonated 793 ft above the ground surface. This event generated an overpressure of about 32 psi at GZ. In the outrunning ground shock region at a radial distance of about 1300 to 1600 ft from GZ, the overpressure ranged from about 8 to 10 psi. As part of the development of his code for this region, Hadala performed a parametric study to examine the effects of multiple model properties on the code output. One of the model properties

examined by Hadala was the stress-strain behavior of the soil. In one calculation (which he called L-6), the soil at the site was modeled as a nonlinear, hysteretic material as shown in Figure 2.1. Note these stress-strain curves are for a material subjected to uniaxial strain (no radial movement is allowed; hence, constrained compression). As indicated in Figure 2.1, the slope of the curve is the constrained modulus, M. Hadala compared the particle velocity-time histories generated by calculation L-6 with those from calculation L-7, which assumed linear-elastic behavior, at a distance of 1570 ft from GZ and a depth of 4 ft. These particle velocity-time histories are shown in Figure 2.2.

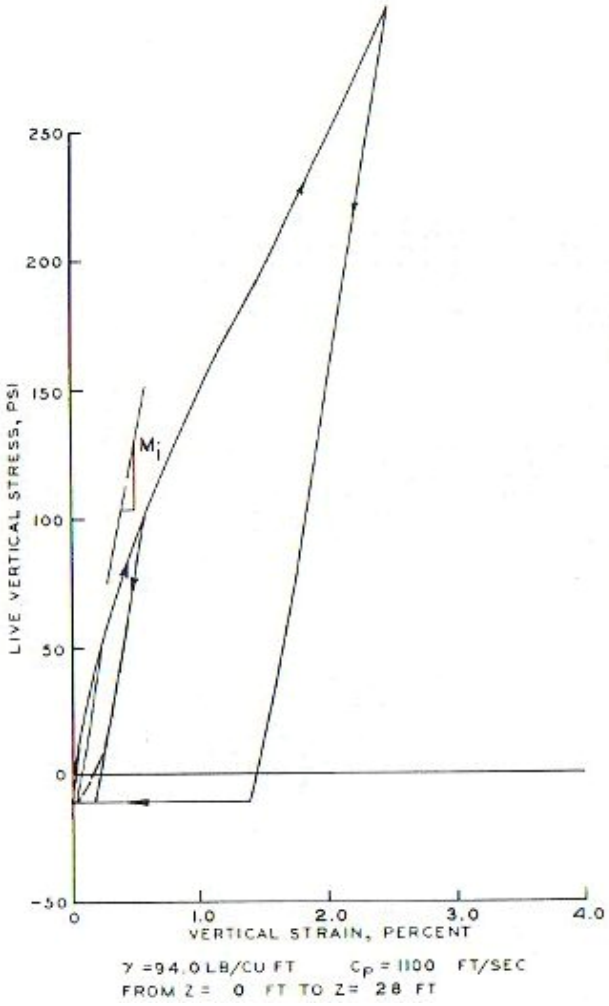

Figure 2.1. Uniaxial stress-strain curve used in calculation L-6 for idealized Layer 1 at the Nevada Test Site (from Hadala, 1973)

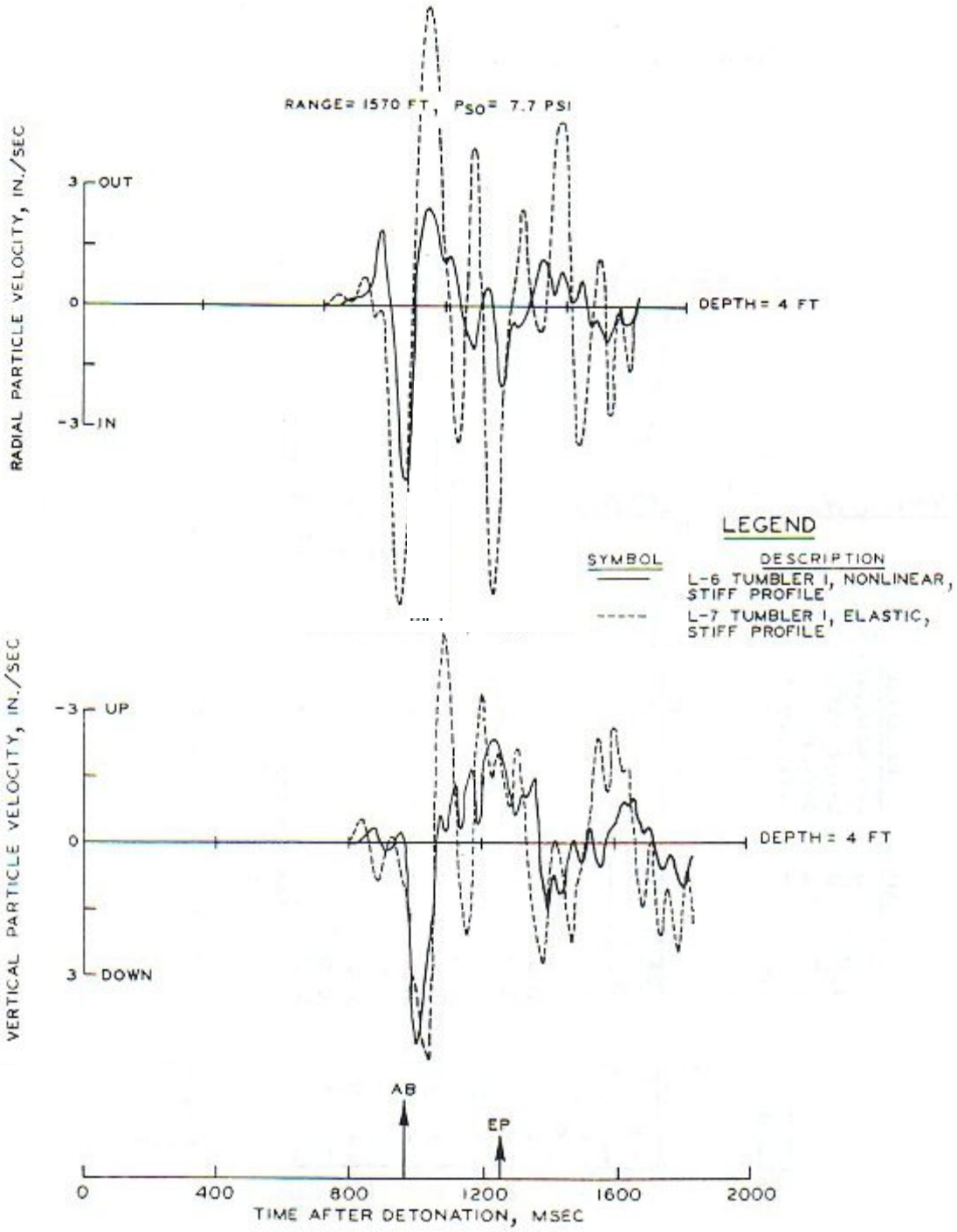

Figure 2.2. Comparison of particle velocity waveforms for linear-elastic and nonlinear-hysteretic TUMBLER1 calculations (modified from Hadala, 1973)

Hadala noted that the waveforms from the linear-elastic calculation (L-7) are more oscillatory, have larger amplitudes, and qualitatively look less like field test data than do the waveforms from the nonlinear-hysteretic calculation (L-6). He then compared his model predictions from calculation L-6 with the actual recorded particle velocity time histories of TUMBLER1 at two different radial distances from GZ. These time histories are shown in Figure 2.3. As shown, the agreement between the nonlinear-hysteretic model and the recorded data is quite good. Hadala stated that this was the first instance where a code was developed which accurately modeled soil behavior in the outrunning-ground-shock region. The importance of the fact that this agreement was obtained only by using a soil model with assumed nonlinearity of the constrained modulus cannot be overstated.

2.2.2 Back-calculation from earthquake records (Beresnev and Wen, 1995; Beresnev et al., 2002)

The concept of back-calculating in-situ linear and nonlinear dynamic properties of soil using earthquake records has been utilized by several researchers during the past 20 years. In almost every case, the focus of the researchers has been on the nonlinear behavior of shear waves (e.g. Wen, 1994; Zeghal et al., 1995; Chang et al., 1996; Beresnev et al., 1998; Ghayamghamian and Kawakami, 2000; Kokusho et al., 2005). This focus on shear waves is partly due to the fact that documenting an earthquake with a sufficiently strong P-wave is rare (Beresnev and Wen, 1995). However, the evidence that soil has experienced nonlinearity is the same regardless of the type of body wave being considered.

As explained by Beresnev and Wen (1995), nonlinear soil response can be manifested in two ways. First, since soil is a material which exhibits elastic hysteresis, this causes more damping in high-strain waves than in low-strain waves. Consequently, the amplification of the base rock motion by the overlying soil will be greater for weak

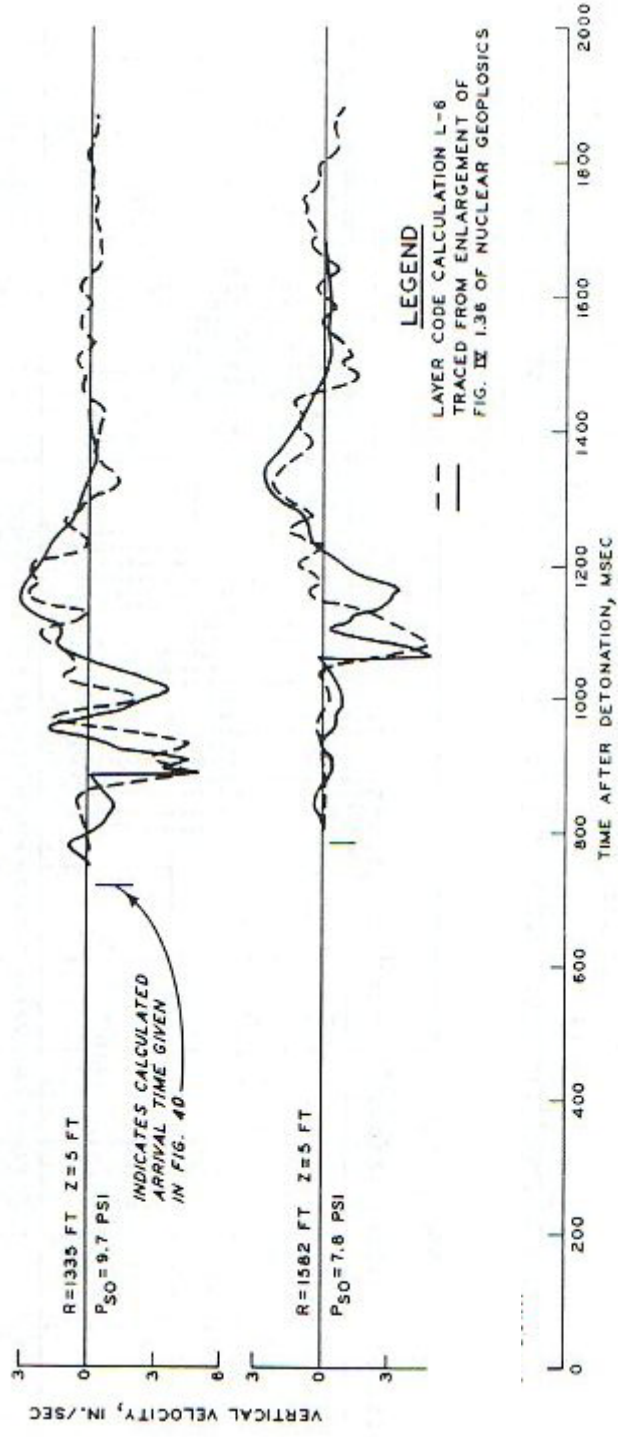

Figure 2.3. Comparison of vertical particle velocity-time histories from the outrunning region of TUMBLER1 with nonlinear-hysteretic calculation L-6 (from Hadala, 1973)

motion. Secondly, it is well-established that the fundamental frequency (f_1) of a soil layer is proportional to the wave velocity by:

$$f_1 = V/4H \tag{2.1}$$

where V is the wave velocity and H is the layer thickness (Murphy et al., 1971). Since the nonlinearity of the stress-strain relationship implies that the soil's moduli and wave velocities are strain dependent, the resonance frequencies are therefore strain dependent as well as layer-thickness dependent. Either of these two phenomena, a strong-motion deamplification or a fundamental frequency shift during strong motion, is generally accepted as evidence of soil nonlinearity.

Beresnev and Wen (1995) investigated evidence of P-wave nonlinearity at a downhole accelerograph array near Lotung, Taiwan, which was deployed from 1985 to 1990 as part of the Large-Scale Seismic Test (LSST) project. This site was previously investigated by Wen (1994) and showed significant nonlinear soil response to shear wave excitation. Accelerographs were placed at the surface and depths of 6, 11, 17, and 47 m (20, 36, 56, and 154 ft), though the accelerograph at 47 m (154 ft) became inoperable before recording the one strong motion event observed during the timeframe mentioned above. The procedure used by Beresnev and Wen (1995) follows the same procedure used by others to examine shear wave nonlinearity (e.g. Wen et al., 1994; Beresnev and Wen, 1996a; Beresnev and Wen, 1996b). This straightforward procedure involves determination of the soil transfer functions (or spectral ratios) by calculating the Fourier amplitude spectrum at each depth (including the surface) and then taking the ratio of the surface spectrum to the spectrum at each depth in the borehole. In this way, the amplification of the base rock motion by the soil layer can be clearly seen.

Beresnev and Wen (1995) computed the transfer functions (spectral ratios) at each depth for five weak events and one strong event. As seen in Figure 2.4, the transfer

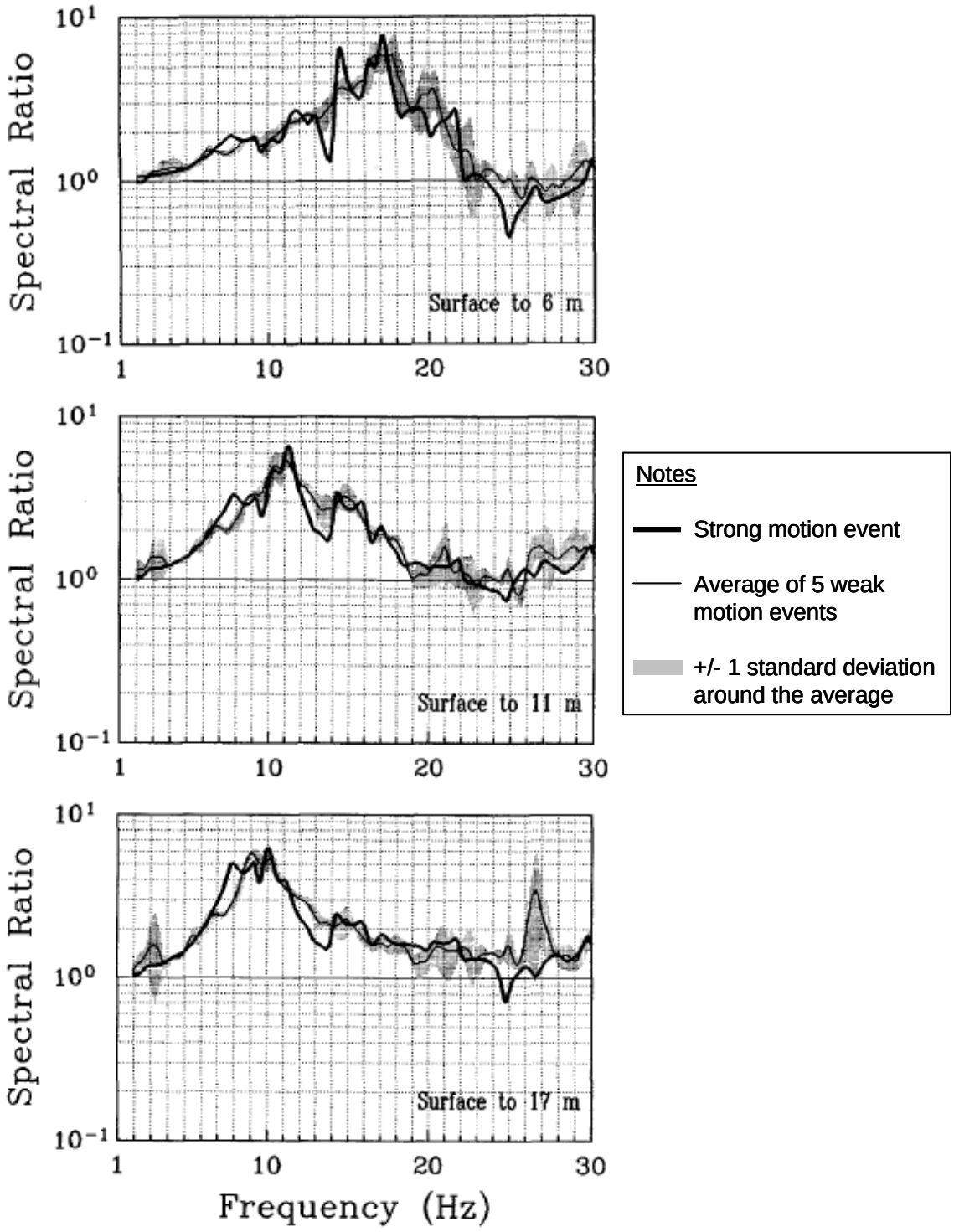

Figure 2.4. Spectral ratios of the Lotung, Taiwan, accelerometers between the surface and depths of 6, 11, and 17 m (20, 36, and 56 ft) (from Beresnev and Wen, 1995)

functions for the weak and strong motions are not significantly different. Specifically, there is neither deamplification of the strong motion nor a shift in the fundamental frequency of the strong motion when compared to the weak motion. Accordingly, the authors concluded that there was no evidence of soil nonlinearity at this site up to a dilatational strain of about $7x10^{-3}$%.

Following procedures similar to those presented by Beresnev and Wen (1995), Beresnev et al. (2002) investigated P-wave nonlinearity using the data from the KiK-net digital borehole accelerograph arrays in Japan. Downhole boreholes were selected such that both "weak" (peak acceleration less than 0.1g) and "strong" (peak acceleration greater than 0.1g) motions were available. Three boreholes (OKYH09, SMNH01, and TTRH02) met these criteria and had profiles such that the boreholes penetrated a soil layer and ended in rock. Each borehole had two instruments: one at the ground surface and one in the rock at a depth of approximately 103 m (338 ft). It is particularly important to note that only one "strong" motion event was recorded by all three boreholes: the October 6, 2000, Tottoriken-seibu earthquake which produced surface accelerations approaching 1g. The transfer functions of both the "weak" and "strong" events are shown in Figure 2.5 for boreholes TTRH02 and OKYH09. At both boreholes, there is strong evidence for P-wave nonlinearity as both exhibit clear strong motion deamplification as well as a shift in the strong motion resonance frequency to lower values.

Using the resonance-frequency shifts (Δf) observed in the transfer functions, Beresnev et al. estimated the corresponding changes in the constrained moduli by the ratio:

$$M_s/M_w = (1 - \Delta f/f_w)^2 \qquad (2.2)$$

where M_s is the strong-motion constrained modulus, M_w is the weak-motion constrained

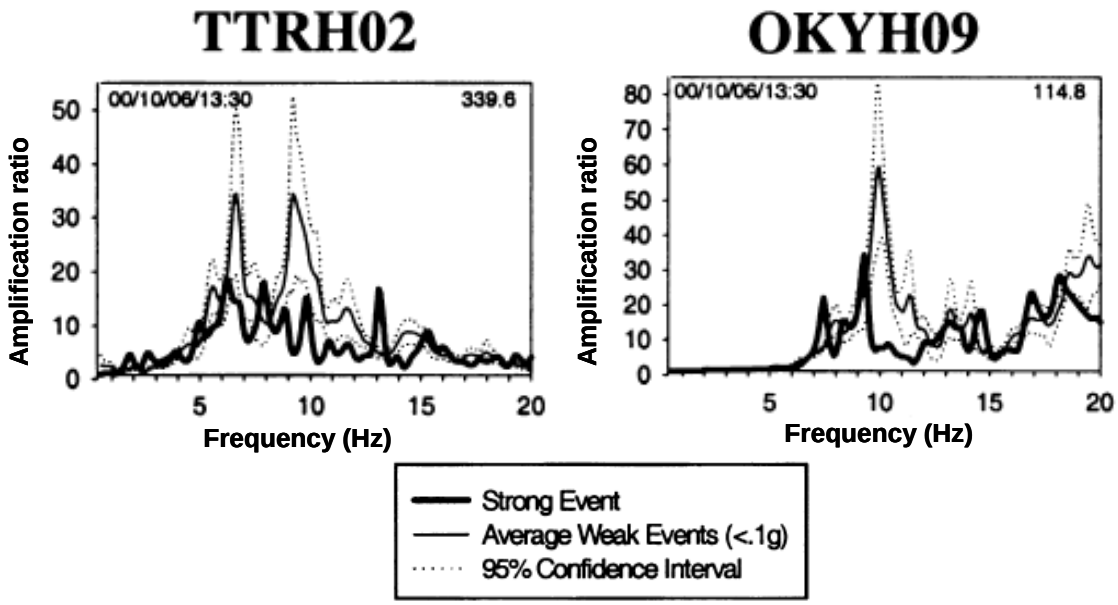

Figure 2.5. Transfer functions for two boreholes in the KiK-net accelerograph array (modified from Beresnev et al., 2002)

modulus, and f_w is the weak-motion resonance frequency (Beresnev et al., 1998). The surface compressional strain was estimated using the assumption of a harmonic wave train discussed by Beresnev and Wen (1996a). The results of these calculations are shown by the constrained modulus reduction effect in Figure 2.6. EPRI (1993) guidelines for shear modulus reduction in sand are also shown in Figure 2.6 for reference.

Beresnev et al. (2002) noted that while the reduction in constrained modulus shown in Figure 2.6 appears qualitatively similar to that of shear modulus reduction, there is considerable scatter in the data. Additionally, all of the constrained modulus ratios less than 1.0 were calculated based on only one strong motion event, the Tottoriken-seibu earthquake. However, according to the authors, this was the first time that compressional-wave nonlinearity had been observed in strong ground motions with potential for engineering use.

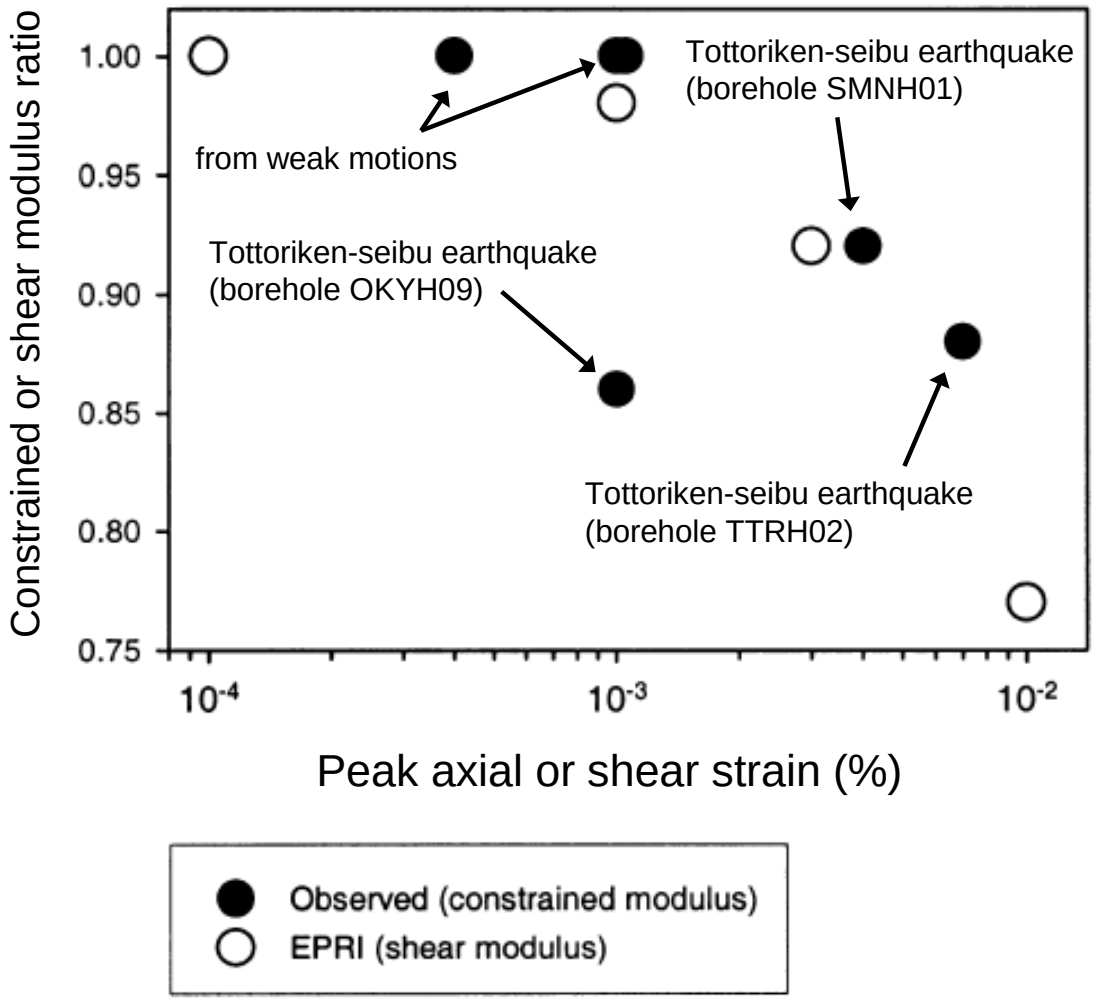

Figure 2.6. Constrained modulus reduction from P-wave amplification data (modified from Beresnev et al., 2002)

2.3 DEVELOPMENT OF FIELD METHODS USING SEISMIC DEVICES

The "high-energy" methods presented in Section 2.2 suffer from several major drawbacks as follows.

1. It is impossible to forecast when or where an earthquake will occur, so an earthquake which creates ideal strong ground motions to study P-wave nonlinearity may occur where the field instrumentation is not ideally suited to

measure the phenomena. The alternative is also possible, i.e. a weak earthquake occurs where there is extensive instrumentation for capturing the event. As a result, documenting an earthquake with a sufficiently strong P-wave is rare (Beresnev and Wen, 1995).

2. While the test locations and timing of HE and nuclear detonations in the U.S. or other countries can often be controlled, these events are still rather infrequent due to the complexity of the test itself, the inherent government involvement required to conduct the test, and the availability of site locations suitable for safe detonation. These limitations make this test procedure unlikely to gain use in the engineering profession.

3. In both cases, the researcher has virtually no control over characteristics of the motion imparted to the soil, such as the frequency content, load amplitude, or duration of the event (indeed in the case of earthquakes, the researcher has absolutely no control over the input motion). Even the use of large-scale HE or nuclear detonations provides little ability to progressively impart strain to the soil but rather loads the soil to failure in a fraction of a second.

Clearly, a need exists for alternative field procedures which provide greater flexibility to the researcher. The development and enhancement of one such field method using localized seismic devices is discussed in this section.

2.3.1 Phillips (2000); Rathje et al. (2001); Stokoe et al. (2001); Axtell et al. (2002)

Around the start of the 21st century, the research group at The University of Texas at Austin developed a field method to measure the linear and nonlinear dynamic moduli of soils over a range in strain levels (Phillips, 2000; Rathje et al., 2001; Stokoe et al., 2001; Axtell et al., 2002). This method utilizes a loading platen, usually a cast-in-place

concrete footing, at or near the ground surface as a wave source and a sensor array embedded directly beneath the platen as receivers as shown in Figure 2.7. Each sensor is composed of three, one-dimensional (1-D) geophones (two horizontal; one vertical) housed in a machined acrylic case (shown in Figure 2.8).

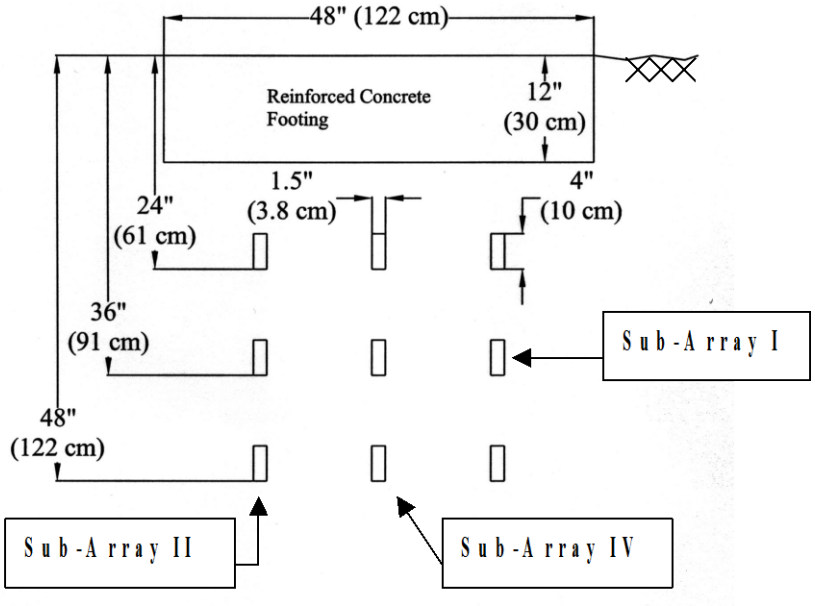

Figure 2.7. Embedded sensor array beneath a cast-in-place concrete footing (from Axtell et al., 2002)

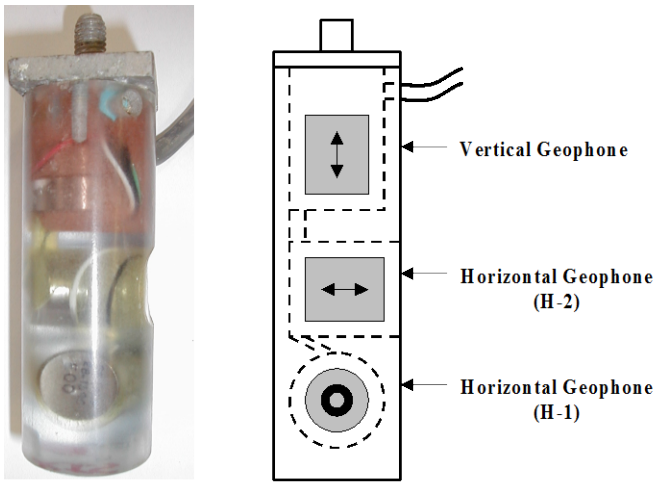

Figure 2.8. Three-component geophone case and geophones (from Axtell et al., 2002)

To measure linear and nonlinear dynamic moduli, the sensor array is subjected to two phases of seismic testing: (1) small-strain (linear) downhole and crosshole tests and (2) large-strain (nonlinear) tests using both steady-state and transient excitation. In the small-strain downhole and crosshole tests, a static load is applied to the concrete footing using a hydraulic ram which reacts against the mass of a large truck as shown in Figure 2.9. This hydraulic ram is used to vary the applied static load level. At each load level, transient downhole and crosshole seismic tests are performed to determine the small-strain wave velocities of vertically-propagating constrained compression waves (P_V waves), horizontally-propagating constrained compression waves (P_H waves), vertically-propagating, horizontally-polarized shear waves (S_{VH} waves), and horizontally-propagating, vertically-polarized shear waves (S_{HV} waves). Coupled with an assumption of the induced stress distribution underneath the footing, the behavior of these wave velocities (V_{Pv}, V_{Ph}, V_{Svh}, and V_{Shv}, respectively) with increasing stress level can be determined as shown in Figure 2.10.

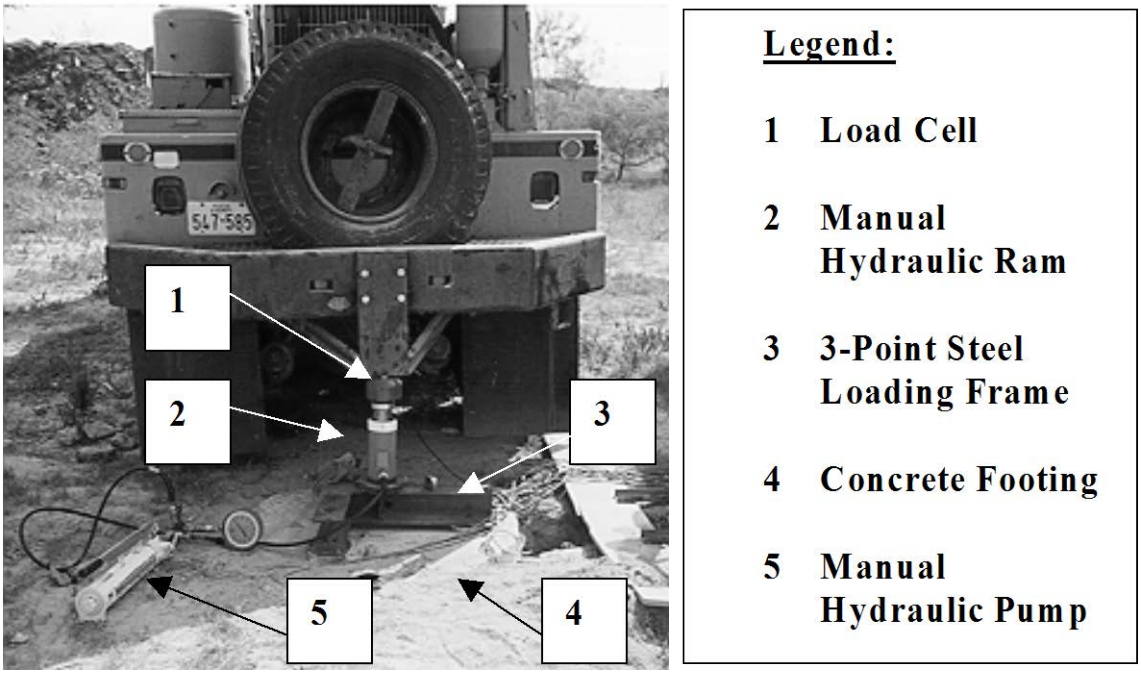

Figure 2.9. Static loading of concrete footing for small strain tests (from Axtell et al., 2002)

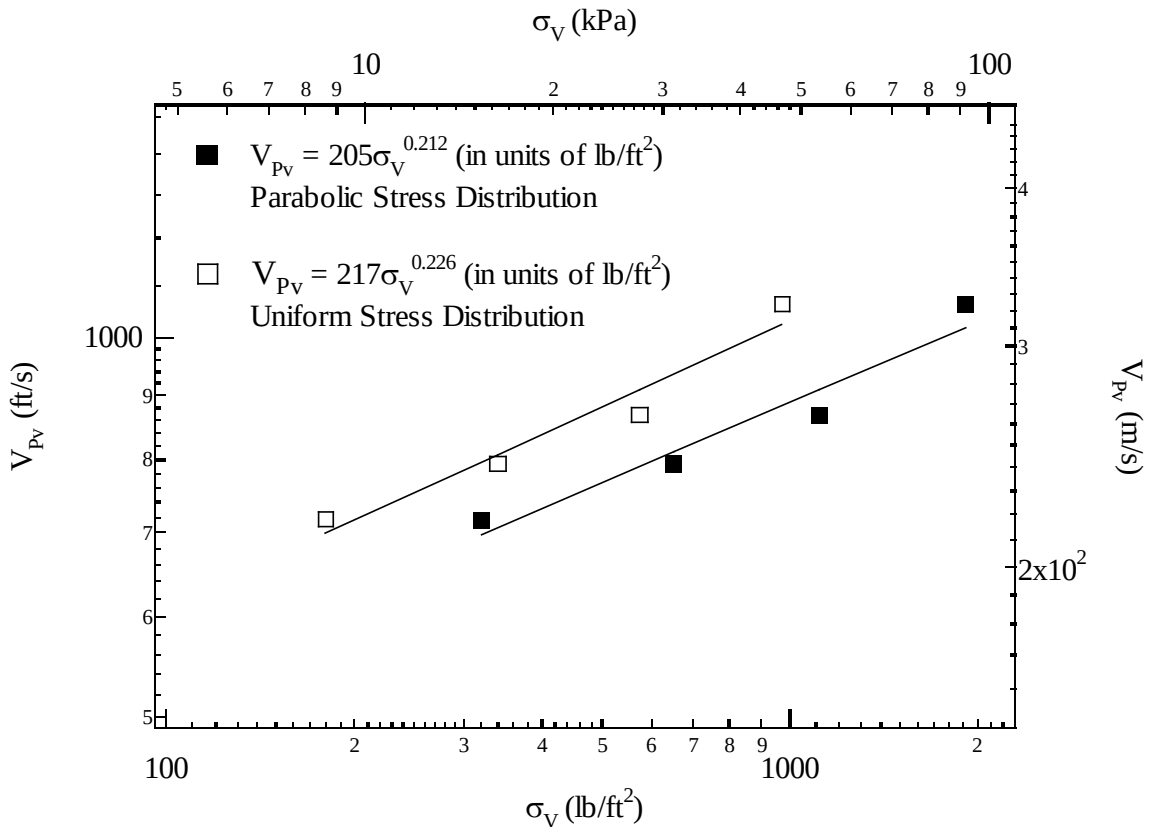

Figure 2.10. Effect of increasing total vertical stress on the P_V-wave velocities at a depth of 3.5 in. (8.9 cm) below the center of the footing (from Axtell et al., 2002)

To measure the P_V-wave velocities at large-strains (presumably nonlinear), a vibroseis truck is used to apply both a vertical static hold-down load and a vertical steady-state excitation to the concrete footing. This test arrangement is pictured in Figure 2.11. To increase the strain level, the amplitude of the dynamic load applied by the vibroseis was progressively increased at each level of static load. The highest axial strain induced by Axtell et al. (0.015 %) was generated with a static load of 18 kips and a dynamic load of +/- 10 kips. The vibroseis used by Axtell et al. was only capable of applying vertical excitation and could therefore only generate P_V-waves. To evaluate the S_{VH}-wave velocities at large strains, Axtell et al. developed a pendulum-hammer arrangement which applied a large, transient dynamic load horizontally to the side of the concrete footing as shown in Figure 2.12. This large-strain test was effectively

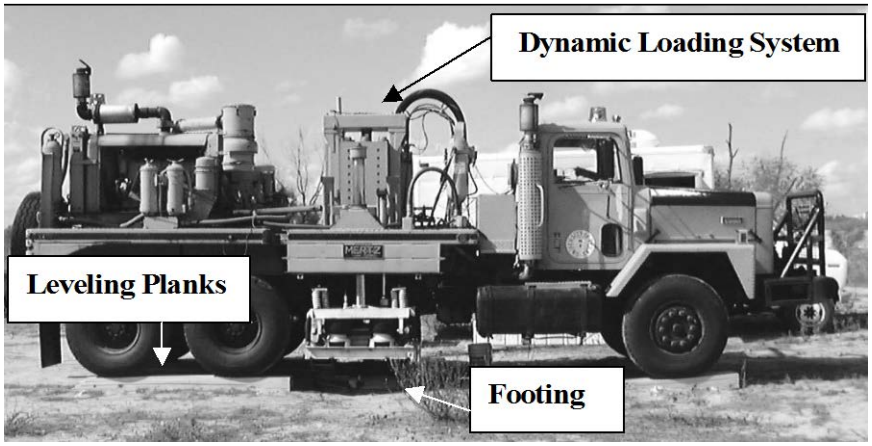

(a)

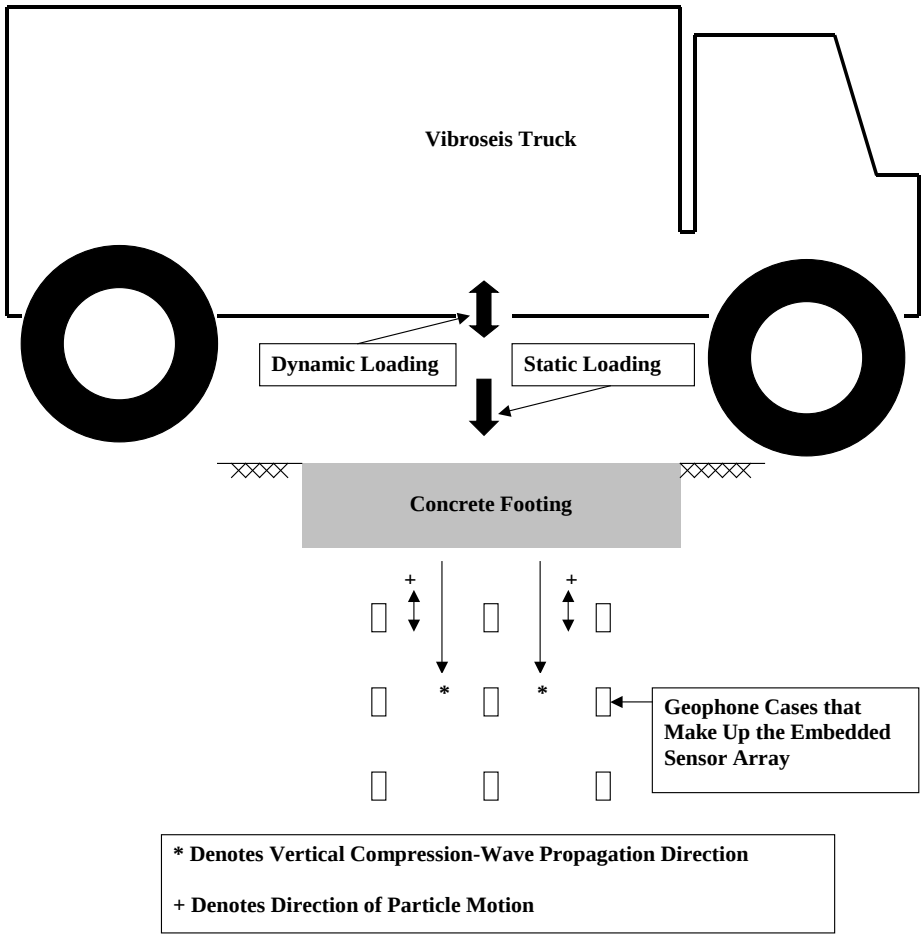

(b)

Figure 2.11. Test arrangement to measure large-strain P_V-wave velocity: (a) vibroseis truck and (b) schematic depicting generation of P_V-waves (from Axtell et al., 2002)

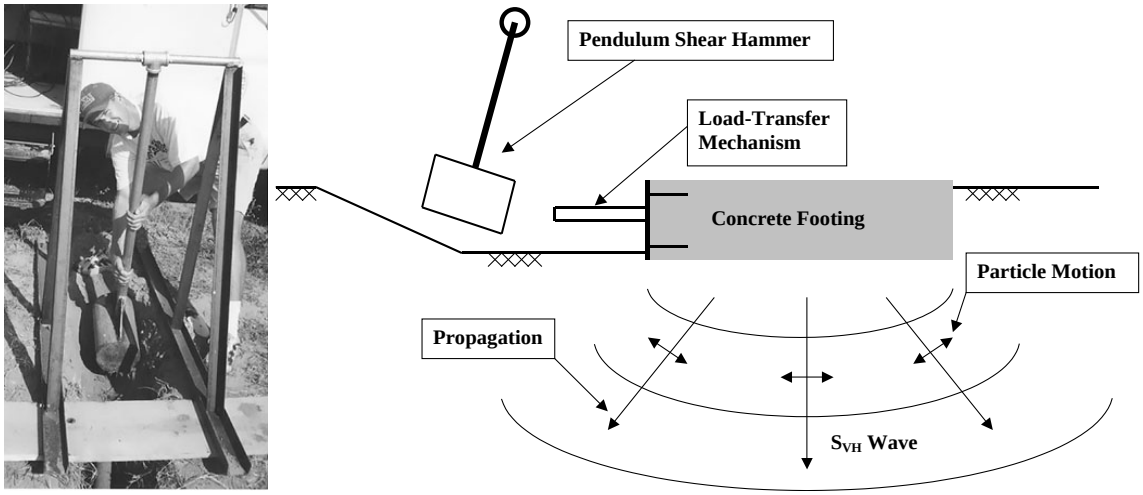

Figure 2.12. Pendulum-hammer arrangement used to evaluate S_{VH}-wave velocity at large strains (from Axtell et al., 2002)

performed in much the same manner as the small-strain downhole tests, with the exception that the roughly 130-lb pendulum-hammer applied the transient horizontal impact instead of the 2-lb and 8-lb hammers used in the small-strain downhole tests. Using this arrangement, the shear strain level was increased by increasing the drop-height of the pendulum-hammer

In each testing phase, the wave velocities are calculated by dividing the geophone spacing by the travel time (Δt) between arrivals at the geophones. For the transient seismic tests (both small-strain and large-strain), this Δt was determined based on the first-arrivals of the waves at the geophones as shown in Figure 2.13a. In the steady-state vertical excitation tests, Δt was determined based on the phase-shift between geophones as shown in Figure 2.13b. The wave velocities are then used to determine the corresponding dynamic moduli by:

$$G = \rho V_S^2 \qquad (2.3a)$$

$$M = \rho V_P^2 \qquad (2.3b)$$

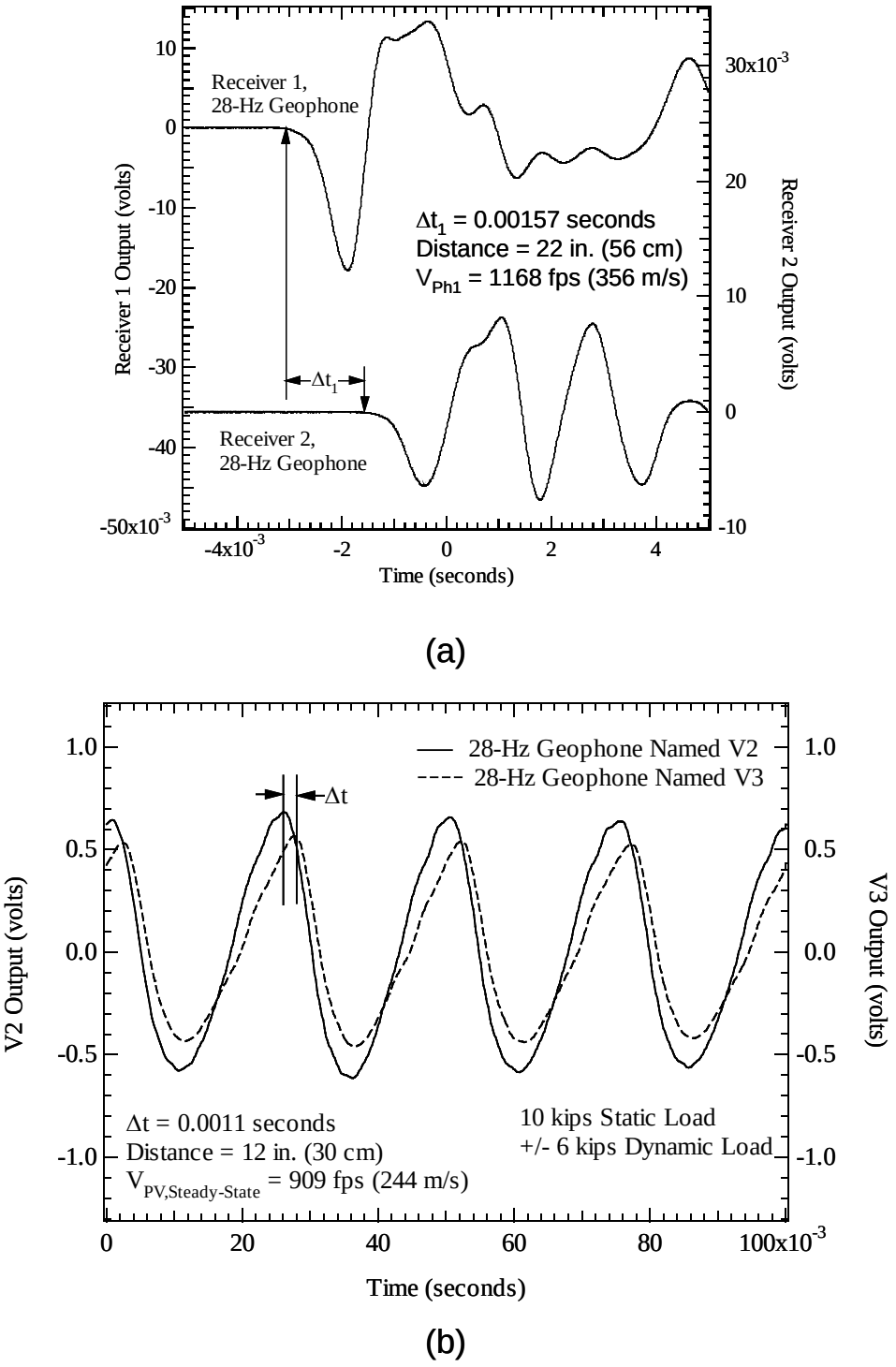

Figure 2.13. Determination of travel time between geophones for (a) transient seismic tests and (b) steady-state vertical excitation tests (from Axtell et al., 2002)

where G and M are the shear and constrained moduli, respectively, V_S and V_P are the shear and constrained compression wave velocities, respectively, and ρ is the total mass density of the soil (Richart et al., 1970). Axtell et al. (2002) assumed a plane wave travelled vertically through the sensor array and determined the strain induced in the soil by the relations:

$$\gamma = \frac{\dot{x}}{V_S} \tag{2.4a}$$

$$\varepsilon = \frac{\dot{z}}{V_P} \tag{2.4b}$$

where γ and ε are the shear and axial strains, respectively, and $\dot{x}$ and $\dot{z}$ are the peak particle velocities measured by horizontally- and vertically-oriented geophones, respectively (Richart et al., 1970).

Using Equations 2.3 and 2.4, nonlinear reduction curves of normalized shear modulus and normalized constrained modulus, i.e. G/G_{max} – log γ and M/M_{max} – log ε, respectively, can be generated as shown in Figures 2.14a and 2.14b. The quantities G_{max} and M_{max} are defined as the small-strain shear and constrained moduli, respectively. The behavior of the in-situ normalized constrained modulus shown in Figure 2.14b is presumably the first time such behavior has been determined using field testing techniques. Axtell et al. compared this behavior to the Seed et al. (1986) shear modulus reduction curves for sand (also shown in Figure 2.14). The M/M_{max} – log ε curve shown in Figure 2.14b is generally similar to both the Seed et al. (1986) G/G_{max} – log γ curves for sand and the G/G_{max} – log γ curve in Figure 2.14a generated by Axtell et al. (2002).

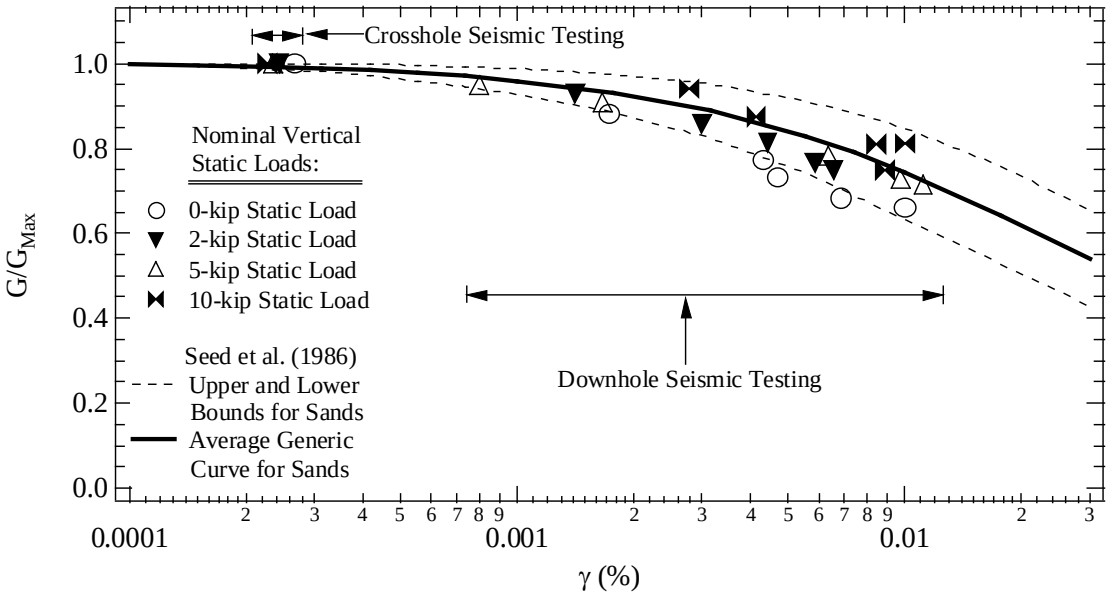

(a)

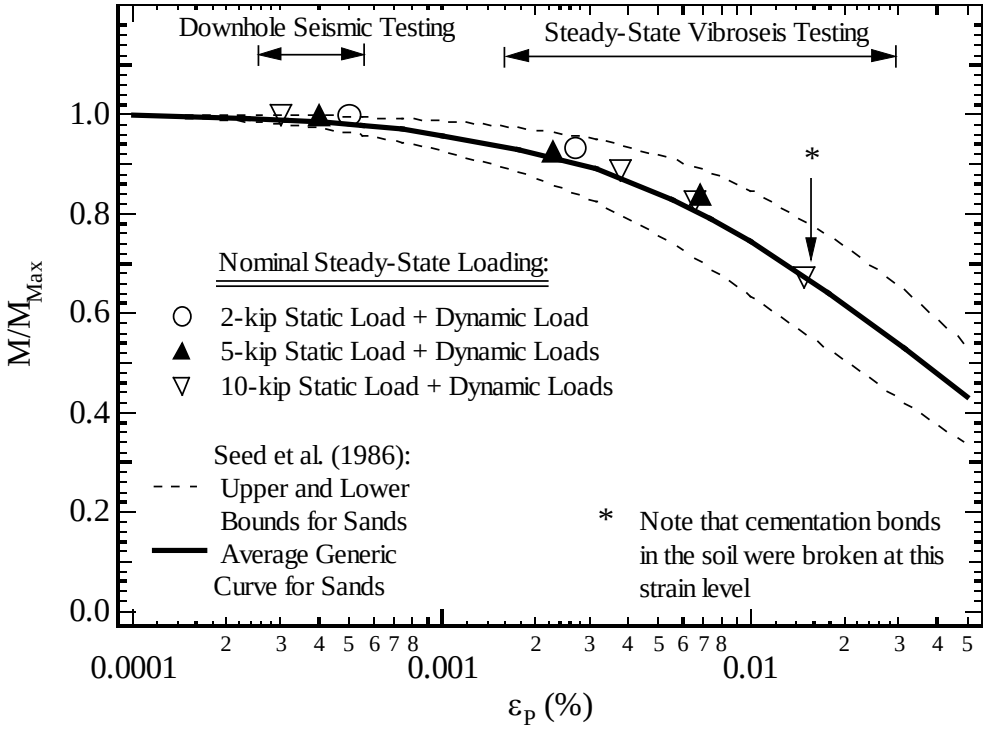

(b)

Figure 2.14. In-situ normalized dynamic modulus reduction curves: (a) normalized shear modulus and (b) normalized constrained modulus (from Axtell et al., 2002)

2.3.2 Stokoe et al. (2006); Kurtulus (2006); Park (2010)

Subsequent to the test procedures described in Section 2.3.1, a new generation of vibroseis trucks was developed by The University of Texas at Austin in conjunction with the George E. Brown, Jr. Network for Earthquake Engineering Simulations (NEES) (Stokoe et al., 2004). The major improvements included the ability to apply higher static and dynamic loads and the ability to apply both vertical and horizontal excitations. As such, the procedures described in Section 2.3.1 were further refined by Stokoe et al. (2006), and two alternate testing procedures were advanced. The first used the more advanced vibroseis trucks to apply a vertical excitation to a drilled concrete shaft near an embedded geophone array (see Figure 2.15). This method was described in more detail by Kurtulus (2006) in her PhD dissertation. However, this method is not capable of generating P_V-waves and will not be discussed further. The second method employs both vertical and horizontal excitation of a concrete footing placed over the embedded sensor array (see Figure 2.16). This method more closely resembles the procedures described in

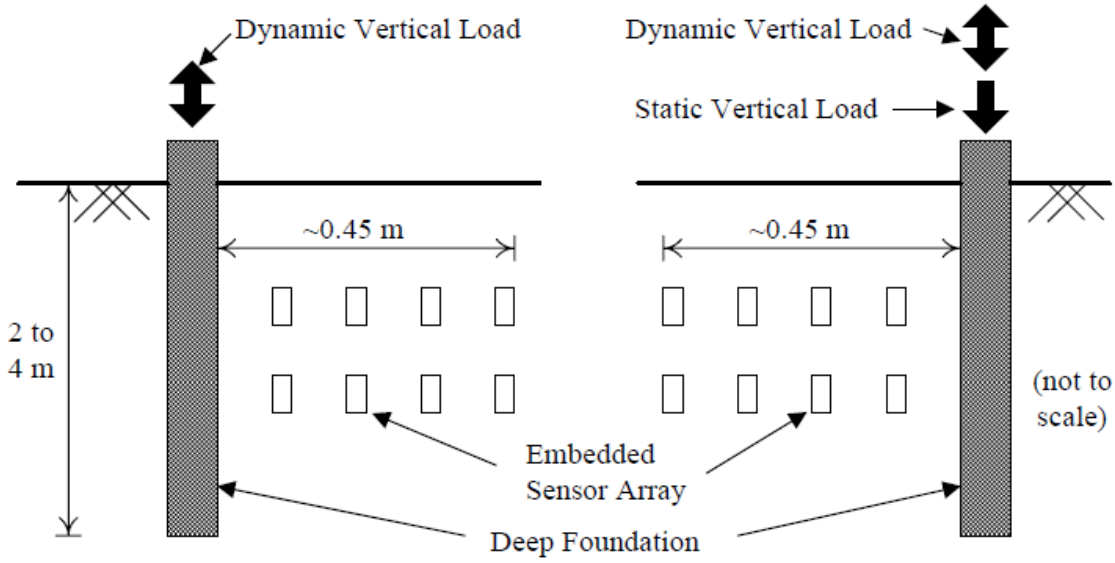

Figure 2.15. Generalized testing arrangements to measure nonlinear shear wave propagation in-situ with a dynamically loaded drilled shaft: (a) no static load and (b) with additional static load (from Stokoe et al., 2006)

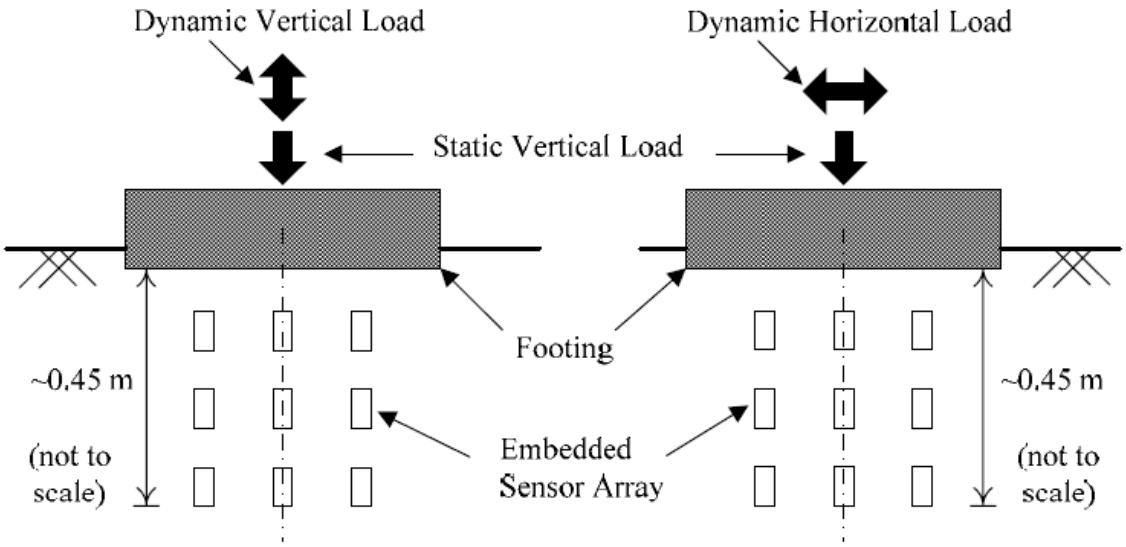

Figure 2.16. Generalized testing arrangements to measure nonlinear constrained compression and shear wave propagation in-situ with a dynamically loaded surface footing: (a) vertical excitation and (b) horizontal excitation (from Stokoe et al. 2006)

Section 2.3.1 and was further refined by Park (2010) in his PhD dissertation. Though Park's method was presumably capable of measuring both shear and constrained moduli of soils in-situ, Park principally focused on the measurement of linear and nonlinear shear moduli. Nonetheless, his refinement of the procedure is still noteworthy as the present research builds largely off his advances.

The instrumentation used by Park (2010) is generally similar to that presented by Axtell et al. (2002) except for the vibroseis trucks (mobile shakers) used and the construction of the three-dimensional (3-D) sensors. Park used two mobile shakers which are part of the nees@UTexas equipment site: (1) a small-capacity vibroseis called "Thumper" (shown in Figure 2.17a) and (2) a large-capacity vibroseis called "T-Rex" (shown in Figure 2.17b). Both Thumper and T-Rex are capable of inducing dynamic excitation in the three tri-axial directions (two horizontal and one vertical). These large mobile shakers are described in more detail in Chapter 3 and by Stokoe et al. (2004). The 3-D sensors used by Park were constructed using three, 1-D, 28-Hz geophones (two

horizontal and one vertical). These sensors, shown in Figure 2.18, are much more compact, and therefore less susceptible to rocking, than those used by Axtell et al. (2002). Additionally, the individual 1-D geophones were placed in a plastic form and then encased in epoxy. This eliminated the need for the costly and time-consuming machining process used by Axtell et al. (2002). A key aspect in Park's study is that the unit weight of the 3-D sensor is close to the unit weight of the soil.

Figure 2.17. Mobile shakers used as dynamic sources: (a) small-capacity vibroseis truck "Thumper" and (b) large-capacity vibroseis truck "T-Rex" (from Stokoe et al., 2004)

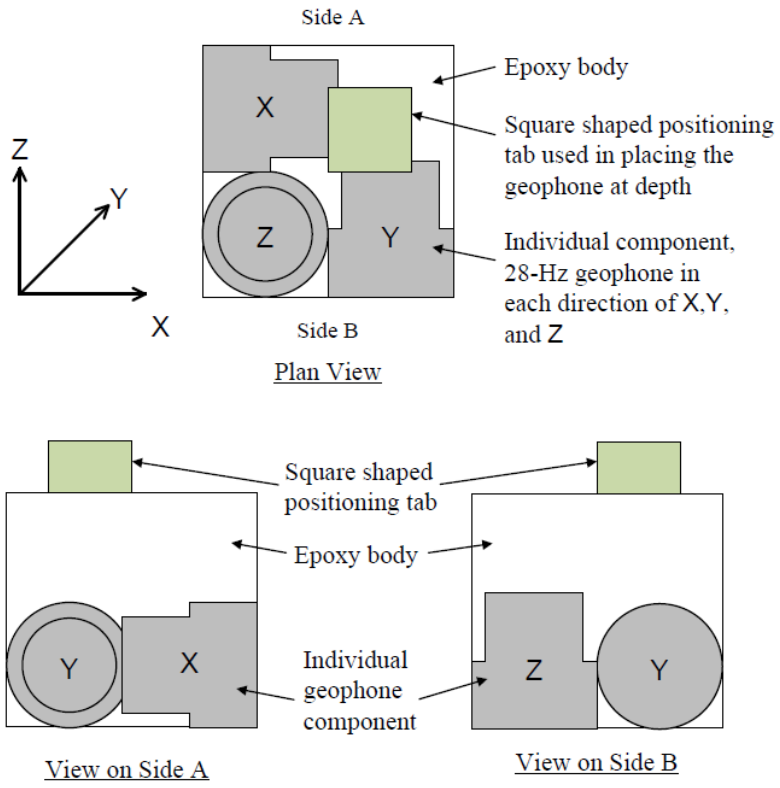

(a) Schematic illustration of 3-D geophone

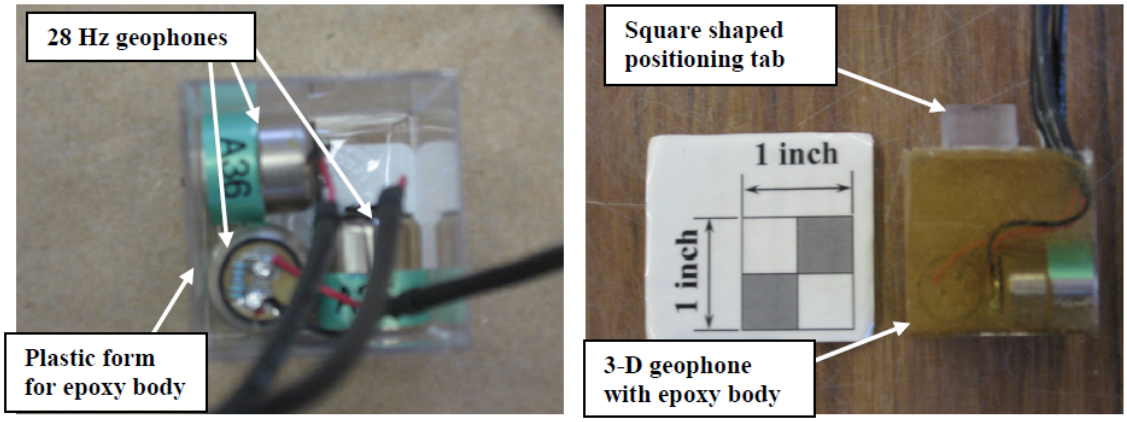

(b) Individual components before assemblage (c) Assembled 3-D geophone

Figure 2.18. 3-D sensor composed of 1-D, 28-Hz geophones used in tests at Yucca Mountain, Nevada (from Park, 2010)

Park further refined the stage loading sequence used by Axtell et al. (2002) in his tests on cemented alluvium at Yucca Mountain, Nevada. The test sequence used is shown in Figure 2.19. Similar to Axtell et al., Park used both small-strain downhole and crosshole tests (see Figure 2.20) and large-strain, steady-state tests using excitations applied by the two vibroseis trucks. Additionally, Park conducted limited load-settlement tests (Stages 5 and 7 in Figure 2.19) to determine how much settlement the footing underwent as a result of static and dynamic testing.

Instead of calculating strains based on the plane wave approximation used by Axtell et al. (2002), Park calculated shear strain based on the two-node displacement-based (DB) method developed by Rathje et al. (2004). A graphical representation of the DB method is shown in Figure 2.21, where adjacent sensors (11 and 5 in this case) are

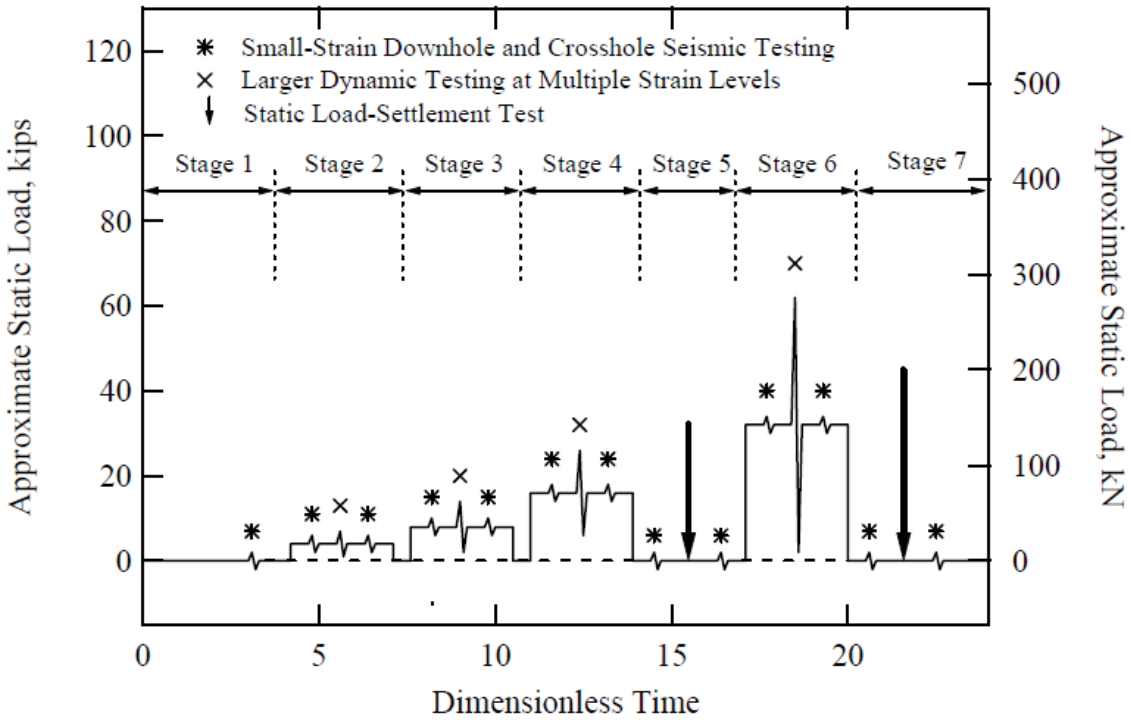

Figure 2.19. Staged loading sequence used in nonlinear shear wave testing at Yucca Mountain, Nevada (from Park, 2010)

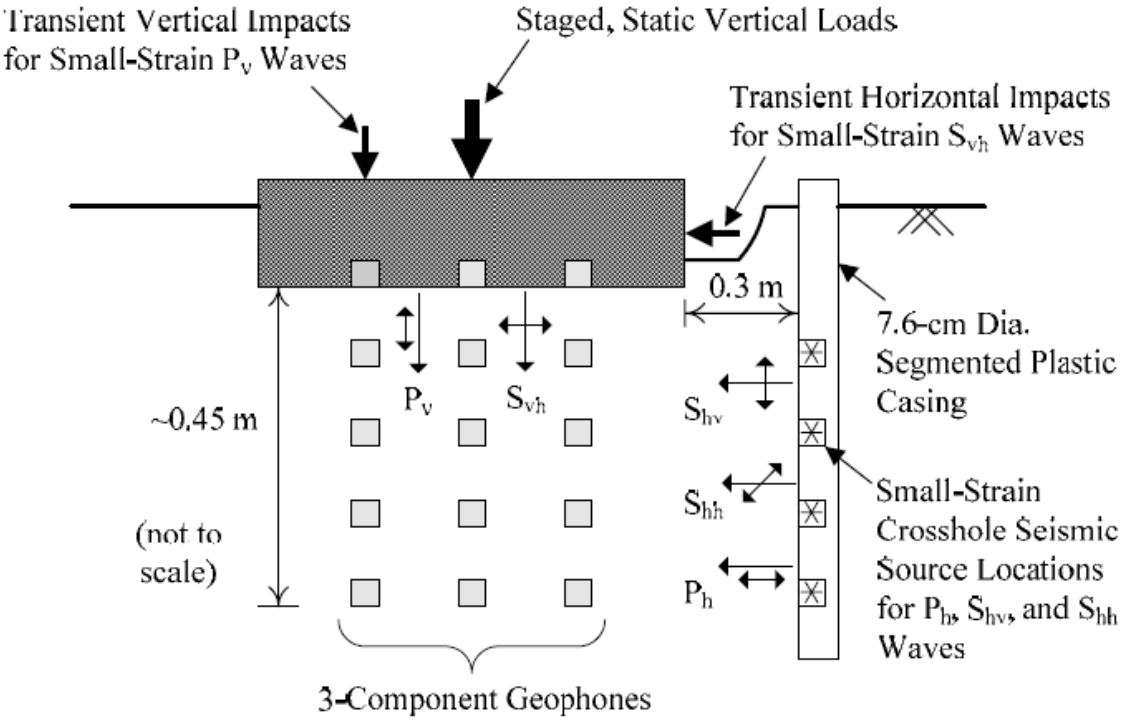

Figure 2.20. Generalized testing arrangement to measure small-strain (linear) wave velocities in downhole and crosshole tests (from Stokoe et al., 2004)

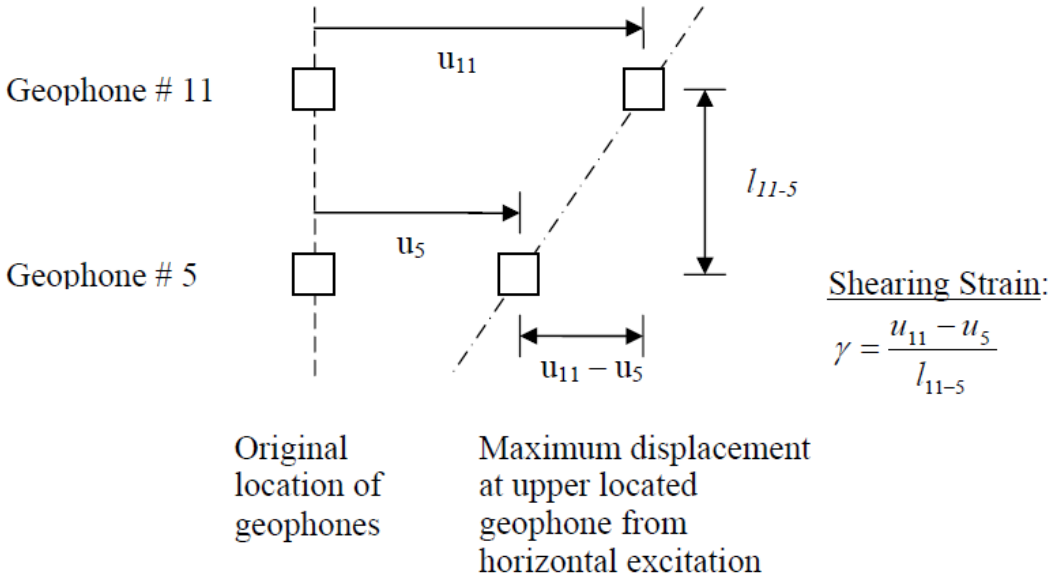

Figure 2.21. Two-node DB method used to calculate shear strain (from Park, 2010)

the two nodes, and strain is assumed to vary linearly between nodes. Since the sensors used by Park were velocity transducers, the displacements of the sensors (u_{11} and u_5 in Figure 2.21) were obtained by numerically integrating the velocity-time histories once using the trapezoid rule. After de-trending the displacement-time histories of the adjacent horizontally-oriented sensors, the strain in the positive direction was often not the same as that in the negative direction. Therefore, Park picked one cycle in the steady-steady portion of the response and used the average of the strains in the positive and negative directions. This average shear strain was assumed to represent the actual shear strain between the two sensors. This process is shown in Figure 2.22, where again this analysis is performed in the steady-state portion of the response (cycle 9 in this example).

To determine the relative displacement of the sensors ($u_{11} - u_5$ in Figure 2.21), it is critical that the displacement of each sensor be determined at the same instant in time.

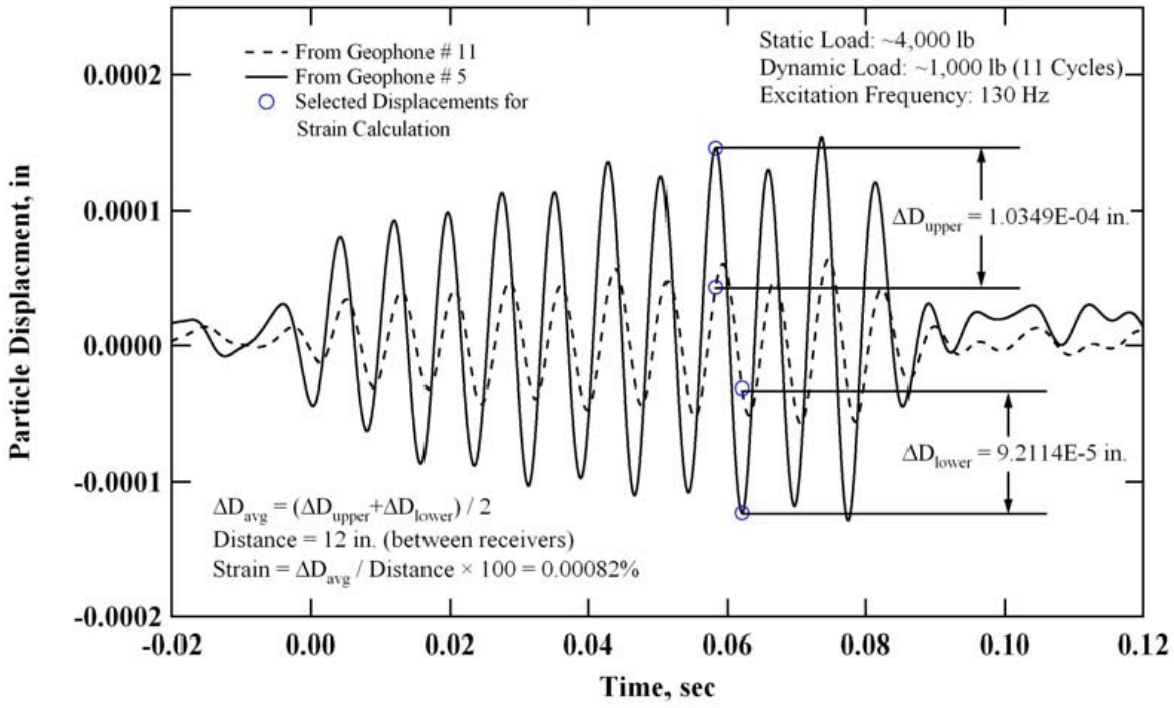

Figure 2.22. Determination of shear strain using displacement-time histories of two adjacent sensors (from Park, 2010)

Therefore, as shown in Figure 2.22, Park first determined the maximum displacement (in the positive and negative directions) of the upper sensor (Sensor 11 in this case). Then the displacement of the lower sensor (Sensor 5) was determined at the same time of the maximum displacement of the upper sensor (Sensor 11). However, there is no guarantee that the shear strain determined at the point of the maximum displacement of the first sensor will be the maximum shear strain induced during the excitation. Therefore, Rathje et al. (2004) recommended calculation of the strain at every moment in time, effectively creating a strain-time history as shown in Figure 2.23. By calculation of the entire strain-time history, the selection of the maximum absolute value of shear strain is then greatly simplified.

The remainder of the analysis procedures used by Park (2010) and his results are similar to those reported by Axtell et al. (2002). However, Park successfully generated in-situ shear modulus reduction curves for a cemented alluvium as shown in Figure 2.24. This work represented the first time nonlinear shear moduli of a cemented alluvium were measured in-situ under controlled conditions.

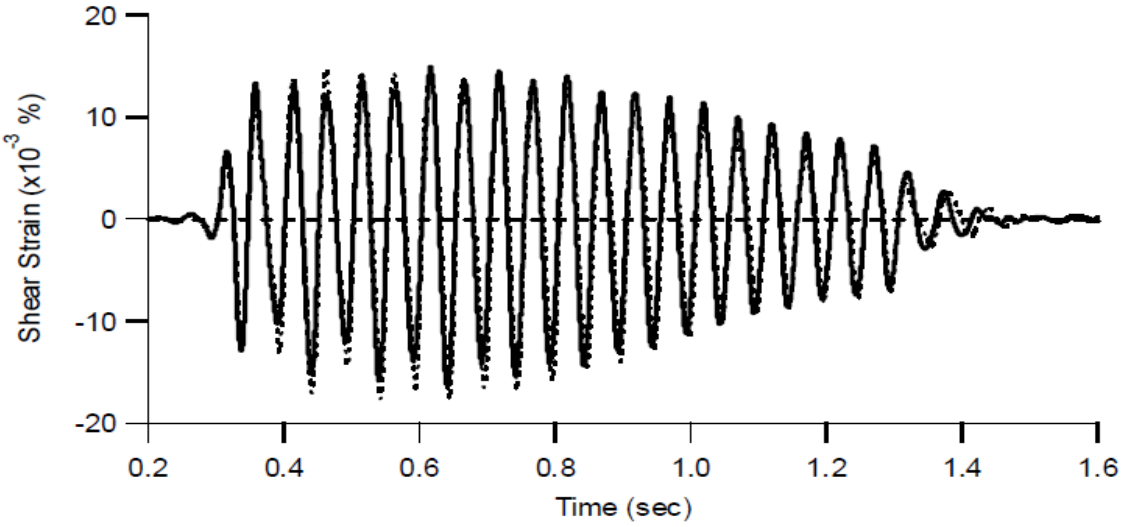

Figure 2.23. Shear strain-time history from the DB method (from Rathje et al., 2004)

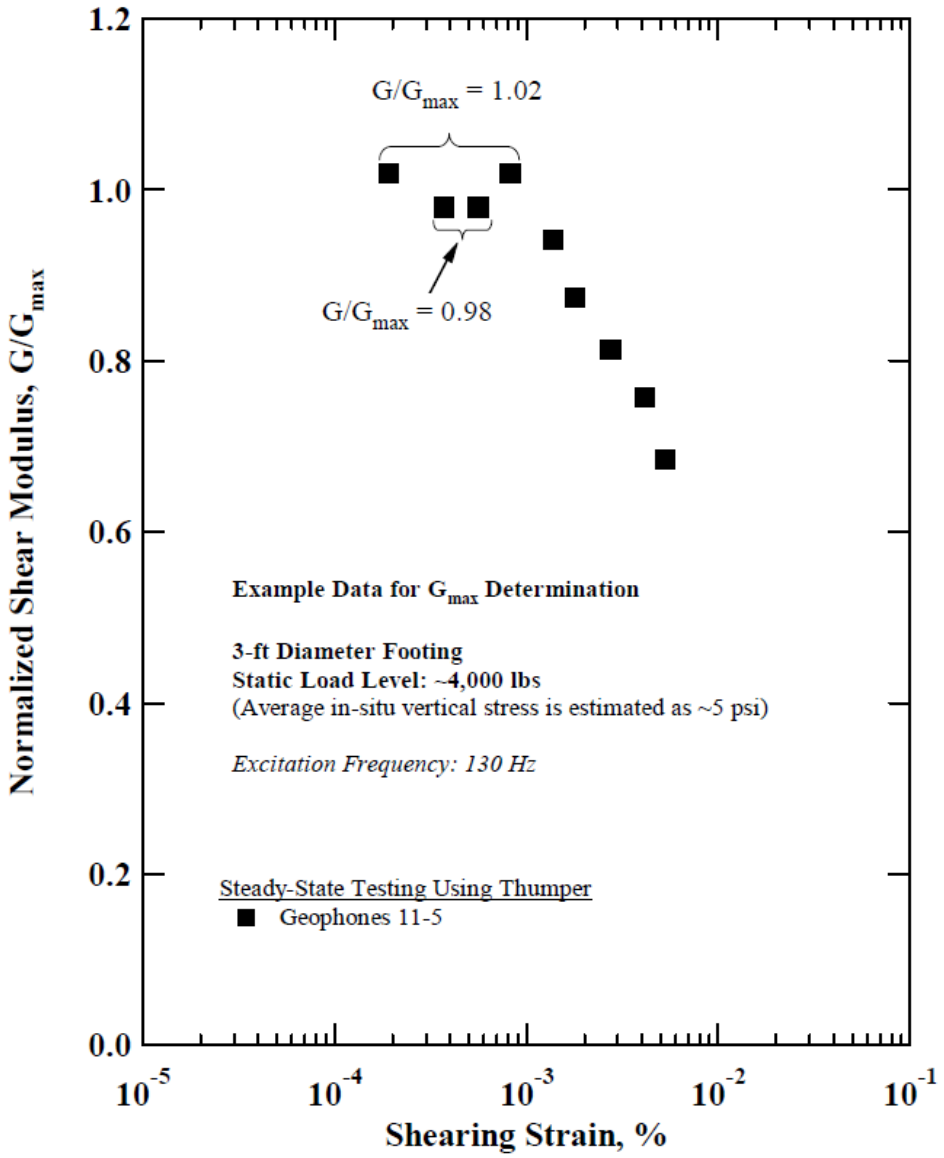

Figure 2.24. Normalized shear modulus reduction curve for a cemented alluvium (from Park, 2010)

2.4 SUMMARY

Although field seismic measurements of linear and nonlinear shear moduli have been extensively studied, similar in-situ measurements of linear and nonlinear constrained moduli of soil have received little attention. Two general categories of

studies involving field measurement of constrained moduli are presented in this chapter. The first category includes methods which generate strong ground motions over a large area using either controlled detonations or earthquakes as the source (Hadala, 1973; Beresnev and Wen, 1995; Beresnev et al., 2002). These sources were shown to be successful in generating constrained-compression waves (P-waves) and inducing nonlinearity in the soil due to P-waves. However, regardless of the source type, these "strong motion" methods both suffer from similar limitations, including the infrequency with which they occur, constraints on the site locations that can be studied, and the limited ability of the researcher to control the characteristics of the event.

The second category of field study presented in this chapter uses seismic devices which generate lower energy levels than detonations or earthquakes and are confined to a very localized area. The research group at The University of Texas at Austin (UT) initially developed a method which involved application of both transient and steady-state excitation to a concrete footing constructed at the ground surface directly over an embedded sensor array (Phillips, 2000; Rathje et al., 2001; Stokoe et al., 2001; Axtell et al., 2002). This method avoids the limitations of the "strong motion" methods previously mentioned and was successful in generating nonlinear P-waves. However, the method did not show much control over the dynamic source level (especially in the case of shear waves) and, therefore, did not allow for measurement of soil properties over a wide range of strains. Following the development of second-generation vibroseis trucks under the NEES program (Stokoe et al., 2004), the UT research group further refined the method to address the shortcomings noted above in dynamic source control (Stokoe et al., 2006; Kurtulus, 2006; Park, 2010). This method showed considerable promise in the in-situ measurement of linear and nonlinear shear moduli of soils but was not extended to the measurement of linear and nonlinear constrained moduli. In the research proposed herein, the feasibility of extending this field method to evaluate in-situ linear and nonlinear constrained moduli of granular soils is investigated.

CHAPTER 3: INSTRUMENTATION FOR FIELD MEASUREMENTS OF LINEAR AND NONLINEAR CONSTRAINED AND SHEAR MODULI

3.1 INTRODUCTION

The instrumentation used in this study was similar to that used by previous researchers (Axtell et al., 2002; Kurtulus, 2006; Stokoe et al., 2004; Stokoe et al., 2006; Park, 2010). The primary components used are: (1) large mobile shakers used to apply static loading and sinusoidal excitation, (2) sensors (geophones) to monitor wave propagation and particle movement in the soil, (3) load cells to measure applied static loads, and (4) the data acquisition system (dynamic signal analyzer, power supply, and function generator) used to record the data. Each of these components is described in detail in this chapter. Additional details can also be found in Stokoe et al. (2011) and LeBlanc et al. (2012), which were written concurrent with this dissertation.

3.2 MOBILE SHAKERS

The field method to measure linear and nonlinear shear and constrained moduli is feasible due to the development and implementation of large mobile shakers (vibroseis). The excitation imparted by these large mobile shakers is controllable in direction (vertically or horizontally), frequency, and load amplitude. This control allows the researcher the flexibility to evaluate the soil moduli over the proper strain range, which ranges from low strains to relatively high strains.

To further expand the strain range over which the linear and nonlinear shear and constrained moduli could be evaluated, two mobile shakers were used: (1) a small-capacity vibroseis called “Thumper” and (2) a large-capacity vibroseis called “T-Rex.” Both mobile shakers were provided by the nees@UTexas Equipment Site. The

nees@UTexas Equipment Site is part of the George E. Brown, Jr. Network for Earthquake Engineering Simulations (NEES) with funding provided by the U.S. National Science Foundation. Both Thumper and T-Rex are shown in Figures 3.1a and 3.1b, respectively. The theoretical force output over the operating frequency range is shown for both Thumper and T-Rex in Figures 3.2a and 3.2b, respectively. The main characteristics of Thumper and T-Rex are summarized in Table 3.1, and more detailed information about the shakers and their development can be found in Stokoe et al. (2004).

Figure 3.1. Mobile shakers used as dynamic sources in this research: (a) small-capacity vibroseis truck "Thumper" and (b) large-capacity vibroseis truck "T-Rex" (from Stokoe et al., 2004)

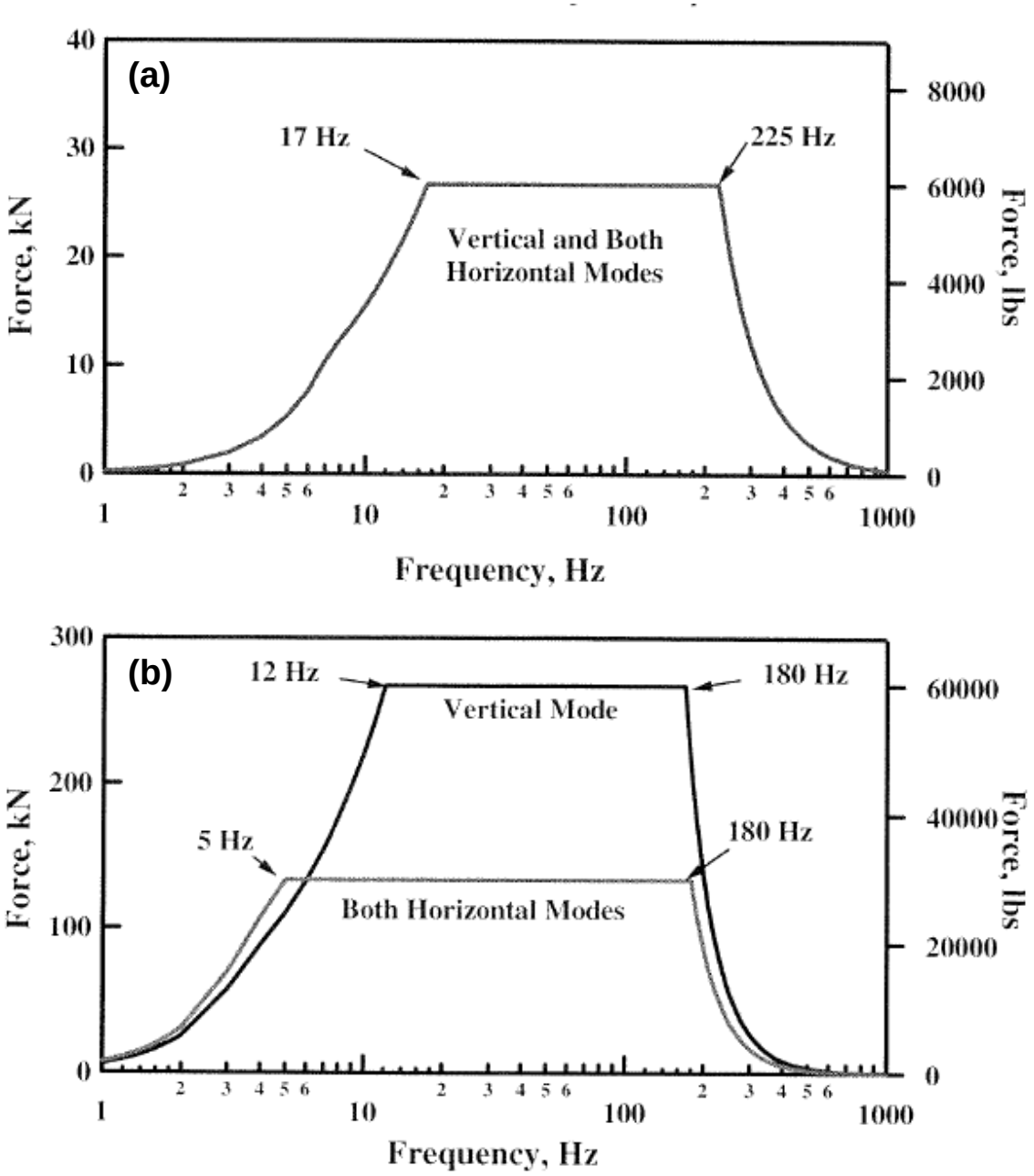

Figure 3.2. Theoretical force outputs and the associated operating frequency ranges of (a) Thumper and (b) T-Rex (from Stokoe et al., 2004)

Table 3.1. Specifications of Thumper and T-Rex (from Stokoe et al., 2004)

Shaker	Thumper	T-Rex
Vehicle Type	Built on Ford F650 truck	Buggy-mounted shaker, articluated body
Driving Speed	Highway speed	Hydraulic drive system (< 15 mph)
Total Weight	22,600 lb (9980 kg)	64,000 lb (29,030 kg)
Length	23 ft (7.1 m)	32 ft (9.8 m)
Width	8 ft (2.4 m)	8 ft (2.4 m)
Height	8 ft (2.4 m)	10.5 ft (3.2 m)
Hyraulic System Pressure	4,000 psi (476 bar)	3,000 psi (207 bar)
Vibrator Pump Flow	151 l/m (40 g/m)	757 l/m (200 gpm)
Vibration Orientations	(1) Vertical, (2) Horizontal in-line, and (3) Horizontal cross-line	(1) Vertical, (2) Horizontal in-line, and (3) Horizontal cross-line
Shaking Orientation Transformation	Field transformable in about four hours	Push-button transformation of shaking orientation
Maximum Output Force: (1) Vertical, and (2) Horizontal	(1) 6,000 lb (26.7 kN) (2) 6,000 lb (26.7 kN)	(1) 60,000 lb (267 kN) (2) 30,000 lb (134 kN)
Base Plate Area	7.50 ft^2 (0.698 m^2)	44.2 ft^2 (4.11 m^2)
Moving Mass: (1) Vertical, and (2) Horizontal	(1) 311 lb (140 kg) (2) 311 lb (140 kg)	(1) 8,100 lb (3,670 kg) (2) 4,850 lb (2,200 kg)
Stroke (Peak to Peak) (1) Vertical, and (2) Horizontal	(1) 3.0 in. (7.6 cm) (2) 3.0 in. (7.6 cm)	(1) 3.5 in. (8.9 cm) (2) 7.0 in. (17.8 cm)
Hydraulic Oil	Vegetable-based hydraulic oil	Vegetable-based hydraulic oil
Special Features	(1) Built for high-frequency output (above 200 Hz) (2) Built for use in urban environments (3) Can be driven on highways	(1) Cone pushing capacity (2) Hydraulic pressure take-off (3) Variable vertical hold-down force (4) Must be transported by tracktor-trailer rig

3.3 GEOPHONES

A geophone is a velocity transducer that generates an electrical output (voltage) proportional to the particle velocity at the location of the geophone. In the initial tests at Site One (see Chapter 5), three-dimensional (3-D) sensors composed of three, one-dimensional (1-D) 28-Hz geophones, previously constructed by Park (2010), were used (see Chapter 2). These sensors were selected primarily for expediency given that the scope of the experiments at Site One was limited to "proof-of-concept" type tests. The one-dimensional (1-D), 24-Hz geophones (Geospace Technologies GS14 24-3400) used in the more robust suite of tests performed at Site Two (see Chapter 6) were selected for primarily three reasons, each of which was noted by Park:

1. The geophones are generally robust and generate a relatively large output without the need for a power supply.

2. Since the particle velocity is obtained directly from the output voltage and geophone calibration factor, only one numerical integration is required to calculate displacement. In this way, errors associated with numerical integration can be minimized relative to accelerometers that require two integration steps.

3. The 1-D geophones are compact enough in size (0.69-in. (1.8-cm) height and 0.66-in. (1.7-cm) diameter) to allow for three geophones to be assembled together into a single 3-D sensor (see Section 3.3.2).

A 4700-ohm/0.125-Watt/1% tolerance metal-film resistor (Allied Electronics PN 896-5904) was soldered to each 24-Hz geophone to provide approximately 40% damping of the raw geophone output. Each geophone was then wired to a 25-ft long Belden 8451 shielded twisted pair coaxial cable (Allied Electronics PN 8451) which terminated with a BNC connector. This arrangement is shown in Figure 3.3.

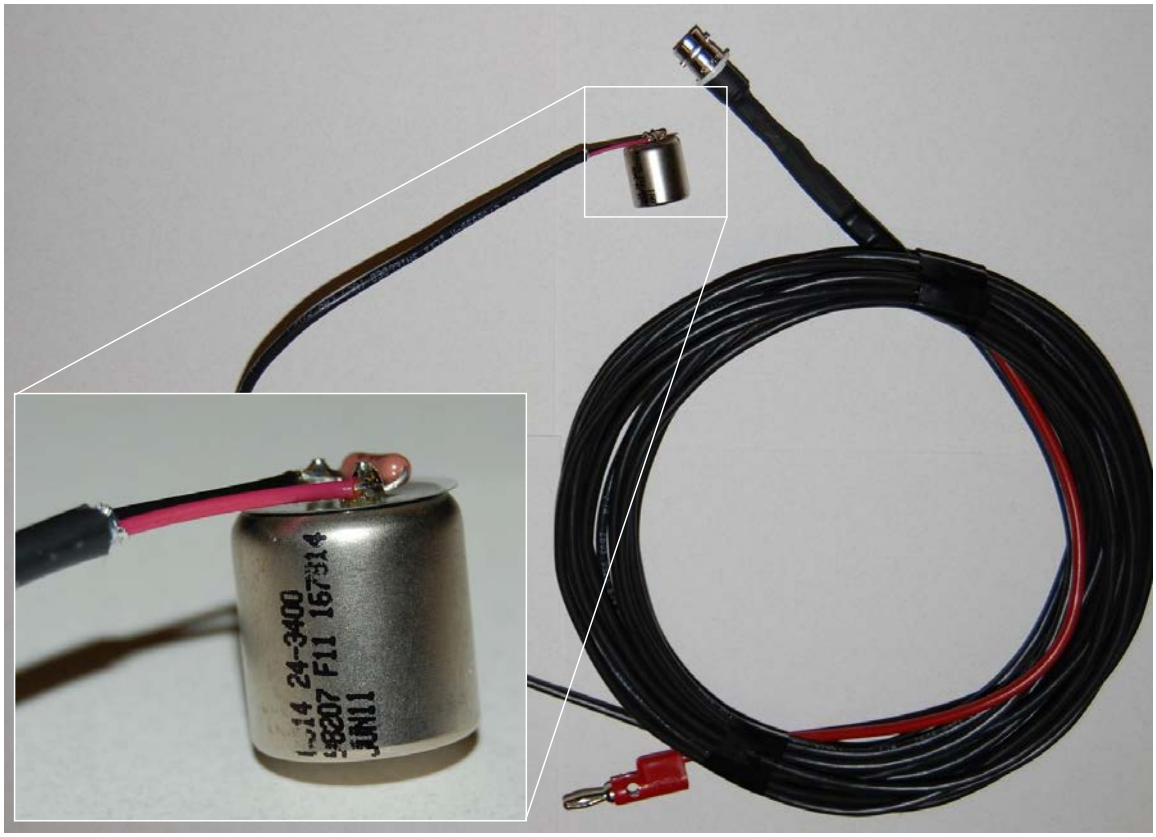

Figure 3.3. 24-Hz geophone connected to resistor and shielded twisted pair cable

3.3.1 Geophone calibration

Before the individual 24-Hz geophones were assembled into 3-D sensors, three 24-Hz geophones were selected at random and carefully calibrated in the Soil and Rock Dynamics laboratory at the University of Texas at Austin (UT). Based on the experiences of Park (2010) and Zalachoris (2010), it was assumed that the behavior of the geophones would not change significantly once they were assembled into 3-D sensors and that calibration of these three 24-Hz geophones was sufficient enough to represent the entire lot of 36 geophones. As shown in Figure 3.4, the geophones were calibrated using an electromagnetic modal shaker, where the engineering quantities (amplitude and phase information) of the geophone being calibrated and the reference sensors are the same for input sinusoidal motions. Both a proximeter (Bently-Nevada 19049) and an

accelerometer (Columbia 3021 and charge amplifier 4102M) were used as the calibration references (see Figure 3.4). These reference sensors are calibrated annually by the manufacturer or at UT, so their performance is reliable. The proximeter is a displacement transducer and is specifically used at low frequencies (less than 30 Hz). For frequencies greater than 30 Hz, the accelerometer was used as the primary reference sensor during calibration. The sinusoidal motions were generated by the electromagnetic shaker in a sweeping mode over a frequency range of 800 to 0.5 Hz, and the responses of the geophone being calibrated and the two reference sensors were recorded at each frequency simultaneously. The calibration curves of the three, 28-Hz geophones are shown in Figure 3.5. There is generally good agreement between the three geophones with respect to both the calibration response curve (Figure 3.5a) and the phase response curve (Figure 3.5b).

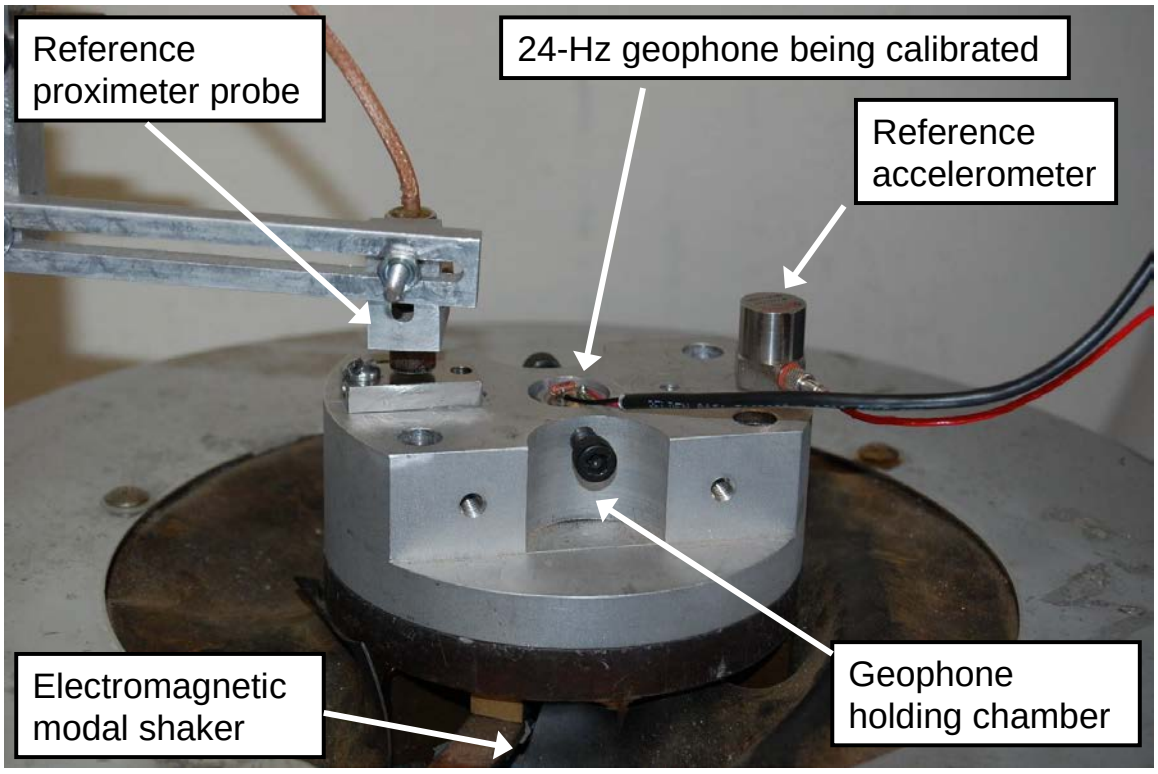

Figure 3.4. Calibration of a 1-D, 24-Hz geophone in the laboratory

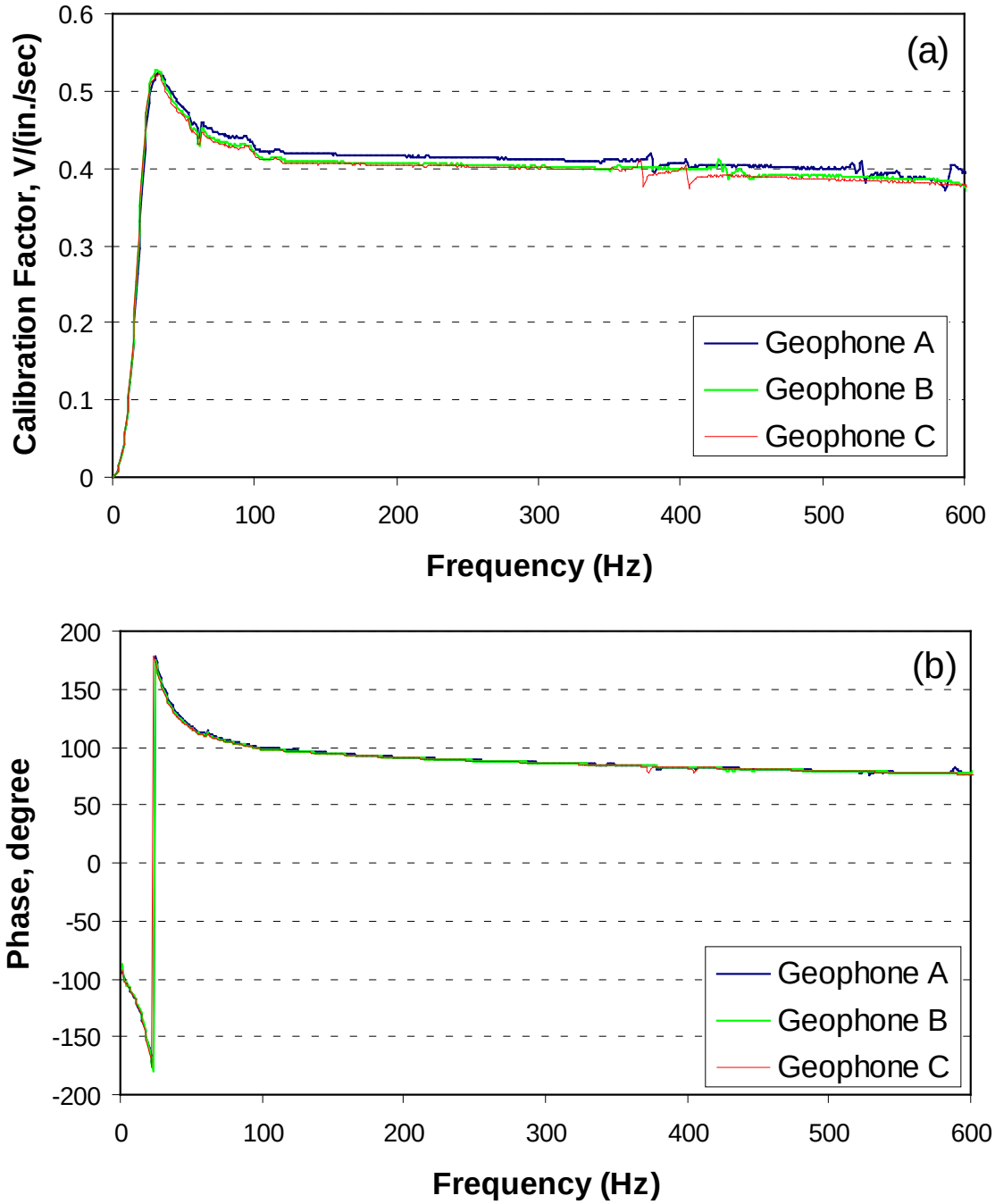

Figure 3.5. Calibration curves for three, 28-Hz geophones: (a) calibration response curve and (b) phase response curve

3.3.2 3-D sensor construction

Following calibration of the three, 1-D geophones described in Section 3.3.1, each 3-D sensor (12 total) was constructed by orienting three, 1-D geophones in three directions (one vertical; two horizontal). The 1-D geophones were mocked up in a standardized configuration inside the acrylic container box using super glue (Figure 3.6a). A two-part West Brand 105 Epoxy/205 Fast Hardener epoxy resin was then mixed per the manufacturer's guidelines at 5 Epoxy:1 Hardener and applied in the acrylic box in three lifts to limit the amount of heat applied to the geophones and the acrylic plastic housing. Following application of the epoxy resin, a 1/4-20 orientation nut was secured to the top of the sensor (Figure 3.6b) using two-part epoxy resin in order to mate with the geophone installation/orientation tool described in Chapter 5. Great care was taken to ensure that the unit weight of the 3-D sensor was close to the in-situ unit weight of the soil that it would displace. One complete 3-D sensor weighed 90 grams and had dimensions of 1.625 in. x 1.625 in. x 1.0 in. (4.1 cm x 4.1 cm x 2.5 cm). The unit weight of one 3-D sensor was then approximately 129 pcf (2066 kg/m^3), which was deemed acceptable for use in the experiment. Each 3-D sensor was tested for continuity and electrical resistance and judged ready for field installation.

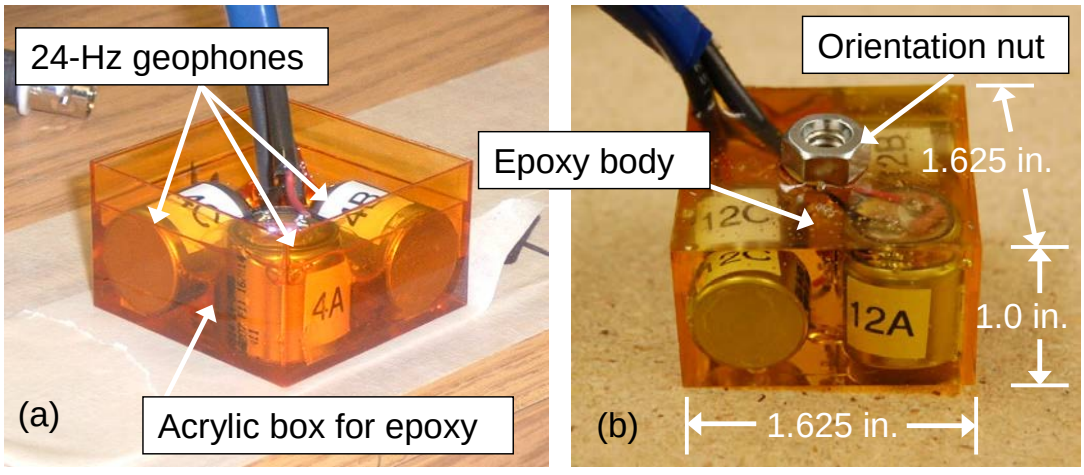

Figure 3.6. Construction of 3-D sensors: (a) Sensor 4 during construction and (b) Sensor 12 after placement of epoxy and orientation nut

3.4 LOAD CELLS

A strain-gauge-based load cell was used to measure static loads applied to the surface of a concrete footing. The load cell (Interface model 1032AF-50K-B) had a capacity of 50.0 kips (222 kN) and had been recently calibrated by the manufacturer for use in research projects. A 10-V DC power supply was used to provide power to the load cell. A photograph of the load cell is shown in Figure 3.7.

3.5 DYNAMIC SIGNAL ANALYZER

During dynamic testing, a central data acquisition system is required to control and monitor the testing process and to record the voltage outputs from the sensors. The data acquisition system used in the present research was similar to that employed by Park (2010) and Zalachoris (2010) and is shown in Figure 3.8. The dynamic signal analyzer is

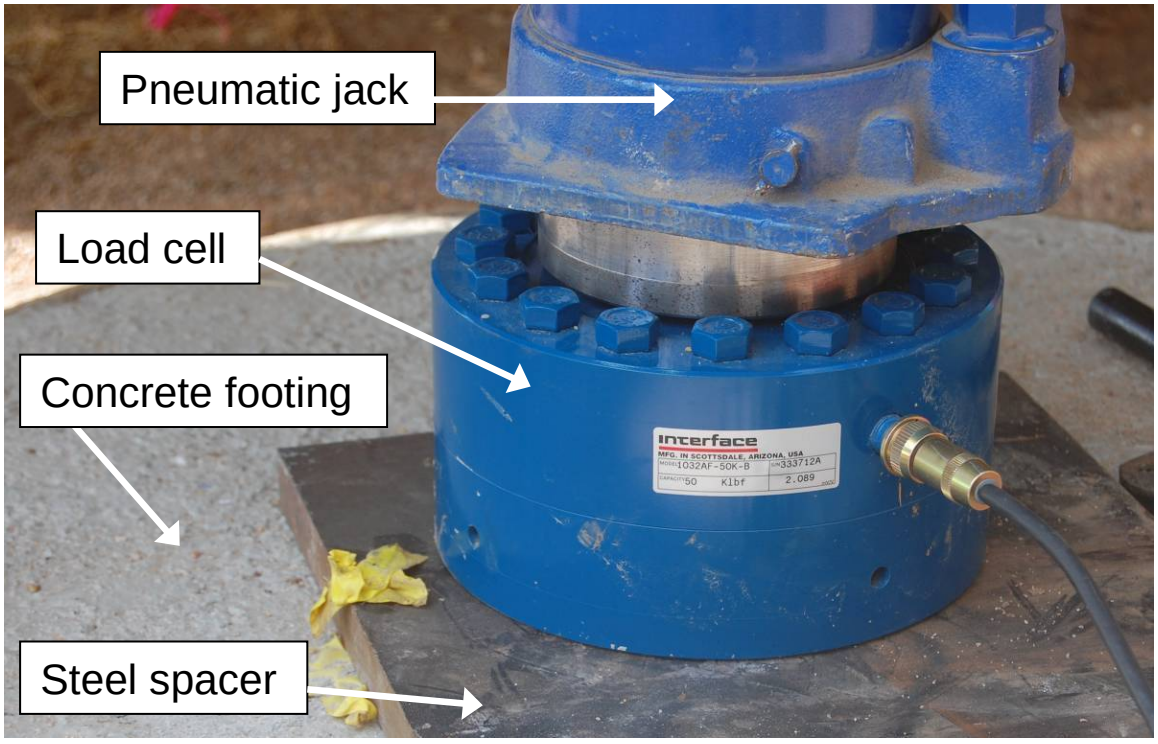

Figure 3.7. 50-kip (222 kN) load cell used in testing at Hornsby Bend, Austin, TX

primarily responsible for recording the output from the sensors. In this research, two different dynamic signal analyzers were employed: (1) a 32-channel analyzer (SignalCalc 730) used at Site One and (2) a 72-channel analyzer (VXI technology) used at Site Two. Both the 32- and 72-channel dynamic signal analyzers are capable of recording signals from all channels simultaneously at sampling rates of 102.4 kHz and 51.0 kHz, respectively, per channel. At both test sites, the frequency range of the recorded signals was 30 to 100 Hz for the steady-state excitation tests and approximately 200 to 500 Hz for the small-strain, transient, downhole and crosshole tests. These frequency ranges are well below the Nyquist frequencies (half the sampling frequencies) of the two analyzers. Therefore, according to the sampling theorem, the sampling frequencies of both dynamic signal analyzers are sufficient to allow the analyzers to properly resolve the recorded signals without any distortion.

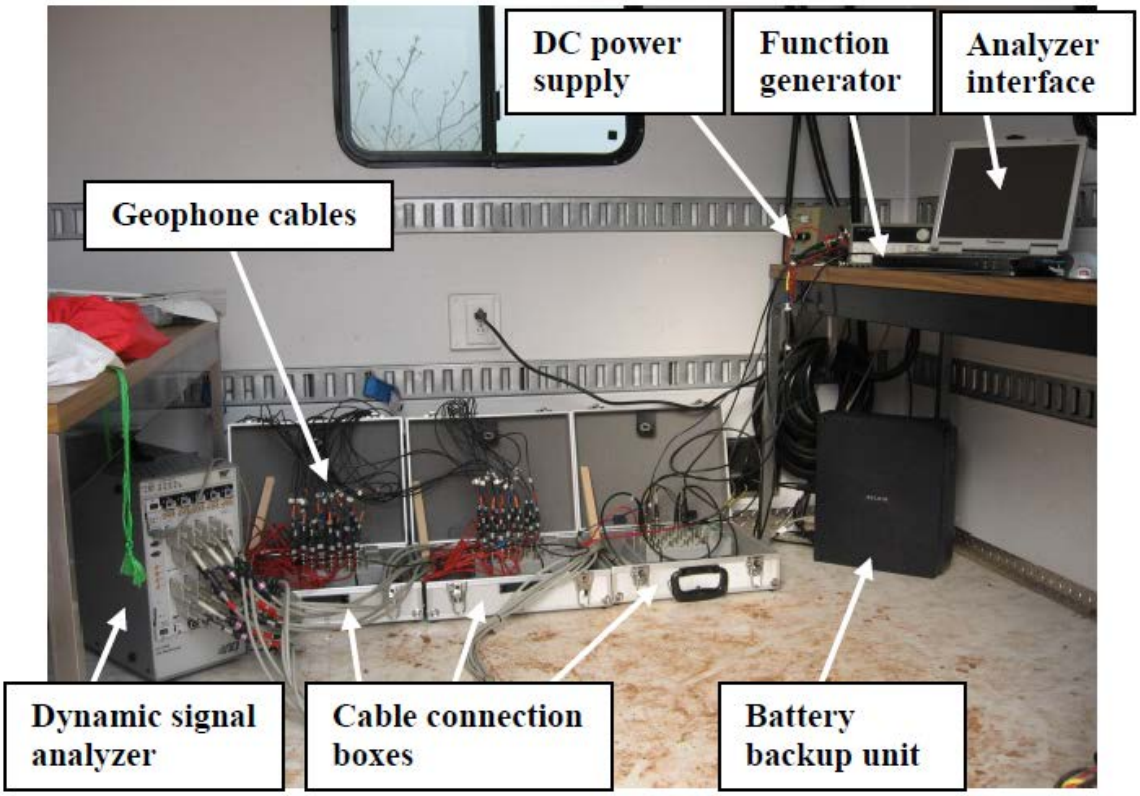

Figure 3.8. Data acquisition system used to measure linear and nonlinear dynamic soil moduli (from Park, 2010)

3.6 POWER SUPPLY AND FUNCTION GENERATOR

A DC power supply is required to operate the load cell described in Section 3.4. An Agilent E3620A regulated power supply was used to provide a voltage of 10 V to the load cell. A function generator (Agilent 33220A) was used to control the number of cycles, frequency, and amplitude of the generated sinusoidal waveforms. The function generator was connected to the control system of the hydraulic actuator of the vibroseis (Thumper or T-Rex). In this way, the vibration system of the vibroseis truck produced the steady-state excitation inputted by the function generator. In this research, the frequency range of the sinusoidal waveforms was 30 to 100 Hz, and 10 cycles were generated at each frequency. At each fixed selected frequency, the load amplitude was varied depending on the strain and load level being targeted. In general, steady-state excitation testing at each frequency progressed from small strains (low load amplitude) to large strains (high load amplitude). The power supply and function generator are shown in Figure 3.9.

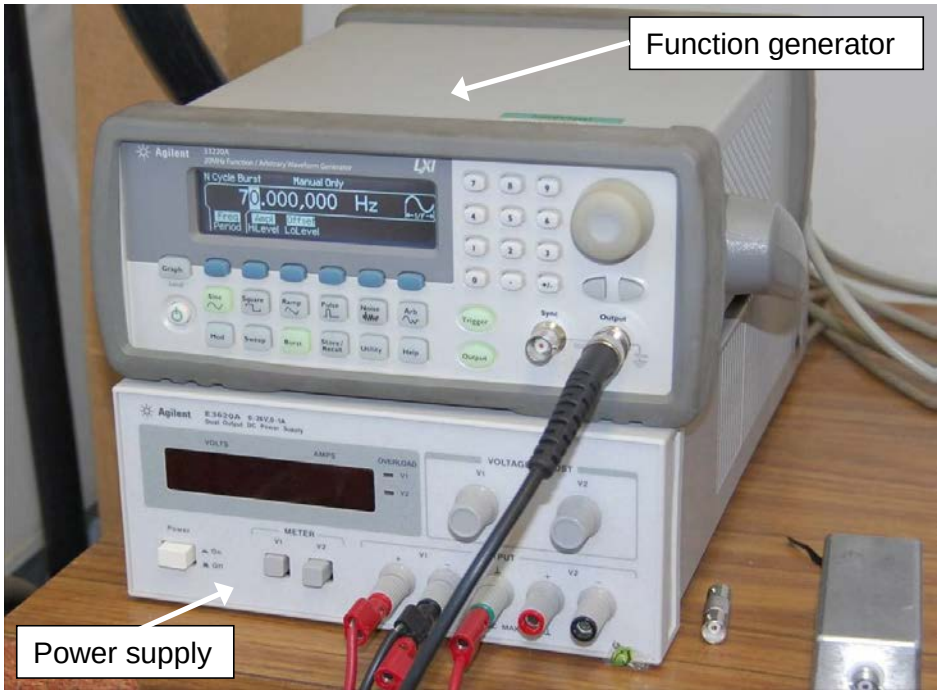

Figure 3.9. Power supply and function generator used at Hornsby Bend, Austin, TX

3.7 SUMMARY

The main components of the instrumentation used in the transient downhole and crosshole tests and the steady-state excitation tests are discussed in this chapter. Large mobile shakers (Thumper and T-Rex) provided by the nees@UTexas equipment site were used to apply both static loads and steady-state excitation to an embedded sensor array. Each 3-D sensor consisted of three, 1-D, 24-Hz geophones oriented in three triaxial directions (one vertical and two horizontal) and encased in an epoxy body with a unit weight approximately equal to that of the soil it displaced. A 50.0-kip (222 kN) load cell, powered by a 10-V DC power supply, was used to measure the static load applied to a concrete footing during the transient downhole and crosshole tests. A data acquisition system was used which consisted primarily of a dynamic signal analyzer and a function generator. The dynamic signal analyzer recorded the signals of all sensors simultaneously at a sampling frequency high enough to properly resolve the signal with no distortion. The function generator was connected to the mobile shakers and was used to generate the desired number of cycles, frequency, and amplitude of the sinusoidal waveforms imparted to the embedded sensor array by the mobile shakers during the steady-state excitation tests.

CHAPTER 4: EXAMPLES OF TEST DATA AND DATA REDUCTION

4.1 INTRODUCTION

The raw data collected in the in-situ linear and nonlinear tests consist of voltage-time histories for each 3-D geophone sensor described in Chapter 3 (see Figures 3.3 and 3.6). These voltage-time histories can then be converted into particle velocity-time histories using the appropriate calibration factor for the geophone which was determined as described in Chapter 3. In the case of the linear tests, i.e. small-strain, transient downhole and crosshole tests, the processed data are propagation velocities of the body waves under each static load level. With the load level and size of the loaded area known, the in-situ state of stress at each sensor location was calculated. Therefore, construction of log V_S – log σ_v and log V_P – log σ_v relationships is possible.

As in the linear tests, the nonlinear tests, i.e. large-strain sinusoidal excitation applied with the vibroseis, were performed at several different static load levels, i.e. states of stress. At each load level, the processed data are: (1) both axial and shear strains (depending on the direction of the applied excitation) and (2) propagation velocities of P_V and S_{VH} waves (again depending on the direction of the excitation). In this chapter, examples of the test data and the analysis procedures from the field linear and nonlinear tests are discussed.

4.2 RAW DATA

The raw data collected in the in-situ linear and nonlinear tests consist of voltage-time histories for each 3-D sensor. With the geophone calibration factor, these voltage-time histories are converted into particle velocity-time histories using the relation:

$$\dot{z}(t) = \frac{V(t)}{CF} \tag{4.1}$$

where $\dot{z}(t)$ is the particle velocity-time history (in units of distance/sec), *V(t)* is the voltage-time history of the geophone, and CF is the geophone calibration factor in units of volts/(distance/sec). In the determination of strain (whether axial or shear strain), this processing of raw data into something physically meaningful is essential, as the resulting strain depends on the velocity (and therefore, displacement) amplitudes of the sensors. However, processing of the raw data is not necessary to calculate the wave propagation velocities. All that is required in this case is the difference between the wave arrival times at two measuring sensors and the known distance between the sensors. This process is discussed in more detail in Sections 4.3 and 4.4 for the linear and nonlinear tests, respectively.

4.3 SMALL-STRAIN CROSSHOLE AND DOWNHOLE TESTS

Constrained compression and shear waves were measured in the small-strain range using transient crosshole and downhole tests. These tests were performed at several different static load levels both before and after large-strain dynamic tests (see Figure 5.6 and Figure 6.11). The purposes of these tests were: (1) to determine the variation of small-strain wave velocity with confining pressure, (2) to examine any changes in the soil skeleton after the large-strain dynamic tests, and (3) to confirm that the steady-state vertical excitation tests were measuring the constrained compression wave velocities (and not unconstrained or partially-constrained compression wave velocities) at small-strain levels.

Data collected from the in-situ small-strain seismic tests were reduced to obtain the small-strain wave velocities of horizontally-propagating constrained compression waves (P_H waves) and horizontally-propagating, vertically-polarized shear waves (S_{HV}

waves) in the crosshole tests and vertically-propagating constrained compression waves (P_V waves) and vertically-propagating, horizontally-polarized shear waves (S_{VH} waves) in the downhole tests. Coupled with an assumption of the induced stress distribution underneath the footing, the behavior of these wave velocities (V_{Ph}, V_{Shv}, V_{Pv}, and V_{Svh}) with increasing stress level can be determined. These data are presented in this section. Data analysis procedures from this testing at Site 2 (see Chapter 6) are presented as examples.

4.3.1 Shear and constrained compression wave velocities from crosshole tests

In the small-strain crosshole tests, both P_H and S_{HV} waves were generated simultaneously. As seen in Figure 4.1, all waves in the crosshole tests travel in the horizontal direction and were generated by applying a vertical impulse load to a steel rod driven to the same depth below the ground surface as the two embedded sensors. The vertical impulsive load was applied in the downward direction to create P_H and S_{HV} waves. To aid in determination of the S_{HV}-wave arrival time, the impulsive load was then applied in the upward direction to create S_{HV} waves with opposite polarity. Each created wave was monitored using the appropriate 1-D component of the 3-D sensors: the horizontal component oriented in the direction of wave propagation in the case of P_H waves and the vertical component in the case of S_{HV} waves.

Wave propagation velocities were then calculated from wave travel times between two sensors separated by the predetermined horizontal distance created during array construction (Δx in Figure 4.1b). In the present research, this horizontal spacing between sensors was between 9 and 15 in. (23 and 38 cm), which is generally small compared to traditional investigations. The travel times between sensors were determined using two methods: (1) first-arrivals of the waves and (2) cross-correlation of the two waveforms. Travel times determined by cross-correlation were particularly useful when the first arrivals of the waves were not clear and not easily identified "by eye." In some cases, the

(a)

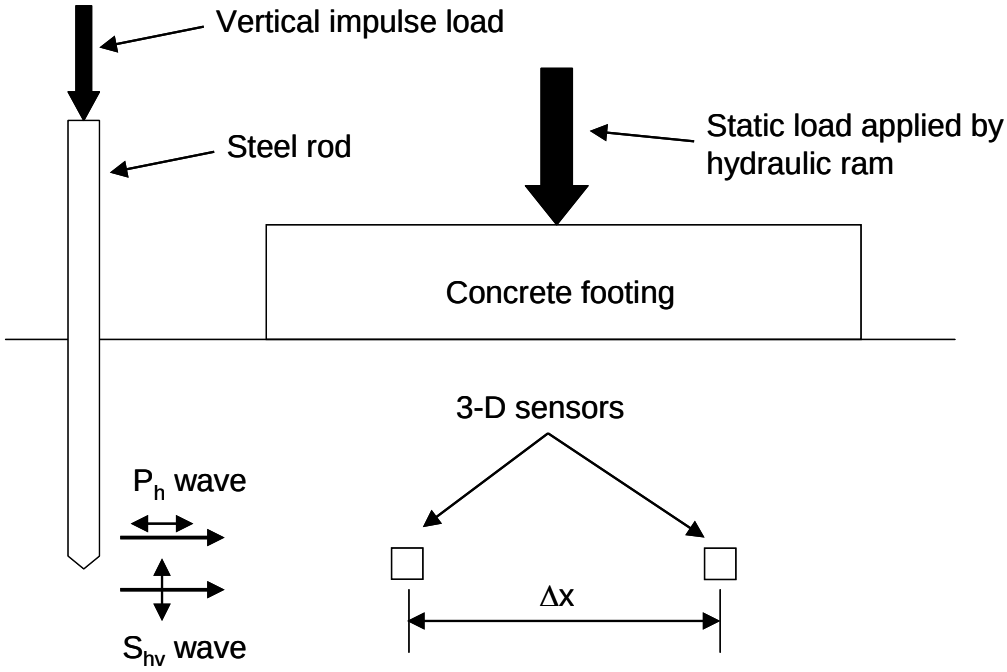

(b)

Figure 4.1. Crosshole testing: (a) Capt Allen Branco imparting a vertical impulse load to a steel rod and (b) an idealized schematic showing generation of crosshole body waves

travel time between sensors could not be determined using either first-arrivals or the cross-correlation sequence (the specifics of these cases are described in detail in Chapters 5 and 7 in the discussions of the results at Sites 1 and 2, respectively). The wave velocity was then determined using the travel time between the source rod and the first receiver, where the total travel time was reduced by the time required for the wave to travel from the point of the vertical impulse load to the tip of the rod.

Example P_H-wave voltage-time histories are shown in Figure 4.2 for two sensors at Site 2. The arrival times of the P_H waves are readily apparent in Figure 4.2b, and the resulting P_H-wave velocity (V_{Ph}) calculated using first-arrivals is shown as well. In Figure 4.3, the cross-correlation sequence between the same two sensors at Site 2 is shown, where negative time shift implies that the P_H wave arrives at the farthest sensor before the closest sensor (negative velocity), zero time shift implies that the P_H wave arrives at both sensors simultaneously (infinite velocity), and positive time shift implies that the P_H wave arrives at the closest sensor before the farthest sensor (positive velocity). The peaks in the cross-correlation sequence correspond to instances where a waveform similar to that recorded at the closest sensor (sensor 3B) also occurs at the farthest sensor (sensor 7B). Therefore, arrival of the wave at the farthest sensor was assumed to occur at the largest peak in the cross-correlation sequence that occurs after zero time shift, and the corresponding time shift at this peak was interpreted as the travel time between the two sensors. The V_{Ph} value calculated using cross-correlation is also shown in Figure 4.3. It is important to note that this velocity does not agree with the V_{Ph} calculated using first arrivals (shown in Figure 4.2) for this case. This difference is likely due to the irregular shape of the cross-correlation sequence (including the locations and amplitudes of the peaks) as is affected by the dissimilarity of the waveforms at the two sensors. As the shapes of the two waveforms become more similar to each other, the cross-correlation V_{Ph} becomes closer to the V_{Ph} calculated using first arrivals. And as seen in Figure 4.2, the shape of the waveform at Sensor 7B is quite different than that of the waveform at Sensor 3B for unknown reasons.

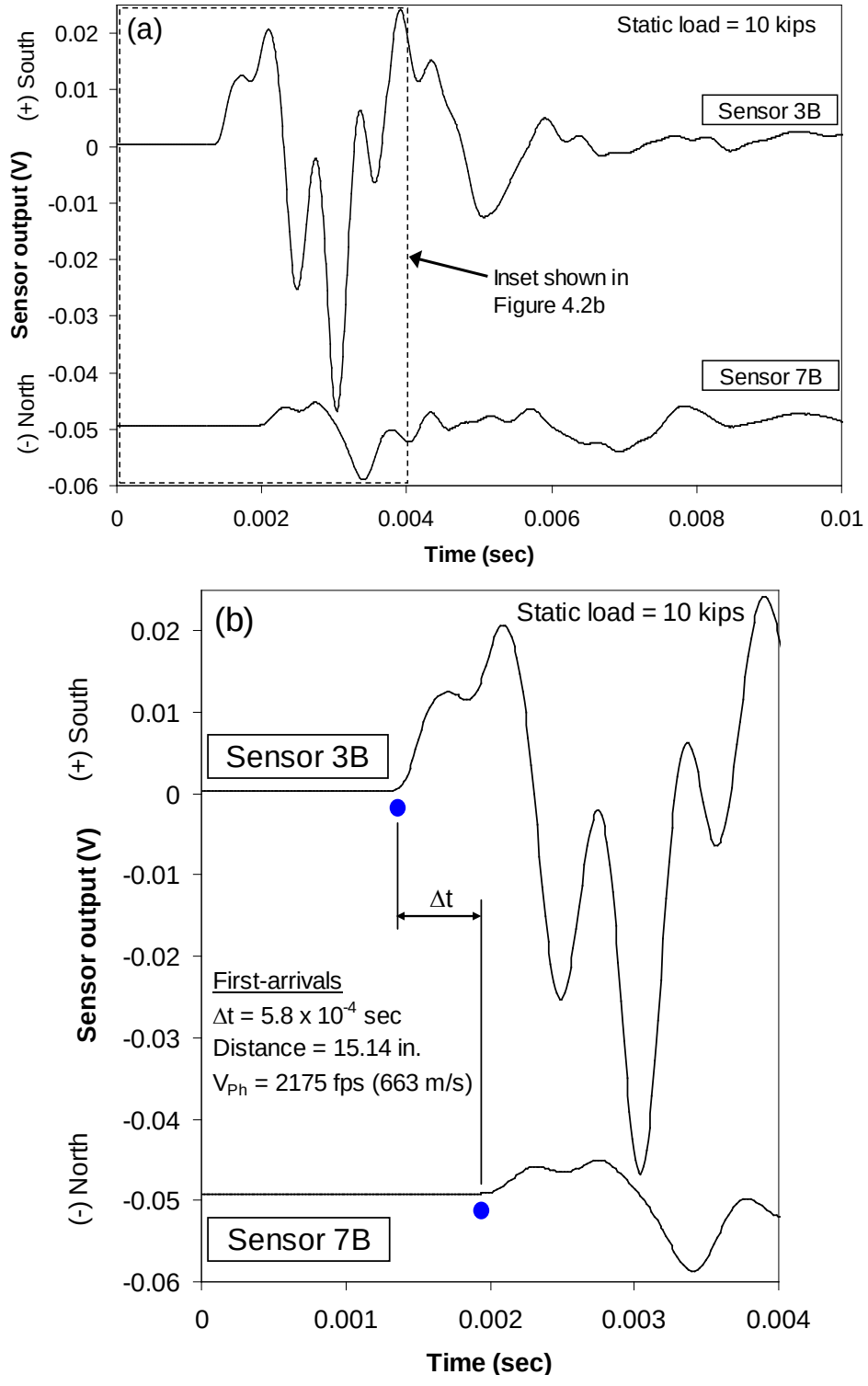

Figure 4.2. Determination of P_H-wave velocity using first-arrivals at each horizontal sensor: (a) entire time record and (b) selection of P_H-wave arrivals and calculation of V_{Ph}

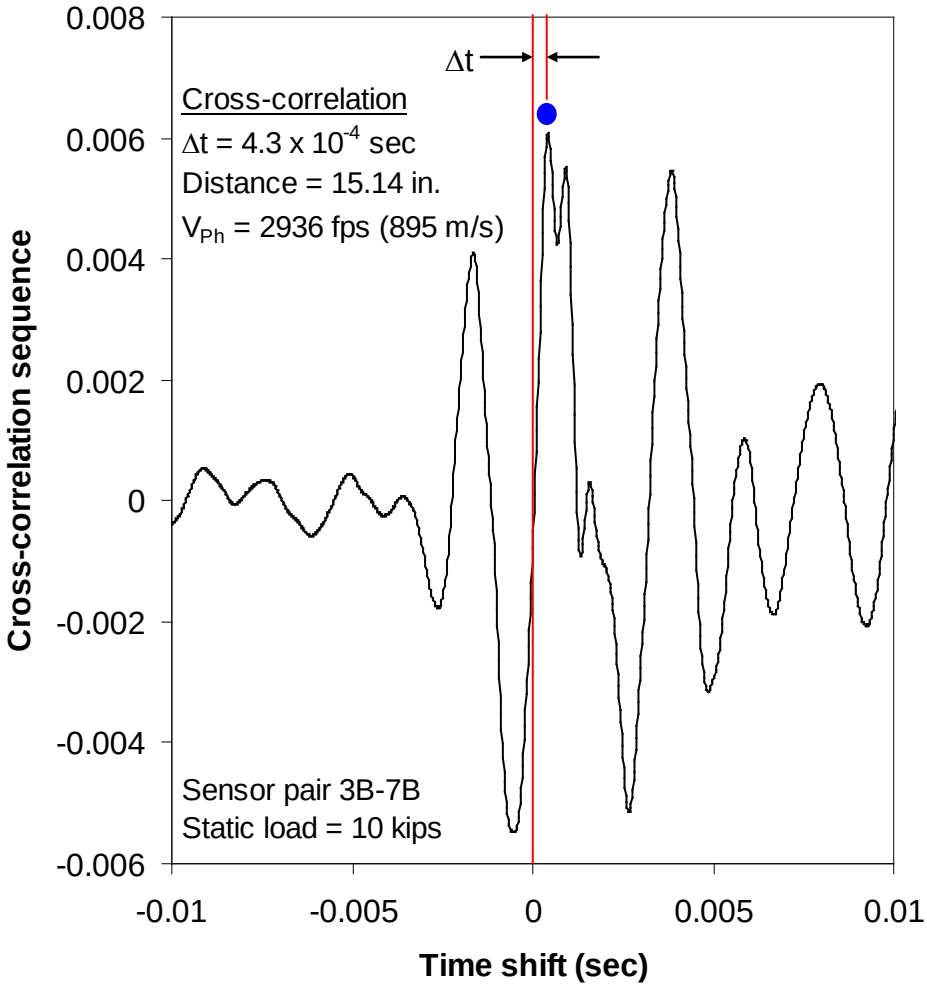

Figure 4.3. Determination of P_H-wave velocity using the time shift of the cross-correlation sequence

Example voltage-time histories of the S_{HV} wave are shown in Figure 4.4 for the same two, 3-D sensors (Sensors 3 and 7) at Site 2. However, the vertical component of these sensors is shown in Figure 4.4. The signals generated by both the upward and downward hammer strikes are shown, where the S_{HV}-wave arrival time at each sensor was taken as the average of the arrival times from the upward and downward hits. These S_{HV}-wave arrivals are shown in Figure 4.4 for both sensors, and the S_{HV}-wave velocity (V_{Shv}) calculated using first-arrivals is shown as well. The cross-correlation sequence

between the same two sensors is shown in Figure 4.5, where again the cross-correlation sequences were calculated for both the upward and downward hammer hits. The average time-shift is also shown in Figure 4.5, although it is worth noting that, in this example, the first peak of the cross-correlation sequence is basically the same regardless of whether the crosshole source rod was struck upward or downward. The V_{Shv} calculated using cross-correlation is in good agreement (~7%) with the V_{Shv} calculated using first arrivals. This agreement is much closer than the agreement shown in the V_{Ph} example discussed above. It should also be noted that the first peak of the S_{HV}-wave cross-correlation sequence is much more identifiable than that of the P_H-wave cross-correlation

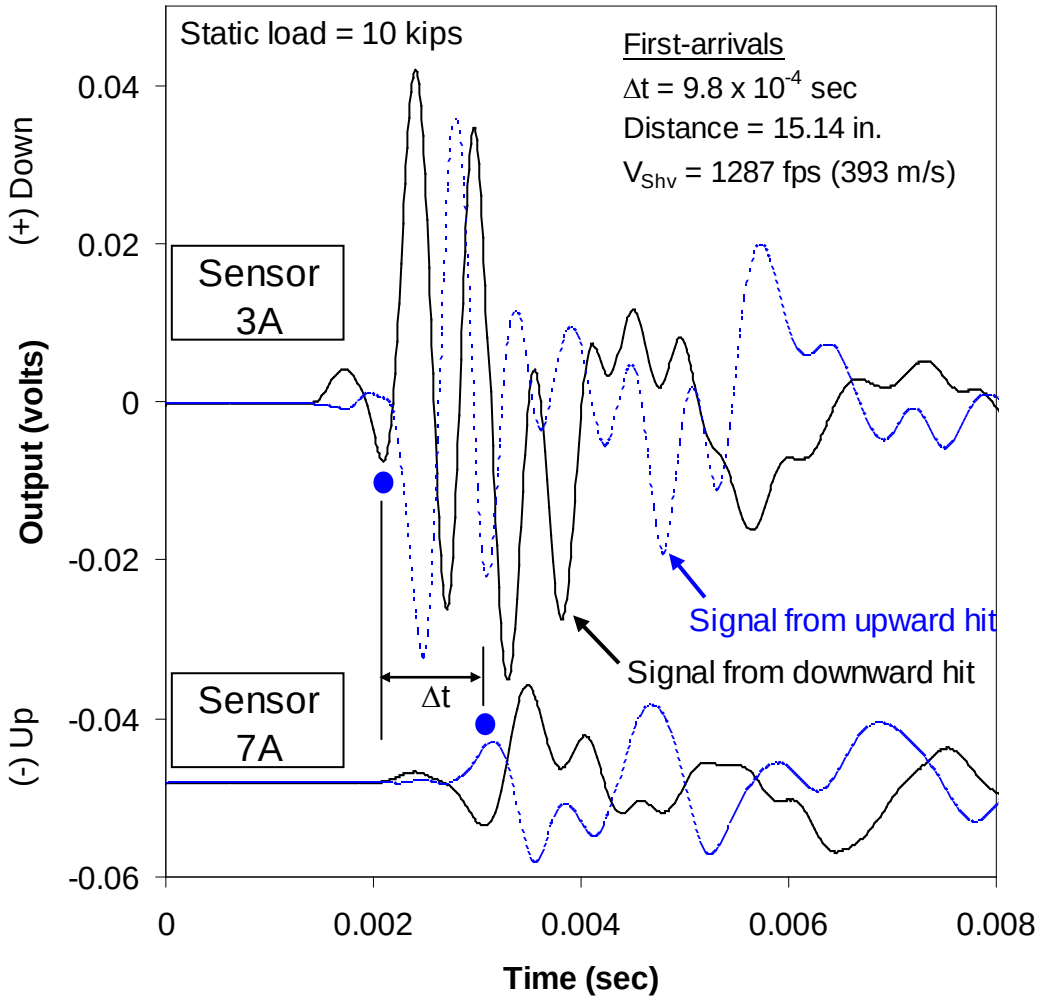

Figure 4.4. Determination of S_{HV}-wave velocity using first-arrivals at each sensor

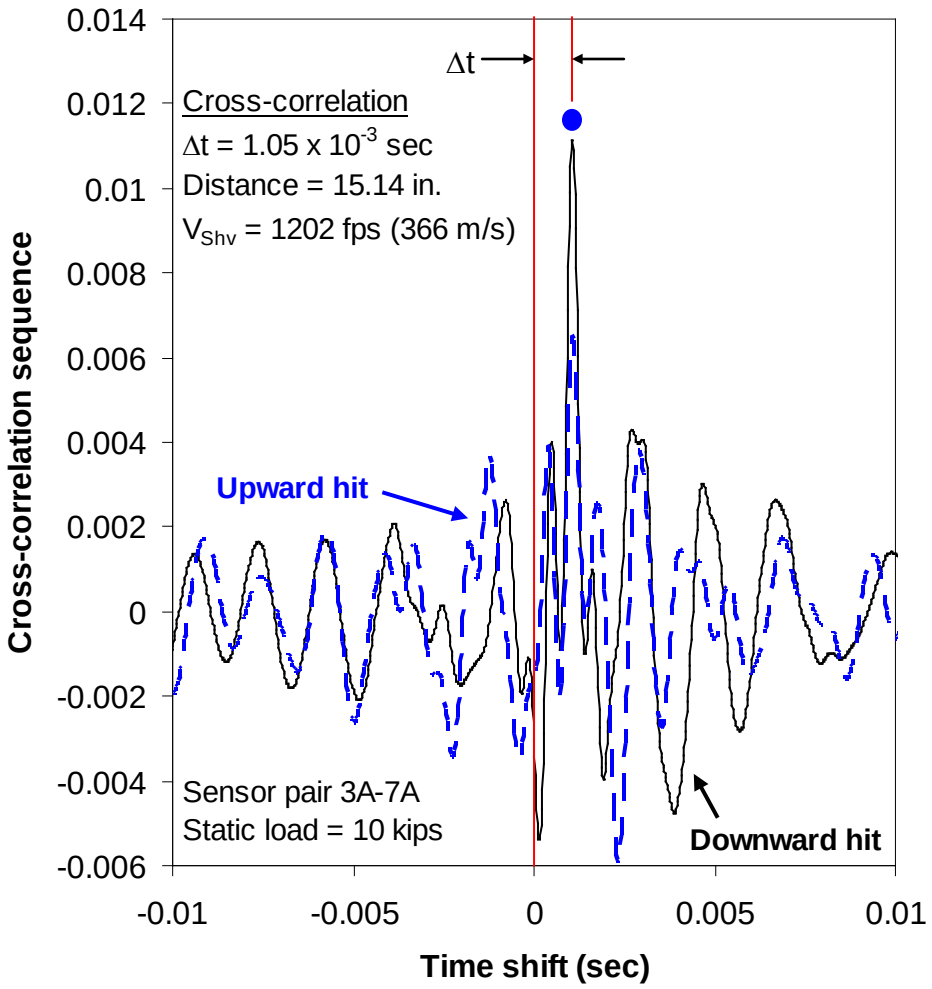

Figure 4.5. Determination of S_{HV}-wave velocity using the time shift of the cross-correlation sequence

sequence (Figure 4.3). Both of these observations (closer agreement between the S_{HV}-wave velocities and a stronger peak in the S_{HV}-wave cross-correlation sequence) are likely due to the fact that the S_{HV} waves at the two sensors are more similar to each other than are the P_H waves at the two sensors.

Though only one example is shown here, the observations noted above were generally true in almost every case during the small-strain crosshole testing. These comparisons proved beneficial in that the first arrivals of the S_{HV} waves were generally

more difficult to determine by eye than the first arrivals of the P_H waves. As a result, in most cases, the final wave velocities reported in this research and used in further analysis were the V_{Ph} determined using first-arrivals and the V_{Shv} determined using the time shift of the cross-correlation sequence. Any deviations from this convention are noted in Chapters 5 and 7.

4.3.2 Shear and constrained compression wave velocities from downhole tests

In the small-strain downhole tests, both P_V and S_{VH} waves were generated by striking the concrete footing with an instrumented hammer. As seen in Figure 4.6, all waves in the downhole tests travel predominantly in the vertical direction and were generated by striking the top of the footing (P_V waves) and the side of the footing (S_{VH} waves). The created wave was then monitored using the appropriate 1-D components of the 3-D sensors: the vertical components in the case of P_V waves and the horizontal components oriented in the direction of particle motion, i.e. the direction of the hammer strike, in the case of S_{VH} waves.

The analysis procedure used in the downhole tests is the same as described for the crosshole tests. The only difference is in the calculation of the sensor spacing. Unlike the crosshole tests, the impulse load from the hammer was not applied directly in line with the two receivers (sensors). The vertical impulse was offset slightly from the middle of the concrete footing due to obstruction by the static load apparatus (Figure 4.6a), and the horizontal impulse was applied to the edge of the footing (Figure 4.6b). As shown in Figure 4.6, the wave travels first through the concrete footing and then is refracted downward to each sensor. Therefore, the vertical spacing between sensors is not the true travel distance of the wave between the sensors. Referring to Figure 4.6, the true travel distance between sensors is the difference in the wave paths ($d_B - d_A$), not the difference in the depths of the sensors ($z_B - z_A$). These wave path distances were calculated using the refraction techniques described by Richart et al. (1970). It should be noted that the

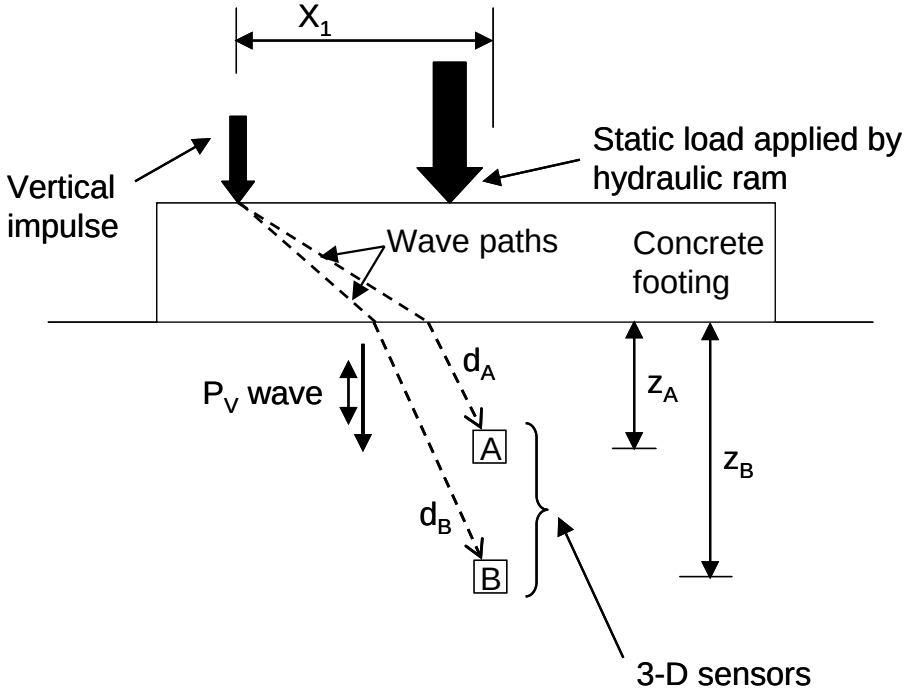

(a)

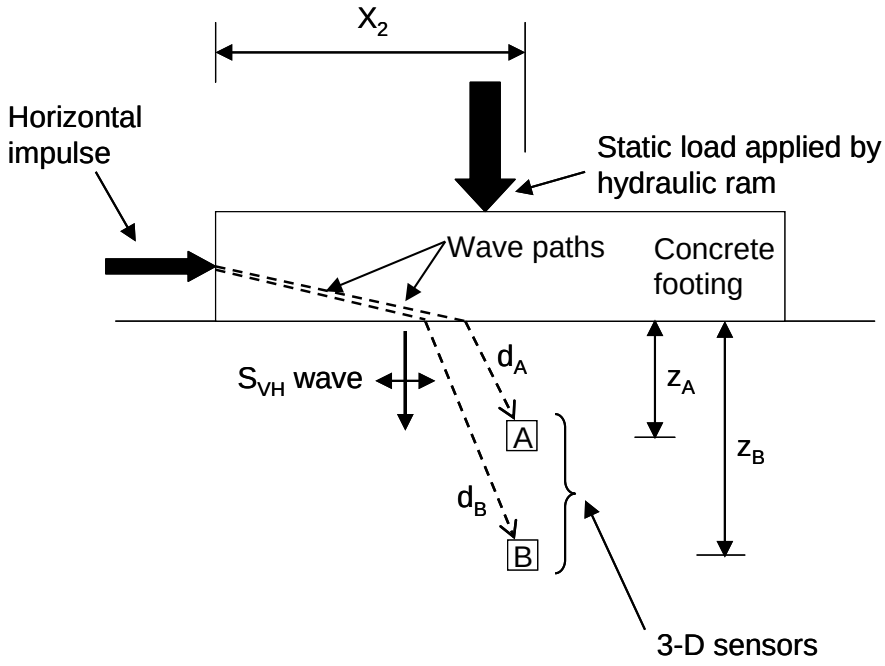

(b)

Figure 4.6. Idealized schematic showing generation of downhole body waves: (a) P_V waves and (b) S_{VH} waves

refraction correction is relatively minor when the horizontal distance (X_1 or X_2) between the impulse and the sensors is small. However, the refraction correction at Site 2 made a significant difference on the spacing between sensors in the column furthest away from the impulse (note that X_1 ranged from 4.8 to 14.6 in. (12.2 to 37.1 cm), and X_2 ranged from 11.2 to 26.2 in. (28.4 to 66.5 cm) at Site 2). In the most extreme case, while the vertical spacing between sensors was 12 in., the true travel distance between sensors after correcting for refraction was as low as roughly 11.1 in.

Example P_V-wave voltage-time histories are shown in Figure 4.7 for two sensors at Site 2. The arrival times of the P_V waves are readily apparent in each sensor output. The P_V-wave velocity (V_{Pv}) calculated using first-arrivals is also shown in Figure 4.7. The cross-correlation sequence between the same two sensors is shown in Figure 4.8. In this case, the V_{Pv} calculated using the time-shift of the cross-correlation sequence is roughly half of the V_{Pv} calculated using first-arrivals. The poor agreement between the V_{Pv} calculated using these two methods (cross-correlation and first-arrivals) is similar to that noted in the calculation of V_{Ph} in the crosshole tests described in Section 4.3.1. As in the crosshole tests, the shapes of the P_V waveforms at the two sensors are likely too different to make effective use of the cross-correlation sequence (see Figure 4.7a).

Example S_{VH}-wave voltage-time histories are shown in Figure 4.9 for the horizontal components of the same two sensors (sensors 3 and 2) at Site 2. The S_{VH}-wave arrivals are shown in Figure 4.9 for both sensors. The S_{VH}-wave velocity (V_{Svh}) calculated using first-arrivals is also shown in Figure 4.9. The cross-correlation sequence between these sensors is shown in Figure 4.10. The V_{Svh} calculated using cross-correlation is in extremely close agreement (~3%) with the V_{Svh} calculated using first arrivals. This agreement is much closer than the agreement between V_{Pv} as discussed above.

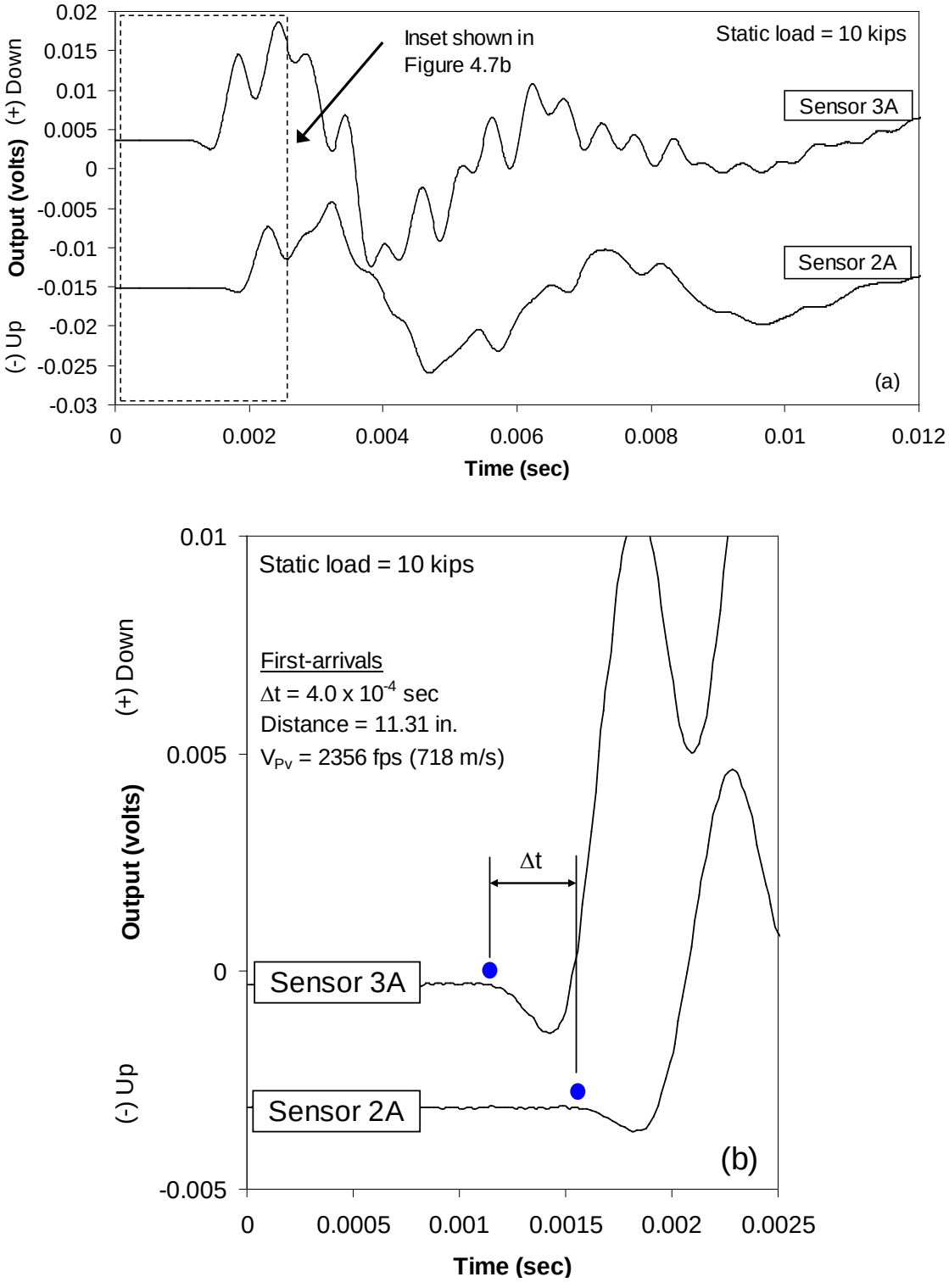

Figure 4.7. Determination of P_V-wave velocity using first-arrivals at each vertical sensor: (a) entire time record and (b) selection of P_V-wave arrivals and calculation of V_{Pv}

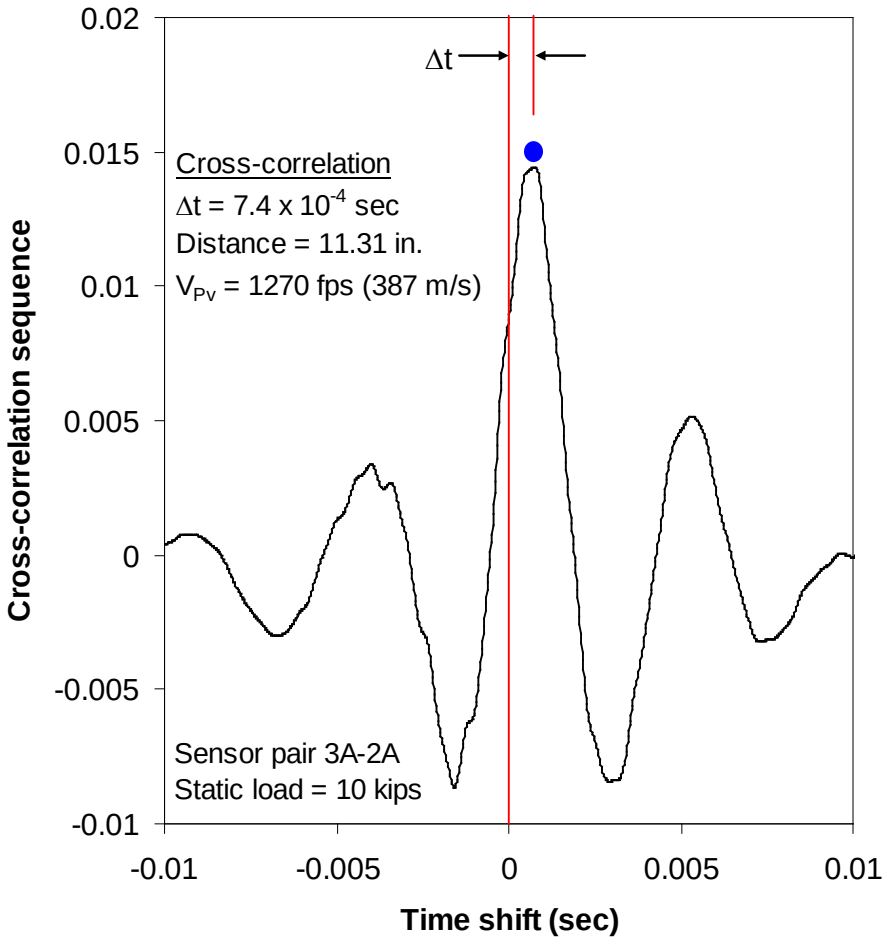

Figure 4.8. Determination of P_V-wave velocity using the time shift of the cross-correlation sequence

Though only one example is shown here, the observations noted above were generally true in almost every case during the small-strain downhole testing. Since the first arrivals of the P_V-wave were generally easily identifiable, the P_V-wave velocity calculated using first-arrivals was used at all sensor pairs in the downhole tests. However, the first arrivals of the S_{VH} waves were generally more difficult to determine by eye than the first arrivals of the P_V waves. As a result, the final S_{VH}-wave velocities reported in this research and used in further analysis were the V_{Svh} determined using the time-shift of the cross-correlation sequence. Any deviations from this convention are noted in Chapters 5 and 7.

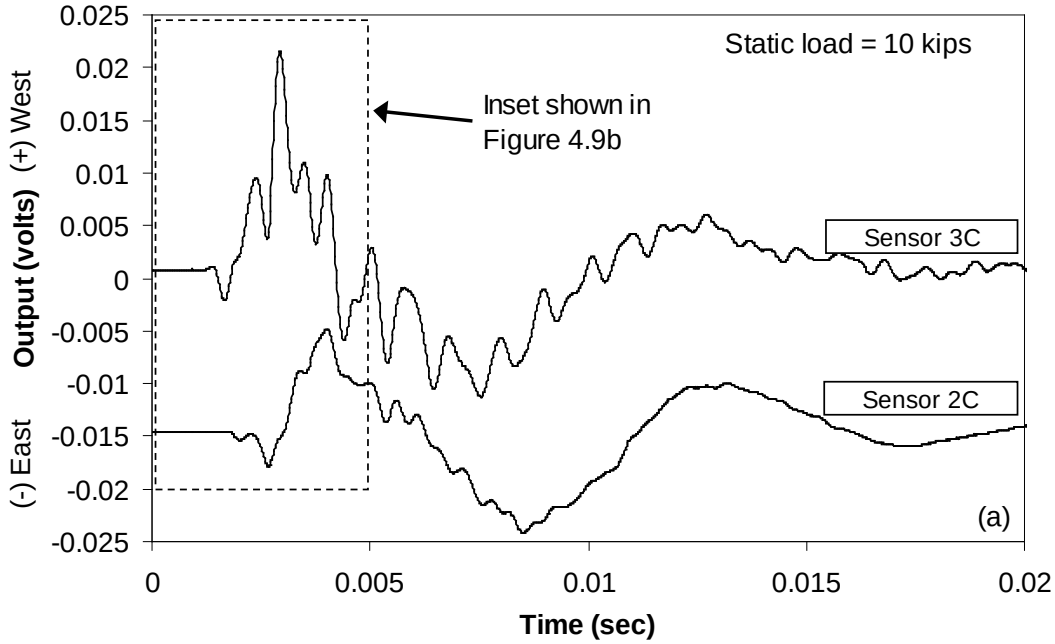

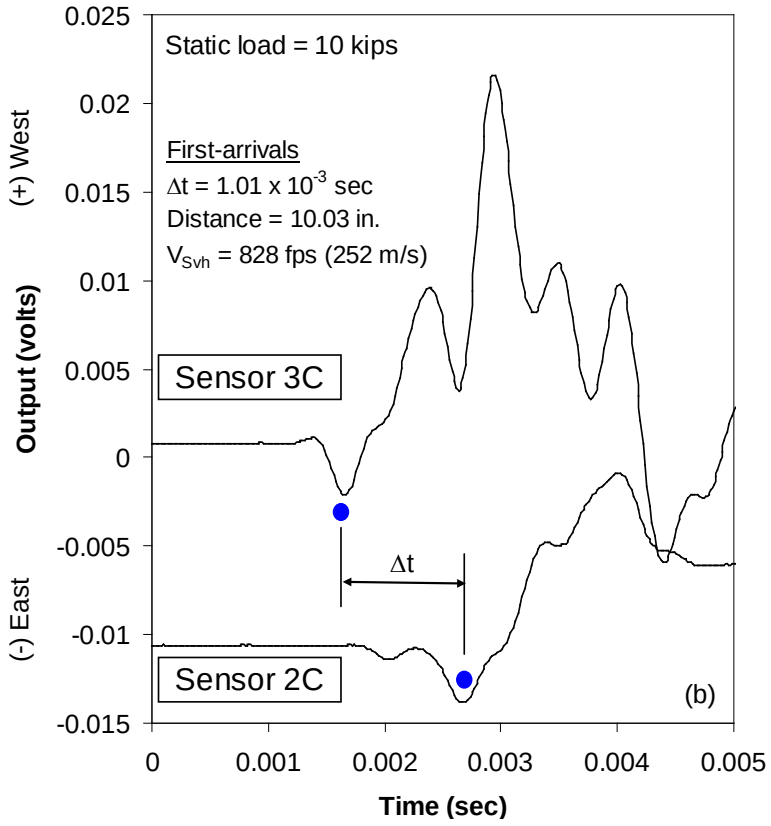

Figure 4.9. Determination of S_{VH}-wave velocity using first-arrivals at each sensor: (a) entire time record and (b) selection of S_{VH}-wave arrivals and calculation of V_{Svh}

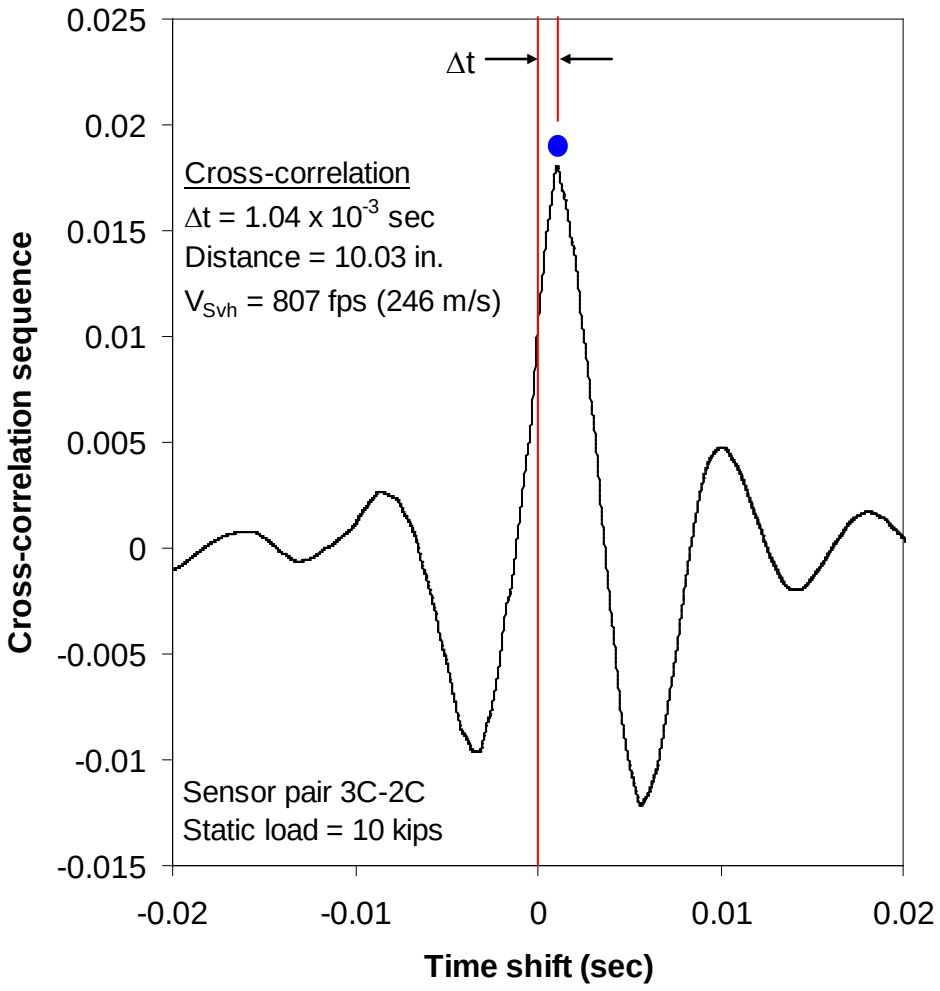

Figure 4.10. Determination of S_{VH}-wave velocity using the time shift of the cross-correlation sequence

4.3.3 Estimation of in-situ states of stress under the imposed static loads

The total vertical stress beneath the concrete footing in the crosshole and downhole tests was calculated in the following two steps: (1) determination of the initial overburden stress due to the total weight of the soil and (2) estimation of the change in total stress beneath the footing imposed by the additional static load (including the weight of the footing). These two stresses were combined together to represent the final total vertical stress distribution beneath the concrete footing due to a given static load level.

The change in total stress due to an applied load was estimated by: (1) using a Boussinesq distribution, (2) assuming a uniform stress is applied to the soil, and (3) assuming the soil to be homogeneous, isotropic, semi-infinite, and elastic (Coduto 1999). As an example, the estimated change in the total stress due to a 10 kip (44.5 kN) static load applied to a 3-ft (0.9-m) diameter footing is shown in Figure 4.11 for the sensor array at Site 2 (note that this array is axisymmetric as described in Chapter 6). When the induced stress shown in Figure 4.11 is combined with the initial overburden stress, the final total stress distribution due to a 10 kip (44.5 kN) static load applied to a 3-ft (0.9-m) diameter footing can be obtained as shown in Figure 4.12.

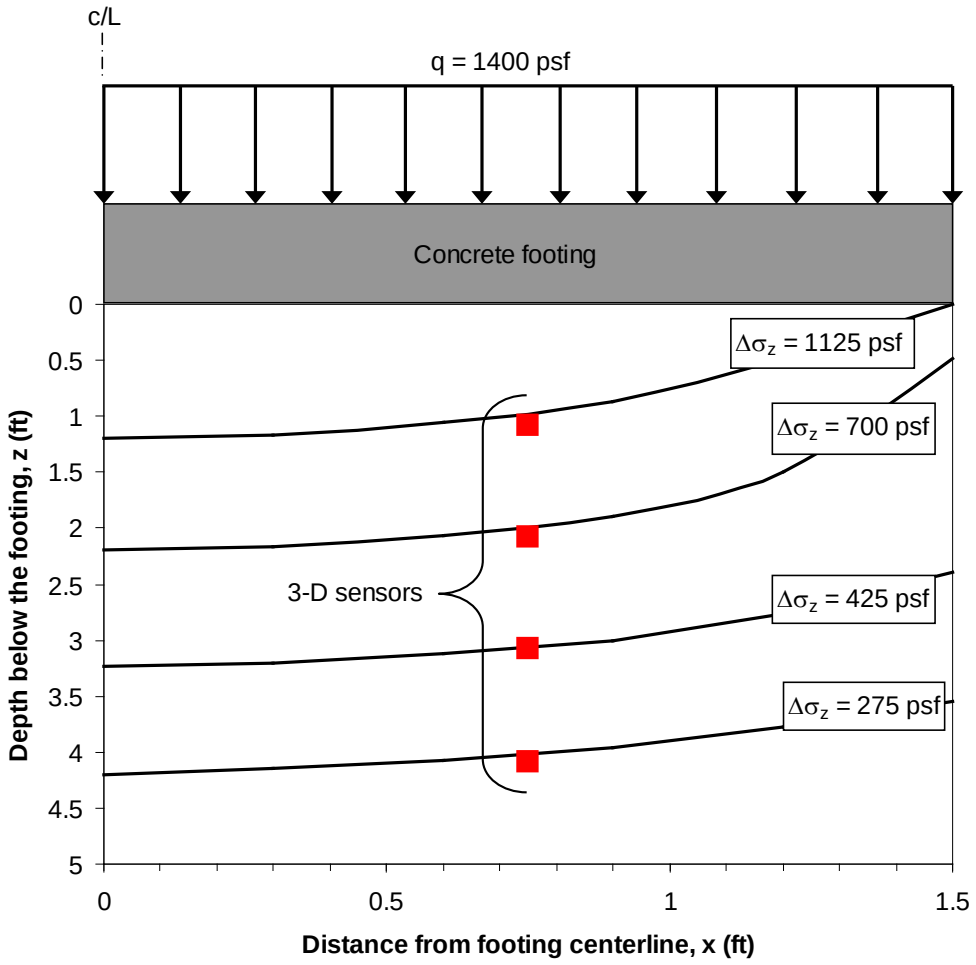

Figure 4.11. Estimated change in total vertical stress induced by a 10-kip (44.5-kN) static load applied to a 3-ft (0.9-m) diameter, concrete footing at Site 2

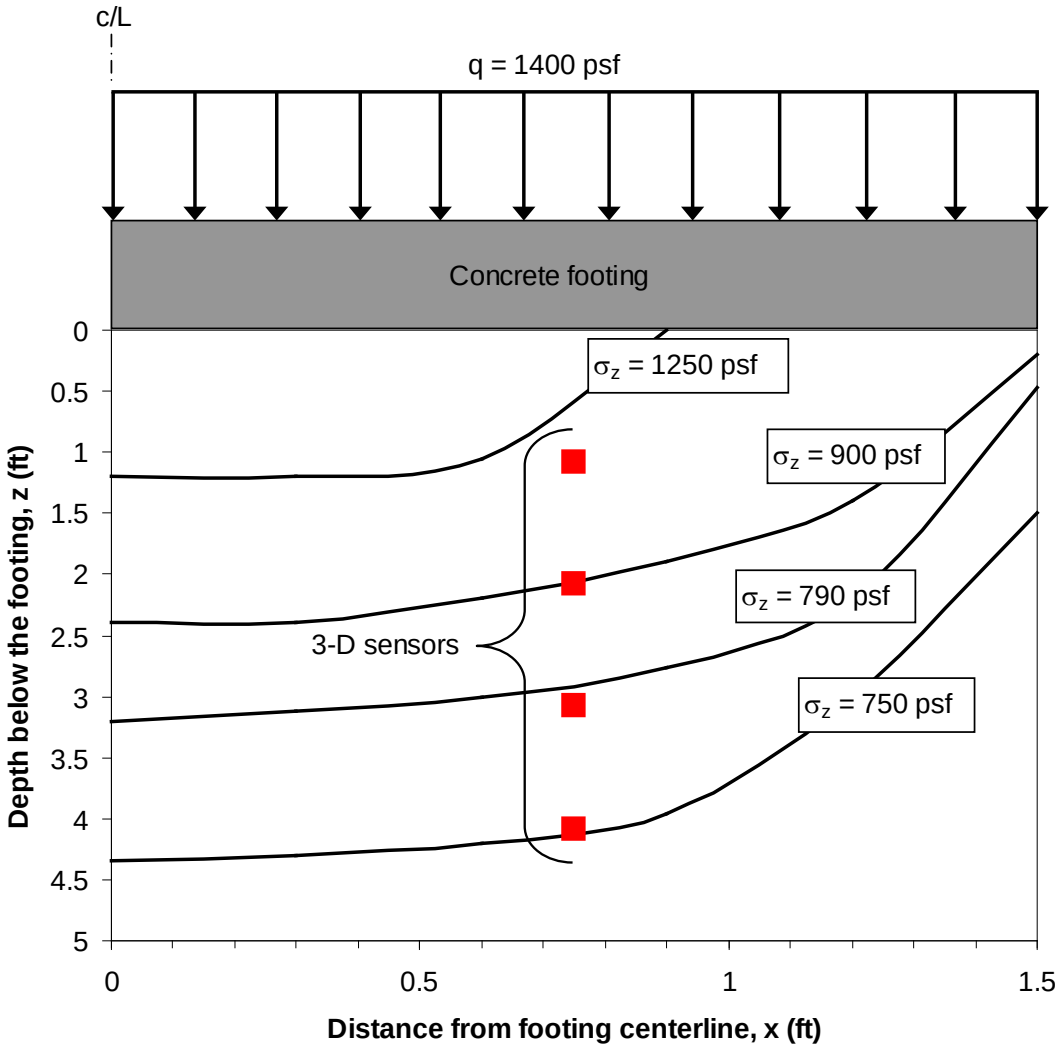

Figure 4.12. Estimated final total vertical stress distribution at Site 2 under a 10-kip (44.5-kN) static load applied to a 3-ft (0.9-m) diameter, concrete footing

It is important to note that the actual state of stress in the field beneath a circular footing is quite complex, and the process described above allows only an approximation of this stress distribution to be estimated. The actual soil at the test sites used in this research is neither homogeneous nor isotropic, but instead shows evidence of at least a moderate degree of overconsolidation. Additionally, there are likely significant negative pore pressures near the ground surface due to an extensive drought in this part of Texas. These large negative pore pressures call into question the validity of a total stress

approach, and attempts were made at Site 2 to estimate the effective stress distribution in the field. The estimation of effective stress at Site 2 is discussed in Chapter 6.

4.4 LINEAR AND NONLINEAR STEADY-STATE EXCITATION TESTS

Linear and nonlinear testing over a wide range in strains was performed in which vertical and horizontal sinusoidal excitations were applied by both Thumper and T-Rex. These tests were performed in a similar manner as those described by Axtell et al. (2002), Stokoe et al. (2006), and Park (2010). Detailed explanations of the test procedure are described in Sections 5.3 and 6.3 for Sites 1 and 2, respectively. In this section, the analysis procedures used to obtain the constrained and shear moduli (M and G, respectively) and to estimate the axial and shear strains (ε and γ, respectively) are discussed. Finally, the data from two levels of vertical excitation are reduced for a given sensor pair as an example of the analysis procedures used to determine the in-situ behavior of constrained modulus (e.g. M – log ε and M/M_{max} – log ε).

4.4.1 Constrained and shear modulus evaluations

The sensor arrays at the two sites were subjected to 10 cycles of sinusoidal excitation (either vertical or horizontal) from the vibroseises. Vertical excitation produced P_V waves, and horizontal excitation produced S_{VH} waves. In either case, there was an observed transient portion in the signals recorded by each 3-D receiver. This transient portion occurred during the initial "ramp-up" of the vibroseis to the desired load amplitude and generally lasted about four cycles. There was also a transient portion after the shaker was turned off which lasted about two cycles. After about five cycles, the signal amplitude was generally stable, and this portion of the response was assumed to represent steady-state conditions. A best-fit sinusoidal curve was fitted to cycles 7, 8, and 9 of the raw signals as shown in Figure 4.13, and the time between peaks occurring at adjacent sensors was used to determine the travel time of the wave between sensors. The

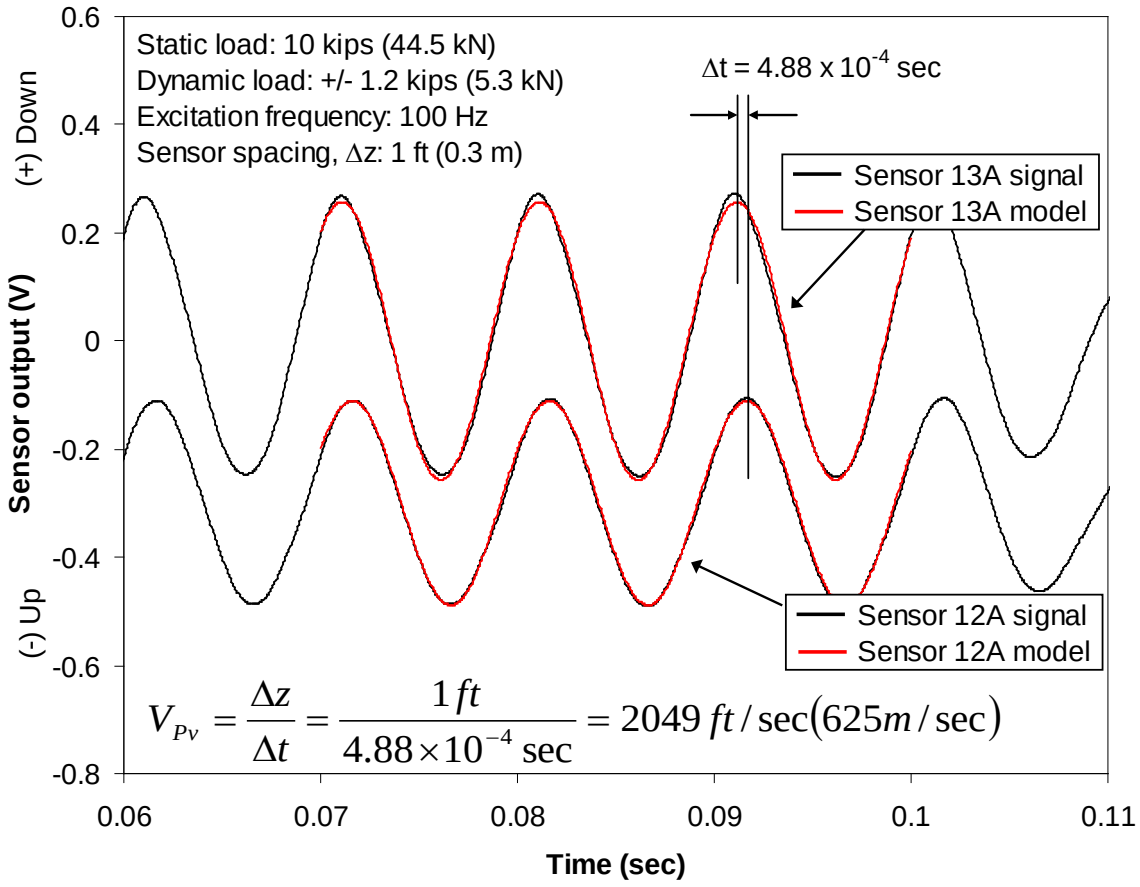

Figure 4.13. Determination of P_V-wave velocity using peak-to-peak travel times between two sensors at Site 2 when subjected to a steady-state vertical excitation

vertical spacing between sensors was divided by this travel time to obtain the wave velocity. Note that while the process shown in Figure 4.13 is for determination of the P_V-wave velocity under steady-state vertical excitation, the analysis procedure is the same for S_{VH} waves generated by steady-state horizontal excitation.

As in the small-strain crosshole and downhole tests described in Section 4.3, the wave velocity was also calculated using the time-shift of the cross-correlation sequence as shown in Figure 4.14. Note that in this example, the V_{Pv} in Figures 4.13 and 4.14 are identical. However, in some instances when the induced strains became large, the waveforms recorded by the vertical sensors were asymmetric, and a satisfactory

sinusoidal model could not be fit to the waveforms as described in the previous paragraph. An example of this case is shown in Figure 4.15. For these instances where a sinusoidal model could not satisfactorily be fit to the recorded waveform, determination of the P_V-wave velocity using the cross-correlation sequence was the preferred method. The S_{VH} waveforms from horizontal excitations at Site 2 were not asymmetric at large strains, and a satisfactory fit with a sinusoidal model was obtained in almost every case. More details concerning the shapes of the waveforms at large strains and the use of the cross-correlation sequence to compute the wave velocities are given in Chapters 5 and 8.

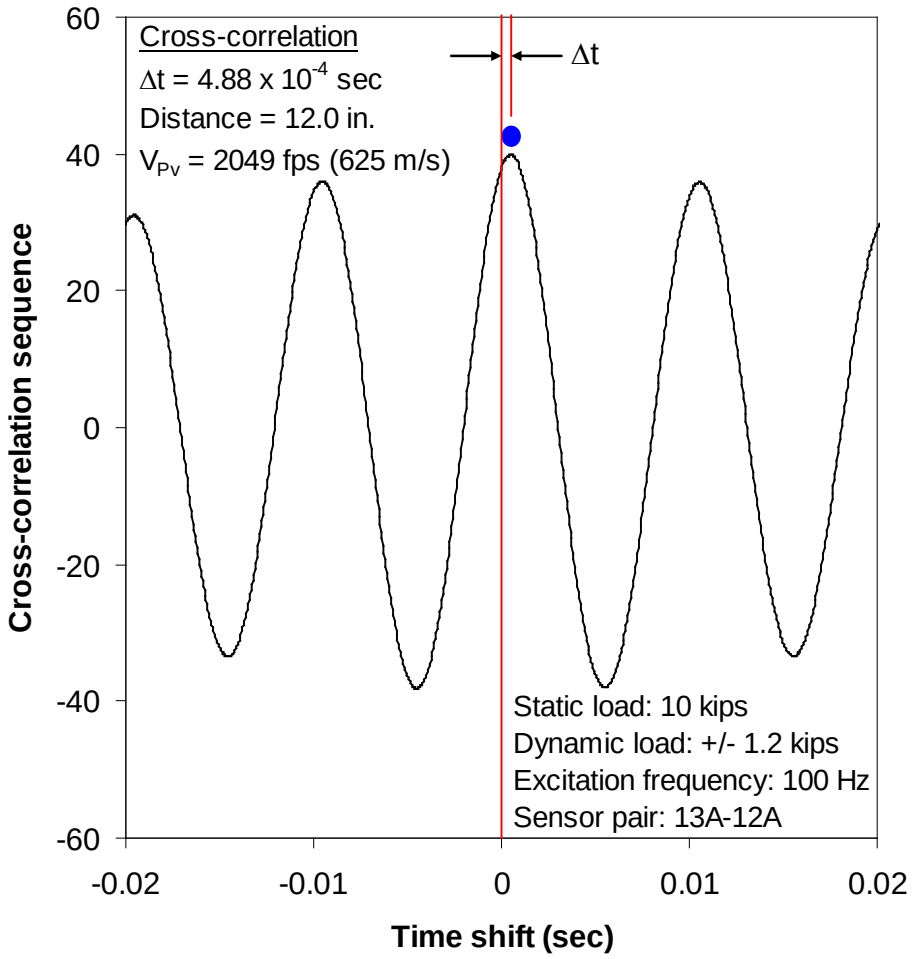

Figure 4.14. Determination of P_V-wave velocity using the time-shift of the cross-correlation sequence between two sensors at Site 2 when subjected to a steady-state vertical excitation

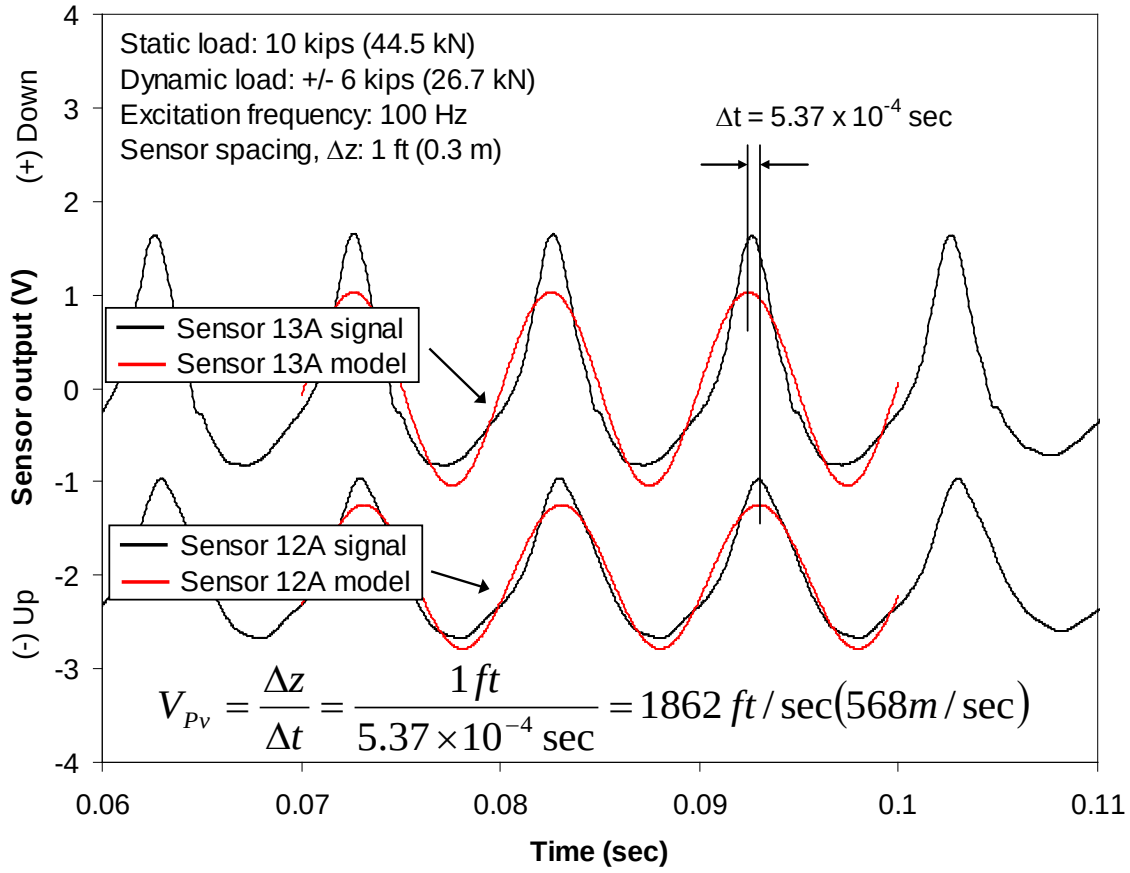

Figure 4.15. Example of a case where the accuracy of computing the P_V-wave velocity using peak-to-peak travel times is questionable due to the poor fit of the sinusoidal model to the recorded waveform

After the wave velocities were calculated as described above, the constrained and shear moduli (M and G, respectively) were determined using the relations:

$$M = \rho V_{Pv}^{\ 2} \tag{4.2a}$$

$$G = \rho V_{Svh}^{\ 2} \tag{4.2b}$$

where ρ is the total density of the soil (Richart et al., 1970). In this manner, the dynamic moduli of the soil were determined for each level of sinusoidal excitation applied by the

vibroseis. For a given level of sinusoidal excitation, these moduli were combined with the induced strain (determined as described in the following section) to obtain one point on either the M – log ε or G – log γ curve. The process was repeated for all levels of excitation to construct the entire M – log ε and G – log γ curves.

4.4.2 Axial and shear strain evaluations

The strain between sensors was determined using a two-node displacement-based (DB) method developed by Rathje et al. (2004), where the sensors are the nodes and strain is assumed to vary linearly between sensors. The calculation of axial and shear strain using the 2-node DB method is shown graphically in Figure 4.16a and 4.16b, respectively.

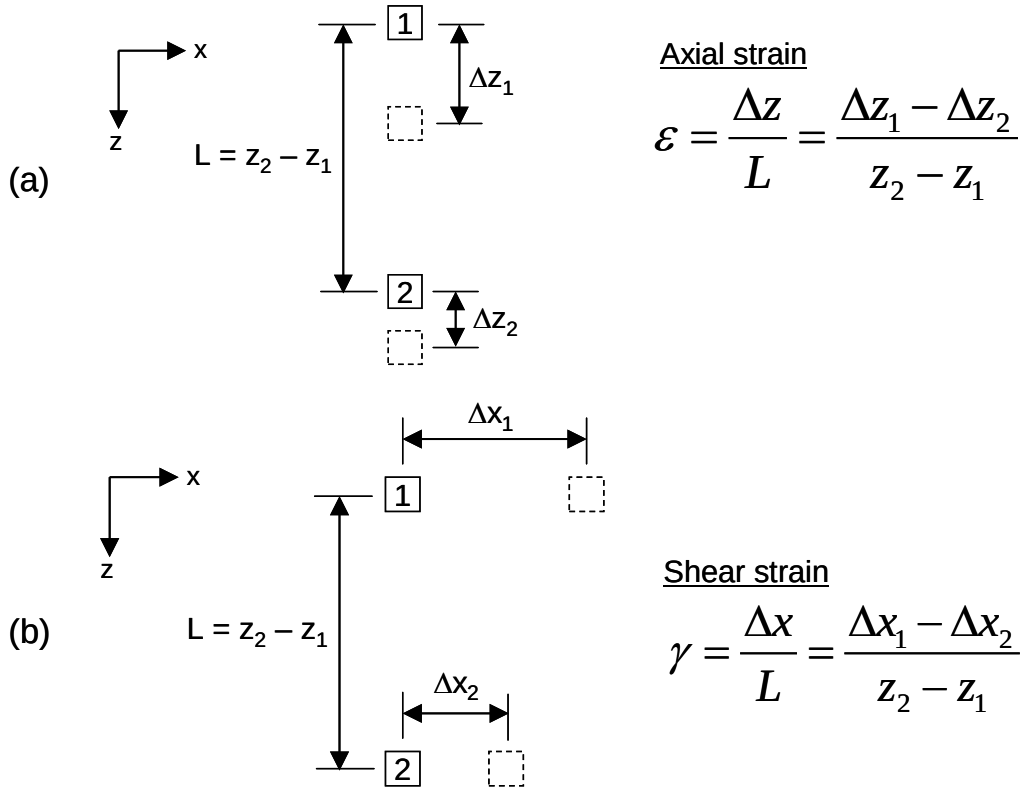

Figure 4.16. Graphical representation of 2-node displacement-based method for calculating: (a) axial strain and (b) shear strain

To calculate the strains as shown in Figure 4.16, it is critical that the displacements of the sensors be known for the same moment in time. As mentioned in Section 4.2, this determination requires processing the voltage output of the sensors into meaningful engineering units. To do so, the voltage-time histories recorded by the sensors were converted into velocity-time histories using Equation 4.1. Then, the displacement-time histories were obtained using the trapezoid rule to numerically integrate the velocity-time histories once. When performing the numerical integration, the baseline of the velocity-time history was corrected to remove drift in the integrated signal (displacement-time history in this case). This process is shown in Figure 4.17 for two axial sensors at Site 2. Using the displacement-time histories of the two sensors, a strain-time history can be constructed by calculating the strain (either axial or shear) between the two sensors at every moment in time (t) using the relations:

$$\varepsilon(t) = \frac{z_1(t) - z_2(t)}{L} \tag{4.3a}$$

$$\gamma(t) = \frac{x_1(t) - x_2(t)}{L} \tag{4.3b}$$

where $z_1(t)$ and $z_2(t)$ are the vertical displacement-time histories of the first and second sensors, respectively, $x_1(t)$ and $x_2(t)$ are the horizontal displacement-time histories of the first and second sensors, respectively, and L is the vertical spacing between the two sensors. The axial strain-time history computed using Equation 4.3a and the vertical displacement-time histories shown in Figure 4.17c is shown in Figure 4.18. The maximum strain (in either the positive or negative directions) that occurred in the steady-state portion of the strain-time history (cycles 4 through 9) was selected to represent the induced strain between the sensors, and this process is also shown in Figure 4.18. Note that while the examples shown in Figures 4.17 and 4.18 are for axial strain, the process is generally the same to calculate shear strain induced by a horizontal excitation. However, due to the large vertical component induced by the horizontal excitations at Site 2, a 4-node DB method was used to evaluate the shear strain-time histories (see Section 8.3.2).

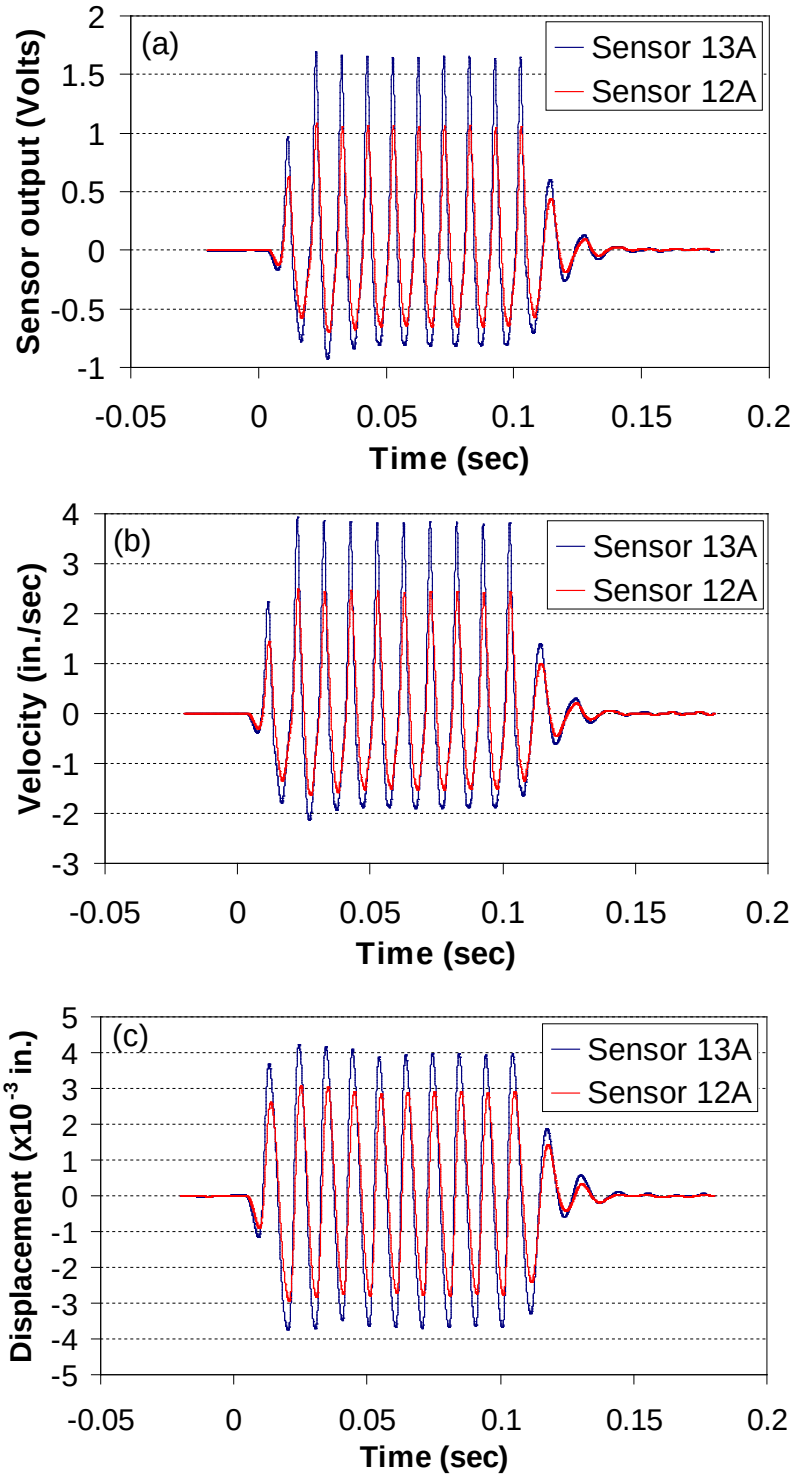

Figure 4.17. Examples for two axial sensors at Site 2 of: (a) voltage-, (b) velocity-, and (c) vertical displacement-time histories

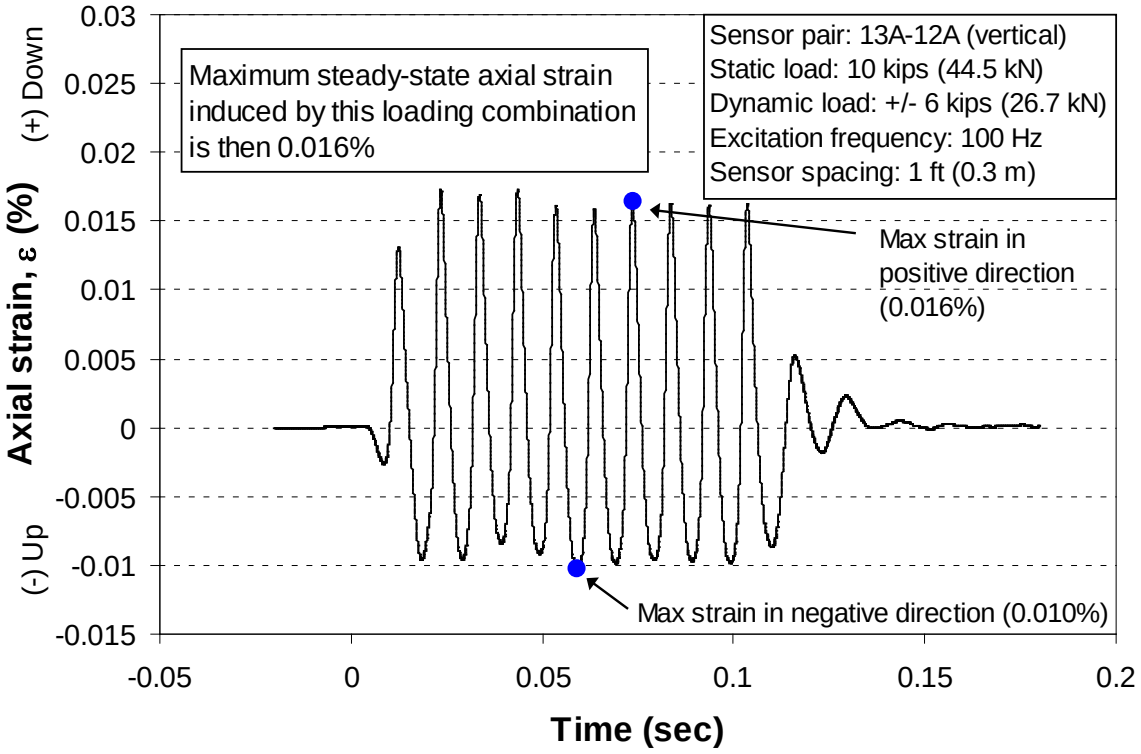

Figure 4.18. Determination of the maximum steady-state axial strain induced by a specified loading condition using the strain-time history between two sensors at Site 2

4.4.3 Examples of moduli and strain calculations

Example calculations of constrained moduli and axial strain are provided in this section for a vertically-oriented sensor pair at Site 2 when subjected to two different strain levels, i.e. two different dynamic load amplitudes.

Example 1 – In the first example, a static load of 10 kips (44.5 kN) was applied directly on the ground surface using the baseplate of Thumper. Thumper was then used to apply 10 cycles of a vertical sinusoidal excitation with a load amplitude of +/- 1.2 kips (5.3 kN) and an excitation frequency of 100 Hz directly to the ground surface. The V_{Pv} between sensors 13 and 12 was determined previously in Figures 4.13 and 4.14 as 2049 fps (625 m/s). Using Equation 4.2a and a total unit weight of the soil of 110 pcf (1762

kg/m^3), the constrained modulus for this case is 14,345 ksf (687 MPa). The axial strain computed for this case is 0.0031% as shown in Figure 4.19.

Example 2 – In the second example, the only change to the loading combination is that the load amplitude of the vertical sinusoidal excitation is increased to +/- 6 kips (26.7 kN). As discussed in Section 4.4.1 and shown in Figure 4.15, the use of the peak-to-peak travel time between sensors 13 and 12 to determine V_{Pv} is questionable due to the shape of the recorded waveforms. In this case, use of the time-shift of the cross-correlation sequence to determine V_{Pv} is the preferred method. The V_{Pv} calculated in this manner is 2049 fps (625 m/s) as shown in Figure 4.20. The constrained modulus is then 14,345 ksf (687 MPa) by Equation 4.2a. The axial strain induced by this loading case is 0.016% as shown in Figure 4.18.

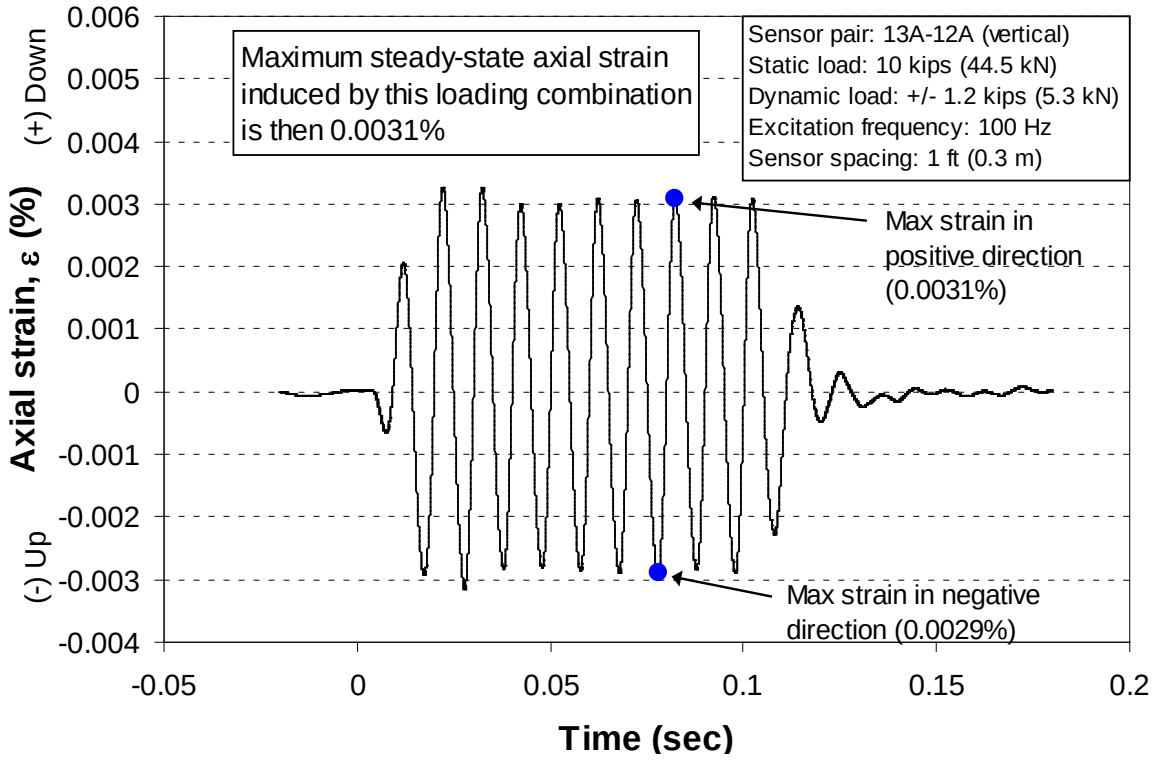

Figure 4.19. Determination of the maximum steady-state axial strain induced between two sensors at Site 2 by the loading conditions described in Example 1

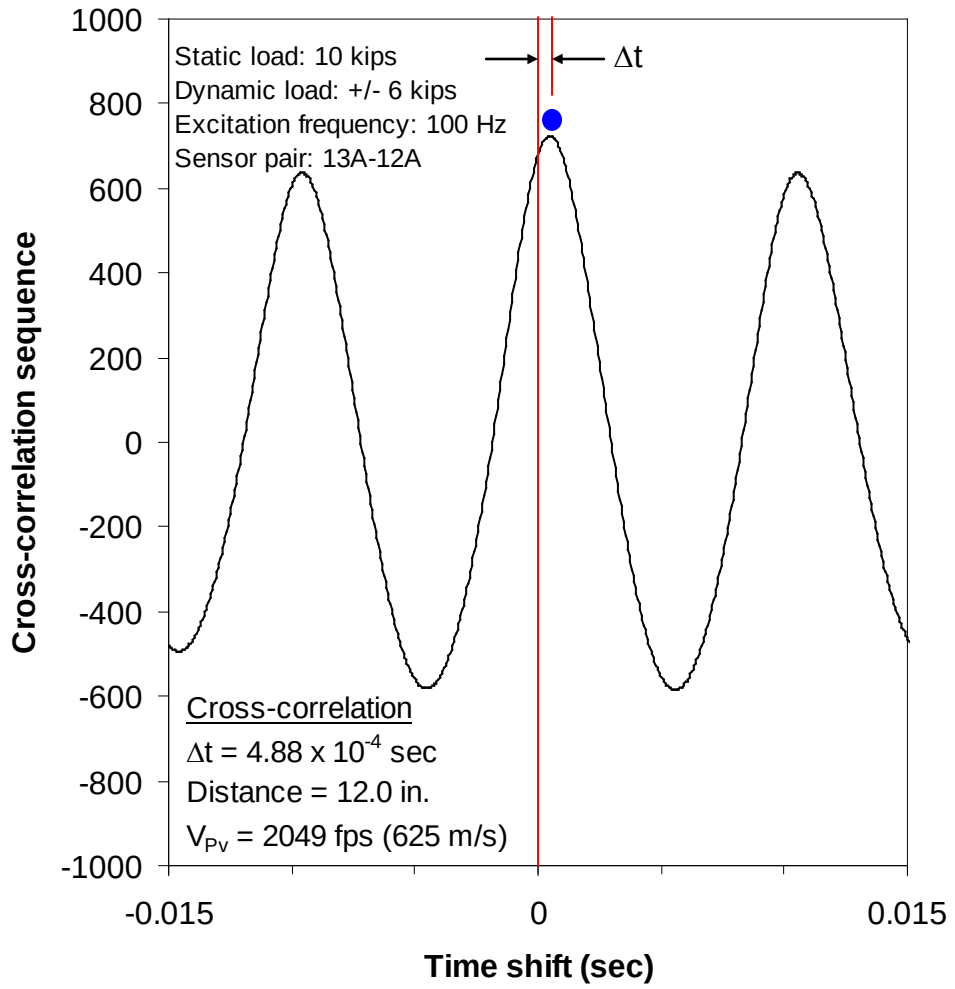

Figure 4.20. Determination of P_V-wave velocity between two sensors at Site 2 when subjected to the loading conditions described in Example 2

The constrained modulus and axial strains computed in Examples 1 and 2 can be combined together to form two data points on an M – log ε plot for the sensor pair 13A-12A as shown in Figure 4.21. It is important to note that this plot represents the behavior of the constrained modulus at these two sensors only for the loading combination discussed above, i.e. when a 10-kip (44.5-kN) static load is applied by Thumper to the ground surface and then a series of 100-Hz vertical sinusoidal excitations of varying amplitudes are generated by Thumper to induce a wide range of strain levels between the two sensors. The M values used in Figure 4.21 can also be normalized by the M at the

smallest induced strain (or an average value of M at the three or four smallest strains if "scatter" appears in the data). Following the established naming convention used for the shear modulus at low strains (e.g. G_{max}), the constrained modulus at the lowest strains is termed M_{max} as shown in Figure 4.21. Note that though the term M_{max} is used, the constrained modulus at small strains was not always the maximum constrained modulus (this point is discussed further in Chapters 5 and 8). The behavior of the normalized constrained modulus, M/M_{max}, in this example is shown in Figure 4.22. As can be seen in both Figures 4.21 and 4.22, no constrained modulus nonlinearity was observed for this sensor pair and loading combination, even though the signal exhibited a change in the sinusoidal behavior as shown in Figure 4.15. The behavior of either constrained modulus or normalized constrained modulus with the log of axial strain (e.g. M – log ε and M/M_{max} – log ε, respectively) can also be investigated for various sensor pairs, excitation frequencies, and static load levels. These various combinations are discussed in Chapters 5 and 8 for Sites 1 and 2, respectively.

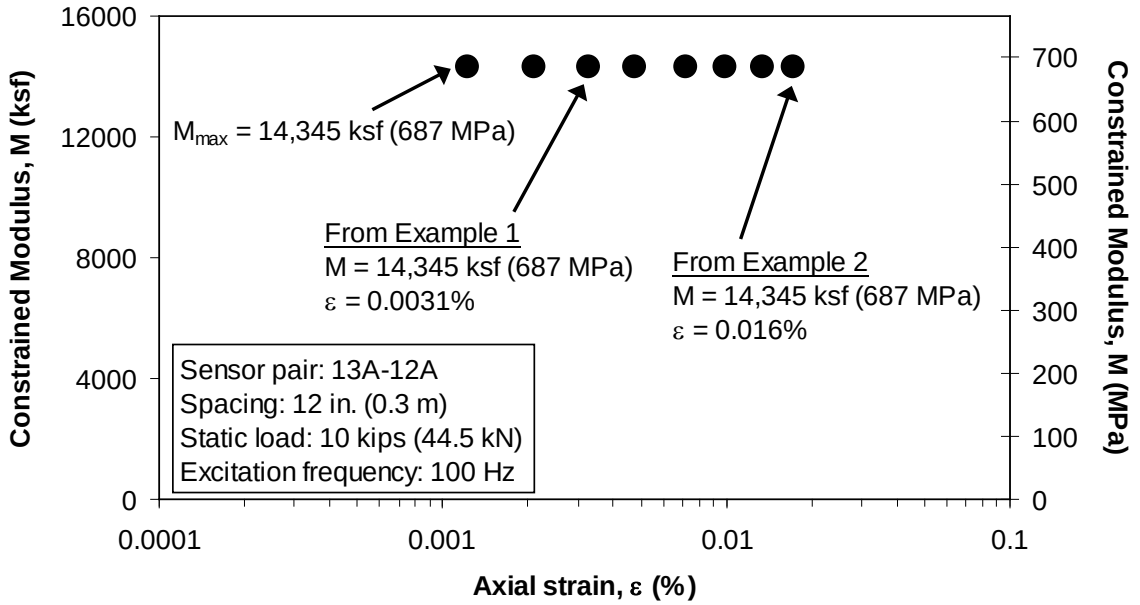

Figure 4.21. In-situ constrained moduli determined at various levels of axial strain induced between Sensors 13A and 12A by a 100-Hz vertical sinusoidal excitation; note that no nonlinearity is exhibited in M over the axial strains measured.

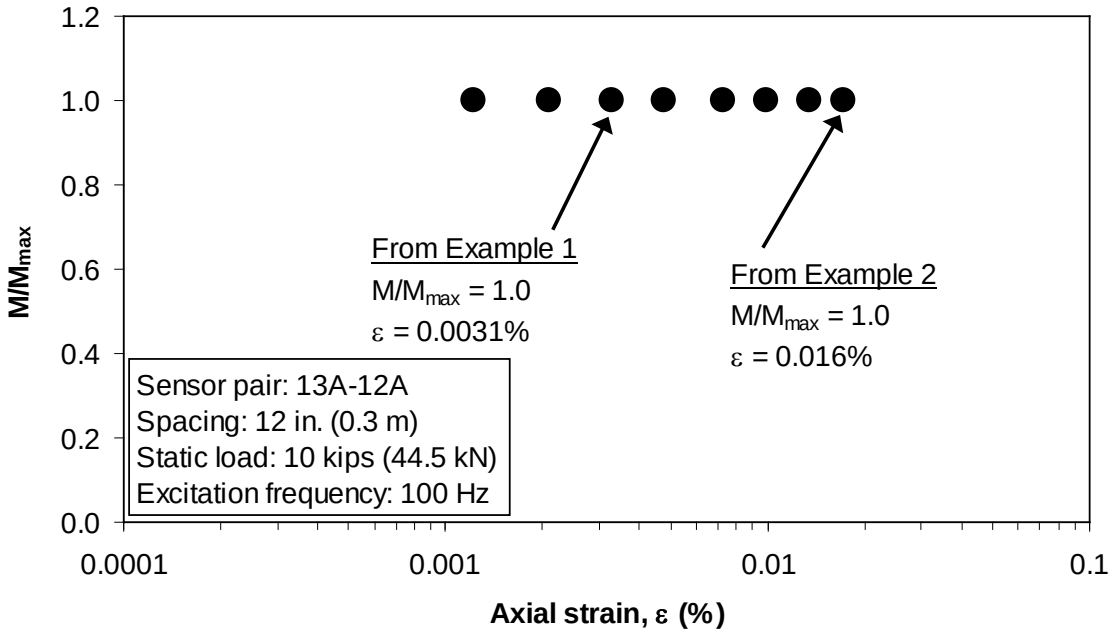

Figure 4.22. In-situ normalized constrained moduli determined at various levels of axial strain induced between Sensors 13A and 12A by a 100-Hz vertical sinusoidal excitation; note that no nonlinearity is exhibited in M over the axial strains measured.

4.5 SUMMARY

The raw data collected in the in-situ linear and nonlinear tests consist of voltage-time histories for each embedded 3-D sensor. In the case of the linear tests, i.e. small-strain, transient downhole and crosshole tests, these voltage-time histories were used directly to obtain the propagation velocities of the body waves (P_V, S_{VH}, P_H, and S_{HV} waves) between sensors. The in-situ state of stress was estimated using a Boussinesq stress distribution. The interpreted data from the small-strain, transient downhole and crosshole tests are presented as log V – log σ relationships.

In the nonlinear tests, large-strain sinusoidal excitations were applied with two different vibroseises, Thumper and T-Rex. A vertical excitation was applied by the vibroseis to create P_V waves and allow examination of the in-situ behavior of the

constrained moduli. Similarly, the vibroseis applied a horizontal excitation to induce S_{VH} waves and allow examination of the in-situ behavior of the shear moduli. In either case, the voltage-time histories recorded at each sensor were used directly to obtain the propagation velocities of the body waves between sensors. These velocities were calculated using both the peak-to-peak travel times between sensors and the time-shift of the cross-correlation sequence between sensors. To estimate the strains induced by the sinusoidal excitation of the vibroseis, the voltage-time histories recorded by the sensors were first converted into particle velocity-time histories using the appropriate calibration factor. These particle velocity-time histories were then numerically integrated once to obtain particle displacement-time histories. The induced strain was determined using a 2-node displacement-based method. This method involved computing the strain-time history using the displacement-time histories of two adjacent sensors and selecting the largest absolute value of strain induced between the two sensors in the steady-state portion of the strain-time history. The interpreted data from the large-strain, nonlinear vibroseis tests are the behaviors of the constrained and shear moduli with increasing axial or shear strain, respectively (e.g. M – log ε and M/M_{max} – log ε ; G – log γ and G/G_{max} – log γ).

CHAPTER 5: INITIAL FIELD EVALUATION OF LINEAR AND NONLINEAR MODULI AT SITE 1 AT HORNSBY BEND, TEXAS

5.1 INTRODUCTION

Prior to building an extensive field site and undertaking comprehensive sets of staged tests (presented in Chapter 6), preliminary field tests were conducted adjacent to a previous test site (hereafter referred to as Site 1) located on a historical farm field near Hornsby Bend in Austin, Texas, in July 2011. The purpose of these initial tests was to refine the vibroseis method presented by Park (2010) as necessary to allow measurement of linear and nonlinear constrained moduli. In this chapter, the material properties and location of this site, Site 1, are discussed. Construction of the embedded sensor array and the staged loading sequence employed are also discussed. The results of the small-strain downhole and crosshole tests and the large-strain vertical excitation tests are then presented. As the primary focus was on measurement of constrained moduli, horizontal excitation tests (required to measure shear moduli) were not performed at this site. Finally, conclusions and recommendations based on these initial tests are discussed. Part of this discussion can also be found in LeBlanc et al. (2012), which was written concurrently with this dissertation.

5.2 MATERIAL PROPERTIES

Site 1 was chosen due to its proximity to the site used by Van Pelt (2010), as Van Pelt took great care to document basic soil properties and strength parameters at the site using both in-situ tests and laboratory testing of disturbed and undisturbed soil specimens. Before the embedded sensor array was installed at the site, Van Pelt conducted Cone Penetration Testing (CPT) as part of the site characterization effort. His interpretation of the CPT results is shown in Table 5.1. Additional in-situ tests, including

Table 5.1. Interpretation of CPT results near Site 1 (from Van Pelt, 2010)

Layer No.	Depth Below the Ground Surface to Top of Layer (ft.)	USCS Soil Classification*	Cone Tip Resistance** "q_c" (tsf)	Sleeve Side Friction** "f_s" (tsf)	Friction Ratio** "f_s/q_c" (%)
1	0	Sandy Clay (CL)	18	0.25	1.39
2	0.75	Sandy Silt (ML)	16	0.06	0.38
3	7	Clay with Sand (CL)	47	0.34	0.72
4	33	---***	10	0.22	2.20
5	39	---***	150	0.70	0.47
	42	---***	240	1.15	0.48

* Based on visual field classification

** Representative value based on CPT data

*** No recovery of soil samples and therefore the soil type is unknown

Spectral-Analysis-of-Surface-Waves (SASW) and seismic CPT measurements, are presented by Van Pelt (2010) but are not reproduced here.

Additionally, Van Pelt conducted specific gravity and grain size distribution tests in the laboratory on disturbed samples and classified the soil in the upper 4 ft (1.2 m) as a sandy silt (ML) with a specific gravity of 2.69. The grain size distribution is shown in Figure 5.1 and Table 5.2. Van Pelt also performed consolidated-drained (CD) triaxial tests on three remolded specimens obtained from approximately 30 in. (76 cm) below the ground surface. Van Pelt reported an effective friction angle of approximately 36 degrees and an effective apparent cohesion of 0.4 psi (2.8 kPa) based on the Mohr-Coulomb failure envelope shown in Figure 5.2.

Finally, Van Pelt reported the dry unit weight of the soil to be approximately 91 pcf and the average void ratio equal to 0.84 based on undisturbed specimens collected at the project site (Table 5.3). It should be noted that Van Pelt collected specimens in January 2010, prior to the entire Austin area experiencing drought conditions starting in approximately October 2010. The tests performed at Site 1 in the present research occurred in July 2011 in the middle of the drought, so the water content at Site 1 (approximately 5% based on exploratory borings near Site 1) was considerably lower

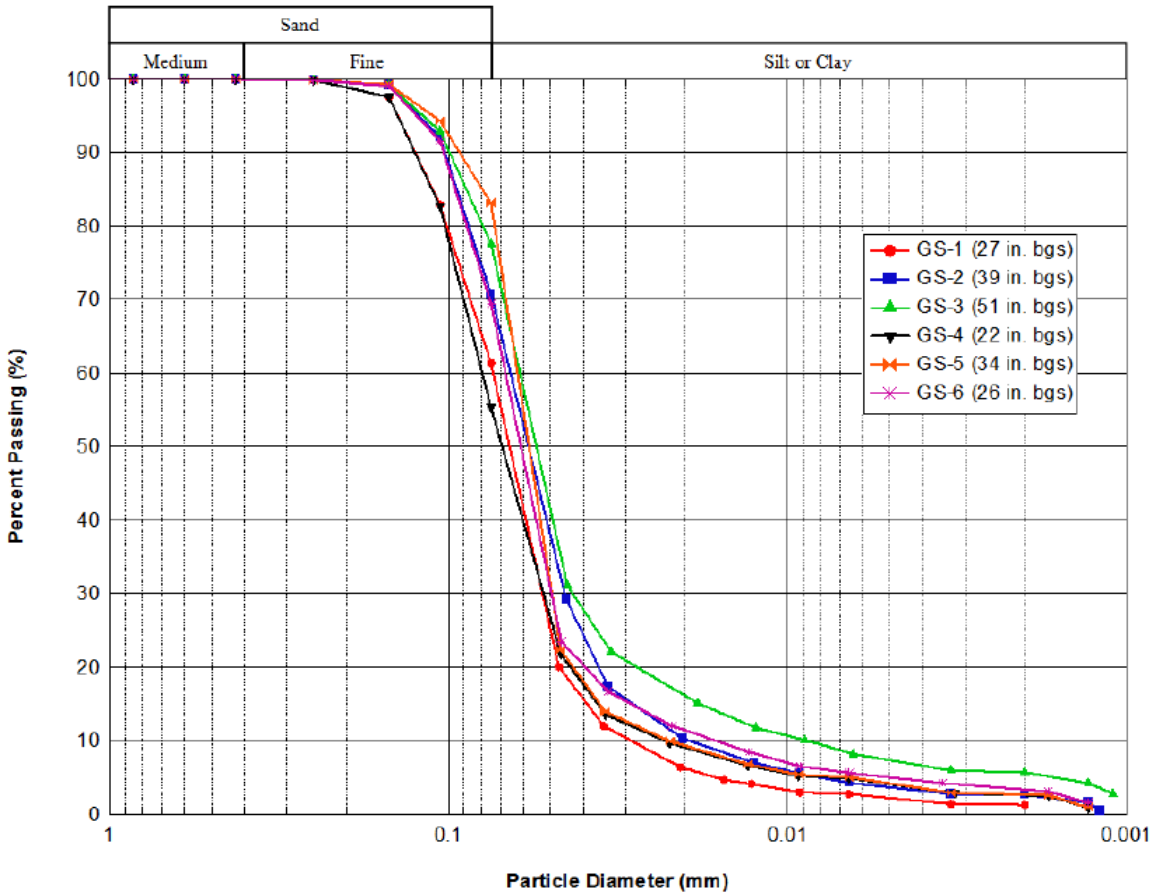

Figure 5.1. Grain size distribution curves of soil near Site 1 (from Van Pelt, 2010)

Table 5.2. Summary of grain size distribution analyses (from Van Pelt, 2010)

Sample I.D.	Sample Location	Sample Depth Below the Ground Surface (in.)	Percent Sand*	Percent Fines**	Soil Description***	USCS Symbol
GS-1	36-in. Ftg.	27	39	61	Sandy Silt	ML
GS-2	36-in. Ftg.	39	29	71	Silt with Sand	ML
GS-3	36-in. Ftg.	51	22	78	Silt with Sand	ML
GS-4	18-in. Ftg.	22	45	55	Sandy Silt	ML
GS-5	18-in. Ftg.	34	17	83	Silt with Sand	ML

* Particle diameter passing the No. 4 sieve (4.75-mm) but not the No. 200 sieve (75-µm)

** Particle diameter passing the No. 200 sieve (75-µm)

*** "Sandy silt" contains between 16-30% sand; "Silt with sand" contains between 15-29% sand

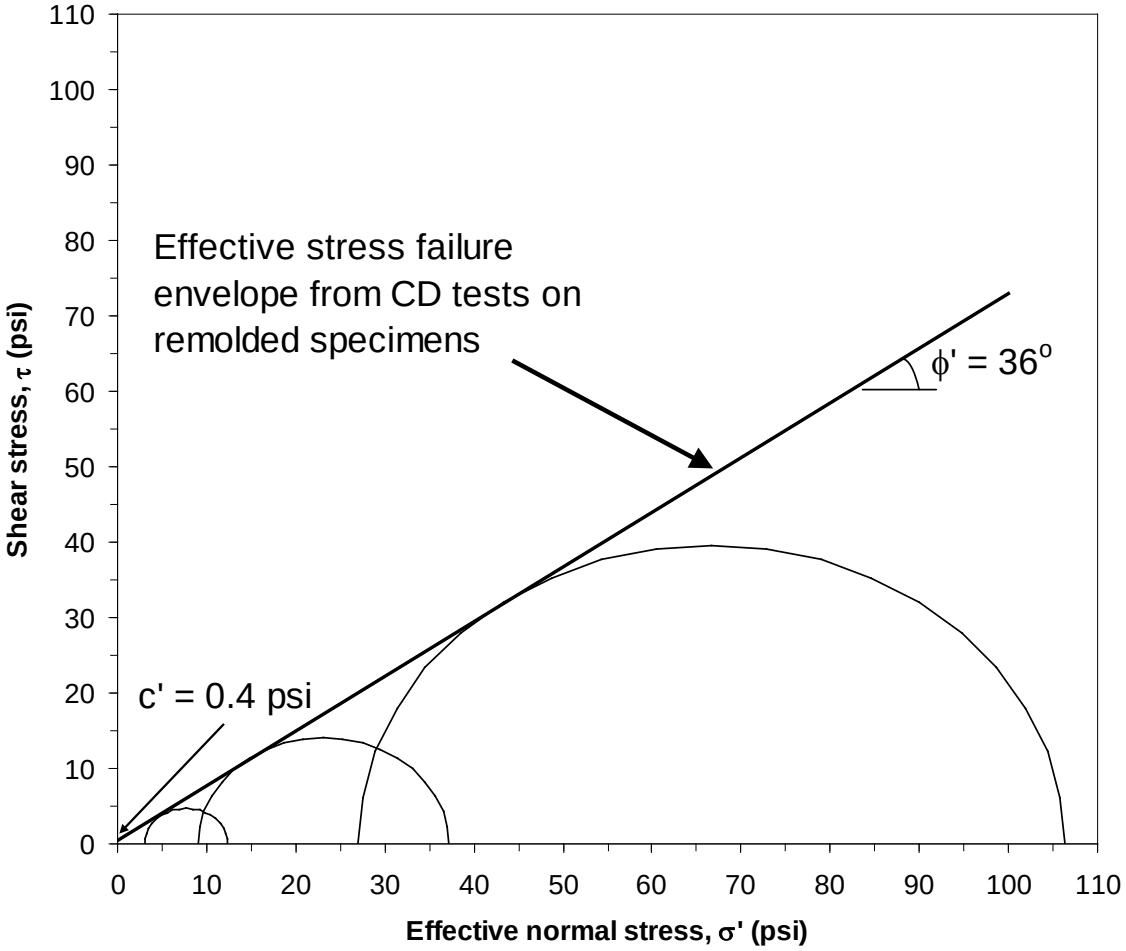

Figure 5.2. Mohr-Coulomb failure envelope from consolidated-drained triaxial tests conducted on remolded specimens near Site 1 (modified from Van Pelt, 2010)

Table 5.3. Summary of unit weight determinations on undisturbed specimens collected near Site 1 (from Van Pelt, 2010)

Sample I.D.	Sample Location	Sample Depth Below the Ground Surface (in.)	Moisture Content "w" (%)	Total Unit Weight "γ_t" (pcf)	Dry Unit Weight "γ_d" (pcf)
D-1	B-3-1	40	15.8	106	91
C-1*	B-3-1	42	17.6	108	92
C-2**	B-3-1	38	15.8	105	91

* From one-dimensional consolidation and permeability test
** From one-dimensional compression test

than that reported by Van Pelt. The results of Van Pelt's compression and consolidation tests are not presented here.

5.3 FIELD SET-UP AND TEST PROCEDURE

The location and set-up of the sensor array and the test procedure used at Site 1 are discussed in this section.

5.3.1 Location and construction of the embedded sensor array

Site 1 was located on a historical farm field in the Lower Tract B area of Hornsby Bend in Austin, Texas (Figure 5.3). The farm field had been ploughed in the preceding

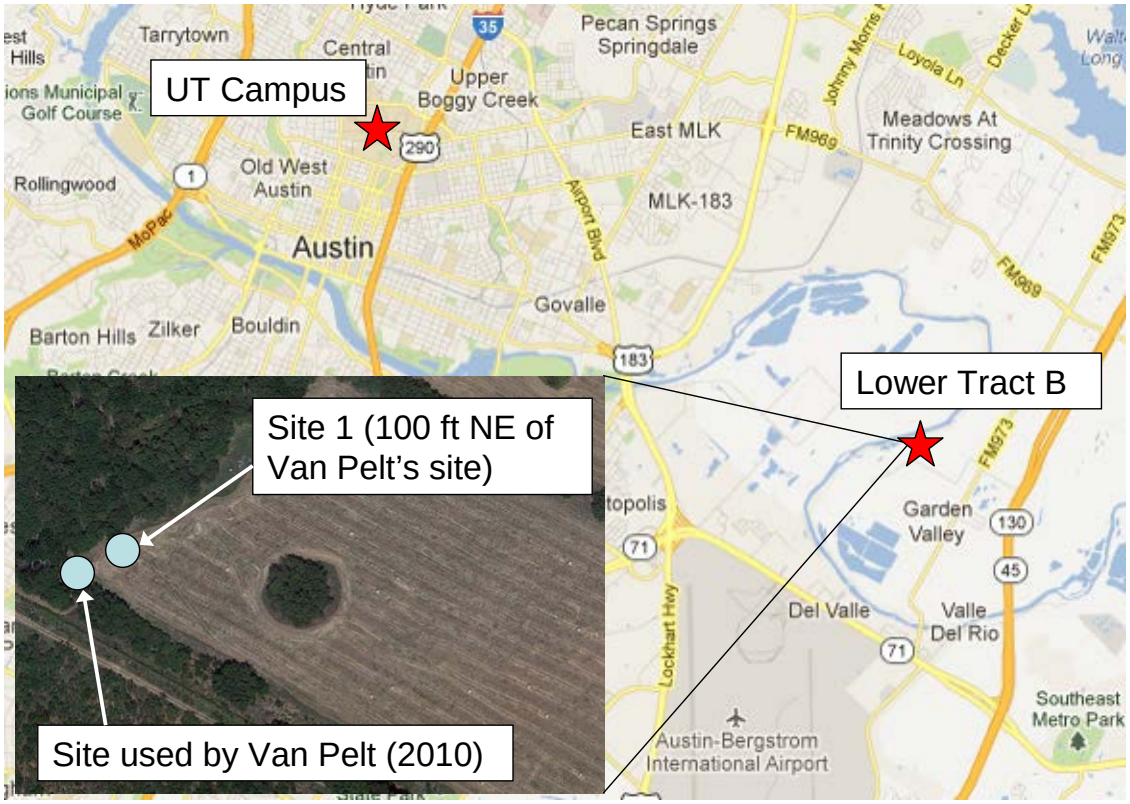

Figure 5.3. Location of Site 1 near Hornsby Bend, Austin, Texas (map provided by Google Maps)

decades, leaving plough tillage (with topsoil and rocks) at the ground surface. An embedded sensor array had previously been installed at Site 1 during an earlier research project and consisted of eight, 3-D sensors at the corners of a 2-ft x 2-ft x 2-ft (0.61-m x 0.61-m x 0.61-m) cubical array. The top of the array (four sensors) was at a depth of 2 ft (0.61 m) below the ground surface, and the bottom of the array (four sensors) was 4 ft (1.22 m) below the ground surface. This previously installed array was prepared for the present research by scarifying the top layer of plough tillage by hand. The tillage was removed until native sandy silt soil was found (approximately 7 in. (18 cm) deep). The area of scarification in plan was about 8-ft by 8-ft (2.4-m by 2.4-m) in order to allow the loading plate of T-Rex to contact natural sandy silt during the steady-state excitation tests.

In June 2011, this existing array was modified by installing three-component (one vertical direction; two horizontal directions) sensors comprised of three, 1-D, 28-Hz geophones previously fabricated by Park (2010). A total of three, 3-D sensors was installed in the middle of the existing cubical array (Figure 5.4). A hand auger was used to drill a 2.5-in. (6.4-cm) diameter borehole to a depth of about 26 in. (66 cm). The bottom of the borehole was prepared, and the deepest sensor (Sensor 3) was placed using the installation/orientation tool shown in Figure 5.5. The borehole was then backfilled with native soil and compacted until the desired depth for Sensor 2 was reached. Great care was taken to compact the backfilled soil to the same density as the in-situ soil. Sensor 2 was then installed, and the process was repeated to install Sensor 1. After Sensor 1 was installed, the remainder of the borehole was backfilled and compacted in steps. The depths of the midpoints of the three sensors were 9.75, 17.75, and 25.75 in. (24.8, 45.1, and 65.4 cm) measured from the scarified soil surface (see Figure 5.4). Finally, a 1-in. (2.5-cm) deep layer of poorly graded sand was placed over the scarified surface to improve contact between the ground surface and either the concrete footing or the vibroseis loading plate during testing.

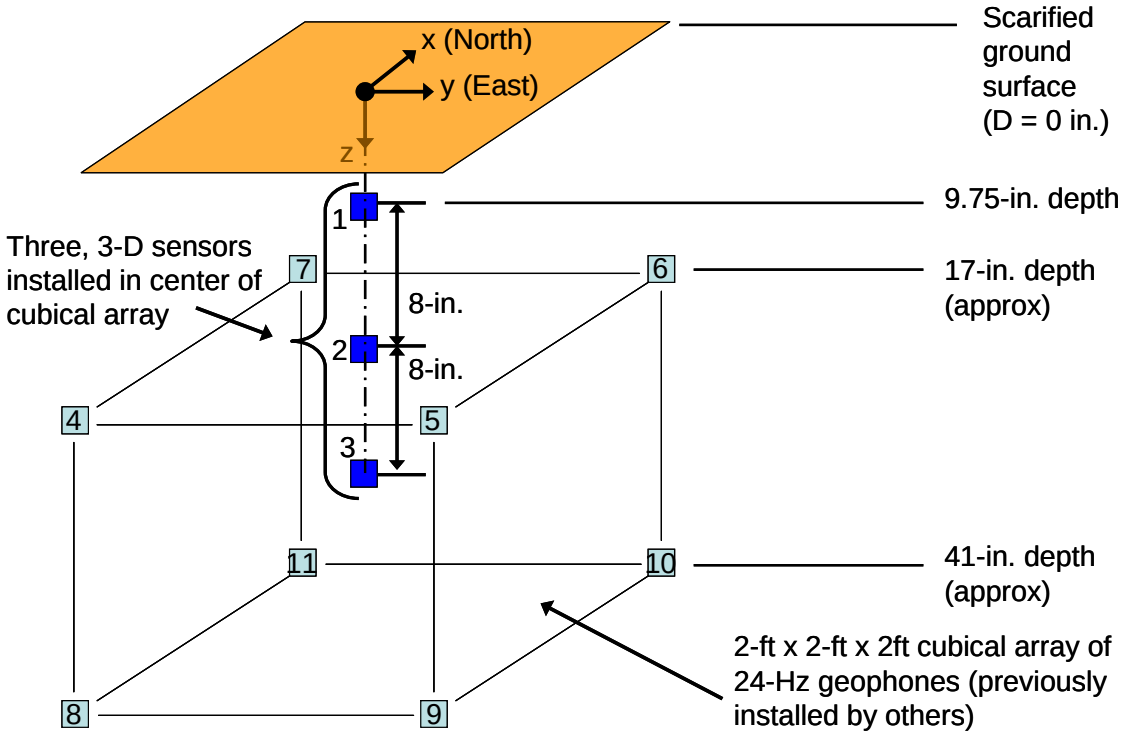

Figure 5.4. Oblique view of the embedded sensor array at Site 1 (not to scale)

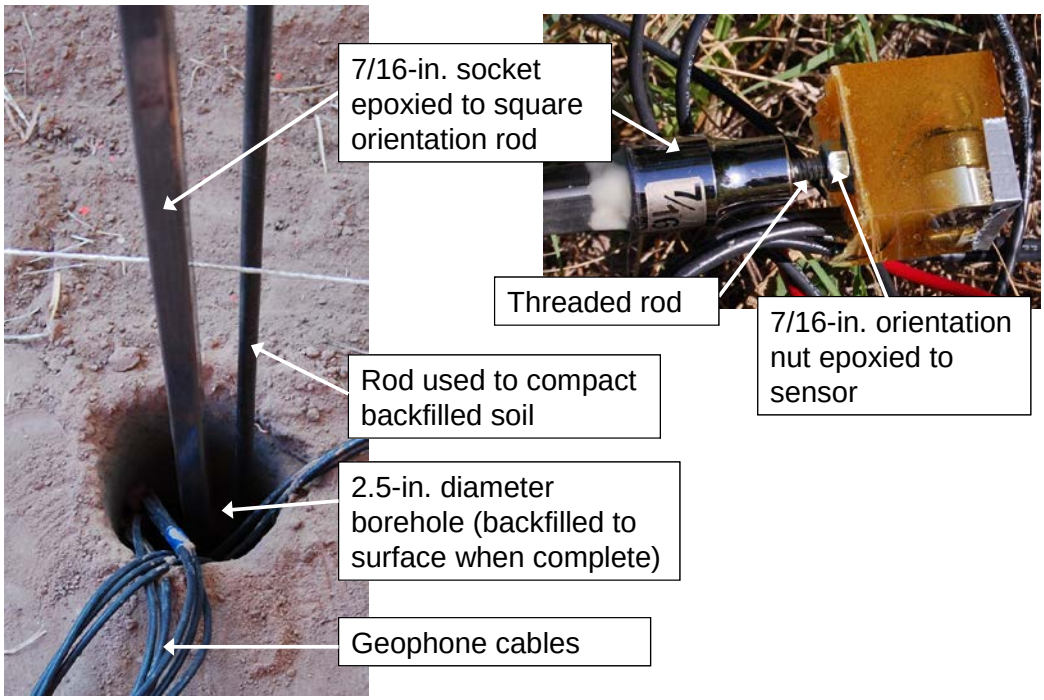

Figure 5.5. Installation of the three additional sensors at Site 1

5.3.2 Staged loading sequence

After modification of the existing embedded sensor array, the soil mass was subjected to four stages of tests as follows: (1) steady-state vertical excitation tests using Thumper, (2) transient, downhole and crosshole seismic tests at small strains, (3) steady-state vertical excitation tests using T-Rex, and (4) transient, downhole and crosshole seismic tests at small strains. The generalized four-stage test sequence with the approximate vertical stress (σ_v) applied in each stage is shown in Figure 5.6. Note that while the loads applied by T-Rex in Stage 3 were much higher than those applied by Thumper in Stage 1, the applied stress was roughly equal in both stages due to the larger baseplate of T-Rex. Due to scheduling conflicts with Thumper, the transient, small-strain downhole and crosshole tests (Stage 2) could not be performed before the steady-state excitation tests (Stage 1). The purpose of each stage is summarized in Table 5.4.

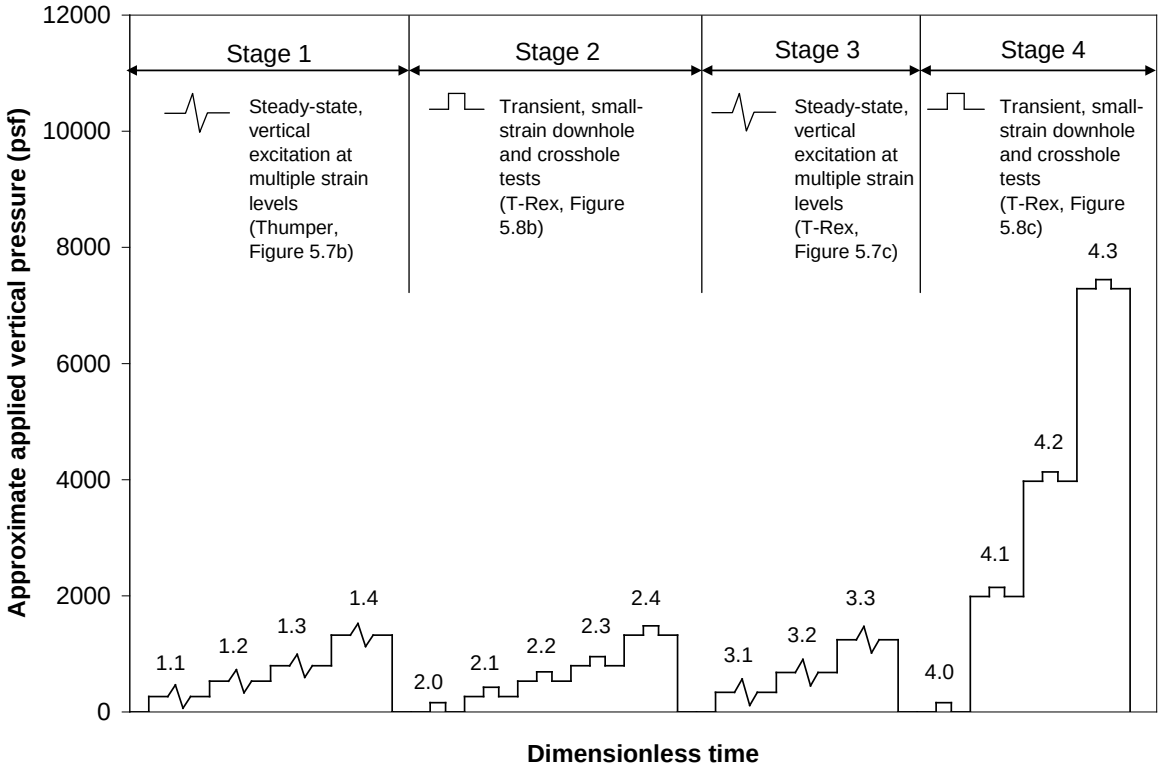

Figure 5.6. Staged loading sequence used at Site 1 (after Stokoe et al., 2006)

Table 5.4. Description of the staged loading sequence at Site 1

Load stage	Test description	Purpose
1	Steady-state, vertical excitation using Thumper (static loads up to 10 kips)	Nonlinear constrained moduli measurements
2	Transient downhole and crosshole tests using T-Rex at static loads up to 10 kips	Variation of linear constrained and shear moduli with stress level
3	Steady-state, vertical excitation using T-Rex (static loads up to 55 kips)	Nonlinear constrained moduli measurements
4	Transient downhole and crosshole tests using T-Rex at static loads up to 55 kips	Variation of linear constrained and shear moduli with stress level

To characterize linear and nonlinear constrained moduli, steady-state excitation tests were performed using Thumper (Stage 1 in Figure 5.6) and then T-Rex (Stage 3 in Figure 5.6) positioned directly over the embedded sensor array as shown in Figure 5.7. Stage 3 was performed one week after Stage 1. A stepped loading sequence was used in both stages (four steps in Stage 1; three steps in Stage 3) to limit the effects of the loading regimen on the underlying soil structure. In each load step, the shaker applied a constant vertical load directly to the ground surface while the load amplitude of the vertical sinusoidal excitation was varied.

Small-strain, transient downhole and crosshole tests were performed in Stages 2 and 4 one week after Stage 1 was completed. The field configuration for these tests is shown in Figure 5.8. In the downhole tests, the top of a 3-ft (0.91-m) diameter, precast concrete footing positioned over the sensor array was struck directly with an instrumented hammer to generate vertically-propagating constrained compression (P_v) waves, and the side of the concrete footing was struck to generate vertically-propagating, horizontally-polarized shear (S_{VH}) waves. In the crosshole tests, steel rods were driven to the depths of each sensor (Sensors 1, 2, and 3), after which the tops of the rods were

struck with an instrumented hammer to generate both horizontally-propagating constrained compression (P_H) waves and horizontally-propagating, vertically-polarized shear (S_{HV}) waves. The purposes of these tests were: (1) to confirm that the steady-state

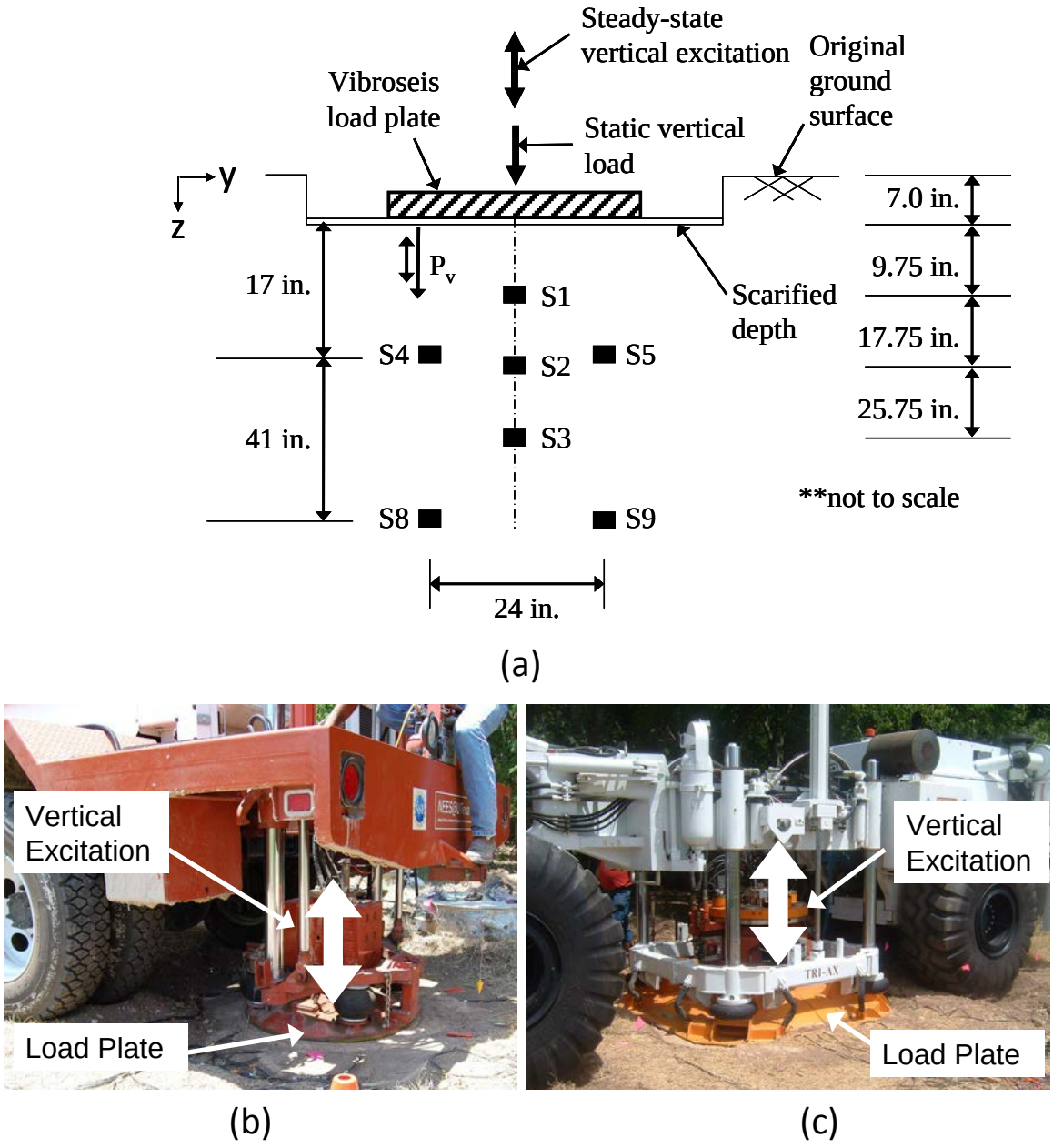

Figure 5.7. Steady-state vertical excitation tests: (a) schematic of test layout looking North, (b) Stage 1 using Thumper, and (c) Stage 3 using T-Rex

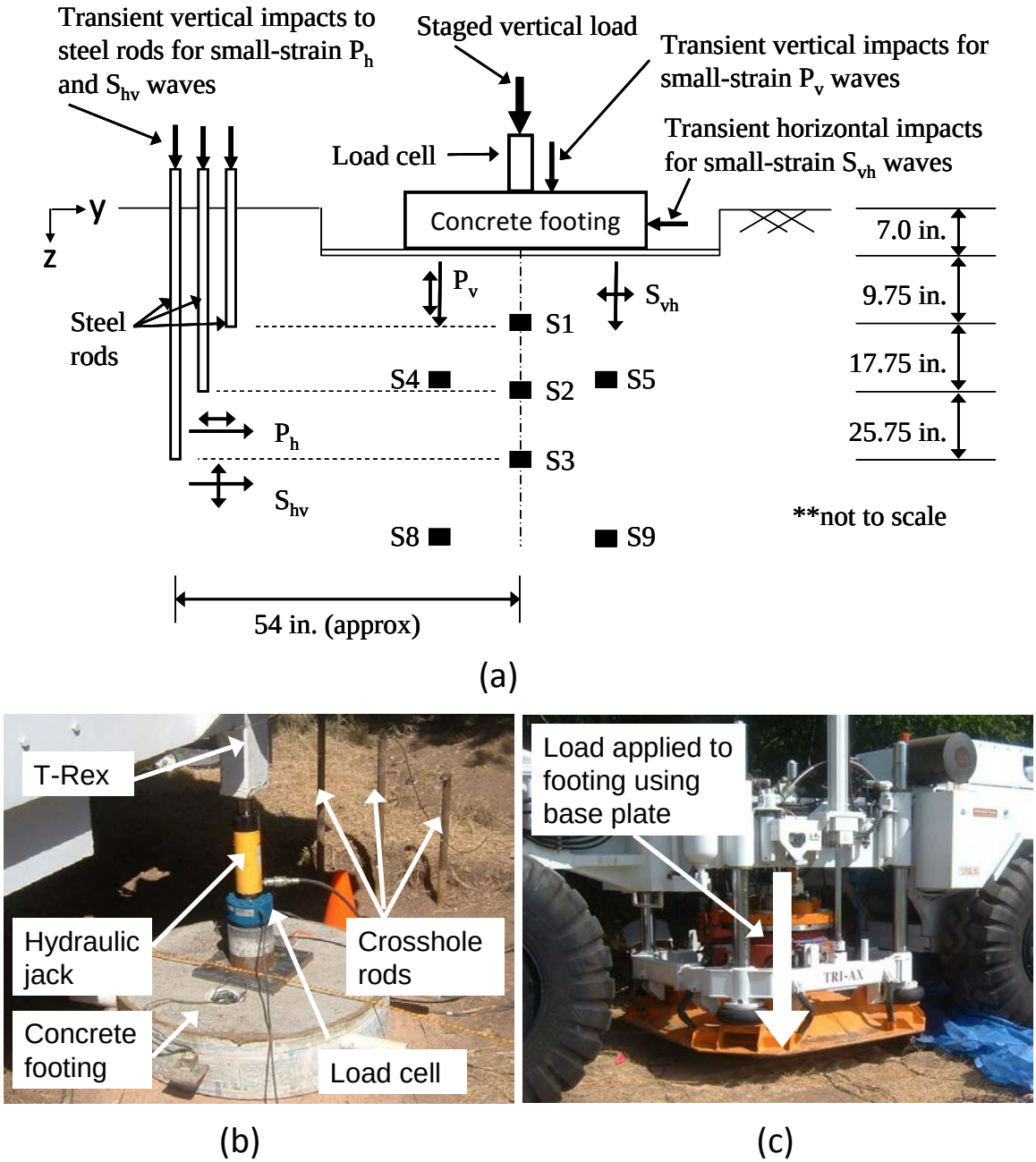

Figure 5.8. Transient, small-strain downhole and crosshole tests: (a) schematic of test layout looking North, (b) using reaction mass of T-Rex to apply static load to the footing in Stage 2, and (c) using base plate of T-Rex to apply static load in Stage 4

excitation tests were measuring the P_v-wave velocity (V_{Pv}) at small strains and (2) to determine the various log V – log σ relationships for both compression and shear waves propagating in both the vertical and horizontal directions. As in the steady-state excitation tests, a stepped loading sequence was used in both stages (five steps in Stage 2; four steps in Stage 4). In Stage 2, the vertical load was increased by jacking against the dead weight of T-Rex using the loading point on the rear "bumper" (Figure 5.8b), and the applied stresses were the same as those used in Stage 1 (see Figure 5.6). To achieve higher levels of vertical stress in Stage 4, T-Rex was positioned directly over the concrete footing, and the vertical load was increased using the base plate of T-Rex as shown in Figure 5.8c. This method of load application was possible because the hydraulic lines of T-Rex remain pressurized even after T-Rex's engine is turned off (which was done to avoid generating noise in the downhole and crosshole tests). While this method did allow for greater loads to be applied to the concrete footing, it created difficulties when generating a wave source during the downhole tests since access to the concrete footing was hindered by the large base plate of T-Rex (Figures 5.8c and 5.9). Therefore, in Stage

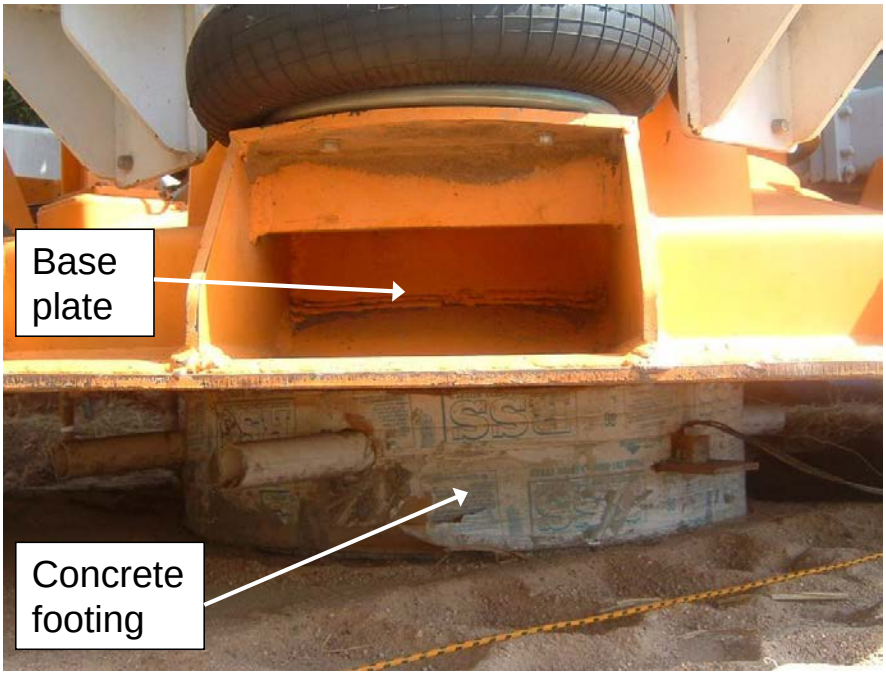

Figure 5.9. Lack of access created by loading with the base plate of T-Rex in Stage 4

4, the edge of the base plate of T-Rex was struck with the instrumented hammer to generate P_v waves, and a steel pipe placed against the side of the footing was struck to generate S_{VH} waves. Due to these difficulties, this method of load application was changed at Site 2 to improve the small-strain downhole tests.

5.4 SMALL-STRAIN CROSSHOLE TESTS

Transient, small-strain crosshole tests were conducted at Site 1 in Stages 2 and 4, as indicated in Figure 5.6. Within each stage, the S_{HV}- and P_H-wave velocities (V_{Shv} and V_{Ph}, respectively) were measured at several different confining pressures (load steps shown in Figure 5.6). In this manner, the effect of confining pressure on V_{Shv} and V_{Ph} was examined. The measurements of V_{Shv} and V_{Ph}, including typical data, and the effect of confining pressure are presented in this section. Note that in this section, the confining pressures used are based on total stresses, but as discussed in Section 4.3.3, negative pore pressures were likely present in the soil at the time of the tests at Site 1. The presence of negative pore pressures makes relationships based on total stress largely unsuitable for determining whether the soil became normally-consolidated over the range of induced stresses since it is the effective, not total, stresses that affect the wave velocities. However, since the tests at Site 1 were limited to "proof-of-concept" type tests, the effective stresses in the field were not estimated at Site 1. Note that for the more robust suite of tests at Site 2, the effective stresses in the field were estimated using the suction stress concept (discussed in Section 6.2.3), and the results of the crosshole tests at Site 2 are presented in the form of effective stress relationships (see Section 7.3).

5.4.1 Measurement of V_{Shv} and V_{Ph} under the footing

As mentioned in Section 5.3.2, S_{HV} and P_H waves were generated in the small-strain crosshole tests by striking steel rods with an instrumented hammer (see Figure 5.8). These steel rods were driven to the depths of the three sensors in the center column of the

Site 1 array. Accordingly, only source-to-receiver travel times could be determined for these sensors. These travel times between the source rod and the receivers were adjusted to account for the delay time required for the wave to travel from the top of the rod (where the vertical impulse load was applied) down to the tip. No crosshole wave velocities were calculated for the remaining sensors in the array. The wave arrivals were generally clear enough to be determined by eye using the procedures described in Chapter 4. Typical data, including V_{Shv} and V_{Ph}, from the tests in Stage 2.4 are shown in Figures 5.10, 5.11, and 5.12 for all three sensors in the center column of the sensor array.

5.4.2 Effect of confining pressure on V_{Shv} and V_{Ph}

In the crosshole tests conducted in Stages 2 and 4, both V_{Shv} and V_{Ph} were determined at Sensors 1, 2, and 3, for each level of static load (load steps shown in Figure 5.6), as described in Section 5.4.1. Additionally, the vertical stress (σ_v) induced at the

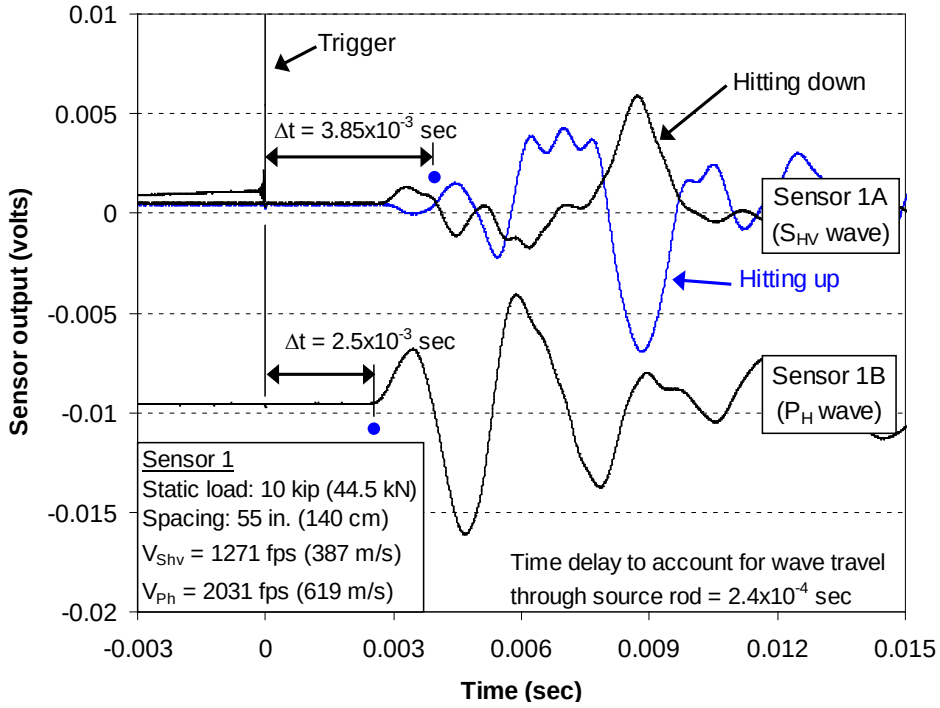

Figure 5.10. Stage 2.4 crosshole data from Sensor 1 (9.75-in. (24.8-cm) depth)

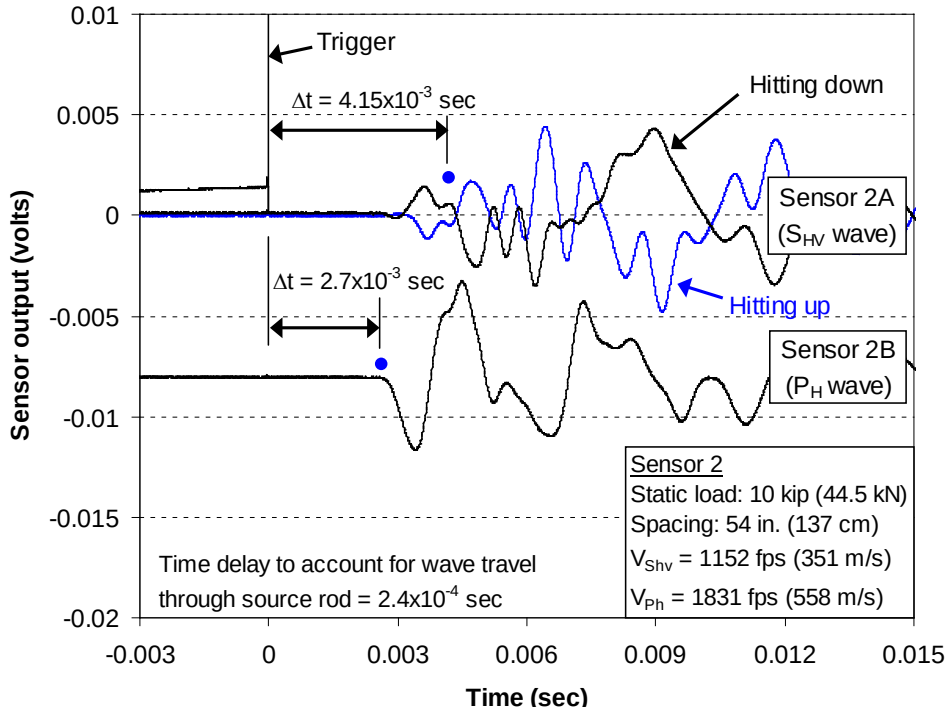

Figure 5.11. Stage 2.4 crosshole data from Sensor 2 (17.75-in. (45.1-cm) depth)

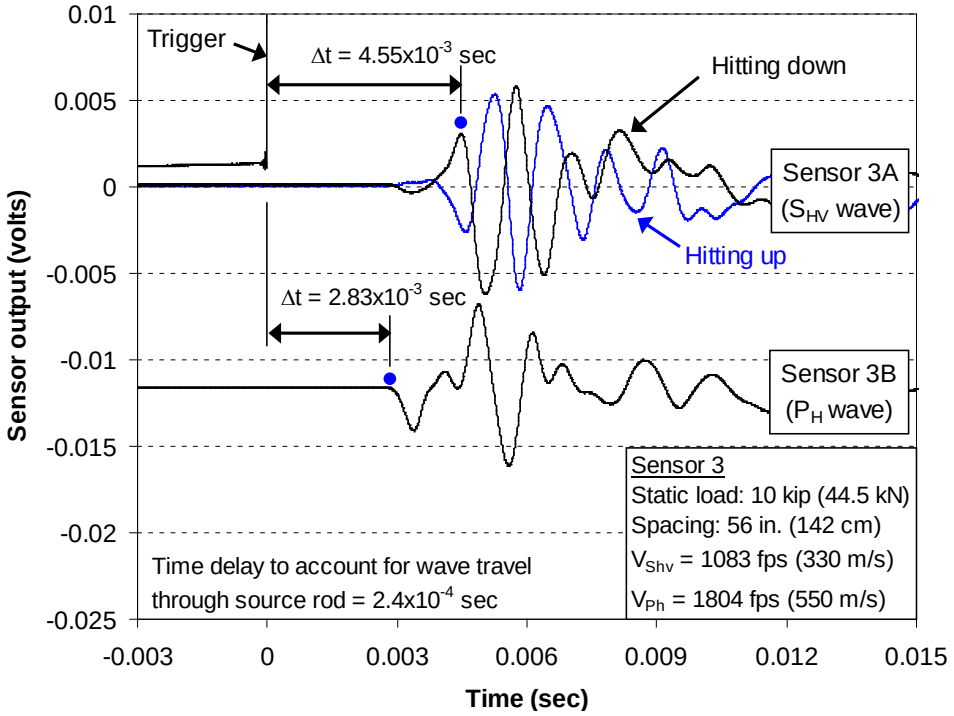

Figure 5.12. Stage 2.4 crosshole data from Sensor 3 (25.75-in. (65.4-cm) depth)

sensors by each load step was estimated using a Boussinesq stress distribution as described in Chapter 4. Since the soil at Site 1 was believed to be overconsolidated, the horizontal stress (σ_h) at each sensor was estimated by assuming that K_o is constant and equal to 1.0. In this manner, the variation of both V_{Shv} and V_{Ph} with confining pressure could be investigated. Lee (1985) suggested that the S_{HV}-wave velocity is influenced equally by both σ_h and σ_v, and therefore proposed that the true measure of confining pressure in this case is the geometric mean of these two stresses, i.e. $\sqrt{\sigma_h \sigma_v}$. However, since K_o was assumed to be equal to 1.0 in all stages at Site 1, the quantity $\sqrt{\sigma_h \sigma_v}$ is numerically equal to σ_h. On the other hand, the P_H-wave velocity is only influenced by the stress in the direction of wave propagation, i.e. the horizontal stress in the case of crosshole tests. Therefore, the effects of confining pressure on V_{Shv} and V_{Ph} at Site 1 are presented in the form of log V_{Shv} – log σ_h and log V_{Ph} – log σ_h relationships in Figures 5.13, 5.14, and 5.15 for Sensors 1, 2, and 3, respectively. The equations of the best-fit lines shown in Figures 5.13 through 5.15 are summarized in Table 5.5. Note that in the best-fit equations, σ_h is normalized by the atmospheric pressure (P_a) following the model suggested by Hardin (1978). Additionally, the average best-fit equations (based on both Stages 2 and 4) for each depth are included in Table 5.5. Note that the value of K_o, if constant, has no influence on the slope of either the log V_{Shv} – log σ_h or log V_{Ph} – log σ_h relationships, so any trends observed in Figures 5.13 through 5.15 are equally valid for all values of K_o.

For every case listed in Table 5.5, the S_{HV}-wave velocity generally increases with stress level at roughly the same rate as the P_H-wave velocity, i.e. the exponents of the normal stress of the log V_{Shv} – log σ_h and log V_{Ph} – log σ_h relationships are about the same. Additionally, at every depth in the embedded sensor array, the exponents of both the V_{Shv} and V_{Ph} relationships are generally the same in Stages 2 and 4. At Sensors 2 and 3, the P_H-wave velocities are about 100 fps (31 m/s) slower in Stage 4 than in Stage 2 (Figures 5.14b and 5.15b). This reduction is relatively small (about 5%), yet represents

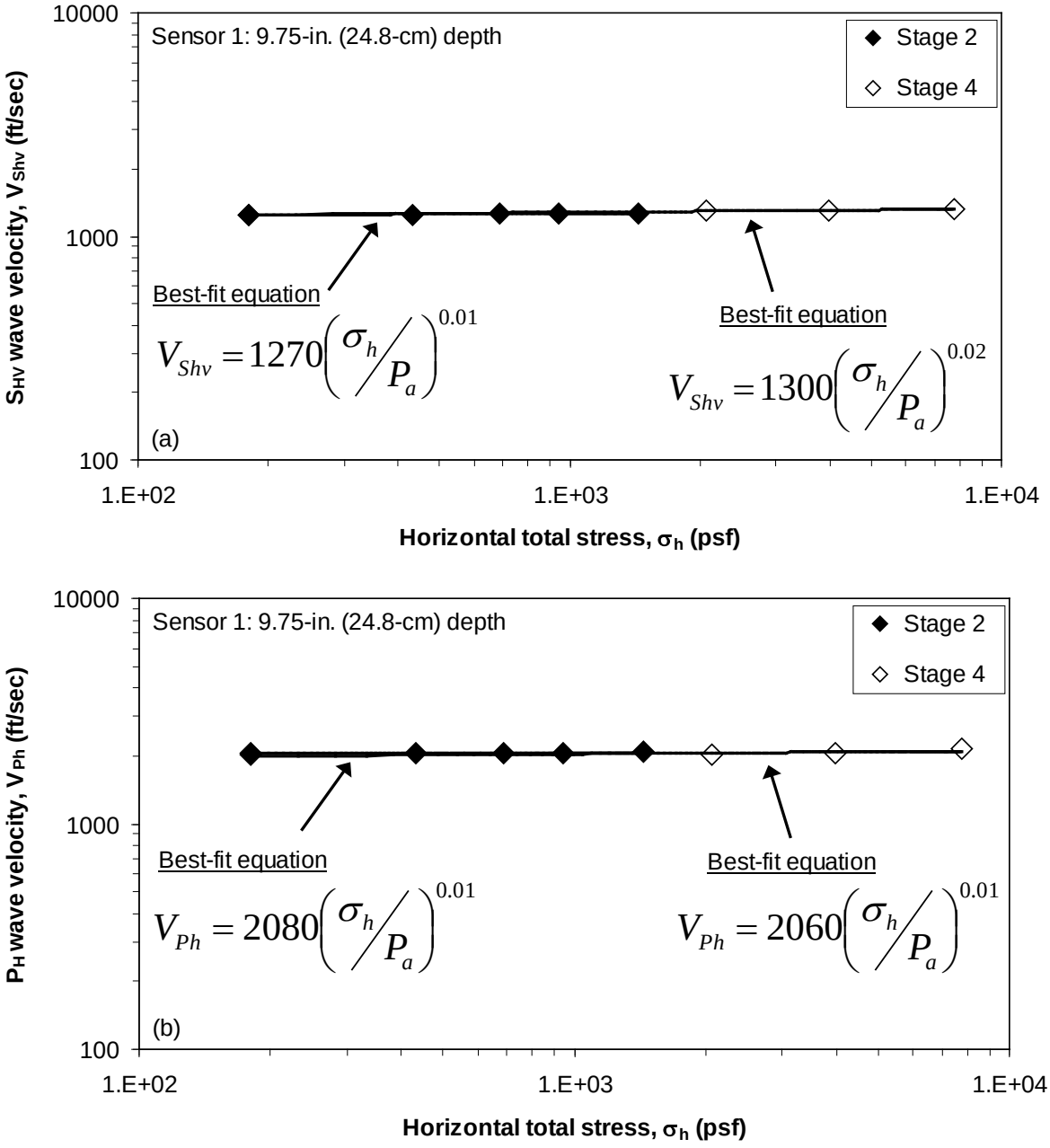

Figure 5.13. Variation of (a) S_{HV}-wave velocity and (b) P_H-wave velocity with increasing stress level at a depth of 9.75 in. (24.8 cm) below the base of the concrete footing

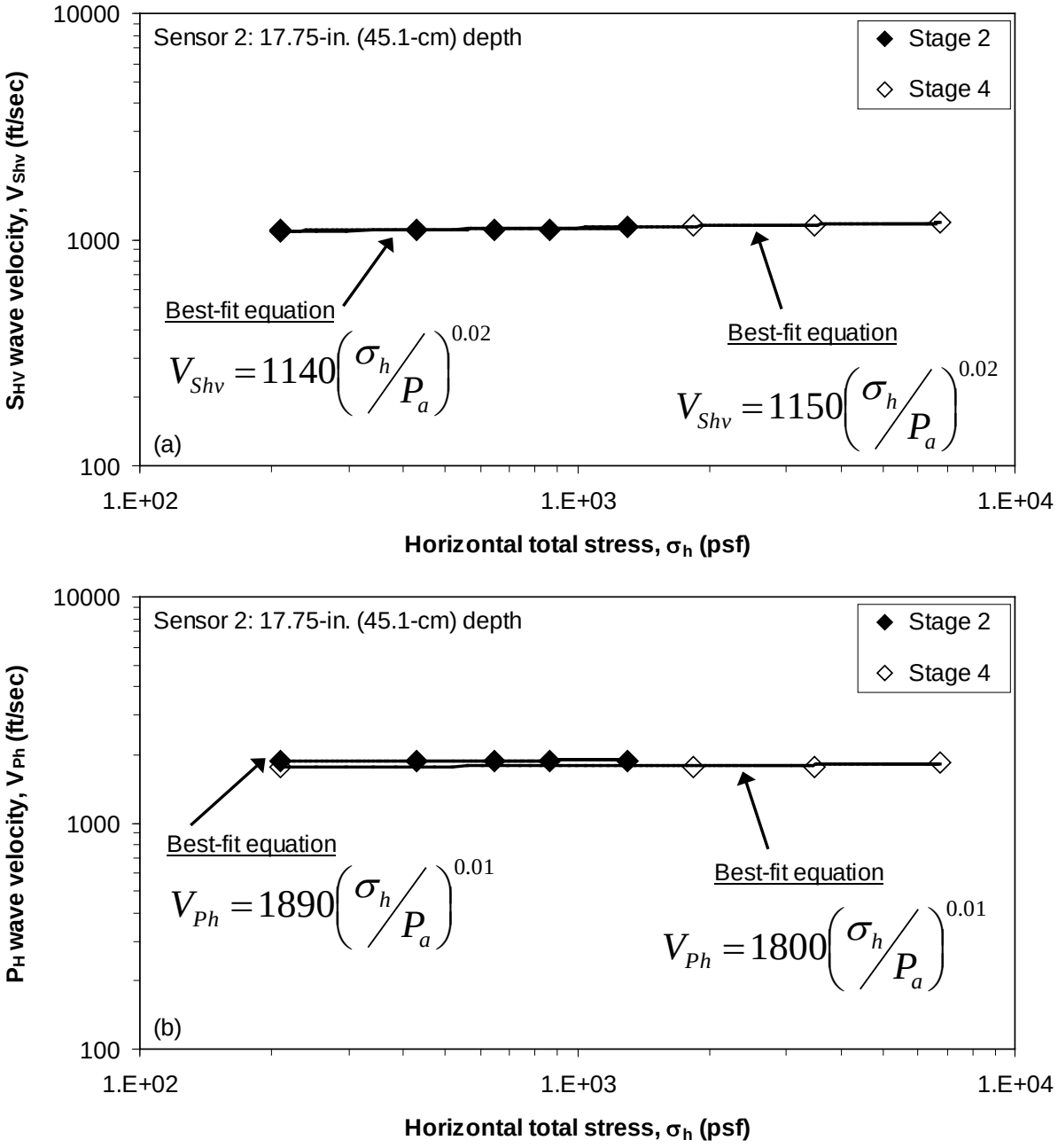

Figure 5.14. Variation of (a) S_{HV}-wave velocity and (b) P_H-wave velocity with increasing stress level at a depth of 17.75 in. (45.1 cm) below the base of the concrete footing

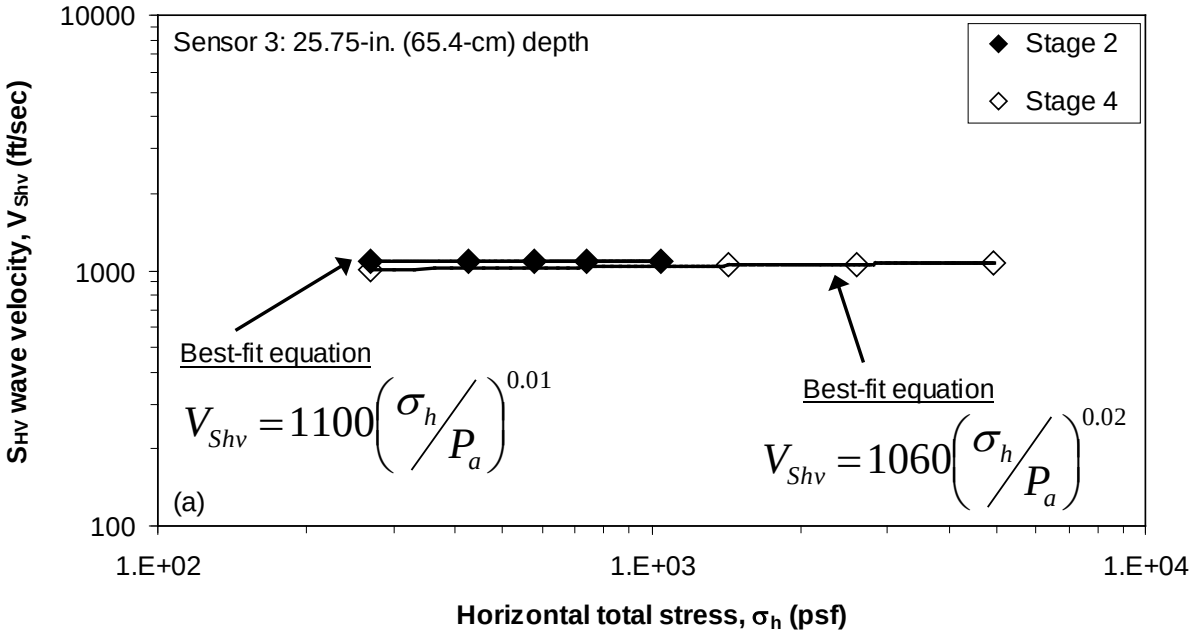

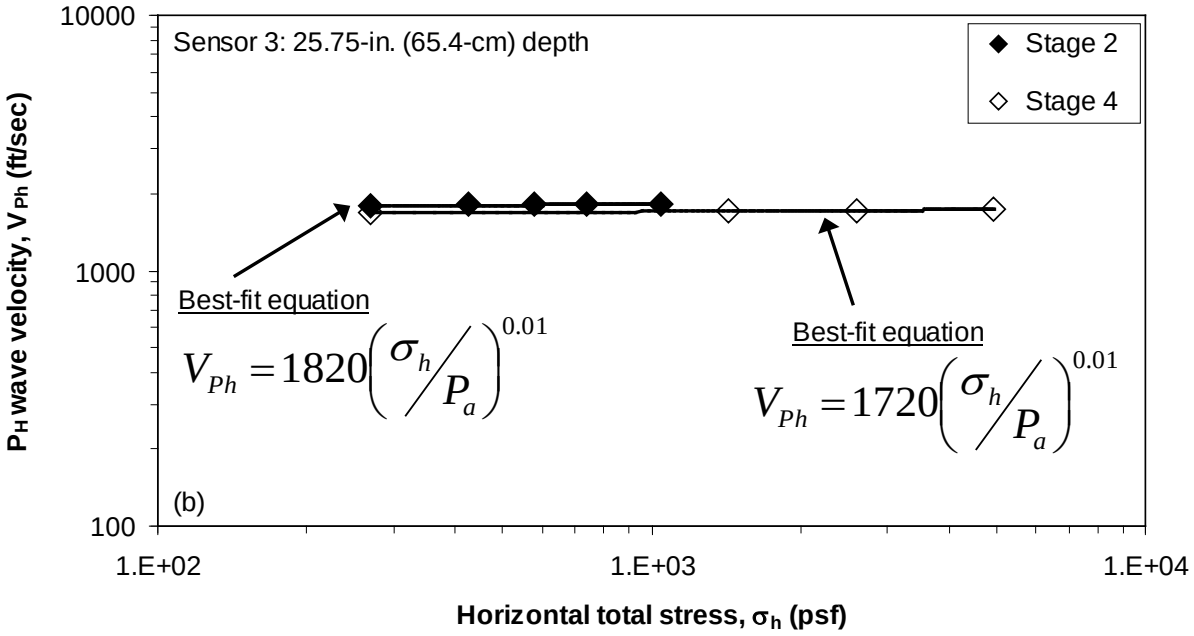

Figure 5.15. Variation of (a) S_{HV}-wave velocity and (b) P_H-wave velocity with increasing stress level at a depth of 25.75 in. (65.4 cm) below the base of the concrete footing

Table 5.5. Summary of best-fit equations obtained from crosshole tests at Site 1

Depth	Stage	Total stress equations	Average total stress equations (based on all stages)
9.75 in.	2	$V_{Shv} = 1270\left(\sigma_h / P_a\right)^{0.01}$ $V_{Ph} = 2080\left(\sigma_h / P_a\right)^{0.01}$	$V_{Shv} = 1280\left(\sigma_h / P_a\right)^{0.02}$ $V_{Ph} = 2070\left(\sigma_h / P_a\right)^{0.01}$
	4	$V_{Shv} = 1300\left(\sigma_h / P_a\right)^{0.02}$ $V_{Ph} = 2060\left(\sigma_h / P_a\right)^{0.01}$	
17.75 in.	2	$V_{Shv} = 1140\left(\sigma_h / P_a\right)^{0.02}$ $V_{Ph} = 1890\left(\sigma_h / P_a\right)^{0.01}$	$V_{Shv} = 1150\left(\sigma_h / P_a\right)^{0.02}$ $V_{Ph} = 1850\left(\sigma_h / P_a\right)^{0.01}$
	4	$V_{Shv} = 1150\left(\sigma_h / P_a\right)^{0.02}$ $V_{Ph} = 1800\left(\sigma_h / P_a\right)^{0.01}$	
25.75 in.	2	$V_{Shv} = 1100\left(\sigma_h / P_a\right)^{0.01}$ $V_{Ph} = 1820\left(\sigma_h / P_a\right)^{0.01}$	$V_{Shv} = 1070\left(\sigma_h / P_a\right)^{0.02}$ $V_{Ph} = 1770\left(\sigma_h / P_a\right)^{0.01}$
	4	$V_{Shv} = 1060\left(\sigma_h / P_a\right)^{0.02}$ $V_{Ph} = 1720\left(\sigma_h / P_a\right)^{0.01}$	

**Note: Depths are the distances from the base of the footing to each sensor (see Figure 5.8a)

the largest difference noted between Stages 2 and 4 in the crosshole tests. This difference could be attributed to several factors, including: (1) variability in the seismic measurements, (2) difficulty in identifying the wave arrivals for complex waveforms such as those shown in Figures 5.10 and 5.11, (3) the use of best-fit equations based on total stresses rather than effective stresses, (4) destruction (either complete or partial) of

cementation bonds present in the soil at the end of Stage 2. Still, the differences between Stages 2 and 4 are relatively minor since a single line-of-best-fit could be fit satisfactorily to the data from both stages (note the average best-fit equations listed in Table 5.5). This suggests that there was little, if any, effect on the soil structure due to the intervening steady-state vertical excitation imposed by T-Rex in Stage 3.

Additionally, Figures 5.13 through 5.15 provide some insight into the change in soil stiffness with depth as both V_{Shv} and V_{Ph} decrease with depth. The reduction of the wave velocities is most readily seen in the coefficients of the best-fit equations. These coefficients represent the S_{HV}- and P_H-wave velocities at one atmosphere ($V_{Shv,1}$ and $V_{Ph,1}$, respectively). Referring to the average best-fit equations in Table 5.5, the average $V_{Shv,1}$ at Sensor 1 was 1280 fps (390 m/s), the average $V_{Shv,1}$ at Sensor 2 was 1150 fps (351 m/s), and the average $V_{Shv,1}$ at Sensor 3 was 1070 fps (326 m/s). Similarly, the average $V_{Ph,1}$ at Sensor 1 was 2070 fps (631 m/s), the average $V_{Ph,1}$ at Sensor 2 was 1850 fps (564 m/s), and the average $V_{Ph,1}$ at Sensor 3 was 1770 fps (540 m/s).

5.4.3 Poisson's ratio

Poisson's ratio (ν) is related to the small-strain crosshole wave velocities by the relation:

$$\frac{V_{Ph}}{V_{Shv}} = \sqrt{\frac{2(1+\nu)}{1-2\nu}} \qquad (5.1)$$

which assumes that the soil is homogeneous and isotropic (Richart et al. 1970). The Poisson's ratio in the crosshole tests was calculated at every depth in the embedded sensor array using Equation 5.1. The crosshole velocities used in Equation 5.1 were the $V_{Shv,1}$ and $V_{Ph,1}$ values from the average total stress relationships given in Table 5.5. The Poisson's ratios in the crosshole tests are summarized in Table 5.6 for all depths in the embedded sensor array. As seen in Table 5.6, the Poisson's ratios at all depths are

Table 5.6. Poisson's ratios determined in the crosshole tests at Site 1

Crosshole tests	
Depth (in.)	Poisson's ratio, ν
9.75	0.19
17.75	0.19
25.75	0.21

Note: Poisson's ratio calculated using V_{Ph} and V_{Shv} at one atmosphere

positive and vary over a very small range (0.19 to 0.21). Therefore, the results of the crosshole tests do not indicate the presence of significant structural anisotropy in the soil, and the isotropic assumption inherent in Equation 5.1 appears to be valid for Site 1.

5.5 SMALL-STRAIN DOWNHOLE TESTS

Transient, small-strain downhole tests were conducted at Site 1 in Stages 2 and 4, as indicated in Figure 5.6. Within each stage, the S_{VH}- and P_V-wave velocities (V_{Svh} and V_{Pv}, respectively) were measured at several different confining pressures (load steps shown in Figure 5.6). In this manner, the effect of confining pressure on V_{Svh} and V_{Pv} was examined. The measurements of V_{Svh} and V_{Pv}, including typical data, and the effect of confining pressure are presented in this section. Note that in this section, the confining pressures used are based on total stresses, but as discussed in Section 4.3.3, negative pore pressures were likely present in the soil at the time of the tests at Site 1. The presence of negative pore pressures makes relationships based on total stress largely unsuitable for determining whether the soil became normally-consolidated over the range of induced stresses since it is the effective, not total, stresses that affect the wave velocities. However, since the tests at Site 1 were limited to "proof-of-concept" type tests, the effective stresses in the field were not estimated at Site 1. Note that for the more robust suite of tests at Site 2, the effective stresses in the field were estimated using the suction stress concept (discussed in Section 6.2.3), and the results of the downhole tests at Site 2 are presented in the form of effective stress relationships (see Section 7.2).

5.5.1 Measurement of V_{Svh} and V_{Pv} under the footing

As mentioned in Section 5.3.2, S_{VH} waves were generated in the small-strain downhole tests by striking the side of a 3-ft (0.91-m) diameter, concrete footing that was positioned over the sensor array (see Figure 5.8). P_H waves were generated by striking the top of the concrete footing in Stage 2 (Figure 5.8b) and the edge of T-Rex's load plate in Stage 4 (Figure 5.9). The downhole wave velocities (V_{Svh} and V_{Pv}) were calculated using the receiver-to-receiver travel times between the three sensors under the center of the footing (Sensors 1, 2, and 3). The wave arrivals were generally clear enough to be determined by eye using the procedures described in Chapter 4. Typical examples from the Stage 2 downhole tests showing the calculation of V_{Svh} and V_{Pv} between the sensors in the center column are shown in Figures 5.16 and 5.17, respectively.

5.5.2 Effect of confining pressure on V_{Svh} and V_{Pv}

In the downhole tests conducted in Stages 2 and 4, the V_{Svh} and V_{Pv} between adjacent sensors (Sensor pairs 1-2 and 2-3) were determined for each level of static load (load steps shown in Figure 5.6), as described in Section 5.4.1. As in the crosshole tests described in Section 5.4.2, the vertical stress (σ_v) induced by each load step was estimated using a Boussinesq stress distribution. However, since the wave velocities were determined between adjacent sensors, these velocities are representative of the area between sensors rather than at the sensor depths as assumed in the crosshole tests. Accordingly, the induced σ_v was calculated at the midpoint between sensors, as the stress at this point was assumed to be a good representation of the state of stress between the sensors. As in the crosshole tests, K_o was again assumed to be equal to 1.0. In the downhole tests, the variations of both V_{Svh} and V_{Pv} with stress level are given in the form of log V_{Svh} – log σ_v and log V_{Pv} – log σ_v relationships. These relationships are shown for the Sensor 1-2 pair (midpoint depth of 13.75 in. (34.9 cm)) in Figure 5.18 and for the Sensor 2-3 pair (midpoint depth of 21.75 in. (55.2 cm)) in Figure 5.19. The equations of

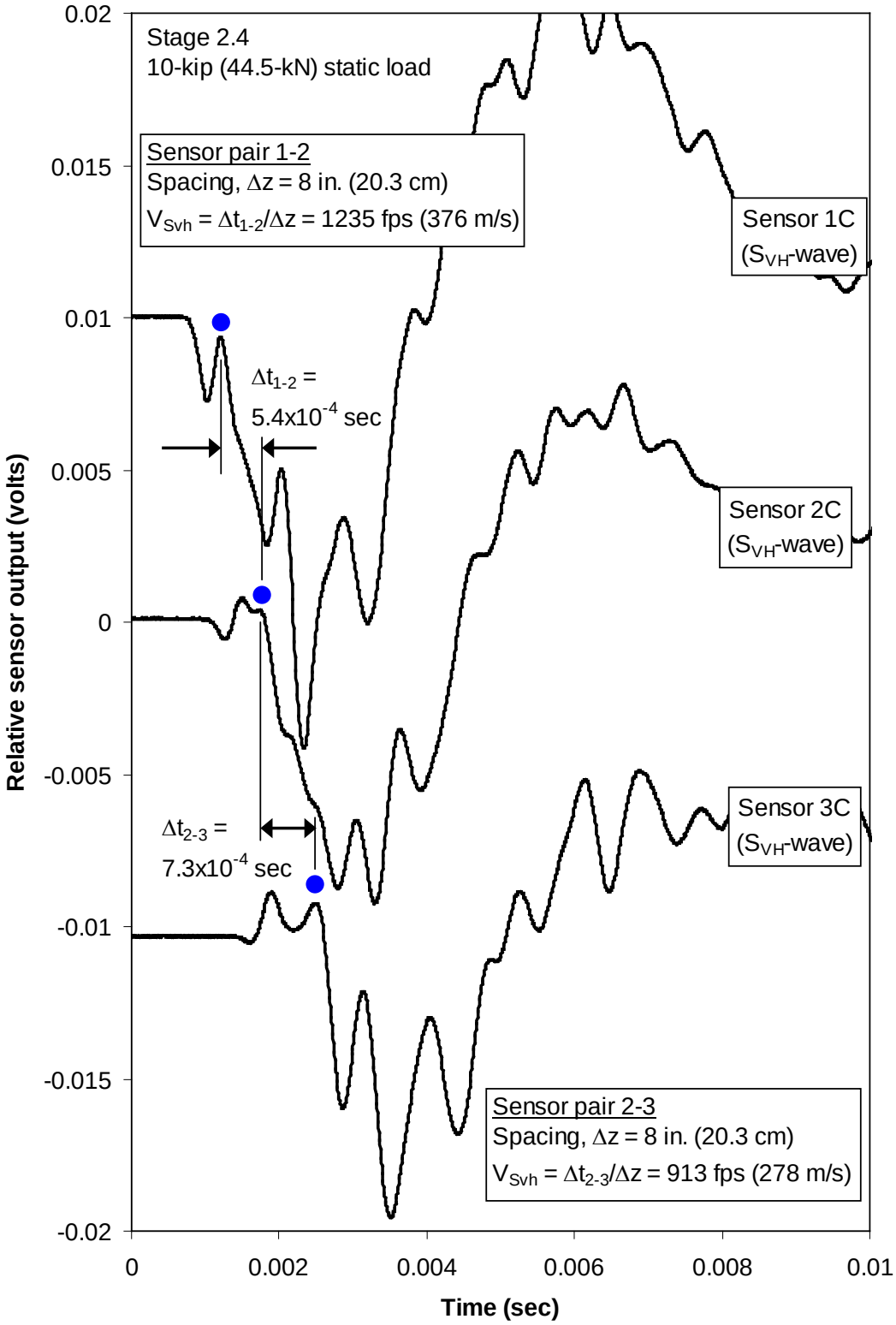

Figure 5.16. Determination of V_{Svh} using Stage 2.4 downhole data

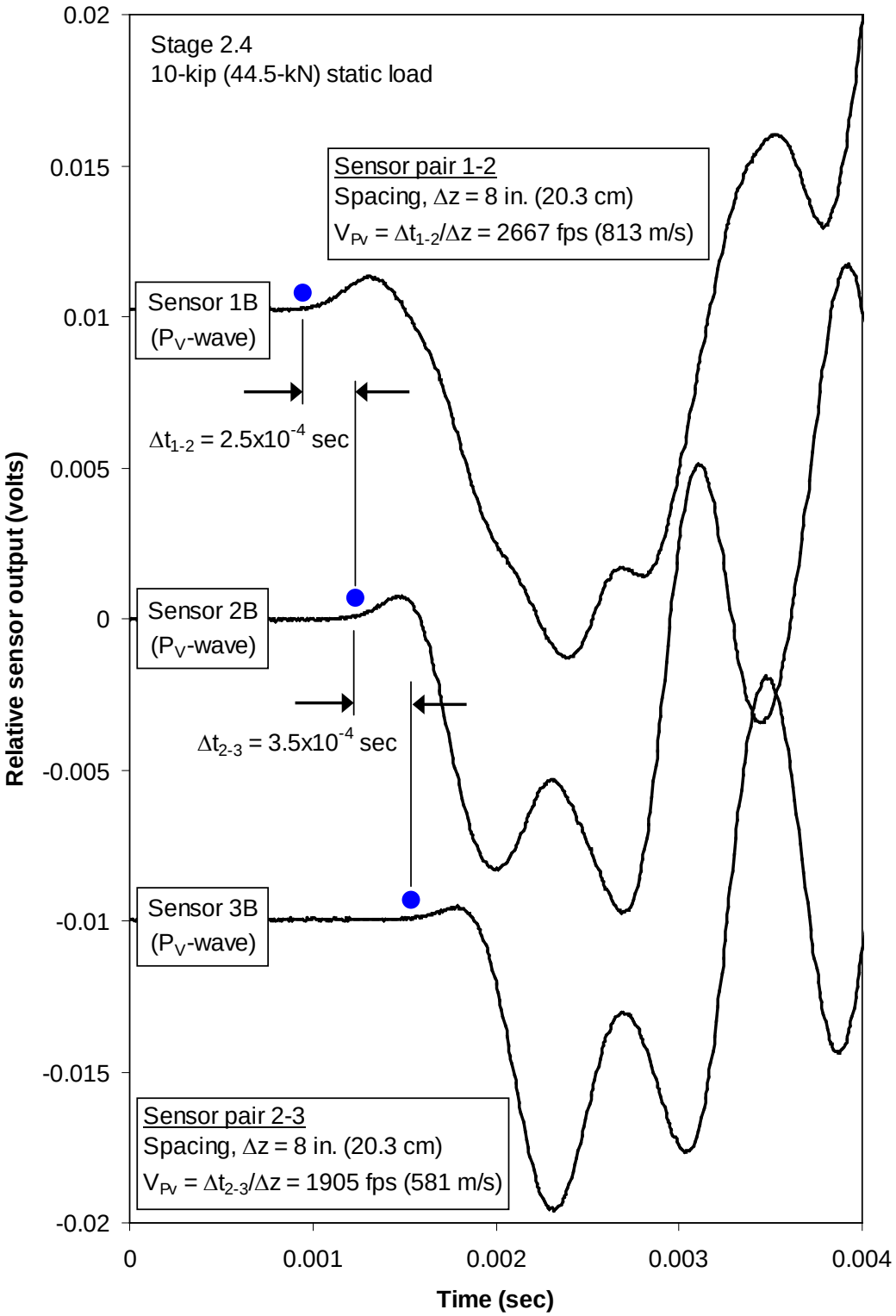

Figure 5.17. Determination of V_{Pv} using Stage 2.4 downhole data

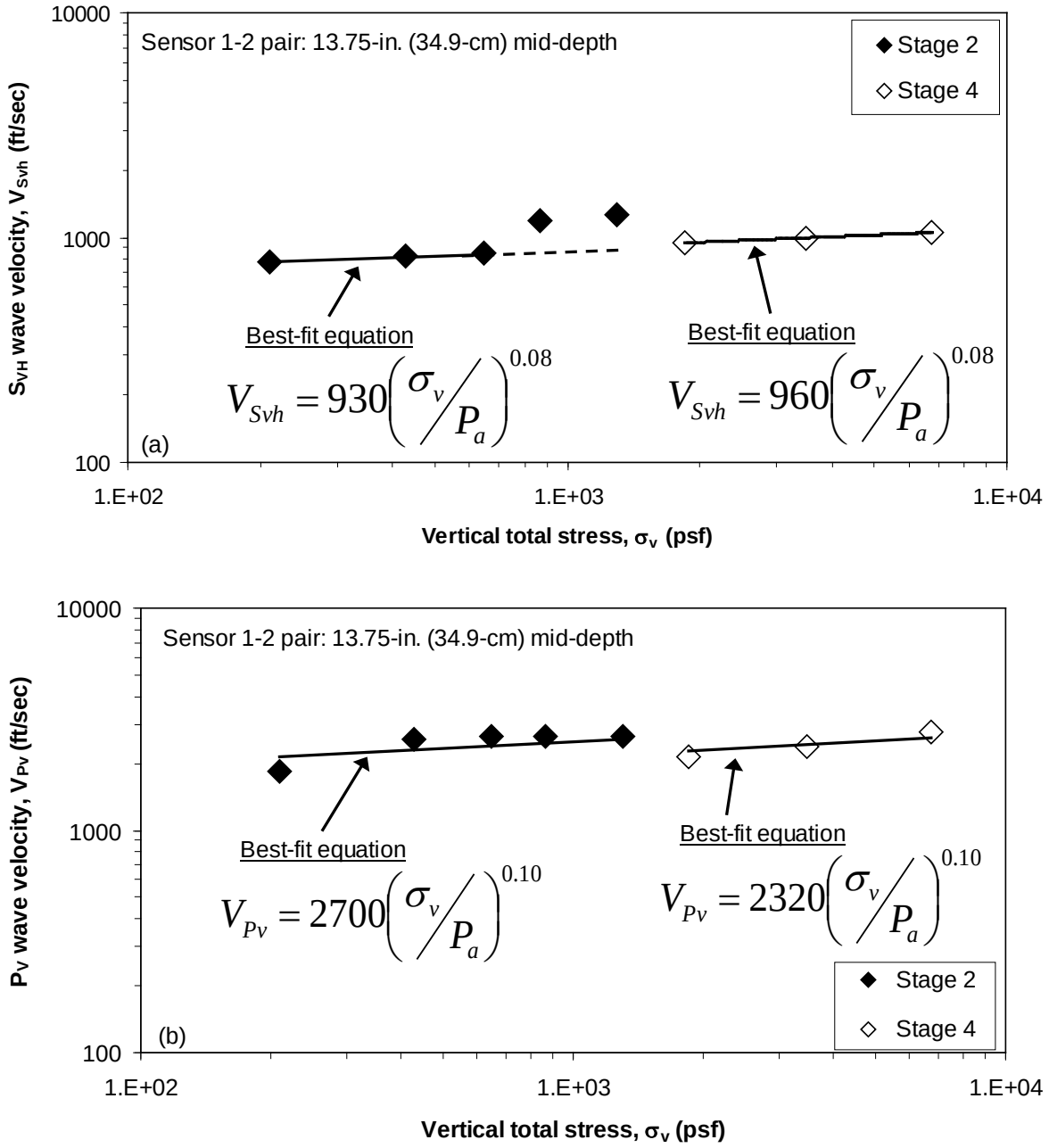

Figure 5.18. Variation of (a) S_{VH}-wave velocity and (b) P_V-wave velocity with increasing stress level at a midpoint depth of 13.75 in. (34.9 cm) below the base of the concrete footing

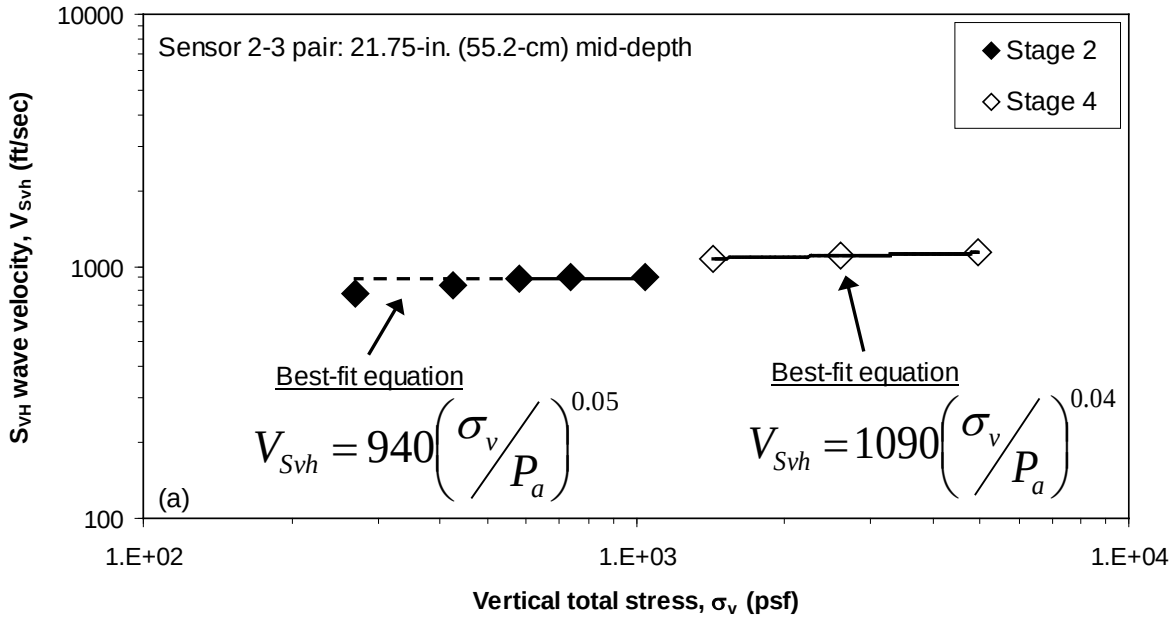

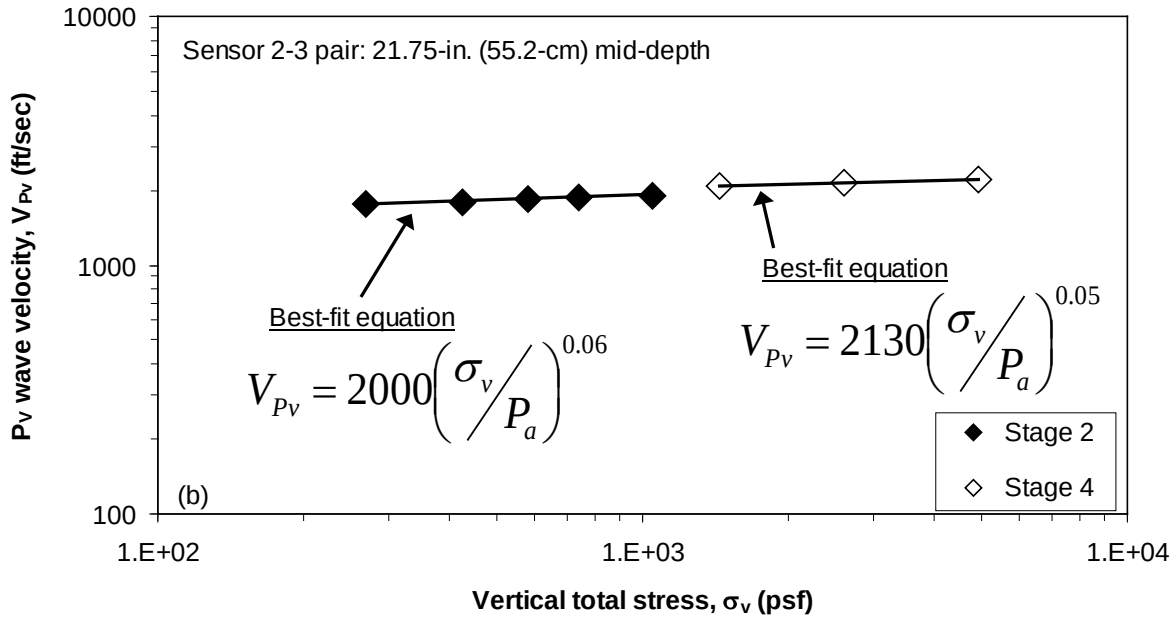

Figure 5.19. Variation of (a) S_{VH}-wave velocity and (b) P_V-wave velocity with increasing stress level at a midpoint depth of 21.75 in. (55.2 cm) below the base of the concrete footing

the best-fit lines given in Figures 5.18 and 5.19 are summarized in Table 5.7. Note that in the best-fit equations, σ_v is normalized by the atmospheric pressure (P_a) following the model suggested by Hardin (1978). Additionally, the average best-fit equations (based on both Stages 2 and 4) for each depth are included in Table 5.7.

In Figure 5.18a, the log V_{Svh} – log σ_v relationship for the Sensor 1-2 pair is basically the same in Stages 2 and 4. Note that with the exception of two apparently outlying points in Stage 2, a single line-of-best-fit could be used with little loss of accuracy. The exponent of the normal stress of these log V_{Svh} – log σ_v lines (0.08) is quite similar to the exponent of the log V_{Pv} – log σ_v lines (0.10) in Stages 2 and 4 (Figure 5.18b). These exponents indicate that the soil is heavily overconsolidated even at the higher stresses applied in Stage 4. Similar conclusions can be made concerning the Sensor 2-3 pair (Figure 5.19) as the exponents of the best-fit lines are about the same in both Stages 2 and 4. Indeed, in each downhole case listed in Table 5.7 at Site 1, a single line-of-best-fit could satisfactorily represent the behavior of both Stages 2 and 4, except perhaps for the case of V_{Pv} at the sensor 1-2 pair (Figure 5.18b). At this depth, there is about a 400 fps (122 m/s) decrease in the coefficients of the best-fit equations (the V_{Pv} at one atmosphere, or $V_{Pv,1}$). This reduction is still rather small (about 15%) and could be due to several factors, including: (1) variability in the seismic measurements, (2) seating or bedding-in of the concrete footing at the beginning of Stage 4, (3) the 2-day time delay that occurred between Stages 2 and 4, and (4) destruction (either complete or partial) of cementation bonds present in the soil at the end of Stage 2. However, taken as a whole, the results of the downhole tests shown in Figures 5.18 and 5.19 suggest that the soil remained overconsolidated in the range of stresses applied at Site 1 and that the intervening steady-state excitations in Stage 3 had little, if any, effect on the soil structure.

Table 5.7. Summary of best-fit equations obtained from downhole tests at Site 1

Depth	Stage	Total stress equations	Average total stress equations (based on all stages)
13.75 in.	2	$V_{Svh} = 930\left(\sigma_v / P_a\right)^{0.08}$ $V_{Pv} = 2700\left(\sigma_v / P_a\right)^{0.10}$	$V_{Svh} = 950\left(\sigma_v / P_a\right)^{0.08}$ $V_{Pv} = 2500\left(\sigma_v / P_a\right)^{0.10}$
	4	$V_{Svh} = 960\left(\sigma_v / P_a\right)^{0.08}$ $V_{Pv} = 2320\left(\sigma_v / P_a\right)^{0.10}$	
21.75 in.	2	$V_{Svh} = 940\left(\sigma_v / P_a\right)^{0.05}$ $V_{Pv} = 2000\left(\sigma_v / P_a\right)^{0.06}$	$V_{Svh} = 1010\left(\sigma_v / P_a\right)^{0.05}$ $V_{Pv} = 2100\left(\sigma_v / P_a\right)^{0.06}$
	4	$V_{Svh} = 1090\left(\sigma_v / P_a\right)^{0.04}$ $V_{Pv} = 2130\left(\sigma_v / P_a\right)^{0.05}$	

**Note: Depths are the distances from the base of the footing to the midpoint of each sensor pair (see Figure 5.8a)

As in the crosshole tests, the results of the downhole tests also reveal a decrease in V_{Pv} with depth. The decrease in V_{Pv} is most readily seen in the coefficients of the best-fit equations ($V_{Pv,1}$). Referring to the average best-fit equations in Table 5.7, the average $V_{Ph,1}$ at the Sensor 1-2 pair was 2500 fps (762 m/s) and the average $V_{Ph,1}$ at the Sensor 2-3 pair was 2100 fps (640 m/s). The variation of V_{Svh} with depth is less prevalent, as there is little difference between the S_{VH}-wave velocities at the two depths.

Referring to the summarized results of the small-strain crosshole and downhole tests (Tables 5.5 and 5.7, respectively), several observations can be made about Site 1. First, both the crosshole or downhole tests show that the soil remained heavily

overconsolidated over the range of stresses used in the field. There is also no clear evidence that the sinusoidal excitations imposed in Stage 3 had any effect on the soil structure since, in most cases, the behavior observed in Stage 2 was similar to that observed in Stage 4. In general, the downhole wave velocities (V_{Svh} and V_{Pv}) increased with stress level at a rate roughly four times faster than that of the crosshole wave velocities (V_{Shv} and V_{Ph}). This effect was the same regardless of the depth or wave type (shear or compression) investigated. Additionally, while the V_{Shv} values obtained in the crosshole tests were slightly faster than the V_{Svh} values obtained in the downhole tests, the opposite effect was observed with the P-wave velocities (V_{Pv} was generally greater than V_{Ph}).

5.5.3 Poisson's ratio

Poisson's ratio (ν) is related to the small-strain downhole wave velocities by the relation:

$$\frac{V_{Pv}}{V_{Svh}} = \sqrt{\frac{2(1+\nu)}{1-2\nu}} \tag{5.2}$$

which assumes that the soil is homogeneous and isotropic (Richart et al. 1970). The Poisson's ratio in the downhole tests was calculated at every midpoint depth in the embedded sensor array using Equation 5.2. The downhole velocities used in Equation 5.2 were the $V_{Svh,1}$ and $V_{Pv,1}$ values from the average total stress relationships given in Table 5.7. The Poisson's ratios in the downhole tests are summarized in Table 5.8 for all depths in the embedded sensor array. As seen in Table 5.8, the Poisson's ratios at all depths are positive and vary over a relatively small range (0.35 to 0.42). Therefore, the results of the downhole tests do not indicate the presence of significant structural anisotropy in the soil, and the isotropic assumption inherent in Equation 5.2 appears to be valid for Site 1.

Table 5.8. Poisson's ratios determined in the downhole tests at Site 1

Downhole tests	
Depth (in.)	Poisson's ratio, ν
13.75	0.42
21.75	0.35

Note: Poisson's ratio calculated using V_{Ph} and V_{Shv} at one atmosphere

5.6 LINEAR AND NONLINEAR VERTICAL EXCITATION TESTS

To characterize linear and nonlinear constrained moduli, two stages of vertical excitation tests (Stages 1 and 3 in Figure 5.6) were conducted with the vibroseis positioned directly over the embedded sensor array (Figure 5.7). In Stage 1, 10 cycles of sinusoidal vertical excitation were applied with Thumper at four different levels of static load (the load steps shown in Figure 5.6). This procedure was repeated with T-Rex in the three load steps of Stage 3. In this section, the process used to verify that vertically-propagating, constrained compression (P_V) waves were generated by the vibroseis is discussed. Additionally, the effect of increasing axial strain on the constrained moduli of soil is also presented.

5.6.1 Generation of P_V waves by vertical sinusoidal excitation

As shown in Section 4.4.1, the constrained moduli of soil can be determined if the constrained compression wave velocity (V_{Pv}) is measured. Therefore, it is essential to verify that the vertical sinusoidal excitation tests successfully induced constrained compression (P_V) waves and not unconstrained (or partially-constrained) compression waves. The first step required to verify that P_V waves were generated is to examine the raw voltage records of all three components (one vertical; two horizontal) in the sensors. The raw voltage-time records of the three sensors in the center column (Sensors 1, 2, and 3) are shown in Figure 5.20. The voltage-time records under the highest level of vertical excitation applied with Thumper are shown in Figure 5.20a, and the records under the

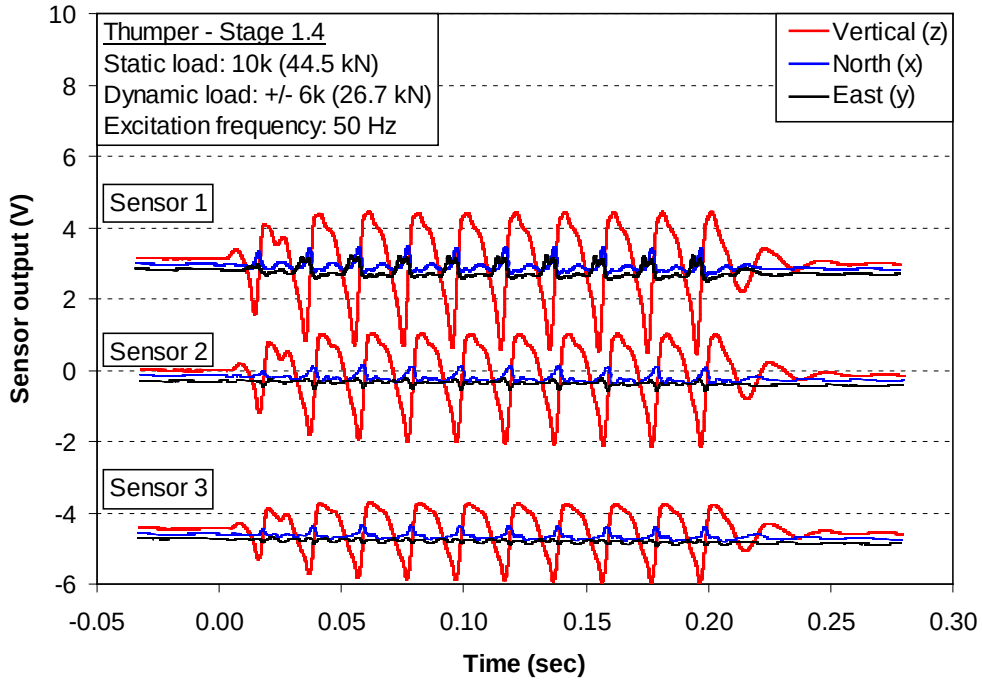

(a)

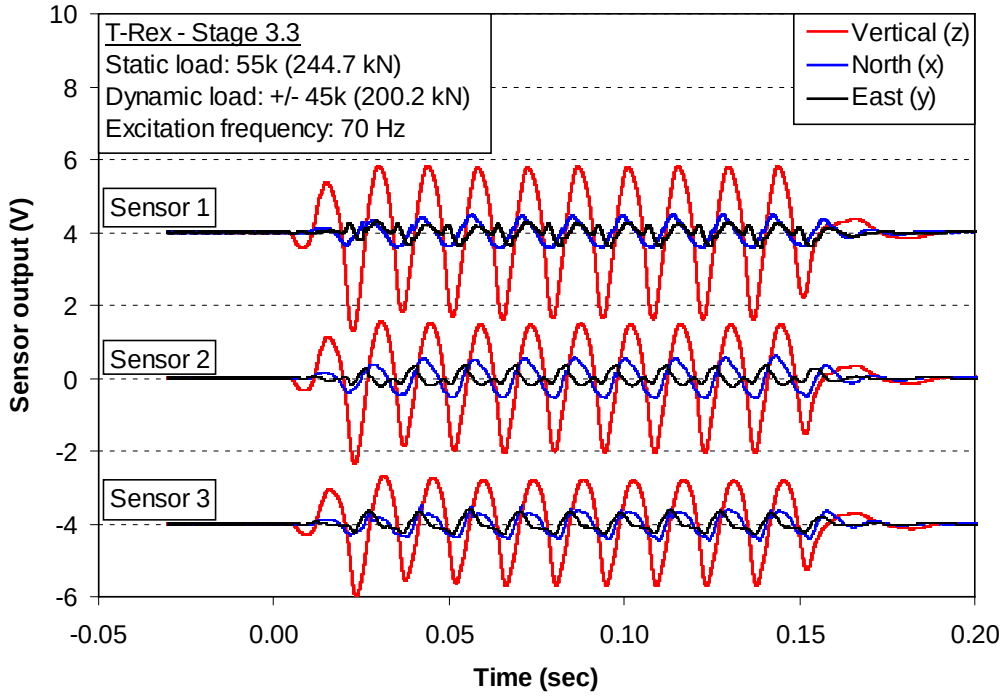

(b)

Figure 5.20. Voltage-time histories from three sensors subjected to sinusoidal vertical excitation at Site 1: (a) Stage 1.4 with Thumper and (b) Stage 3.3 with T-Rex

highest level of vertical excitation applied with T-Rex are shown in Figure 5.20b. As seen in Figure 5.20, more horizontal motion was generated by T-Rex than Thumper, but in both cases, the voltage output of the vertically-oriented geophone was about five to ten times greater than those of either horizontally-oriented geophone. This observation was true at all three sensors in the center column. Therefore, it was concluded that both shakers induced primarily vertically-propagating waves. To determine whether these waves were indeed P_V waves, the steady-state compression wave velocities measured under the lowest levels of vertical excitation imposed in each load step, i.e. at the smallest induced strains, were compared to the transient, small-strain V_{Pv} measured in the downhole seismic tests. The steady-state compression wave velocities were determined using the time-shift of the cross-correlation sequence as described in Chapter 4. A comparison of the steady-state, small-strain wave velocities and the transient, small-strain V_{Pv} is shown in Figure 5.21a for the Sensor 1-2 pair and in Figure 5.21b for the Sensor 2-3 pair. Note that the steady-state velocities calculated in Stage 3 (with T-Rex) are at slightly different confining pressures since T-Rex's load plate is larger than both the 3-ft (0.91-m) load plate of Thumper and the 3-ft (0.91-m) diameter concrete footing. The small-strain unconstrained compression wave velocity (V_C) is also shown in Figure 5.21 and was determined using the relation:

$$V_C = V_{Svh}\sqrt{2(1+\nu)} \tag{5.3}$$

where ν is the Poisson's ratio calculated by Equation 5.1 (Richart et al. 1970). As seen in Figure 5.21a, the steady-state wave velocities measured at a depth of 13.75 in. (34.9 cm) fall somewhere between V_C and V_{Pv} in both Stages 1 and 3. This difference could be due to the compression waves generated at this depth by both Thumper and T-Rex being partially-constrained or could simply be "scatter" in the measurements. In Stage 1, the steady-state wave velocities tend to become closer to the small-strain V_{Pv} as the vertical confining pressure applied with Thumper is increased. The steady-state wave velocities measured at the middle two load steps in Stage 1 are within about 10% of V_{Pv}. At a

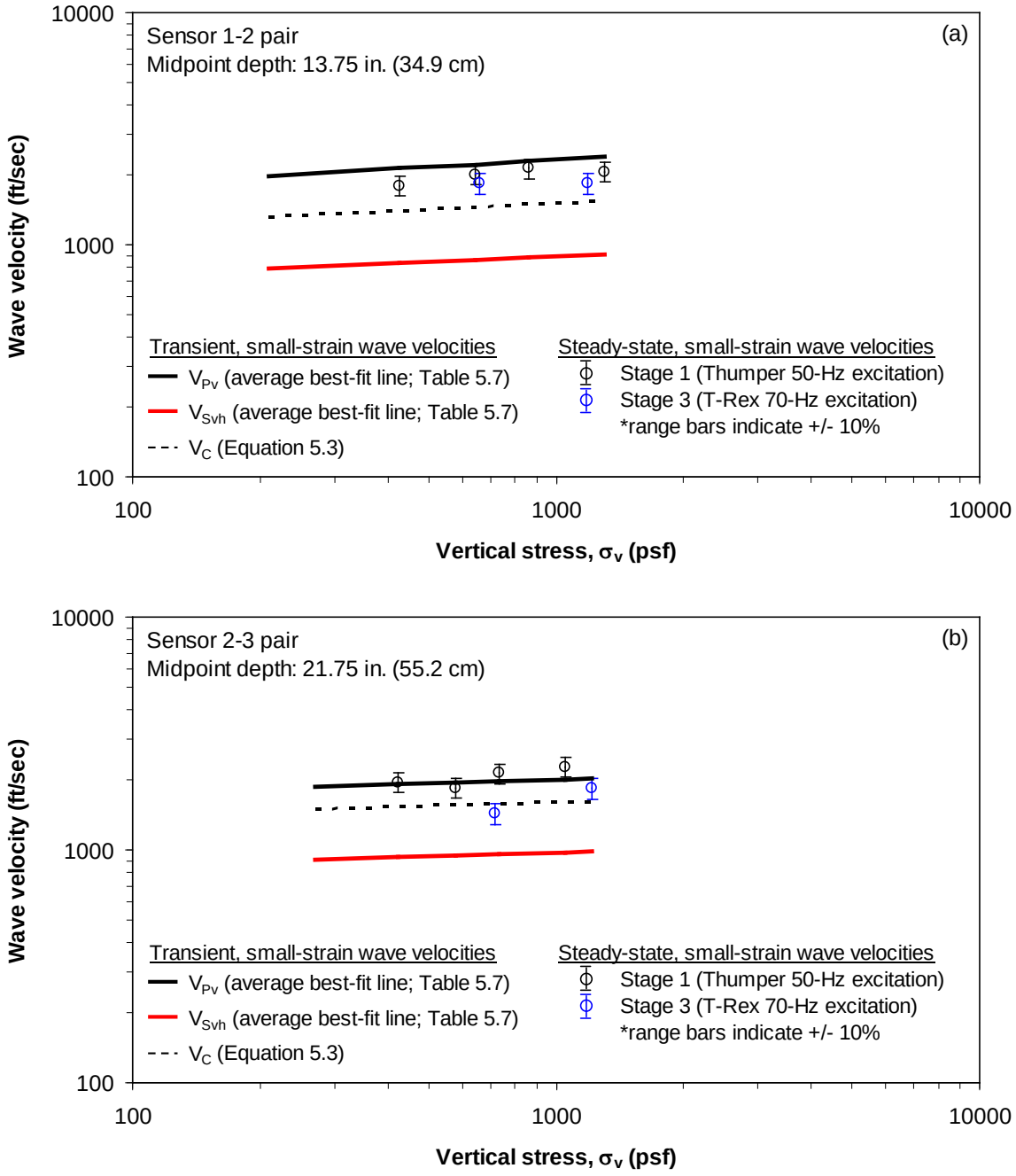

Figure 5.21. Comparison of steady-state, small-strain wave velocities with the transient, small-strain P_V-wave velocities at Site 1: (a) Sensor 1-2 pair and (b) Sensor 2-3 pair

depth of 21.75 in. (55.2 cm), the steady-state wave velocities measured at all load steps in Stage 1 agree much more closely with the small-strain V_{Pv} rather than the small-strain V_C (Figure 5.21b). This good agreement between the transient and steady-state small-strain velocities is much better than at the shallower depth and was taken to confirm that Thumper was capable of generating constrained compression waves beneath the centerline of the load plate. Furthermore, at the last load step in Stage 3, T-Rex also generated constrained compression waves at this depth (note blue dots shown in Figure 5.21b). Based on these observations, it was concluded that P_V waves were successfully generated in Stages 1.2 and 1.3 at the midpoint of the Sensor 1-2 pair and in Stages 1.1, 1.2, 1.3, 1.4, and 3.3 at the midpoint of the Sensor 2-3 pair (refer to Figure 5.6 for the load step naming convention). Therefore, these were the only cases where the effects of increasing axial strain on the constrained moduli were examined. A discussion of these effects is provided in Section 5.6.2.

The behavior of the waves generated by Thumper and T-Rex can also be partially characterized by examining the records of the sensors in the pre-existing cubical array. As shown in Figure 5.22, these sensors are located directly under the edge of the load plate of Thumper but still roughly in the center region of the much larger load plate of T-Rex. Accordingly, these sensors are ideally suited for examining the extent of the lateral confinement provided by the static vertical loads applied by the shakers. The voltage-time records of the vertical components of the four sensors in the original cubical array at a depth of 17-in. (43.2 cm) below the vibroseis load plate (Sensors 4, 5, 6, and 7) are shown in Figure 5.23 for two levels of vertical excitation with Thumper. The voltage-time output from Sensor 2 in the center column is also included in Figure 5.23 since it is at roughly the same depth (17.75 in. (45.1 cm)) as the four sensors mentioned above. At low levels of dynamic load amplitude (Figure 5.23a), the four sensors under the edge of the load plate of Thumper lag behind Sensor 2, but the amount of lag is relatively minor. However, at higher levels of dynamic load amplitude (Figure 5.23b) the lag is more pronounced, especially in the case of Sensor 7 which lags significantly behind all other

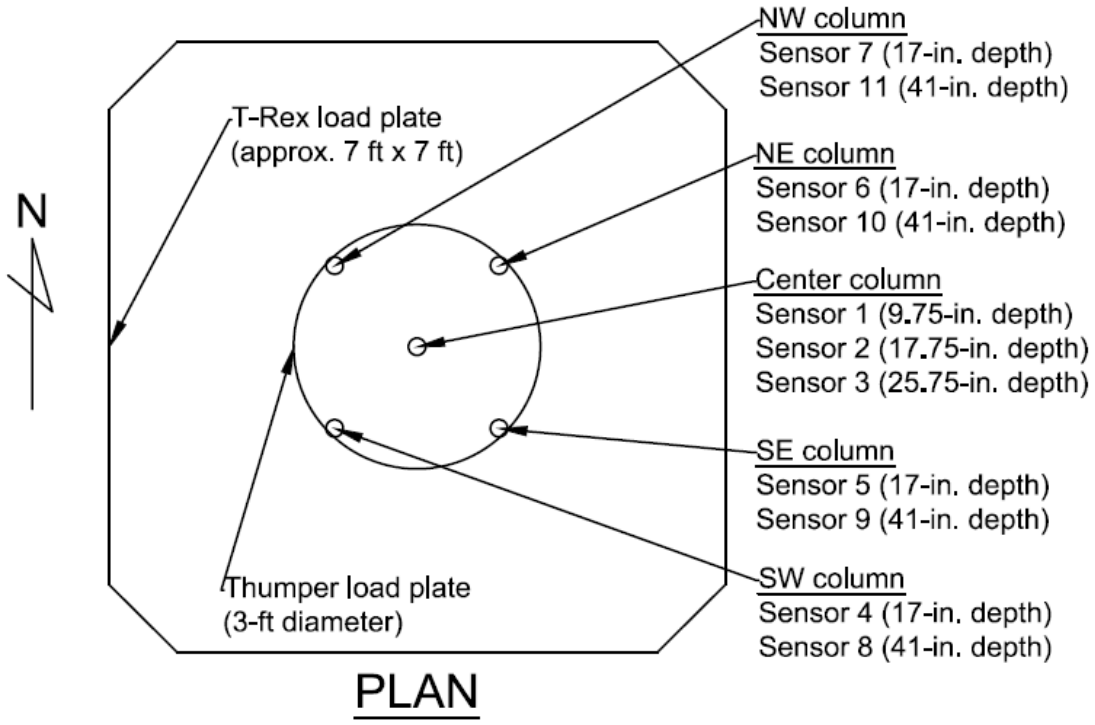

Figure 5.22. Plan view of the location of Site 1 sensor array relative to the load plates of Thumper and T-Rex

sensors. In general, the phase difference between the center column (Sensor 2) and the original cubical array (Sensors 4, 5, 6, and 7) was much less in Stage 3 when the loading was applied by the much larger load plate of T-Rex. The voltage-time records of these five sensors are shown in Figure 5.24 for two levels of vertical excitation with T-Rex. Except in the case of Sensor 7 at high levels of dynamic load amplitude (Figure 5.24b), the sensors in the cubical array are relatively in-phase with Sensor 2 in the center column. The behavior of the sensors in Figures 5.23 and 5.24 suggests that T-Rex was moderately better at generating planar waves which propagated vertically downward through the embedded sensor array. However, it should be noted that Thumper was still somewhat successful in generating vertically-propagating waves which were roughly planar even under the edges of its smaller load plate.

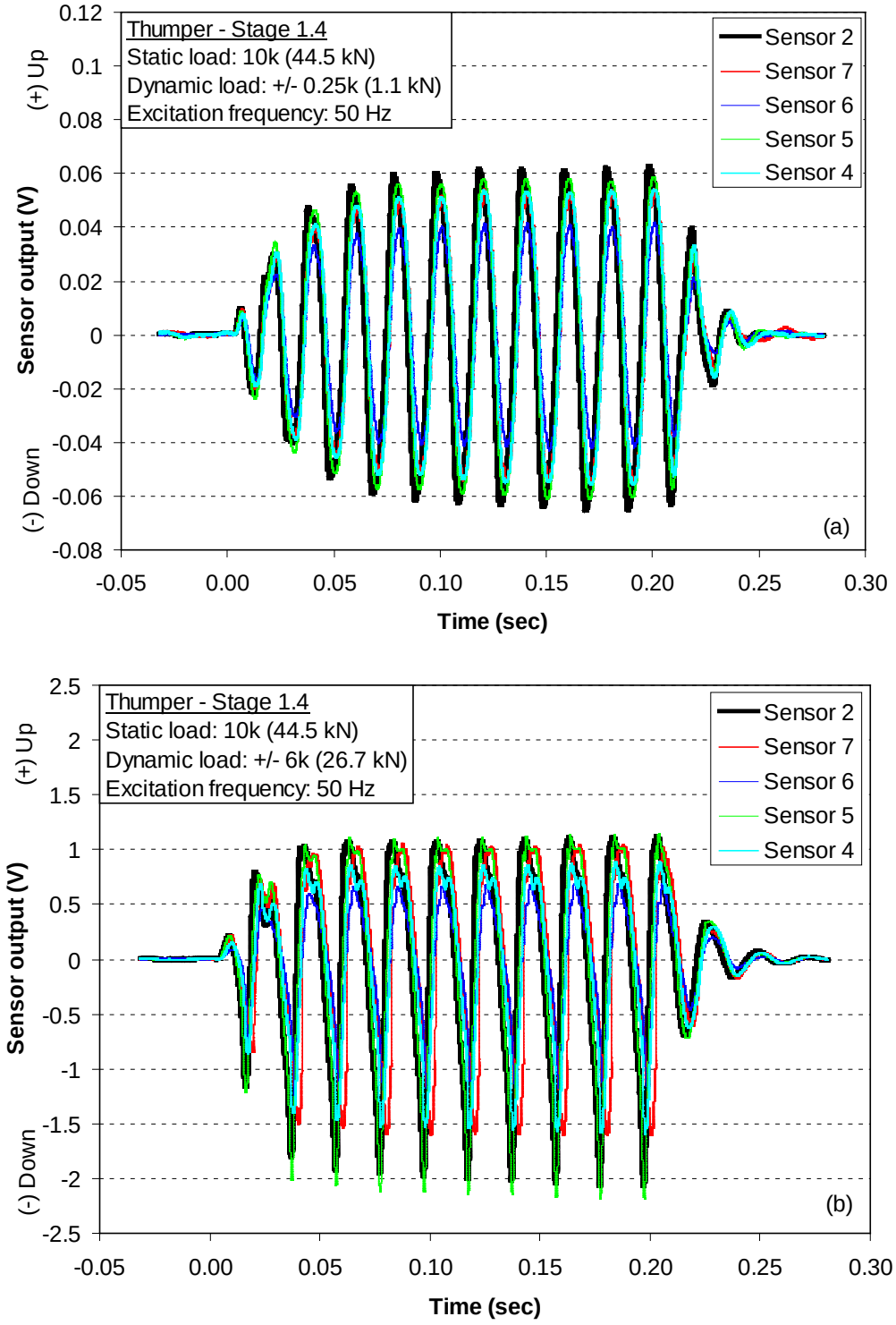

Figure 5.23. Voltage-time records of five sensors at Site 1 when subjected to vertical excitations imposed by Thumper in Stage 1.4: (a) low amplitude and (b) high amplitude

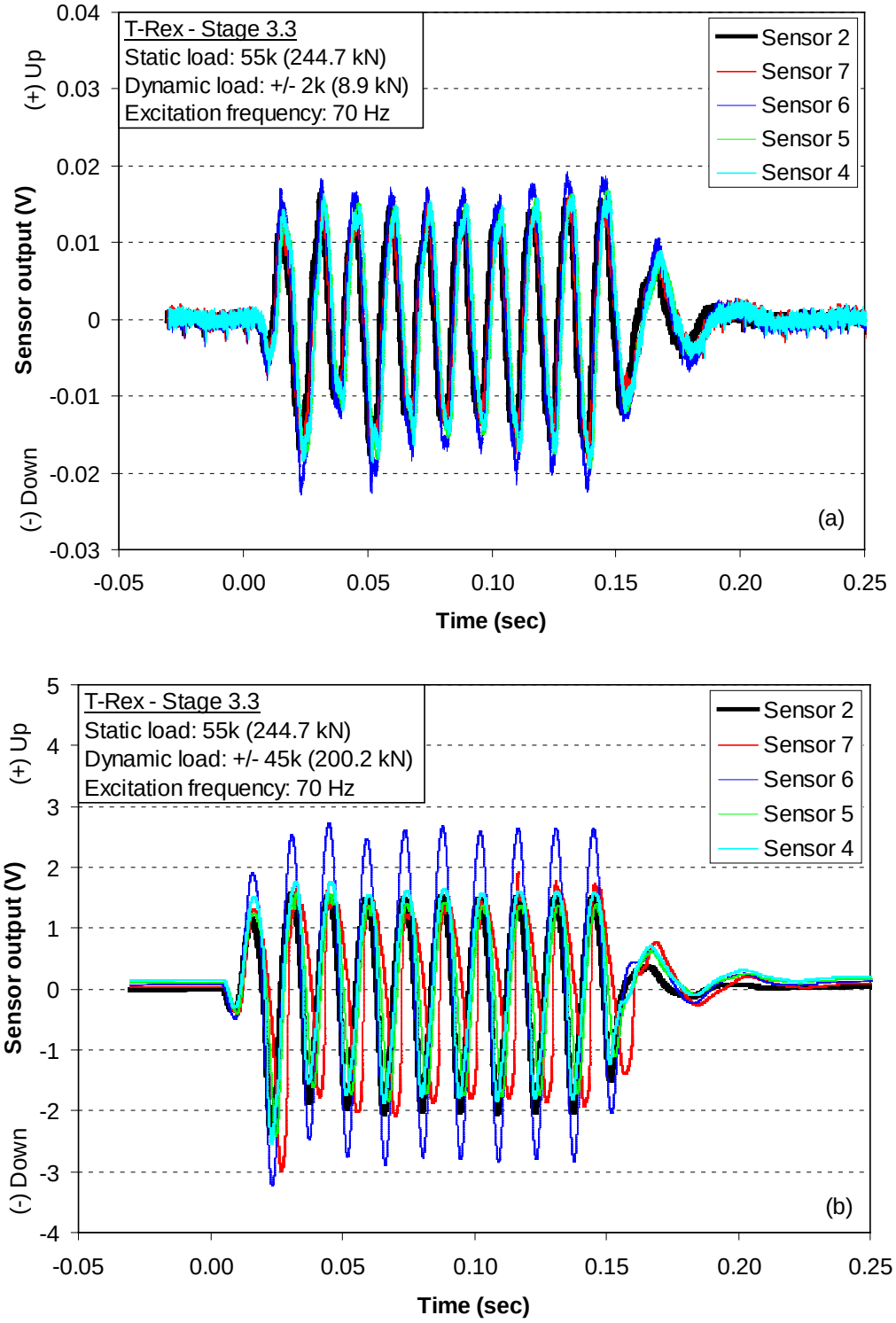

Figure 5.24. Voltage-time records of five sensors at Site 1 when subjected to vertical excitations imposed by T-Rex in Stage 3.3: (a) low amplitude and (b) high amplitude

As mentioned above, the sensors in the original cubical array were used to examine the extent of the lateral confinement provided by the load plate of the shakers. These measurements were helpful in designing the layout of the embedded sensor array at Site 2 (discussed in Chapter 6). To determine whether the compression waves generated by the vertical sinusoidal excitations were constrained or partially constrained at the locations of the sensors in the cubical array, a similar procedure as that described earlier was performed in which the steady-state, small-strain wave velocities between sensors were compared to the transient, small-strain V_{Pv} determined in the downhole seismic tests. The results of these analyses between two sensor pairs in the cubical array are shown in Figure 5.25. At both sensor pairs shown in Figure 5.25, the steady-state wave velocities calculated in Stage 1 are generally in poor agreement with the average small-strain V_{Pv}. However, the steady-state wave velocities in Stage 3 agree quite closely with the small-strain V_{Pv}. Therefore, it was assumed that T-Rex generated constrained compression waves at these locations while Thumper did not. This is not generally surprising, since one might expect the larger load plate of T-Rex (Stage 3) to induce more lateral confinement at the location of the cubical sensor array than the load plate of Thumper (Stage 1).

Based on the results presented in this section, it was concluded that generation of P_V waves was most successful at or near the centerline of the load plates of the shakers. While T-Rex was capable of generating P_V waves over a larger horizontal area than Thumper, the design of the embedded sensor array at Site 2 was selected such that it fell completely within the limits of the smaller load plate of Thumper (see Chapter 6). The effect of increasing axial strain along the centerline of the load plate on the constrained moduli at Site 1 is discussed in the next section.

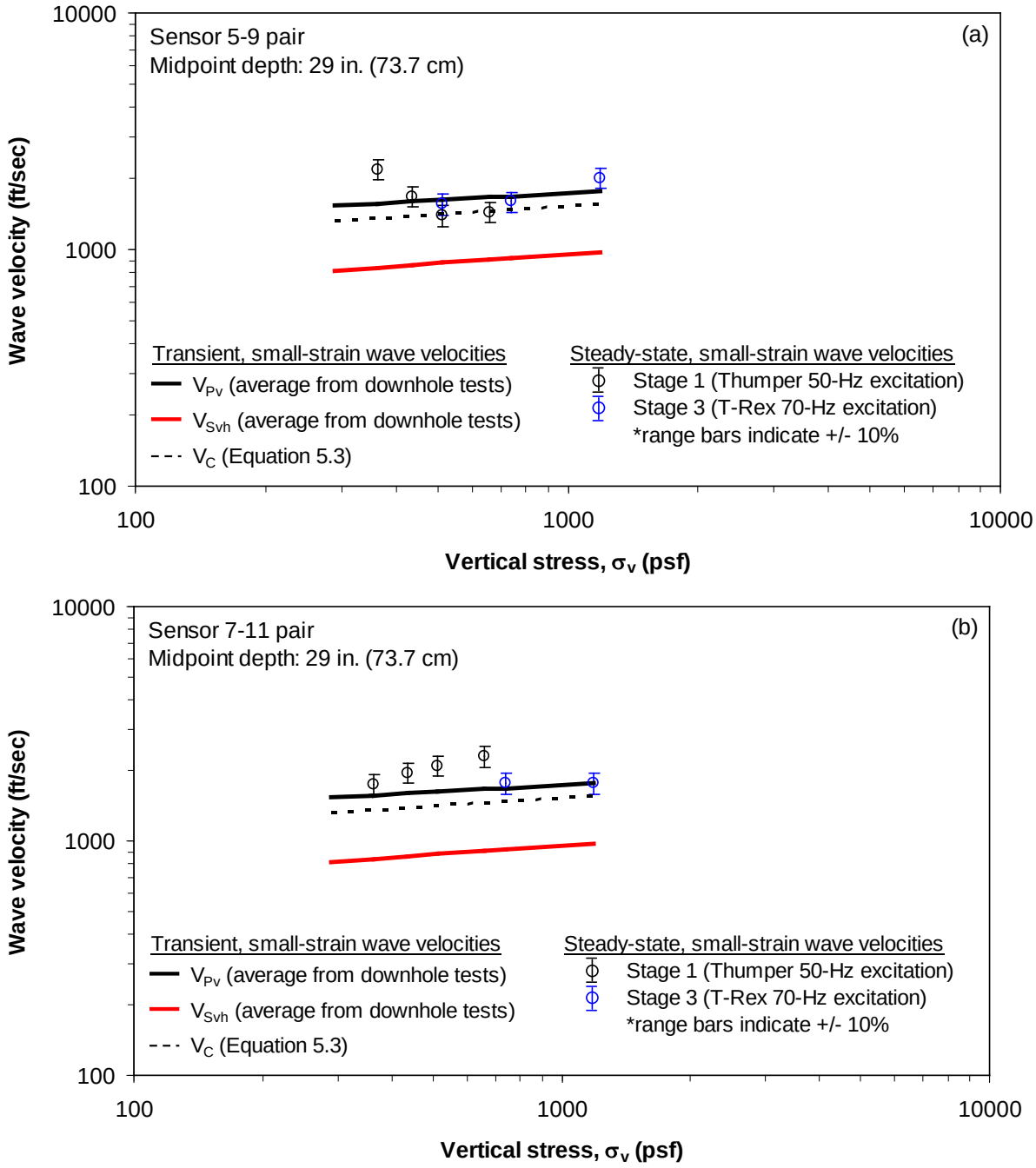

Figure 5.25. Comparison of steady-state, small-strain wave velocities with the transient, small-strain P_V-wave velocities at Site 1: (a) Sensor 5-9 pair and (b) Sensor 7-11 pair

5.6.2 Effect of increasing axial strain on constrained moduli

As discussed in Section 5.6.1, it was concluded that the shakers successfully induced P_V waves in Stages 1.2 and 1.3 at the midpoint of sensor pair 1-2 and in Stages 1.1, 1.2, 1.3, 1.4, and 3.3 at the midpoint of sensor pair 2-3. Following the process described in Chapter 4, both V_{Pv} and axial strain, ε, were calculated at every level of dynamic excitation applied in the stages listed above. The V_{Pv} at each strain level was related to the constrained modulus (M) using Equation 4.2a. The effect of increasing axial strain on the constrained moduli is discussed in this section for two locations under the centerline of the load plates of the shakers. As noted earlier, the most consistent results were found with the deeper sensor pair, so these results are presented first.

5.6.2.1 Results at sensor pair 2-3

The M – log ε relationships between Sensors 2 and 3 (midpoint depth of 21.75 in. (55.2 cm)) are shown in Figure 5.26 for five different load stages where P_V waves are believed to have been generated. The small-strain constrained moduli calculated using Equation 4.2a and V_{Pv} from the small-strain, transient downhole tests are also plotted in Figure 5.26. The axial strains associated with these transient downhole tests were calculated assuming a plane stress wave travelling vertically through the system using Richart et al. (1970) as:

$$\varepsilon = \frac{\dot{z}}{V_{Pv}} \tag{5.4}$$

where $\dot{z}$ represents the maximum particle velocity in the vertical direction. The axial strains in these tests ranged from 0.00008 to 0.00017%. The average axial strain was about 0.00014% and was used to represent ε for all transient downhole tests. Note that no downhole tests were conducted at the vertical confining pressure induced at this depth

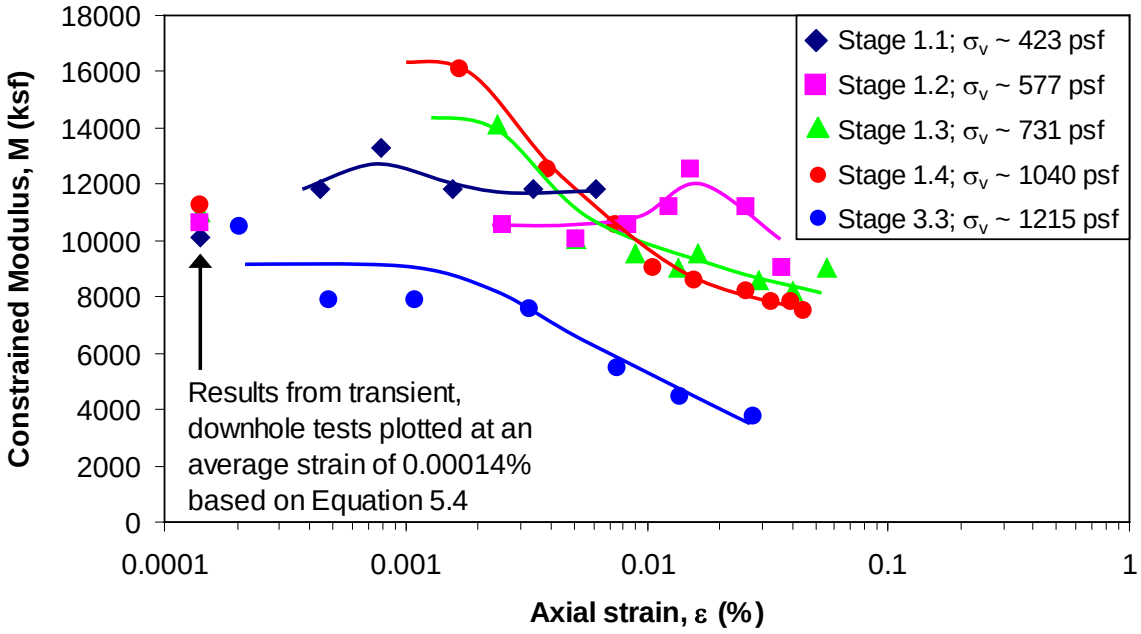

Figure 5.26. Variation of constrained modulus with axial strain at Site 1 between Sensors 2 and 3 (21.75-in. (55.2-cm) depth)

in Stage 3.3. However, the lowest induced strain in the steady-state tests in Stage 3.3 was about 0.0002%, and the constrained modulus at this strain is reasonably close to the constrained moduli from the transient downhole tests. As seen in Figure 5.26, the behavior of the M – log ε relationship at the midpoint of sensor pair 2-3 is indeed nonlinear, but it is also quite complex. At the lower confining pressures (Stages 1.1 and 1.2), M remains relatively constant with perhaps only a slight increase as the axial strain is increased. However, at larger confining pressures (Stages 1.3, 1.4, and 3.3), M decreases with increasing axial strain. Therefore, the M – log ε curve is more nonlinear at the highest confinements than it is at lower confinement states. This behavior of more strain dependency as σ_v increases has never before been observed and could possibly be due to several reasons including: (1) uncertainties in these new types of measurements and/or (2) degradation of the soil occurring at higher dynamic loads. As is typically done with shear modulus reduction curves, the M – log ε relationships at the different confining pressures shown in Figure 5.26 were normalized by M_{max} and are presented in

Figure 5.27 in the form of M/M_{max} – log ε relationships. It should be noted that the term M_{max} is used here to represent the M at small strains to follow the convention used to refer to the shear modulus at small strains (G_{max}). Though the strains generated in the downhole tests are indeed small, the constrained modulus at small-strains (M_{max}) was assumed to occur at the lowest strain induced in the steady-state excitation tests. This convention was chosen to avoid potential errors that may arise by using two different test methods. In Figure 5.27, the σ_v-dependent transition from M/M_{max} – log ε increasing with increasing axial strain to M/M_{max} – log ε decreasing with increasing axial strain is readily seen. Additionally, as opposed to the sensor 1-2 pair (discussed in Section 5.6.2.2), there are no strain ranges that are severely under-represented at this depth (21.75 in. (55.2 cm)). This information was used to design the embedded sensor array at Site 2 such that the midpoint of the first two sensors was far enough away from the load plates of the shakers to allow for a wide range of strains to be induced (see Chapter 6).

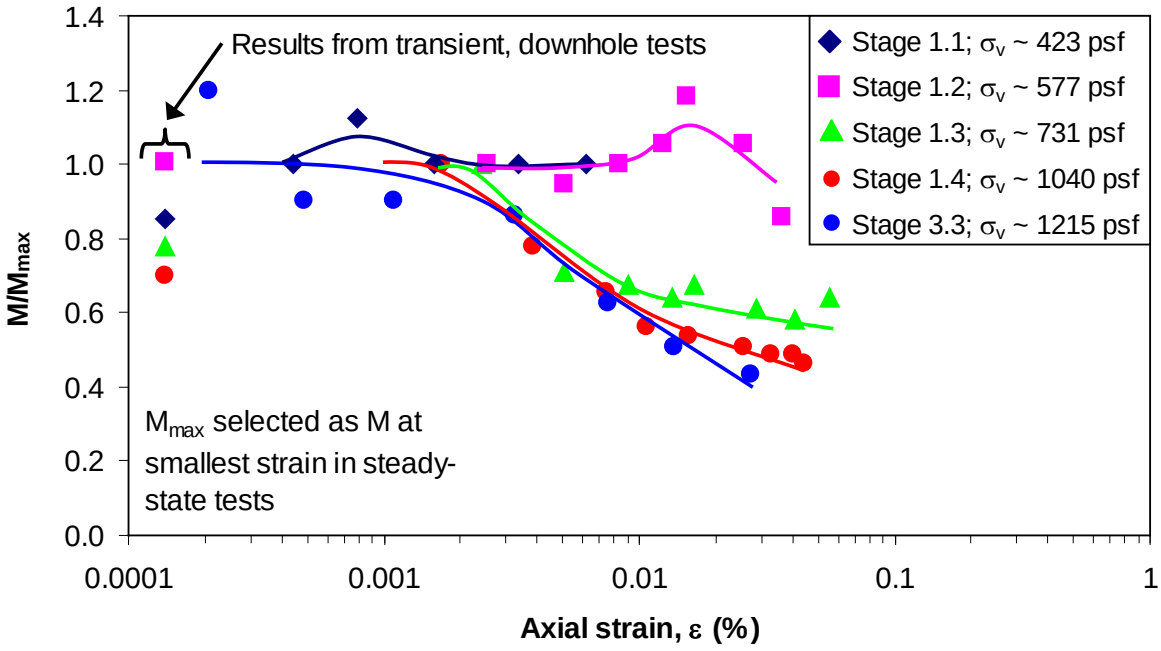

Figure 5.27. Variation of normalized constrained modulus with axial strain at Site 1 between Sensors 2 and 3 (21.75-in. (55.2-cm) depth)

5.6.2.2 Results at sensor pair 1-2

The variation of M with log ε is shown in Figure 5.28 for the midpoint of sensor pair 1-2 (13.75-in. (34.9-cm) depth). The small-strain constrained moduli calculated using Equation 4.2a and V_{Pv} from the small-strain, transient downhole tests are also plotted in Figure 5.28. Using Equation 5.4, the axial strains in these tests ranged from 0.00012 to 0.00014%. The average axial strain was about 0.00013% and was used to represent ε for all transient downhole tests. While the nonlinear behavior of M at relatively large strains can be clearly seen in Figure 5.28, the lowest axial strain induced at this depth by the steady-state tests was about 0.007%. Accordingly, there is a large range of strains (0.00013 to 0.007%) where the behavior of M is unknown. This is especially problematic when selecting a value for M_{max} to be used to normalize the M – log ε relationships. Since the constrained moduli from the transient, downhole tests were so much higher than those from the steady-state tests in this case, M_{max} was assumed to

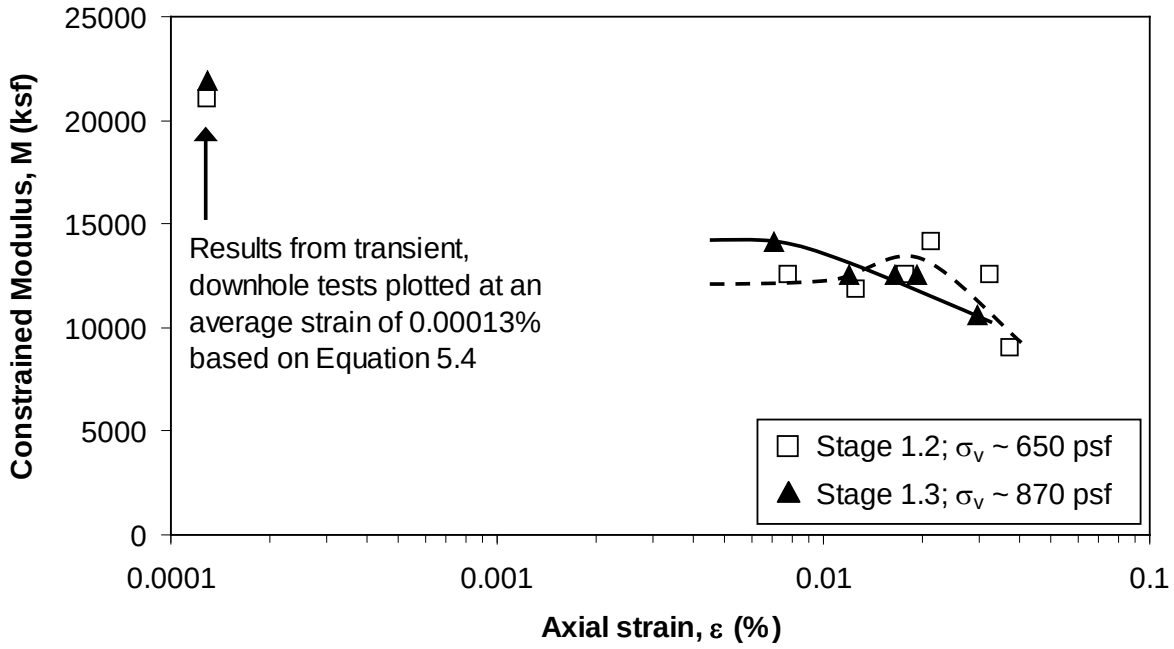

Figure 5.28. Variation of constrained modulus with axial strain at Site 1 between Sensors 1 and 2 (13.75-in. (34.9-cm) depth)

be the constrained moduli at the lowest strain induced in the steady-state tests. The M – log ε relationships shown in Figure 5.28 were normalized by M_{max} and are presented in Figure 5.29 in the form of M/M_{max} – log ε relationships. As seen in Figure 5.29, M/M_{max} in Stage 1.2 initially increases with increasing axial strain, but then decreases with increasing axial strain after about 0.02% axial strain. At the higher confining pressure applied in Stage 1.3, M/M_{max} decreases with increasing axial strain over the entire range of induced axial strain. Therefore, as noted in the discussion of sensor pair 2-3, it appears the behavior of M/M_{max} with increasing axial strain is much more complicated than the normalized shear modulus (G/G_{max}) with increasing shear strain (γ). However, any further inferences on the behavior of M/M_{max} – log ε based on this depth are at best premature due to the previously mentioned large range of axial strains over which no measurements of M were made. It is possible that the high strains generated between Sensors 1 and 2 were due to the relatively close proximity of these sensors to the load plate of Thumper.

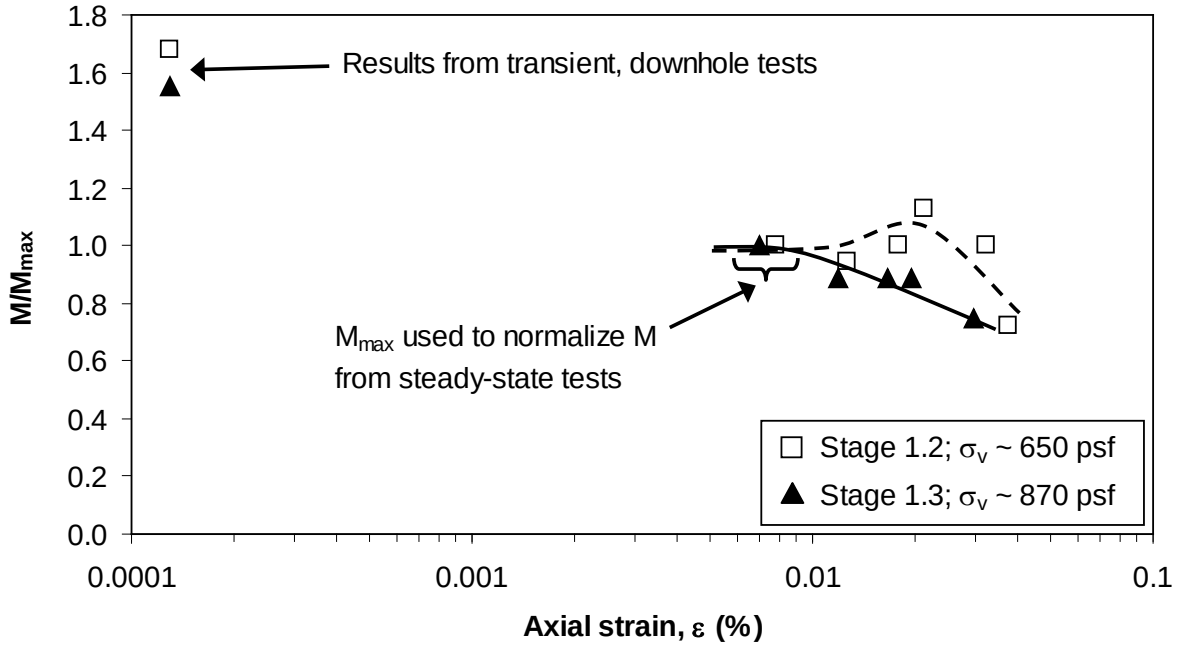

Figure 5.29. Variation of normalized constrained modulus with axial strain at Site 1 between Sensors 1 and 2 (13.75-in. (34.9-cm) depth)

5.7 RECOMMENDATIONS FROM THE INITIAL FIELD TESTS

Based on these preliminary tests at Site 1, several observations and recommendations can be made which will further improve the test procedure at subsequent sites.

1. In most cases in the center sensor column, the compression wave velocity determined using steady-state sinusoidal excitation at the smallest excitation level is approximately equal to the P_v-wave velocity determined using small-strain, transient downhole tests. Therefore, it is reasonable to conclude that Thumper (and most likely T-Rex as well) will successfully generate constrained compression waves at or very near the centerline of the shaker's load plate.

2. At locations of the sensors in the original cubical array further from the center of the load plate (hence, beneath the edge of the load plate of Thumper), Thumper did not generate P_V waves while T-Rex had only marginal success. This confirms the assumption that the larger load plate of T-Rex induces lateral confinement over a larger horizontal area than the load plate of Thumper. However, as noted in Item #1, the most successful results occurred near the centerline of the load plate. Therefore, any subsequent embedded sensor arrays should be constructed such that the sensors are relatively close to the center of the vibroseis load plates (within at least about 9 in. (23 cm)).

3. Both Thumper and T-Rex successfully induced nonlinearity in the soil to a depth of at least 21.75 in. (55.2 cm) below the load plate. This nonlinearity is readily apparent in Figures 5.26 through 5.29. It can also be seen in the asymmetric shapes of the output signals from Sensors 1, 2, and 3 (see Figure 5.20). LeBlanc et al. (2012) suggested this signal asymmetry represents an accumulation of downward deformation and indicates the system is becoming nonlinear.

4. The axial strains generated between Sensors 1 and 2 during the steady-state tests were generally large, with the lowest axial strain induced at this depth equal to about 0.007%. As shown in Figures 5.28 and 5.29, the result was a large range of strains over which the behavior of the constrained modulus could not be characterized. However, at the deeper depth of the midpoint of Sensors 2 and 3, the lowest strain induced by the steady-state tests was about 0.0002%, and the behavior of the constrained modulus could be investigated over a wide range in strains. Therefore, the depth between the shaker's load plate and the midpoint of the first sensor pair should probably be increased.

5. The sensors used at Site 1 were installed at 8-in. (20.3-cm) intervals. This close spacing led to difficulties in interpreting arrival times of the waveform at each sensor in that the arrival times were separated by very few data points in the digital time records. By increasing the distance between sensors, more data points will separate the arrival times at each sensor. This makes the velocity calculated using these arrival times much less sensitive to small changes in the travel time between sensors.

6. Due to time constraints with T-Rex and Thumper, horizontal excitation could not be applied at Site 1. Therefore, a field $G/G_{max} - \log \gamma$ relationship could not be constructed. Subsequent testing should be scheduled to allow sufficient time for both vertical and horizontal excitation so that the $M/M_{max} - \log \varepsilon$ and $G/G_{max} - \log \gamma$ relationships can be compared directly for the same site.

5.8 SUMMARY

In the summer of 2011, an existing embedded cubical sensor array at Site 1 near Hornsby Bend, Texas, was modified by installing three additional sensors in a central, vertical column. This modified array was then subjected to a series of transient, small-

strain downhole and crosshole tests and steady-state, sinusoidal excitation tests over a wide strain range. The purpose of these tests was to investigate the linear and nonlinear behavior of the in-situ constrained moduli. The results of the transient, small-strain downhole and crosshole tests showed little variation of the dynamic wave velocities with increasing stress level, suggesting that the soil at this site is heavily overconsolidated. The sinusoidal, vertical excitation tests were successful in generating constrained modulus nonlinearity in certain loading configurations and at certain depths. In general, constrained modulus nonlinearity was most successfully induced with Thumper and T-Rex near the centerline of the shakers' load plates and at depths no shallower than about 21.75 in. (55.2 cm). The lessons learned from these initial field tests at Site 1 were used to refine the testing procedure and design the embedded sensor array for use in the more robust suite of tests at Site 2. The test program at Site 2 is described in Chapter 6, and the results are discussed in Chapters 7 and 8.

CHAPTER 6: FIELD SET-UP AND TEST PROCEDURE AT SITE 2 AT HORNSBY BEND, TEXAS

6.1 INTRODUCTION

With the experience gained from the initial test program at Site 1 described in Chapter 5, a second sensor array was installed at a location approximately 300 ft (92 m) northeast of Site 1 but still located in the same farm field (Lower Tract B) near Hornsby Bend, Texas. The location of this site, hereafter known as Site 2, relative to Site 1 is shown in Figure 6.1. Using the lessons learned from the initial tests, a more extensive suite of linear and nonlinear tests was performed at Site 2 between August 25, 2011, and September 1, 2011. The material properties of the soil at this site, as well as the details of the sensor array and the testing program are described in this chapter.

Figure 6.1. Location of Site 2 at Hornsby Bend (map provided by Google Maps)

6.2 SITE CHARACTERIZATION

As mentioned above and seen in Figures 5.3 and 6.1, the location of Site 2 is about 300 ft (91 m) northeast of Site 1. Due to concerns about spatial heterogeneity found in the Lower Tract B farm field, both laboratory and field seismic tests were conducted at or near Site 2 as part of an extensive site characterization program. These tests were performed as part of a collaborative research program with Los Alamos National Laboratory and are discussed in this section.

6.2.1 Field tests

As part of the site characterization program at Site 2, Kim (2012) conducted several field seismic tests in the fall of 2011. After installation of a deep borehole (approximately 75 ft (23 m) deep) at Site 2, Kim performed traditional downhole tests using this borehole. He also performed seismic cone tests, Cone Penetration Tests (CPT), and Spectral-Analysis-of-Body-Waves (SASW) tests. The locations of these tests in Lower Tract B are shown in Figure 6.2. Details of the deep borehole installation at Site 2 and the corresponding boring log are included in Appendix A. Details of the field seismic tests are discussed in Kim (2012).

6.2.2 Laboratory tests

A grain-size analysis was performed in accordance with ASTM D422 on a soil sample taken from a depth of 24 in. (0.61 m) below the ground surface. The results of the sieve and hydrometer analyses indicate that the soil near the ground surface at Site 2 is approximately 52% sand and 48% fines as shown by the grain size distribution (GSD) in Figure 6.3. The average of the GSDs reported by Van Pelt (2010) for his test site is also shown in Figure 6.3 for comparison. Atterberg Limits tests (ASTM D4318) performed on the Site 2 soil showed that the fines fraction had no plasticity. Using

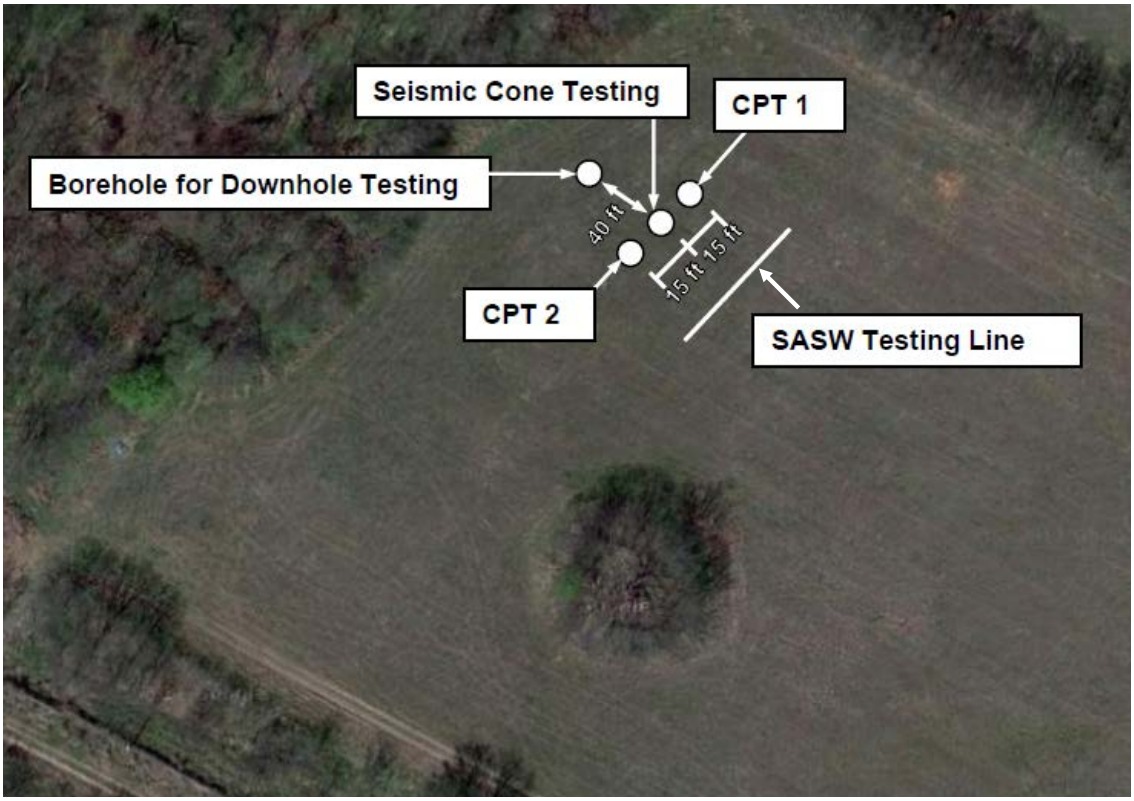

Figure 6.2. Location of field seismic tests at Site 2 (from Kim 2012)

the Unified Soil Classification System (USCS) described by ASTM D2487, the soil at Site 2 is a sandy silt (ML). This classification is the same USCS classification as the soil at Van Pelt's site, though the soil at Van Pelt's site had a slightly higher fines content (shown in Figure 6.3). The boring log from the installation of the deep borehole at Site 2 (see Appendix A) indicates that this layer of sandy silt extends to about 6 ft (1.83 m) below the ground surface.

Water content determinations were performed at several depths and locations at Site 2, and the results are summarized in Table 6.1. Additionally, the total unit weight of the soil was estimated as 96 pcf (1538 kg/m^3) based on the relatively undisturbed specimens obtained with a large split-tube sampler used by the driller in conjunction with the deep borehole installation described in Appendix A. The locations of the various boreholes listed in Table 6.1 are shown in Figure 6.4.

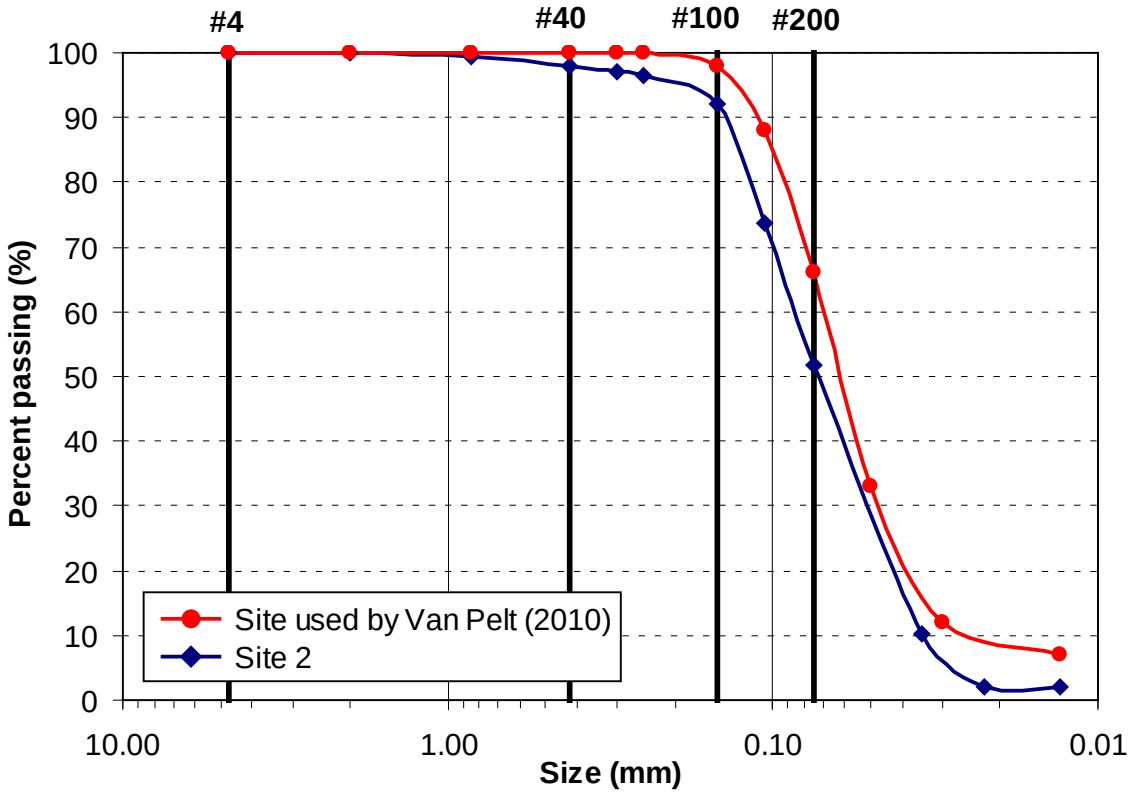

Figure 6.3. Grain size distribution curves for the soil at Site 2 and the site used by Van Pelt (2010)

Table 6.1. Water content and unit weight determinations at Site 2

Borehole ID	Depth (in.)	Sampling method	Total unit weight (pcf)	Water content (%)
EB-1	2	Disturbed	-	5.0
EB-2	5	Disturbed	-	4.8
EB-3	6	Disturbed	-	4.8
EB-2	12	Disturbed	-	4.3
EB-3	22	Disturbed	-	4.2
EB-2	35	Disturbed	-	6.4
LANL 2	36	Disturbed	-	4.0
Deep borehole	48	Split-tube	96	-
LANL 3	96	Disturbed	-	6.9

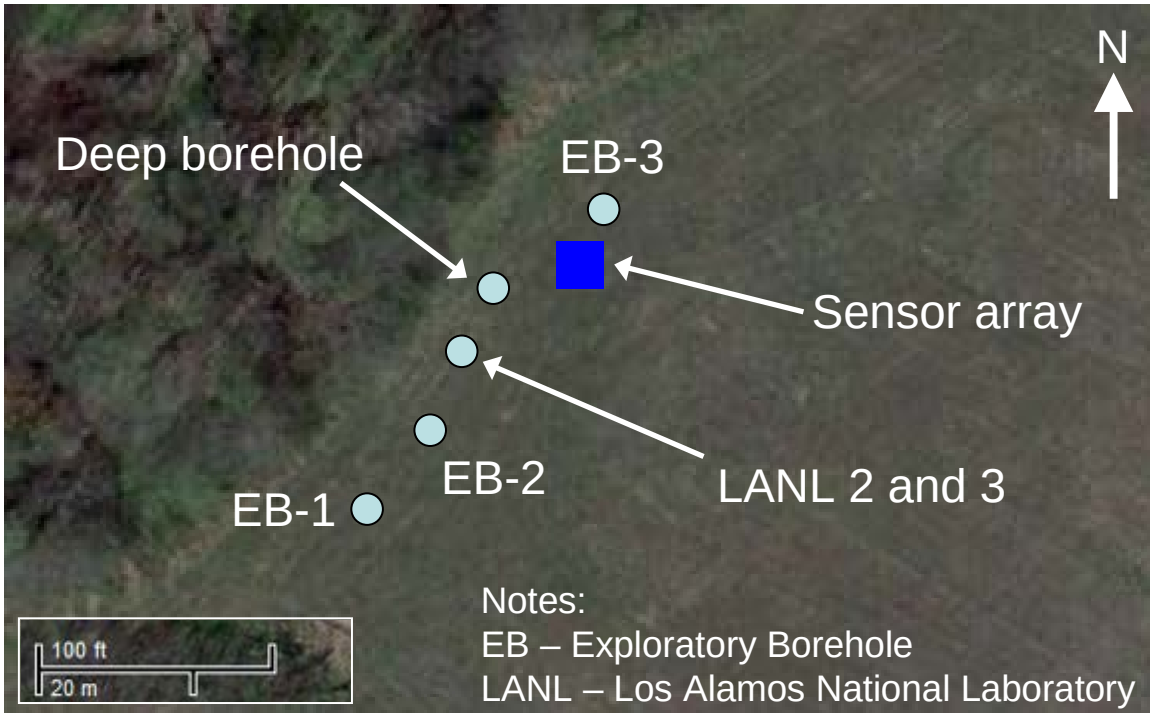

Figure 6.4. Locations of boreholes used at Site 2 (map provided by Google Maps)

6.2.3 Estimation of in-situ effective stress

By the time of the tests at Site 1 in July 2011, the entire central Texas region had been under severe drought conditions for at least six to eight months. This drought continued throughout the remainder of the summer of 2011, as seen by the daily high and low temperatures and rainfall amounts observed at Austin-Bergstrom International Airport (about 3 miles (5 km) from Hornsby Bend) shown in Figure 6.5. The dates of the tests at both sites are also identified in Figure 6.5. In the 42 days between the testing at Site 1 and Site 2, 35 days had a high temperature over 100 ^{o}F, and a measurable amount of precipitation (0.05 in.) was only recorded on one day. The combination of these two factors dried the soil more than it was during testing at Site 1 and resulted in generating more negative pore pressures near the ground surface at Site 2. There is then little doubt that the state of stress in the soil at Site 2 was different than at Site 1.

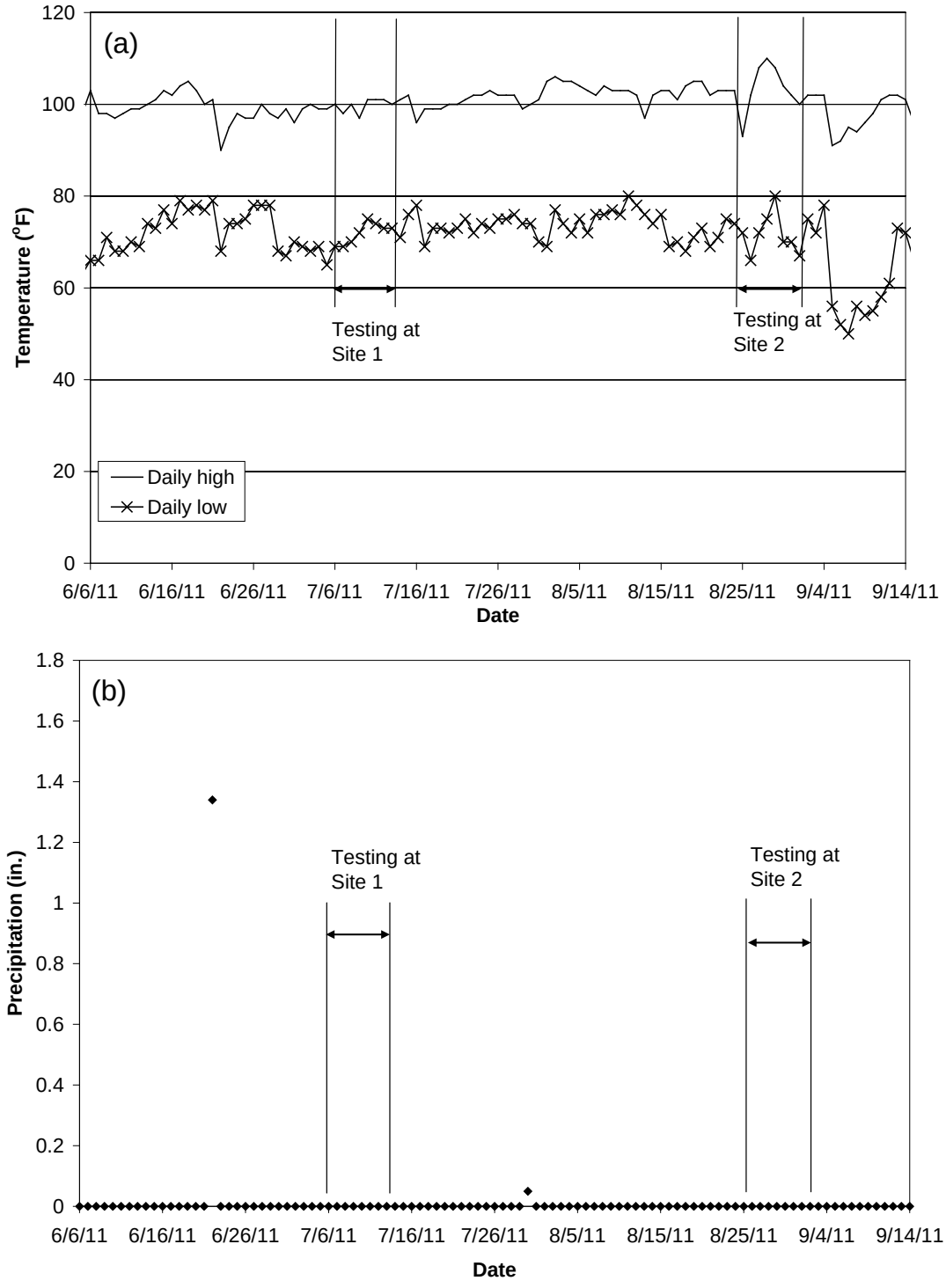

Figure 6.5. Summer 2011 climatological data for Austin-Bergstrom International Airport: (a) daily temperature and (b) daily precipitation (data provided by Weather Underground – www.wunderground.com)

As mentioned in Section 4.3.3, these large negative pore pressures call into question the validity of a total stress approach when estimating the stress distribution beneath the concrete footing. As such, for the unsaturated soil at Site 2, an attempt was made to estimate the in-situ effective stress using the suction stress concept described by Lu and Likos (2006). As the name suggests, the suction stress (σ_s) is a function of matric suction and water content but encompasses all effects of interparticle physicochemical stresses attributable to cementation, van der Waals attraction, double-layer repulsion, capillary stress arising from surface tension, and negative pore-water pressure. Lu and Likos suggested that the effective stress (σ') in an unsaturated soil can be determined using the relation:

$$\sigma' = \sigma_t - u_a + \sigma_s \tag{6.1}$$

where σ_t is the total stress and u_a is the pore air pressure. Since u_a is typically assumed to be zero, Equation 6.1 reduces to:

$$\sigma' = \sigma_t + \sigma_s \tag{6.2}$$

To estimate the suction stress, a series of undrained triaxial tests were performed on remolded specimens to obtain a total stress failure envelope representative of the in-situ shear strength of the unsaturated soil at Site 2. The unit weight and water content of the remolded specimens were 96.5 pcf (1546 kg/m^3) and 4.5%, respectively (note that the void ratio in this case is 0.82, only slightly lower than 0.84 found by Van Pelt (2010) near Site 1). Referring to Table 6.1, these values closely represent the field conditions at Site 2 in the summer of 2011. Details of the specimen preparation and triaxial test procedures are given in Appendix B. The total stress failure envelope obtained for the remolded specimens is shown in Figure 6.6 along with the effective stress failure envelope reported by Van Pelt (2010) for a saturated soil. Given the similarities noted in Section 6.2.2 between the soils at Van Pelt's site and Site 2, Van Pelt's effective stress envelope was

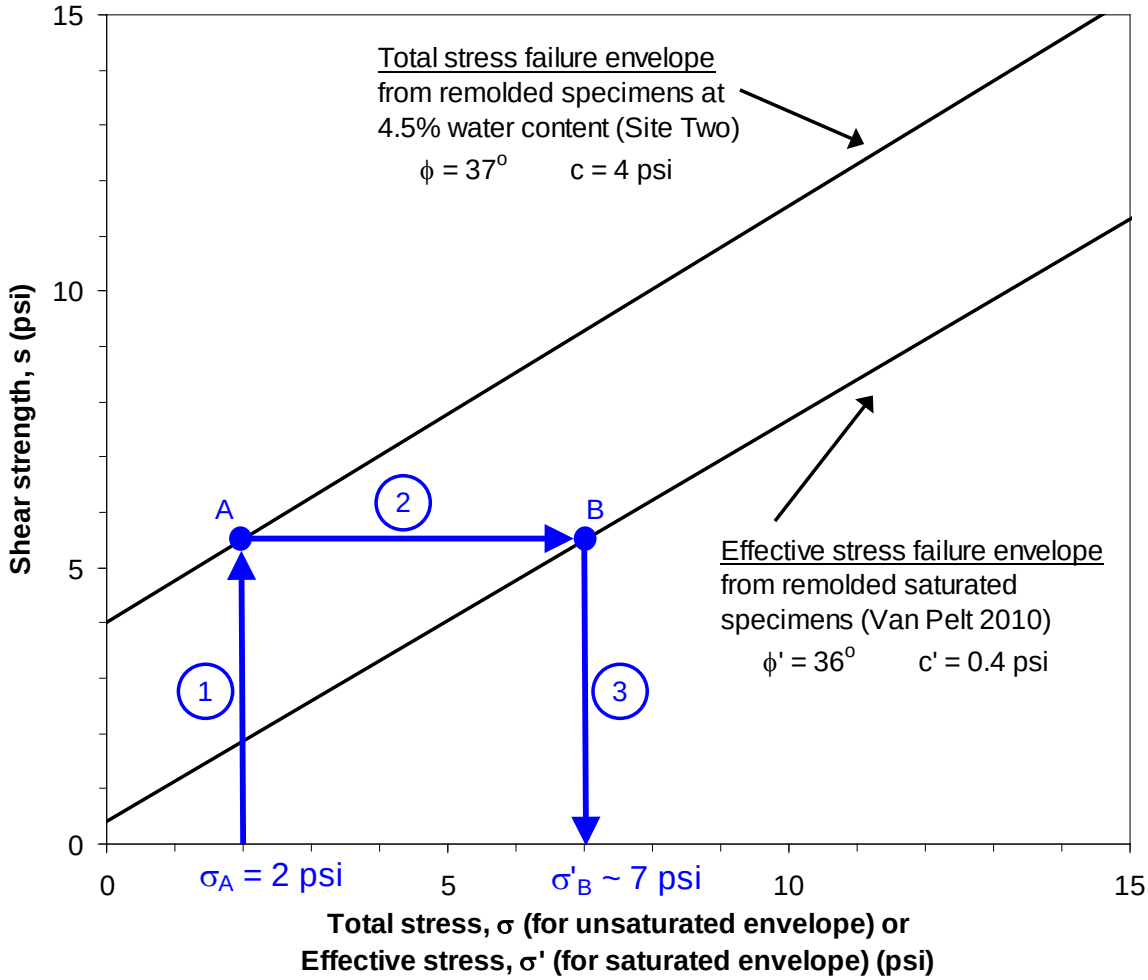

Figure 6.6. Approximate method used to estimate the suction stress at Site 2 based on the total and effective stress Mohr-Coulomb failure envelopes

deemed to be acceptable for use in an approximate method for estimating the suction stress. Referring to the steps shown in blue circles in Figure 6.6, the procedure used to estimate the suction stress is as follows:

Step 1 – Start by estimating the total vertical stress in the field induced by a given loading scenario using the procedures described in Chapter 4 (note that 2 psi is used as an example in Figure 6.6). Then move up in Figure 6.6 to the total stress failure envelope, and estimate the shear strength at this total stress (point A).

Step 2 – Move right in Figure 6.6 to determine the point on the effective stress failure envelope where this same shear strength occurs (point B).

Step 3 – Move down in Figure 6.6 to determine the effective stress corresponding to point B. In this example, this effective stress is 7 psi, as indicated in the figure.

As suggested by Lu and Likos (2006) and Equation 6.2, the difference between the effective stress at point B (σ'_B) and the total stress at point A (σ_A) is the suction stress. In this example, the suction stress is about 5 psi (34.5 kPa). Because the total and effective stress failure envelopes are almost parallel, the suction stress in the range of total stresses induced in this research (2 to 12 psi (13.8 to 82.7 kPa)) does not deviate much from this value. Therefore, the in-situ effective stress at Site 2 was estimated by adding a suction stress of 5 psi (34.5 kPa) to the total stress according to Equation 6.2. The use of effective stress instead of total stress is discussed in more detail in Chapter 7.

6.3 FIELD SET-UP AND TEST PROCEDURE

The construction of the sensor array and the testing procedures used at Site 2 are discussed in this section.

6.3.1 Construction of the embedded sensor array

As shown in Figure 6.1, the embedded sensor array at Site 2 was located in the same farm field as Site 1. Therefore, as with Site 1, the Site 2 location was first prepared by scarifying the top layer of plough tillage by hand. The tillage was removed until native sandy silt soil was found. The 3-D sensors used at Site 2 were fabricated as described in Chapter 3, using 3, 1-D, 24-Hz geophones (velocity transducers) cast in epoxy resin. A total of 12, 3-D sensors was installed in a triangular prism array

consisting of three vertical columns, with four sensors in each column. After the top 6.5 in. (16.5 cm) of plow tillage/top soil was removed by hand, the sensors were installed at 12-, 24-, 36-, and 48-in. (30.5-, 61.0-, 91.5-, and 122.0-cm) depths below the scarified surface using the same procedures described in Chapter 5 for Site 1. The 3-D sensors were installed such that the 1-D component geophones were oriented in the vertical (component "A"), East-West (component "B"), and North-South (component "C") directions. For example, the nomenclature "13B" indicates the 1-D component geophone in Sensor 13 that is oriented to capture horizontal motion in the East-West direction. Finally, a 1-in. (2.5-cm) layer of poorly graded sand was placed over the scarified surface to improve contact between the ground surface and either the concrete footing or the vibroseis load plate during testing. The configuration of the sensor array is shown in Figure 6.7, and various steps in the construction of the sensor array are shown in Figures 6.8 through 6.10.

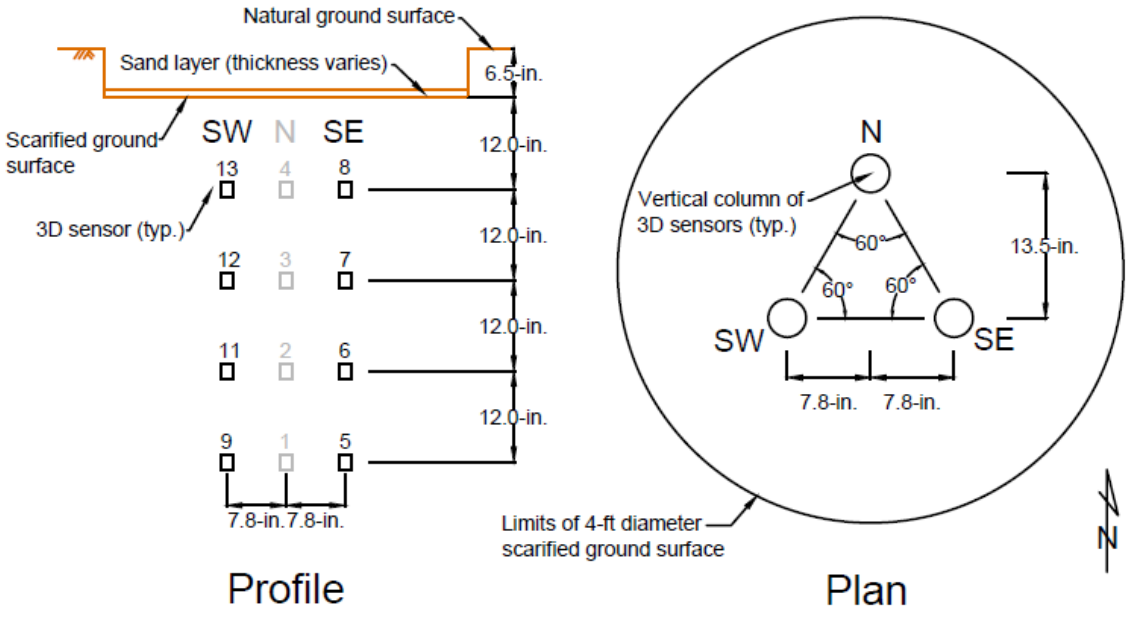

Figure 6.7. Layout of the embedded sensor array at Site 2

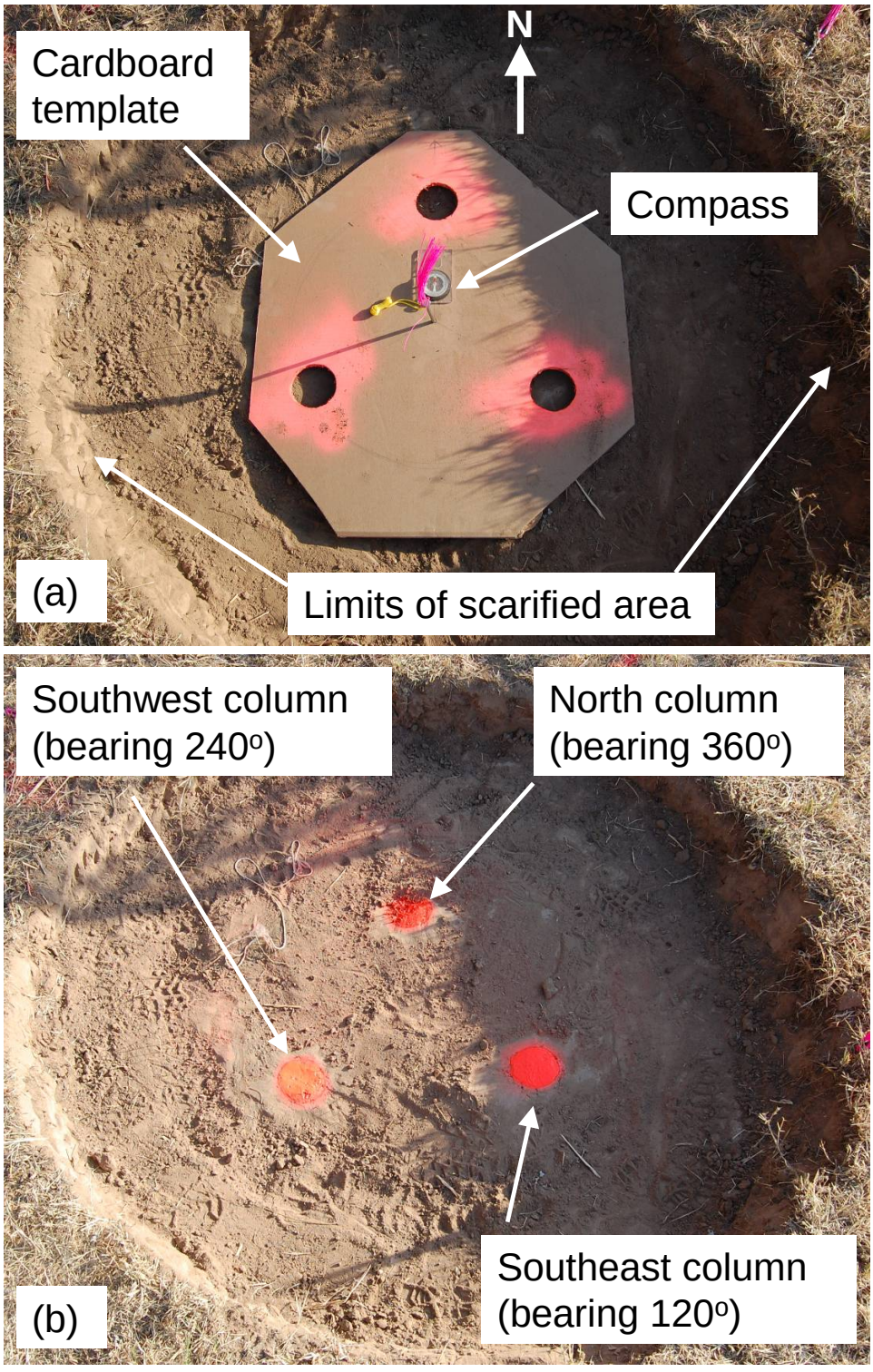

Figure 6.8. Marking the sensor column locations at Site 2: (a) orienting the columns using a cardboard template and (b) column nomenclature and azimuth

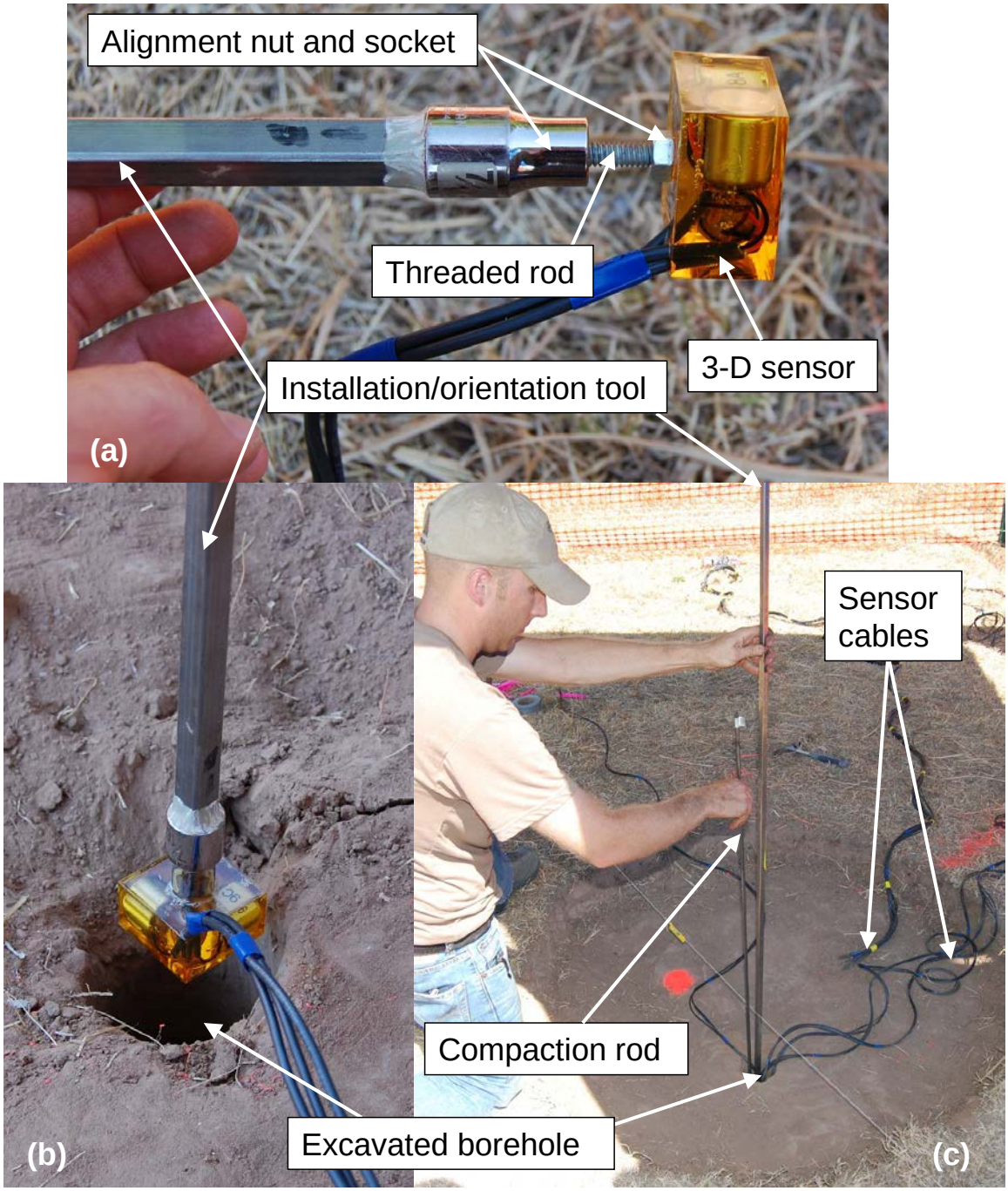

Figure 6.9. Installation of Sensor 9: (a) securing the sensor to the installation/orientation tool, (b) lowering the sensor into the borehole, and (c) backfilling the borehole up to the next sensor (Sensor 11) depth

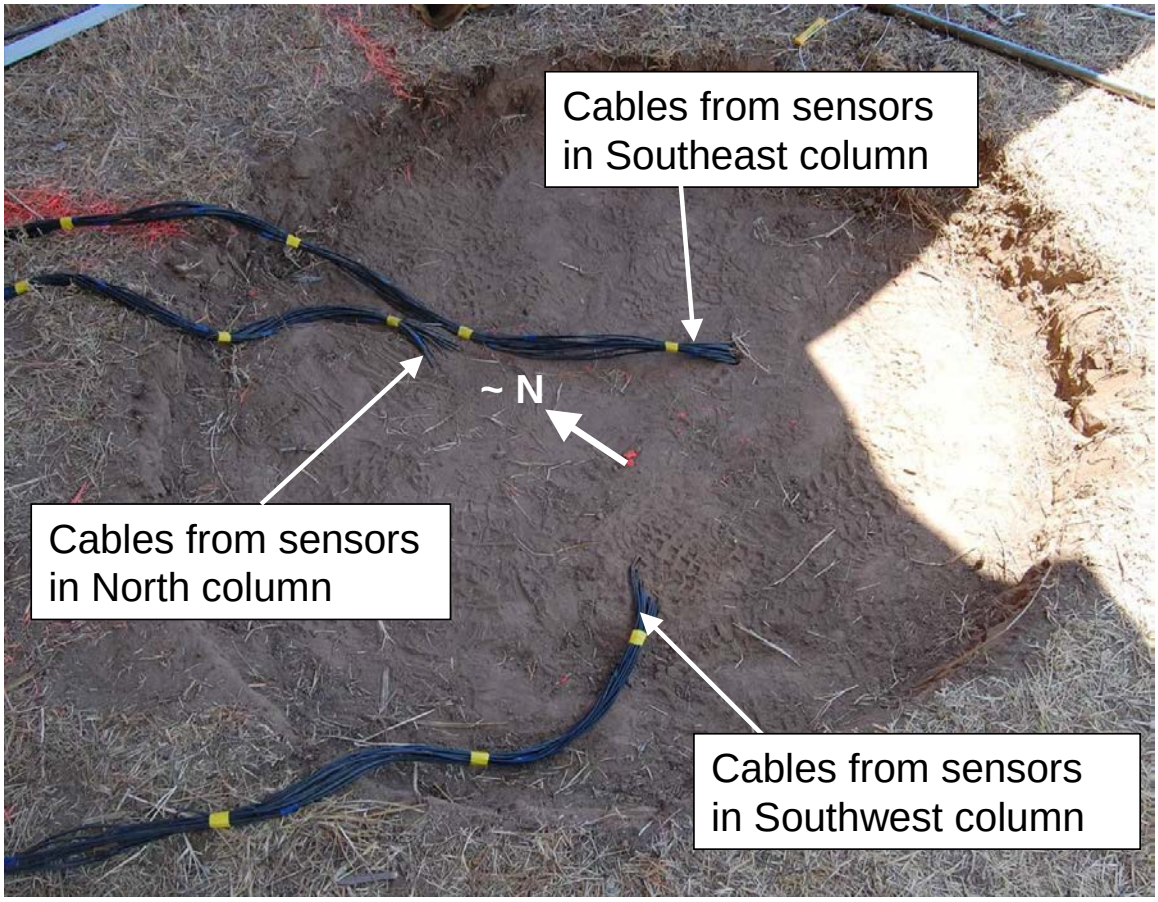

Figure 6.10. Sensor array after completion of sensor installation and before final leveling of the scarified ground surface

6.3.2 Staged loading sequence

After construction of the sensor array, two types of tests were performed at Site 2 in late August 2011: (1) traditional transient, downhole and crosshole seismic tests at small strains and (2) sinusoidal excitation tests encompassing linear and nonlinear strain levels. As at Site 1, a staged loading sequence was used to limit the effects of the loading regimen on the soil structure. The staged loading sequence used at Site 2 is shown in Figure 6.11. In general, both types of tests were performed in the same manner as described in Section 5.3.2 for Site 1. Any deviations made from the test procedures described for Site 1 are discussed below for the tests at Site 2.

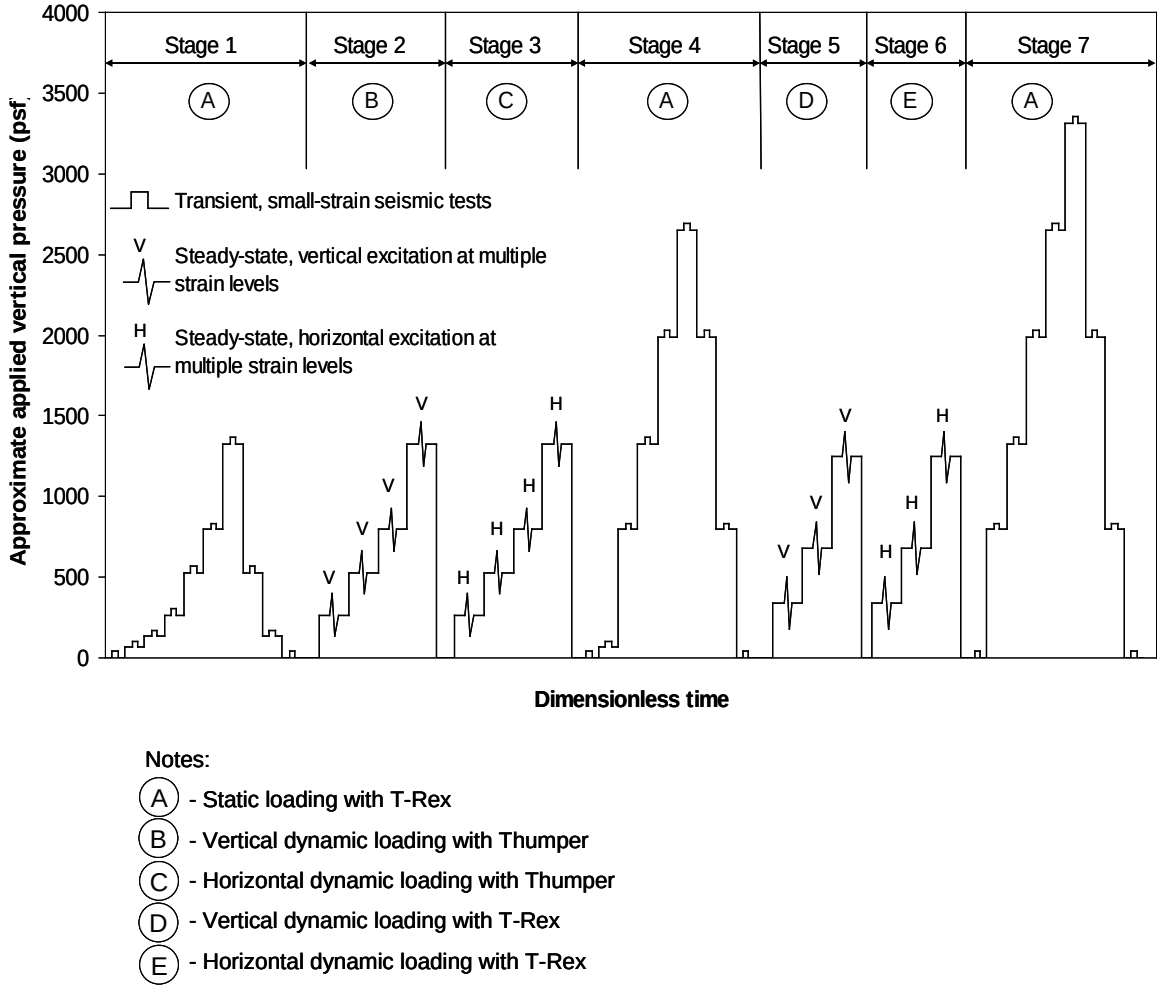

Figure 6.11. Staged loading sequence at Site 2 (after Stokoe et al., 2006)

Transient, small-strain downhole and crosshole tests were performed at the beginning and end (Stages 1 and 7 in Figure 6.11) of the entire suite of tests at Site 2. An additional set of small-strain downhole and crosshole tests was performed in Stage 4 after the dynamic tests with Thumper but before the dynamic tests with T-Rex. The Stage 4 testing was conducted to determine the impact of the sinusoidal excitations applied in the dynamic tests on the small-strain stiffness of the soil structure. The downhole and crosshole tests were performed as described in Chapter 5 for Site 1, except that the static loads were always applied using the hydraulic jack and the dead weight of the vibroseis. The load plate of T-Rex was not used to apply higher stresses since the load plate

prevents access to the concrete footing as shown in Figure 5.9. Additionally, the locations of the crosshole source rods were different in every stage at Site 2. In Stage 1, all crosshole rods were 36 in. (91.5 cm) from the center of the concrete footing as shown in Figure 6.12a. However, one of the rods (Rod #1) was damaged during Stage 2 and was subsequently relocated to the position shown in Figure 6.12b for the small-strain tests in Stage 4. To conduct the sinusoidal excitation tests in Stages 5 and 6, all crosshole rods had to be removed to allow sufficient room for the larger load plate of T-Rex. Then in Stage 7, the crosshole rods were installed at the positions shown in Figure 6.12c. The small-strain downhole and crosshole test configuration at Site 2 is shown in Figure 6.13.

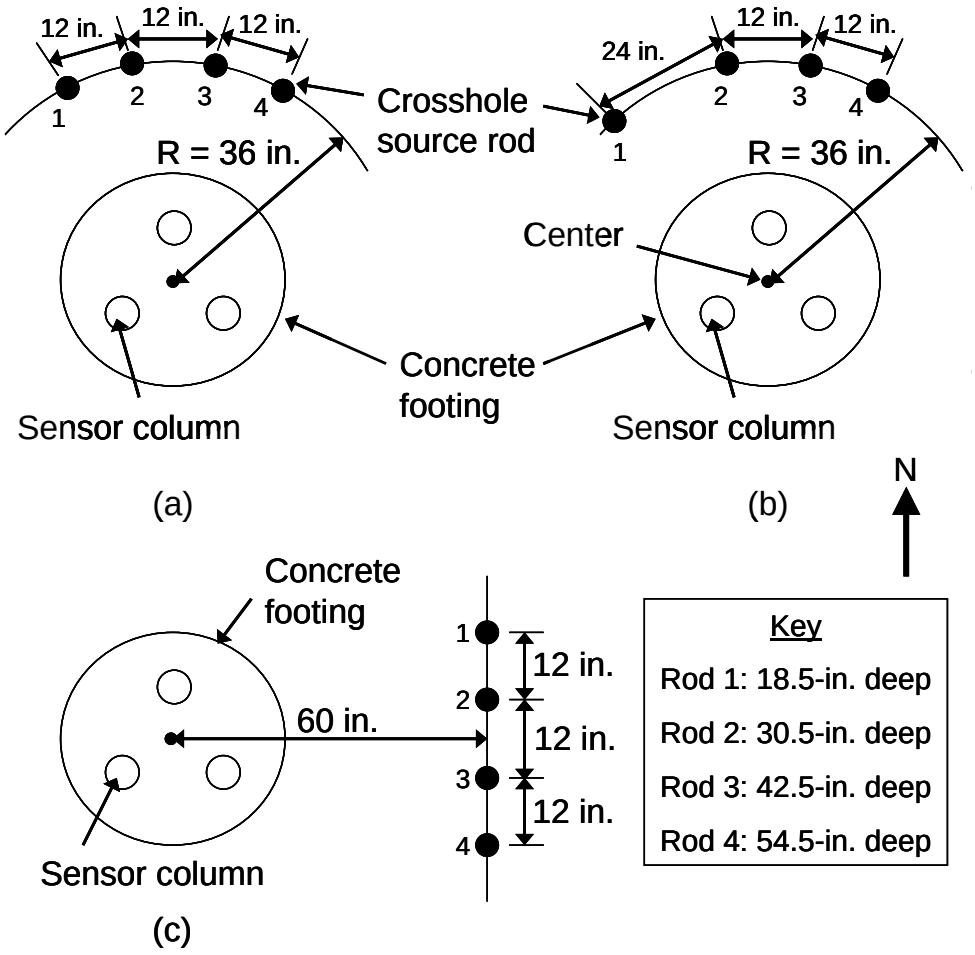

Figure 6.12. Crosshole source rod configuration at Site 2 for: (a) Stage 1, (b) Stage 4, and (c) Stage 7

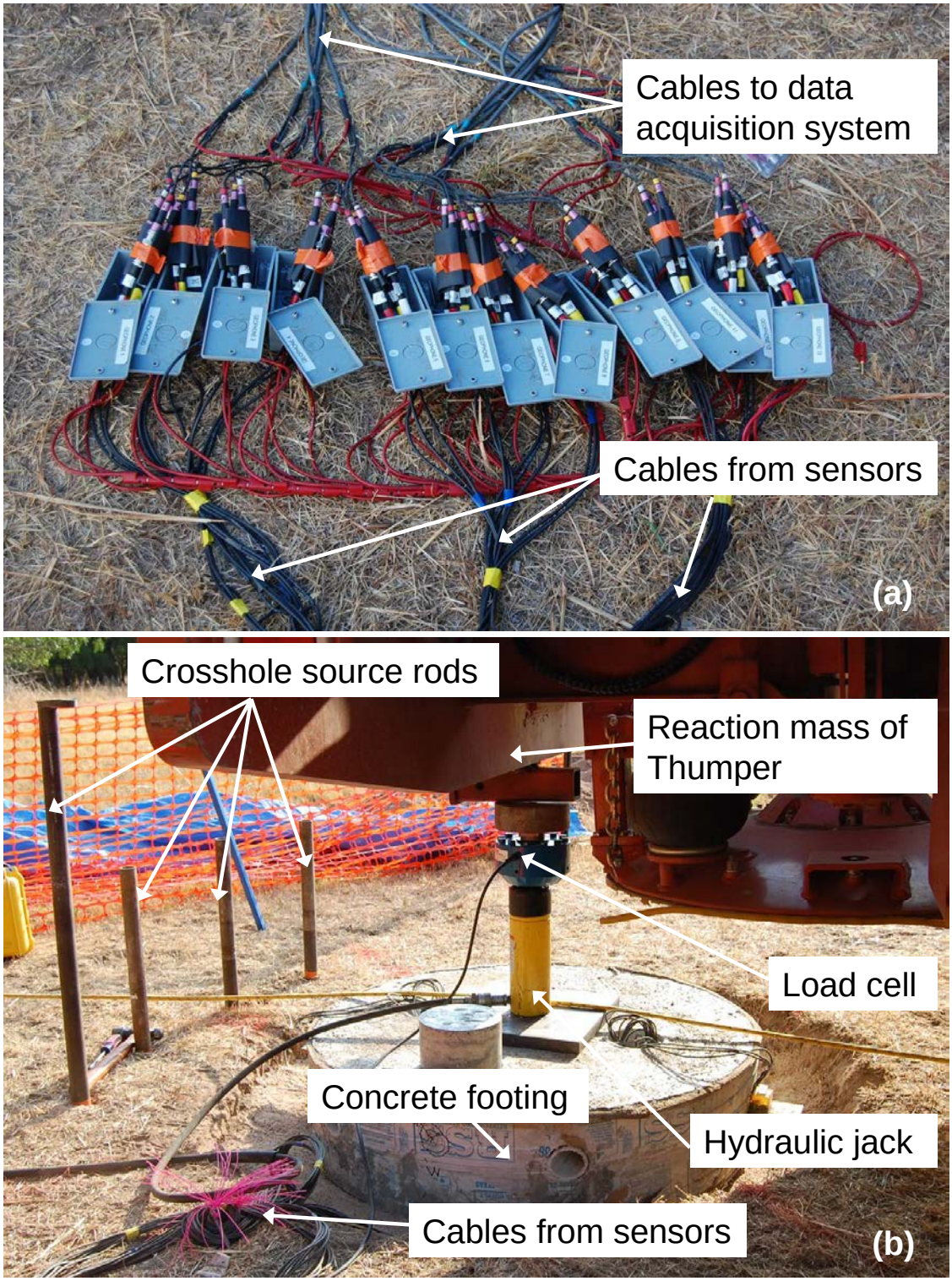

Figure 6.13. Stage 1 testing arrangement: (a) connections to data acquisition equipment and (b) crosshole and downhole test configuration

In contrast to Site 1, the sinusoidal excitation tests at Site 2 included horizontal as well as vertical excitation from the vibroseis (Thumper and T-Rex). In Stages 2 and 3, the sinusoidal excitation was applied by Thumper in the vertical and horizontal directions, respectively. Similarly, in Stages 5 and 6, the sinusoidal excitation was applied by T-Rex in the vertical and horizontal directions, respectively. While T-Rex is capable of imparting much higher static and dynamic loads than Thumper, the base plate of T-Rex (44.2 ft^2 (4.11 m^2) area) is significantly larger than the base plate of Thumper (7.5 ft^2 (0.70 m^2) area). Consequently, the vertical hold-down pressure applied by T-Rex was generally about the same or less than that applied by Thumper (see Figure 6.11). The test configurations at Site 2 for vertical excitation with Thumper and T-Rex are shown in Figures 6.14 and 6.15, respectively.

6.4 SUMMARY

Subsequent to the initial tests performed at Site 1, a more robust suite of tests was conducted in August 2011 with an embedded sensor array at Site 2. A significant number of laboratory and field tests were conducted at this site to characterize the soil properties

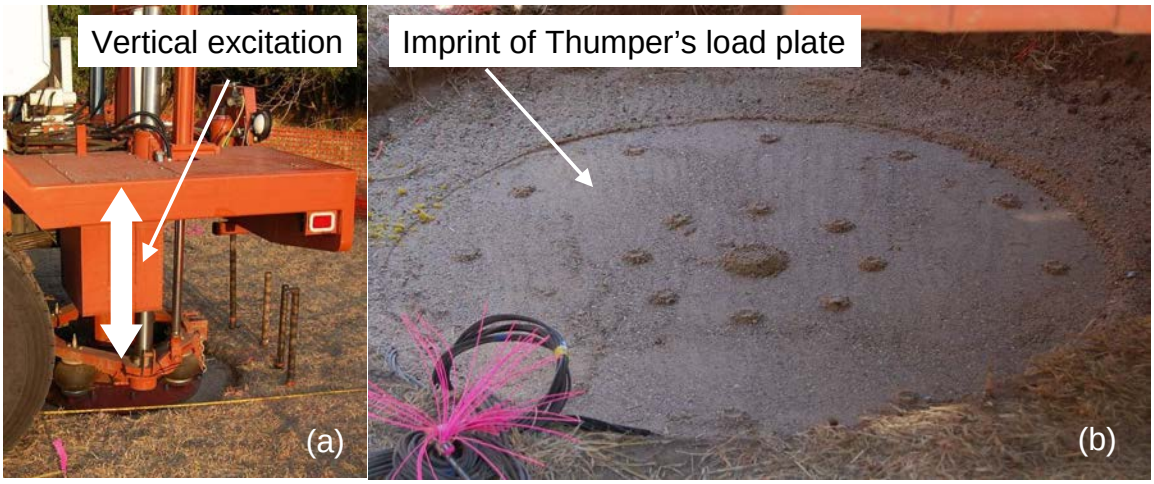

Figure 6.14. Stage 2 testing arrangement: (a) vertical excitation applied directly to the ground surface and (b) imprint left by Thumper's load plate after completion of Stage 2

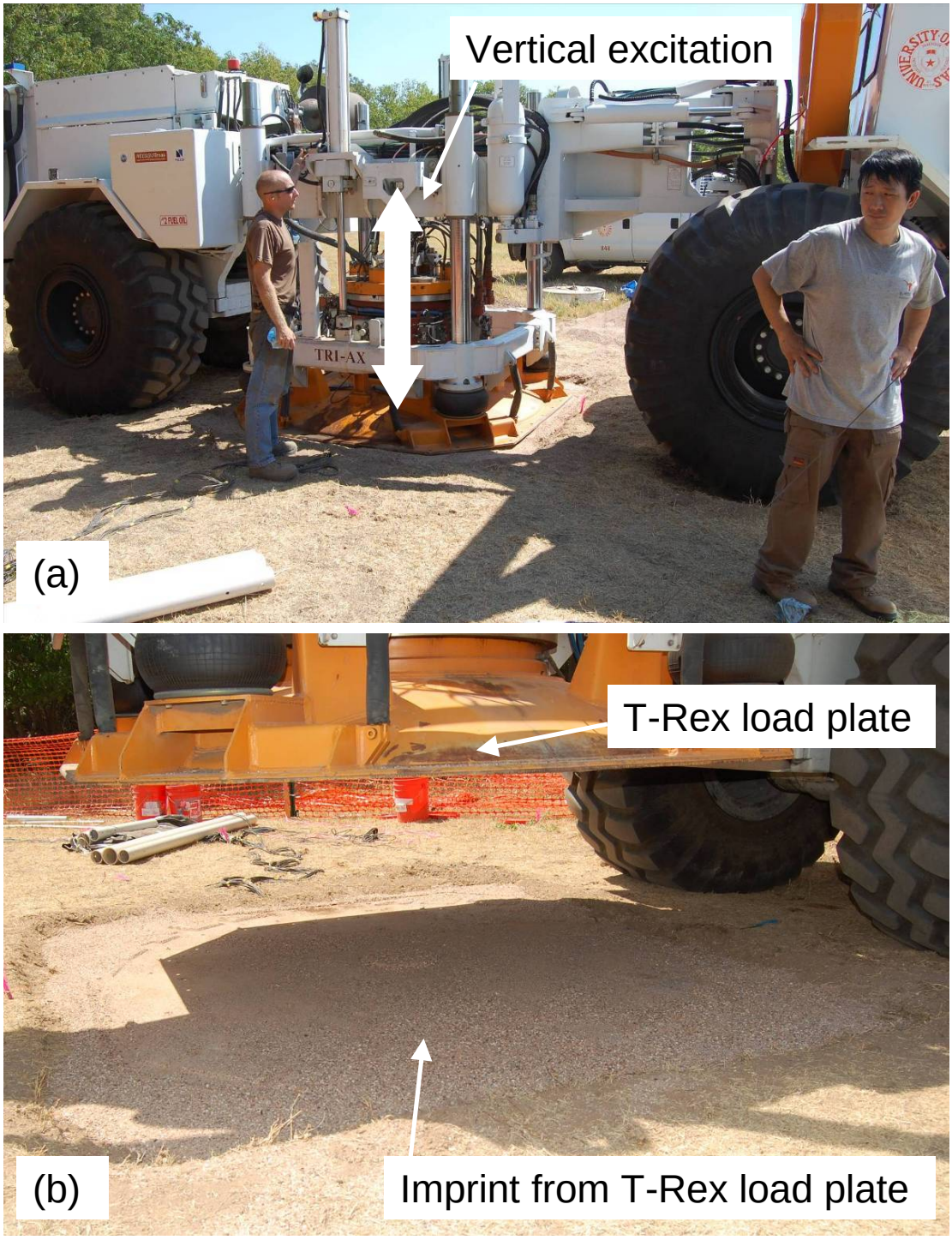

Figure 6.15. Stage 5 testing arrangement: (a) vertical excitation applied directly to the ground surface (pictured from left: Capt Allen Branco and Dr. Changyoung Kim) and (b) imprint left by T-Rex's load plate after completion of Stage 5

and subsurface layer profile. The embedded sensor array consisted of 12, 3-D sensors installed in a triangular prism arrangement consisting of three vertical columns with four sensors in each column. To limit the effects of the static and dynamic loading regimen on the soil structure, a staged loading sequence was used in which small-strain crosshole and downhole tests were performed both before and after vertical and horizontal sinusoidal excitations were imparted directly above the embedded sensor array by two vibroseis trucks (Thumper and T-Rex). The results of the tests conducted at Site 2 are discussed in Chapters 7 and 8 for measurements performed in the linear range and in the nonlinear range, respectively.

CHAPTER 7: EVALUATION OF CONSTRAINED AND SHEAR MODULI IN THE LINEAR RANGE AT SITE 2

7.1 INTRODUCTION

The results of the traditional downhole and crosshole tests conducted at Site 2 as described in Chapter 6 are presented in this chapter. These transient, small-strain tests were performed in three stages (Stages 1, 4, and 7 noted in Figure 6.11 and enlarged in Figure 7.1). Since the strains induced by the traditional downhole and crosshole tests were small, the stress-strain behavior of both the constrained and shear moduli (M and G, respectively) was in the linear range. The results of the small-strain downhole tests are presented first, followed by the results of the small-strain crosshole tests. A comparison between the results of these tests is provided. The uncertainties and limitations associated with these tests are also discussed.

7.2 SMALL-STRAIN DOWNHOLE TESTS

The two types of body waves generated in the transient, small-strain downhole tests were: (1) vertically-propagating, constrained compression waves (P_V waves) and (2) vertically-propagating, horizontally-polarized shear waves (S_{VH} waves). The propagation velocities of these two types of waves (V_{Pv} and V_{Svh}) were calculated between each pair of sensors using the procedures described in Chapter 4. V_{Pv} was calculated by determining the times of the first-arrivals of the P_V wave at adjacent sensors, and V_{Svh} was calculated using the time-shift of the cross-correlation sequence between adjacent sensors. The results of these analyses are discussed in the sections below. First, the P_V- and S_{VH}-wave velocity-versus-depth profiles generated at the beginning of each load stage are presented. Then, the effect of confining pressure on V_{Pv} and V_{Svh} is examined. Finally, a short discussion of the results of the small-strain downhole tests is provided.

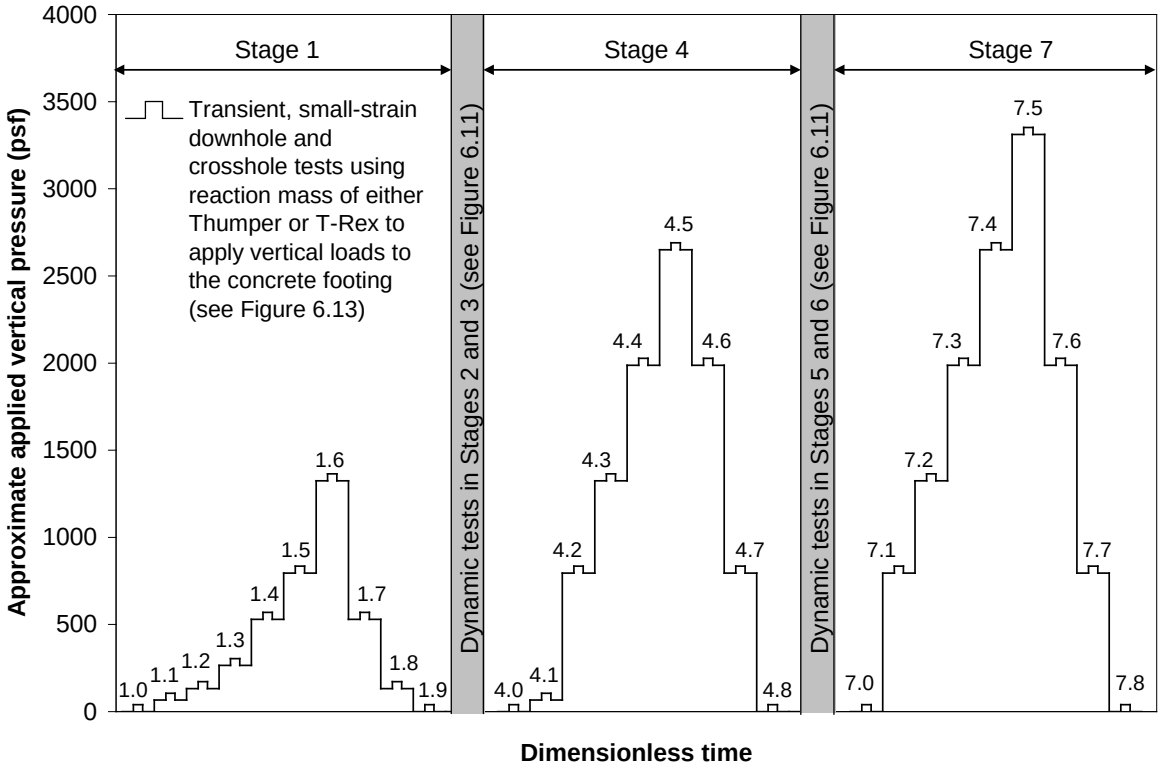

Figure 7.1. Staged loading sequence used for small-strain, downhole and crosshole tests performed in Stages 1, 4, and 7 at Site 2

7.2.1 V_{Pv} and V_{Svh} profiles with no vertical load applied to the footing

For all three sensor columns in the embedded sensor array (see Figure 6.7), the variation of V_{Pv} with depth is shown in Figure 7.2, where the V_{Pv} between each sensor pair is plotted at the depth of the sensor pair midpoint. Referring to the load step nomenclature shown in Figure 7.1, the velocity-depth profiles in Figure 7.2 represent the starting conditions in Stages 1.0, 4.0, and 7.0, i.e. before application of any vertical load. At the shallowest depth (24.5 in. (62.2 cm)) in the Southwest and North sensor columns (Figures 7.2a and 7.2b, respectively), V_{Pv} is higher in Stage 1.0 than in Stages 4.0 or 7.0. However, there is no further decrease in V_{Pv} from Stage 4.0 to Stage 7.0. The reduction in V_{Pv} is most pronounced in the North column where the V_{Pv} measured in Stage 1.0 is about 1000 fps (305 m/s) higher than in Stages 4.0 and 7.0. At this depth, the reduction

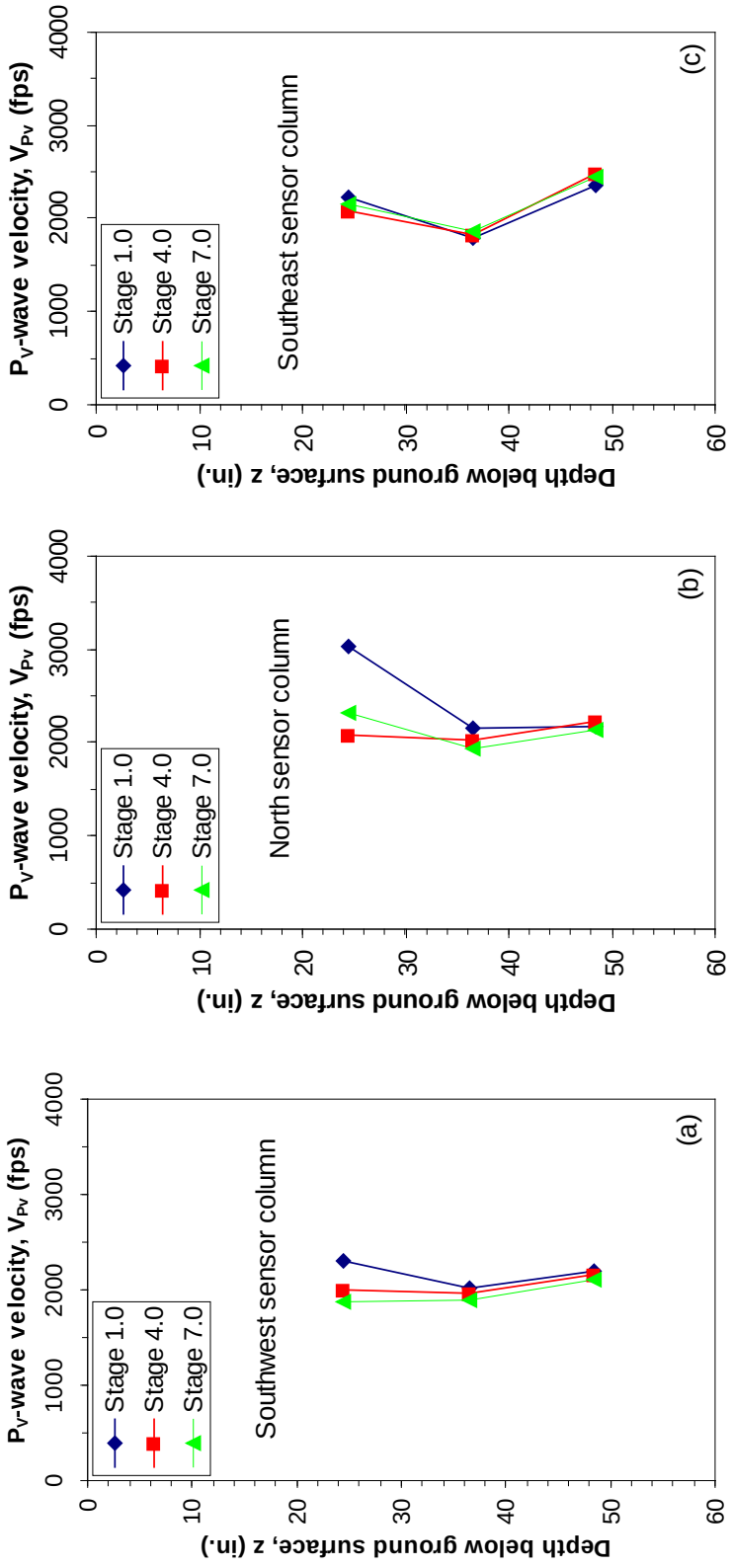

Figure 7.2. Variation of V_{Pv} with depth in three sensor columns of the embedded sensor array at the beginning of each load stage at Site 2: (a) Southwest, (b) North, and (c) Southeast

in V_{Pv} between Stages 1.0 and 4.0 could be due to the application of static loads in Stage 1, the generation of vertical and horizontal dynamic excitations in Stages 2 and 3, or a combination of both. This reduction could also result from a change (increase) in water content in the upper portion of the profile. At depths of 36.5 in. (92.7 cm) and 48.5 in. (123.2 cm) in the Southwest and North columns and at all depths in the Southeast column (Figure 7.2c), the P_V-wave velocity is basically the same in Stages 1.0, 4.0, and 7.0 and appears to have been unaffected by the test regimen and/or water content changes.

The variation of V_{Svh} with depth in all three sensor columns is shown in Figure 7.3. Similar to the observations described above for the V_{Pv} profiles, the difference between the V_{Svh} measured in Stages 1.0, 4.0, and 7.0 is largest at the shallowest depth (24.5 in. (62.2 cm)). At this depth in the Southwest and North columns (Figures 7.3a and 7.3b, respectively), the V_{Svh} measured in Stage 1.0 is about 700 fps (213 m/s) higher than the V_{Svh} measured in either Stages 4.0 or 7.0. In these two columns, the difference in V_{Svh} among the three stages decreases with increasing depth, until the V_{Svh} measured at the deepest depth (48.5 in. (123.2 cm)) is basically the same in all three stages. The behavior of V_{Svh} in the Southeast sensor column (Figure 7.3c) is slightly different. At the two shallowest depths in the Southeast column, the V_{Svh} in Stage 1.0 is only slightly higher (about 150 fps (46 m/s)) than the V_{Svh} in Stages 4.0 and 7.0. However, at the deepest depth (48.5 in. (123.2 cm)) in the Southeast column, the V_{Svh} measured in Stage 1.0 is about 300 fps (91 m/s) lower than the V_{Svh} from Stages 4.0 and 7.0. It is not known why the behavior of the measured V_{Svh} in the Southeast column is different than that seen in the Southwest and North columns. Regardless of the reason(s) for this difference in V_{Svh} behavior between sensor columns, the trends seen in all three columns in Figure 7.3 support the observations made in the preceding paragraph for the V_{Pv} profiles. Specifically, the following trends were observed in both the V_{Pv} and V_{Svh} profiles: (1) there was a noticeable change in the velocity-depth profiles between Stages 1.0 and 4.0 and (2) this effect is most pronounced at shallower depths and generally disappears at a depth of 48.5 in. (123.2 cm). As noted in the preceding paragraph, the change in

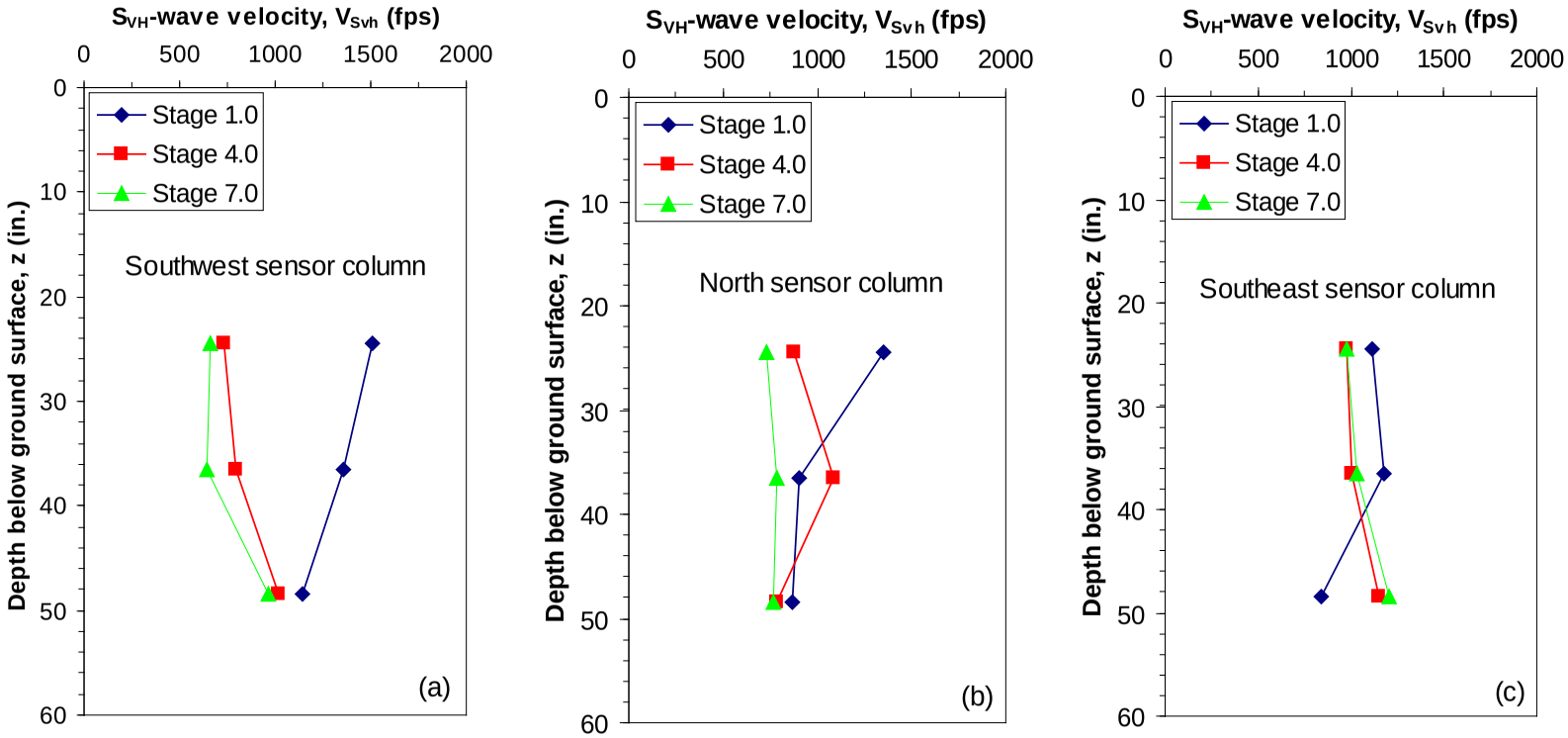

Figure 7.3. Variation of V_{Svh} with depth in three sensor columns of the embedded sensor array at the beginning of each load stage at Site 2: (a) Southwest, (b) North, and (c) Southeast

behavior from Stage 1.0 to Stage 4.0 is likely due to the test regimen in combination with possible moisture changes affecting the suction stress.

Average V_{Pv} and V_{Svh} profiles beneath the footing were created by averaging the velocities measured at the same depth in each of the three columns. These average profiles are shown in Figure 7.4 along with the profiles determined from Seismic Cone Penetration Tests (SCPT) and downhole tests performed by Kim (2012). It should be noted, however, that the SCPT and downhole tests were performed in Fall 2011 (one to two months after the tests in Stages 1.0, 4.0, and 7.0). These tests were performed in the same Hornsby Bend field as Site 2 but were located about 40 ft (12 m) from the embedded sensor array (refer to Figures 6.2 and 6.4). The average V_{Pv} values in Stages 1.0, 4.0, and 7.0 are higher than those reported by Kim (Figure 7.4a). However, based on Kim's entire V_{Pv} profile (Figure B.20 in Kim, 2012), which extends to a depth of 40 ft (12 m), it appears his downhole tests were conducted at intervals of 5 ft (1.5 m).

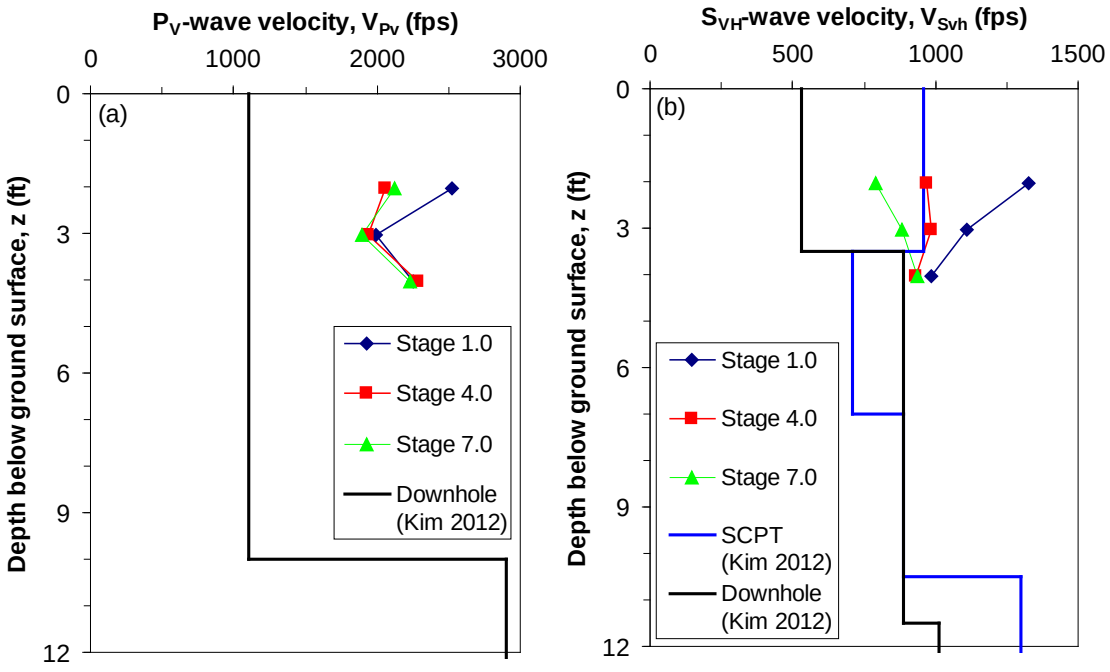

Figure 7.4. Average downhole wave velocity profiles at Site 2 compared with SCPT and downhole tests performed by Kim (2012): (a) V_{Pv} profiles and (b) V_{Svh} profiles

Therefore, the upper 10 ft (3.0 m) of Kim's V_{Pv} profile is based on only one or two measurements. As a result, the downhole tests performed in Stages 1.0, 4.0, and 7.0 better captured localized V_{Pv} variability that was not identified by Kim due to the relatively large-scale averaging in his downhole tests. As seen in Figure 7.4b, the average V_{Svh} profiles at Site 2 are in good agreement with the SCPT and downhole results reported by Kim, especially in Stages 4.0 and 7.0 and at depths of about 3 to 4 ft (0.9 to 1.2 m).

7.2.2 Effect of confining pressure on V_{Pv} and V_{Svh}

V_{Pv} and V_{Svh} values were measured at several different confining pressures in Stages 1, 4, and 7 (note the load steps shown in Figure 7.1). Lee (1985) suggested that the S_{VH}-wave velocity is influenced by both the vertical and horizontal stresses (σ_v and σ_h, respectively), and therefore proposed that the true measure of confining pressure in this case is the geometric mean of these two stresses, i.e. $\sqrt{\sigma_v \sigma_h}$. However, since K_o was assumed to be constant and equal to 1.0 in all stages at Site 2 (similar to Site 1 as described in Chapter 5), the quantity $\sqrt{\sigma_v \sigma_h}$ is numerically equal to σ_v. Therefore, the effects of confining pressure on V_{Pv} and V_{Svh} at Site 2 are presented in the form of log V_{Pv} – log σ_v and log V_{Svh} – log σ_v relationships. These relationships are presented separately in this section for each stage of the downhole tests.

7.2.2.1 Stage 1; In terms of total stresses

Ten static load steps were used in Stage 1 (see Figure 7.1). As discussed in Section 7.2.1, the embedded sensor array was constructed in a triangular prism layout with three vertical columns containing four sensors each (see Figure 6.7). It was then possible to determine the wave velocities at nine points in the embedded sensor array, e.g. between the first and second sensors, the second and third sensors, and the third and

fourth sensors in each of the three columns. Therefore, at each depth in the sensor array, V_{Pv} and V_{Svh} were determined between three sensor pairs (one pair in each column). The effects of confining pressure on V_{Pv} and V_{Svh} at a depth of 19 in. (48.3 cm) below the concrete footing are shown in Figures 7.5a and 7.5b, respectively. In Figure 7.5, the V_{Pv} and V_{Svh} values measured in all three sensor columns are shown, and the equations of the best-fit lines for this depth are given. Note that in the equations shown in Figure 7.5, σ_v is normalized by the atmospheric pressure (P_a) following the model suggested by Hardin (1978). Similar results at depths of 31 and 43 in. (78.7 and 109.2 cm) below the footing are shown in Figures 7.6 and 7.7, respectively. The trends shown in Figures 7.5 through 7.7 are summarized in Figure 7.8. As shown in Figure 7.8a, the exponents of the normal stress of the log V_{Pv} – log σ_v relationships are approximately equal at all depths, though the P_V-wave velocities are higher at the shallowest depth (19 in. (48.3 cm)). The behavior of V_{Svh} is more nearly the same at all three depths as shown in Figure 7.8b.

7.2.2.2 Stage 1; In terms of effective stresses

As mentioned in Sections 4.3.3 and 6.2.3, negative pore pressures likely existed at the time of the tests at Site 2. The presence of negative pore pressures makes the relationships based on total stress (shown in Figure 7.8) unsuitable for determining whether the soil became normally-consolidated over the range of stresses induced in Stage 1. As described in Section 6.2.3, the vertical effective stress (σ'_v) in the soil at Site 2 was estimated by adding the suction stress term (Lu and Likos 2006) to the total stress using Equation 6.2, where the suction stress was estimated as 720 psf (34.5 kPa). The addition of the suction stress has the effect of increasing the exponents of the various total stress relationships given in Figure 7.8. This increase in the exponents can be seen in Figure 7.9, where the effects of both total stress and effective stress on the downhole wave velocities are shown. For any given depth, the exponent of the log V_{Pv} – log σ'_v relationship is approximately double that of the log V_{Pv} – log σ_v relationship (Figure

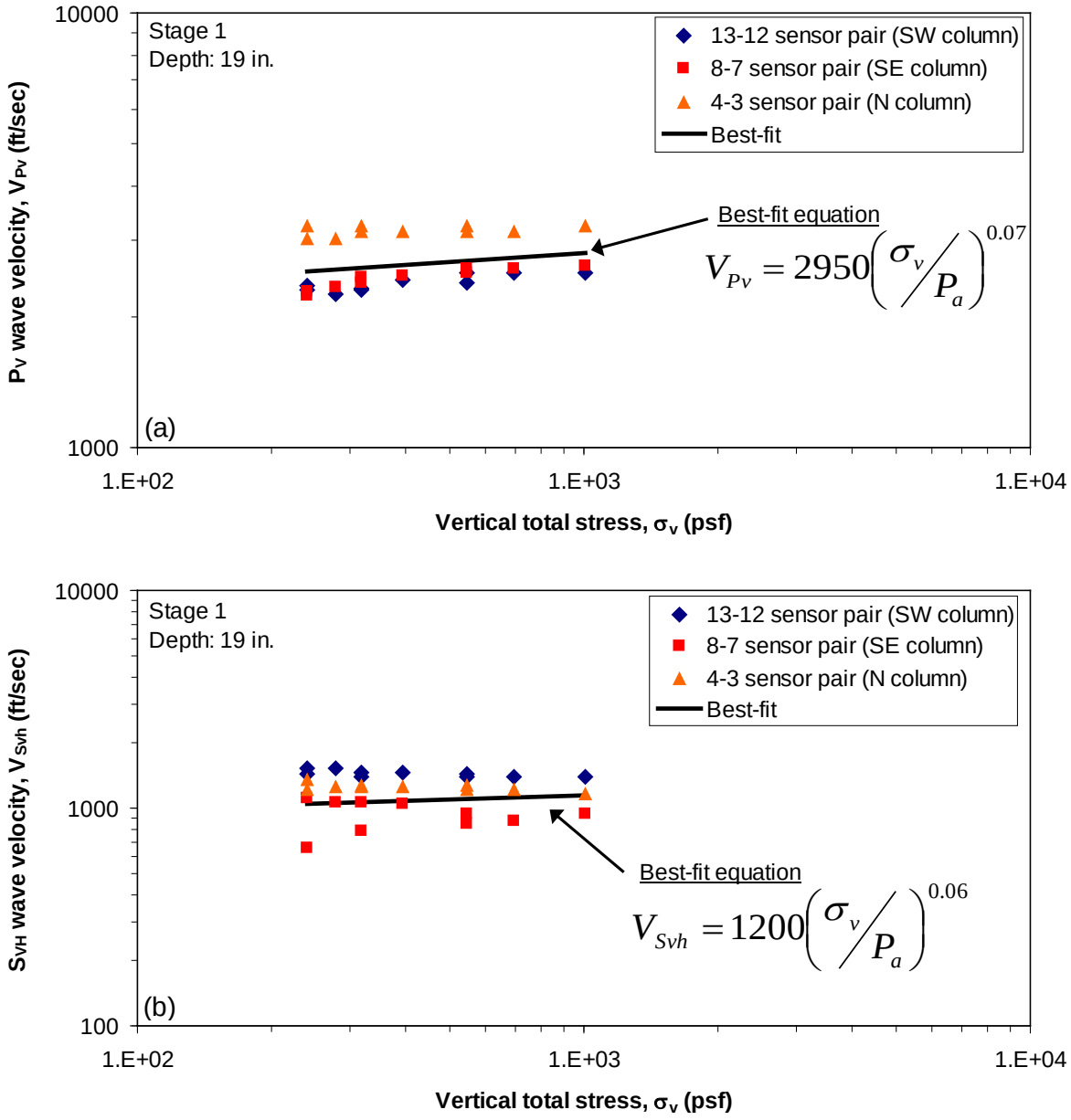

Figure 7.5. Variation of downhole wave velocities with increasing stress level at an average depth of 19 in. (48.3 cm) below the concrete footing in Stage 1: (a) log V_{Pv} – log σ_v and (b) log V_{Svh} – log σ_v

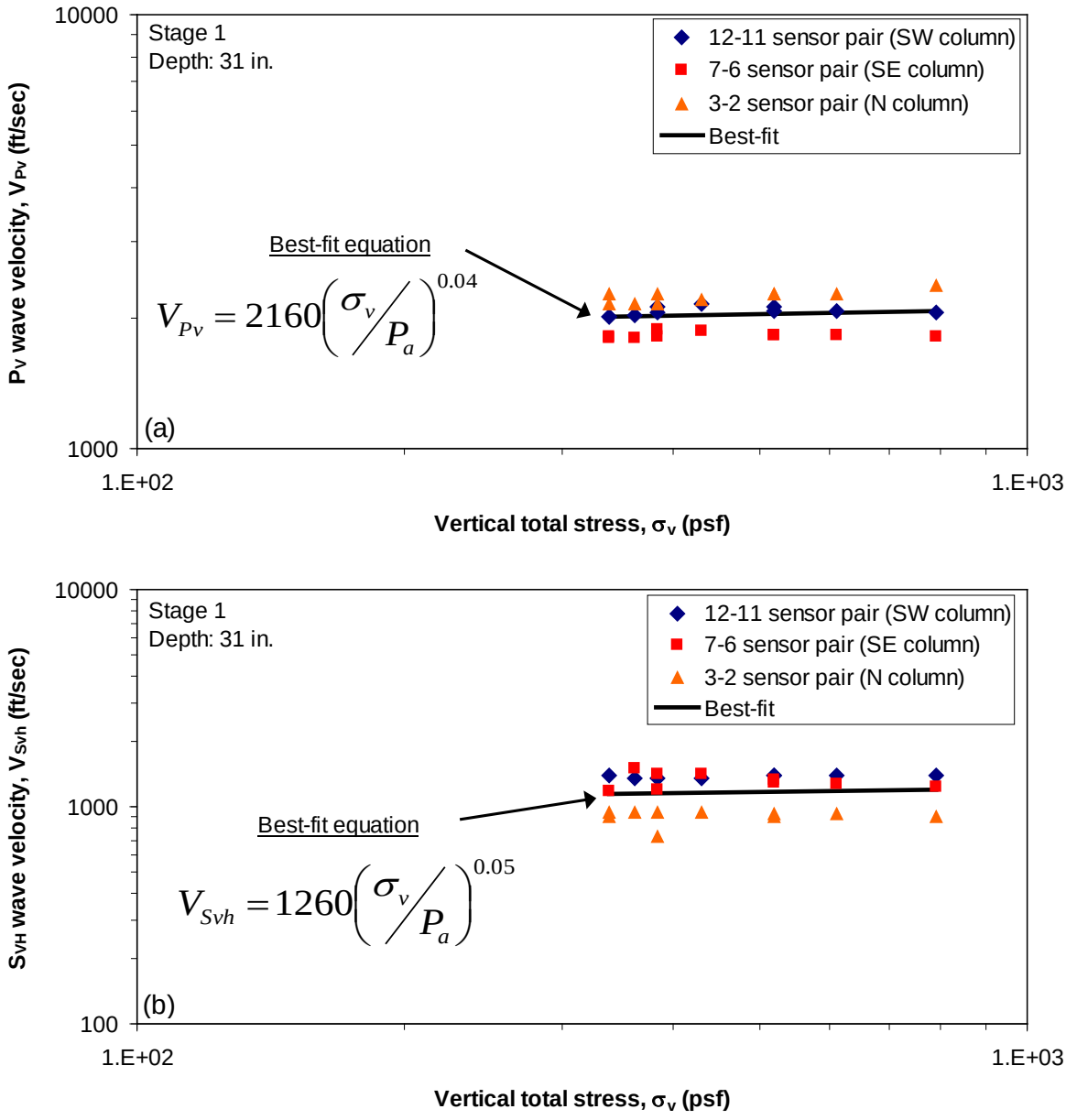

Figure 7.6. Variation of downhole wave velocities with increasing stress level at an average depth of 31 in. (78.7 cm) below the concrete footing in Stage 1: (a) log V_{Pv} – log σ_v and (b) log V_{Svh} – log σ_v

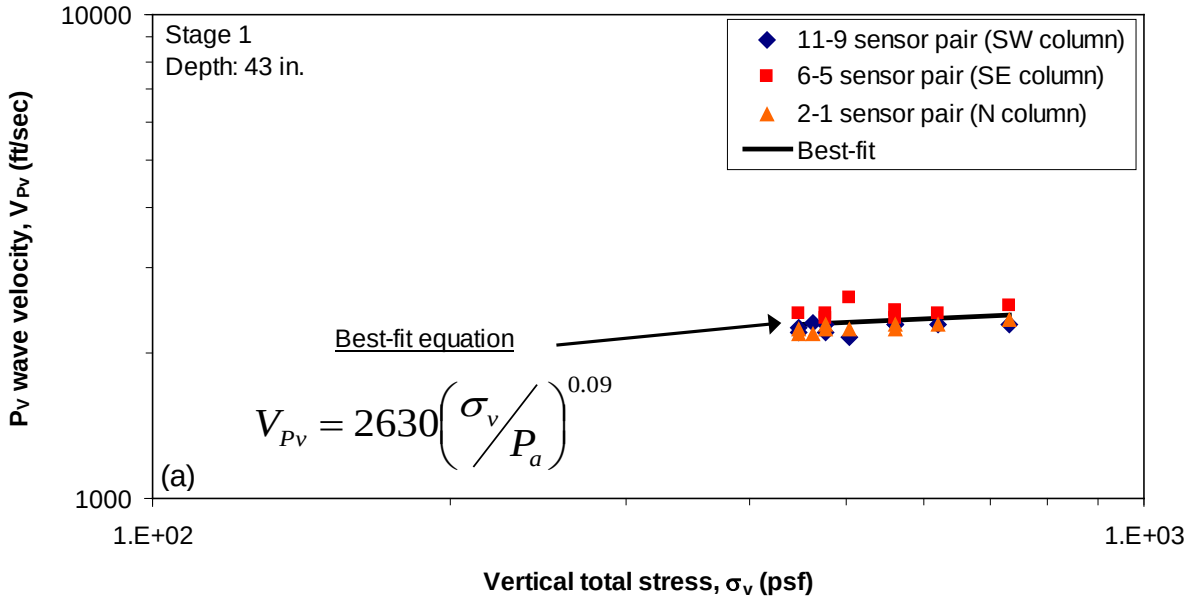

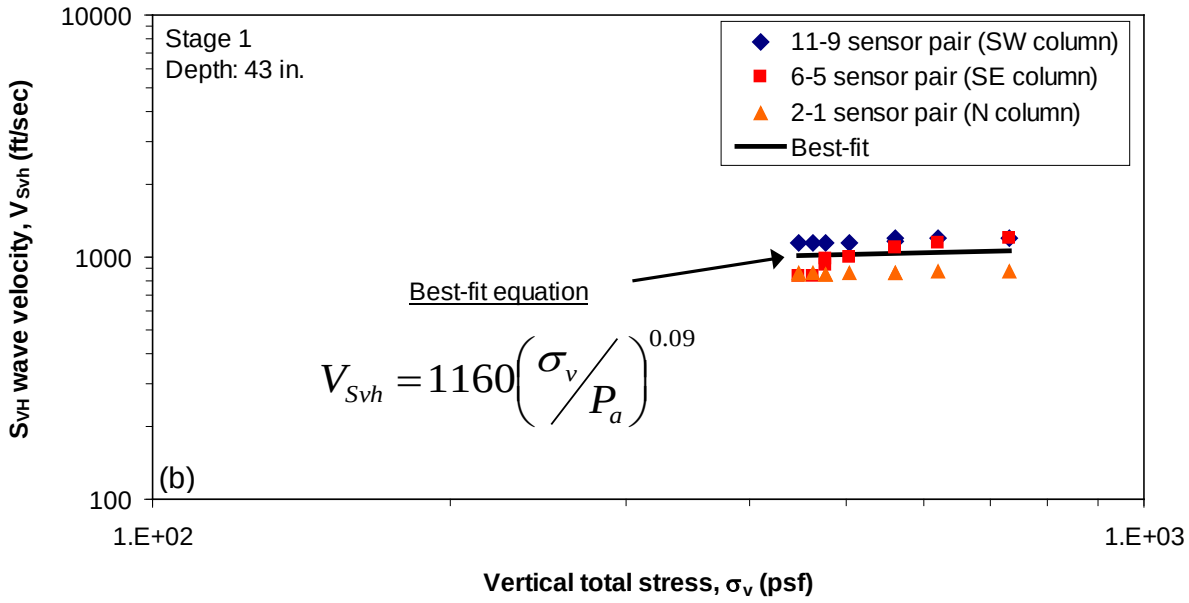

Figure 7.7. Variation of downhole wave velocities with increasing stress level at an average depth of 43 in. (109.2 cm) below the concrete footing in Stage 1: (a) log V_{Pv} – log σ_v and (b) log V_{Svh} – log σ_v

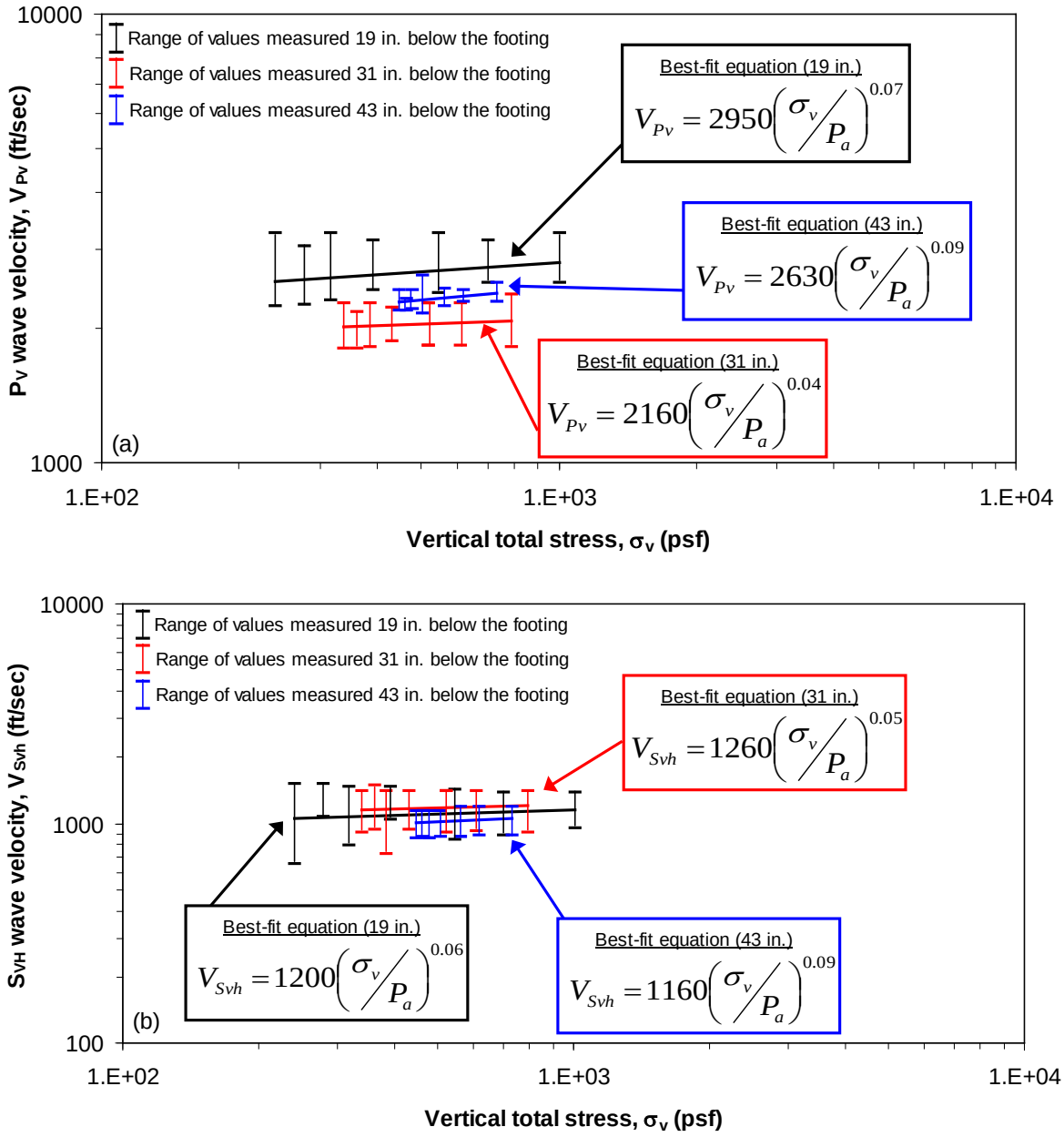

Figure 7.8. Variation of downhole wave velocities with increasing stress level at all depths below the footing in Stage 1: (a) log V_{Pv} – log σ_v and (b) log V_{Svh} – log σ_v

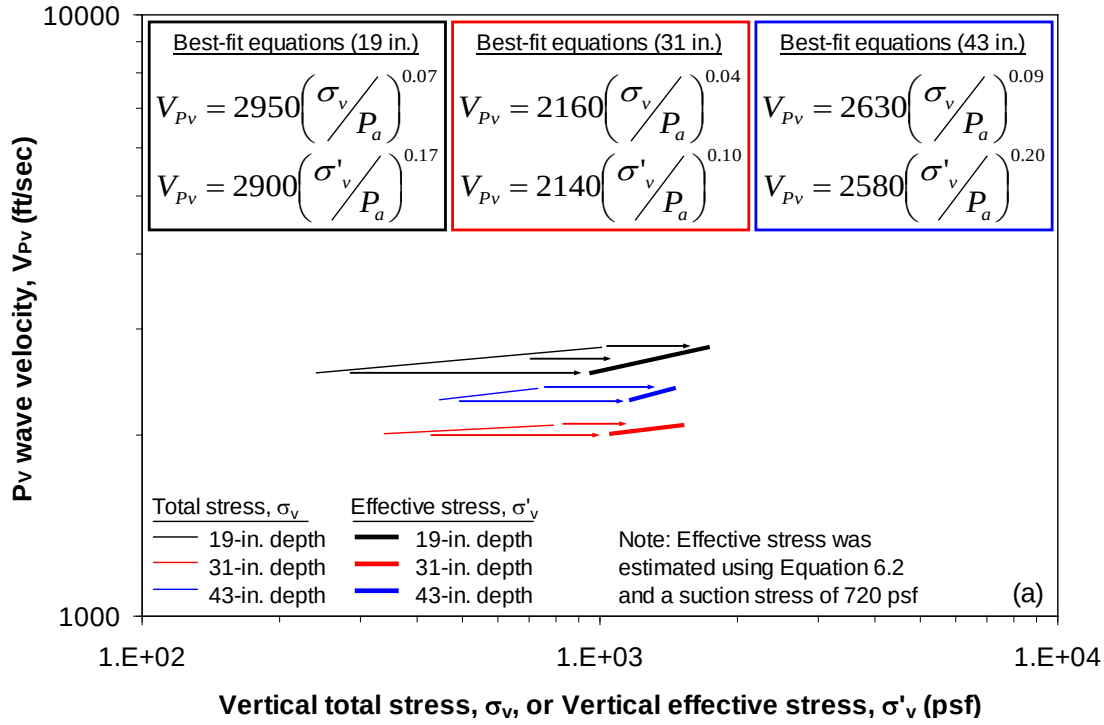

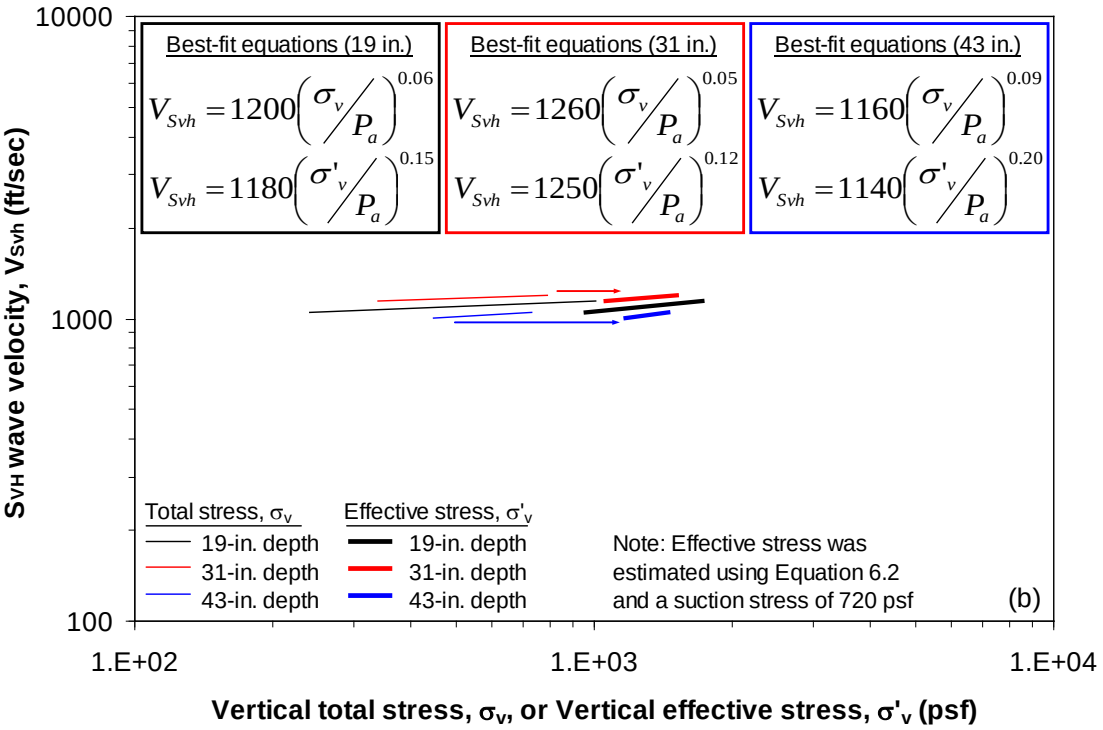

Figure 7.9. Comparison of the effect of total stress versus effective stress on the downhole wave velocities determined in Stage 1: (a) V_{Pv} and (b) V_{Svh}

7.9a). This observation is also true of the log V_{Svh} – log σ'_v and log V_{Svh} – log σ_v relationships shown in Figure 7.9b. However, all of the exponents given in Figure 7.9 (whether based on total or effective stress) are generally small and indicate that the soil at Site 2 was overconsolidated and remained so throughout the course of Stage 1.

7.2.2.3 Stage 4; In terms of total stresses

Nine static load steps were used in Stage 4 (see Figure 7.1). V_{Pv} and V_{Svh} were determined at nine distinct locations in the sensor array as described in Section 7.2.2.1 for Stage 1. The effects of confining pressure on the downhole wave velocities (V_{Pv} and V_{Svh}) at average depths of 19, 31, and 43 in. (48.3, 78.7, and 109.2 cm) below the concrete footing are shown in Figures 7.10, 7.11, and 7.12, respectively. The trends shown in Figures 7.10 through 7.12 are summarized in Figure 7.13. As shown in Figure 7.13a, the exponents of the log V_{Pv} – log σ_v relationships are approximately equal at all depths, though the P_V-wave velocities are higher at the deepest depth (43 in. (109.2 cm)). As noted in Stage 1, the behavior of V_{Svh} is about the same at all three depths as shown in Figure 7.13b.

7.2.2.4 Stage 4; In terms of effective stresses

The effective stresses beneath the footing were estimated in the same manner as that described in Section 7.2.2.2 for Stage 1. The effects of both total stress and effective stress on the downhole wave velocities in Stage 4 are shown in Figure 7.14. At every depth, the exponents of the effective stress relationships (log V_{Pv} – log σ'_v and log V_{Svh} – log σ'_v) are approximately double the exponents of the total stress relationships (log V_{Pv} – log σ_v and log V_{Svh} – log σ_v). A similar observation was made in Stage 1. Also, the exponents shown in Figure 7.14 (whether based on total or effective stress) are generally small. Therefore, as in Stage 1, the soil at Site 2 was likely overconsolidated and remained so throughout the course of Stage 4.

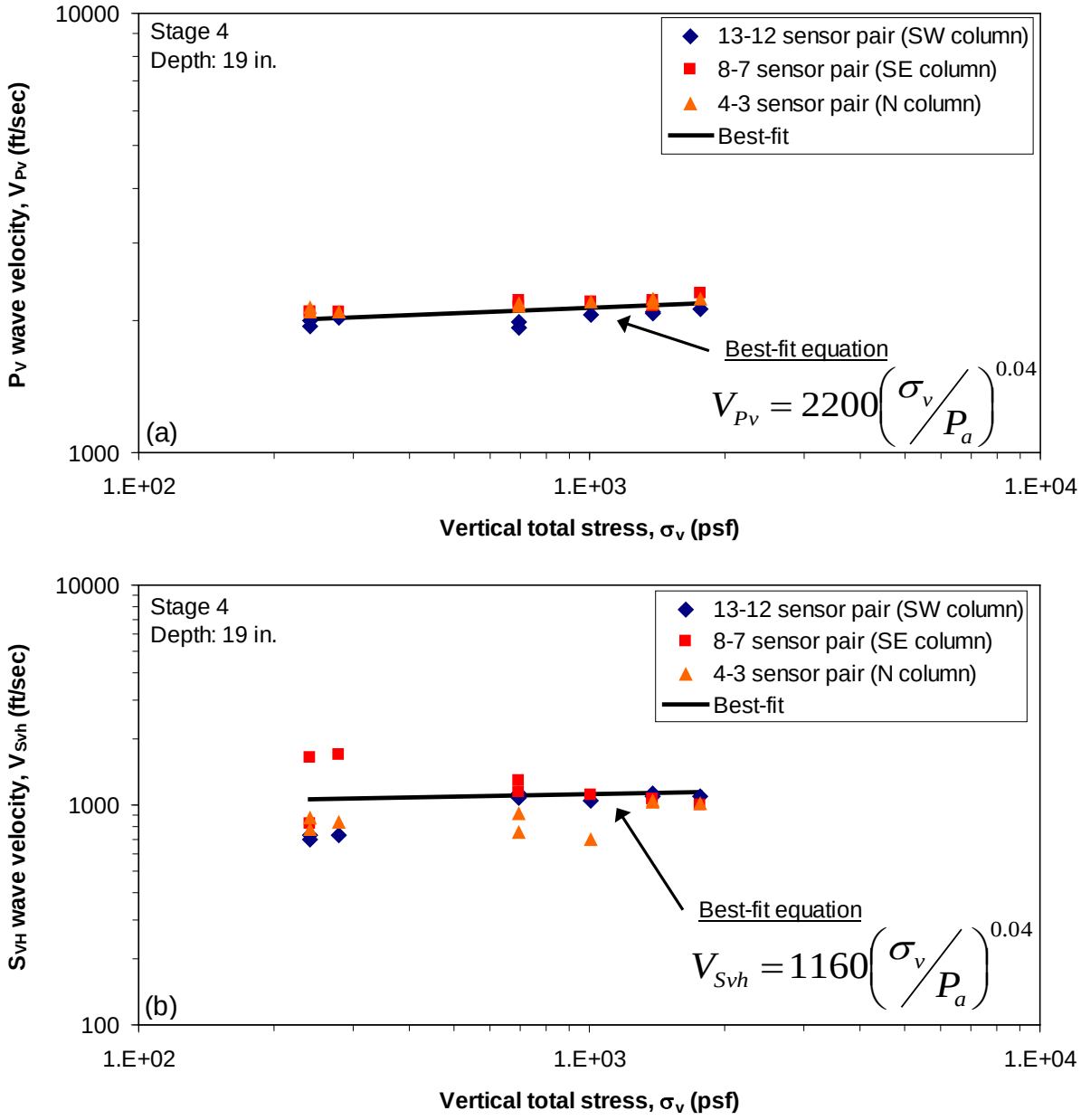

Figure 7.10. Variation of downhole wave velocities with increasing stress level at an average depth of 19 in. (48.3 cm) below the concrete footing in Stage 4: (a) log V_{Pv} – log σ_v and (b) log V_{Svh} – log σ_v

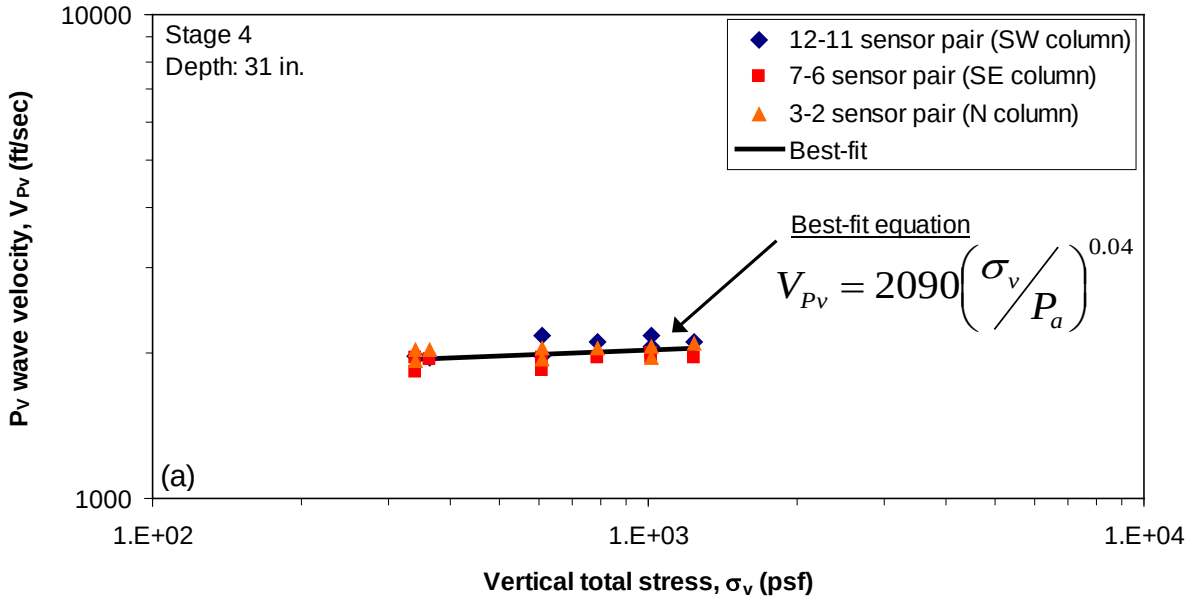

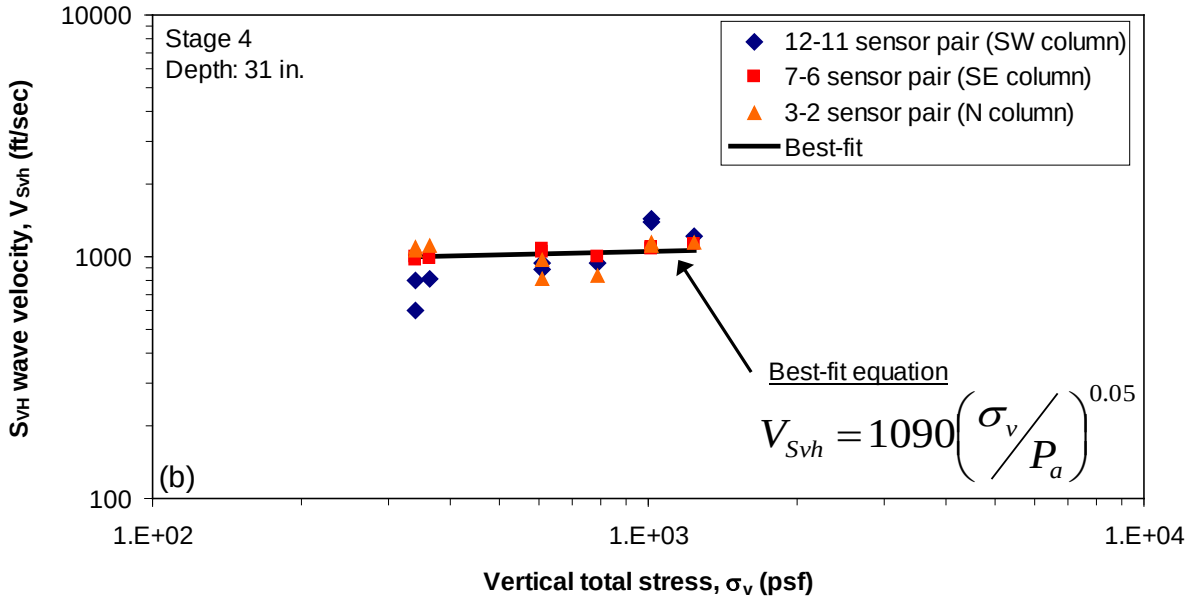

Figure 7.11. Variation of downhole wave velocities with increasing stress level at an average depth of 31 in. (78.7 cm) below the concrete footing in Stage 4: (a) log V_{Pv} – log σ_v and (b) log V_{Svh} – log σ_v

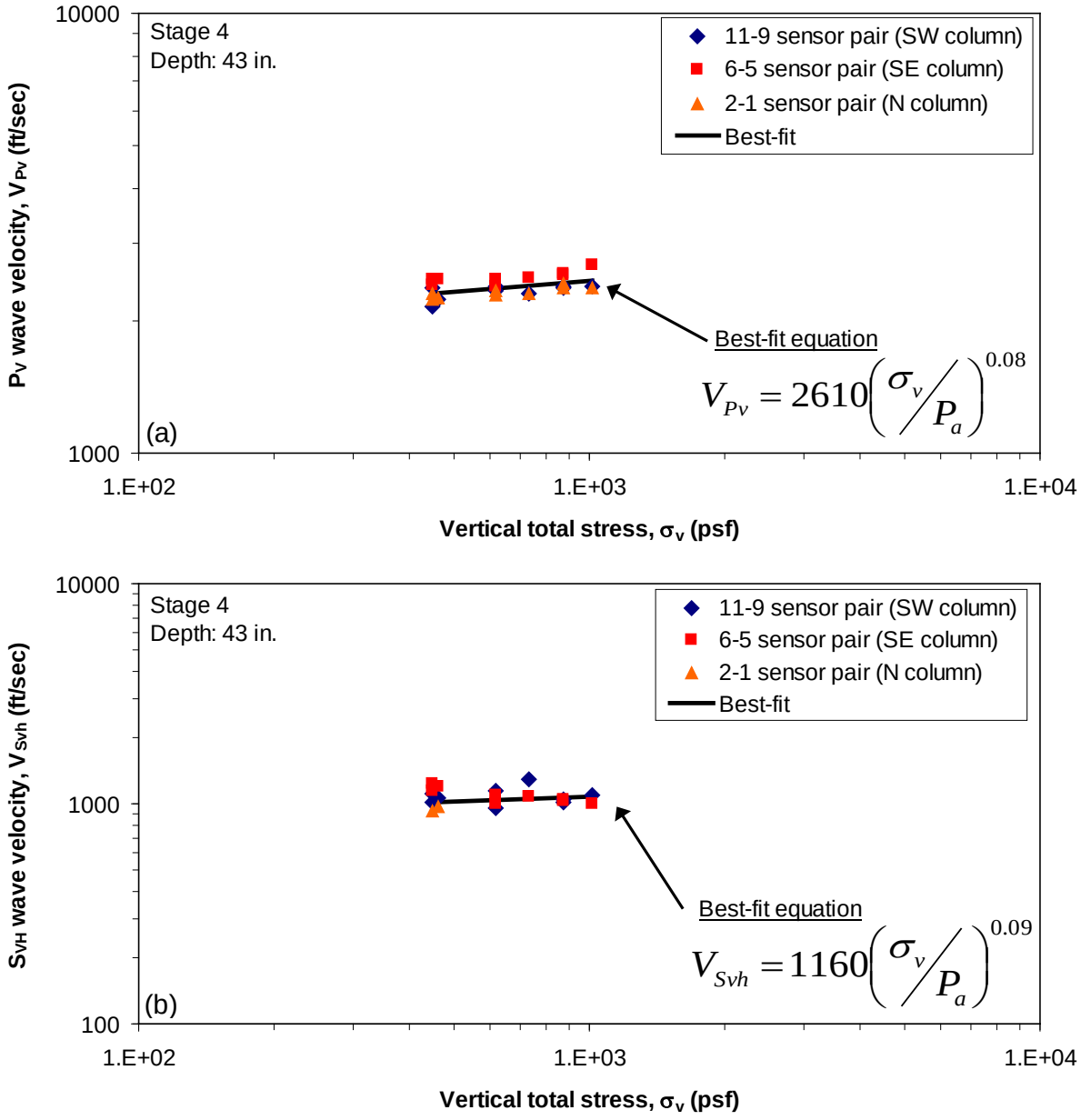

Figure 7.12. Variation of downhole wave velocities with increasing stress level at an average depth of 43 in. (109.2 cm) below the concrete footing in Stage 4: (a) log V_{Pv} – log σ_v and (b) log V_{Svh} – log σ_v

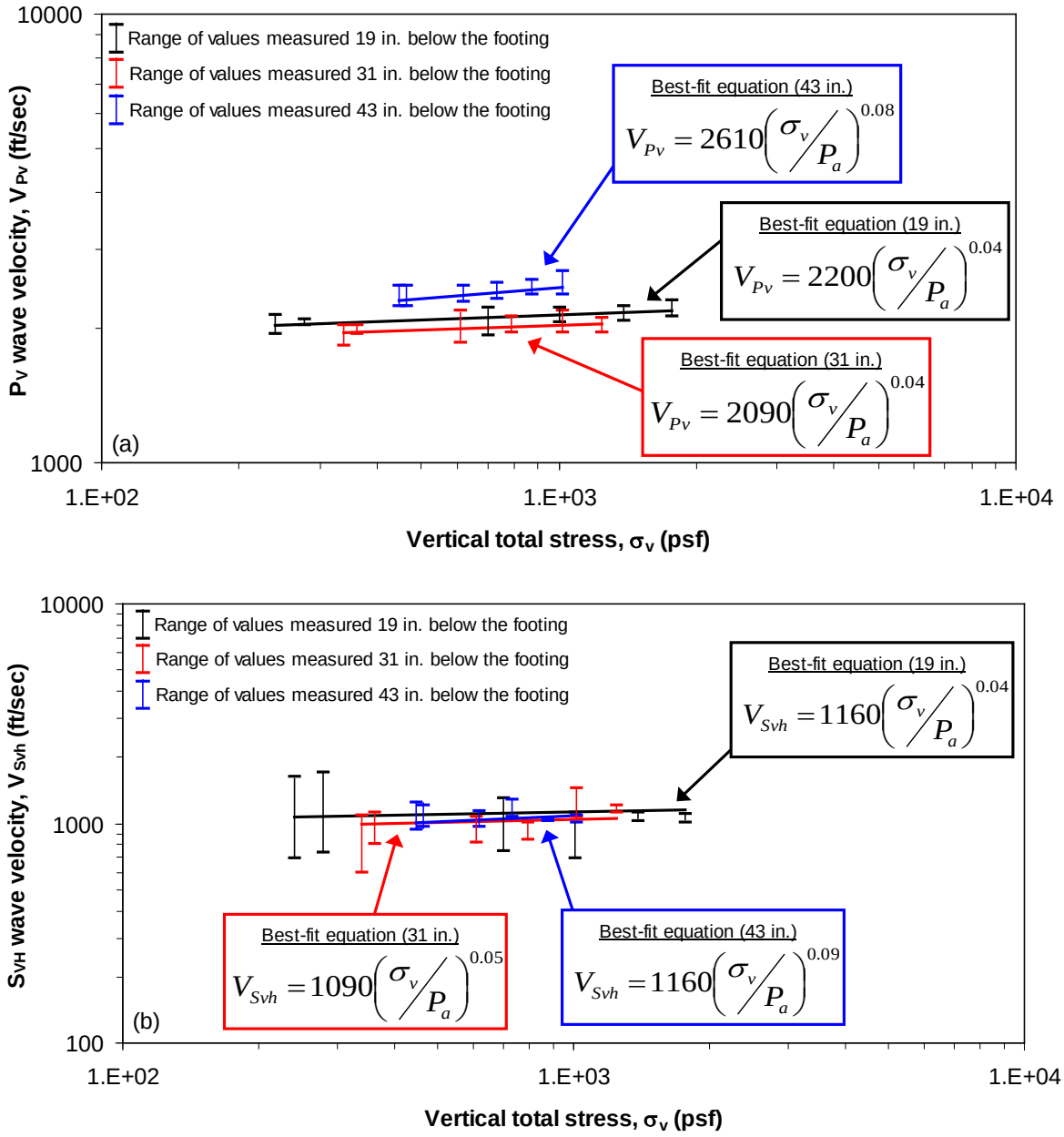

Figure 7.13. Variation of downhole wave velocities with increasing stress level at all depths below the footing in Stage 4: (a) log V_{Pv} – log σ_v and (b) log V_{Svh} – log σ_v

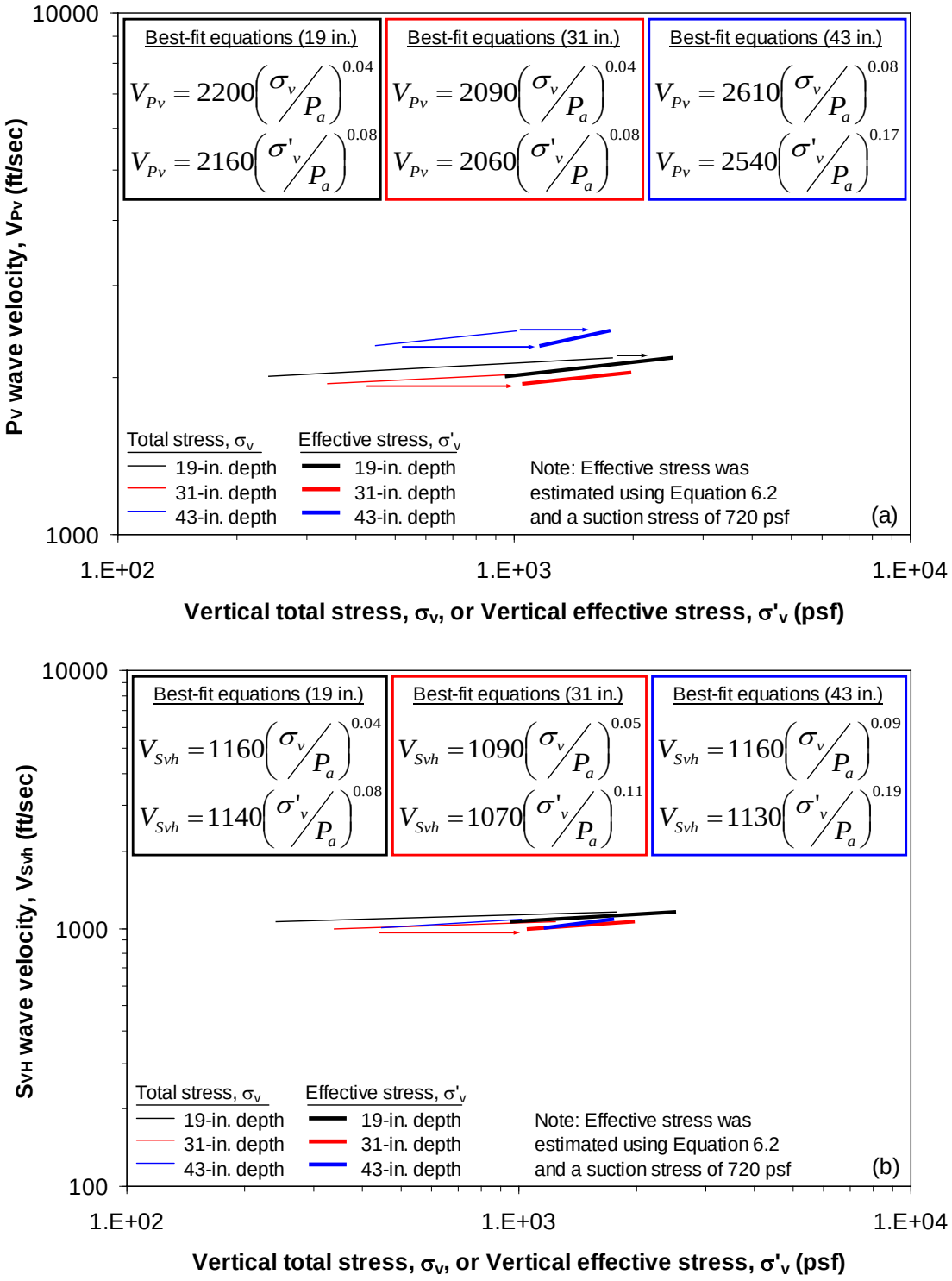

Figure 7.14. Comparison of the effect of total stress versus effective stress on the downhole wave velocities determined in Stage 4: (a) V_{Pv} and (b) V_{Svh}

7.2.2.5 Stage 7; In terms of total stresses

Nine static load steps were used in Stage 7 (see Figure 7.1). V_{Pv} and V_{Svh} values were determined at nine distinct locations in the sensor array as described in Section 7.2.2.1 for Stage 1. The effects of confining pressure on the downhole wave velocities (V_{Pv} and V_{Svh}) at average depths of 19, 31, and 43 in. (48.3, 78.7, and 109.2 cm) below the concrete footing are shown in Figures 7.15, 7.16, and 7.17, respectively. The trends shown in Figures 7.15 through 7.17 are summarized in Figure 7.18. As shown in Figure 7.18a, the exponents of the log V_{Pv} – log σ_v relationships at average depths of 19 and 31 in. (48.3 and 78.7 cm) are approximately equal. A similar observation about the log V_{Svh} – log σ_v relationships at these two depths is shown in Figure 7.18b. However, at an average depth of 43 in. (109.2 cm), the exponents of both the log V_{Pv} – log σ_v and log V_{Svh} – log σ_v relationships are twice as much as the exponents at the two shallower depths. There is generally good agreement between the V_{Svh} values measured at all three depths (Figure 7.18b), but V_{Pv} appears to show more dependency with depth (Figure 7.18a).

7.2.2.6 Stage 7; In terms of effective stresses

The effective stresses beneath the footing were estimated in the same manner as that described in Section 7.2.2.2 for Stage 1. The effects of both total stress and effective stress on the downhole wave velocities in Stage 7 are shown in Figure 7.19. At every depth, the exponents of the effective stress relationships (log V_{Pv} – log σ'_v and log V_{Svh} – log σ'_v) are approximately double the exponents of the total stress relationships (log V_{Pv} – log σ_v and log V_{Svh} – log σ_v). Similar observations were made in Stages 1 and 4. Also, the exponents shown in Figure 7.19 (whether based on total or effective stress) are generally small. Therefore, as in Stages 1 and 4, the soil at Site 2 is overconsolidated and remained so throughout the course of Stage 7.

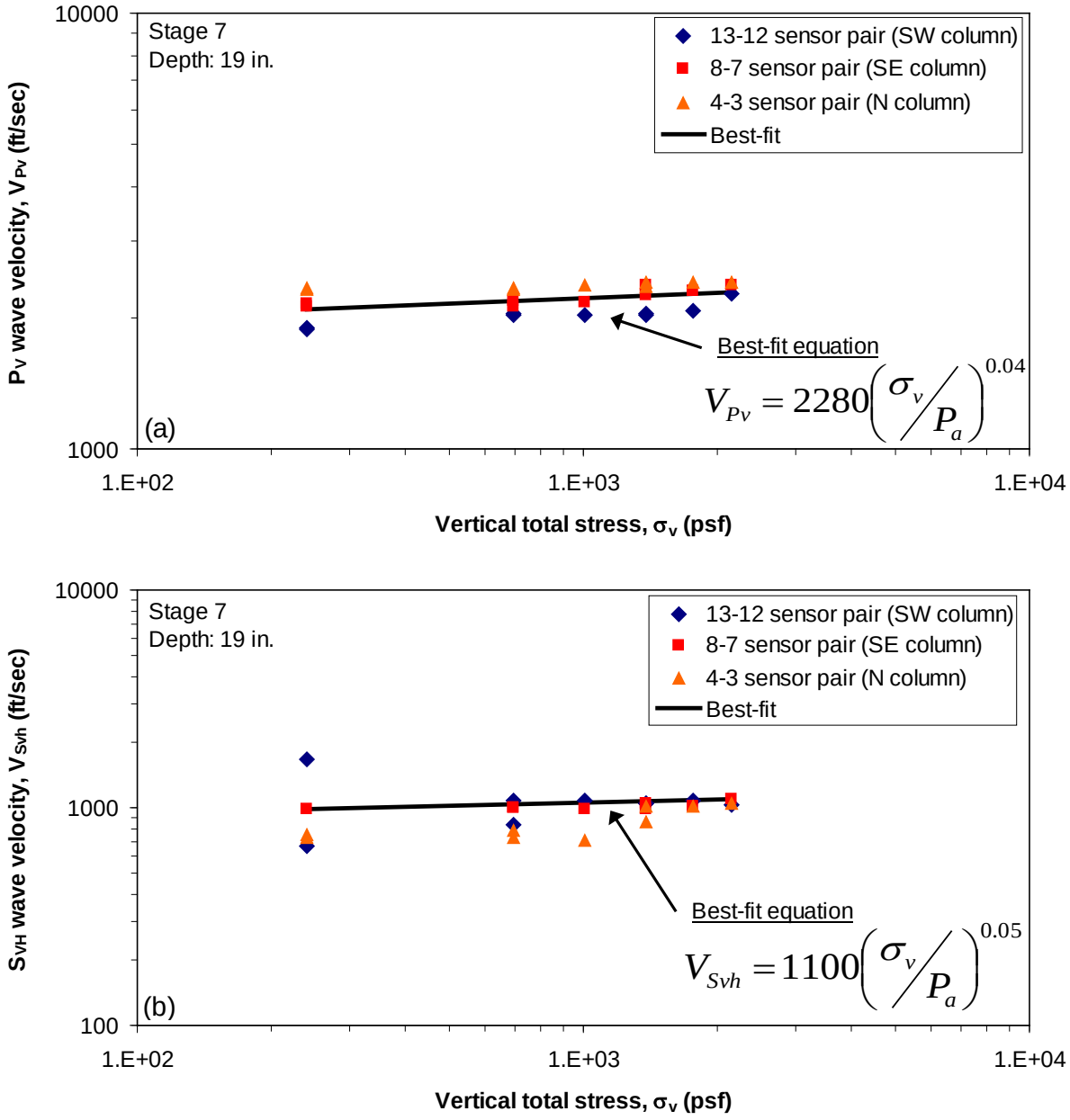

Figure 7.15. Variation of downhole wave velocities with increasing stress level at an average depth of 19 in. (48.3 cm) below the concrete footing in Stage 7: (a) log V_{Pv} – log σ_v and (b) log V_{Svh} – log σ_v

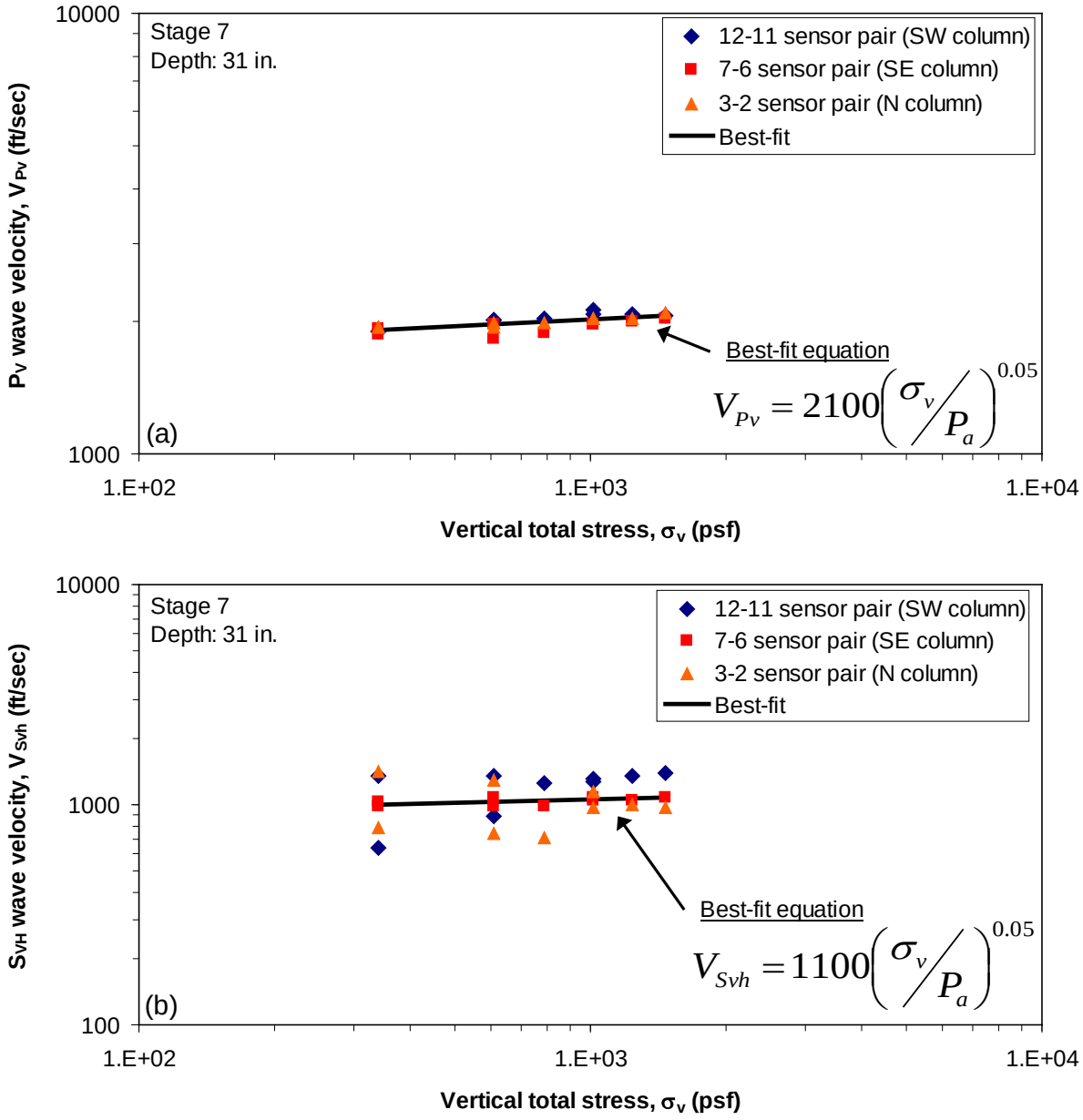

Figure 7.16. Variation of downhole wave velocities with increasing stress level at an average depth of 31 in. (78.7 cm) below the concrete footing in Stage 7: (a) log V_{Pv} – log σ_v and (b) log V_{Svh} – log σ_v

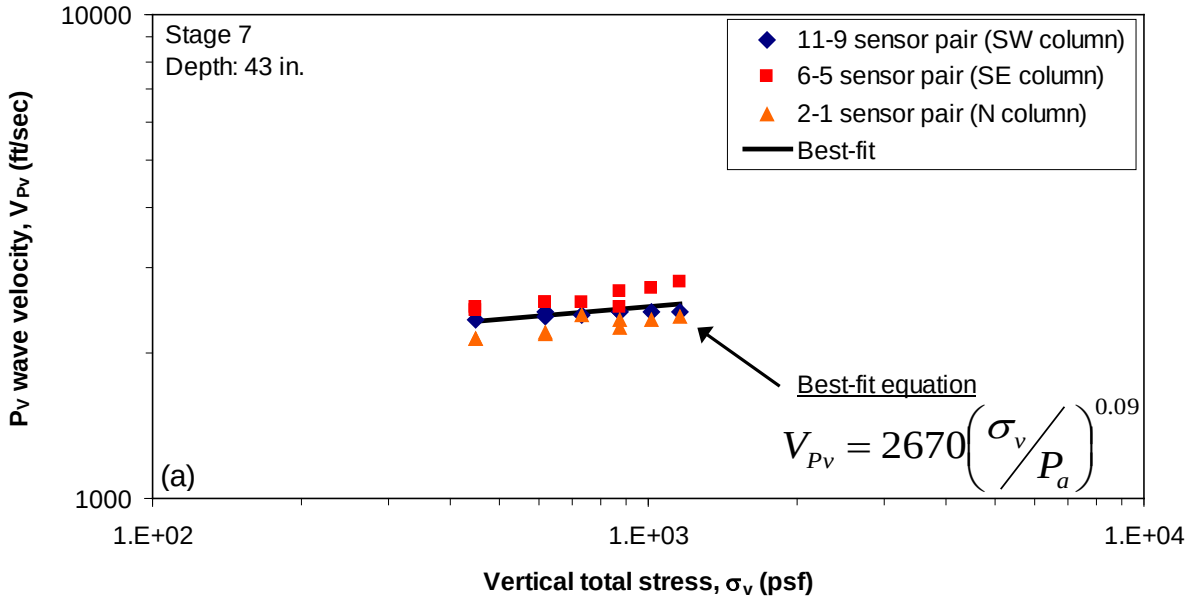

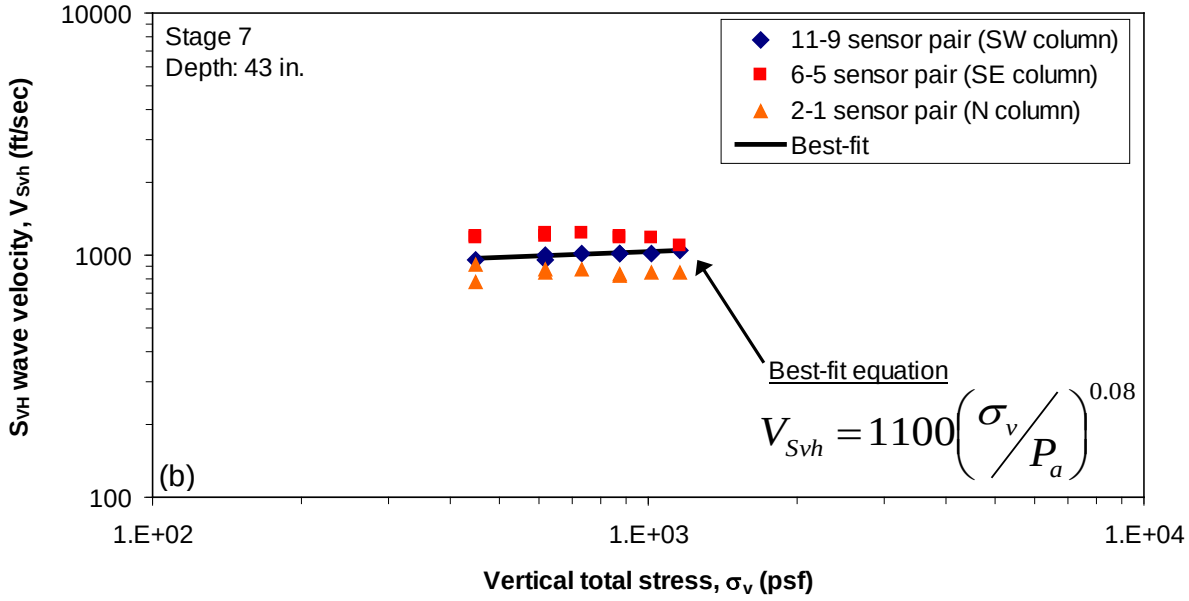

Figure 7.17. Variation of downhole wave velocities with increasing stress level at an average depth of 43 in. (109.2 cm) below the concrete footing in Stage 7: (a) log V_{Pv} – log σ_v and (b) log V_{Svh} – log σ_v

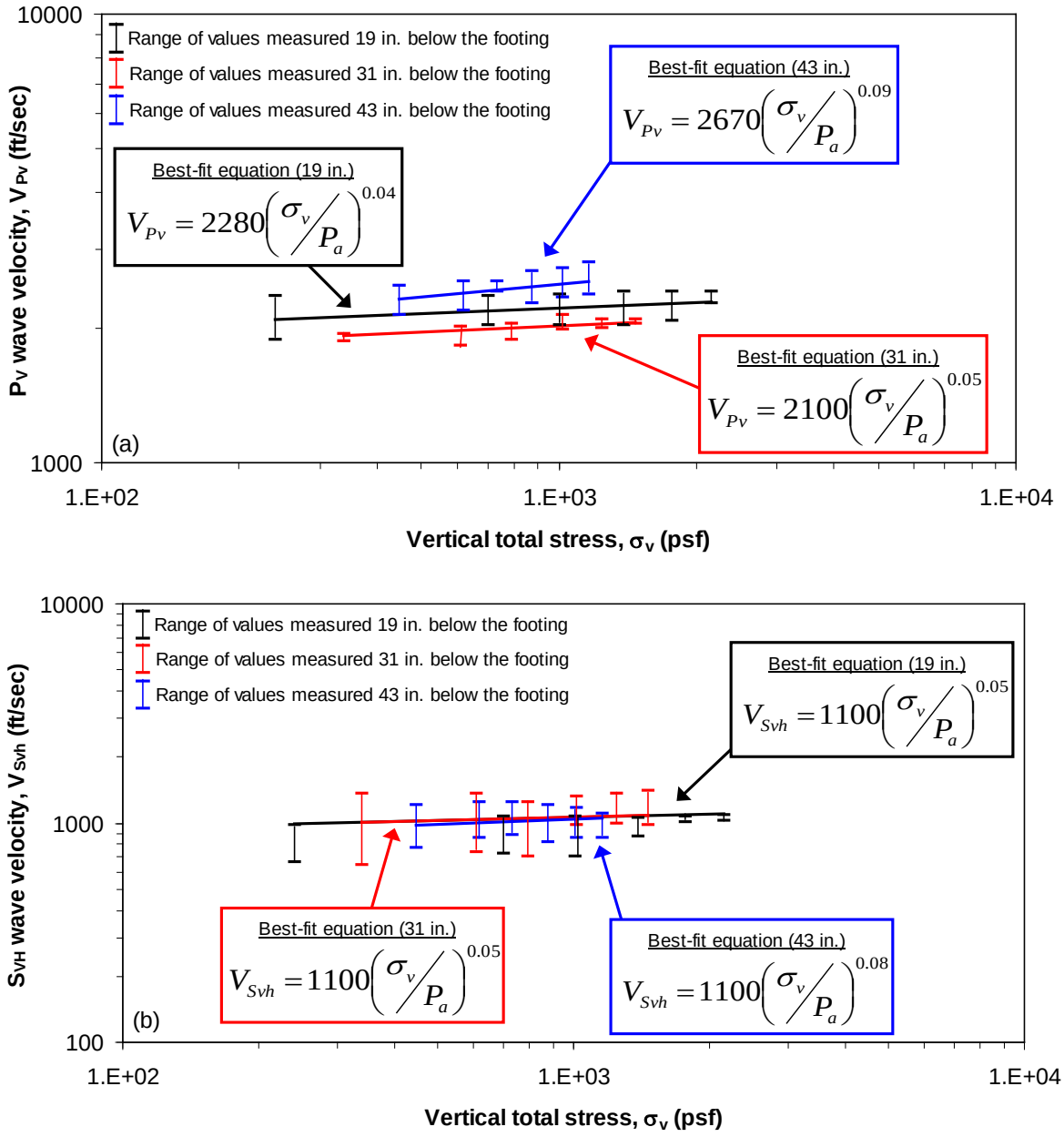

Figure 7.18. Variation of downhole wave velocities with increasing stress level at all depths below the footing in Stage 7: (a) log V_{Pv} – log σ_v and (b) log V_{Svh} – log σ_v

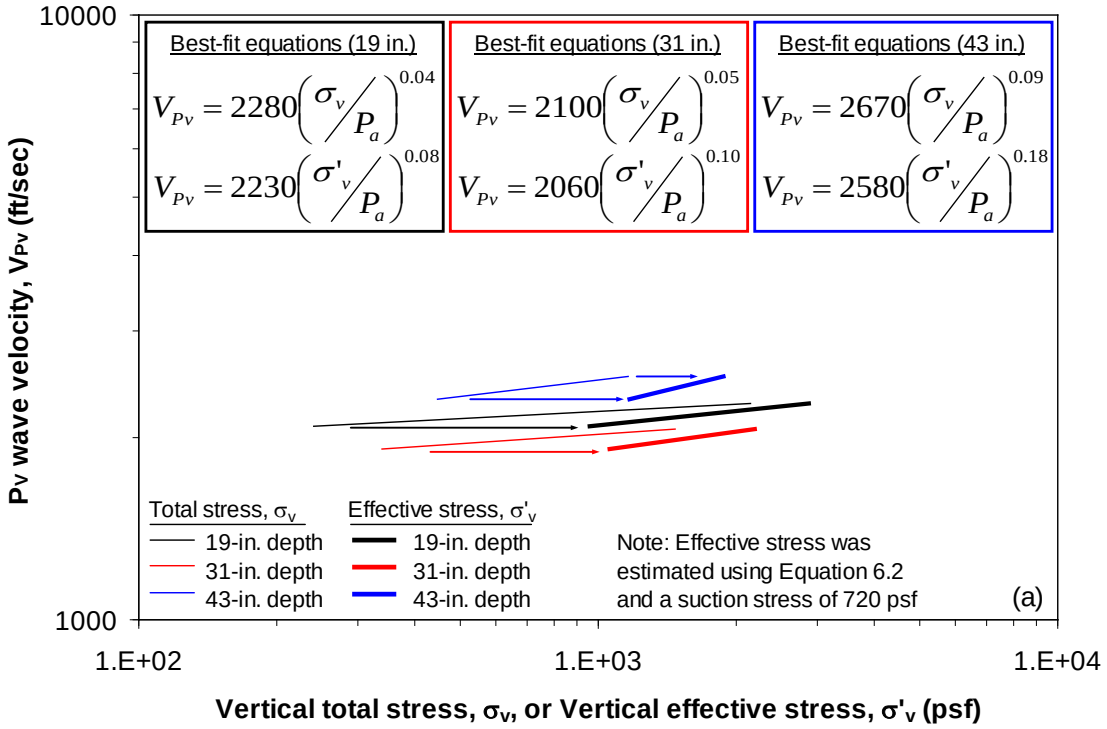

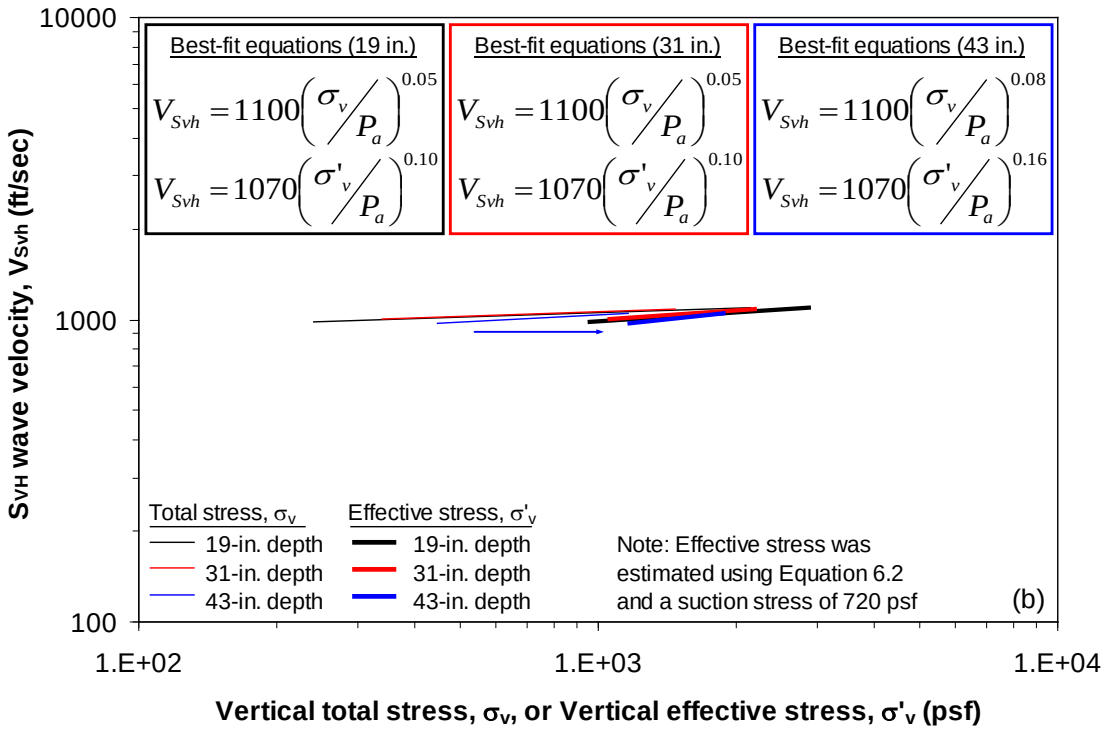

Figure 7.19. Comparison of the effect of total stress versus effective stress on the downhole wave velocities determined in Stage 7: (a) V_{Pv} and (b) V_{Svh}

7.2.3 Discussion

The variations of the downhole wave velocities with stress level in all stages and at all depths are summarized in Figures 7.20 and 7.21 for V_{Pv} and V_{Svh}, respectively. Note that for clarity, only the total and effective stress best-fit lines that are shown in Figures 7.9, 7.14, and 7.19 are included in Figures 7.20 and 7.21. The equations of all best-fit lines, including the average effective stress equations at each depth, are listed in Table 7.1. Based on the results presented in Sections 7.2.1 and 7.2.2, several observations can be made about the downhole tests at Site 2.

At the shallowest depth in the sensor array (19 in. (48.3 cm)), the P_V-wave velocities determined in Stage 1 are noticeably higher than the wave velocities in either Stages 4 or 7. This same effect occurs at the middle depth (31 in. (78.7 cm)) with the S_{VH}-wave velocities. The difference in velocity between the stages generally diminished with depth in both cases. This behavior is also seen in the V_{Pv} profiles (Figures 7.2 and 7.4a) and the V_{Svh} profiles (Figures 7.3a, 7.3b, and 7.4b). The reduction in the downhole wave velocities between Stages 1 and 4 was likely caused by the intervening vertical and horizontal dynamic excitations applied with Thumper in Stages 2 and 3, although near-surface changes in water content could also contribute to this reduction. The reduction in wave velocities between Stages 4 and 7 is much less pronounced, suggesting that perhaps most of the change in the soil occurred before dynamic excitations were applied with T-Rex in Stages 5 and 6. The exact manner in which the dynamic excitations imparted by Thumper caused this reduction is not known. However, possible mechanisms include: (1) destruction of cementation bonds present in the soil, (2) some change in the structural anisotropy in the soil skeleton, or (3) a combination of these factors. As seen in Figures 7.20c and 7.21c, there is virtually no difference in the wave velocities measured in Stages 1, 4, and 7 at the deepest depth (43 in. (109.2 cm). Therefore, it was concluded that the dynamic excitations had little or no effect on the soil at this depth.

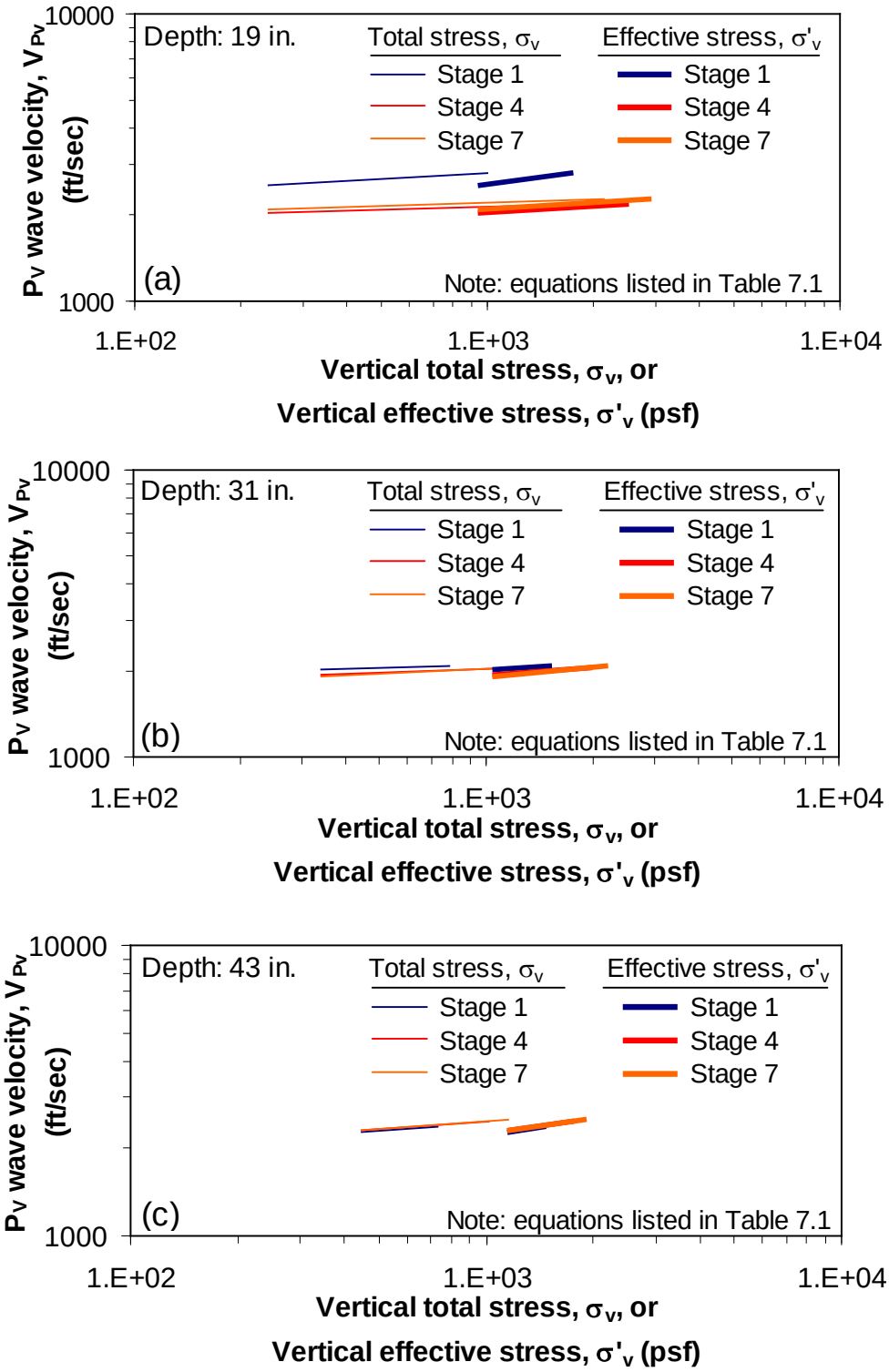

Figure 7.20. Variation of best-fit V_{Pv} with stress level in all stages of downhole tests and at all depths at Site 2: (a) 19 in. (48.3 cm), (b) 31 in. (78.7 cm), and (c) 43 in. (109.2 cm)

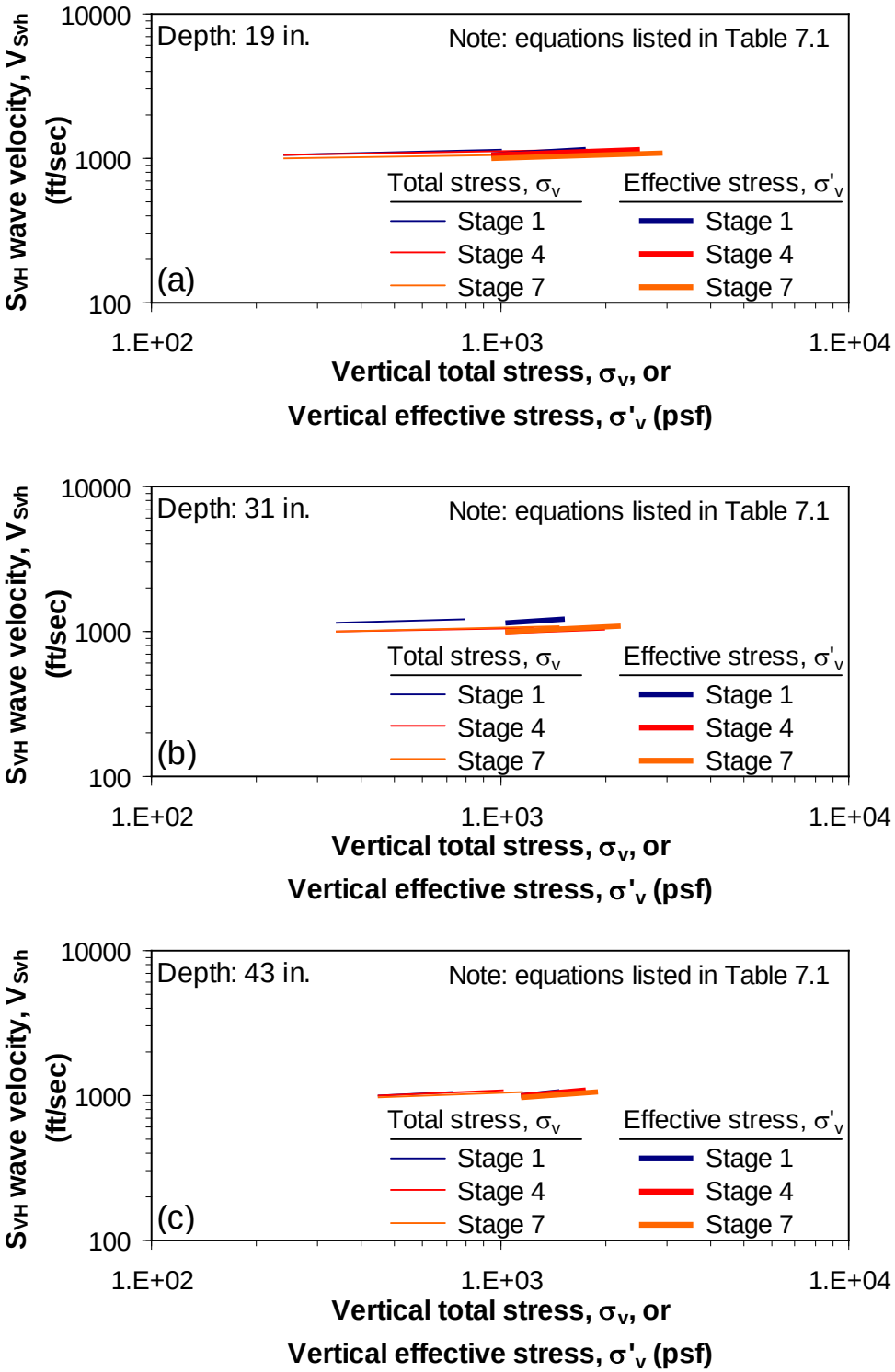

Figure 7.21. Variation of best-fit V_{Svh} with stress level in all stages of downhole tests and at all depths at Site 2: (a) 19 in. (48.3 cm), (b) 31 in. (78.7 cm), and (c) 43 in. (109.2 cm)

Table 7.1. Summary of best-fit equations for downhole tests at Site 2

Depth	Stage	Total stress equations	Effective stress equations	Average effective stress equations (based on all stages)
19-in.	1	$V_{Pv} = 2950\left(\sigma_v / P_a\right)^{0.07}$ $V_{Svh} = 1200\left(\sigma_v / P_a\right)^{0.06}$	$V_{Pv} = 2900\left(\sigma'_v / P_a\right)^{0.17}$ $V_{Svh} = 1180\left(\sigma'_v / P_a\right)^{0.15}$	$V_{Pv} = 2430\left(\sigma'_v / P_a\right)^{0.11}$ $V_{Svh} = 1130\left(\sigma'_v / P_a\right)^{0.11}$
	4	$V_{Pv} = 2200\left(\sigma_v / P_a\right)^{0.04}$ $V_{Svh} = 1160\left(\sigma_v / P_a\right)^{0.04}$	$V_{Pv} = 2160\left(\sigma'_v / P_a\right)^{0.08}$ $V_{Svh} = 1140\left(\sigma'_v / P_a\right)^{0.08}$	
	7	$V_{Pv} = 2280\left(\sigma_v / P_a\right)^{0.04}$ $V_{Svh} = 1100\left(\sigma_v / P_a\right)^{0.05}$	$V_{Pv} = 2230\left(\sigma'_v / P_a\right)^{0.08}$ $V_{Svh} = 1070\left(\sigma'_v / P_a\right)^{0.10}$	
31-in.	1	$V_{Pv} = 2160\left(\sigma_v / P_a\right)^{0.04}$ $V_{Svh} = 1260\left(\sigma_v / P_a\right)^{0.05}$	$V_{Pv} = 2140\left(\sigma'_v / P_a\right)^{0.10}$ $V_{Svh} = 1250\left(\sigma'_v / P_a\right)^{0.12}$	$V_{Pv} = 2090\left(\sigma'_v / P_a\right)^{0.09}$ $V_{Svh} = 1130\left(\sigma'_v / P_a\right)^{0.11}$
	4	$V_{Pv} = 2090\left(\sigma_v / P_a\right)^{0.04}$ $V_{Svh} = 1090\left(\sigma_v / P_a\right)^{0.05}$	$V_{Pv} = 2060\left(\sigma'_v / P_a\right)^{0.08}$ $V_{Svh} = 1070\left(\sigma'_v / P_a\right)^{0.11}$	
	7	$V_{Pv} = 2100\left(\sigma_v / P_a\right)^{0.05}$ $V_{Svh} = 1100\left(\sigma_v / P_a\right)^{0.05}$	$V_{Pv} = 2060\left(\sigma'_v / P_a\right)^{0.10}$ $V_{Svh} = 1070\left(\sigma'_v / P_a\right)^{0.10}$	
43-in.	1	$V_{Pv} = 2630\left(\sigma_v / P_a\right)^{0.09}$ $V_{Svh} = 1160\left(\sigma_v / P_a\right)^{0.09}$	$V_{Pv} = 2580\left(\sigma'_v / P_a\right)^{0.20}$ $V_{Svh} = 1140\left(\sigma'_v / P_a\right)^{0.20}$	$V_{Pv} = 2570\left(\sigma'_v / P_a\right)^{0.18}$ $V_{Svh} = 1110\left(\sigma'_v / P_a\right)^{0.18}$
	4	$V_{Pv} = 2610\left(\sigma_v / P_a\right)^{0.08}$ $V_{Svh} = 1160\left(\sigma_v / P_a\right)^{0.09}$	$V_{Pv} = 2540\left(\sigma'_v / P_a\right)^{0.17}$ $V_{Svh} = 1130\left(\sigma'_v / P_a\right)^{0.19}$	
	7	$V_{Pv} = 2670\left(\sigma_v / P_a\right)^{0.09}$ $V_{Svh} = 1100\left(\sigma_v / P_a\right)^{0.08}$	$V_{Pv} = 2580\left(\sigma'_v / P_a\right)^{0.18}$ $V_{Svh} = 1070\left(\sigma'_v / P_a\right)^{0.16}$	

**Note: Depths are the distances from the base of the concrete footing to the midpoint of each sensor pair assuming a 1-in. (2.5-cm) thick sand layer (see Figure 6.7)

Given the results of previous downhole tests in the Hornsby Bend area (at Site 1 discussed in Chapter 5 and at a nearby site discussed by Van Pelt, 2010), the soil at Site 2 was initially assumed to be heavily overconsolidated. This assumption was confirmed by the results of the downhole tests at Site 2. In all stages of downhole tests at Site 2, the exponents of the log V_{Pv} – log σ_v and log V_{Svh} – log σ_v relationships ranged from 0.04 to 0.09. When the influence of effective stress on the small-strain, downhole wave velocities was examined, the exponents of the effective stress relationships (log V_{Pv} – log σ'_v and log V_{Svh} – log σ'_v) were approximately double the exponents of the total stress relationships and ranged from 0.08 to 0.20. This doubling of the exponents was observed in every load stage and at every depth in the embedded sensor array (Table 7.1). Though the exponents of the effective stress relationships were twice those of the total stress relationships, the variation of V_{Pv} and V_{Svh} with increasing stress level (whether based on total or effective stress) was still relatively small, suggesting that the soil at Site 2 was initially overconsolidated and remained so throughout all stages of downhole testing. Even at the highest loads applied in Stage 7, there was no identifiable stress level where the exponents of the best-fit lines increased to a value typical of a normally-consolidated soil. However, the largest exponents of the effective stress relationships (about 0.20) were observed at the deepest depth, suggesting that the overconsolidation in the soil decreases with depth. This is consistent with the assumption that the overconsolidation near the ground surface is partly due to negative pore pressures as discussed in Chapter 6.

7.3 SMALL-STRAIN CROSSHOLE TESTS

The two types of body waves generated in the transient, small-strain crosshole tests were: (1) horizontally-propagating, constrained compression waves (P_H waves) and (2) horizontally-propagating, vertically-polarized shear waves (S_{HV} waves). The wave propagation velocities (V_{Ph} and V_{Shv}) were calculated at the three shallowest depths in the embedded sensor array (13, 25, and 37 in. (33, 64, and 94 cm) beneath the base of the footing). However, at the deepest depth in the sensor array (49 in. (125 cm)), the

recorded waveforms were weak, and identification of the P_H and S_{HV} wave arrivals was not possible. Accordingly, the results at this depth are not discussed further.

At the three shallowest depths in the embedded sensor array, V_{Ph} was determined between the crosshole source rod and the receivers in the sensor column closest to the source. This source-to-receiver method was selected because the P_H waves were filtered out significantly by the soil as the distance from the source increased. Accordingly, the arrival of the P_H waves at the receivers in the sensor columns furthest from the source could not be readily identified in many cases, and the interval travel times between sensors could not be calculated. The travel times between the source rod and the receivers were adjusted to account for the time required for the wave to travel from the top of the rod (where the transient impact was applied) down to the tip. The determination of the confining pressure (σ_h) associated with the source-to-receiver P_H-wave velocity is problematic since the wave travels along a path which lies in at least two distinct regions: (1) an area near the source rod that is not affected by the increase in vertical load applied to the footing and (2) an area near the receiver which experiences an increase in confining pressure due to the increase in vertical load applied to the footing. Therefore, the σ_h associated with the source-to-receiver V_{Ph} was estimated by first assuming a trapezoidal stress distribution beneath the footing. Then, the distances that the wave travels through the two regions discussed above were estimated at every depth, and a "weighted average" σ_h was determined for each depth. Using this method, the range of confining pressures induced in the case of P_H waves was generally small (about half of a log cycle in σ_h and less than $1/10^{th}$ of a log cycle in σ'_h).

The S_{HV}-wave signals recorded by the sensors in the array were relatively strong, and the arrivals of the S_{HV} waves were readily identified even in the sensor column furthest from the source. Therefore, V_{Shv} was determined between adjacent sensors using first arrivals of the S_{HV} wave as described in Chapter 4. At each depth, the interval travel time was computed between the two sensors that were most "in-line" with the source.

For example, referring to Figures 6.7 and 6.12, Sensors 3 and 7 (in the North and Southeast sensor columns, respectively) were located approximately in a straight line with Rod 2 during Stages 1 and 4, and the V_{Shv} between these two sensors was taken as the V_{Shv} at this depth (25 in. (64 cm)).

The results of the crosshole analyses are discussed in the sections below. The P_H- and S_{HV}-wave velocity-versus-depth profiles generated at the beginning of each load stage are presented first. Then, the effect of confining pressure on V_{Ph} and V_{Shv} is examined. Finally, a short discussion of the results of the small-strain crosshole tests is provided.

7.3.1 V_{Ph} and V_{Shv} profiles with no vertical load applied to the footing

For all stages of crosshole testing at Site 2, the variation of V_{Ph} and V_{Shv} with depth is shown in Figures 7.22a and 7.22b, respectively. Referring to the load step nomenclature shown in Figure 7.1, the velocity-depth profiles in Figure 7.22 represent the conditions in Stages 1.0, 4.0, and 7.0, i.e. before application of any vertical load. As seen in Figure 7.22a, V_{Pv} is relatively constant with depth at the start of all three stages. However, the V_{Ph} in Stage 4.0 is about 100 fps (31 m/s) slower than in Stage 1.0. This difference (about 5%) between Stages 1.0 and 4.0 is relatively constant and did not diminish with depth. As seen in Figure 7.22b, the shapes of the V_{Shv} profiles in Stages 1.0 and 4.0 are generally similar, though V_{Shv} at every depth in Stage 4.0 is about 100 fps (31 m/s) slower than in Stage 1.0. Further, in Stages 1.0 and 4.0, V_{Shv} is about 200 fps (61 m/s) faster at a depth of 25 in. (64 cm) than at depths of 13 and 37 in. (33 and 94 cm). The shape of the V_{Shv} profile in Stage 7.0 is quite different from Stages 1.0 and 4.0. At a depth of 13 in. (33 cm), the V_{Shv} in Stage 7.0 is in good agreement with Stages 1.0 and 4.0. However, at depths of 25 and 37 in. (64 and 94 cm), V_{Shv} in Stage 7.0 is about 300 fps (91 m/s) slower than in Stages 1.0 and 4.0. The difference in the Stage-7.0 V_{Shv} profile could have been caused by several factors, including: (1) the application of static

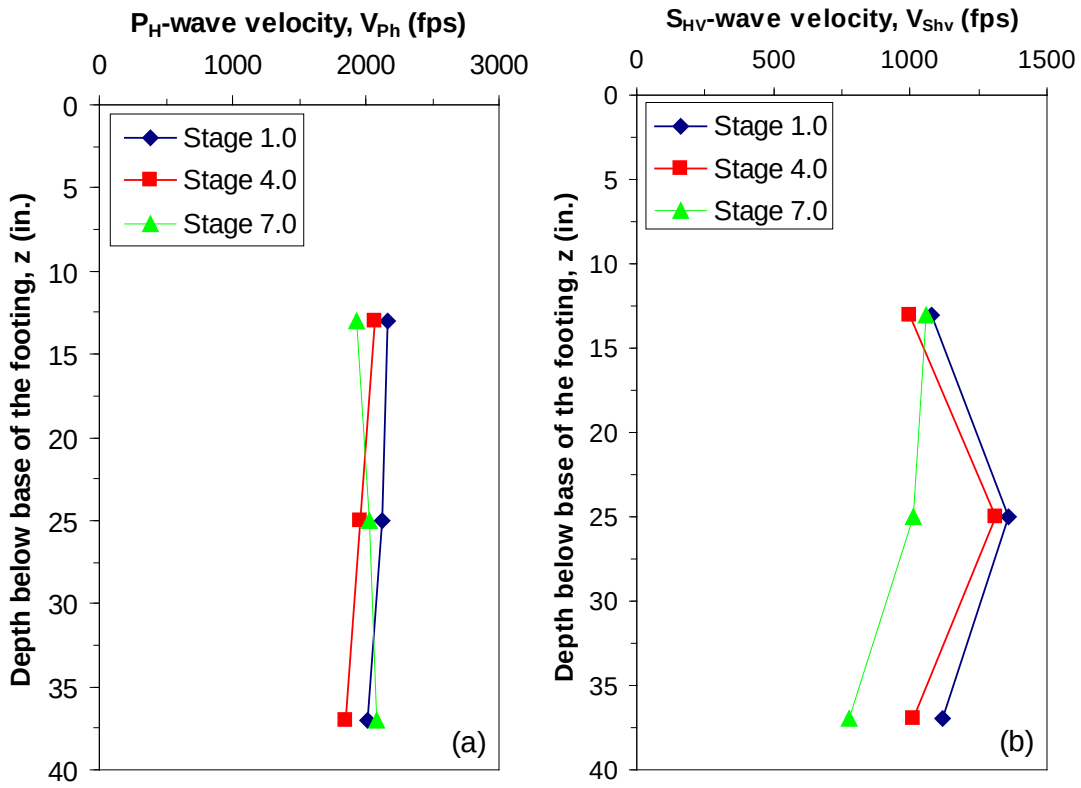

Figure 7.22. Variation of crosshole wave velocities with depth at the beginning of each load stage at Site 2: (a) V_{Ph} and (b) V_{Shv}

loads in Stage 4, (2) the vertical and horizontal dynamic excitations in Stages 5 and 6, (3) the different location of the crosshole source rods in Stage 7, or (4) a combination of these factors.

The V_{Ph} and V_{Shv} profiles at Site 2 are shown again in Figure 7.23 along with the profiles determined from Seismic Cone Penetration Tests (SCPT) and downhole tests performed by Kim (2012). It should be noted, however, that the SCPT and downhole tests were performed in Fall 2011 (one to two months after the tests in Stages 1.0, 4.0, and 7.0). These tests were performed in the same Hornsby Bend field as Site 2 but were located about 40 ft (12 m) away from the embedded sensor array (refer to Figures 6.2 and 6.4). The V_{Ph} values in Stages 1.0, 4.0, and 7.0 are higher than those reported by Kim,

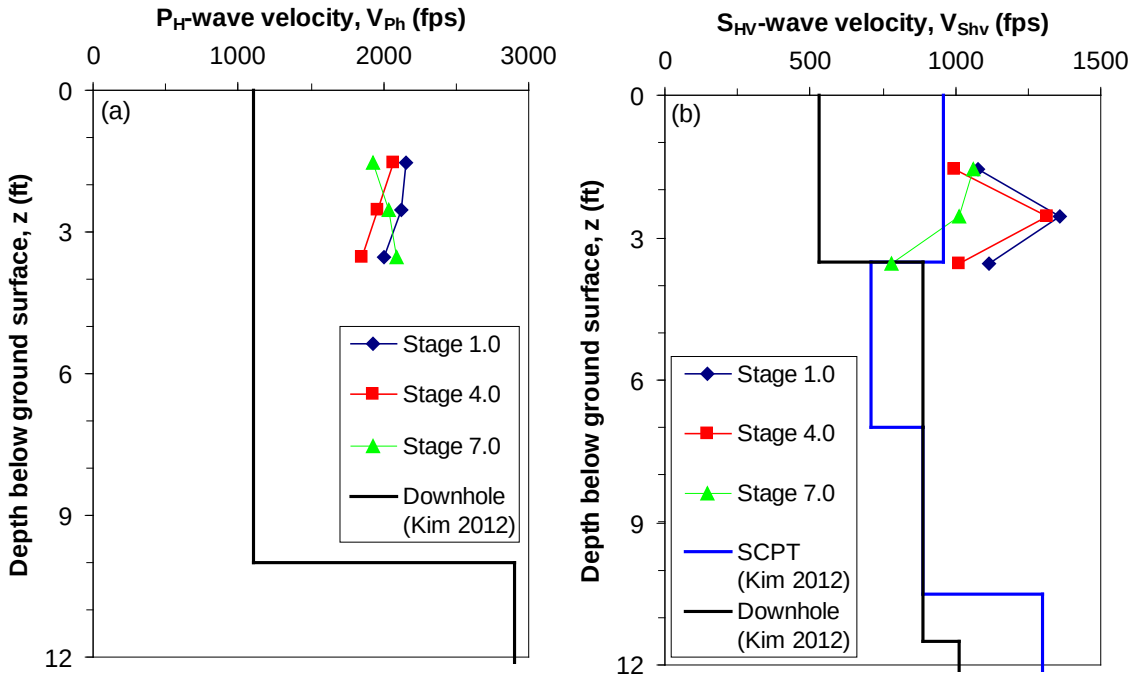

Figure 7.23. Crosshole wave velocity profiles at Site 2 compared with SCPT and downhole tests performed by Kim (2012): (a) V_{Ph} profiles and (b) V_{Shv} profiles

though the V_{Shv} values are generally in good agreement with Kim's SCPT results, especially in Stage 7.0 and at depths of 18.5 and 42.5 in. (47.0 and 108.0 cm) below the ground surface. As noted in the discussion of the downhole results in Section 7.2.1, it is possible that the crosshole tests performed in Stages 1.0, 4.0, and 7.0 captured localized V_{Ph} and V_{Shv} variability that was not identified by Kim due to the relatively large-scale averaging of his SCPT and downhole tests at these shallow depths.

7.3.2 Effect of confining pressure on V_{Ph} and V_{Shv}

The V_{Ph} and V_{Shv} values were evaluated at several different confining pressures in Stages 1, 4, and 7 (note the load steps shown in Figure 7.1). As at Site 1 (see Chapter 5), K_o was assumed to be constant and equal to 1.0 in all stages. The effects of confining pressure in each stage of crosshole tests are presented separately in this section.

7.3.2.1 Stage 1; In terms of total stresses

Ten static load steps were used in Stage 1 (see Figure 7.1). As discussed in Section 7.3.1, the embedded sensor array was constructed in a triangular prism layout with three vertical columns, each column containing four sensors (see Figure 6.7). At the three shallowest depths in the embedded sensor array, V_{Ph} was determined between the crosshole source rod and the receivers in the sensor column closest to the source, while V_{Shv} was determined using first arrivals of the S_{HV} wave at adjacent sensors. The effects of confining pressure on V_{Ph} and V_{Shv} at three depths below the base of the concrete footing are shown in Figures 7.24a and 7.24b, respectively. In general, the behavior of the crosshole wave velocities is similar at all depths. V_{Ph} varies between about 2000 to 2200 fps (610 to 670 m/s), and the exponent of the normal stress of the log V_{Ph} – log σ_h relationship is either 0.04 or 0.05 at every depth (Figure 7.24a). V_{Shv} varies between about 1050 and 1250 fps (320 to 380 m/s), and the exponent of the log V_{Shv} – log σ_h relationship is 0.03 at every depth (Figure 7.24b).

7.3.2.2 Stage 1; In terms of effective stresses

As mentioned in Sections 4.3.3 and 6.2.3, negative pore pressures likely existed at the time of the tests at Site 2. The presence of negative pore pressures makes the relationships based on total stress (shown in Figure 7.24) unsuitable for determining whether the soil became normally-consolidated over the range of stresses induced in Stage 1. As described in Section 6.2.3, the vertical effective stress (σ'_v) in the soil at Site 2 was estimated by adding the suction stress term (Lu and Likos 2006) to the total stress using Equation 6.2, where the suction stress was estimated as 720 psf (34.5 kPa). The horizontal effective stress (σ'_h) was then estimated assuming a K_o equal to 1.0. The addition of the suction stress has the effect of increasing the exponents of the various total stress relationships in Figure 7.24. This increase in exponents can be seen in Figure 7.25, where the effects of both total stress and effective stress on the crosshole wave

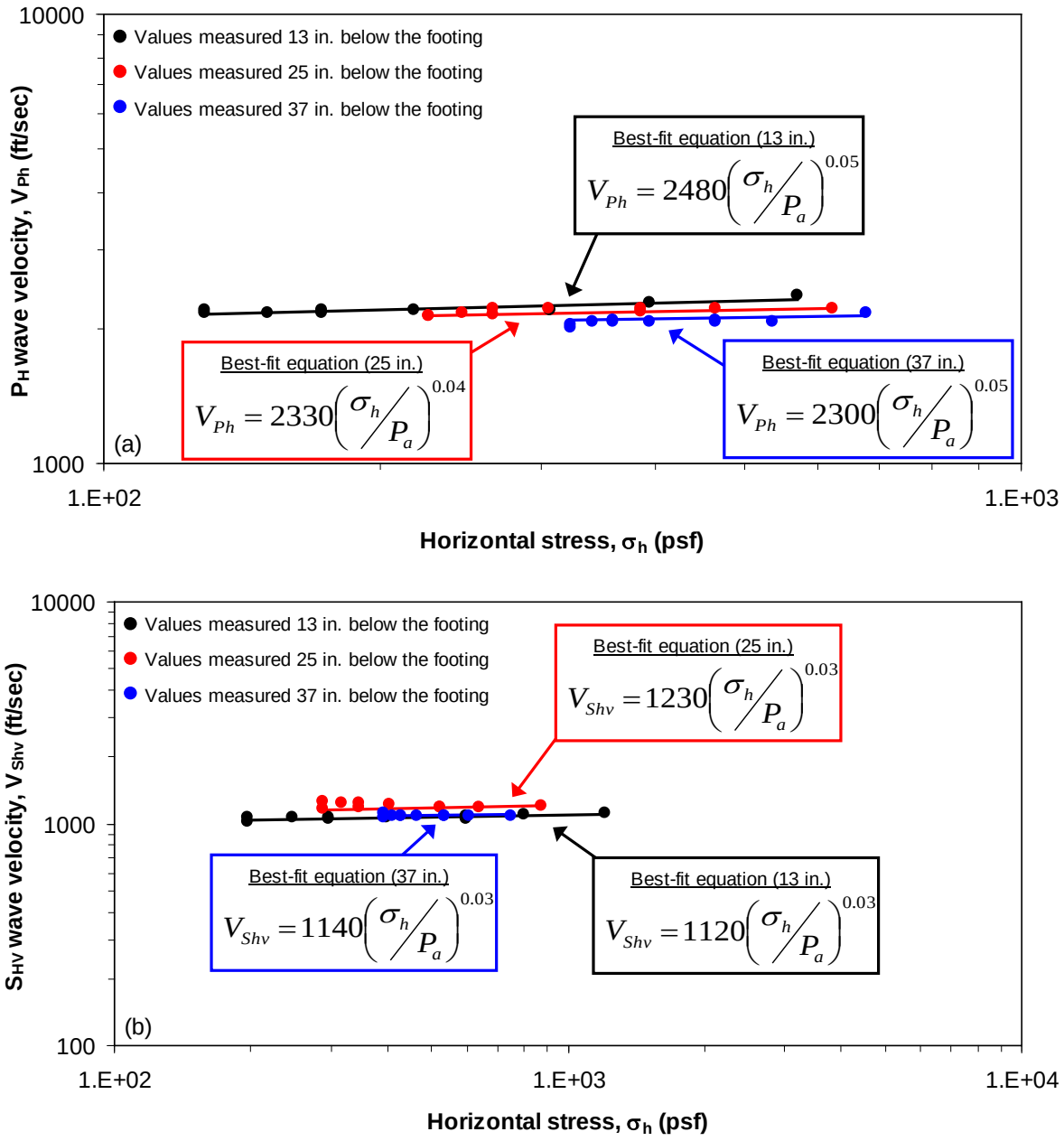

Figure 7.24. Variation of crosshole wave velocities with increasing stress level at all depths below the base of the footing in Stage 1: (a) log V_{Ph} – log σ_h and (b) log V_{Shv} – log σ_h

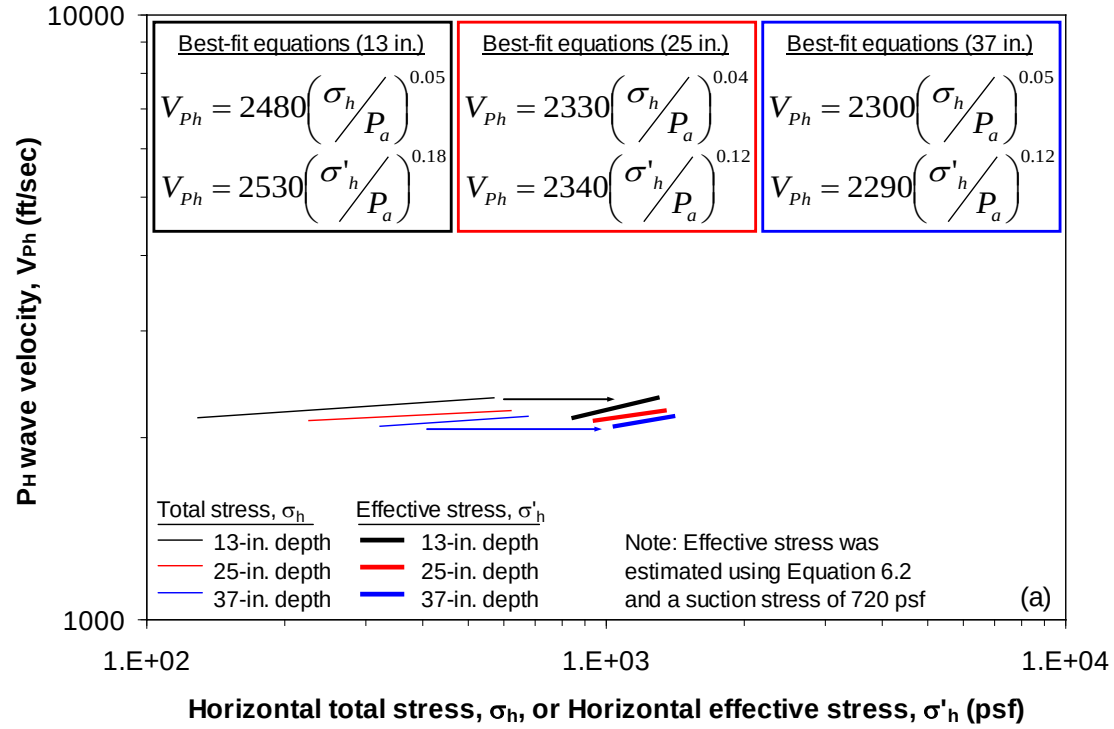

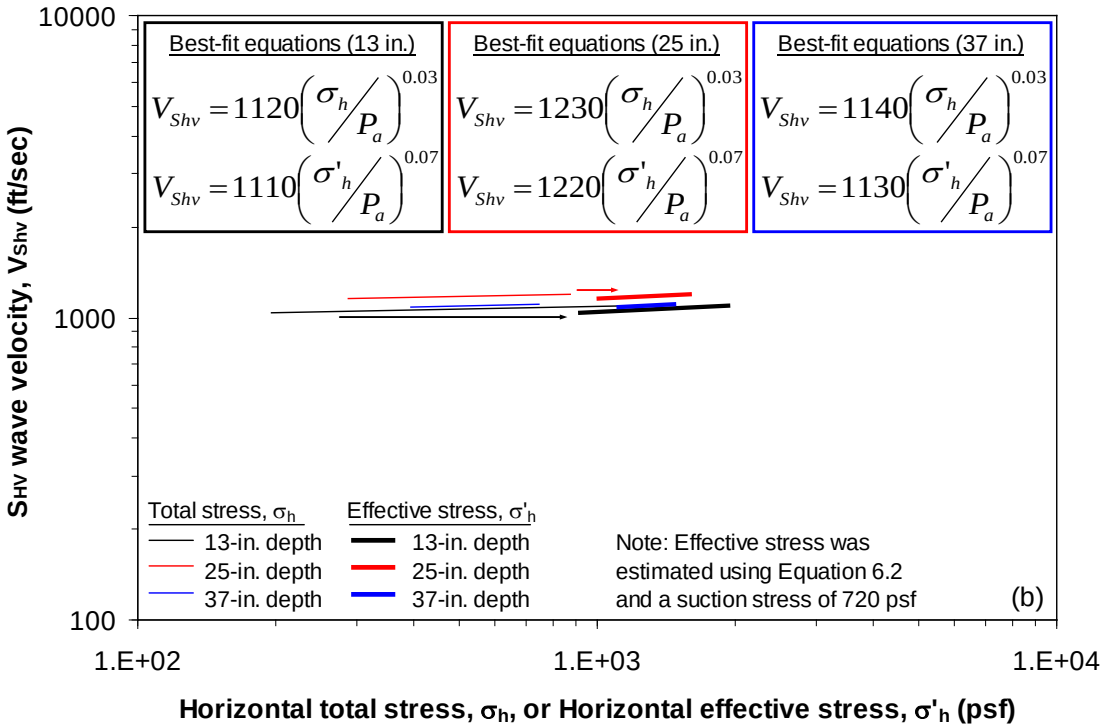

Figure 7.25. Comparison of the effect of total stress versus effective stress on the crosshole wave velocities determined in Stage 1: (a) V_{Ph} and (b) V_{Shv}

velocities are shown. For any given depth, the exponent of the log V_{Ph} – log σ'_h relationship is about two to three times that of the log V_{Ph} – log σ_h relationship (Figure 7.25a). The increase is slightly less in Figure 7.25b, where the exponent of the log V_{Shv} – log σ'_h is slightly less than double the exponent of the log V_{Shv} – log σ_h relationship. Note that while the effect of confining pressure on V_{Ph} is higher than on V_{Shv} in Figure 7.25, the larger exponents of the log V_{Ph} – log σ'_v relationships are likely due in part to the small range of stresses induced in the crosshole P_V tests. However, all of the exponents given in Figure 7.25 (whether based on total or effective stress) are generally small and indicate that the soil at Site 2 was overconsolidated and remained so throughout Stage 1.

7.3.2.3 Stage 4; In terms of total stresses

Nine static load steps were used in Stage 4 (see Figure 7.1). At the three shallowest depths in the embedded sensor array, V_{Ph} was determined between the crosshole source rod and the receivers in the sensor column closest to the source, while V_{Shv} was determined using first arrivals of the S_{HV} wave at adjacent sensors. The effects of confining pressure on V_{Ph} and V_{Shv} at three depths below the base of the concrete footing are shown in Figures 7.26a and 7.26b, respectively. At a depth of 13 in. (33 cm) below the footing, V_{Ph} is about 400 fps (122 m/s) faster than at depths of 25 and 37 in. (64 and 94 cm). However, the effect of confining pressure on V_{Ph} is similar at all depths, since the exponent of the log V_{Ph} – log σ_h relationship is about the same in every case (Figure 7.26a). As seen in Figure 7.26b, there is slightly more effect of stress level on V_{Shv} at a depth of 13 in. (33 cm) than at depths of 25 and 37 in. (64 and 94 cm). The exponent of the log V_{Shv} – log σ_h relationship at 13 in. (33 cm) is 0.06 while the exponents at 25 and 37 in. (64 and 94 cm) are 0.03 and 0.04, respectively. This difference could be due to the steady-state excitations applied with Thumper in Stages 2 and 3, which would presumably have had more of an effect at shallower depths than at deeper depths, or it could simply be the resolution of the seismic measurements.

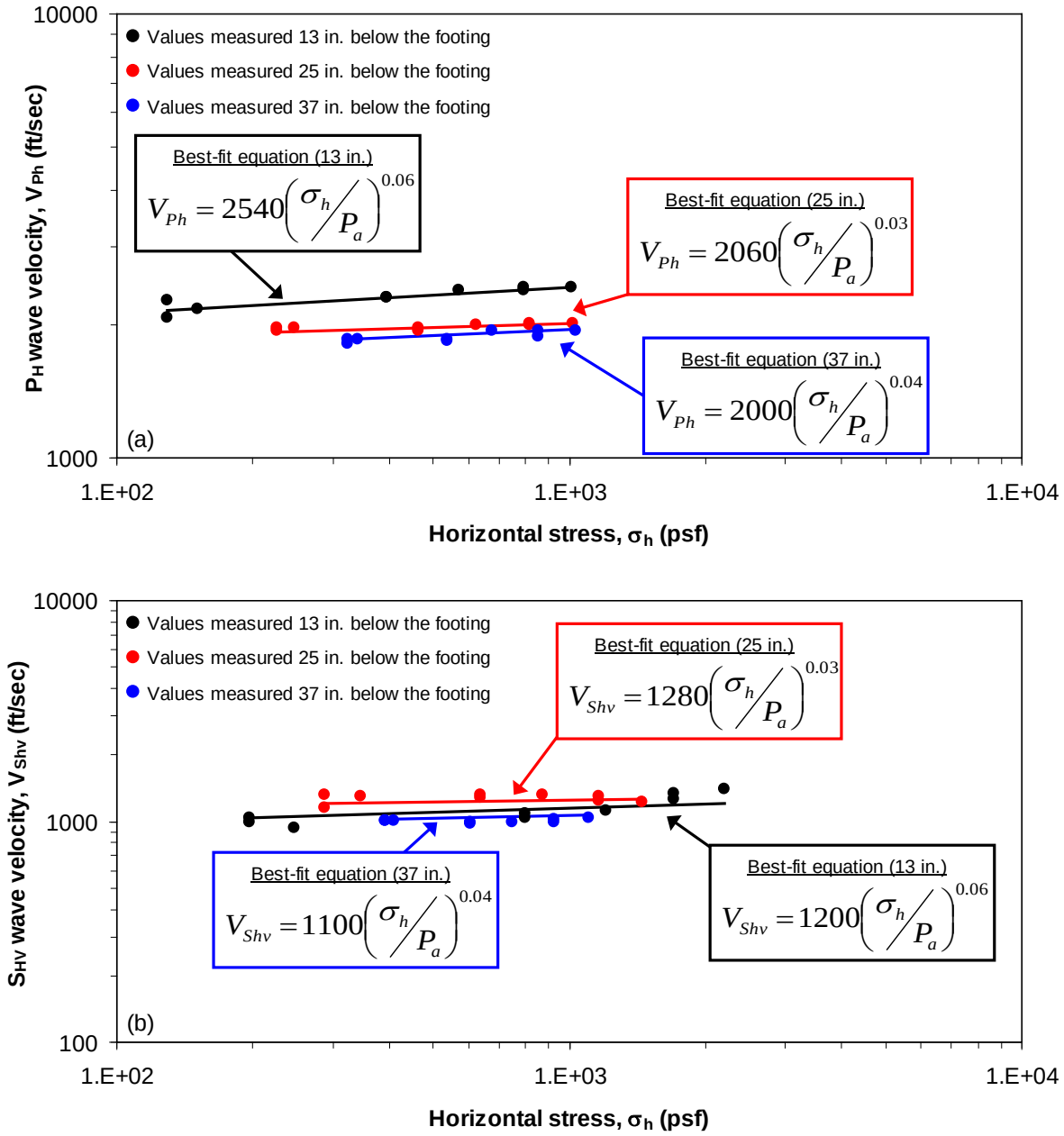

Figure 7.26. Variation of crosshole wave velocities with increasing stress level at all depths below the base of the footing in Stage 4: (a) log V_{Ph} – log σ_h and (b) log V_{Shv} – log σ_h

7.3.2.4 Stage 4; In terms of effective stresses

The vertical and horizontal effective stresses were estimated using the same procedure described in Section 7.3.2.2 for Stage 1, and the log V_{Ph} – log σ'_h and log V_{Shv} – log σ'_h relationships determined in Stage 4 are shown in Figures 7.27a and 7.27b, respectively. The observations seen in Figure 7.27 are similar to those noted in Stage 1. Specifically, for any given depth, the exponents of the effective stress relationships (log V_{Ph} – log σ'_h and log V_{Shv} – log σ'_h) are approximately double those of the total stress relationships (log V_{Ph} – log σ_h and log V_{Shv} – log σ_h). However, all of the exponents given in Figure 7.27 (whether based on total or effective stress) are generally small and indicate that the soil at Site 2 was overconsolidated and remained so throughout the course of Stage 4.

7.3.2.5 Stage 7; In terms of total stresses

Nine static load steps were used in Stage 7 (see Figure 7.1). At the three shallowest depths in the embedded sensor array, V_{Ph} was determined between the crosshole source rod and the receivers in the sensor column closest to the source, while V_{Shv} was determined using first arrivals of the S_{HV} wave at adjacent sensors. However, the locations of the crosshole source rods were different than in Stages 1 and 4 (see Figure 6.12). In Stage 7, the crosshole source rods were further away from the center of the footing (approximately 60 in. (152 cm) versus 36 in. (91 cm)) and positioned on the East side of the footing instead of the North side. The effects of confining pressure on V_{Ph} and V_{Shv} at three depths below the base of the concrete footing are shown in Figures 7.28a and 7.28b, respectively. The behavior of V_{Ph} is basically the same at all three depths, as the log V_{Ph} – log σ_h relationships shown in Figure 7.28a fall approximately along a single line with an exponent of 0.05. As seen in Figure 7.28b, while the exponent of the log V_{Shv} – log σ_h relationship is roughly equal at all depths, V_{Shv} is about 300 fps (91 m/s) slower at a depth of 37 in. (94 cm) than at the two shallower depths. This

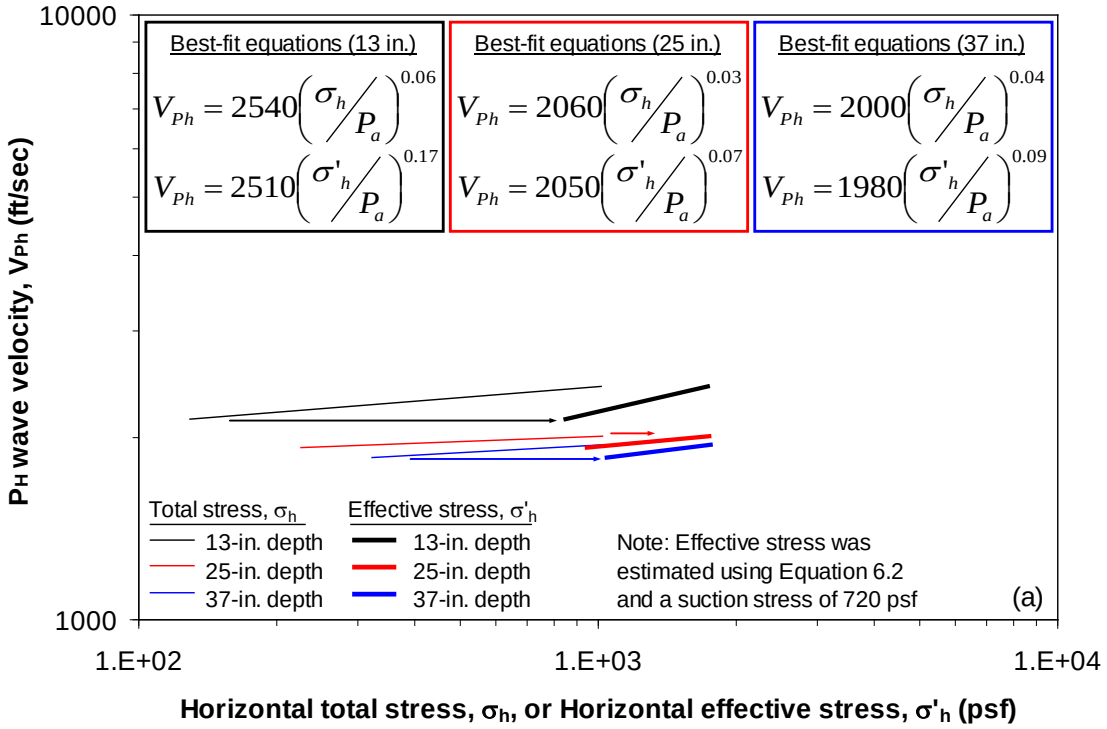

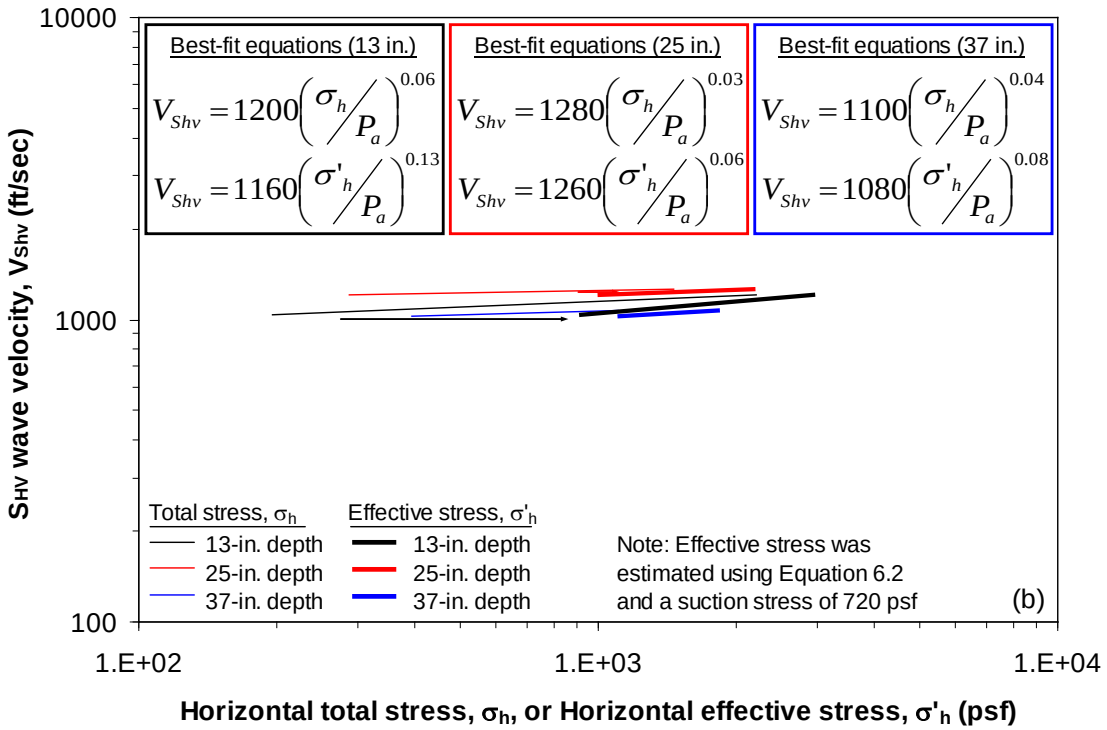

Figure 7.27. Comparison of the effect of total stress versus effective stress on the crosshole wave velocities determined in Stage 4: (a) V_{Ph} and (b) V_{Shv}

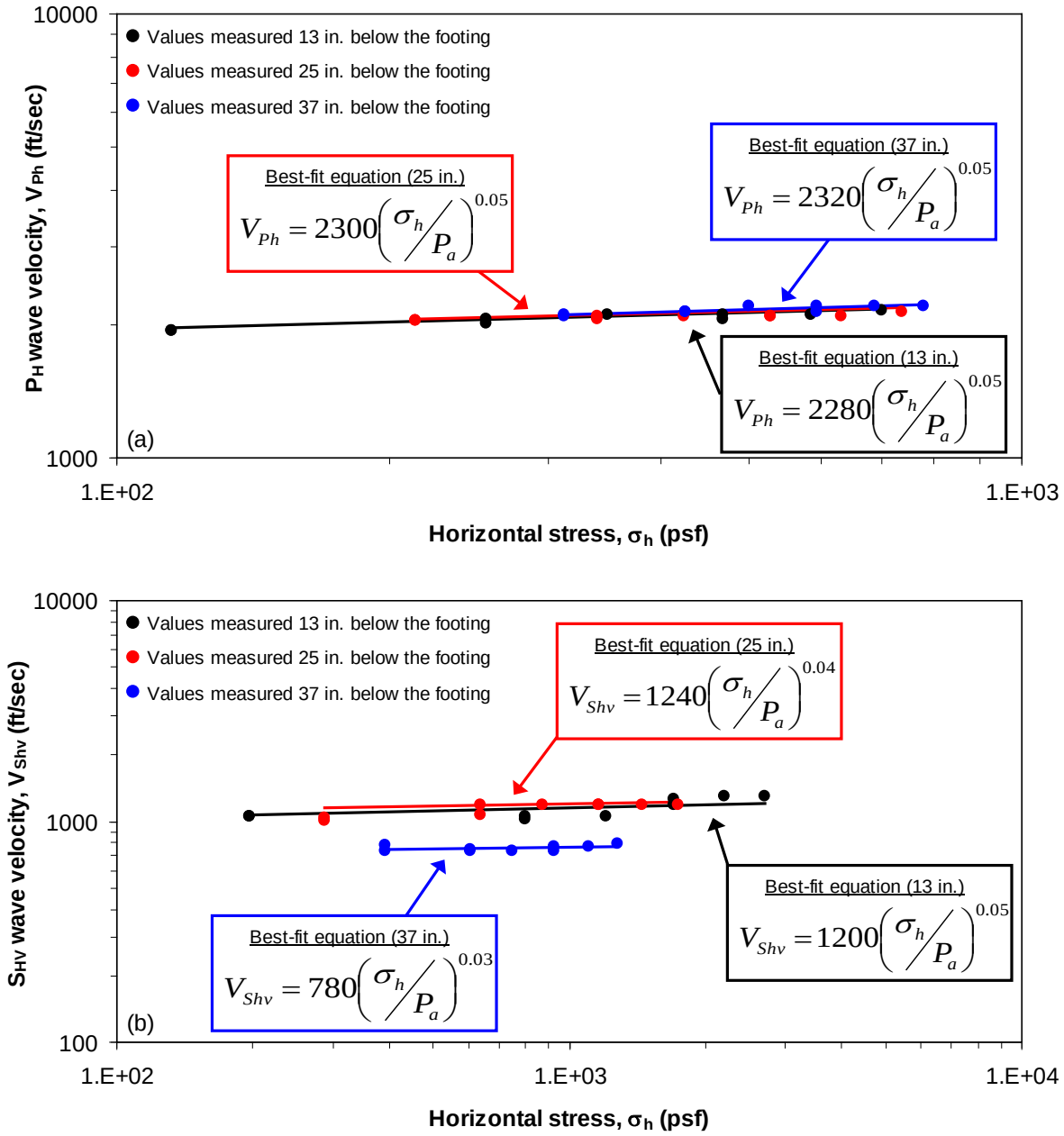

Figure 7.28. Variation of crosshole wave velocities with increasing stress level at all depths below the base of the footing in Stage 7: (a) log V_{Ph} – log σ_h and (b) log V_{Shv} – log σ_h

reduction in V_{Shv} at the deepest depth was also noted in Section 7.3.1, where the possible reasons given for the slower V_{Shv} were: (1) application of static loads in Stage 4, (2) generation of vertical and horizontal dynamic excitations in Stages 5 and 6, (3) the different location of the source rods in Stage 7, or (4) a combination of these factors.

7.3.2.6 Stage 7; In terms of effective stresses

The vertical and horizontal effective stresses were estimated using the same procedure described for Stages 1 and 4, and the log V_{Ph} – log σ'_h and log V_{Shv} – log σ'_h relationships determined in Stage 7 are shown in Figures 7.29a and 7.29b, respectively. For any given depth, the exponents of the effective stress relationships (log V_{Ph} – log σ'_h and log V_{Shv} – log σ'_h) are about two to three times those of the total stress relationships (log V_{Ph} – log σ_h and log V_{Shv} – log σ_h). However, all the exponents given in Figure 7.29 (whether based on total or effective stress) are small and indicate that the soil at Site 2 was overconsolidated and remained so throughout Stage 7.

7.3.3 Discussion

The variations of the crosshole wave velocities with stress level in all stages and at all depths are summarized in Figures 7.30 and 7.31 for V_{Ph} and V_{Shv}, respectively. Note that for clarity, only the total and effective stress best-fit lines that are shown in Figures 7.25, 7.27, and 7.29 are included in Figures 7.30 and 7.31. The equations of all best-fit lines, including the average effective stress equations at each depth, are listed in Table 7.2. Based on the results presented in Sections 7.3.1 and 7.3.2, several observations can be made about the crosshole tests at Site 2.

At the shallowest depth in the sensor array (13 in. (33 cm)), the effect of stress level on V_{Ph} is about the same in all three stages, as seen by the exponents of the trend lines in Figure 7.30a and in Table 7.2. Additionally, the V_{Ph} values in Stages 1 and 4 are

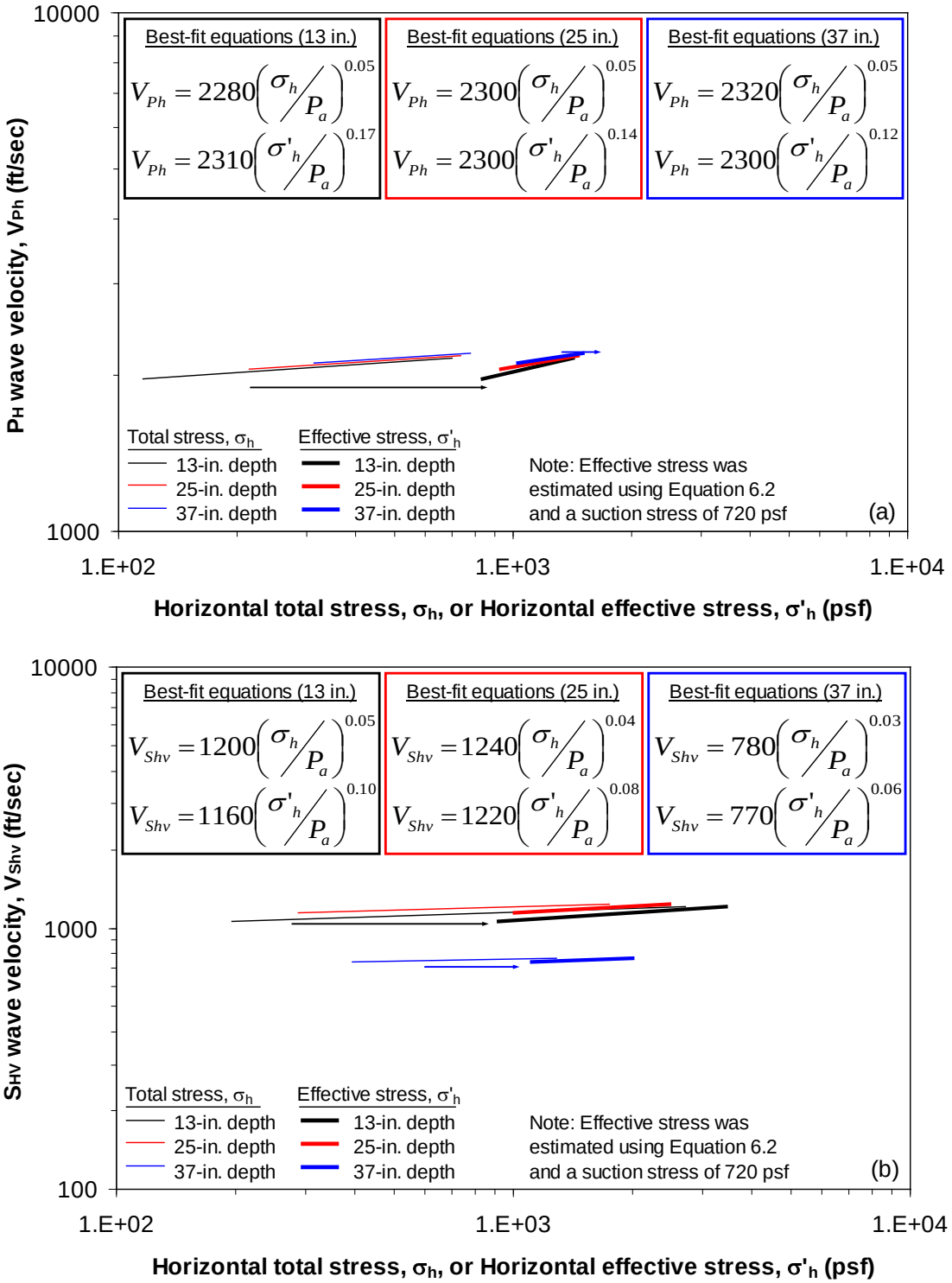

Figure 7.29. Comparison of the effect of total stress versus effective stress on the crosshole wave velocities determined in Stage 7: (a) V_{Ph} and (b) V_{Shv}

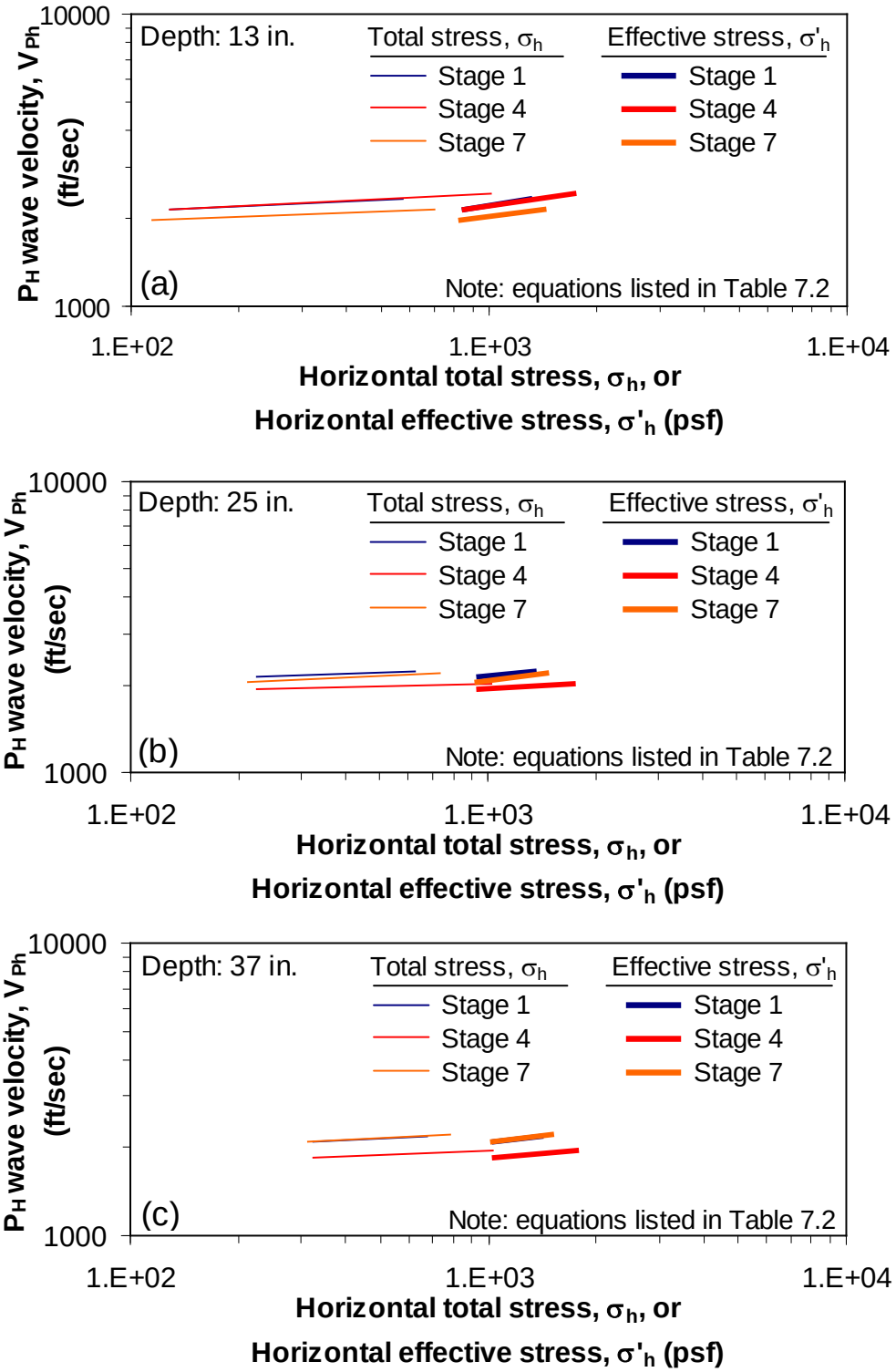

Figure 7.30. Variation of best-fit V_{Ph} with stress level in all stages of crosshole tests and at all depths at Site 2: (a) 13 in. (33 cm), (b) 25 in. (64 cm), and (c) 37 in. (94 cm)

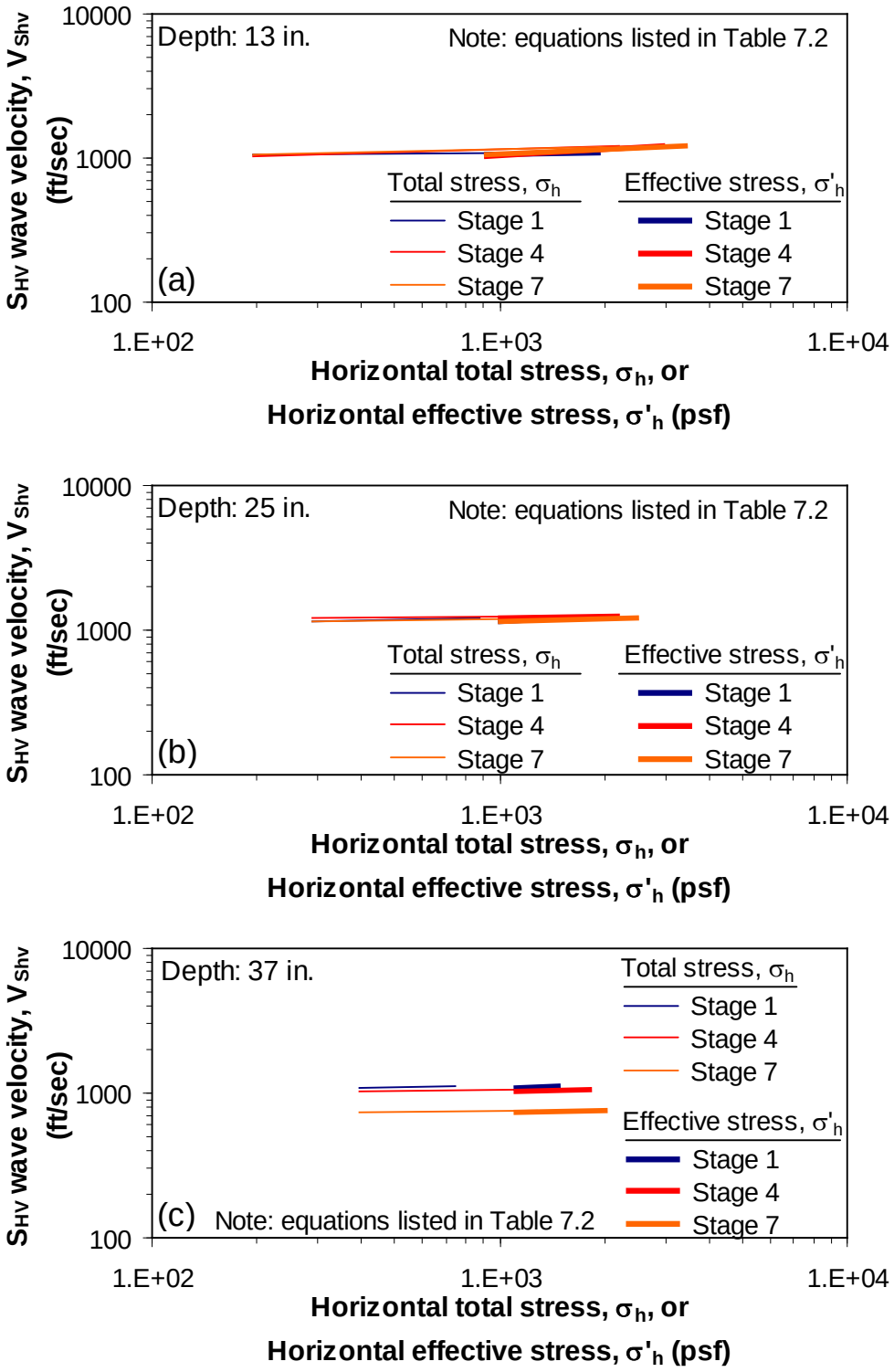

Figure 7.31. Variation of best-fit V_{Shv} with stress level in all stages of crosshole tests and at all depths at Site 2: (a) 13 in. (33 cm), (b) 25 in. (64 cm), and (c) 37 in. (94 cm)

Table 7.2. Summary of best-fit equations for crosshole tests at Site 2

Depth	Stage	Total stress equations	Effective stress equations	Average effective stress equations (based on all stages)
13-in.	1	$V_{Ph} = 2480\left(\sigma_h / P_a\right)^{0.05}$ $V_{Shv} = 1120\left(\sigma_h / P_a\right)^{0.03}$	$V_{Ph} = 2530\left(\sigma'_h / P_a\right)^{0.18}$ $V_{Shv} = 1110\left(\sigma'_h / P_a\right)^{0.07}$	$V_{Ph} = 2450\left(\sigma'_h / P_a\right)^{0.17}$ $V_{Shv} = 1140\left(\sigma'_h / P_a\right)^{0.10}$
	4	$V_{Ph} = 2540\left(\sigma_h / P_a\right)^{0.06}$ $V_{Shv} = 1200\left(\sigma_h / P_a\right)^{0.06}$	$V_{Ph} = 2510\left(\sigma'_h / P_a\right)^{0.17}$ $V_{Shv} = 1160\left(\sigma'_h / P_a\right)^{0.13}$	
	7	$V_{Ph} = 2280\left(\sigma_h / P_a\right)^{0.05}$ $V_{Shv} = 1200\left(\sigma_h / P_a\right)^{0.05}$	$V_{Ph} = 2310\left(\sigma'_h / P_a\right)^{0.17}$ $V_{Shv} = 1160\left(\sigma'_h / P_a\right)^{0.10}$	
25-in.	1	$V_{Ph} = 2330\left(\sigma_h / P_a\right)^{0.04}$ $V_{Shv} = 1230\left(\sigma_h / P_a\right)^{0.03}$	$V_{Ph} = 2340\left(\sigma'_h / P_a\right)^{0.12}$ $V_{Shv} = 1220\left(\sigma'_h / P_a\right)^{0.07}$	$V_{Ph} = 2200\left(\sigma'_h / P_a\right)^{0.10}$ $V_{Shv} = 1230\left(\sigma'_h / P_a\right)^{0.07}$
	4	$V_{Ph} = 2060\left(\sigma_h / P_a\right)^{0.03}$ $V_{Shv} = 1280\left(\sigma_h / P_a\right)^{0.03}$	$V_{Ph} = 2050\left(\sigma'_h / P_a\right)^{0.07}$ $V_{Shv} = 1260\left(\sigma'_h / P_a\right)^{0.06}$	
	7	$V_{Ph} = 2300\left(\sigma_h / P_a\right)^{0.05}$ $V_{Shv} = 1240\left(\sigma_h / P_a\right)^{0.04}$	$V_{Ph} = 2300\left(\sigma'_h / P_a\right)^{0.14}$ $V_{Shv} = 1220\left(\sigma'_h / P_a\right)^{0.08}$	
37-in.	1	$V_{Ph} = 2300\left(\sigma_h / P_a\right)^{0.05}$ $V_{Shv} = 1140\left(\sigma_h / P_a\right)^{0.03}$	$V_{Ph} = 2290\left(\sigma'_h / P_a\right)^{0.12}$ $V_{Shv} = 1130\left(\sigma'_h / P_a\right)^{0.07}$	$V_{Ph} = 2200\left(\sigma'_h / P_a\right)^{0.10}$ $V_{Shv} = 1100\left(\sigma'_h / P_a\right)^{0.07}$
	4	$V_{Ph} = 2000\left(\sigma_h / P_a\right)^{0.04}$ $V_{Shv} = 1100\left(\sigma_h / P_a\right)^{0.04}$	$V_{Ph} = 1980\left(\sigma'_h / P_a\right)^{0.09}$ $V_{Shv} = 1080\left(\sigma'_h / P_a\right)^{0.08}$	
	7	$V_{Ph} = 2320\left(\sigma_h / P_a\right)^{0.05}$ $V_{Shv} = 780\left(\sigma_h / P_a\right)^{0.03}$	$V_{Ph} = 2300\left(\sigma'_h / P_a\right)^{0.12}$ $V_{Shv} = 770\left(\sigma'_h / P_a\right)^{0.06}$	

**Note: Depths are the distances from the base of the concrete footing to each sensor assuming a 1-in. (2.5-cm) thick sand layer (see Figure 6.7)

in excellent agreement, but the V_{Ph} values in Stage 7 are about 200 fps (61 m/s) slower than those in Stages 1 and 4. The agreement between the V_{Shv} values in Stages 1, 4, and 7 is much better (Figure 7.31a), with all values falling within a range of about 100 fps (31 m/s). However, the effect of increasing stress level on V_{Shv} was slightly less in Stage 1 than in Stages 4 and 7 (note the exponents of the equations listed in Table 7.2).

At depths of 25 and 37 in. (64 and 94 cm), the exponents of the log V_{Ph} – log σ'_h relationships in all stages are very nearly identical, as seen in Figures 7.30b and 7.30c and Table 7.2. However, at a depth of 25 in. (64 cm), the V_{Ph} values in Stage 4 are about 150 fps (46 m/s) slower than those in Stages 1 and 7. In general, the difference in the V_{Ph} values between the stages (about 10%) remained relatively constant with depth. At a depth of 37 in. (94 cm), there is good agreement between the V_{Ph} values in Stages 1 and 7, and the V_{Ph} measured in Stage 4 are only about 200 fps (61 m/s) slower (Figure 7.30c). A difference in velocity between the stages was also noted for V_{Shv}, but the effect tended to increase with depth. At the first two depths, there is excellent agreement between all three stages (Figures 7.31a and 7.31b). As seen in Figure 7.31c, there was very little difference between the V_{Shv} values determined in Stages 1 and 4 at a depth of 37 in. (94 cm). However, V_{Shv} in Stage 7 was about 300 fps (91 m/s) slower than Stages 1 and 4 at a depth of 37 in. (94 cm) (Figure 7.31c).

In most cases shown in Figures 7.30 and 7.31, there is little or no difference between the crosshole wave velocities in Stages 1 and 4. Though the V_{Ph} values at depths of 25 and 37 in. (64 and 94 cm) are slower in Stage 4 than in Stage 1, there is no difference between the stages at the shallowest depth of 13 in. (33 cm). Additionally, the V_{Shv} values at all depths are in excellent agreement between Stages 1 and 4. Therefore, it does not appear that the intervening vertical and horizontal dynamic excitations applied with Thumper in Stages 2 and 3 had any lasting effect on the soil structure. However, there is a decrease in the crosshole wave velocities measured in Stage 7. The V_{Ph} values in Stage 7 are slower than in Stages 1 and 4 at the shallowest depths (Figure 7.30a) but

agree well with Stage 1 at the deepest depths (Figures 7.30b and 7.30c). The effect on V_{Shv} is somewhat opposite in that the V_{Shv} values in Stage 7 are slower than in Stages 1 and 4 at the deepest depth (Figure 7.31c) but agree well with all stages at the shallowest depths (Figures 7.31a and 7.31b). The reduction of the wave velocities in Stage 7 could have been caused by several factors: (1) application of static loads in Stage 4, (2) generation of vertical and horizontal dynamic excitations applied by T-Rex in Stages 5 and 6, (3) the different location of the crosshole source rods in Stage 7, or (4) a combination of these factors. However, it seems unlikely that the vibroseis would cause changes in the soil (either in the soil skeleton itself or in the pore pressure distribution) at deeper depths but not at shallower depths. Therefore, it was assumed that most of the differences between the wave velocities measured in Stage 7 and those in Stages 1 and 4 were due to the different location of the crosshole source rods in Stage 7 and the resolution of the seismic measurements.

Given the results of previous downhole tests in the Hornsby Bend area (at Site 1 discussed in Chapter 5 and at a nearby site discussed by Van Pelt, 2010), the soil at Site 2 was initially assumed to be heavily overconsolidated. This assumption was confirmed by the results of the crosshole tests at Site 2. In all stages of crosshole tests at Site 2, the exponents of the log V_{Ph} – log σ_h and log V_{Shv} – log σ_h relationships ranged from 0.03 to 0.06. When the influence of effective stress on the small-strain, crosshole wave velocities was examined, the exponents of the effective stress relationships (log V_{Ph} – log σ'_h and log V_{Shv} – log σ'_h) were approximately double or triple the exponents of the total stress relationships and ranged from 0.06 to 0.18. This increase in the exponents was observed in every load stage and at every depth in the embedded sensor array (see Table 7.2). Though the exponents of the effective stress relationships were larger than those of the total stress relationships, the variation of V_{Ph} and V_{Shv} with increasing stress level (whether based on total or effective stress) was still relatively small and suggests that the soil at Site 2 was initially overconsolidated and remained so throughout all stages of crosshole testing. Even at the highest static loads applied in Stage 7, there was no

identifiable stress level where the exponent of the trend lines changed and increased to a value typical of a normally-consolidated soil.

7.4 COMPARISON OF DOWNHOLE AND CROSSHOLE WAVE VELOCITIES

In this section, wave velocities determined in the small-strain, downhole tests performed at Site 2 (Section 7.2) are compared to wave velocities determined in the small-strain, crosshole tests at Site 2 (Section 7.3). The depths in the embedded sensor array at which the results were reported in Sections 7.2 and 7.3 are slightly different in the downhole and crosshole tests. For instance, the shallowest depth used in the downhole tests is the midpoint between the first and second sensors in the array (19-in. (48-cm) depth), but in the crosshole tests, the shallowest depth is the location of the first sensor (13-in. (33-cm) depth). Despite this discrepancy, good results were obtained in both downhole and crosshole tests at three different depths in the embedded sensor array. Accordingly, the results of the downhole and crosshole tests are compared at the first, second, and third depths in the sensor array, and the actual depths at which the tests were performed are indicated in each case. Since soil behavior is more dependent on effective stress than on total stress, only the effective stress relationships discussed in Sections 7.2 and 7.3 are used in this section. Where appropriate, comparisons to available empirical relationships are also provided. For simplicity, the effects of stress level on the P-wave velocities (V_{Pv} from the downhole tests and V_{Ph} from the crosshole tests) are treated separately from the effects of stress level on the S-wave velocities (V_{Svh} from the downhole tests and V_{Shv} from the crosshole tests). The Poisson's ratios computed using the downhole wave velocities are also compared to the Poisson's ratios computed using the crosshole wave velocities.

7.4.1 Log V_{Pv} – log σ'_v and log V_{Ph} – log σ'_h

The P-wave results of the downhole and crosshole tests at the first, second, and third depths in the embedded sensor array are shown in Figures 7.32, 7.33, and 7.34, respectively. In each figure, the equations of the average log V_{Pv} – log σ'_v (downhole tests) and log V_{Ph} – log σ'_h (crosshole tests) relationships based on all stages of testing are shown (note these equations are listed in Tables 7.1 and 7.2). In general, the agreement between the downhole and crosshole tests is quite good. At the first and second depths (Figures 7.32 and 7.33), the exponents of the average log V_{Pv} – log σ'_v and log V_{Ph} – log σ'_h relationships are roughly equal and the relationships overlap. However, at the third depth (Figure 7.34), the log V_{Pv} – log σ'_v relationship is higher than the log V_{Ph} – log σ'_h relationships by about 300 fps (91 m/s). This difference is small (~15%) and supports the conclusion that any structural anisotropy present in the soil at Site 2 is small enough to be counteracted by stress-induced anisotropy.

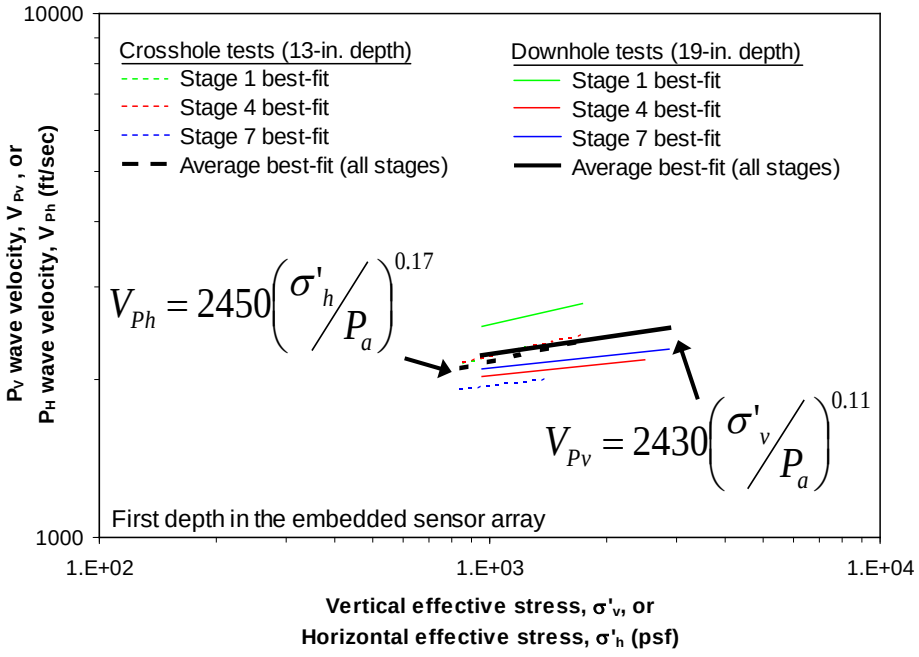

Figure 7.32. Comparison of log V_{Pv} – log σ'_v and log V_{Ph} – log σ'_h relationships at the first depth in the embedded sensor array at Site 2

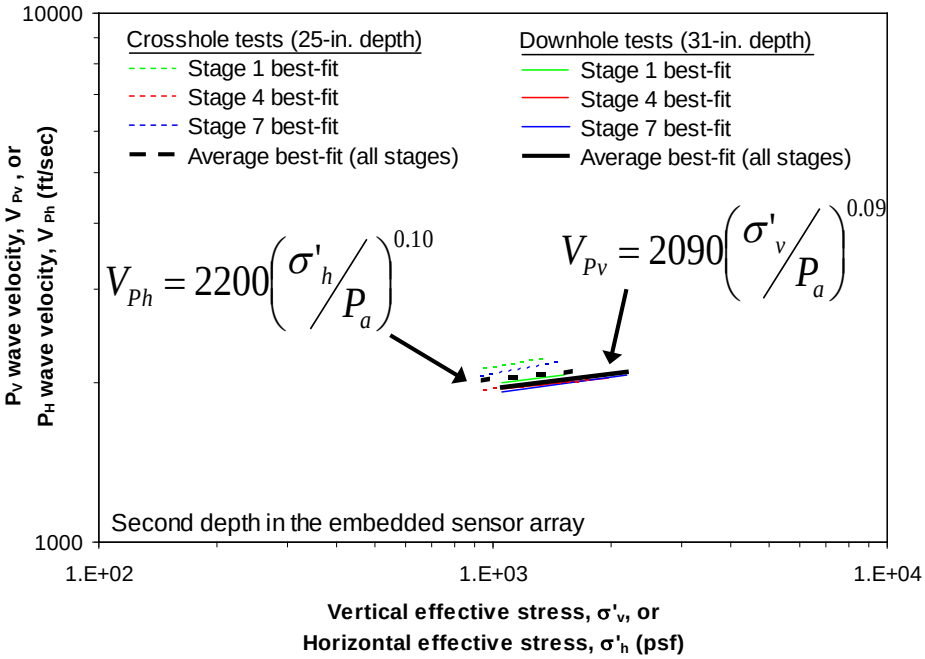

Figure 7.33. Comparison of log V_{Pv} – log σ'_v and log V_{Ph} – log σ'_h relationships at the second depth in the embedded sensor array at Site 2

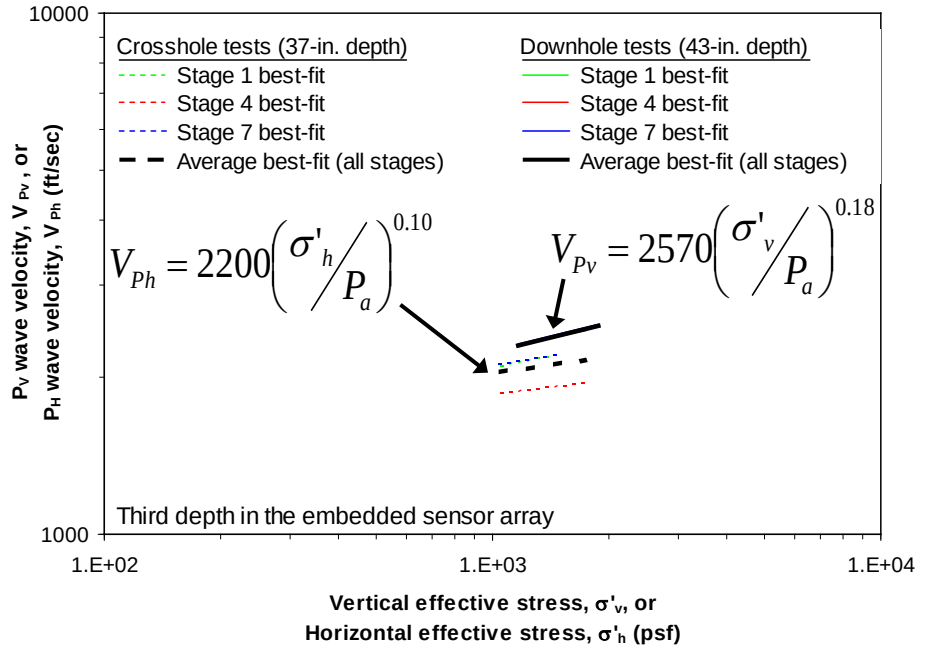

Figure 7.34. Comparison of log V_{Pv} – log σ'_v and log V_{Ph} – log σ'_h relationships at the third depth in the embedded sensor array at Site 2

7.4.2 Log V_{Svh} – log σ'_v and log V_{Shv} – log σ'_h

The S-wave results of the downhole and crosshole tests at the first, second, and third depths in the embedded sensor array are shown in Figures 7.35, 7.36, and 7.37, respectively. In each figure, the equations of the average log V_{Svh} – log σ'_v (downhole tests) and log V_{Shv} – log σ'_h (crosshole tests) relationships based on all stages of testing are shown (note these equations are listed in Tables 7.1 and 7.2). In general, the agreement between the downhole and crosshole tests is quite good. The exponents of the average log V_{Svh} – log σ'_v and log V_{Shv} – log σ'_h relationships are roughly equal at the first and second depths in the array (Figures 7.35 and 7.36). At the deepest depth, V_{Svh} appears to show more dependency on stress level than does V_{Shv} (Figure 7.37). However, the agreement between the values of V_{Svh} and V_{Shv} is excellent if the crosshole tests in Stage 7 are disregarded (note the dotted blue line in Figure 7.37). Therefore, the difference in the exponents of the log V_{Svh} – log σ'_v and log V_{Shv} – log σ'_h relationships

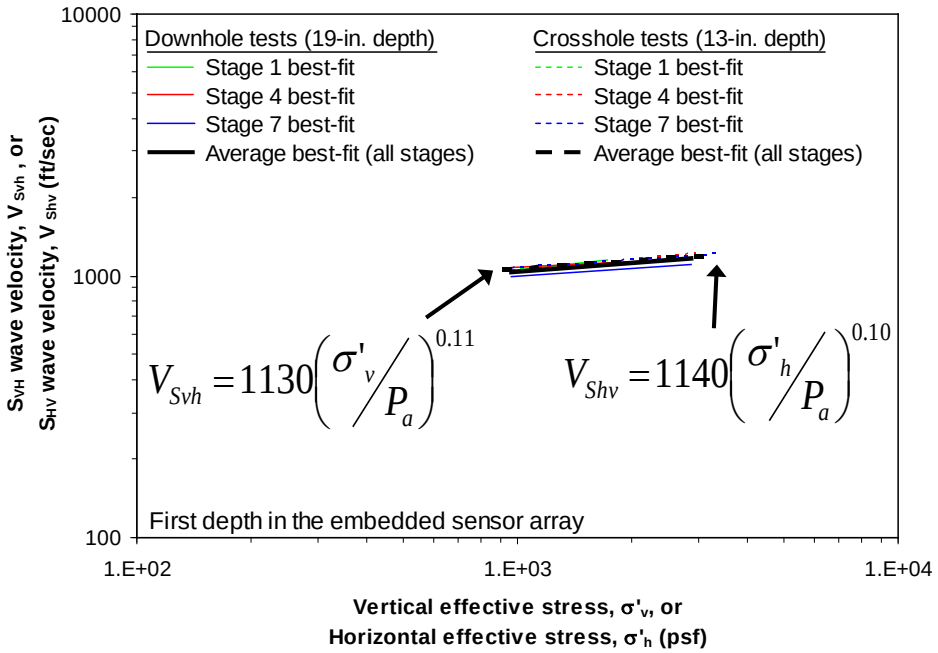

Figure 7.35. Comparison of log V_{Svh} – log σ'_v and log V_{Shv} – log σ'_h relationships at the first depth in the embedded sensor array at Site 2

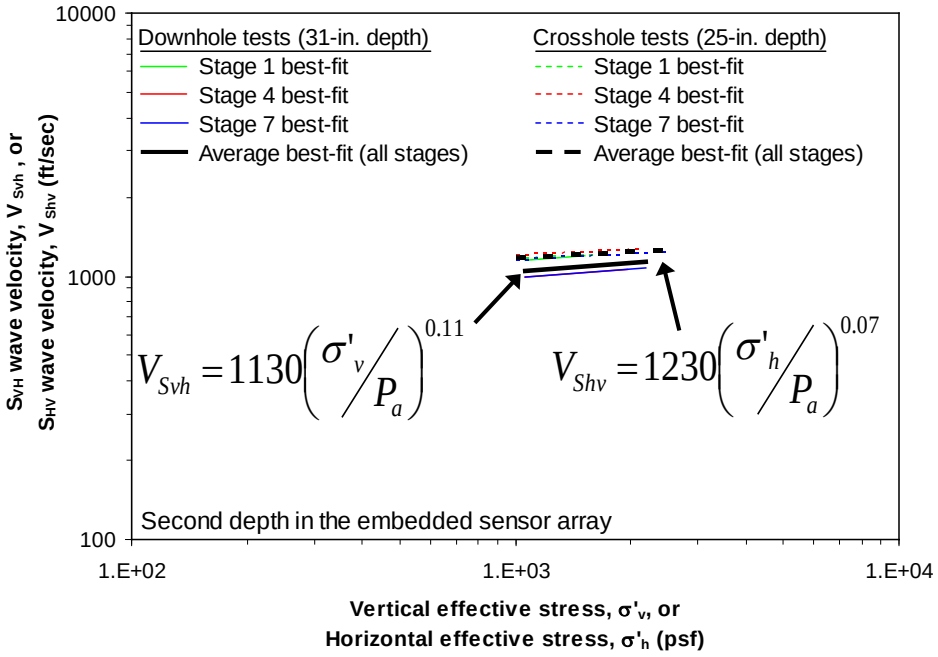

Figure 7.36. Comparison of log V_{Svh} – log σ'_v and log V_{Shv} – log σ'_h relationships at the second depth in the embedded sensor array at Site 2

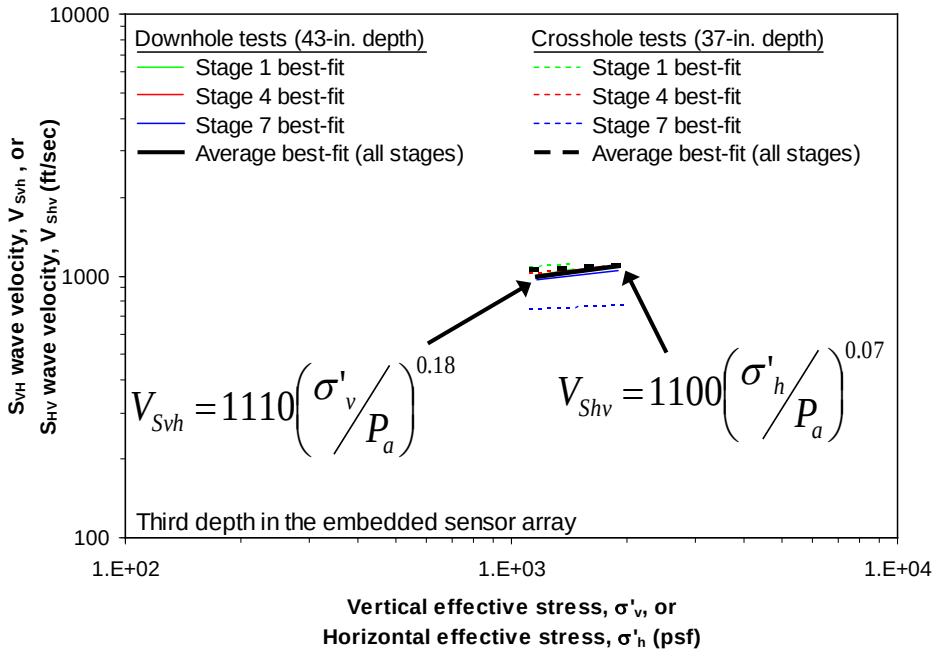

Figure 7.37. Comparison of log V_{Svh} – log σ'_v and log V_{Shv} – log σ'_h relationships at the third depth in the embedded sensor array at Site 2

shown in Figure 7.37 was assumed to be a consequence of fitting trend lines over a very limited range in stress (about 1/10th of a log cycle). In general, the difference between the crosshole and downhole velocities is rather small (~10%) and supports the conclusion that any structural anisotropy present in the soil at Site 2 is small enough to be counteracted by stress-induced anisotropy.

7.4.3 Menq (2003) empirical relation for G_{max}

As part of his PhD dissertation, Menq (2003) developed several empirical models to estimate the effect of stress level (in his case, the mean effective stress, σ'_o) on the small-strain shear wave velocity (V_S) of soil. His models allow construction of the estimated log V_S – log σ'_o relationships for several different types of soil by first estimating the small-strain shear modulus (G_{max}). Menq's model for an uncemented sand is expressed as:

$$G_{\max} = C_{G3} \times C_u^{\,b1} \times e^{x} \times \left[\sigma'_o / P_a \right]^{n_G} \tag{7.1}$$

where C_{G3} = 1400 ksf (67.1 MPa), C_u = uniformity coefficient, b1 = -0.20, e = void ratio, $x = -1 - [D_{50}/20]^{0.75}$, P_a = atmospheric pressure (2117 psf or 100 kPa), $n_G = 0.48 \times C_u^{\,0.09}$, and D_{50} = median grain diameter in mm (Menq, 2003). Note that since K_o was assumed to be equal to 1.0 (and constant) in this study, the mean effective stress is equal to the vertical effective stress. Therefore, in this study σ'_o was replaced by σ'_v in Equation 7.1. V_S is then related to G_{max} by:

$$V_S = \sqrt{\frac{G_{\max}}{\gamma_t / g}} \tag{7.2}$$

where γ_t is the total unit weight of the soil and g is acceleration due to gravity (Richart et al. 1970).

The grain size distribution curve for Site 2 shown in Figure 6.3 was used to determine the C_u and D_{50} terms (2.5 and 0.07 mm, respectively) of Equation 7.2. As discussed in Chapter 6, the total unit weight and water content in the field were about 96.5 pcf (1546 kg/m^3) and 4.5%, respectively. Based on these values, the void ratio used in Equation 7.2 was 0.82 (assuming G_s was equal to 2.69 as reported by Van Pelt (2010) for Lower Tract B). The log V_S – log σ'_v relationship for an uncemented sand estimated by Equations 7.1 and 7.2 is shown in Figure 7.38. Two key observations are seen in Figure 7.38 concerning the predicted log V_S – log σ'_v relationship for an uncemented sand: (1) the exponent of 0.26 is higher than the values measured in all cases at Site 2

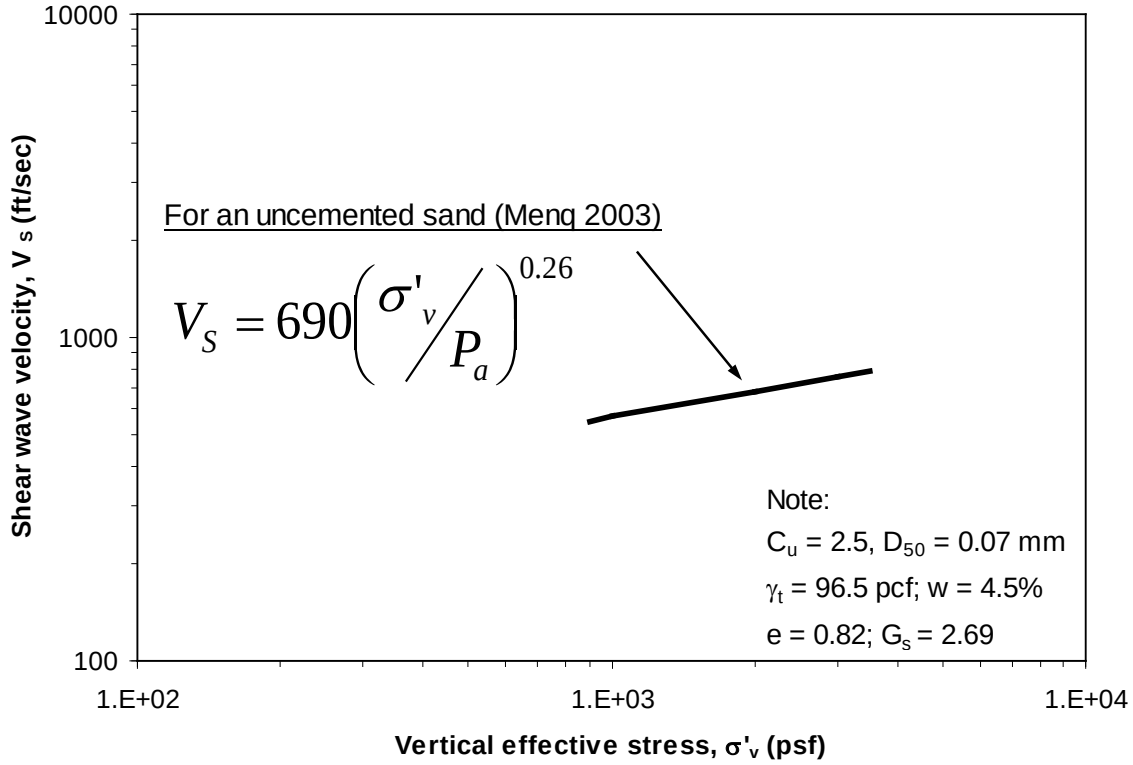

Figure 7.38. Variation of V_S with confining pressure (log V_S – log σ'_v) predicted for an uncemented sand (Menq, 2003)

(0.07 to 0.18 as shown in Figures 7.35 through 7.37) and (2) the coefficient (the V_S at one atmosphere, or $V_{S,1}$) is 690 fps, which is much lower than the values measured at Site 2 (1100 to 1230 fps as shown in Figures 7.35 through 7.37). Park (2010) attributed both of these phenomena to the presence of cementation in the soil. Therefore, it was concluded that the soil at Site 2 was at least partially cemented during all three stages of small-strain downhole and crosshole tests.

7.4.4 Poisson's ratio

Poisson's ratio (ν) is related to the small-strain downhole and crosshole wave velocities by the relations:

$$\frac{V_{Pv}}{V_{Svh}} = \sqrt{\frac{2(1+\nu)}{1-2\nu}} \tag{7.3a}$$

$$\frac{V_{Ph}}{V_{Shv}} = \sqrt{\frac{2(1+\nu)}{1-2\nu}} \tag{7.3b}$$

which assume that the soil is homogeneous and isotropic (Richart et al. 1970). The Poisson's ratio in the downhole tests was calculated at every depth in the embedded sensor array using Equation 7.3a. The downhole velocities used in Equation 7.3a were the P_V- and S_{VH}-wave velocities at one atmosphere ($V_{Pv,1}$ and $V_{Svh,1}$, respectively) which are the coefficients of the average effective stress relationships given in Table 7.1. Similarly, the Poisson's ratio in the crosshole tests was calculated at every depth in the embedded sensor array using Equation 7.3b. The crosshole velocities used in Equation 7.3b were the P_H- and S_{HV}-wave velocities at one atmosphere ($V_{Ph,1}$ and $V_{Shv,1}$, respectively) which are the coefficients of the average effective stress relationships given in Table 7.2. The Poisson's ratios in the downhole and crosshole tests are summarized in

Table 7.3 for all depths in the embedded sensor array. As seen in Table 7.3, the Poisson's ratios calculated using the crosshole wave velocities were about the same as those calculated using the downhole wave velocities at the first two depths. The difference between the crosshole and downhole results was greatest at the deepest depths of around 37 to 43 in. (94 to 109 cm). However, the overall difference is generally small as the average Poisson's ratios (average of all depths) were 0.35 and 0.32 in the downhole and crosshole tests, respectively. Indeed, with respect to Poisson's ratio, the results of the downhole and crosshole tests agree quite well in several ways. First, in both the downhole and crosshole tests, the Poisson's ratios at the middle depth in the sensor array are lower than at the shallowest and deepest depths. Second, in both the downhole and crosshole tests, the Poisson's ratios at the shallowest depths are basically the same at those at the deepest depths. Finally, the Poisson's ratios calculated using both the downhole and crosshole wave velocities are positive and vary over a relatively small range (0.27 to 0.39). Therefore, neither the results of the downhole nor the crosshole tests indicate the presence of significant structural anisotropy in the soil, and the isotropic assumption inherent in Equation 7.3 appears to be valid for Site 2.

7.5 UNCERTAINTIES AND LIMITATIONS

Throughout the data analysis of the small-strain downhole and crosshole tests, several simplifying assumptions had to be made. These assumptions, coupled with the

Table 7.3. Poisson's ratios determined in the downhole and crosshole tests at Site 2

Downhole tests	
Average depth (in.)	Poisson's ratio, ν
19	0.36
31	0.29
43	0.39

Note: Poisson's ratio calculated using V_{Pv} and V_{Svh} at one atmosphere

Crosshole tests	
Average depth (in.)	Poisson's ratio, ν
13	0.36
25	0.27
37	0.33

Note: Poisson's ratio calculated using V_{Ph} and V_{Shv} at one atmosphere

inherent uncertainties and limitations involved in the testing procedure, can effect the analysis of the linear constrained and shear moduli as described in this chapter. The relative significance of these effects on the results of the analysis is not known definitively. However, it is nonetheless important to understand the uncertainties and limitations that can be associated with these types of measurements.

Park (2010) identified several uncertainties and limitations involved in the testing of a cemented alluvium, some of which are equally valid at Site 2. Additionally, there are also uncertainties and limitations identified in this study that were not noted by Park. The uncertainties and limitations in evaluating the linear constrained and shear moduli (hence, the constrained compression and shear wave velocities) using small-strain downhole and crosshole tests are as follows (where contributions noted by Park are indicated as necessary):

1. Evaluation of the in-situ state of stress is only an approximation (Park, 2010). The entire farm field at Lower Tract B generally shows considerable spatial heterogeneity and localized anisotropy. This heterogeneity was discussed in Section 7.3.3 when the results of the crosshole tests in Stage 7 were different than in Stages 1 and 4 potentially due to the different location of the crosshole source rods in Stage 7 (note that destruction of the cementation bonds also likely occurred between Stages 4 and 7). As discussed in Section 7.4.2, the silty sand at Site 2 appears to have been at least initially cemented, and the amount of this cementation undoubtedly also varies spatially. These factors (heterogeneity, anisotropy, and cementation) were not directly considered when estimating the in-situ state of stress (Park, 2010).

2. In an attempt to somewhat overcome the limitations noted in Item #1, the estimated effective stresses in the field were used in this study. This estimation involved laboratory determination of the amount of suction stress present in

remolded specimens which were prepared as close as possible to the in-situ water content and density conditions in the field. The suction stress present in these small, remolded specimens was assumed to be the same as that in the field. However, the suction stress is highly unlikely to be a constant value in the field, and the distribution likely varies both horizontally and with increasing depth. Additionally, even at a single point in the soil, the suction stress is probably not constant during all phases of testing. The generation of excess positive pore pressures and/or destruction of cementation by the dynamic excitations of Thumper and T-Rex undoubtedly affects the distribution of suction stress. However, this effect was not quantifiable with the instrumentation used in this study and was therefore not considered.

3. The amount of stress increase generated in the soil by the equipment used in this study was relatively small even at the shallowest depths in the embedded sensor array. At the location of the first sensor in the array (13 in. (33 cm) beneath the concrete footing), the amount of total vertical stress increase was barely more than one log cycle (from about 200 to 2700 psf (10 to 130 kPa)). And at the deepest sensor in the array (49 in. (125 cm)), the increase in total vertical stress (from about 500 to 1100 psf (24 to 53 kPa)) was less than the amount of suction stress estimated using the procedure described in Item #2 (720 psf (34.5 kPa)). Therefore, rather than the increase in stress level, the suction stress term may be the controlling factor in the behavior of the small-strain wave velocities at even relatively shallow depths.

4. The propagation paths of the waves may not be correctly identified. It is possible that the waves propagate along some other path instead of the direct path assumed in the data analysis (Park 2010). Park also noted that the unknown variability in the cementation in the soil may also cause the waves to travel along unexpected paths.

5. As noted in Section 7.3, the P_H waves generated in the crosshole tests were filtered out rather quickly by the soil, such that the arrivals of the P_H waves at the receivers furthest from the source could not be identified in most cases. Accordingly, the receiver-to-receiver travel times could not be used to determine V_{Ph}, but rather the source-to-receiver travel times were used. The calculation of V_{Ph} in this manner is problematic when determining the stress level associated with the V_{Ph}. If the wave travels along a direct path as assumed in Item #4 above, a potentially large portion of this path lies outside the area influenced by the vertical stress applied to the concrete footing. Accordingly, the P_H wave traverses at least two distinct regions where the stress level is significantly different. This effect was somewhat accounted for by assuming a trapezoidal stress distribution beneath the footing and computing a "weighted average" induced stress at each depth. The errors associated with this approximation of stress level are not known.

These possible uncertainties and limitations cause the variability in the small-strain, downhole and crosshole data to increase. However, Park (2010) found reasonably good agreement with other field methods which used different measurement methods. A similar observation is discussed in Sections 7.2.1 and 7.3.1 where the downhole and crosshole tests at Site 2 are compared to Kim's (2012) SCPT results (see Figures 7.4 and 7.23). Therefore, it is believed that the uncertainties and limitations are not overly significant in the evaluation of the constrained and shear moduli in the linear strain range using the methods discussed in this chapter.

7.6 SUMMARY

Constrained and shear moduli in the linear range were evaluated from traditional downhole and crosshole tests conducted on a silty sand at Site 2 at Hornsby Bend, Texas. These transient, small-strain tests were performed in three stages (Stages 1, 4, and 7) with

each stage inducing progressively more vertical stress within an embedded sensor array consisting of 12, 3-D sensors (these sensors and the arrangement of the sensor array are described in Chapter 6). During each stage of testing, both downhole wave velocities (V_{Pv} and V_{Svh}) and crosshole wave velocities (V_{Ph} and V_{Shv}) were measured at several different stress levels and at several different locations in the embedded sensor array. The amount of stress increase induced by the equipment used in this study was relatively small even at the shallowest depth in the embedded sensor array. At the location of the first sensor in the array (13 in. (33 cm) beneath the concrete footing), the amount of vertical stress increase was barely more than one log cycle (from about 200 to 2700 psf (10 to 130 kPa)). And at the deepest sensor in the array (49 in. (125 cm)), the amount of vertical stress increase was only about half of one log cycle (from about 500 to 1100 psf (24 to 53 kPa)). As a relative comparison, the stress increase at the deepest sensor is less than the amount of suction stress (determined in Chapter 6 as 720 psf (34.5 kPa)) used to estimate the effective stresses in the field.

The results of the downhole tests are presented in two forms: (1) V_{Pv} and V_{Svh} versus depth profiles and (2) log V_{Pv} – log σ'_v and log V_{Svh} – log σ'_v relationships. The results of the crosshole tests are also presented in two forms: (1) V_{Ph} and V_{Shv} versus depth profiles and (2) log V_{Ph} – log σ'_h and log V_{Shv} – log σ'_h relationships. In most cases, the V_{Svh}– and V_{Shv}–depth profiles agree well with the results of downhole and Seismic Cone Penetration Tests (SCPT) reported by Kim (2012) for the same field at Hornsby Bend. However, the V_{Pv} and V_{Ph} profiles in all stages are roughly 1000 fps (305 m/s) faster than the results of Kim's downhole tests. In the downhole tests, the variation of V_{Pv} and V_{Svh} with increasing effective stress level was relatively small (exponents of σ'_v of about 0.12). Similarly in the crosshole tests, the variation of V_{Ph} and V_{Shv} with increasing effective stress level was relatively small (exponents of σ'_v of about 0.09). These exponents are low compared to an empirical model developed by Menq (2003) for an uncemented sand, which predicts an exponent of 0.26 for the log V_S – log σ'_v relationship. Since the predicted effective stress exponent is greater than that observed in

this study, it was concluded that the sandy silt at Site 2 was at least partially cemented and heavily overconsolidated during all three stages of the small-strain downhole and crosshole tests.

In general, the agreement between the results of the downhole tests and those of the crosshole tests is quite good. The exponents in the log V_{Pv} – log σ'_v (from downhole tests) and log V_{Ph} – log σ'_h (from crosshole tests) relationships are roughly equal at all depths. At the second depth in the embedded sensor array, the two V_P trend lines overlap, but at the first and third depths the log V_{Pv} – log σ'_v relationships are higher than the log V_{Ph} – log σ'_h relationships (about 150 fps (46 m/s) at the first depth and about 300 fps (91 m/s) at the third depth). The exponents in the log V_{Svh} – log σ'_v (from downhole tests) and log V_{Shv} – log σ'_h (from crosshole tests) relationships are also roughly equal at all depths. Further, the downhole and crosshole V_S trend lines are within about 100 fps (31 m/s) of each other at all depths. These differences in the downhole and crosshole trend lines are rather small (about 10 to 15%) and support the conclusion that any structural anisotropy in the soil at Site 2 had a minor effect on the wave velocities relative to σ'_v and any cementation. Additionally, the average Poisson's ratio calculated using the crosshole wave velocities (V_{Ph} and V_{Shv}) was about 0.30. This value is slightly lower than the average Poisson's ratio of 0.35 calculated using the downhole wave velocities (V_{Pv} and V_{Svh}). Even so, Poisson's ratio falls within a range of about 0.25 to 0.39, indicating again that there is no evidence of <u>significant</u> structural anisotropy in the soil at Site 2.

In some cases, the wave velocities determined in the downhole tests were different depending on the load stage (Stage 1, 4, or 7). At the shallowest depth of 19 in. (48 cm), there is a roughly 25% (700 fps (213 m/s)) reduction in the $V_{Pv,1}$ values between Stages 1 and 4. At this same depth, there is virtually no reduction in the P_V-wave velocities between Stages 4 and 7. The P_V-wave velocities at the two deeper depths (31 and 43 in. (79 and 109 cm)) are basically constant in all three stages. Additionally, at all

depths in the embedded sensor array, there is no significant reduction in the V_{Svh} determined between Stages 1, 4, and 7. These last few statements can be seen in Figure 7.39, where the $V_{Pv,1}$ and $V_{Svh,1}$ determined in all three load stages are shown. At this time, it is believed that the reduction in the $V_{Pv,1}$ values at the shallowest depth between Stages 1 and 4 was likely caused by the intervening vertical and/or horizontal steady-state excitations applied with Thumper in Stages 2 and 3. The agreement between the $V_{Pv,1}$ values in Stages 4 and 7 suggests that perhaps most of the change in the soil occurred before steady-state excitations were applied with T-Rex in Stages 5 and 6. More evidence to support this conclusion is given in Chapter 8 in the discussion of the results of the steady-state excitation tests.

In contrast to results of the downhole tests at Site 2, the V_{Ph} and V_{Shv} values at all depths are generally in good agreement between Stages 1 and 4. Therefore, the crosshole

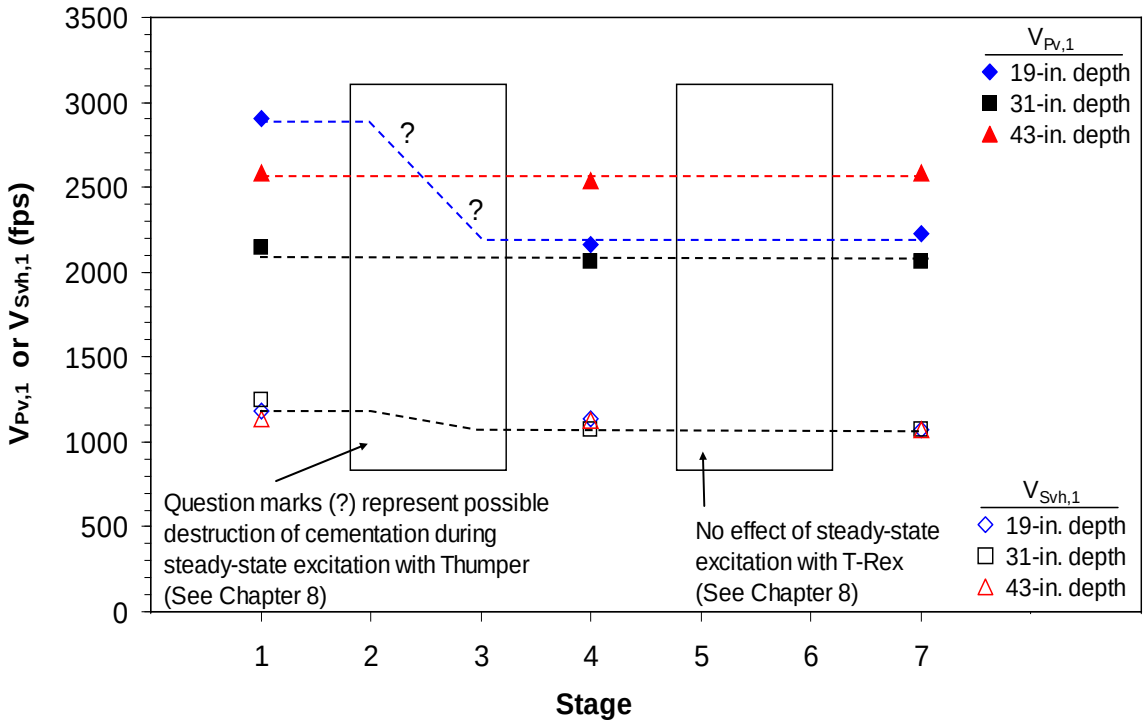

Figure 7.39. Effect of the staged loading sequence at Site 2 on the P_V- and S_{VH}-wave velocities at one atmosphere ($V_{Pv,1}$ and $V_{Svh,1}$)

tests do not indicate that the intervening vertical and horizontal excitations applied with Thumper in Stages 2 and 3 had any lasting effect on the soil structure. However, there is a roughly 200 fps (61 m/s) decrease in the crosshole wave velocities measured in Stage 7 (about a 10% reduction in V_{Ph} and a 20% reduction in V_{Shv}). The reduction of the crosshole wave velocities in Stage 7 could have been caused by several factors: (1) application of static loads in Stage 4, (2) generation of vertical and horizontal dynamic excitations applied by T-Rex in Stages 5 and 6, (3) the different location of the crosshole source rods in Stage 7, or (4) a combination of these factors. However, it does not seem possible that the vibroseis would cause changes in the crosshole wave velocities, but not in the downhole wave velocities. Therefore, it was assumed that most of the differences between the crosshole wave velocities measured in Stage 7 and those in Stages 1 and 4 were due to the different location of the crosshole source rods in Stage 7.

Though the results of the downhole and crosshole tests were apparently somewhat influenced by the steady-state excitation tests as discussed above, in most cases the behavior of the P-wave velocity with increasing confining pressure is generally the same in both the downhole and crosshole tests, i.e. the log V_{Pv} – log σ'_v and the log V_{Ph} – log σ'_h relationships are approximately the same. Additionally, these relationships do not vary significantly with depth. Similar statements can be made about the log V_{Svh} – log σ'_v (downhole tests) and log V_{Shv} – log σ'_h (crosshole tests) relationships. Therefore, the equations listed in Tables 7.1 and 7.2 can be reduced to a single set of relationships for Site 2. The recommended relationships for Site 2 are:

$$V_P = 2300\left(\sigma'_v / P_a\right)^{0.11} \tag{7.4a}$$

$$V_S = 1200\left(\sigma'_v / P_a\right)^{0.11} \tag{7.4b}$$

where the coefficients ($V_{P,1}$ and $V_{S,1}$) are in units of ft/sec.

Throughout the data analysis of the small-strain downhole and crosshole tests, several simplifying assumptions had to be made. These assumptions, coupled with the inherent uncertainties and limitations involved in the testing procedure, undoubtedly increase the variability in the small-strain, downhole and crosshole data. However, Park (2010) found reasonably good agreement with other field methods which used different measurement methods, and the results of this study agreed well with Kim's (2012) SCPT results. Therefore, it is believed that the uncertainties and limitations are not overly significant in the evaluation of the constrained and shear moduli in the linear strain range, and that the method described in this chapter is a promising approach to evaluating log V – log σ' relationships in the field.

CHAPTER 8: EVALUATION OF CONSTRAINED AND SHEAR MODULI IN THE NONLINEAR RANGE AT SITE 2

8.1 INTRODUCTION

The results of the sinusoidal excitation tests conducted at Site 2 as described in Chapter 6 are presented in this chapter (examples of raw waveforms recorded in these tests are provided in Appendices C and D). These steady-state excitation tests were performed in four stages (Stages 2, 3, 5, and 6 noted in Figure 6.11 and enlarged in Figure 8.1). In Stages 2 and 3, the sinusoidal excitations were applied by Thumper in the vertical and horizontal directions, respectively. Similarly, in Stages 5 and 6, the sinusoidal excitations were applied by T-Rex in the vertical and horizontal directions, respectively. When vertical sinusoidal excitations were applied by the shakers (Stages 2 and 5), vertically-propagating, constrained compression waves (P_V waves) were generated, and axial strains (ε) were induced between sensors in the embedded array. When horizontal sinusoidal excitations were applied by the shakers (Stages 3 and 6), vertically-propagating, horizontally-polarized shear waves (S_{VH} waves) were generated and shear strains (γ) were induced between sensors in the embedded array.

In each loading stage, the dynamic load amplitude was gradually increased in a stepped-sequence to progressively induce more strain (either ε or γ depending on the load stage) within the embedded sensor array (note the load-step naming convention is shown in Figure 8.1). In this manner, a wide range of strains was induced at Site 2 which allowed investigation of the nonlinear stress-strain behavior of both the constrained and shear moduli (M and G, respectively). The results of the vertical sinusoidal tests (which generated linear and nonlinear behavior in M) are presented first, followed by the results of the horizontal sinusoidal tests (which generated linear and nonlinear behavior in G). A comparison between the field M – log ε and G – log γ relationships from these tests is presented. The uncertainties and limitations associated with these tests are discussed.

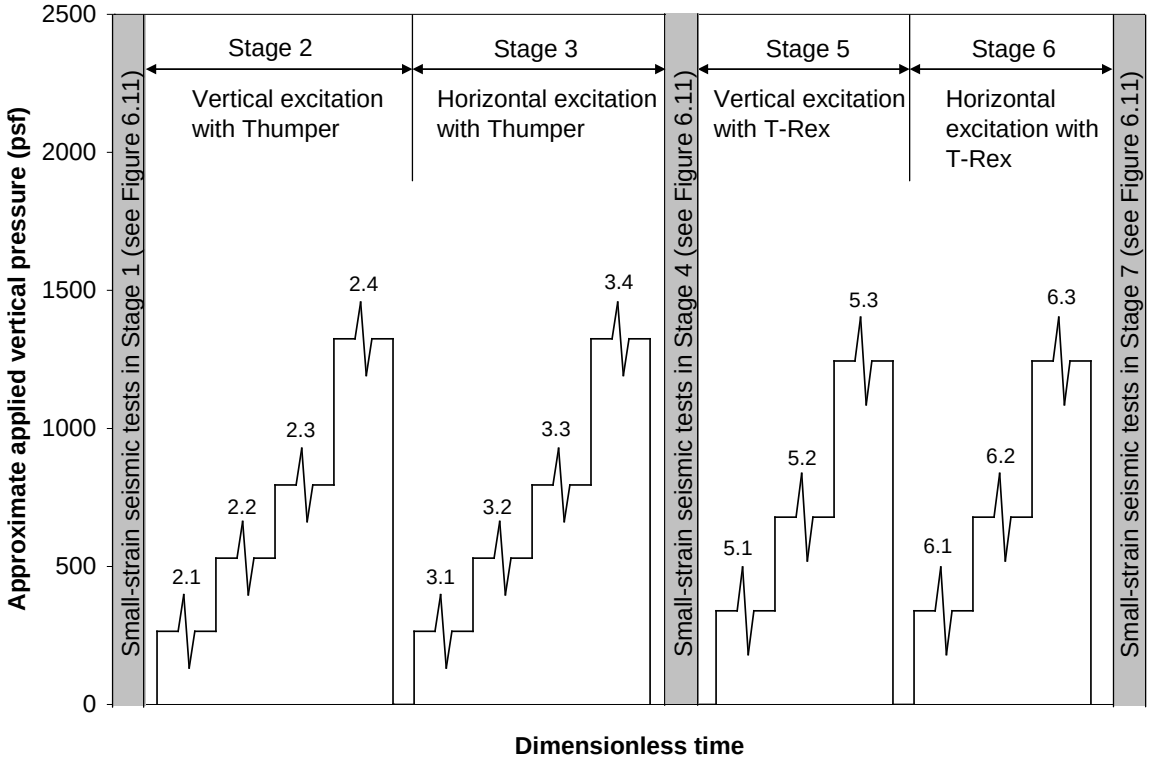

Figure 8.1. Staged loading sequence used for the sinusoidal excitation tests performed in Stages 2, 3, 5, and 6

8.2 EVALUATION OF NONLINEAR CONSTRAINED MODULI AT SITE 2

The results of the vertical sinusoidal excitation tests performed in Stages 2 and 5 are presented in this section (raw voltage-time histories recorded in these stages are provided in Appendix C). Four load steps were used in Stage 2, and three load steps were used in Stage 5 (see Figure 8.1). In each load step, the axial strains induced within the embedded sensor array were relatively large and allowed investigation of the nonlinear behavior of the constrained moduli in the field. In this section, the determination of the P_V-wave velocity (V_{Pv}) and its relation to M is presented first. Then, the process by which it was confirmed that the vertically-propagating waves generated by Thumper and T-Rex were fully constrained (and not partially-constrained or unconstrained) is discussed. Finally, the effect of increasing axial strain on the

constrained moduli is presented in the form of M – log ε and M/M_{max} – log ε relationships (where M_{max} is the constrained modulus at small strains).

8.2.1 Determination of field constrained moduli

In each of the load steps shown in Figure 8.1, the load amplitude of the vertical sinusoidal excitation applied with the shakers was progressively increased, which increased the amount of axial strain induced in the embedded sensor array. At each strain level, the velocity of the vertically-propagating wave traveling downward through the sensor array was calculated between the vertical components of adjacent sensors. This wave was *initially* assumed to be fully constrained, and for simplicity, will be referred to hereafter as a P_V wave (the validity of this assumption is discussed in Section 8.2.2).

Three methods were examined initially at Site 2 to quantify the potential variability in V_{Pv} due to the analytical method itself. The three methods are: (1) fitting of a sinusoidal model to the steady-state portion of the voltage-time records of adjacent sensors and calculation of the time difference between the peak of the same cycle at both sensors, (2) determination of the time-shift of the cross-correlation sequence computed between adjacent sensors (using the voltage-time records), and (3) fitting of a sinusoidal model to the displacement-time records of adjacent sensors and calculation of the time difference between the peak of the same cycle at both sensors. Note that Methods 1 and 2 are described in Chapter 4, and examples of the V_{Pv} calculated between Sensors 13 and 12 using these two methods are shown in Figures 4.13 and 4.14, respectively, at a small strain level induced in Stage 2.4 (V_{Pv} in both cases was 2049 fps (625 m/s)). Method 3 is similar to Method 1, but involves fitting of the sinusoidal model to the displacement-time histories rather than the voltage-time histories. The displacement-time histories used in Method 3 were computed by numerically integrating the velocity-time histories once as described in Section 4.4.2. An example of V_{Pv} calculated between Sensors 13 and 12 using Method 3 is shown in Figure 8.2a for the same strain level described in Figures

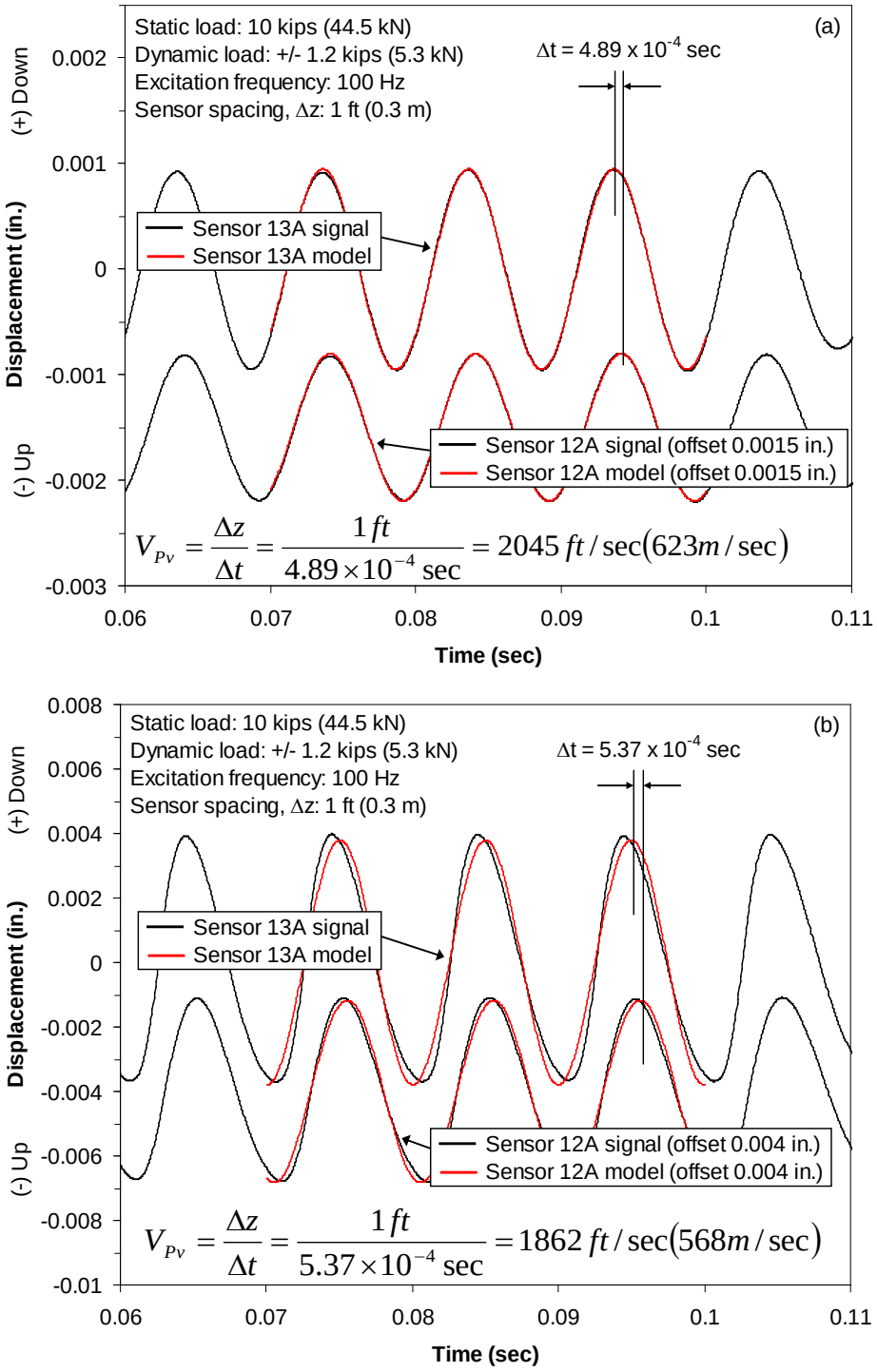

Figure 8.2. Calculation of V_{Pv} by fitting a sinusoidal model to displacement-time histories at two levels of vertical excitation in Stage 2.4: (a) low-amplitude loading and (b) high-amplitude loading

4.13 and 4.14. The V_{Pv} determined by Method 3 is 2045 fps (623 m/s), which is in excellent agreement with Methods 1 and 2. However, at larger strain levels, the agreement between the methods is not as good. At the largest strain level induced in Stage 2.4, the V_{Pv} calculated using Method 1 was 1862 fps (568 m/s) (see Figure 4.15), and the V_{Pv} calculated using Method 2 was 2049 fps (625 m/s) (see Figure 4.20). It should be noted that at the sampling frequency used in this case (20.4 kHz), the travel times used to compute these two V_{Pv} values are only different by one time step ($4.9x10^{-5}$ sec) in the digital records. Therefore, the 10% difference in the V_{Pv} values determined in Methods 1 and 2 is the minimum amount of change that can be detected in this case. As discussed in Chapter 4, the voltage-time histories recorded by the sensors at larger strain levels were often asymmetrical, showing more positive (downward) amplitude than negative (upward) amplitude (note the shapes of the responses shown in Figure 4.15), and the validity of fitting a sinusoidal model to these records using Method 1 was of great concern. Method 3 was developed to address this concern, as the displacement-time histories were much more symmetrical than the voltage-time histories, and the fit of a sinusoidal model was generally much better in this case (compare the fit of the models shown in Figure 8.2b for displacement-time to those shown in Figure 4.15 for voltage-time). As shown in Figure 8.2b, using Method 3 resulted in a V_{Pv} of 1862 fps (568 m/s), which agrees well with Method 1.

Though the V_{Pv} values calculated with Methods 1 and 3 are the same at both low and high strain levels, both methods rely on the fit of a single-frequency sinusoidal model to a signal that is not purely sinusoidal. Careful inspection of Figures 4.15 (Method 1) and 8.2b (Method 3) shows that the peaks of the models do not always coincide with the peaks of the signals at larger strain levels. And due to the relatively close spacing of the sensors, even small changes in the travel time of the wave have a large effect on the resulting V_{Pv}. This deficiency could be overcome by using a multi-frequency sinusoidal model, but Methods 1 and 3 are already highly labor-intensive. Computation of the cross-correlation sequence in Method 2 is relatively simple and quick, and results in V_{Pv}

values that are the same as Methods 1 and 3 at small strains and within 10% at large strains. For these reasons, Method 2 was used at Site 2 to calculate V_{Pv} at all strain levels.

After V_{Pv} was calculated between two sensors using the cross-correlation technique described above, the constrained modulus (M) was determined using the relation:

$$M = \frac{\gamma}{g} V_{Pv}^{\ 2} \tag{8.1}$$

where γ is the total unit weight of the soil and g is acceleration due to gravity (Richart et al. 1970). In this manner, M was determined for each level of sinusoidal excitation applied by Thumper and T-Rex. For a given level of sinusoidal excitation, M was combined with the induced axial strain (discussed in Section 8.2.3) to obtain one point on the M – log ε relationship. The process was repeated for all levels of excitation to construct the entire M – log ε relationship.

8.2.2 Generation of P_V waves under vertical excitations

In Section 8.2.1, it was assumed that the vertically-propagating waves generated by Thumper and T-Rex in Stages 2 and 5 were fully constrained. However, it is essential to verify that the vertical sinusoidal excitation tests successfully induced constrained compression (P_V) waves and not unconstrained (or partially-constrained) compression waves. Verification that P_V waves were generated is treated separately for Thumper (Stage 2) and T-Rex (Stage 5) in this section.

8.2.2.1 Thumper (Stage 2)

The first step required to verify that P_V waves were generated was to examine the raw voltage records of all three components (one vertical; two horizontal) in the sensors. The raw voltage-time records of the four sensors in the North sensor column (Sensors 4, 3, 2, and 1) are shown in Figure 8.3. The records in the Southwest and Southeast sensor columns are similar, so only one set is presented. The voltage-time records under the lowest and highest levels of vertical excitation applied in Stage 2.4 are shown in Figures 8.3a and 8.3b, respectively. As seen in both Figures 8.3a and 8.3b, there is a significant amount of motion monitored by the two horizontal components (relative to the vertical motion) of all sensors at both low and high levels of excitation. However, on average, the vertical motions of Sensors 4, 3, and 1 are still about 2.9 times larger than the horizontal motions. The amount of vertical motion relative to horizontal motion was greatest at the depth of Sensor 2 (37 in. (94 cm)). The vertical motion of Sensor 2 is, on average, about 5.2 times larger than the horizontal motion. It should be noted that these general observations were true at both low and high levels of excitation, even though the voltages at high levels of excitation (Figure 8.3b) were about 10 times greater than those at low levels of excitation (Figure 8.3a). Therefore, it was concluded that Thumper induced primarily vertically-propagating stress waves.

To determine whether these waves were indeed P_V waves, the steady-state compression wave velocities measured under the lowest levels of vertical excitation imposed in each load step, i.e. at the smallest induced strains, were compared to the log V_{Pv} – log σ'_v relationships determined in the transient, small-strain downhole tests described in Section 7.2. A comparison of the steady-state, small-strain wave velocities and the transient, small-strain V_{Pv} relationships is shown in Figure 8.4 for two sensor pairs at an average depth of 19 in. (48.3 cm) below the load plate of Thumper. Note that due the variability in the determination of V_{Pv} under steady-state excitation as described in Section 8.2.1, range bars indicating +/- 10% are also shown in Figure 8.4.

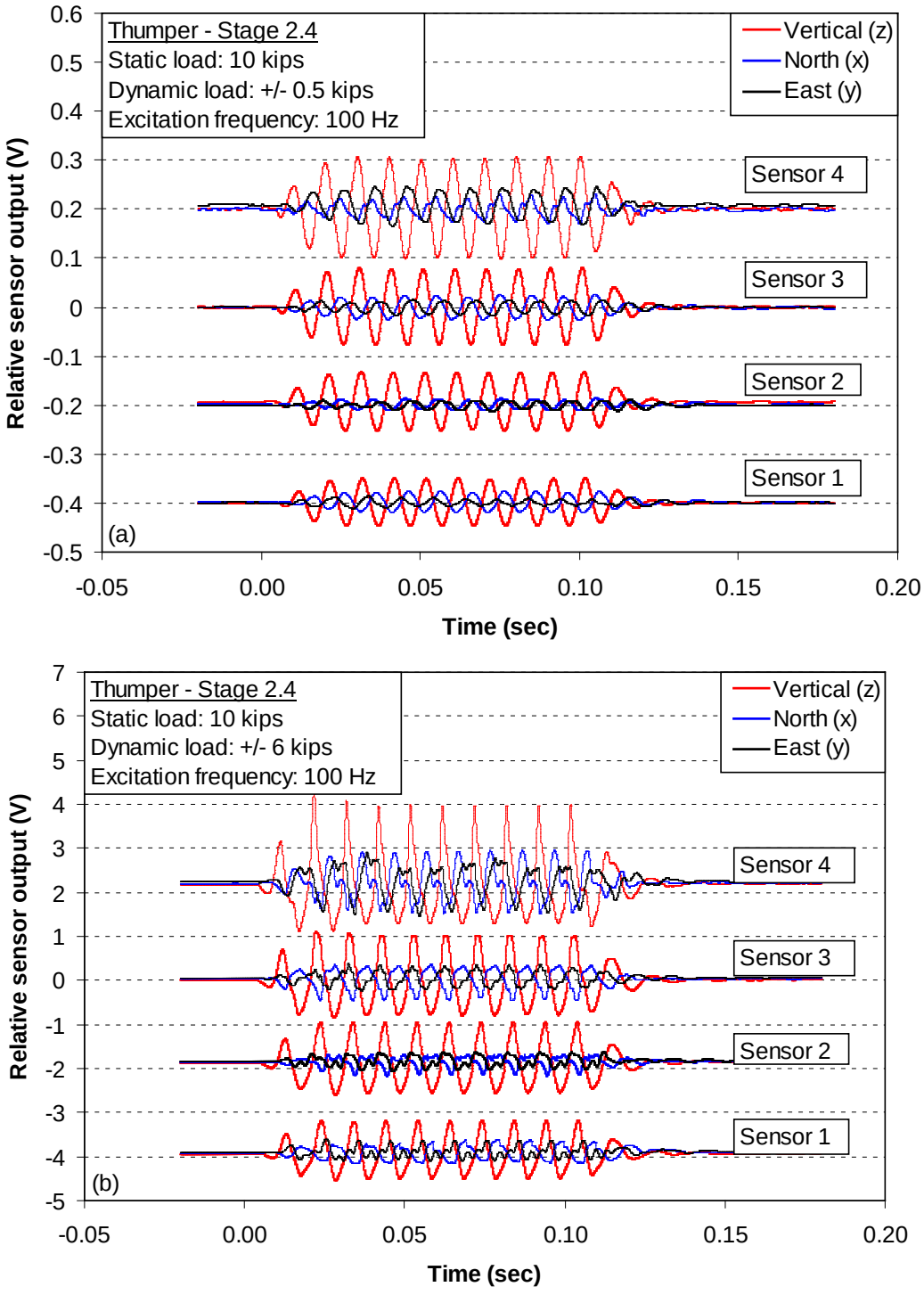

Figure 8.3. Voltage-time histories recorded by four vertically-aligned sensors subjected to sinusoidal vertical excitations in Stage 2.4: (a) low-load amplitude and (b) high-load amplitude

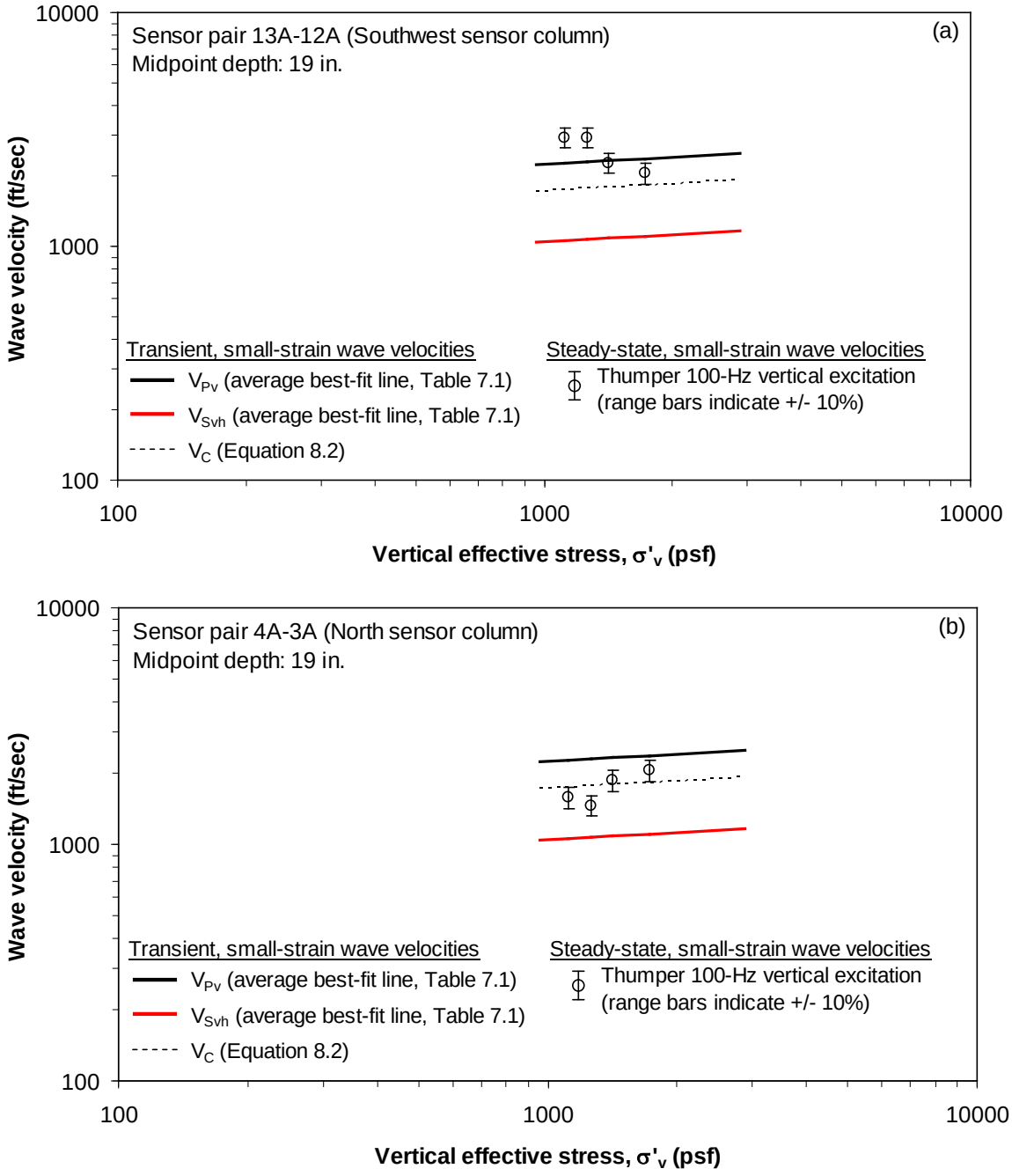

Figure 8.4. Comparison of steady-state, small-strain wave velocities in Stage 2 to the transient, small-strain wave velocities at an average depth of 19 in. (48.3 cm) at Site 2: (a) sensor pair 13-12 and (b) sensor pair 4-3

Additionally, the small-strain unconstrained compression wave velocity (V_C) relationship is included in Figure 8.4 and was determined using the relations:

$$\frac{V_{Pv}}{V_{Svh}} = \sqrt{\frac{2(1+\nu)}{1-2\nu}} \tag{8.2a}$$

$$V_C = V_{Svh}\sqrt{2(1+\nu)} \tag{8.2b}$$

where ν is the Poisson's ratio (Richart et al. 1970). As seen in Figure 8.4a, the steady-state wave velocities measured between Sensors 13 and 12 agree well with the transient, small-strain V_{Pv} in Stages 2.3 and 2.4. Note that the load step naming convention is shown in Figure 8.1. As seen in Figure 8.4b, the steady-state wave velocities measured between Sensors 4 and 3 are generally lower than the transient, small-strain V_{Pv}.

The agreement between the steady-state wave velocities and the transient, small-strain V_{Pv} was somewhat better at depths further away from the load plate of Thumper. Comparisons of the steady-state, small-strain wave velocities and the transient, small-strain V_{Pv} relationships are shown in Figure 8.5 for two sensor pairs at intermediate depths (31 and 37 in. (78.7 and 94.0 cm) and in Figure 8.6 for two sensor pairs at the deepest depth (43 in. (109.2 cm)). Note that the amplitude of the recorded waveform from the vertical component of Sensor 11 was similar to the two horizontal components. Therefore, the vertical component of Sensor 11 was assumed to be lost, and sensor pair 12-9 was used instead in Figure 8.5a. As seen in Figure 8.5, the steady-state wave velocities agree well with the transient, small-strain V_{Pv} in Stages 2.1, 2.2, 2.3, and 2.4 for sensor pair 12-9 (Figure 8.5a) and in Stage 2.4 for sensor pair 3-2 (Figure 8.5b). At the deepest depth in the embedded sensor array shown in Figure 8.6, the steady-state wave velocities agree well with the transient, small-strain V_{Pv} in Stages 2.1, 2.2, 2.3, and 2.4 for both sensor pair 6-5 (Figure 8.6a) and sensor pair 2-1 (Figure 8.6b).

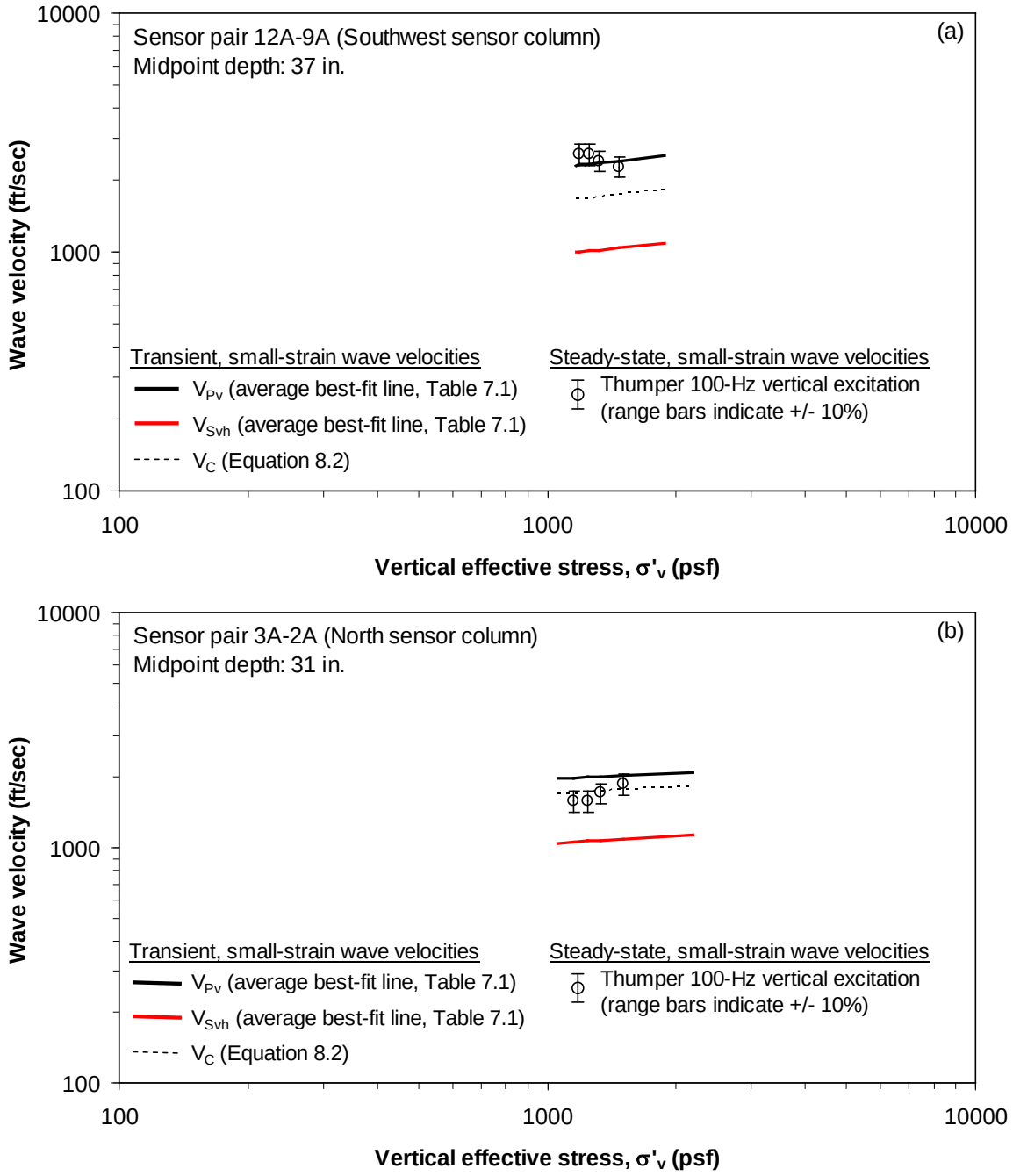

Figure 8.5. Comparison of steady-state, small-strain wave velocities in Stage 2 to the transient, small-strain wave velocities at intermediate depths at Site 2: (a) sensor pair 12-9 (37-in. (94.0-cm) mid-depth) and (b) sensor pair 3-2 (31-in. (78.7-cm) mid-depth)

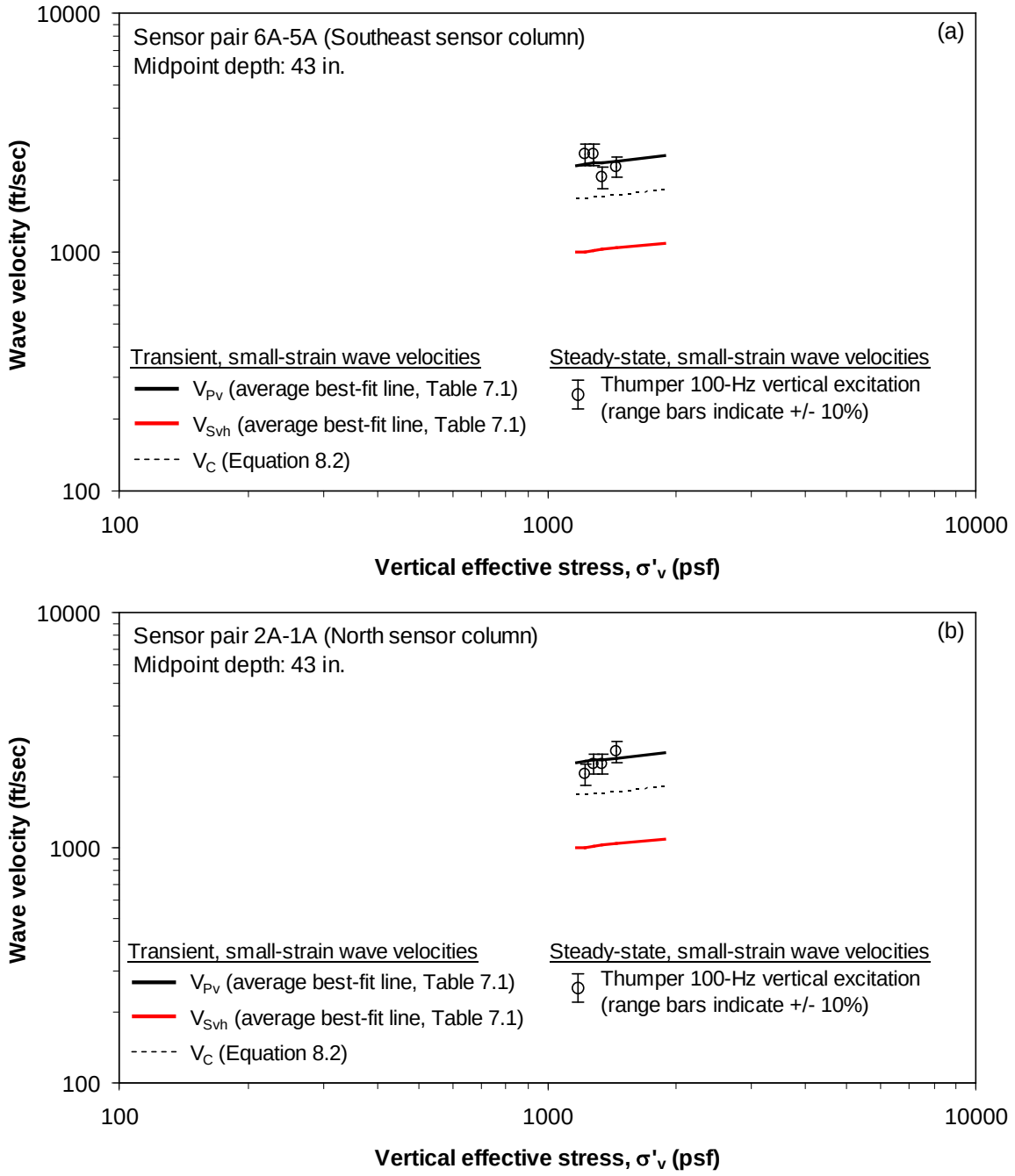

Figure 8.6. Comparison of steady-state, small-strain wave velocities in Stage 2 to the transient, small-strain wave velocities at an average depth of 43 in. (109.2 cm) at Site 2: (a) sensor pair 6-5 and (b) sensor pair 2-1

Based on the observations discussed in the previous two paragraphs and shown in Figures 8.4 through 8.6, it was concluded that P_V waves (or at least partially-constrained compression waves) were generated by Thumper at the following locations within the sensor array: (1) the midpoints (19-in. (48.3-cm) depth) of sensor pairs 13-12 and 4-3 (Figure 8.4), (2) the midpoint (31-in. (78.7-cm) depth) of sensor pair 3-2 (Figure 8.5b), (3) the midpoint (37-in. (94.0-cm) depth) of sensor pair 12-9 (Figure 8.5a), and (4) the midpoints (43-in. (109.2-cm) depth) of sensor pairs 6-5 and 2-1 (Figure 8.6). Therefore, these were the only cases in Stage 2 where the effects of increasing axial strain on the constrained moduli were examined. The effects of increasing axial strain are discussed in Section 8.2.3.

8.2.2.2 T-Rex (Stage 5)

As in Stage 2, the first step required to verify that P_V waves were generated in Stage 5 with T-Rex was to examine the raw voltage records of all three components (one vertical; two horizontal) in the sensors. The raw voltage-time records of the four sensors in the North sensor column (Sensors 4, 3, 2, and 1) are shown in Figure 8.7 (the records in the Southwest and Southeast sensor columns are similar). The voltage-time records under the lowest and highest levels of vertical excitation applied in Stage 5.3 are shown in Figures 8.7a and 8.7b, respectively. As seen in Figure 8.7a, there is very little response from the horizontal components of the four sensors. The vertical components of all sensors are, on average, 8.8 to 12.9 times larger than the horizontal components at this low level of excitation. At the highest level of sinusoidal excitation (Figure 8.7b), the amount of horizontal response recorded at all four sensors is relatively unaffected by depth, but the vertical response decreases with increasing depth. Accordingly, the amount of response from the vertical component relative to the horizontal components generally decreases with depth. In Sensor 4, the vertical component is, on average, 3.9 to 8.4 times larger than the two horizontal components. But at the deepest depth of Sensor 1, the vertical component is only about 2.1 to 5.1 times larger, on average, than the two

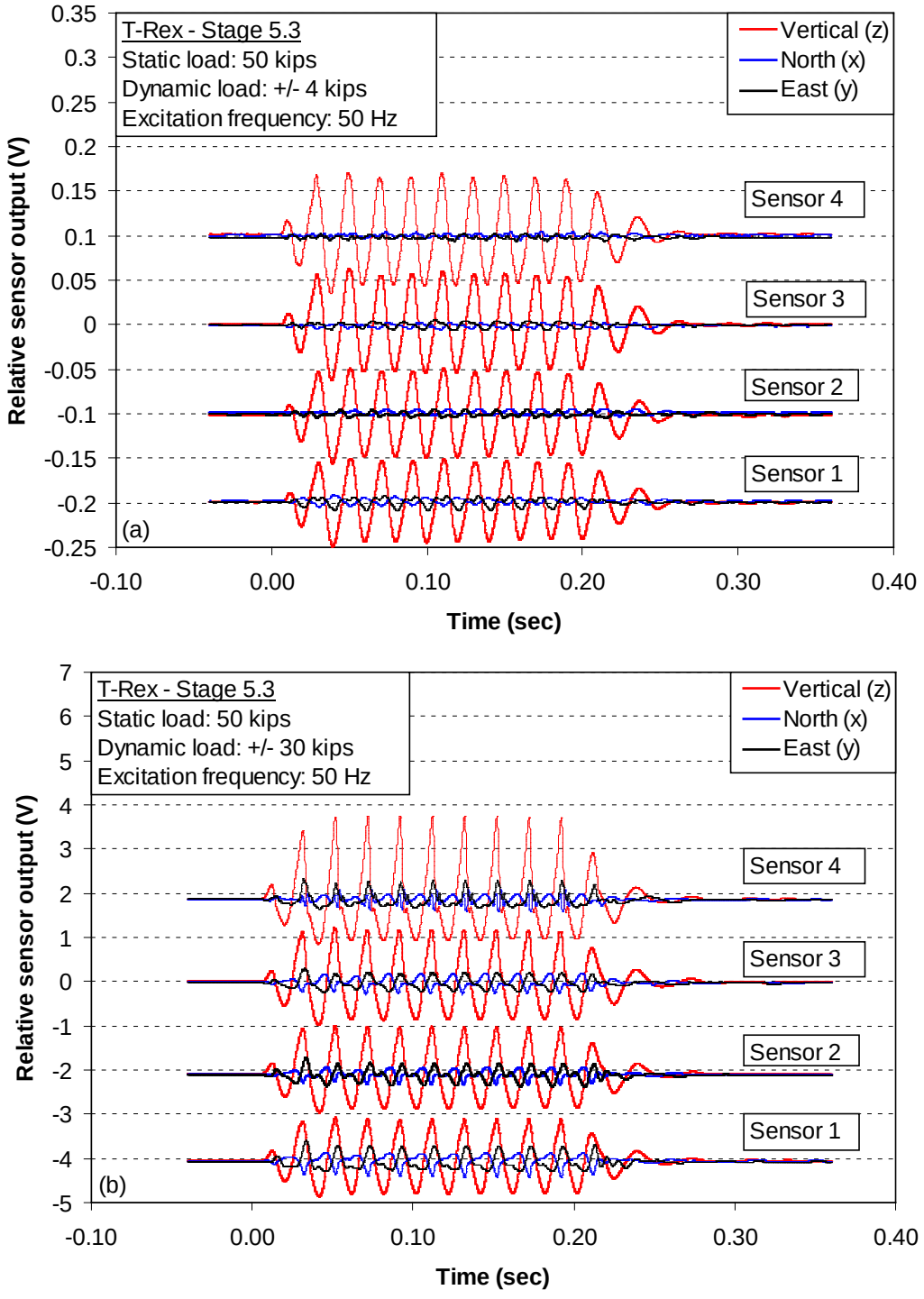

Figure 8.7. Voltage-time histories recorded by four vertically-aligned sensors subjected to sinusoidal vertical excitations in Stage 5.3: (a) low-load amplitude and (b) high-load amplitude

horizontal components. However, at all levels of vertical excitation and at all depths in the embedded sensor array, the response of the vertical component was considerably larger than those of the two horizontal components. Therefore, it was concluded that T-Rex induced primarily vertically-propagating compression waves.

Compared to the results of the Stage 2 tests with Thumper, there were fewer pairs of sensors in Stage 5 where the steady-state compression wave velocities could be determined using any of the three methods described in Section 8.2.1. At the locations of several sensor pairs within the embedded sensor array, the vertical response of the shallower sensor was either in-phase with or lagged the response of the deeper sensor. The resulting compression wave velocities at these locations were then either infinite or negative. The results were the same regardless of the excitation frequency or the method of analysis used. The compression wave velocities could not be determined at the shallowest depth in all three sensor columns (sensor pairs 13-12, 8-7, and 4-3) and at the deepest depth in the North sensor column (sensor pair 2-1). A similar effect was noticed at the shallowest depths in the sensor array used in the preliminary testing at Site 1 (see Chapter 5). As at Site 1, it is believed that due to the relatively large load plate of T-Rex, the first two sensors in the embedded sensor array at Site 2 are either too close to the shaker, too close to each other, or both. It is not known why the same effect also occurred at the deepest depth at Site 2 in one instance.

Despite the difficulties mentioned in the preceding paragraph, there were still four locations within the embedded sensor array at Site 2 where compression wave velocities were successfully determined. To determine whether these waves were indeed P_V waves, the steady-state compression wave velocities measured under the lowest levels of vertical excitation imposed in each load step, i.e. at the smallest induced strains, were compared to the average $\log V_{Pv} - \log \sigma'_v$ relationships determined in the transient, small-strain downhole tests described in Section 7.2 (the equations of these relationships are listed in Table 7.1). This process is the same as that described for Stage 2 in Section 8.2.2.1. A

comparison of the steady-state, small-strain wave velocities determined in Stage 5 and the transient, small-strain V_{Pv} relationships is shown in Figure 8.8 for two sensor pairs at an average depth of 31 in. (78.7 cm) below the load plate of T-Rex. A similar comparison is shown in Figure 8.9 for two sensor pairs at deeper depths in the sensor array. Note that due the variability in the determination of V_{Pv} under steady-state excitation as described in Section 8.2.1, range bars indicating +/- 10% are also shown in Figures 8.8 and 8.9. As seen in Figure 8.8, the steady-state wave velocities at an average depth of 31 in. (78.7 cm) agree well with the transient, small-strain V_{Pv} in Stages 5.1, 5.2, and 5.3 for sensor pair 7-6 (Figure 8.8a) and in Stages 5.2 and 5.3 for sensor pair 3-2 (Figure 8.8b). At the deeper depths in the embedded sensor array shown in Figure 8.9, the steady-state wave velocities agree well with the transient, small-strain V_{Pv} in Stages 5.1 and 5.3 for sensor pair 12-9 (Figure 8.9a) and in Stages 5.1, 5.2, and 5.3 for sensor pair 6-5 (Figure 8.9b).

Based on the observations discussed in the previous paragraph and shown in Figures 8.8 through 8.9, it was concluded that P_V waves were generated by T-Rex at the following locations within the sensor array: (1) the midpoints (31-in. (78.7-cm) depth) of sensor pairs 7-6 and 3-2 (Figure 8.8), (2) the midpoint (37-in. (94.0-cm) depth) of sensor pair 12-9 (Figure 8.9a), and (4) the midpoint (43-in. (109.2-cm) depth) of sensor pair 6-5 (Figure 8.9b). Therefore, these were the only cases in Stage 5 where the effects of increasing axial strain on the constrained moduli were examined. The effects of increasing axial strain are discussed in Section 8.2.3.

8.2.3 Effect of increasing axial strain on constrained moduli

Following the process described in Chapter 4 and Section 8.2.1, both V_{Pv} and axial strain (ε) were calculated at every level of dynamic excitation applied in Stages 2 and 5. The V_{Pv} at each strain level was related to the constrained modulus (M) using Equation 8.1. The effects of increasing axial strain on the constrained moduli are

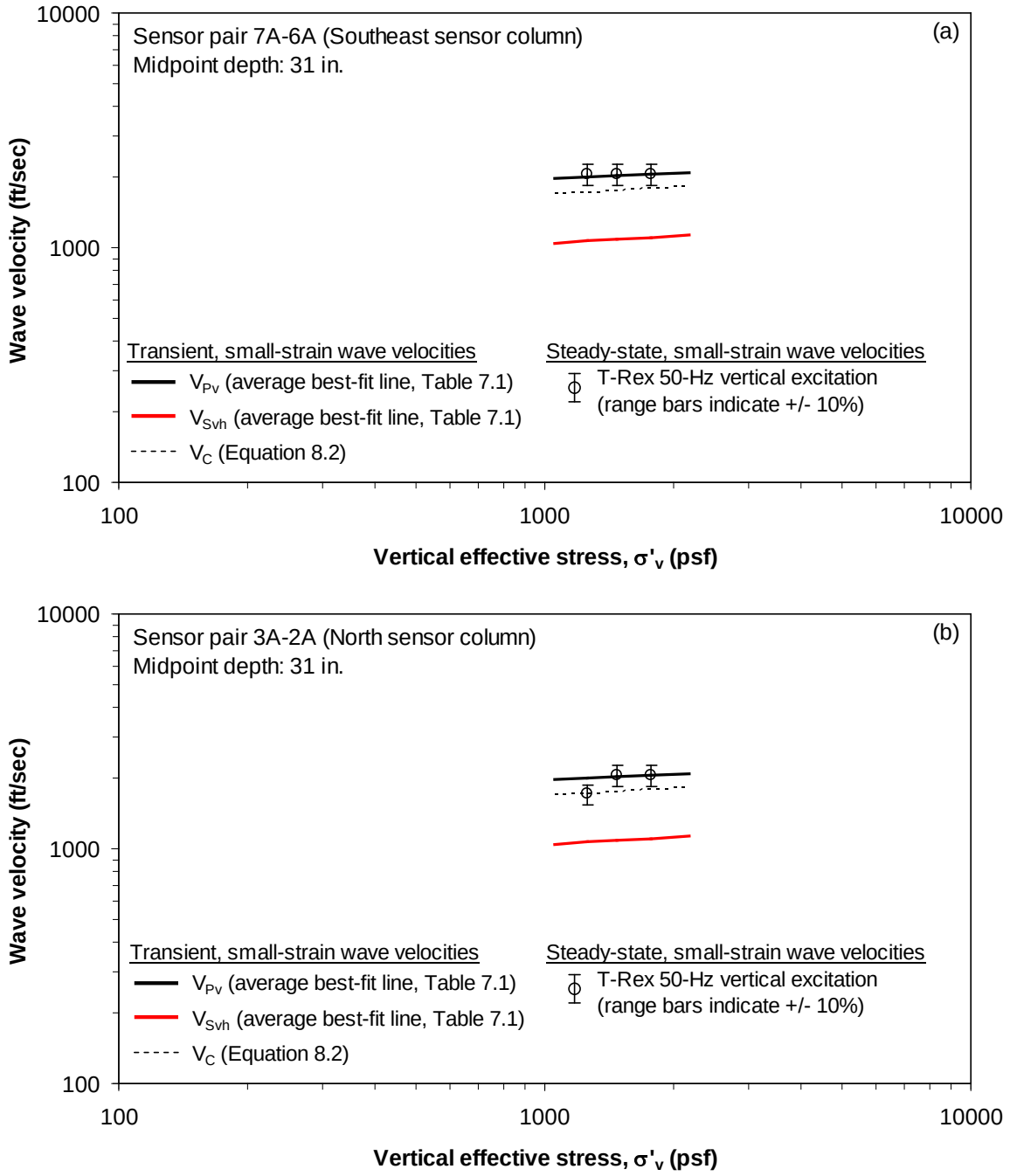

Figure 8.8. Comparison of steady-state, small-strain wave velocities in Stage 5 to the transient, small-strain wave velocities at an average depth of 31 in. (78.7 cm) at Site 2: (a) sensor pair 7-6 and (b) sensor pair 3-2

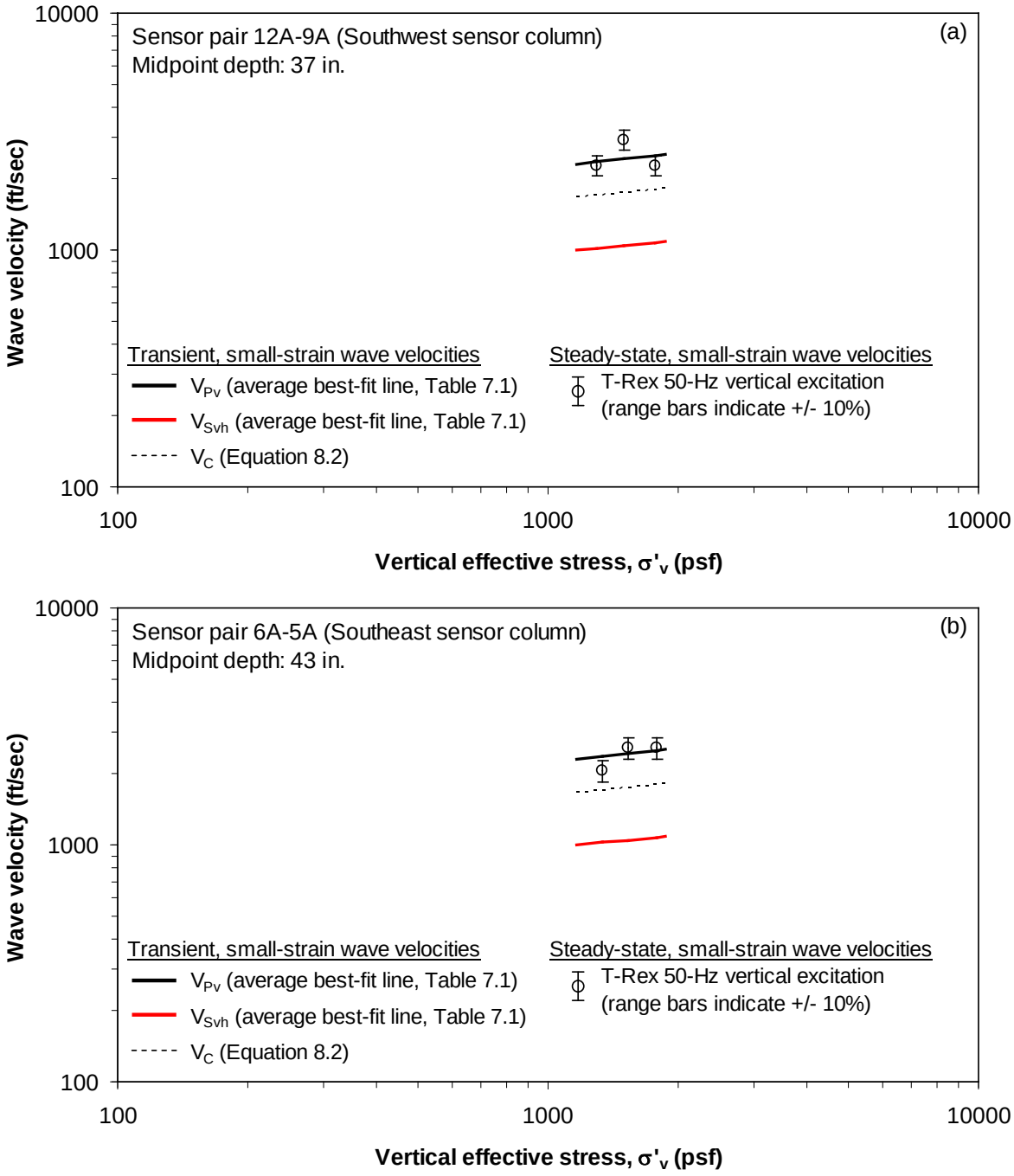

Figure 8.9. Comparison of steady-state, small-strain wave velocities in Stage 5 to the transient, small-strain wave velocities at deeper depths at Site 2: (a) sensor pair 12-9 (37-in. (94.0-cm) mid-depth) and (b) sensor pair 6-5 (43-in. (109.2-cm) mid-depth)

discussed in this section for the sensor pairs identified in Section 8.2.2 (pairs 3-2, 12-9, 6-5, 13-12, 4-3, 7-6, and 2-1). As discussed in Section 8.2.2, P_V waves were successfully generated between sensor pairs 3-2, 12-9, and 6-5 (average depths of 31, 37, and 43 in. (78.7, 94.0, and 109.2 cm), respectively) in both Stages 2 and 5. Therefore, since a large amount of data was collected at these three sensor pairs, the results at these pairs are presented first, followed by the results at sensor pairs 13-12, 4-3, 7-6, and 2-1. The results between points located along the centerline of the load plate of T-Rex (Stage 5) are also discussed.

In the figures presented in this section, the constrained moduli from the transient, downhole seismic tests (see Chapter 7) are included to aid in the comparison with the constrained moduli determined using steady-state excitations. The axial strains associated with the transient, downhole seismic tests were calculated assuming a plane stress wave travelling vertically through the system using:

$$\varepsilon = \frac{\dot{z}}{V_{Pv}} \tag{8.3}$$

where $\dot{z}$ represents the maximum particle velocity in the vertical direction (Richart et al., 1970). The axial strains in these tests ranged from about 0.00005 to 0.00025%. The average axial strain was about 0.00012% and was used to represent ε for all transient downhole tests. Though these strains generated in the downhole tests are indeed small, the constrained modulus at small-strains (M_{max}) was assumed to occur at the lowest strain induced in the steady-state excitation tests. This convention was chosen to avoid potential errors that may arise by using two different test methods. Note that in some cases, the M values were slightly different at the first two or three levels of axial strain. In this event, an average value of M_{max} was used based on these two or three values of M (notes are included in the figures presented in this section to indicate when this averaging

method was used). These values of M (at the start of the steady-state tests) generally exhibited similar values over a strain range of about one log cycle.

8.2.3.1 Results at sensor pairs 3-2, 12-9, and 6-5

The variation of M with log ε in Stages 2 and 5 is shown in Figure 8.10a for the midpoint of sensor pair 3-2 (31-in. (78.7-cm) depth). Due to the variability in the determination of V_{Pv} as discussed in Section 8.2.1, range bars are included in Figure 8.10a. However, though the variability in V_{Pv} was estimated as +/- 10%, the variability in M is about +/- 20% since M depends on the square of V_{Pv} (see Equation 8.1). As is typically done with shear modulus reduction curves, the M – log ε relationships shown in Figure 8.10a were normalized by M_{max} and are presented in Figure 8.10b in the form of M/M_{max} – log ε relationships. Similar results are shown for sensor pairs 12-9 (37-in. (94.0-cm) depth) and 6-5 (43-in. (109.2-cm) depth) in Figures 8.11 and 8.12, respectively. In general, P_V waves were successfully generated in more load steps at the sensor pairs furthest from the load plates of Thumper and T-Rex (note that all load steps in Stages 2 and 5 are represented for sensor pair 6-5 (Figure 8.12)). It should be noted that the nomenclature M_{max} is used here to represent the M at small strains to follow the convention used to refer to the shear modulus at small strains (G_{max}). However, the term M_{max} could be potentially misleading in that the M at small strains is not always the maximum M. As seen in Figures 8.10b, 8.11b, and 8.12b, M/M_{max} decreases or remains constant with increasing axial strain in Stage 2 but increases with increasing axial strain in Stage 5. Therefore, it appears the behavior of M/M_{max} with increasing axial strain is much more complicated than the normalized shear modulus (G/G_{max}) with increasing shear strain (a comparison of the nonlinear behaviors of M/M_{max} and G/G_{max} is given in Section 8.4). Specifically, as indicated by the trend lines shown in Figures 8.10 through 8.12, the behavior of M/M_{max} in the nonlinear strain range seemed to depend on which vibroseis was used to apply the vertical sinusoidal excitations. Possible reasons for this difference in behavior are discussed in detail in Section 8.2.4.

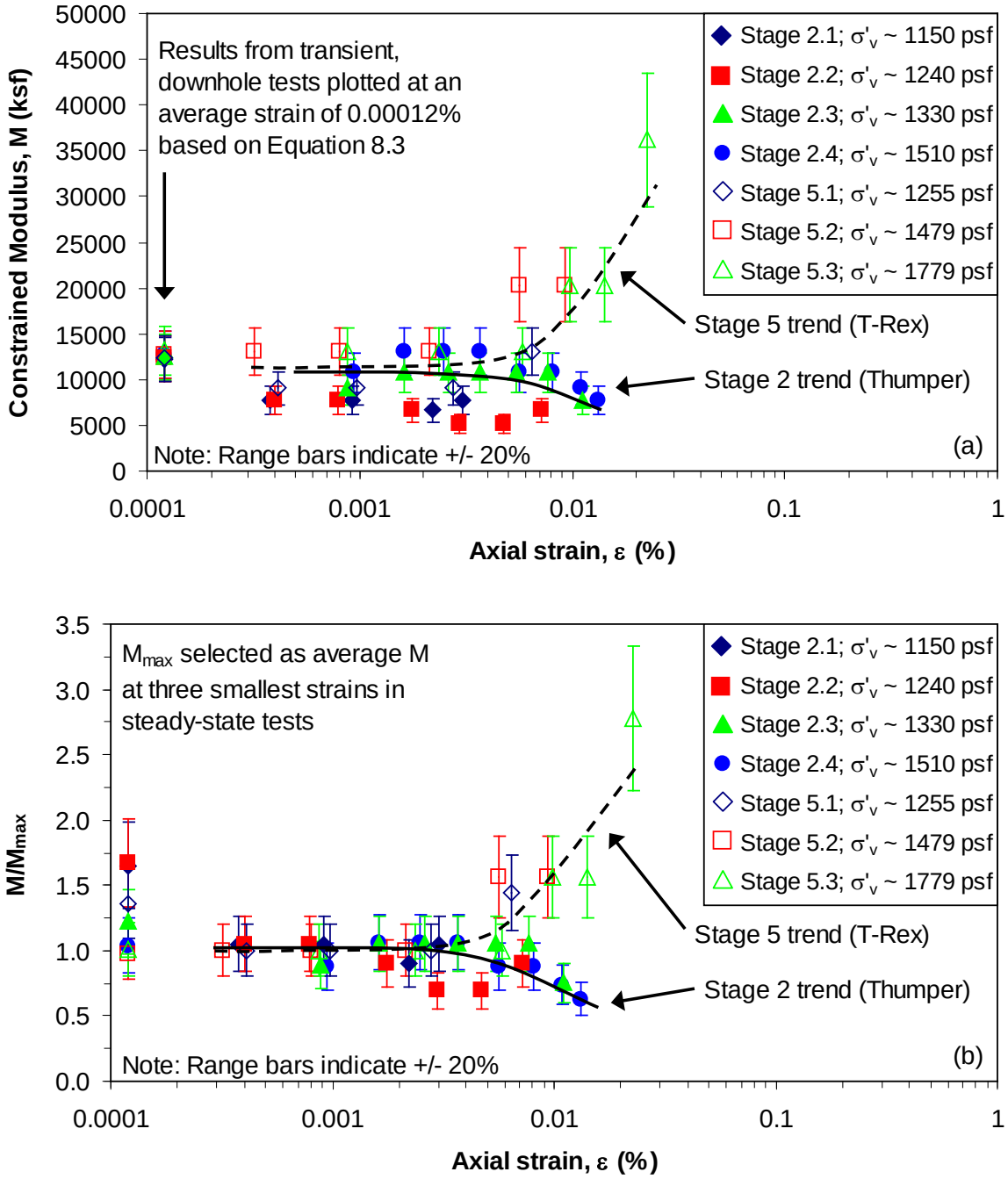

Figure 8.10. Variation of constrained modulus with axial strain at Site 2 between Sensors 3 and 2 (31-in. (78.7-cm) mid-depth): (a) M – log ε and (b) M/M_{max} – log ε

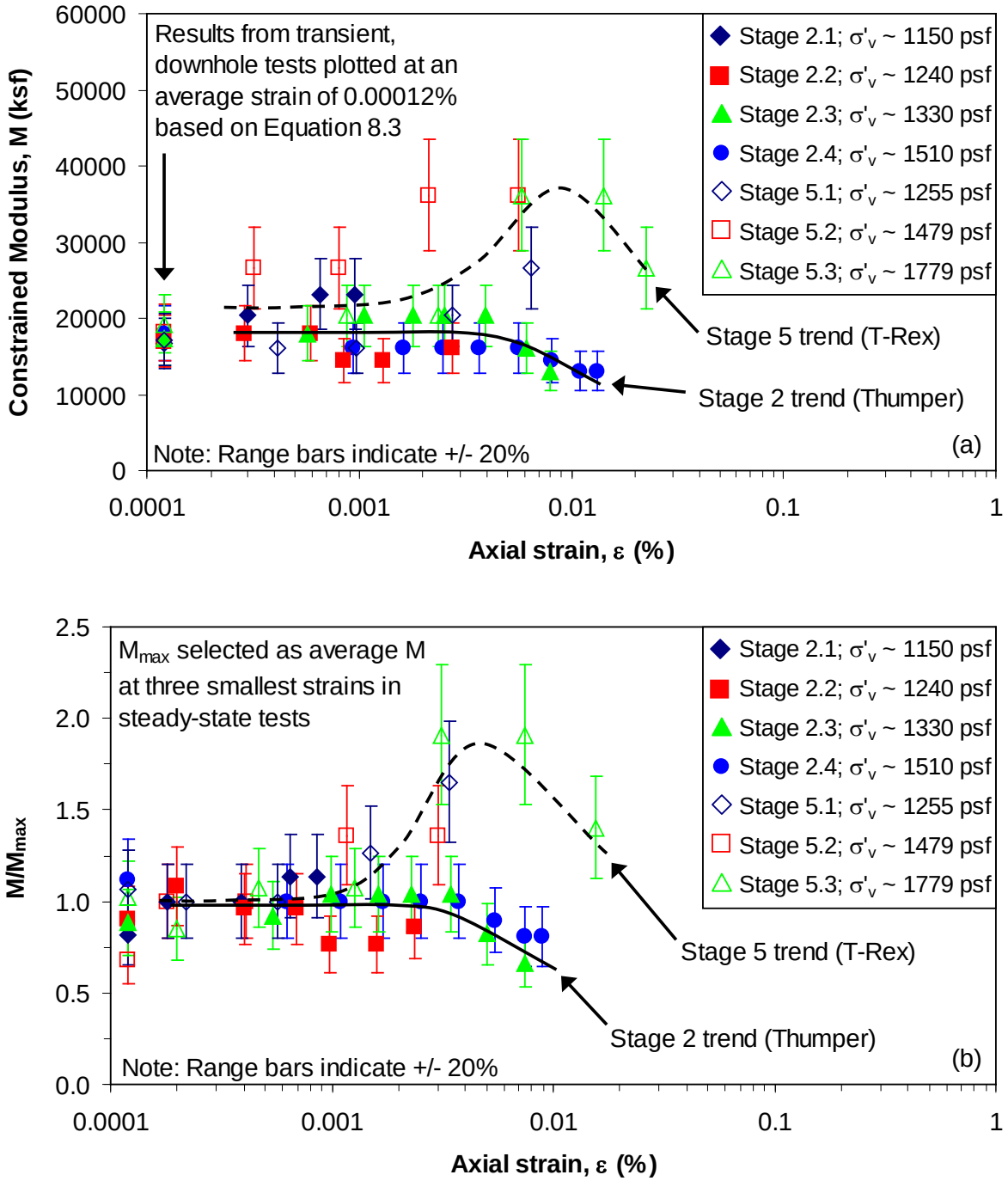

Figure 8.11. Variation of constrained modulus with axial strain at Site 2 between Sensors 12 and 9 (37-in. (94.0-cm) mid-depth): (a) M – log ε and (b) M/M_{max} – log ε

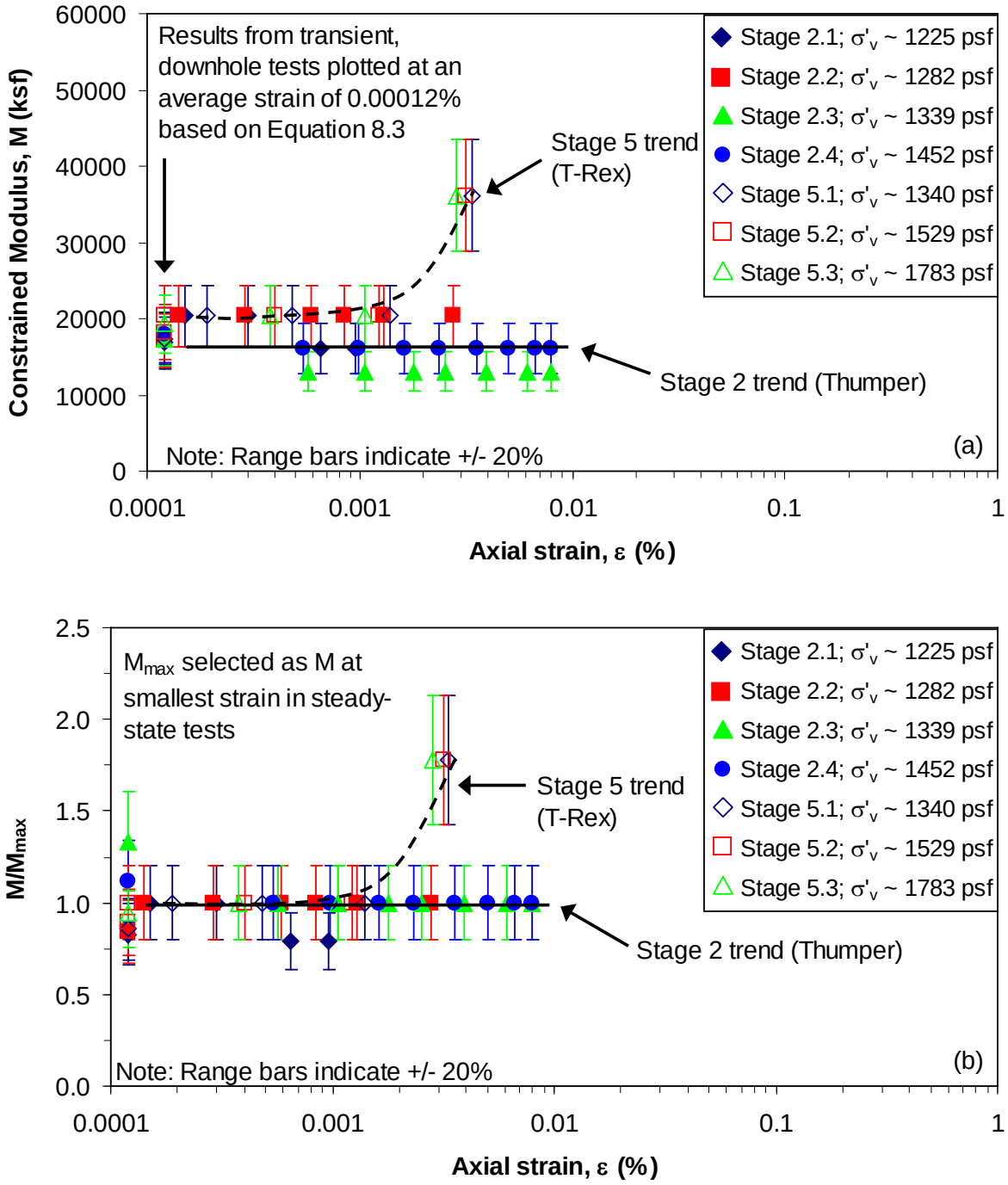

Figure 8.12. Variation of constrained modulus with axial strain at Site 2 between Sensors 6 and 5 (43-in. (109.2-cm) mid-depth): (a) M – log ε and (b) M/M_{max} – log ε

8.2.3.2 Results at sensor pairs 13-12, 4-3, 7-6, and 2-1

As discussed in Sections 8.2.2 and 8.2.3, at the midpoints of sensor pairs 13-12, 4-3, 7-6, and 2-1, P_V-wave velocities could only be determined in one load stage, i.e. in Stage 2 or 5, but not both. P_V waves were generated by Thumper (Stage 2) at the midpoints of sensor pairs 13-12, 4-3, and 2-1 and by T-Rex (Stage 5) at the midpoint of sensor pair 7-6. The analysis procedure used at these sensor pairs is the same as that described in Section 8.2.3.1. The variation of M with log ε in Stage 2 is shown in Figure 8.13a for the midpoint of sensor pair 13-12 (19-in. (48.3-cm) mid-depth). As in Section 8.2.3.1, the M – log ε relationships shown in Figure 8.13a were normalized by M_{max} and are presented in Figure 8.13b in the form of M/M_{max} – log ε relationships. Similar results are shown for sensor pairs 4-3 (19-in. (48.3-cm) mid-depth), 7-6 (31-in. (78.7-cm) mid-depth), and 2-1 (43-in. (109.2-cm) mid-depth) in Figures 8.14, 8.15, and 8.16, respectively.

For these sensor pairs, the nonlinear behavior of M (and M/M_{max}) is generally similar to the nonlinear behavior noted in Section 8.2.3.1. As seen in Figures 8.13b, 8.14b, and 8.15b, M/M_{max} decreases or remains constant with increasing axial strain in Stage 2 (with Thumper) but increases with increasing axial strain in Stage 5 (with T-Rex). However, there are a few observations which do not fit the general trends identified to this point, i.e. that the M/M_{max} – log ε relationship decreases when using Thumper (Stage 2) and increases when using T-Rex (Stage 5):

1. In Stage 2.3 at sensor pairs 13-12 and 4-3 (Figures 8.13 and 8.14, respectively) and in Stage 5.3 at sensor pair 7-6 (Figure 8.15), M/M_{max} remains constant until an axial strain of about 0.004 or 0.005%. As the strain increases past this point, M/M_{max} increases briefly before decreasing with increasing axial strain. The only other case where this brief rise and fall of the M/M_{max} – log ε relationship is seen is when T-Rex was used in Stage 5.3 at sensor pair 12-9 (Figure 8.11). Except for

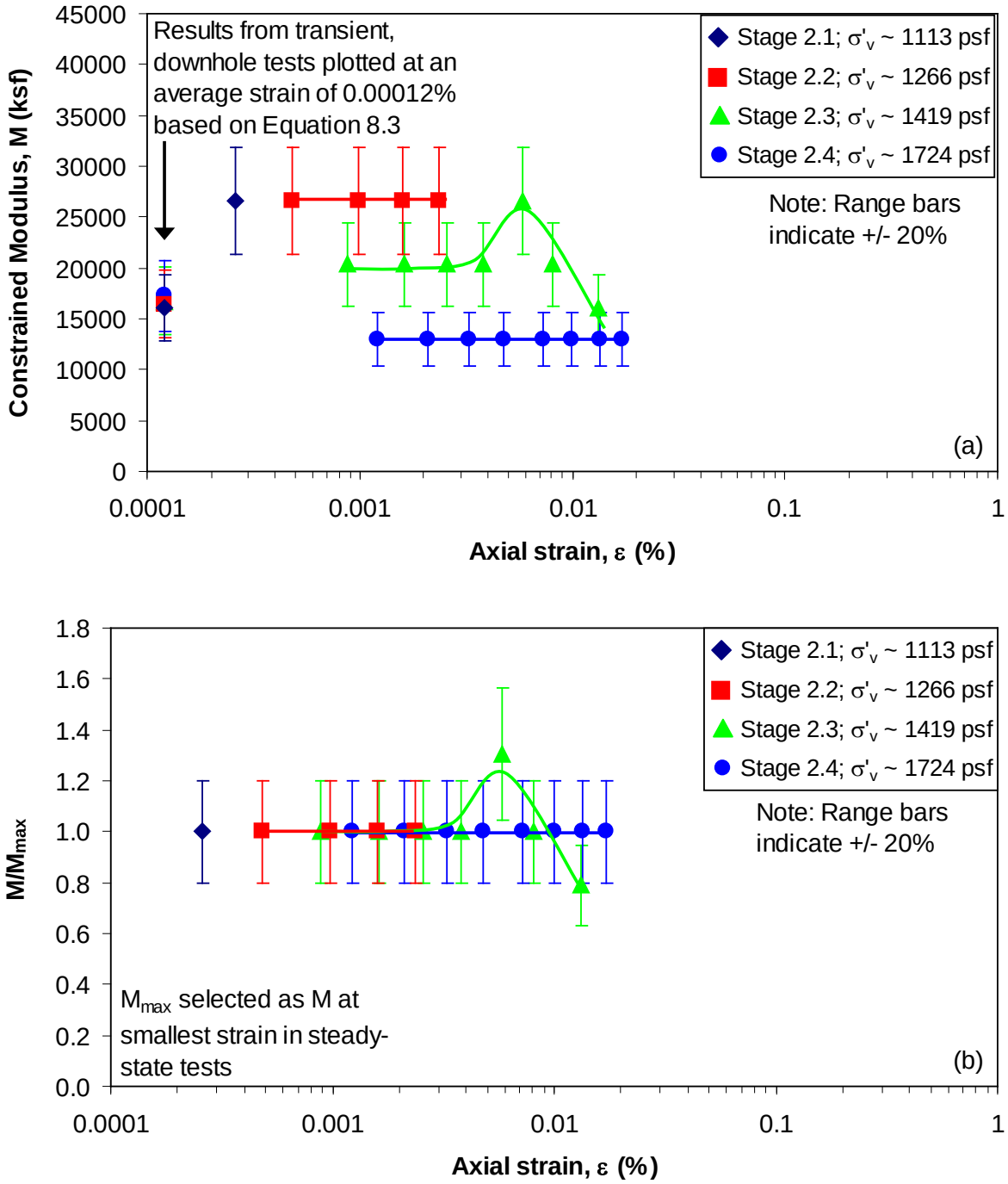

Figure 8.13. Variation of constrained modulus with axial strain at Site 2 between Sensors 13 and 12 (19-in. (48.3-cm) mid-depth): (a) M – log ε and (b) M/M_{max} – log ε

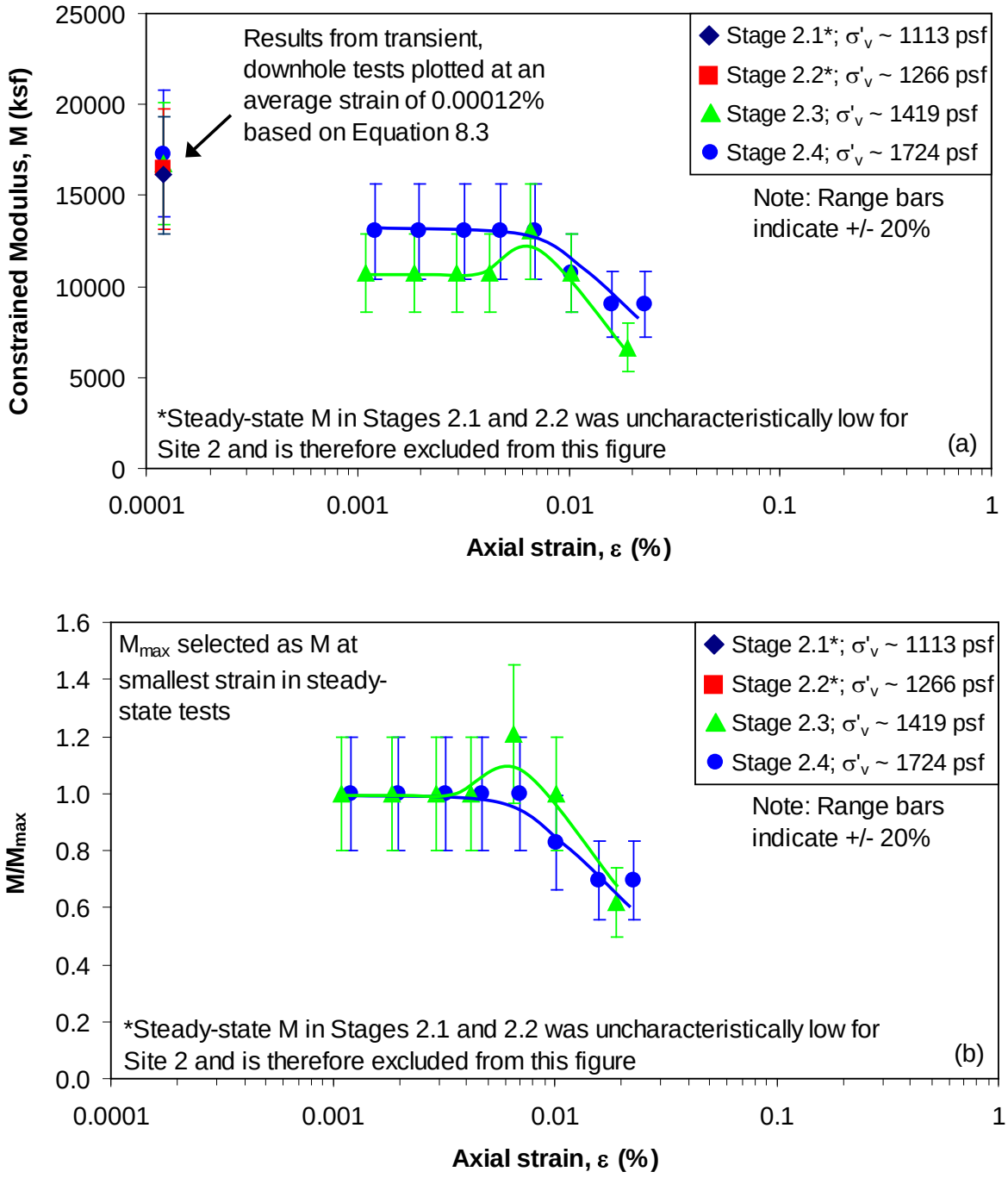

Figure 8.14. Variation of constrained modulus with axial strain at Site 2 between Sensors 4 and 3 (19-in. (48.3-cm) mid-depth): (a) M – log ε and (b) M/M_{max} – log ε

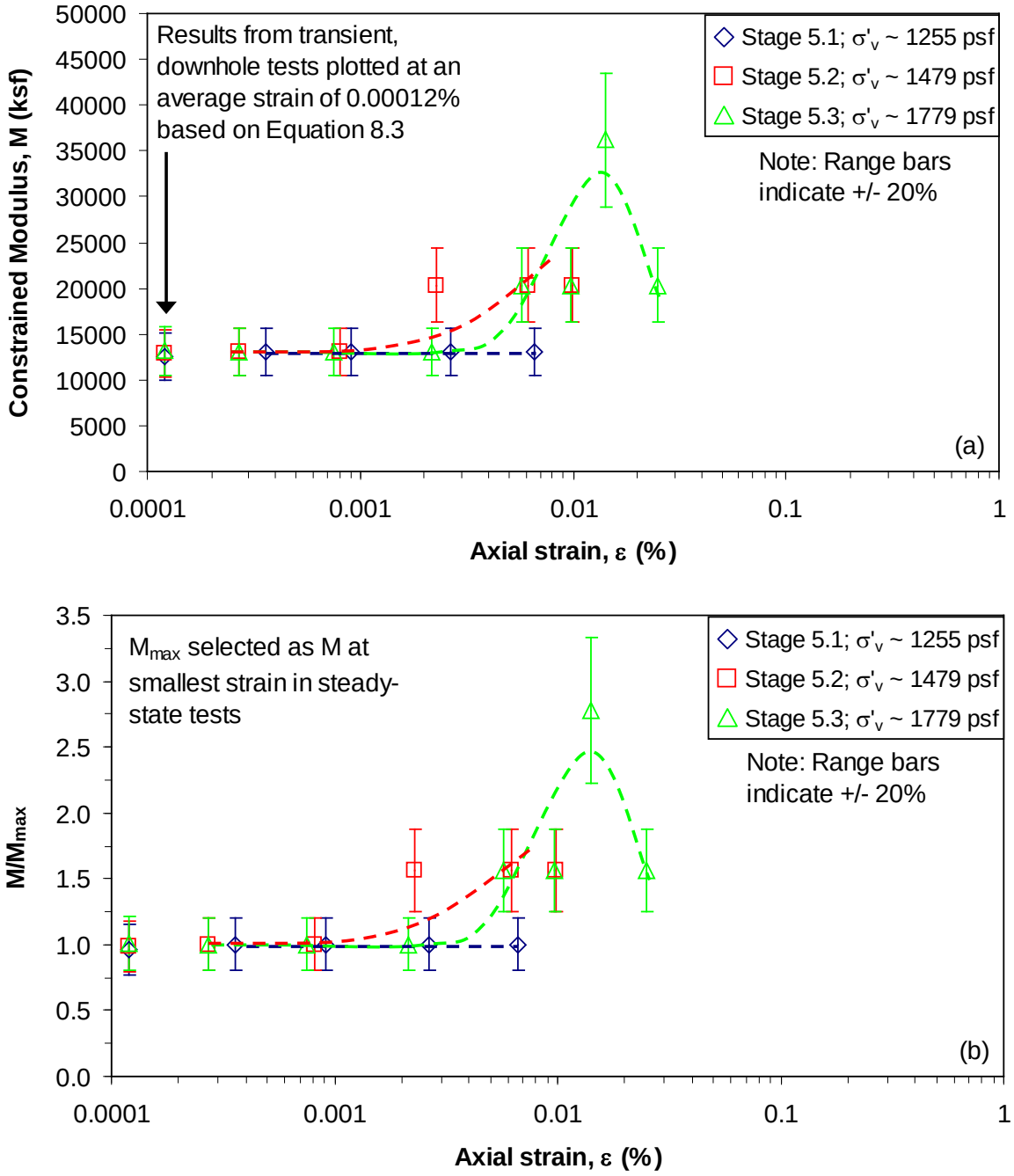

Figure 8.15. Variation of constrained modulus with axial strain at Site 2 between Sensors 7 and 6 (31-in. (78.7-cm) mid-depth): (a) M – log ε and (b) M/M_{max} – log ε

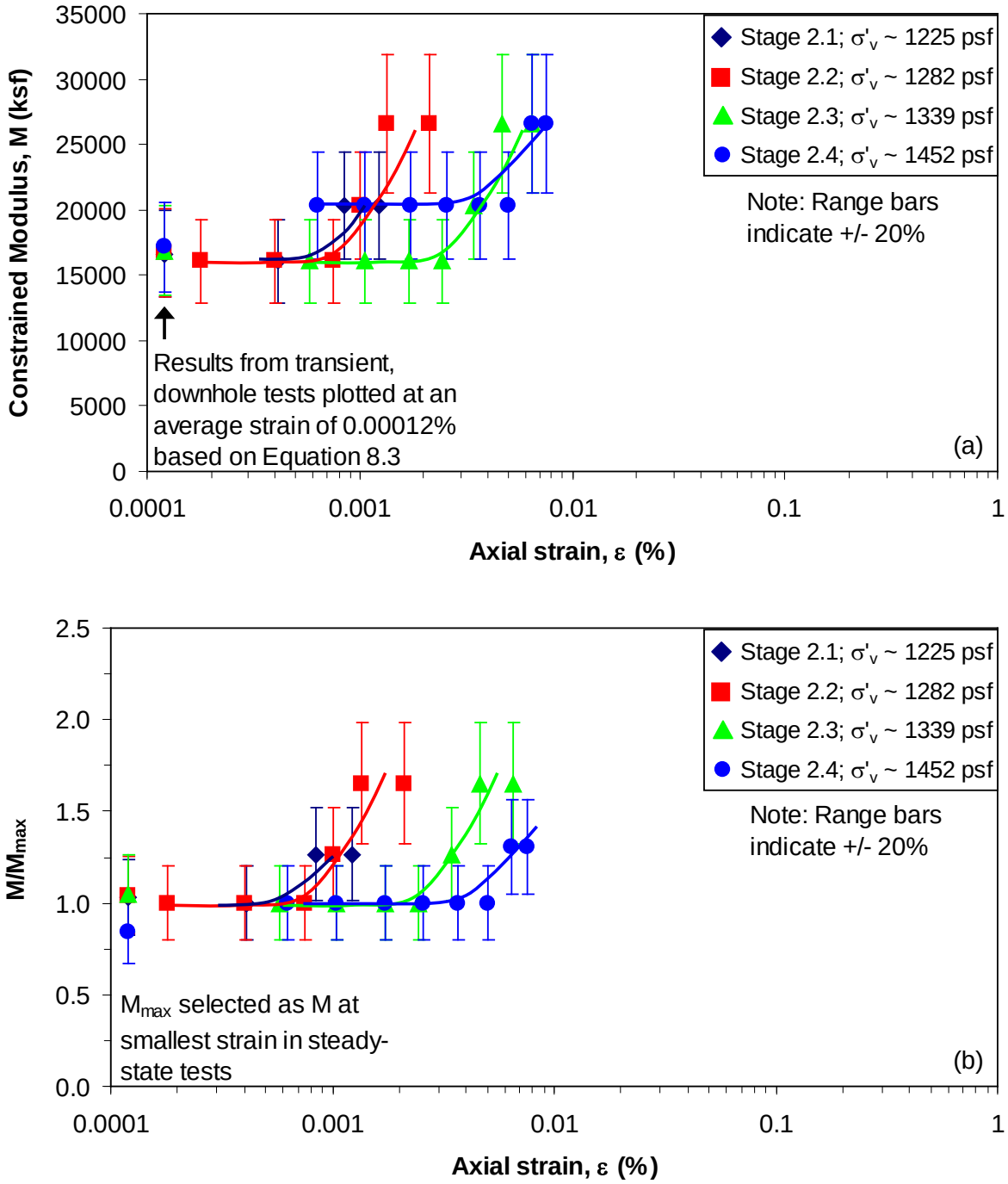

Figure 8.16. Variation of constrained modulus with axial strain at Site 2 between Sensors 2 and 1 (43-in. (109.2-cm) mid-depth): (a) M – log ε and (b) M/M_{max} – log ε

the case noted in this paragraph, this behavior of the M/M_{max} – log ε relationship is never observed when Thumper was used (Stage 2).

2. In all four load steps of Stage 2 at sensor pair 2-1 (Figure 8.16), M/M_{max} increases with increasing axial strain. M/M_{max} increases up to a value of about 1.7, which is slightly less than the increase in M/M_{max} seen in Stage 5 (note M/M_{max} increases up to about 2.0 in Figures 8.10 through 8.12). However, this is the only sensor pair where this increase was observed while using Thumper. Additionally, as the confining pressure (σ'_v) is increased in Stage 2, the axial strain at which M exhibits nonlinear behavior also increases (note Figure 8.16b).

Therefore, it appears the behavior of M/M_{max} with increasing axial strain is much more complicated than the normalized shear modulus (G/G_{max}) with increasing shear strain (a comparison of the nonlinear behaviors of M/M_{max} and G/G_{max} is given in Section 8.4). A more detailed discussion of the behavior of M/M_{max} in the nonlinear strain range is provided in Section 8.2.4.

8.2.3.3 Results at the centerline of the array

As shown in Figure 6.7, at each depth within the embedded sensor array at Site 2, three 3-D sensors form an equilateral triangle with the sensors at the corners. Triangles #1, #2, #3, and #4 are located at depths below the load plate of the vibroseis of 13, 25, 37, and 49 in. (33.0, 63.5, 94.0, and 124.5 cm), respectively. These triangles are essentially the 3-noded triangular element often used in finite element analyses, where the sensors serve as the nodes. Given that the vertical motions were measured at all three sensors, the vertical motion at any point within the triangle can be determined using the same linear shape functions used in finite element procedures. The vertical motions of the centroids of Triangles #1, #2, and #4 were evaluated to determine whether the results along the centerline of the load plate of the vibroseis were similar to those presented in

Sections 8.2.3.1 and 8.2.3.2. The results at Triangle #3 were disregarded since the vertical component of Sensor 11 became inoperable during the test regimen. It should be noted that in Stage 2, the center of Thumper's load plate was not aligned with the centerline of the sensor array due to difficulties experienced while positioning Thumper. This misalignment resulted in the Southeast sensor column being approximately underneath the edge of the load plate of Thumper. Accordingly, only the results in Stage 5 with T-Rex are presented in this section. With the exception of the additional steps required to determine the vertical displacement-time histories of the centroids, the analysis procedures to determine V_{Pv} and ε are the same as those described in Chapter 4.

The variation of M with log ε in Stage 5 is shown in Figure 8.17a for the midpoint between the centroids of Triangles #1 and #2 (19-in. (48.3-cm) average depth). As in Sections 8.2.3.1 and 8.2.3.2, the M – log ε relationships shown in Figure 8.17a were normalized by M_{max} and are presented in Figure 8.17b in the form of M/M_{max} – log ε relationships. Similar results are shown for the midpoint between the centroids of Triangles #2 and #4 (37-in. (94.0-cm) mid-depth) in Figure 8.18. For locations along the centerline of the sensor array, the nonlinear behavior of M (and M/M_{max}) is generally similar to the nonlinear behavior noted in Sections 8.2.3.1 and 8.2.3.2. As seen in Figures 8.17b and 8.18b, M/M_{max} initially increases with increasing axial strain in Stage 5 and then decreases slightly at axial strains greater than about 0.006%.

8.2.4 Discussion

Except for the few cases mentioned in Section 8.2.3 (Stage 2.3 at sensor pairs 13-12 and 4-3, Stage 5.3 at sensor pair 7-6, and all load steps in Stage 2 at sensor pair 2-1), the general trend observed at Site 2 was that the M/M_{max} – log ε relationship either remained constant or decreased with increasing axial strain when using Thumper in Stage 2 (Figures 8.10b, 8.11b, 8.12b, and 8.14b) and increased with increasing axial strain when using T-Rex in Stage 5 (Figures 8.10b, 8.11b, and 8.12b). It is unlikely that this

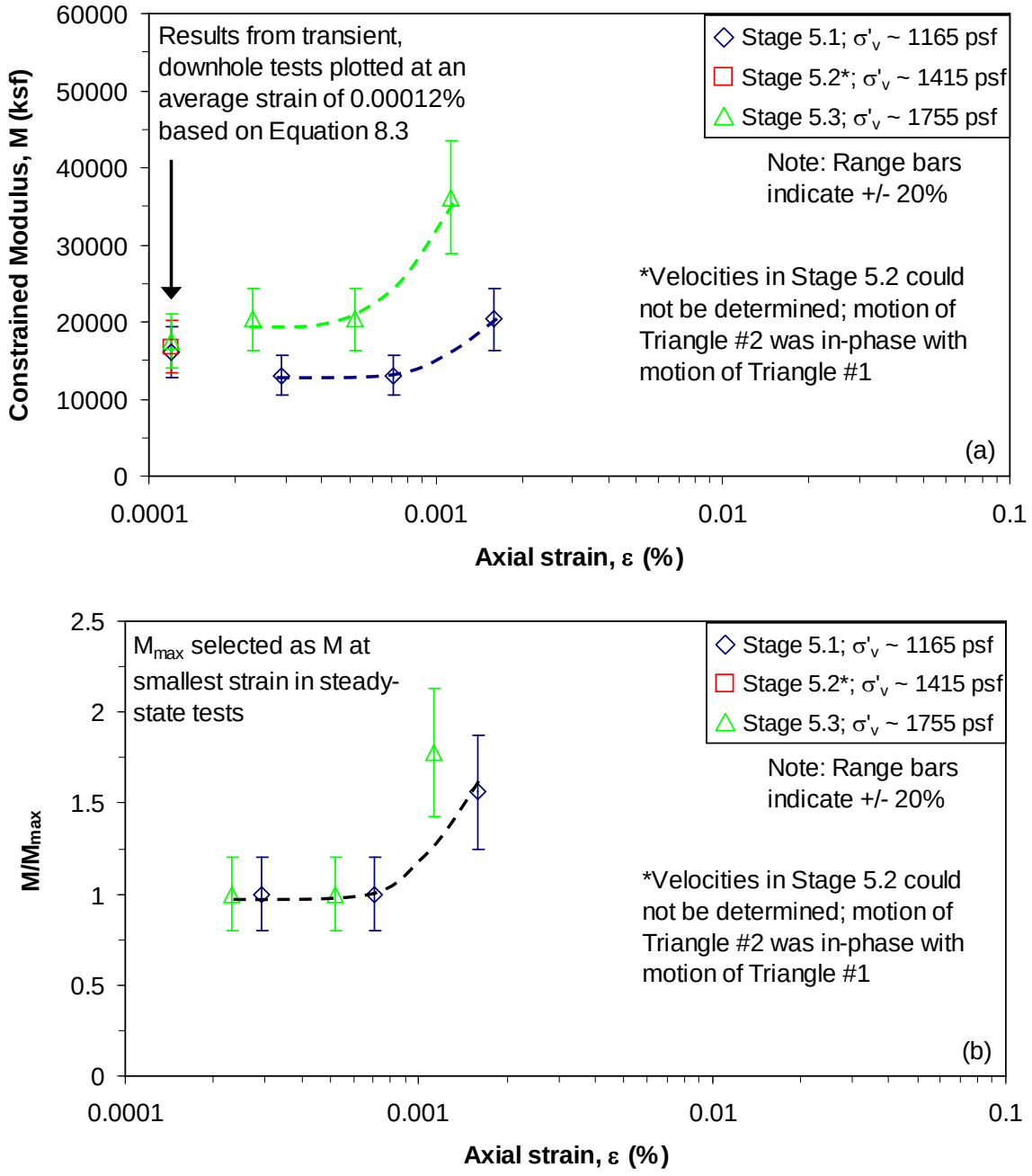

Figure 8.17. Variation of constrained modulus with axial strain at Site 2 at a point along the centerline of the array and between the centroids of Triangles #1 and #2 (19-in. (48.3-cm) mid-depth): (a) M – log ε and (b) M/M_{max} – log ε

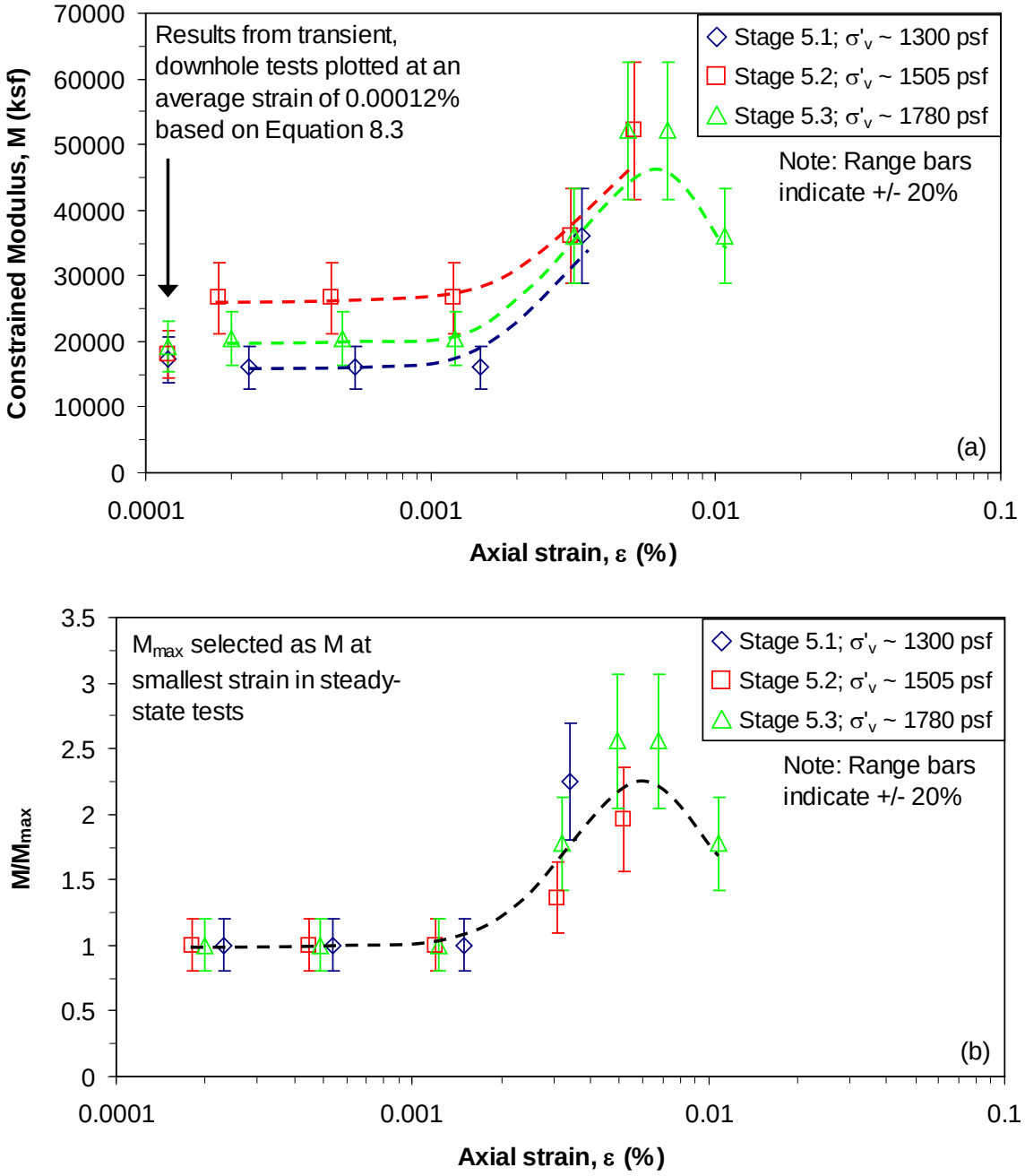

Figure 8.18. Variation of constrained modulus with axial strain at Site 2 at a point along the centerline of the array and between the centroids of Triangles #2 and #4 (37-in. (94.0-cm) mid-depth): (a) M – log ε and (b) M/M_{max} – log ε

difference in the nonlinear behavior of M between Stages 2 and 5 is due to differing environmental conditions at Site 2 since the vertical excitation tests were performed within one week of each other (Stage 2 on August 26, 2011, and Stage 5 on September 1, 2011), and no rainfall occurred during this time (see Figure 6.5).

It should be noted that in Stage 2 with Thumper, the nonlinear behavior of M appears to be somewhat dependent on the magnitude of the induced σ'_v. At levels of vertical effective stress less than about 1450 psf, M increases with increasing axial strain, at least initially (all stages at sensor pair 2-1 (Figure 8.16), Stage 2.1 at sensor pair 12-9 (Figure 8.11), and Stage 2.3 at sensor pair 13-12 (Figure 8.13)). However, when σ'_v is greater than about 1450 psf, M decreases with increasing axial strain (Stages 2.3 and 2.4 at sensor pair 12-9 (Figure 8.11) and Stage 2.4 at sensor pairs 3-2, 13-12, and 4-3 (Figures 8.10, 8.13, 8.14, respectively)). These last two statements are more readily seen in Figure 8.19, where it appears that the nonlinear behavior of M in Stage 2 is dependent on σ'_v (an observation also seen at Site 1 in Figure 5.31).

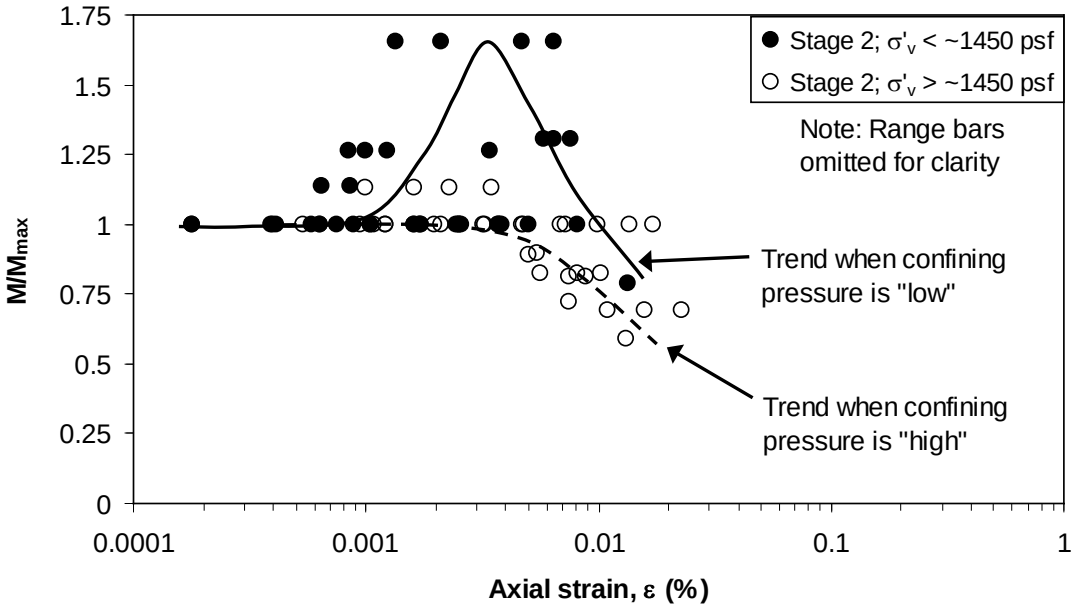

Figure 8.19. Comparison of M/M_{max} – log ε relationships for "low" and "high" confining pressures applied with Thumper in Stage 2

However, it does not appear that the difference in the nonlinear behavior of M between Stages 2 and 5 is due to differing levels of confining pressure (σ'_v). Specifically, there are three instances at Site 2 where both the σ'_v and M_{max} at a given sensor pair are roughly the same (within 10%), yet M/M_{max} – log ε decreases with increasing axial strain when using Thumper and increases with increasing axial strain when using T-Rex. The instances where the only apparent difference in the test conditions is the vibroseis are: (1) Stages 2.4 and 5.2 at sensor pair 3-2, (2) Stages 2.3 and 5.1 at sensor pair 12-9, and (3) Stages 2.2 and 5.1 at sensor pair 6-5. The M – log ε relationships for these three cases are shown in Figures 8.20 through 8.22.

The M – log ε relationships shown in Figures 8.20 through 8.22 illustrate the complexity of the nonlinear behavior of the constrained modulus. All three cases shown in Figures 8.20 through 8.22 were first selected such that the compression wave velocity at the smallest strain induced in the sinusoidal tests closely matched the small-strain V_{Pv} from the downhole tests (discussed in Section 8.2.2). Then, to eliminate as many potential variables as possible, the load steps used in these cases were chosen such that σ'_v and M_{max} at a given sensor pair were roughly the same (within 10%). The result, as seen in Figures 8.20 through 8.22, is that even when the conditions were as close to identical as possible in the field, the observed nonlinear behavior of M is different in Stage 2 (using Thumper) and Stage 5 (using T-Rex). This difference suggests that the measure of whether the compression wave generated by the vibroseis is fully or partially-constrained depends on more than how closely the steady-state, compression wave velocity agrees with the small-strain V_{Pv} from the downhole tests. There are then at least two possible explanations for the differences observed in the behavior of M in the nonlinear range at Site 2:

1. First, consider the possibility that both Thumper and T-Rex successfully generated fully-constrained compression waves (P_V waves) at Site 2. In this event, the observed differences in the M – log e relationships in Stages 2 and 5 are

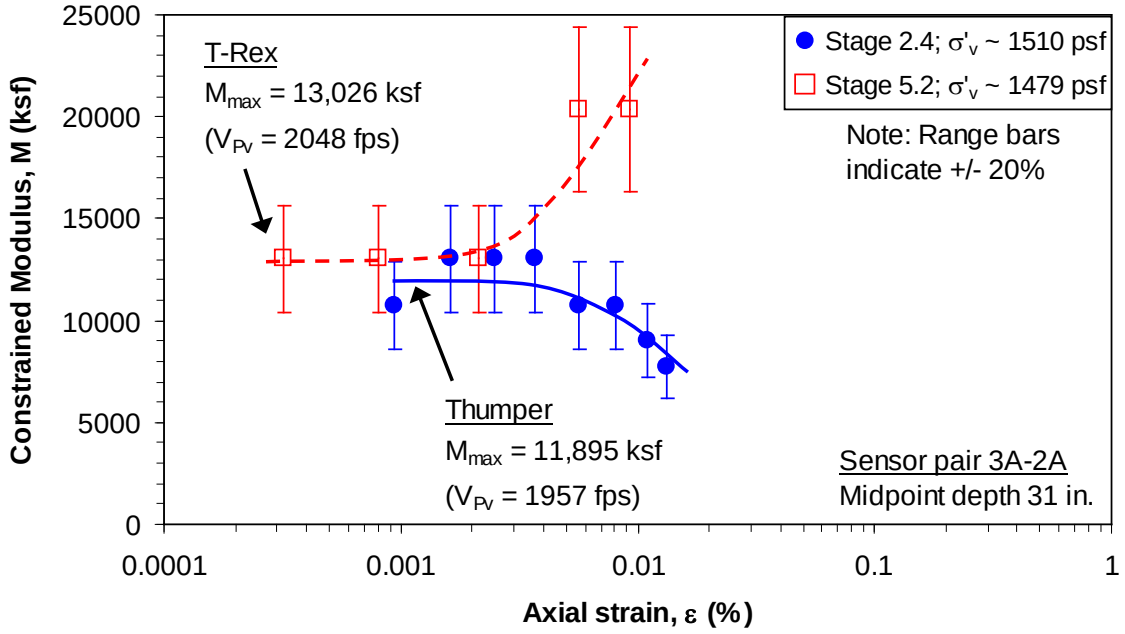

Figure 8.20. Case 1 (sensor pair 3-2) where σ'_v and M_{max} are similar, but the M – log ε relationship decreases when using Thumper and increases when using T-Rex

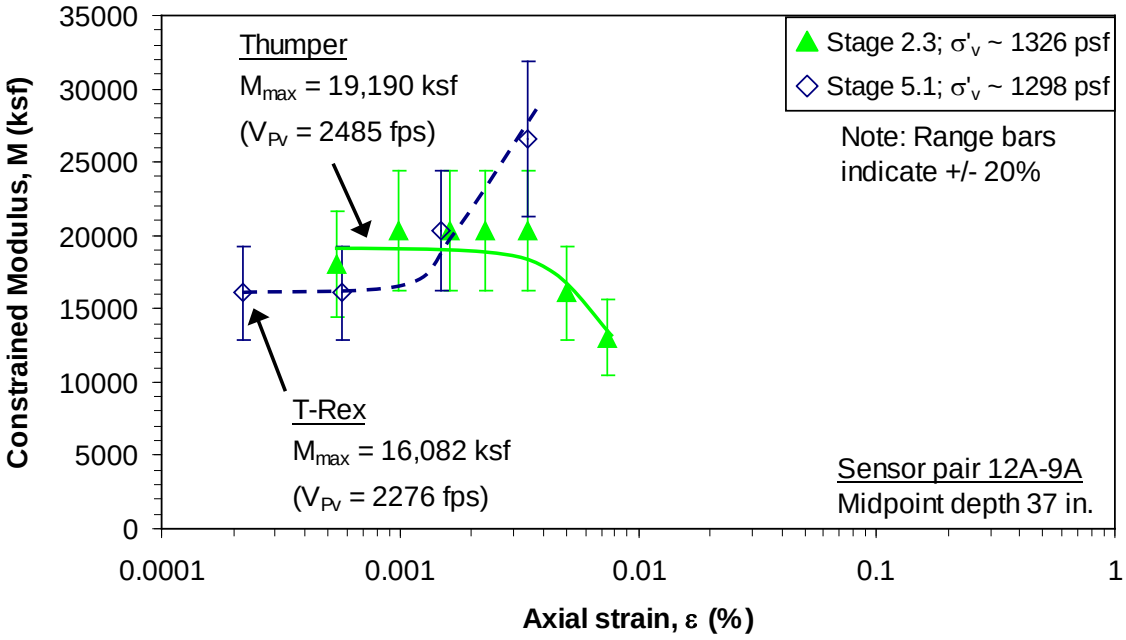

Figure 8.21. Case 2 (sensor pair 12-9) where σ'_v and M_{max} are similar, but the M – log ε relationship decreases when using Thumper and increases when using T-Rex

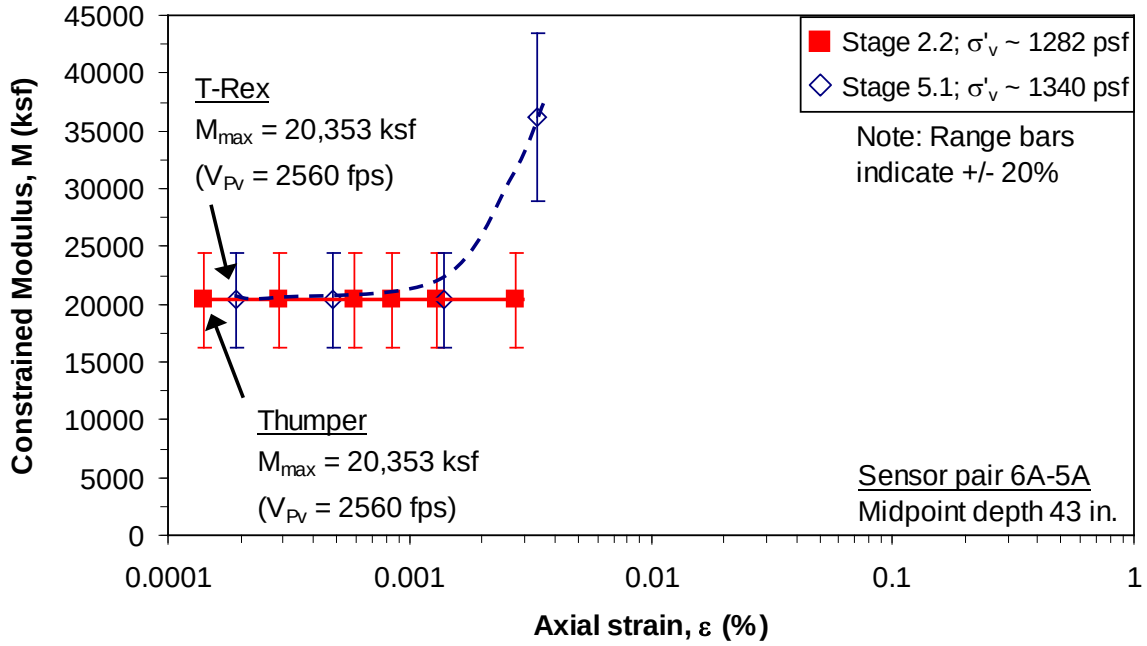

Figure 8.22. Case 3 (sensor pair 6-5) where σ'_v and M_{max} are similar, but the M – log ε relationship decreases when using Thumper and increases when using T-Rex

an actual physical phenomenon induced in the soil, which could have been caused changes to the soil that effectively resulted in a different soil being tested in Stage 5 than was tested in Stage 2. Note that this behavior was not seen at Site 1 (see Figure 5.31 where the M/M_{max} – log ε relationships decrease with increasing axial strain regardless of the vibroseis used). However, neither the horizontal excitations induced in Stage 3 nor the higher static loads of Stage 4 were part of the staged loading sequence at Site 1. Therefore, the tests performed in either of these load stages could have changed the soil at Site 2. The possible changes to the soil caused by the test regimen include: (1) a breakdown of some of the cementation bonds as discussed in Section 7.4.2, (2) a destruction and/or rearrangement of the soil structure, or (3) a redistribution of the negative pore pressures within the embedded sensor array. If the disturbance caused by the dynamic tests at Site 1 was less (for instance, since no horizontal excitations were

applied at Site 1), this would also explain why no difference in the M/M_{max} – log ε behavior was noted between Thumper and T-Rex at Site 1.

2. The second alternative is that the arrangement of the sensor array relative to the size of the load plates caused complications in the analysis of the recorded waveforms. It is well known that in the shear failure of soil underneath a foundation, a "wedge" of soil develops beneath the foundation as shown in Figure 8.23a. Vesic (1973) referred to this wedge as an active Rankine zone, which pushes the adjacent soil sideways and upward. The limits of the active Rankine zone that develops beneath the load plates of Thumper and T-Rex are shown in Figure 8.23a relative to the locations of the 3-D sensors in the array at Site 2. The angle that the lower boundary of this zone makes with the horizontal (α) is assumed to be equal to $45^o + \phi'/2$ (Vesic, 1973). As seen in Figure 8.23a, the embedded sensor array at Site 2 falls entirely within the active Rankine zone developed by the load plate of T-Rex. However, only the sensors at the shallowest depth are in this zone when Thumper is used. It is then possible that T-Rex is the only vibroseis that generated P_V waves because the larger load plate applies vertical (and, in turn, horizontal) confinement over a much larger horizontal area than the smaller load plate of Thumper. As such, in the central region below the load plate (the active Rankine zone), the particles are much less likely to expand laterally away from each other during shaking. As a result, the P_V wave propagates faster through the soil, and the true nonlinear behavior of M is an M – log ε relationship that initially increases with increasing axial strain, as seen at sensor pairs 3-2, 12-9, 6-5, and 7-6 in Stage 5 (see Figures 8.10, 8.11, 8.12, and 8.15, respectively). However, after the initial increase of the M – log ε relationship, it does appear that M decreases as the axial strain continues to increase, as seen at sensor pairs 12-9 and 7-6 (Figures 8.11 and 8.15, respectively). Therefore, the horizontal confinement provided by Thumper is not sufficient to fully constrain the compression waves at most depths within the

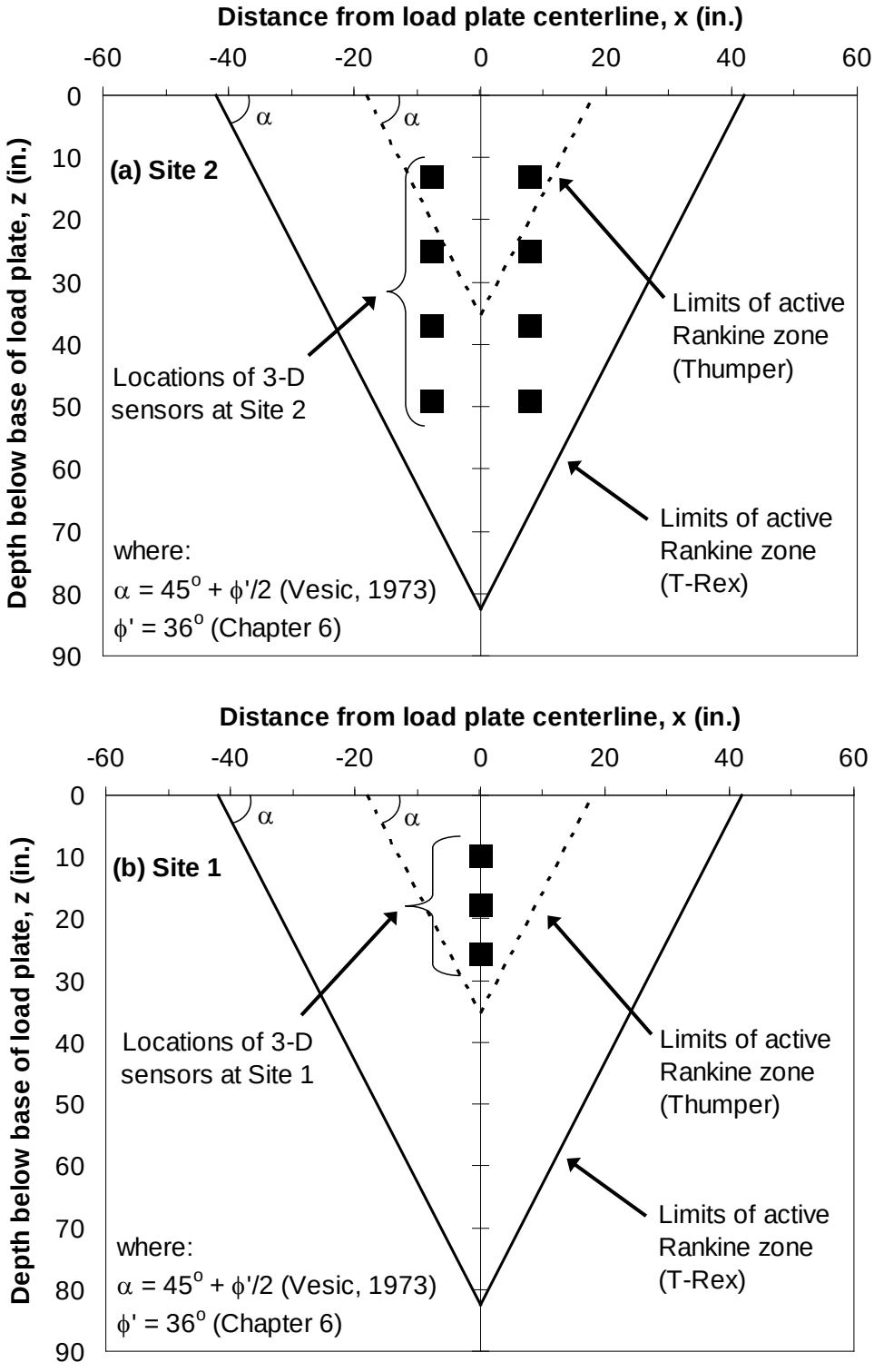

Figure 8.23. Development of active Rankine zones beneath the load plates of Thumper and T-Rex relative to the location of the sensor arrays: (1) Site 2 and (2) Site 1

embedded sensor array at Site 2. It should be noted that at Site 1, all three sensors in the center sensor column were within the active Rankine zone developed by both Thumper and T-Rex (Figure 8.23b). This spatial arrangement could explain why the behavior of the M/M_{max} – log ε relationships at Site 1 was similar (decreasing with increasing axial strain) regardless of the vibroseis used.

At this time, it is believed that both alternatives listed above likely contributed in some manner to the differences observed in Stages 2 and 5. As discussed in Section 7.4.2, the soil at Site 2 was cemented at the beginning of the test regimen and probably remained at least partially cemented for the duration of the test regimen. However, as shown in Figures 7.4, 7.20, and 7.21, both the small-strain V_{Pv} and V_{Svh} in the Stage 4 downhole tests were lower than those in the Stage 1 downhole tests. As discussed in Section 7.2.3, this sharp reduction in the downhole wave velocities between Stages 1 and 4 was likely caused by the intervening vertical and horizontal dynamic excitations applied with Thumper in Stages 2 and 3. If this is the case, then the soil structure (to include the amount of cementation) was no doubt different for the Stage 5 dynamic tests with T-Rex than it was for the Stage 2 dynamic tests with Thumper. This disturbance caused by the dynamic tests of Stages 2 and 3, coupled with the locations of the sensors in the active Rankine zone beneath the shakers, is likely why the soil behaved differently in Stages 2 and 5.

Therefore, due to the highly complex behavior of the constrained modulus in the nonlinear strain range, generalized M/M_{max} – log ε relationships were developed to show the possible range in M/M_{max} values observed at Site 2. These generalized relationships are shown in Figure 8.24. At the present time, the differences in the M/M_{max} – log ε relationships shown in Figure 8.24 are assumed to be due to changes in the soil characteristics, i.e. cementation, structure, pore pressure distribution, relative density, etc., and the locations of the sensors within the central zone beneath the shaker's load plate. Note that though the behaviors of the relationships shown in Figure 8.24 are

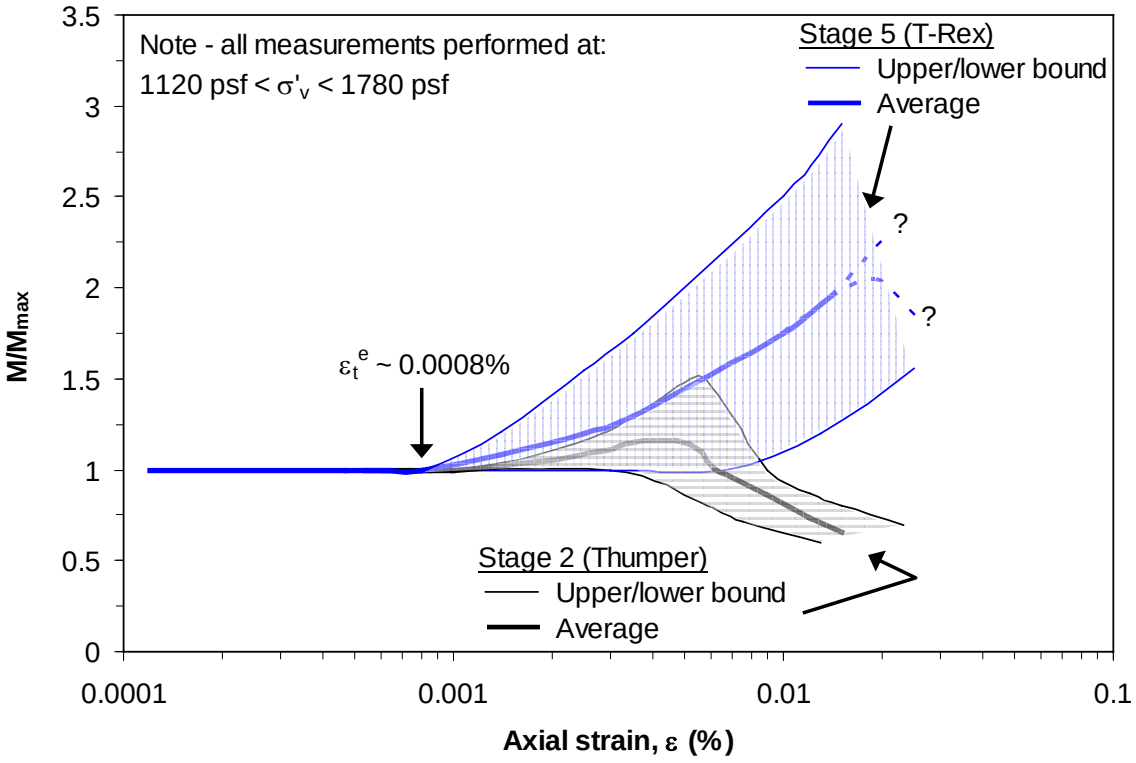

Figure 8.24. Generalized M/M_{max} – log ε relationships for Site 2

different at larger strains, the elastic threshold axial strain (ε_t^e) is about 0.0008% in both Stages 2 and 5. Clearly more work is required in this area.

8.3 EVALUATION OF NONLINEAR SHEAR MODULI AT SITE 2

The results of the horizontal sinusoidal excitation tests performed in Stages 3 and 6 are presented in this section. Raw voltage-time histories recorded in these stages are provided in Appendix D. Four load steps were used in Stage 3, and three load steps were used in Stage 6 (see Figure 8.1). In each load step, shear strains were induced within the embedded sensor array over a relatively large range in strains and allowed investigation of the nonlinear behavior of the shear moduli in the field. In this section, the generation of shear waves in the two stages is discussed first. Determination of shear strain (γ) and the S_{VH}-wave velocity (and its relation to G) is then presented. Then, the effects of

increasing shear strain on the shear moduli are presented in the form of G – log γ and G/G_{max} – log γ relationships at several levels of σ'_v (where G_{max} is the small-strain G). A discussion of the results of the horizontal excitation tests is also provided.

8.3.1 Generation of S_{VH} waves under horizontal excitations

Since the load plates of Thumper (Stage 3) and T-Rex (Stage 6) were positioned directly on the ground surface (and not on a cast-in-place concrete footing as in Park's (2010) study), slight variations in the surface preparation could impact the generation of body waves during horizontal excitation. To verify that primarily horizontal motions were induced by Thumper and T-Rex, the voltage-time records of all three components (one vertical; two horizontal) in the sensors were examined at all locations within the embedded sensor array. However, in this section, the primary focus is on the sensors in the Southwest and Southeast sensor columns. The rationale behind the focus on these specific sensor columns is discussed in Section 8.3.2 (note that the voltage-time histories recorded in the North sensor column are provided in Appendix D).

The voltage-time records under the lowest and highest levels of horizontal excitation applied in Stage 3.4 (with Thumper) are shown in Figure 8.25 for all four sensors in the Southwest sensor column (Sensors 13, 12, 11, and 9) and in Figure 8.26 for all four sensors in the Southeast sensor column (Sensors 8, 7, 6, and 5). As seen in Figure 8.25, the greatest response was recorded by the East-West components of all sensors in the Southwest column at both low and high levels of horizontal shaking with Thumper. At low levels of shaking with Thumper (Figure 8.25a), the horizontal motion is about 3.4 times larger than the vertical motion. However, at high levels of shaking with Thumper (Figure 8.25b), the amount of response recorded by the vertical components is relatively large, and the horizontal motion is only about 2.1 times larger than the vertical motion (the exception being Sensor 11, where the vertical and north components are abnormally low and presumed lost). In the Southeast column (Figure

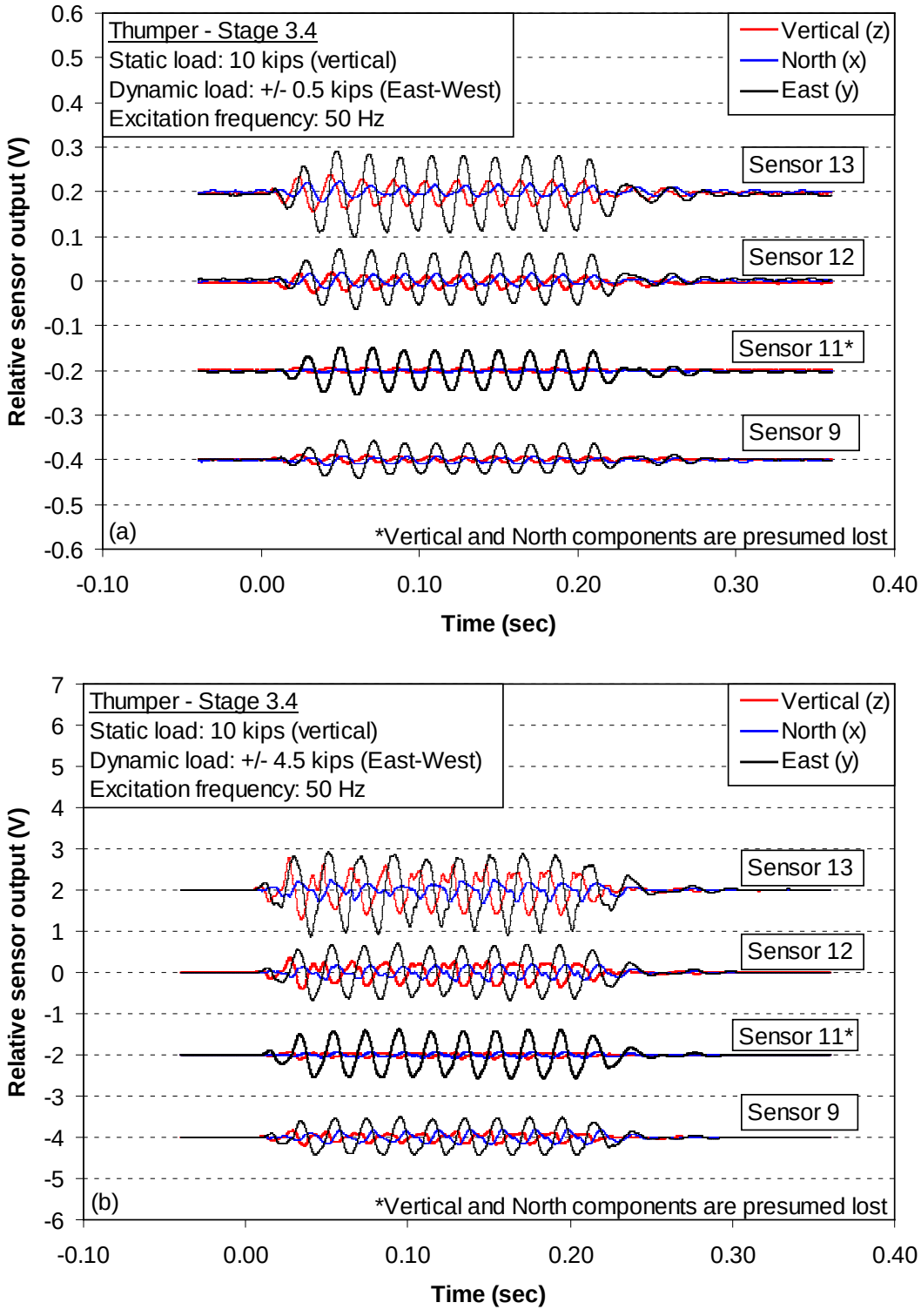

Figure 8.25. Voltage-time histories recorded by four vertically-aligned sensors in the Southwest column during Stage 3.4: (a) low-load amplitude and (b) high-load amplitude

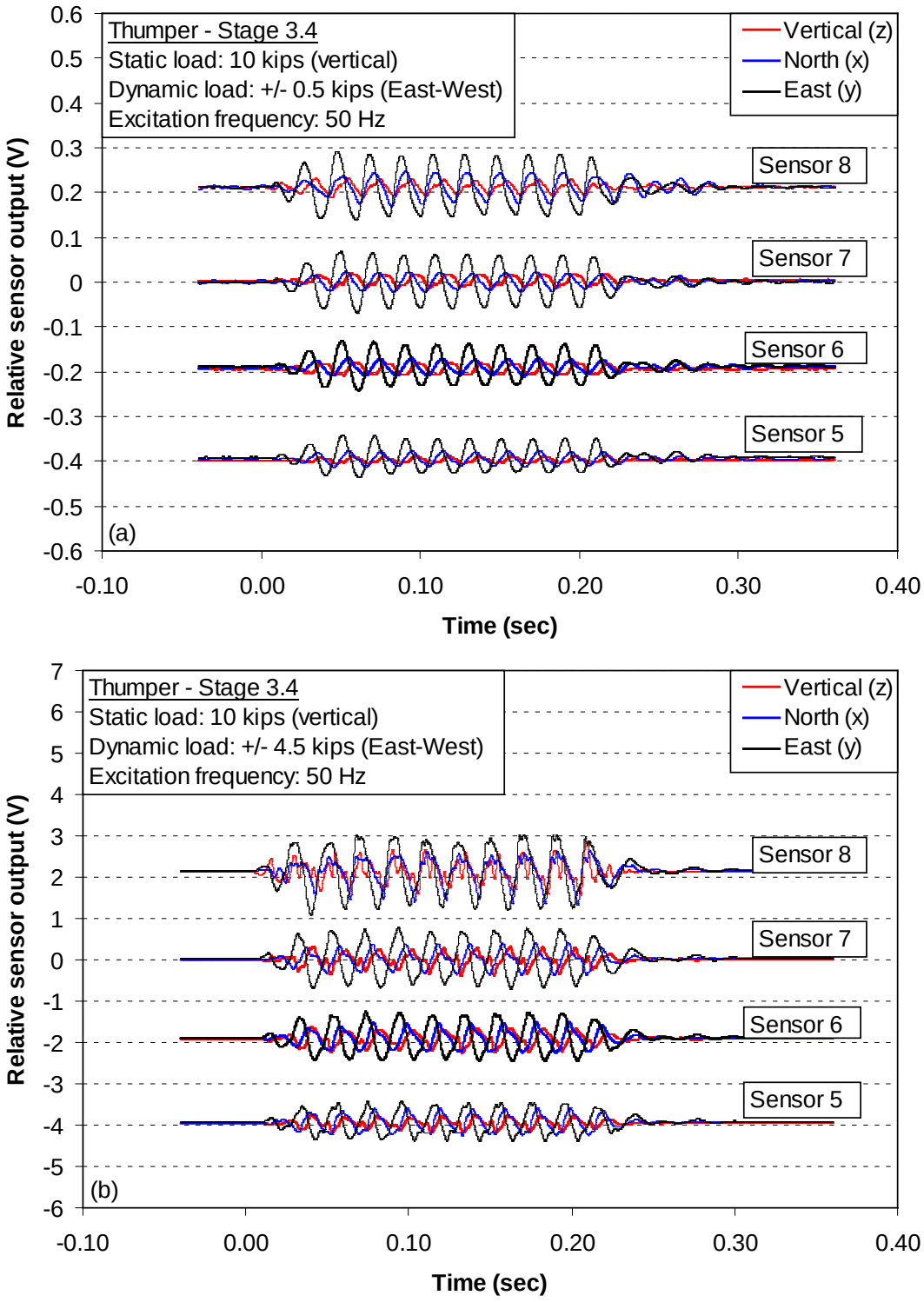

Figure 8.26. Voltage-time histories recorded by four vertically-aligned sensors in the Southeast column during Stage 3.4: (a) low-load amplitude and (b) high-load amplitude

8.26), the results are similar in the vertical direction, but there is a significant amount of motion in the North-South direction. Therefore, while the most response generated by the East-West excitations by Thumper was in the East-West direction, the large amount of vertical and off-axis motion in Stage 3 suggests that the load plate of Thumper is susceptible to rocking at large strains, i.e. in the nonlinear range, and is not ideal for the generation of predominantly horizontal motion.

The voltage-time records under the lowest and highest levels of horizontal excitation applied in Stage 6.3 (with T-Rex) are shown in Figure 8.27 for all four sensors in the Southwest sensor column (Sensors 13, 12, 11, and 9) and in Figure 8.28 for all four sensors in the Southeast sensor column (Sensors 8, 7, 6, and 5). As seen in Figure 8.27, the greatest response was recorded by the East-West components of all sensors in the Southwest column at both low and high levels of horizontal shaking with T-Rex. At low levels of shaking with T-Rex (Figure 8.27a), the horizontal motion is about 5.3 times larger than the vertical motion. Even at high levels of shaking with T-Rex (Figure 8.27b), the response is still predominantly in the horizontal direction as the horizontal motion is about 3.8 times larger than the vertical motion. Compared to Thumper (Figure 8.25), T-Rex generated much less relative vertical motion in the Southwest column. However, in the Southeast sensor column, the amount of response recorded by the vertical components is relatively large (Figure 8.28). At low levels of shaking with T-Rex (Figure 8.28a), the horizontal motion is about 2.7 times larger than the vertical motion, and at high levels of shaking with T-Rex (Figure 8.28b), the horizontal motion is only about 2.0 times larger than the vertical motion. Therefore, in the Southeast sensor column, the amount of vertical motion generated relative to horizontal motion is about the same with T-Rex in Stage 6 (Figure 8.28) as with Thumper in Stage 3 (Figure 8.26). It should be noted that the amount of off-axis motion (North-South direction) generated by T-Rex is lower than that by Thumper.

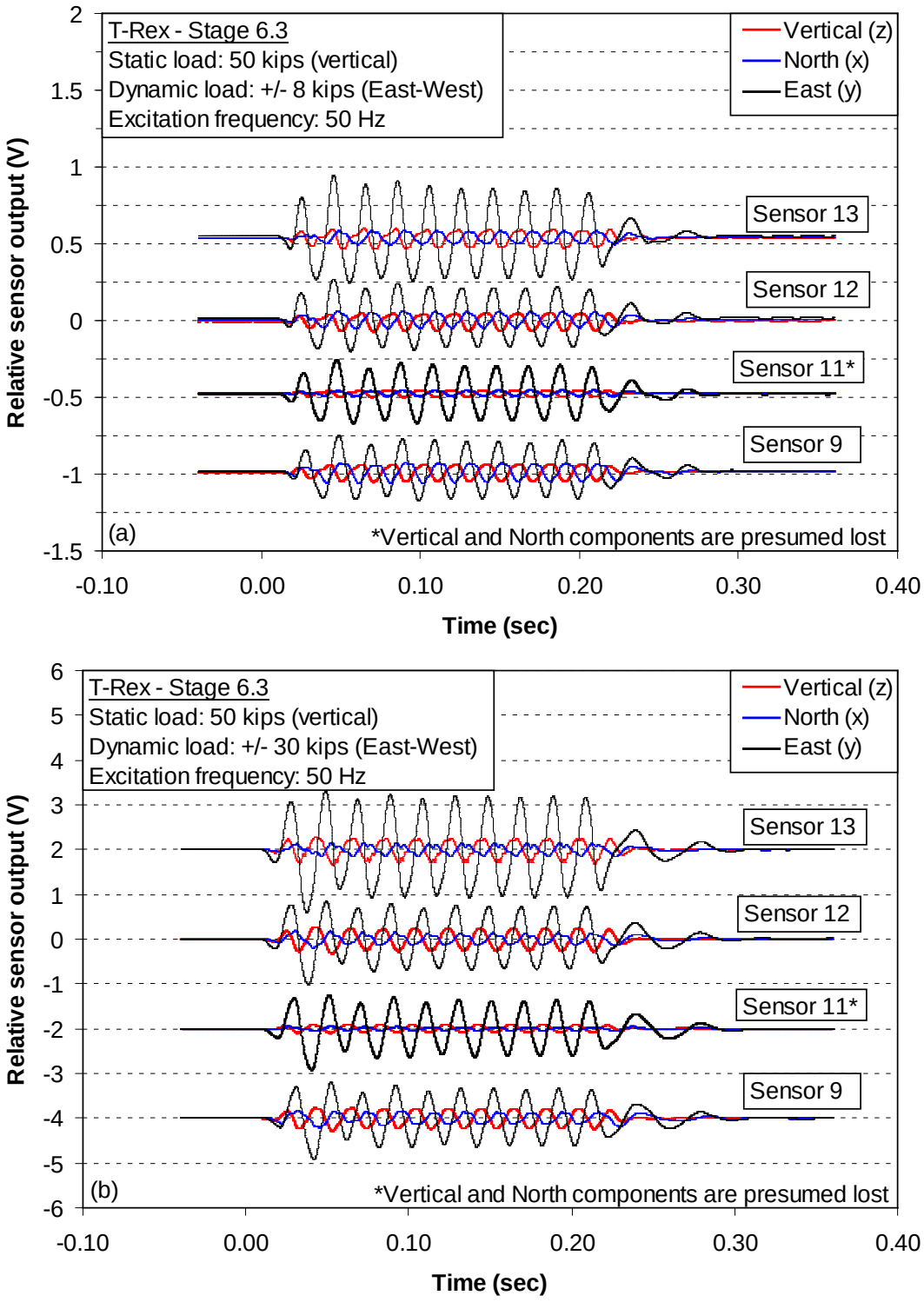

Figure 8.27. Voltage-time histories recorded by four vertically-aligned sensors in the Southwest column during Stage 6.3: (a) low-load amplitude and (b) high-load amplitude

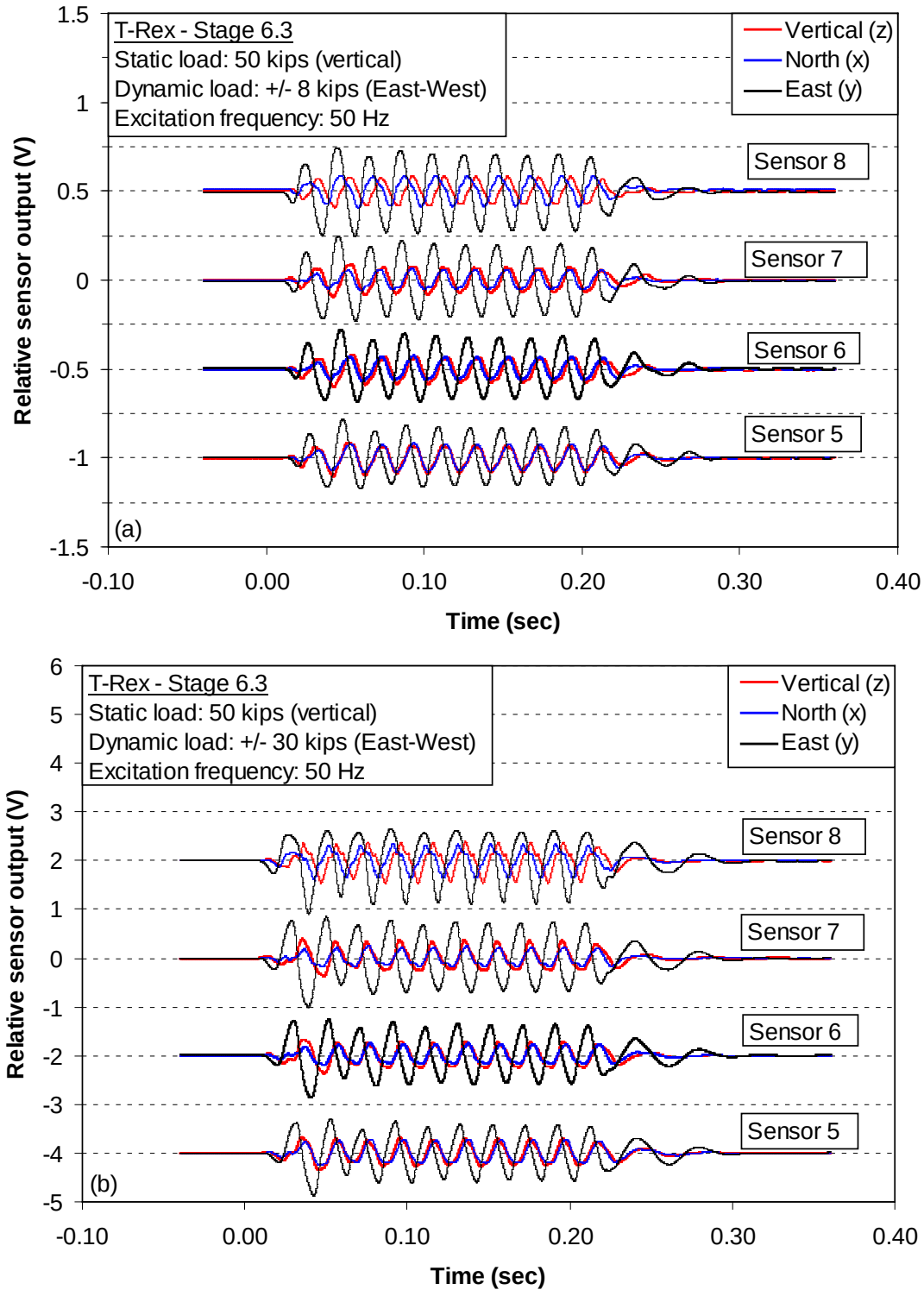

Figure 8.28. Voltage-time histories recorded by four vertically-aligned sensors in the Southeast column during Stage 6.3: (a) low-load amplitude and (b) high-load amplitude

When the results at both sensor columns are taken as a whole, the horizontal sinusoidal excitations applied by T-Rex generally resulted in less vertical motion than when Thumper applied the horizontal excitations. It then appears that the larger load plate of T-Rex is less susceptible to rocking and can be used at larger strain levels, i.e. in the nonlinear range. Therefore, since T-Rex generated the largest amount of relative horizontal motion over the widest range in strains in this study, only the results from Stage 6 (with T-Rex) are presented in Section 8.3.4. It should be noted that while T-Rex was the best S_{VH}-wave source in this study, the motions induced by T-Rex are still not purely horizontal; hence, coupled rocking and sliding motion is generated. Since the load plate of T-Rex generates some rocking motion (especially at larger confining pressures), there is a significant amount of vertical motion present in the records. This fact is addressed further in the determination of shear strain as discussed in Section 8.3.2.

8.3.2 Determination of field shear strain

As discussed in Sections 4.4.2 and 8.2, a 2-node displacement-based (DB) method was used to evaluate the axial strains induced between two sensors by vertical sinusoidal excitations from Thumper and T-Rex. However, as discussed in Section 8.3.1, a significant amount of vertical motion was generated by the horizontal sinusoidal excitations applied by both Thumper and T-Rex. In this case, the 2-node DB method cannot address the amount of shear strain (γ) induced by this vertical component of motion (see Figure 4.16b), and instead, a 4-node DB method is preferred (Rathje et al., 2004). In the 4-node DB method, the displacement-time histories (in two co-planar directions) measured at the four nodes of a quadrilateral are used to estimate the shear strain-time histories at any location within the quadrilateral. As shown in Figure 8.29, the sensors in the Southwest and Southeast sensor columns at Site 2 are arranged such that three quadrilaterals can be formed in which the nodes (sensors) measure displacements in the y- (East-West) and z-directions. It should be noted that, as discussed in Section 8.3.1, the vertical (z) component of Sensor 11 was generally non-

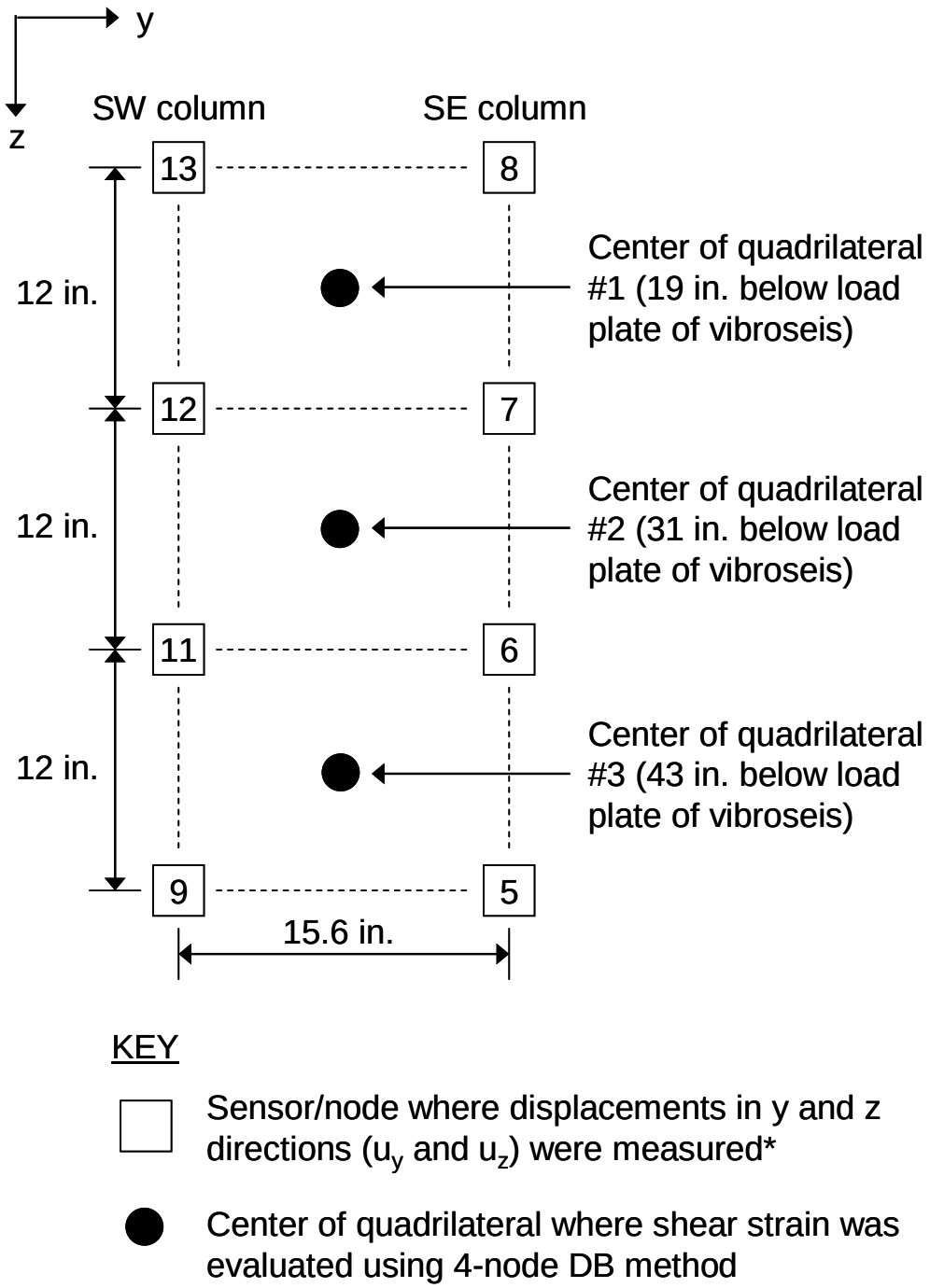

Figure 8.29. Evaluation of shear strain-time histories at the centers of three quadrilaterals at Site 2 using the 4-node displacement-based method

responsive and was presumed to be lost. Therefore, the vertical motion at Sensor 11 was approximated by averaging the voltage-time records from the vertical components of the sensors immediately above and below it (Sensors 12 and 9, respectively).

Using the 4-node DB method, shear strain-time histories were evaluated at the centers of these three quadrilaterals for every level of horizontal load amplitude applied by the vibroseis. After evaluation of the shear strain-time histories, the remainder of the analysis process is unchanged from the 2-node DB method. As described in Section 4.4.2, the maximum shear strain (in either the positive or negative directions) that occurred in the steady-state portion of the strain-time history (cycles 4 through 9) was selected to represent the induced shear strain at the center of each quadrilateral.

8.3.3 Determination of field shear moduli

In each of the load steps shown in Figure 8.1, the load amplitude of the horizontal sinusoidal excitation applied with the shakers was progressively increased, which increased the amount of shear strain induced in the embedded sensor array. At each strain level, the velocity of the vertically-propagating, horizontally-polarized shear wave (S_{VH} wave) traveling downward through the sensor array was calculated between the horizontal components of adjacent sensors. The horizontal components were selected such that they were oriented in the same direction as the horizontal motion imparted by the shakers. In both Stages 3 and 6, the motion of the shaker's load plate was predominantly East-West, so the horizontal components oriented in the East-West direction were used to calculate the S_{VH}-wave velocity (V_{Svh}).

Only one method was used at Site 2 to determine V_{Svh} between adjacent sensor pairs. This method was identified in Section 8.2.1 as "Method 1." In Method 1, a sinusoidal model was fit to the steady-state portion of the voltage-time records of adjacent sensors, followed by calculation of the time difference between the peaks of the

same cycle at both sensors. This method was developed and employed by Park (2010) in his study on cemented alluvium. It was selected for use in this study because the potential deficiencies involved with using this method with P_V waves (discussed in Section 8.2.1) were not observed when S_{VH} waves were generated by the shakers. Specifically, when a horizontal sinusoidal excitation was applied by either Thumper or T-Rex, the voltage-time histories recorded by the horizontal sensor components were symmetric (showing roughly the same amount of positive (West) amplitude as negative (East) amplitude) at all strain levels. Additionally, the peaks of the best-fit sinusoidal model were generally in-phase with the peaks of the voltage-time histories. Since shear strains were evaluated at the centers of the 4-node quadrilaterals shown in Figure 8.29, the V_{Svh} values at these points were estimated by averaging the velocities obtained between the two vertically-aligned sensor pairs on the edges of the quadrilateral. For example, V_{Svh} at the center of quadrilateral 3 was estimated by averaging the V_{Svh} determined between Sensors 11 and 9 with the V_{Svh} determined between Sensors 6 and 5.

After V_{Svh} was calculated at the center of each quadrilateral as described above, the shear modulus (G) was determined using the relation:

$$G = \frac{\gamma_t}{g} V_{Svh}^{\ 2} \tag{8.4}$$

where γ_t is the total unit weight of the soil and g is acceleration due to gravity (Richart et al. 1970). In this manner, G was determined for each level of horizontal sinusoidal excitation applied by Thumper and T-Rex. For a given level of sinusoidal excitation, G was combined with the induced shear strain to obtain one point on the G – log γ relationship. The process was repeated for all levels of excitation to construct the entire G – log γ relationship (discussed in Section 8.3.3). G – log γ relationships were then obtained at several levels of confining pressure (σ'_v) by increasing the amount of vertical load applied by the vibroseis (note the load steps shown in Figure 8.1).

8.3.4 Effect of increasing shear strain on shear moduli

As discussed in Section 8.3.1, the load plate of T-Rex was less susceptible to rocking than the load plate of Thumper. Accordingly, T-Rex was capable of generating large horizontal motions (relative to the vertical motion) over a wider range in shear strains. Therefore, T-Rex is better suited for the examination of the effects of increasing shear strain on the shear moduli, and only the results from Stage 6 using T-Rex are presented in this section. Following the process described in Chapter 4 and Section 8.3.1, V_{Svh} and γ were calculated at every level of steady-state excitation applied in Stage 6.

The shear wave velocities could not be determined at the shallowest depth in all three sensor columns (sensor pairs 13-12, 8-7, and 4-3) since the horizontal response of the shallower sensor was either in-phase with or lagged the response of the deeper sensor. The resulting shear wave velocities at these locations were then either infinite or negative. The results were the same regardless of the excitation frequency or the vibroseis used. A similar effect was noticed with respect to P_V-wave velocities at the shallowest depths in the sensor arrays at both Site 1 (Chapter 5) and Site 2 (Section 8.2). It is believed that due to the relatively large load plate of T-Rex, the first two sensors in the embedded sensor array at Site 2 are either too close to the shaker, too close to each other, or both. It is also possible that partial or complete destruction of the cementation in this upper layer could be contributing to this effect.

Therefore, the effects of increasing shear strain on the shear moduli are discussed in this section only at the locations of the centers of quadrilaterals #2 and #3 (shown in Figure 8.29). In the figures presented in this section, the shear moduli (calculated using Equation 8.4) from the transient, downhole tests (see Chapter 7) are included to aid in the comparison with the shear moduli determined using steady-state excitations. The shear strains associated with the transient downhole tests were calculated using the simplifying assumption of a plane stress wave travelling vertically through the system by:

$$\gamma = \frac{\dot{x}}{V_{Svh}} \tag{8.5}$$

where $\dot{x}$ represents the maximum particle velocity in the horizontal direction (Richart et al., 1970). The shear strains in these tests ranged from about 0.00005 to 0.00038%. The average shear strain was about 0.00018% and was used to represent γ for all transient downhole tests. Though these strains generated in the downhole tests are indeed small, the shear modulus at small-strains (G_{max}) was assumed to occur at the lowest strain induced in the steady-state excitation tests. This convention was chosen to avoid potential errors that may arise by using two different test methods.

As shown in Figure 8.1, horizontal excitation tests were performed with T-Rex in Stage 6 at three different levels of confining pressures (Stages 6.1, 6.2, and 6.3). The variations of G with log γ in Stages 6.1, 6.2, and 6.3 are shown in Figure 8.30a for the center of quadrilateral 2 (31-in. (78.7-cm) average depth). The G – log γ relationships shown in Figure 8.30a were normalized by G_{max} and are presented in Figure 8.30b in the form of G/G_{max} – log γ relationships. At an average depth of 31 in. (78.7 cm), the velocities calculated in Stage 6.1 (at the lowest level of confining pressure) in the embedded sensor array were largely nonsensical. In general, these velocities were high (in some cases, as high as about 1700 fps (518 m/s)). This effect was not observed in Stages 6.2 and 6.3. Since the load plate of T-Rex was placed directly on the ground surface (with an intermediate layer of sand about 1-in. (2.5-cm) thick that was used as a leveling course), it is possible that the low hold-down force in Stage 6.1 was not sufficient to ensure good contact between the load plate and the soil. Despite the difficulties with Stage 6.1, there is excellent agreement between the results of Stages 6.2 and 6.3. However, the steady-state G values determined in Stages 6.2 and 6.3 are about half of the G values determined in the transient, downhole tests (Figure 8.30a). The reason(s) for this discrepancy between the steady-state and transient G values is not clear, but could include effects due to the destruction of cementation by the testing regimen.

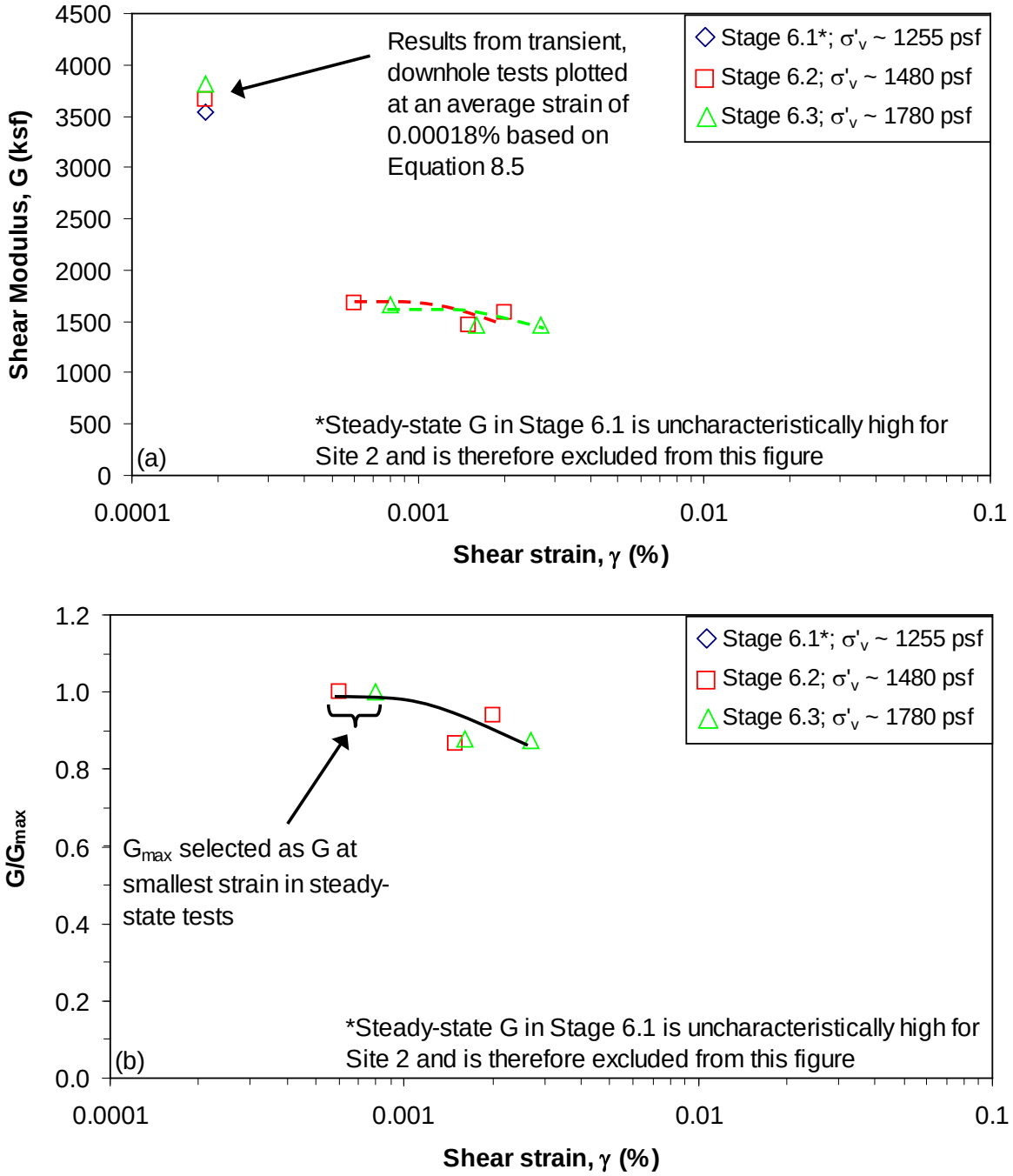

Figure 8.30. Variation of shear modulus with shear strain in Stage 6 at an average depth of 31 in. (78.7-cm) at Site 2: (a) G – log γ and (b) G/G_{max} – log γ

Similar results are shown for the center of quadrilateral 3 (43-in. (109.2-cm) average depth) in Figure 8.31. The variation of G with log γ in Stages 6.1, 6.2, and 6.3 is shown in Figure 8.31a, and the G/G_{max} – log γ relationships are shown in Figure 8.31b. At this depth, G decreases with increasing confining pressure (σ'_v). As a result, the steady-state G values determined in Stage 6.1 agree relatively well with the small-strain G values determined in the transient, downhole tests (Figure 8.31a). The reduction in G at larger values of σ'_v could be due to several factors, including: (1) "scatter" in the measurements, (2) breakdown of cementation bonds as the shear strains were increased during Stage 6, or (3) settlement or "bedding-in" of the load plate at higher values of σ'_v. Despite the differences in the shear moduli determined in Stages 6.1, 6.2, and 6.3, when the G values are normalized by G_{max}, the agreement between all three load steps is excellent, and the G/G_{max} – log γ relationships in all three stages fall approximately on a single line as shown in Figure 8.31b. The shear strain at which G/G_{max} becomes nonlinear, i.e. the threshold strain, is about 0.001% at all levels of σ'_v.

8.3.5 Discussion

In the steady-state horizontal excitation tests conducted at Site 2, neither Thumper nor T-Rex was capable of generating purely horizontal motion due to the rocking or rotation of the shakers' load plates. This coupled rocking and sliding motion occurred because the line of action of the forcing function was above the line of reaction at the bottom of the loading plates. In general, the amount of vertical motion (relative to the horizontal motion) was much higher when Thumper was used, and it is believed that this amount of vertical motion prevented an accurate determination of G – log γ relationships using Thumper. The amount of relative vertical motion generated by T-Rex was much less and allowed for determination of shear moduli over a wide range in shear strains. However, the vertical motion generated by T-Rex contributes to the overall shear strain induced within the sensor array, which cannot be addressed by a 2-node DB method. Therefore, a 4-node DB method was used to evaluate the shear strains induced at two

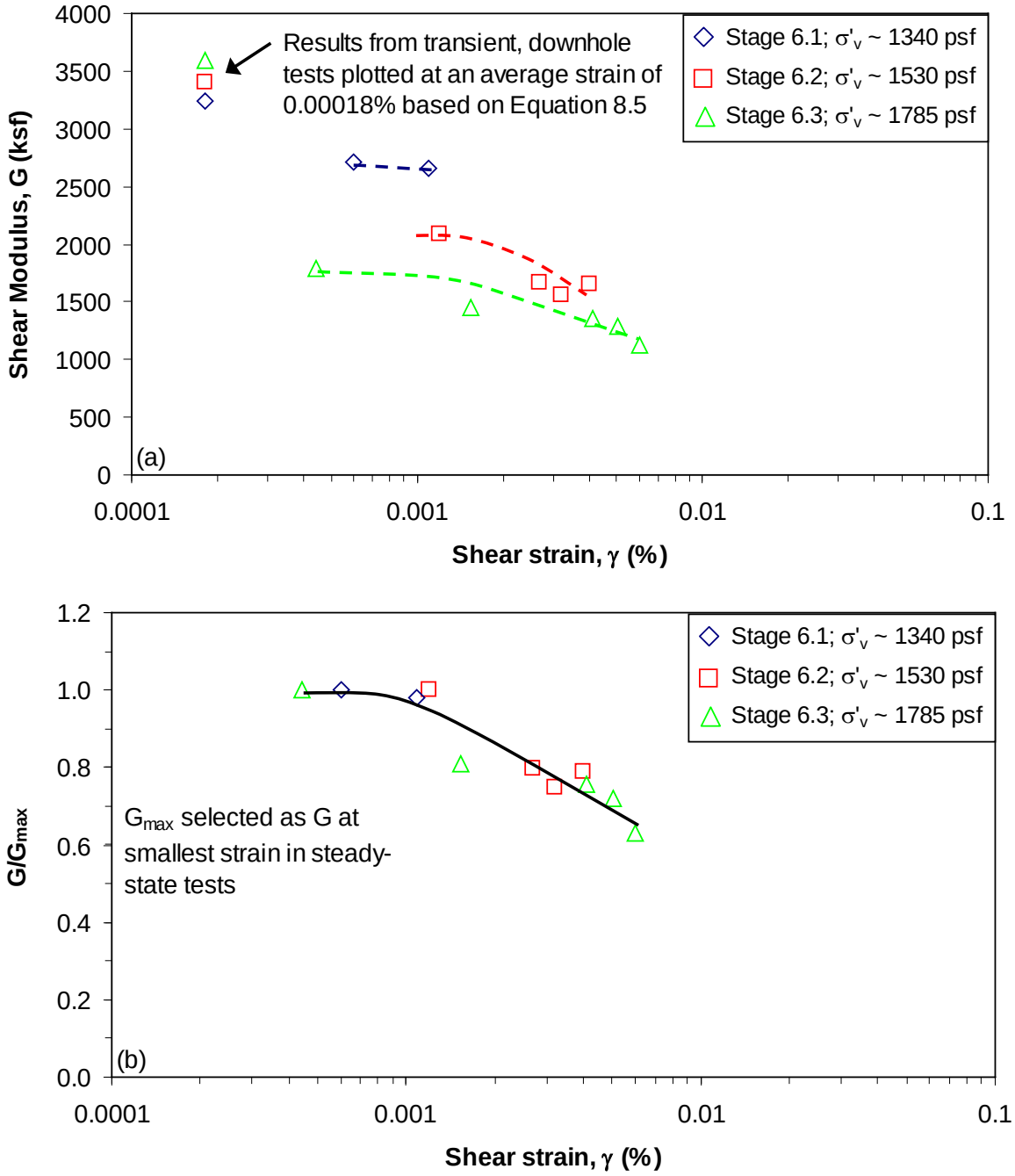

Figure 8.31. Variation of shear modulus with shear strain in Stage 6 at an average depth of 43 in. (109.2-cm) at Site 2: (a) G – log γ and (b) G/G_{max} – log γ

points within the embedded sensor array. Coupled with the shear moduli determined at these points, G – log γ relationships were successfully determined at Site 2 as shown in Figures 8.30 and 8.31.

In general, the steady-state G values determined in Stage 6 with T-Rex were lower than the small-strain G values determined in the transient, downhole seismic tests (Figures 8.30a and 8.31a). At an average depth of 43 in. (109.2 cm) below the load plate of T-Rex, the steady-state and transient G values agree reasonably well at small levels of σ'_v, but diverge as σ'_v is increased (Figure 8.31a). The reasons behind these observations (the poor agreement of the steady-state and transient G values and the decrease in G with increasing σ'_v) are not clear at this time. Possible explanations include: (1) "scatter" in the measurements, (2) breakdown of cementation bonds as the shear strains were increased during Stage 6, (3) settlement or "bedding-in" of the load plate at higher values of σ'_v, or (4) poor contact between the load plate of T-Rex and the native soil.

These differences in shear moduli notwithstanding, when G is normalized by G_{max}, the agreement between the resulting G/G_{max} – log γ relationships at both locations is quite good. As seen in Figure 8.32, the relationships at both locations can be represented by a single curve with little or no loss of accuracy, and show a clear trend of decreasing G/G_{max} with increasing shear strain (the threshold strain is about 0.001%). Therefore, the shear modulus reduction curve shown in Figure 8.32 is assumed to represent the behavior of the shear modulus at Site 2 with increasing shear strain.

8.4 COMPARISON OF NONLINEAR CONSTRAINED AND SHEAR MODULI

Differences in the behavior of the nonlinear constrained and shear moduli observed at Site 2 (discussed in Sections 8.2 and 8.3, respectively) are discussed in this section. First, the M/M_{max} – log ε and G/G_{max} – log γ relationships determined at Site 2 are compared to results reported by previous researchers. Then, the behavior of the

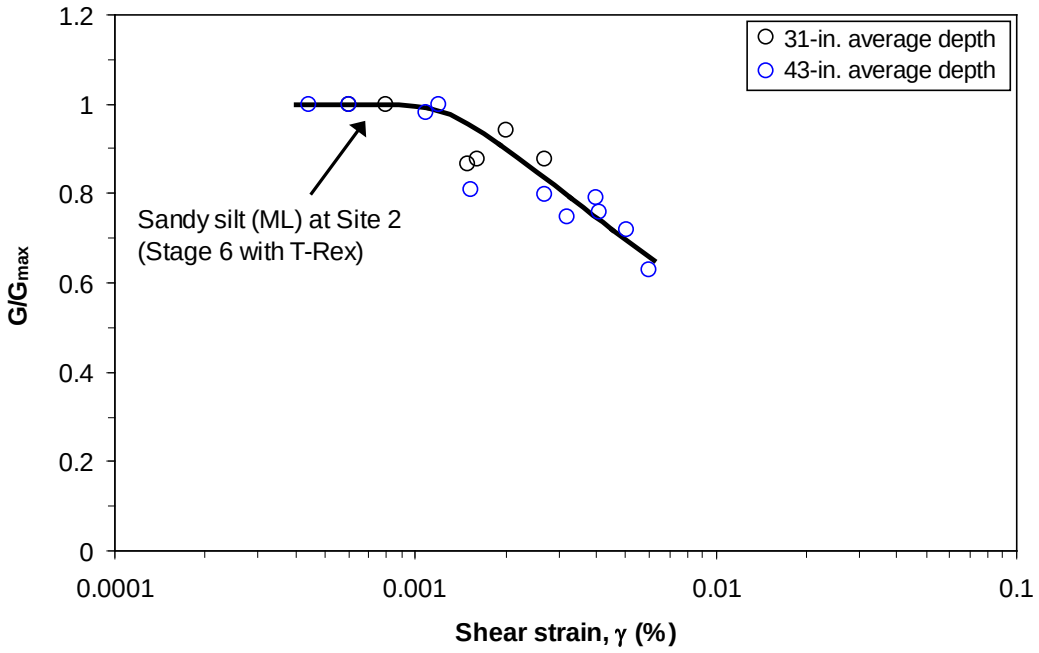

Figure 8.32. Generalized G/G_{max} – log γ relationship for Site 2

nonlinear constrained modulus at Site 2 is contrasted with the behavior of the nonlinear shear modulus at the same site.

8.4.1 Relationships presented in previous studies

In recent years, several researchers have proposed relationships for both M/M_{max} – log ε and G/G_{max} – log γ based on both field work and empirical relationships. In the case of M (and M/M_{max}), much of the recent work has involved the use of field methods due to the complexities involved in laboratory characterization of the nonlinear behavior of the constrained modulus. However, the behavior of G (and G/G_{max}) with increasing shear strain is well-documented, and several empirical relationships exist for G/G_{max} – log γ. In this section, these field and empirical relationships are compared to the results from Site 2. For purposes of this comparison, the generalized M/M_{max} – log ε and G/G_{max} – log γ relationships shown in Figures 8.24 and 8.32, respectively, are used to represent the nonlinear soil response at Site 2.

8.4.1.1 Field determination of M/M_{max} – log ε

Two recent field studies that have proposed M/M_{max} – log ε relationships are discussed in Chapter 2. Beresnev et al. (2002) back-calculated the in-situ linear and nonlinear constrained moduli using earthquake records from the KiK-net digital borehole accelerograph arrays in Japan. The resulting M/M_{max} – log ε relationship is shown in Figure 2.6. Axtell et al. (2002) developed a localized testing method using large mobile shakers placed over an embedded sensor array. This method was similar to the method used in this study, and the M/M_{max} – log ε relationship obtained by Axtell et al. is shown in Figure 2.14. The normalized constrained modulus relationships proposed by Beresnev et al. (2002) and Axtell et al. (2002) are reproduced in Figure 8.33 and shown alongside the M/M_{max} – log ε relationships obtained at Site 2 in this study. As seen in Figure 8.33,

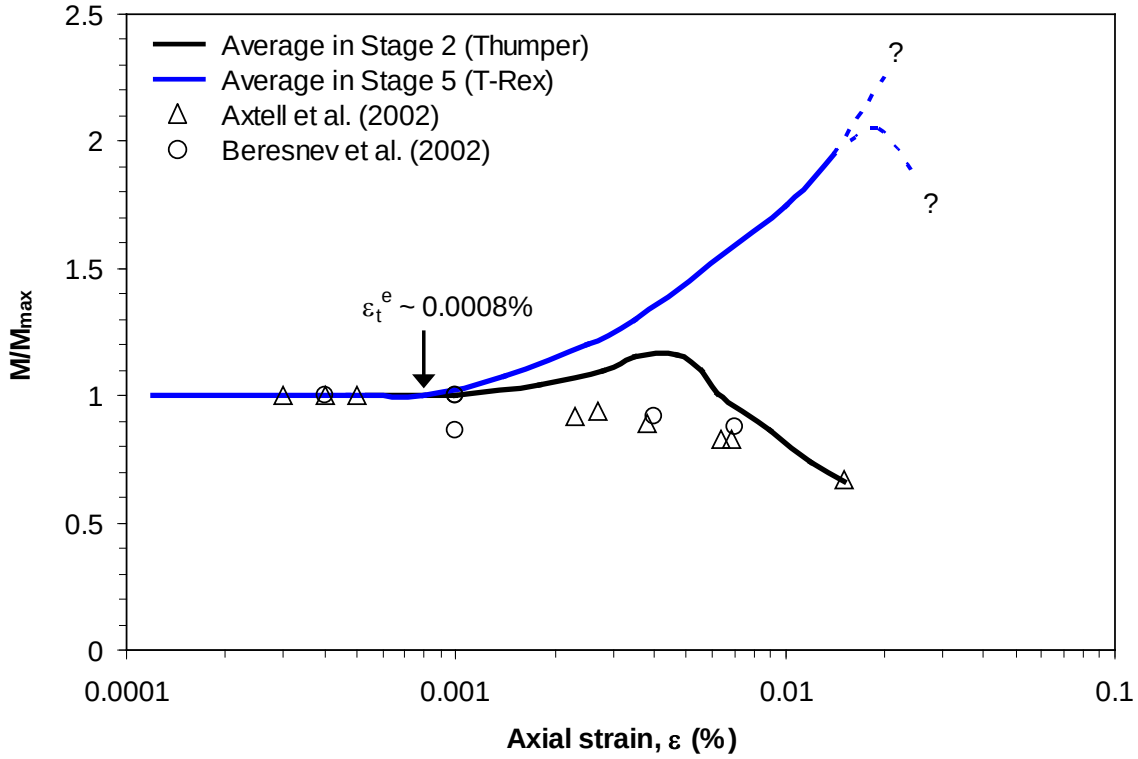

Figure 8.33. Comparison of M/M_{max} – log ε relationships for Site 2 with those proposed by Beresnev et al. (2002) and Axtell et al. (2002)

the M/M_{max} – log ε relationships proposed by Beresnev et al. and Axtell et al. agree very well with each other and are generally within about 20% of the Stage 2 M/M_{max} – log ε relationship evaluated with Thumper. At axial strains greater than about 0.007%, the nonlinear behavior of the constrained modulus in Stage 2 agrees well with the behavior noted by both Beresnev et al. and Axtell et al. However, neither Beresnev et al. nor Axtell et al. identified an increase in M with increasing axial strain, as was observed at Site 2 in both Stage 2 (to a moderate degree at axial strains from about 0.002 to 0.006%) and Stage 5 (to a large degree at axial strains greater than 0.001%).

As discussed in Chapter 5, M generally decreased with increasing axial strain at Site 1, regardless of which shaker was used to impart the vertical excitations (see Figure 5.31). The M/M_{max} – log ε relationships determined between Sensors 2 and 3 at Site 1 are shown in Figure 8.34 along with the M/M_{max} – log ε relationships obtained at Site 2. Note that as with Beresnev et al. (2002) and Axtell et al. (2002), the M/M_{max} – log ε relationship obtained with Thumper at Site 2 is in reasonably good agreement with the results from Site 1. The substantial increase of M/M_{max} with increasing ε obtained when T-Rex was used at Site 2 was not observed at Site 1. The author is not aware of any other instance where M/M_{max} is shown to increase with increasing ε.

8.4.1.2 Empirical relations for G/G_{max} – log γ

Umberg (2012) developed an empirical G/G_{max} – log γ relationship based on resonant column tests of an alluvium located near Dillon Dam in Dillon, CO. The basic properties of the sandy silt used by Umberg to develop his relationship are: 50% fines content (silt), e = 0.48, D_{50} = 0.08 mm, C_u = 24, and w = 11.7%. These same properties for the sandy silt at Site 2 (discussed in Section 7.4.2) are: 52% fines content (silt), e = 0.82, D_{50} = 0.07 mm, C_u = 2.5, and w = 4.5%. The empirical relationship proposed by Umberg is itself a soil-specific variation of the modified hyperbolic model developed by

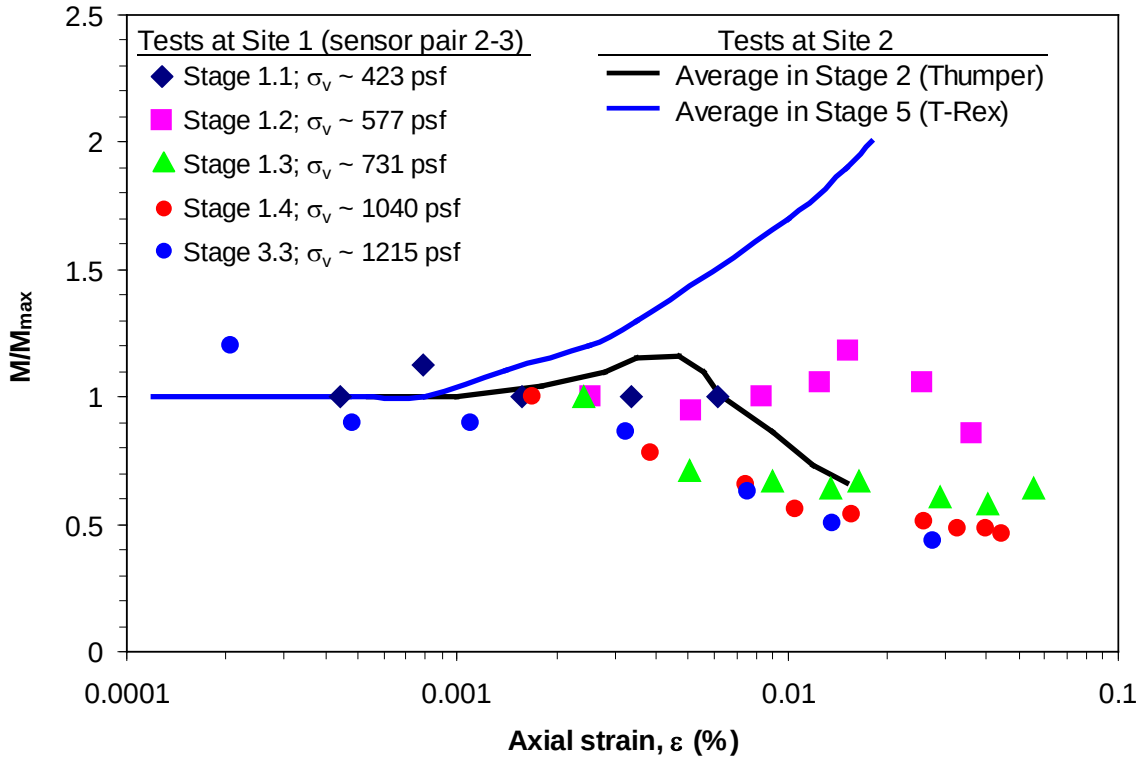

Figure 8.34. Comparison of M/M_{max} – log ε relationships for Sites 1 and 2

Darendeli (2001), which is expressed as:

$$\frac{G}{G_{\max}} = \frac{1}{1+\left(\gamma / \gamma_r\right)^a} \tag{8.6}$$

where a is an experimentally-derived constant, and γ_r is the reference shear strain in percent (Darendeli, 2001). Darendeli proposed that γ_r is a function of plasticity, overconsolidation ratio, and mean stress (σ_o). For the Dillon Dam alluvium, Umberg determined that a = 1.02, and the reference shear strain is defined by the relation:

$$\ln(\gamma_r) = 0.3673 \ln(\sigma_o) - 4.302 \tag{8.7}$$

where σ_o is in units of psi (Umberg, 2012). Using Equations 8.6 and 8.7, Umberg's relationship was computed for two confining pressures that represent the range of stresses at Site 2 in Stage 6 (1400 and 1700 psf (67 and 81 kPa), respectively). The results are shown in Figure 8.35 along with the generalized G/G_{max} – log γ relationships determined for Site 2 (see Figure 8.32). Additionally, the upper and lower bounds for sand proposed by Seed and Idriss (1970) are also included in Figure 8.35.

As seen in Figure 8.35, the G/G_{max} – log γ relationship determined at Site 2 is generally close to the lower bound of the Seed and Idriss (1970) curves, but the threshold strain at Site 2 (about 0.001%) is lower than in any of the proposed relationships shown in Figure 8.32. Additionally, once the shear modulus becomes nonlinear, G/G_{max} decreases with increasing shear strain at a faster rate than that suggested by either the

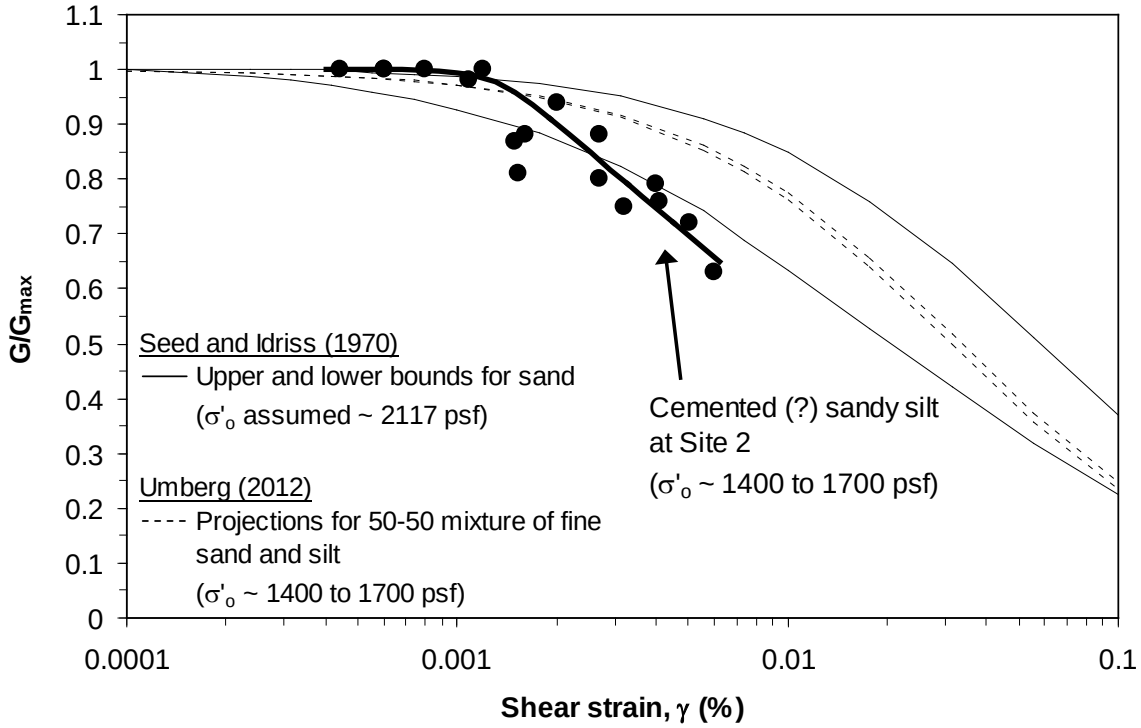

Figure 8.35. Comparison of G/G_{max} – log γ relationships for Site 2 with those proposed by Seed and Idriss (1970) and Umberg (2012)

Seed and Idriss (1970) or Umberg (2012) relationships. The overall shape of the G/G_{max} – log γ relationship at Site 2 is similar to results shown by Park (2010) for a cemented alluvium (Figure 8.36) and supports the conclusion that the sandy silt at Site 2 was likely somewhat cemented.

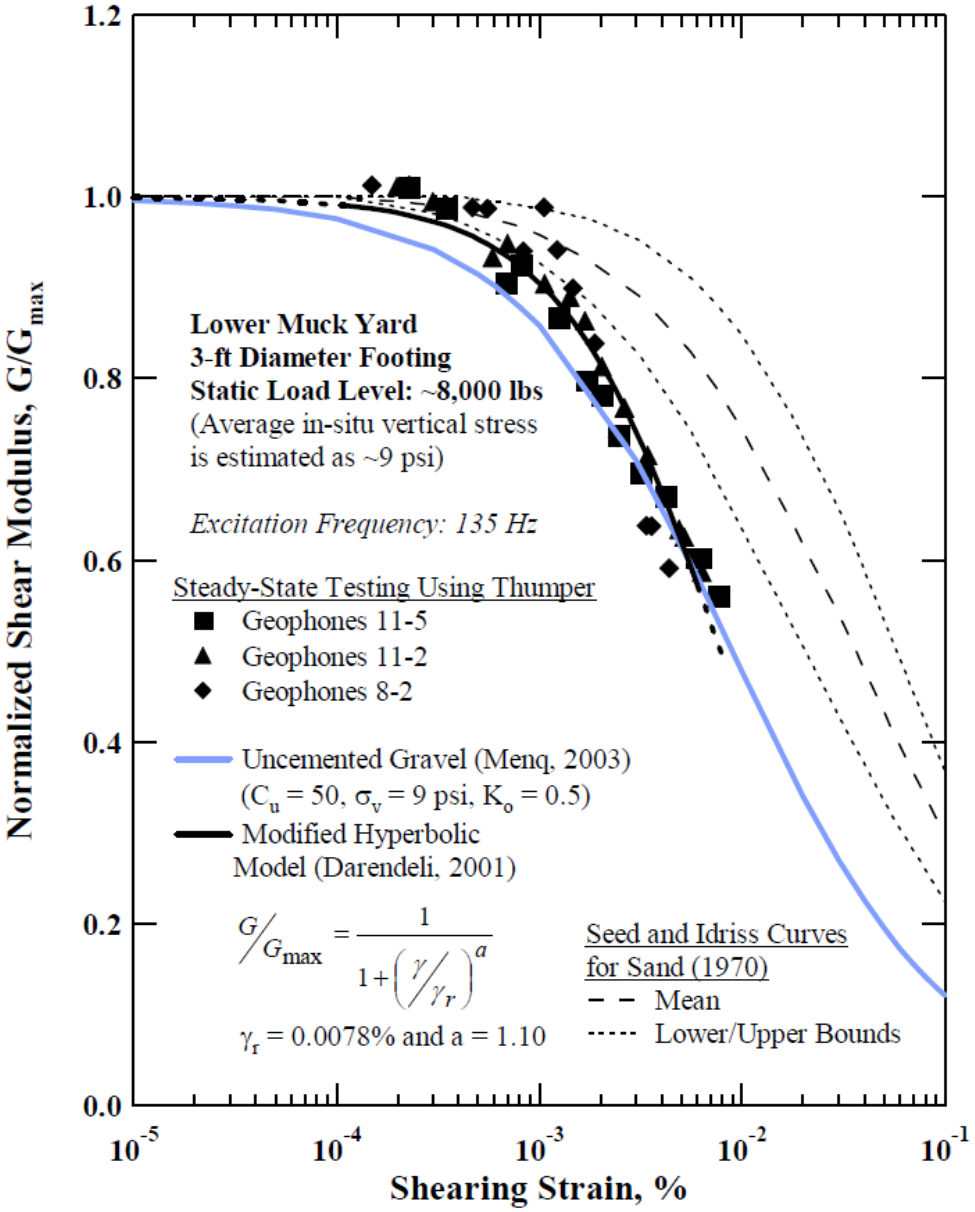

Figure 8.36. Comparison of normalized shear modulus reduction curves of the cemented alluvium at Yucca Mountain to several empirical relationships (from Park, 2010)

8.4.2 Behavior of nonlinear constrained and shear moduli at Site 2

As discussed in Section 8.2, the nonlinear behavior of M is quite complex and seems to be influenced by several factors. The nonlinear behavior of the constrained modulus compared to the nonlinear behavior of the shear modulus is of particular interest in this study, since it is generally assumed that the M/M_{max} – log ε and G/G_{max} – log γ relationships have a similar shape. Since both vertical and horizontal sinusoidal excitations were applied at Site 2, this testing regimen affords a unique opportunity to examine the behaviors of both nonlinear constrained and shear moduli at the same site under approximately the same conditions. However, before the M/M_{max} – log ε and G/G_{max} – log γ relationships can be compared directly, the relationship between ε and γ must be examined.

In the case of vertical sinusoidal excitations imparted directly over an embedded sensor array, several simplifying assumptions can be made concerning an element of soil located approximately under the centerline of the vibroseis' load plate (see Figure 8.37). As discussed in Section 8.2, if the vertically-propagating compression wave generated by the vibroseis is indeed fully constrained, then no movement in the x and y directions is allowed. The strain in the horizontal directions (ε_x or ε_y) is then zero, and this is the uniaxial strain case, as shown in Figure 8.37. Additionally, since all soil elements near the centerline of the load plate are assumed to move together, there is no shear strain acting on the vertical plane of the element (the y-z plane), and this is a principal plane. Similarly, since the sinusoidal excitation is assumed to contain only (or at least predominantly) a vertical component, no shear strain is induced on the horizontal plane of the element (the x-y plane), and this is also a principal plane. Therefore, the Mohr's circle for strain is constructed as shown in Figure 8.37. By inspection of the Mohr's circle for strain, it is readily apparent that the maximum shear strain is equal to the axial strain, i.e. γ_{max} is equal to ε_z. Therefore, the M/M_{max} – log ε and G/G_{max} – log γ relationships can be plotted on the same graph with no adjustment required.

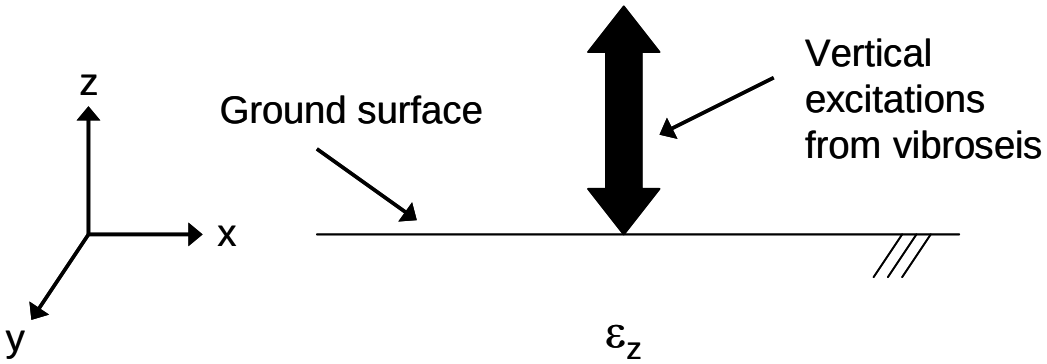

Assumptions:

1. Uniaxial strain ($\varepsilon_x = 0$)
2. No relative vertical movement between this element and adjacent elements ($\gamma_{xz} = 0$)
3. Pure vertical motion from vibroseis ($\gamma_{zx} = 0$)

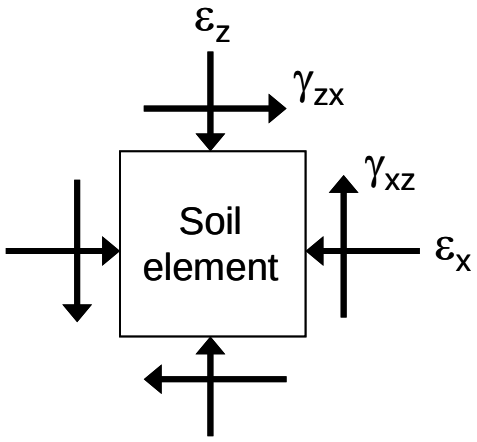

The Mohr's circle for strain

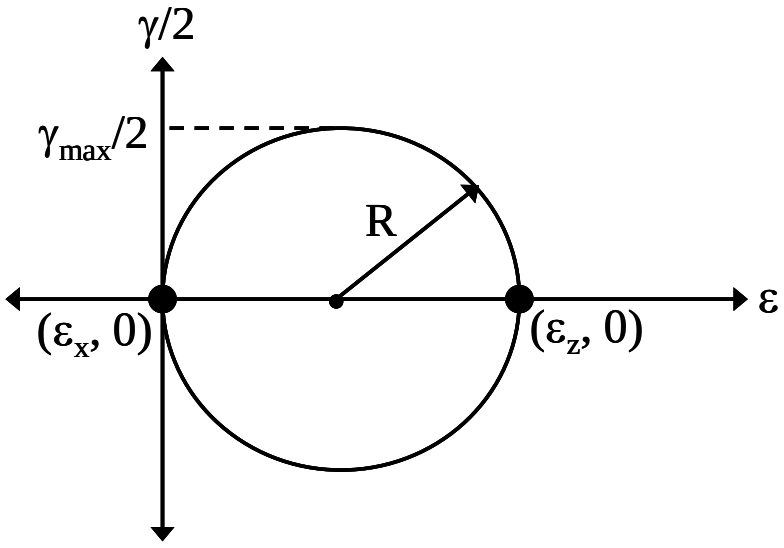

Figure 8.37. State of strain induced in the field by a vertical excitation

A comparison of the M/M_{max} – log ε and G/G_{max} – log γ relationships obtained at Site 2 is shown in Figure 8.38. As seen in Figure 8.38, the agreement between the M/M_{max} – log ε relationships and the G/G_{max} – log γ relationship is the same at small strains, and the "elastic" threshold strain (ε_t^e or γ_t^e) is nearly the same in both cases (about 0.0008 to 0.001%). However, at larger strains, i.e. as the soil exhibits mildly nonlinear behavior, the difference between the nonlinear behaviors of M/M_{max} (in Stage 2) and G/G_{max} is quite large since M/M_{max} initially increases slightly with increasing axial strain. As the strain level increases beyond about 0.007% strain, M/M_{max} (in Stage 2) decreases with increasing strain at approximately the same rate as the G/G_{max} – log γ relationship.

However, when the steady-state vertical excitations were applied by T-Rex in Stage 5, the behavior of M/M_{max} with increasing strain was even more different than the

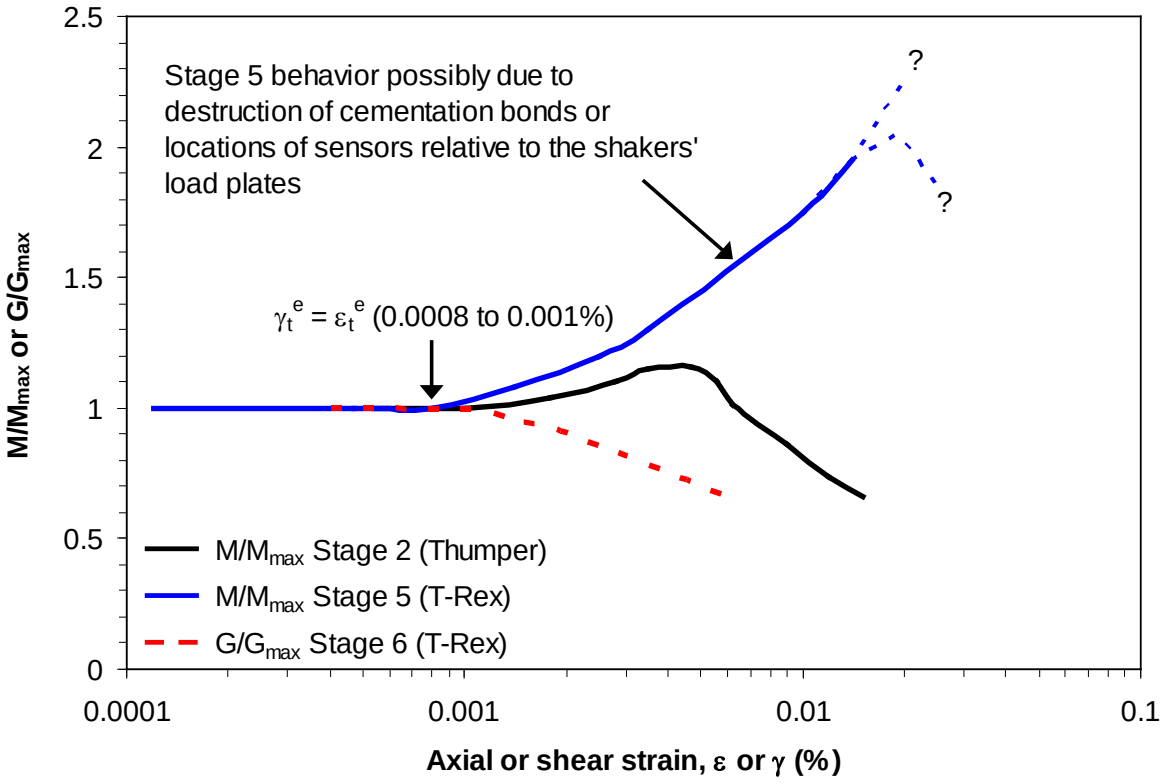

Figure 8.38. M/M_{max} – log ε and G/G_{max} – log γ relationships for Site 2

behavior of G/G_{max}. At this time, it is believed that the soil at Site 2 was significantly altered between the tests performed with Thumper (Stages 2 and 3) and those performed with T-Rex (Stages 5 and 6). The disturbance caused by the dynamic tests of Stages 2 and 3, coupled with the locations of the sensors in the active Rankine zone beneath the shakers, is likely why M/M_{max} behaved differently in Stages 2 and 5. But as shown in Figure 7.39, this disturbance affected the V_{Svh} values (and in turn, the G values) in Stage 4 very little, if at all. Therefore, while the behavior of M/M_{max} appears to be affected by the disturbance of the test regimen, the behavior of G/G_{max} is not affected as much, and a single curve can still be used to represent the $G/G_{max} - \log \gamma$ relationship at Site 2.

It should be noted that there is a major assumption underlying graphs such as Figure 8.38. Namely, the assumption is made here that the shear strains (and the nonlinear response of G) induced at one point in time under horizontal sinusoidal excitations can be directly compared to the axial strains (and the nonlinear response of M) obtained at a later instant in time when vertical sinusoidal excitations are induced in the soil. In other words, the $M/M_{max} - \log \varepsilon$ and $G/G_{max} - \log \gamma$ relationships shown in Figure 8.38 were not obtained simultaneously, but rather over the course of about a week of testing, in several different load configurations, and with intervening static loads applied to the soil for the downhole and crosshole tests. The magnitude of the errors associated with this assumption is not known.

8.5 UNCERTAINTIES AND LIMITATIONS

While the steady-state sinusoidal excitation tests described in this chapter were generally successful in inducing nonlinearity in the field, there are several uncertainties and limitations associated with these types of tests, some of which were also noted by Park (2010). These uncertainties and limitations include the following (where contributions by Park are noted as necessary):

1. The propagation paths of the waves may not be correctly identified. It is possible that the waves propagate along some other path instead of the direct path assumed in the data analysis (Park 2010). Park also noted that the unknown variability in the cementation in the soil may also cause the waves to travel along unexpected paths.

2. Evaluation of the in-situ state of stress is only an approximation (Park 2010). The entire farm field at Lower Tract B generally shows considerable spatial heterogeneity and localized anisotropy. As discussed in Chapter 7, the silty sand at Site 2 appears to be cemented, and the amount of this cementation undoubtedly also varies spatially. These factors (heterogeneity, anisotropy, and cementation) were not directly considered when estimating the in-situ state of stress (Park 2010).

3. The area which can be investigated using steady-state excitations applied by a vibroseis at the ground surface is relatively small compared to the entire farm field (Lower Tract B at Hornsby Bend). The embedded sensor array was installed at depths from 13 to 49 in. (33 to 125 cm) below the load plate of the vibroseis. Given the heterogeneity at the site noted in item #2 above, it is unlikely that the behavior observed in this small area beneath the vibroseis is representative of the entire Lower Tract B field as a whole.

4. For unknown reasons, the area closest to the load plate of the vibroseis generally cannot be investigated using this method. The results at the first two sensors were often unintelligible, as the wave arrivals occurred at both sensors simultaneously or very nearly simultaneously (therefore, “infinite” velocity). The behavior between these first two sensors could only be analyzed in a few cases with Thumper and not at all with the larger load plate of T-Rex. Therefore, only a small area from about 2 to 4 ft (0.6 to 1.2 m) below the load plate of the vibroseis

could be successfully analyzed using this method. This limitation is especially troublesome, since the area closest to the load plate of the vibroseis is probably the most laterally constrained, and therefore is the most ideal for investigation of nonlinear constrained modulus.

5. In both the vertical and horizontal sinusoidal excitation tests, the load plates of Thumper and T-Rex were positioned directly on the ground surface. Though T-Rex is capable of generating much larger loads than Thumper, the load plate of T-Rex is also much bigger than that of Thumper. Accordingly, the range of vertical stresses induced in the embedded sensor array by Thumper and T-Rex was about the same. This similarity is advantageous if one desires to investigate the effect of differing lateral constraint under the same vertical confining pressure. However, this stress state is also a limiting factor if higher levels of vertical stress are desired in the field. In this event, the load plate of T-Rex should be applied to a small circular footing as done by Park (2010).

These possible uncertainties and limitations should be considered when using the data from the steady-state excitation tests, as they undoubtedly cause the variability in the results of the steady-state excitation tests to increase. However, there are several observations which suggest these uncertainties and limitations are not overly significant: (1) Park (2010) found reasonably good agreement between field measurements of nonlinear shear modulus and laboratory resonant column tests, (2) the $G/G_{max} - \log \gamma$ curves determined at Site 2 generally agree well with established empirical relationships, and (3) at small strains, the $M/M_{max} - \log \varepsilon$ relationships determined at Site 2 are similar to previous field studies of nonlinear constrained modulus. Therefore, despite the uncertainties and limitations noted in this section, it is believed that the methods discussed in this chapter are a viable means of evaluating the constrained and shear moduli in the linear and nonlinear strain range.

8.6 SUMMARY

Constrained and shear moduli in the linear and nonlinear range were evaluated using two large shakers (Thumper and T-Rex) to apply steady-state sinusoidal excitations directly to the ground surface above a sensor array embedded in a silty sand at Site 2 at Hornsby Bend, Texas (the construction and arrangement of the sensor array are described in Chapter 6). These steady-state excitation tests were performed in four stages (Stages 2, 3, 5, and 6). In Stages 2 and 3, the sinusoidal excitations were applied by Thumper in the vertical and horizontal directions, respectively. Similarly, in Stages 5 and 6, the sinusoidal excitations were applied by T-Rex in the vertical and horizontal directions, respectively. In each load stage, the sinusoidal load amplitude was gradually increased in a stepped-sequence to progressively induce more strain (either ε or γ depending on the load stage) within the embedded sensor array at Site 2. In this manner, a wide range of strains was induced at Site 2 which allowed investigation of the nonlinear stress-strain behavior of both the constrained and shear moduli.

The results of the linear and nonlinear steady-state vertical excitation tests are presented in the form of M – log ε and M/M_{max} – log ε relationships. The M and M/M_{max} values were successfully determined over an axial strain range of about 0.0002% to 0.02%. In an attempt to verify that the vertically-propagating compression waves induced by the shakers were fully constrained (and not partially-constrained) between a given sensor pair, the compression wave velocity determined under very small levels of steady-state excitation was compared to the small-strain V_{Pv} determined in the traditional transient downhole tests described in Chapter 7. When the agreement between these two velocities was good, it was assumed that P_V waves were generated between the sensor pair of interest. This comparison was made for all pairs of sensors in the embedded sensor array, and only the sensor pairs where P_V waves were generated were used in further analysis. In general, the M/M_{max} – log ε relationships determined using Thumper in Stage 2 increased slightly and then decreased with increasing axial strain. The M/M_{max}

– log ε relationships determined with T-Rex in Stage 5 increased with increasing axial strain. This effect was observed even when the location and load step were selected such that the steady-state V_{Pv} and σ'_v were similar in both stages. The generalized M/M_{max} – log ε relationship based on all locations used in Stage 2 increases slightly at small strains (less than about 0.005%), but then decreases after about 0.005% axial strain. This effect is somewhat similar to the results of the steady-state tests performed at Site 1 (Figure 8.34) which are described in Chapter 5. Additionally, at axial strains greater than about 0.007%, the Stage 2 M/M_{max} – log ε relationship agrees relatively well with the results of previous field studies by Axtell et al. (2002) and Beresnev et al. (2002) (Figure 8.33).

The results of the linear and nonlinear steady-state horizontal excitation tests are presented in the form of G – log γ and G/G_{max} – log γ relationships. In the steady-state horizontal excitation tests conducted at Site 2, neither Thumper nor T-Rex was capable of generating purely horizontal motion due to the rocking/rotation of the shakers' load plates. In general, the amount of vertical motion (relative to the horizontal motion) was much higher when Thumper was used, and it is believed that this amount of vertical motion prevented an accurate determination of G – log γ relationships using Thumper. The amount of relative vertical motion generated by T-Rex was much less and allowed for the determination of shear moduli over a wide range in shear strains (provided the shear strains are determined using a 4-node displacement-based method). The G and G/G_{max} values in Stage 6 with T-Rex were successfully determined over a shear strain range of about 0.0004% to 0.006%.

When G is normalized by G_{max}, the agreement between the resulting G/G_{max} – log γ relationships at both locations at Site 2 is quite good. These relationships can be represented by a single curve (Figure 8.32) with little or no loss of accuracy, and show a clear trend of decreasing G/G_{max} with increasing shear strain. Additionally, the shape of the G/G_{max} – log γ curve in Stage 6 with T-Rex is generally similar to the curves determined by Park (2010) for a cemented alluvium (Figure 8.36). Based on the G/G_{max}

– log γ relationship, the threshold strain is about 0.0008% to 0.001%, which is about the same as with the M/M_{max} – log ε relationships determined in Stages 2 and 5 (Figure 8.38). Additionally, as the strain level increases beyond about 0.007% strain, the M/M_{max} (in Stage 2) decreases with increasing strain at approximately the same rate as the G/G_{max} – log γ relationship.

However, the behaviors of M/M_{max} in Stage 5 (with T-Rex) and G/G_{max} are quite different at Site 2. The large increase in M/M_{max} with increasing ε observed in Stage 5 with T-Rex was not seen in Stage 2 or at Site 1, nor is the author aware of any instance where similar behavior was observed by other researchers. At this time, this difference in the nonlinear behavior of M/M_{max} is assumed to be due several factors, including: (1) changes in the soil caused by the intervening load stages of the test regimen itself and (2) the locations of the sensors in the active Rankine zone developed beneath the load plates of the shakers. Disturbance from the test regimen could have affected several soil characteristics such as the cementation, structure, pore pressure distribution, relative density, etc. There is a strong possibility that the cementation bonds which were apparently intact at the time of the sinusoidal excitation tests in Stage 2 were either partially or completely destroyed by Stage 5.

Therefore, the nonlinear behavior of the constrained modulus is quite complex and appears to be a function of many factors. Several of these factors are discussed above, but there are potentially many more which remain undiscovered, yet still contribute to the behavior of M. While the results of the tests at Site 2 indicate that the test procedure used in this study can be successfully used to investigate M, clearly more work is required in this area to fully quantify the response of the constrained modulus in the nonlinear strain range.

CHAPTER 9: SUMMARY, CONCLUSIONS, AND RECOMMENDATIONS

9.1 SUMMARY

Characterization of the dynamic properties of soil is an important part of soil dynamics and geotechnical earthquake engineering problems and often serves as a basic first step in the solution of problems in these areas. To this end, seismic measurements have been performed by traditional field methods for more than 50 years to determine the small-strain shear and constrained moduli of geotechnical materials under existing conditions. Additionally, efforts to characterize the dynamic properties of soil in the nonlinear strain range generally revolve around the response of the shear modulus (G) to changes in shear strain amplitude, usually evaluated by a combination of field and laboratory measurements. As a result, it is well known that the stress-strain behavior in shear becomes nonlinear at even relatively small levels of shear strain. Similar characterization of the linear and nonlinear response of the constrained modulus (M) has received almost no attention in the civilian geotechnical engineering community. Primarily due to the complexities involved in the laboratory determination of the nonlinear constrained modulus, the few attempts made to characterize the linear and nonlinear response of M have generally focused on field methods and have mainly been conducted in the military and seismological communities. These methods use strong ground motions generated either by controlled high-explosive detonations or earthquakes (Hadala, 1973; Beresnev and Wen, 1995; Beresnev et al., 2002). However, due to the infrequency and unpredictability of these strong motion events, a need exists for an alternative field method to characterize the linear and nonlinear constrained moduli of soil.

Around the start of the 21st century, the research group at The University of Texas at Austin developed a field method to measure the linear and nonlinear dynamic shear

moduli of soils over a range in strain levels (Phillips, 2000; Rathje et al., 2001; Stokoe et al., 2001; Axtell et al., 2002). This method utilizes a loading platen, usually a cast-in-place concrete footing, at or near the ground surface as the wave source and a sensor array embedded directly beneath the platen as receivers. Following the development of a new generation of vibroseis trucks (Stokoe et al., 2004), the methodology was refined by The University of Texas at Austin to perform parametric studies on the shear moduli of geotechnical materials in-situ over a wide range of strains (Stokoe et al., 2006; Park, 2010). The vibroseis field method described above has been shown to be effective in characterizing the linear and nonlinear shear moduli of soils in-situ (Park, 2010). This study was undertaken to determine: (1) whether the method has the potential to measure the in-situ response of the linear and nonlinear constrained moduli, and (2) what steps are necessary to continue this development.

In this study, field measurements were performed at two sites on the edge of a farm field in Lower Tract B near Hornsby Bend, Texas. The first site involved "proof-of-concept" testing, and the second site involved a comprehensive suite of tests. At each site, an embedded sensor array was constructed by first scarifying and removing the top layer of plough tillage by hand until native sandy silt (ML) was found. Then a series of 3-D sensors (comprised of three, 1-D geophones) were installed beneath the ground surface by hand drilling small-diameter boreholes to the desired depth of the deepest sensor. After the bottoms of the boreholes were prepared and the deepest sensors were placed, each borehole was then backfilled with native soil and compacted in steps until the desired depth of the next sensor was reached. Great care was taken to compact the backfilled soil to the same density as the in-situ soil. The next sensor was placed, and the process was repeated until the desired number of sensors was placed in each borehole, after which the remainder of each borehole was backfilled and compacted in steps.

At the first site (Site 1) at Hornsby Bend, an embedded sensor array had previously been installed during an earlier research project and consisted of eight, 3-D

sensors at the corners of a 2-ft x 2-ft x 2-ft (0.61-m x 0.61-m x 0.61-m) cubical array. The existing array at Site 1 was modified in this study by installing three, 3-D sensors in a vertical column in the center of the cubical array. A second sensor array at Hornsby Bend (Site 2) was installed at a location approximately 300 ft (92 m) northeast of Site 1 but still located in the same farm field (Lower Tract B). A total of 12, 3-D sensors was installed at Site 2 in a triangular prism arrangement consisting of three vertical columns, with four sensors in each column. The 3-D array was contained in a volume of soil about 1.3 ft x 1.3 ft x 4 ft (0.4 m x 0.4 m x 1.2 m).

In general, the testing programs at the two sites were similar, though the scope of the program at Site 1 was limited to "proof-of-concept" type tests. The tests at Site 1 built upon the progress made by Park (2010) and were used to specifically tailor the method to best suit the measurement of linear and nonlinear constrained moduli. A more extensive suite of tests was then performed at Site 2 using the lessons learned from the initial tests at Site 1. However, at both sites, the approach generally involved the following two major test phases.

1. The behavior of the small-strain dynamic moduli in the linear strain range was determined using a staged sequence of static vertical loads applied to a precast concrete footing. The footing was positioned over the sensor arrays, and traditional small-strain, transient downhole and crosshole seismic tests were performed at each load stage. The body waves generated in the downhole tests were vertically-propagating, constrained compression (P_V) waves and vertically-propagating, horizontally-polarized shear (S_{VH}) waves. The body waves generated in the crosshole tests were horizontally-propagating, constrained compression (P_H) waves and horizontally-propagating, vertically-polarized shear (S_{HV}) waves. At each level of vertical load, the velocities of the body waves (V_{Pv}, V_{Svh}, V_{Ph}, and V_{Shv}) propagating through the sensor array were determined between adjacent sensors. The purposes of this test phase were: (1) to determine the variation of the

small-strain V_{Pv}, V_{Svh}, V_{Ph}, and V_{Shv} with confining pressure and (2) to confirm that the steady-state excitation tests (discussed below) are measuring the P_V- and S_{VH}-wave velocities at small strains.

2. To characterize linear and nonlinear constrained and shear moduli, steady-state excitation tests were performed in which two nees@UTexas vibroseis trucks (Thumper and T-Rex) applied sinusoidal excitations directly above the embedded sensor arrays, and the response of the soil was measured by the sensors in the array. To investigate the behavior of the constrained moduli, the sinusoidal excitations were applied vertically, and P_V waves were induced by the vibroseis. To investigate the behavior of the shear modulus, the sinusoidal excitations were applied horizontally, and S_{VH} waves were induced by the vibroseis. Note that horizontal excitations were only applied at Site 2. To limit the effects of the loading regimen on the underlying soil structure, a staged loading sequence was used in which the vibroseis applied static hold-down loads while simultaneously imparting progressively larger sinusoidal load amplitudes. In this manner, a wide range of strains was induced which allowed investigation of the nonlinear stress-strain behavior of both M and G (where M is determined using V_{Pv} and G is determined using V_{Svh}).

9.2 CONCLUSIONS

Based on the results of the testing programs at Sites 1 and 2, several conclusions can be drawn concerning the method and the suitability of its use in the field measurement of linear and nonlinear constrained moduli of soils. The conclusions from the linear and nonlinear tests are treated separately in this section.

9.2.1 Evaluation of constrained and shear moduli in the linear strain range

Constrained and shear moduli of the sandy silt at Site 2 in the linear strain range were evaluated using small-scale versions of downhole and crosshole seismic tests. The small-strain, constrained compression and shear wave velocities were successfully measured over a range in confining pressures using a staged loading sequence in which progressively larger vertical loads were applied to a precast concrete footing. The staged loading sequence used at Site 2 (Figure 6.11) was especially beneficial in that the small-strain velocities of these body waves were determined both before and after the large-strain excitations imparted by Thumper and T-Rex. This comparison of small-strain wave velocities allowed for some estimation of the amount, if any, of disturbance in the soil caused by the shakers. In the downhole tests, the results are presented in the form of log V_{Pv} – log σ'_v and log V_{Svh} – log σ'_v relationships. In the crosshole tests, the results are presented in the form of log V_{Ph} – log σ'_h and log V_{Shv} – log σ'_h relationships. These relationships were evaluated over a range of effective vertical stresses from about 900 to 3000 psf (43 to 144 kPa), and an example from the downhole tests at Site 2 is shown in Figure 9.1.

In most cases at Site 2, the behavior of the P-wave velocity with increasing confining pressure is generally the same in both the downhole and crosshole tests, i.e. the log V_{Pv} – log σ'_v and the log V_{Ph} – log σ'_h relationships are approximately the same. Similar statements can be made about the log V_{Svh} – log σ'_v (downhole tests) and log V_{Shv} – log σ'_h (crosshole tests) relationships. Further, these relationships do not vary significantly with depth or with the loading stage (Stage 1, 4 or 7) in most cases. The P_V-wave velocities at one atmosphere ($V_{Pv,1}$) determined at the two deeper depths (31 and 43 in. (79 and 109 cm)) in the embedded sensor array are basically the same in all three stages. Additionally, at all depths in the embedded sensor array, there is no significant reduction in the V_{Svh} at one atmosphere ($V_{Svh,1}$) determined in Stages 1, 4, and 7 (Figure 7.39). However, at the shallowest depth of 19 in. (48 cm), there is a roughly 25% (700

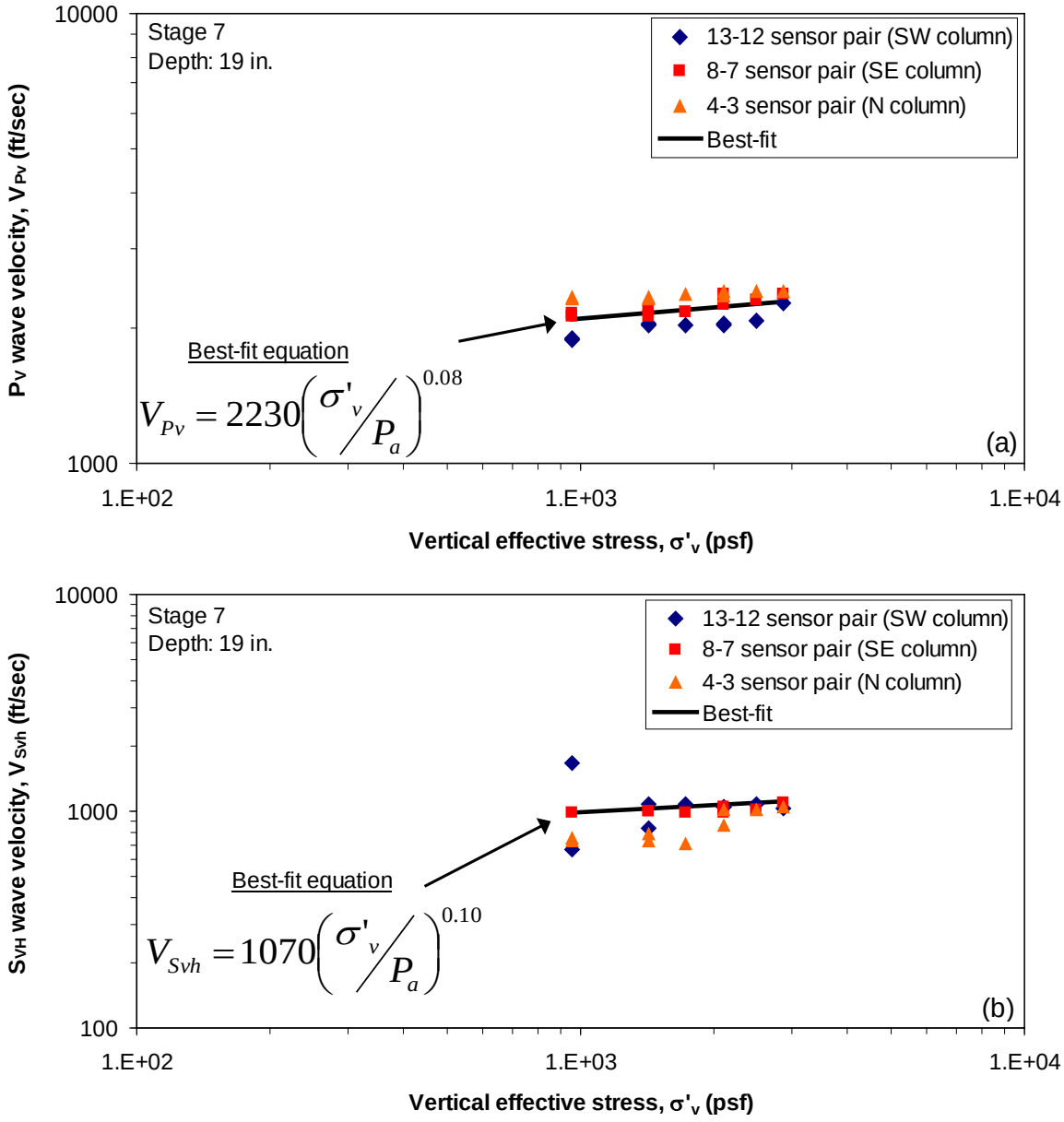

Figure 9.1. Variation of downhole wave velocities with increasing stress level at an average depth of 19 in. (48.3 cm) below the concrete footing at Site 2: (a) log V_{Pv} – log σ'_v and (b) log V_{Svh} – log σ'_v

fps (213 m/s)) reduction in the $V_{Pv,1}$ values between Stages 1 and 4. At this same depth, there is virtually no reduction in $V_{Pv,1}$ between Stages 4 and 7. At this time, it is believed that the reduction in the $V_{Pv,1}$ values at the shallowest depth between Stages 1 and 4 was likely caused by the intervening vertical and/or horizontal steady-state excitations applied with Thumper in Stages 2 and 3. The agreement between the $V_{Pv,1}$ values in Stages 4 and 7 suggests that perhaps most of the change in the soil occurred before steady-state excitations were applied with T-Rex in Stages 5 and 6.

Therefore, with the possible exception of the case mentioned above, the best-fit equations listed in Tables 7.1 and 7.2 for all depths can be reduced to a single set of relationships for Site 2. The recommended relationships for Site 2 are:

$$V_P = 2300\left(\sigma'_v / P_a\right)^{0.11} \tag{9.1a}$$

$$V_S = 1200\left(\sigma'_v / P_a\right)^{0.11} \tag{9.1b}$$

where the coefficients are the V_P and V_S at one atmosphere ($V_{P,1}$ and $V_{S,1}$, respectively (in units of fps)) and the exponents of the normal stress (n_P and n_S) are both equal to 0.11. These exponents are low compared to empirical models developed by Hardin and Drnevich (1972a) and Menq (2003) for an uncemented sand, which predict an exponent of in the range of 0.24 to 0.26 for the log V_S – log σ'_v relationship. Since this predicted exponent is greater than those observed in this study, it was concluded that the sandy silt at Site 2 was likely lightly cemented and/or heavily overconsolidated during all three stages of the small-strain downhole and crosshole seismic tests. This cemented/overconsolidated state resulted in the soil skeleton exhibiting a similar stiffness in the vertical and horizontal directions, much like a condition of $K_o = 1$ in soil.

Throughout the data analysis of the small-strain downhole and crosshole tests, several simplifying assumptions had to be made. As discussed in Section 7.5, these assumptions, coupled with the inherent uncertainties and limitations involved in the testing procedure, undoubtedly increase the variability in the small-strain, downhole and crosshole data. However, Park (2010) found reasonably good agreement with other field methods which used different measurement methods, and the results of this study agreed quite well with the results of Kim's (2012) Seismic Cone Penetration Tests conducted near Sites 1 and 2. Therefore, it is believed that the uncertainties and limitations are not overly significant in the evaluation of the constrained and shear moduli in the linear strain range, and that the method used in this study is a promising approach to evaluating log V – log σ' relationships in the field.

9.2.2 Evaluation of constrained moduli in the nonlinear strain range

Constrained moduli of the sandy silt at Site 2 in the linear- and nonlinear-strain ranges were evaluated from the steady-state vertical excitation tests with Thumper (Stage 2) and T-Rex (Stage 5). In the steady-state vertical excitation tests, the voltage-time signals recorded by most sensors in the arrays displayed significant asymmetry at larger levels of sinusoidal load amplitude (Figures 5.20, 5.23b, 5.24b, 8.3b, and 8.7b). In these cases, the use of the cross-correlation sequence proved to be a reliable method to determine the P_V-wave velocity between sensors. At depths below the vibroseis load plate less than 19 in. (48 cm), P_V-wave velocities could not be determined as discussed in Section 8.2. At depths greater than about 19 in. (48 cm), constrained moduli were determined using the unit weight of the soil (100 pcf (1600 kg/m^3)) and the velocities of the P_V waves between adjacent sensors. In this manner, the M and M/M_{max} values were successfully determined over an axial strain (ε) range from about 0.0002% to 0.02%, and the results are presented in the form of M – log ε and M/M_{max} – log ε relationships.

To verify that the vertically-propagating compression waves induced by the shakers were fully constrained (and not partially-constrained) between a given sensor pair, the compression wave velocity determined under the smallest level of steady-state excitation was compared to the small-strain V_{Pv} determined in the downhole tests (an example of this comparison for one sensor pair is shown in Figure 9.2). In most cases at or near the centerline of the load plates of the shakers, the compression wave velocity determined using steady-state, vertical sinusoidal excitations at the smallest excitation level was approximately equal to the P_v-wave velocity determined using small-strain, transient downhole seismic tests (Figures 5.21, 5.25, 8.4, 8.5, 8.6, 8.8, and 8.9). Therefore, it was concluded that the lateral confinement near the centerline of the load plates of Thumper and T-Rex was sufficient to allow for the generation of fully-constrained compression (P_V) waves by the shakers.

In general, the M/M_{max} – log ε relationships determined using Thumper in Stage 2 exhibited a constant value (1.0) until an elastic threshold strain (ε_t^e) of about 0.0008%. On average, at strains beyond ε_t^e, M/M_{max} increased slightly above 1.0 until about 0.005% axial strain after which M/M_{max} decreased with increasing axial strain. At a few locations within the embedded sensor array there was a slight decrease in the M/M_{max} – log ε relationship at strains above 0.003%. Therefore, the generalized M/M_{max} – log ε relationship based on all locations used in Stage 2 increases slightly at strains less than about 0.005%, but then decreases after about 0.005% axial strain (Figure 9.3). This effect is somewhat similar to the results of the steady-state tests performed at Site 1 (Figures 5.27 and 5.29) which are described in Chapter 5. Additionally, at axial strains greater than about 0.007%, the Stage 2 M/M_{max} – log ε relationship agrees relatively well with the results of previous field studies by Axtell et al. (2002) and Beresnev et al. (2002) (Figure 8.32).

Similar to the results in Stage 2, the M/M_{max} – log ε relationships in Stage 5 with T-Rex at Site 2 (also shown in Figure 9.3) exhibited a constant value (1.0) to an elastic

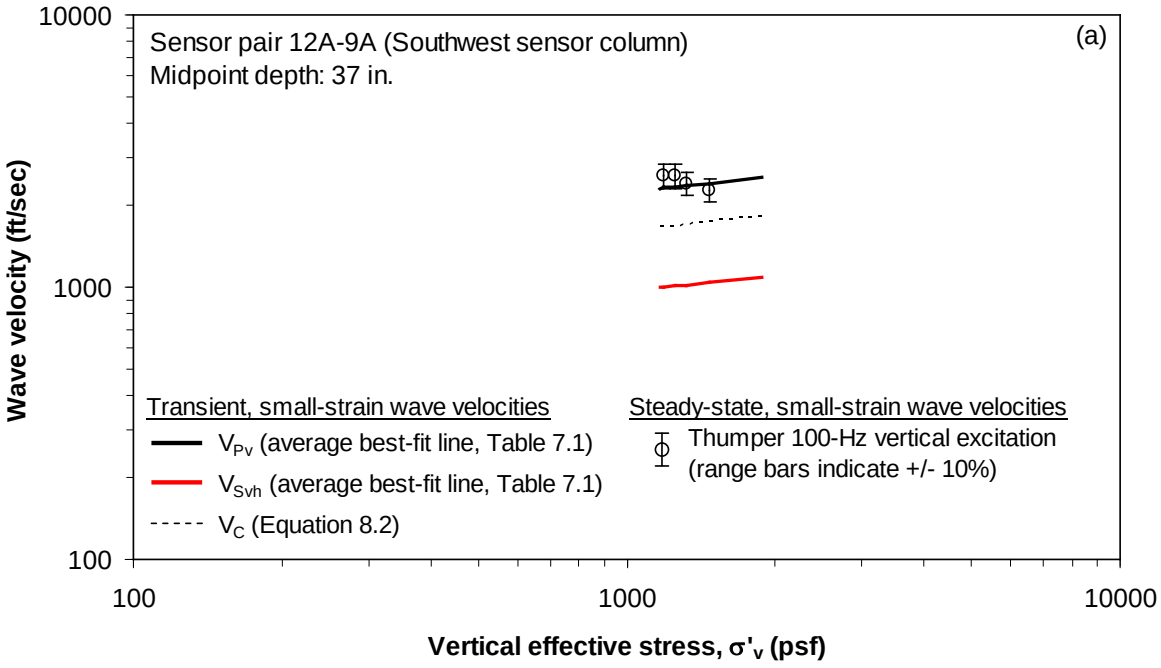

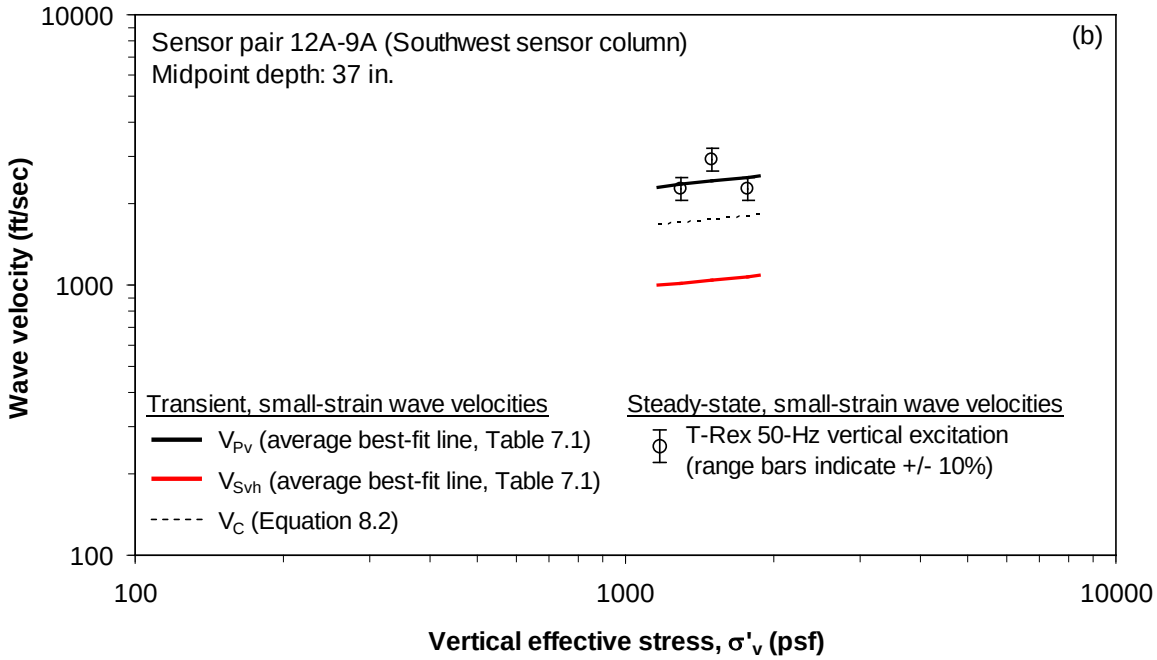

Figure 9.2. Comparison of steady-state, small-strain wave velocities to the transient, small-strain wave velocities at an average depth of 37 in. (94 cm) at Site 2: (a) Stage 2 with Thumper and (b) Stage 5 with T-Rex

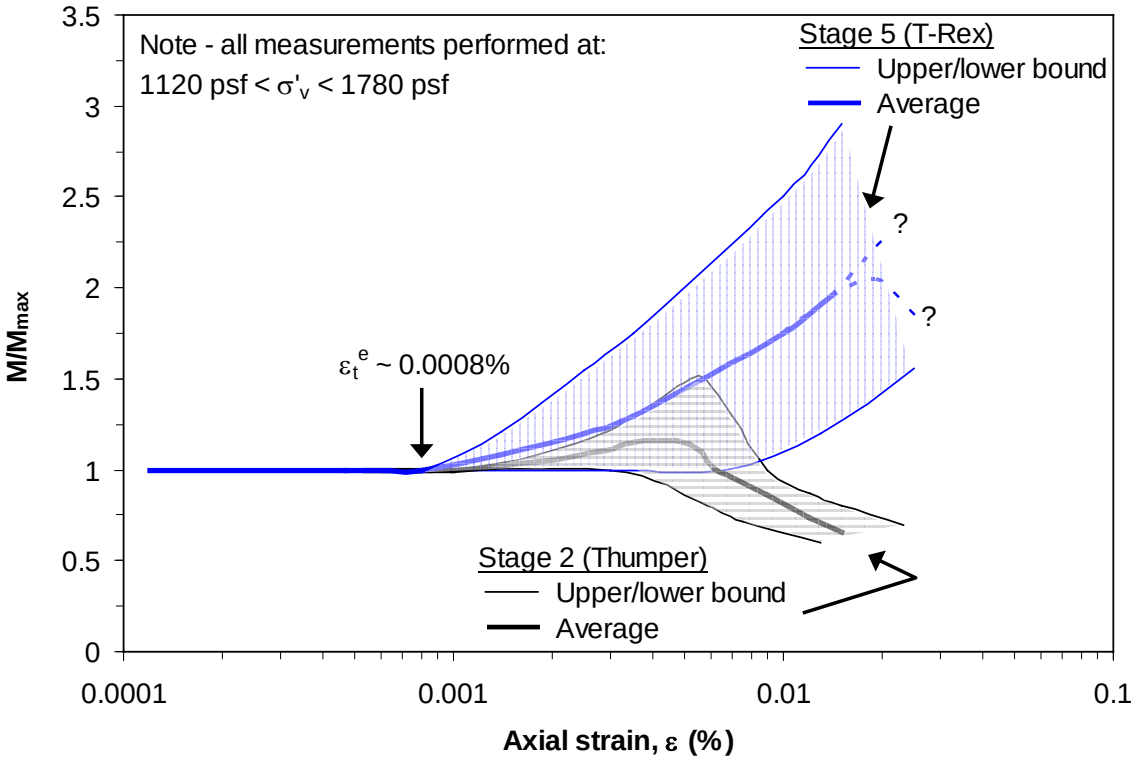

Figure 9.3. Generalized M/M_{max} – log ε relationships based on all depths at Site 2

threshold strain of about 0.0008%. However, at axial strains greater than ε_t^e, the M/M_{max} values generally increased with increasing axial strain and showed little or no tendency to reach a "peak" value (Figures 8.10, 8.11, 8.12, 8.15, 8.24, and 9.3). This effect was observed even when the location and load step were selected such that the steady-state V_{Pv} and σ'_v were similar in both stages (Figures 8.20, 8.21, and 8.22). The large increase in M/M_{max} with increasing ε observed in Stage 5 with T-Rex was not seen at Site 1, nor is the author aware of any instance where similar behavior was observed by other researchers.

At this time, the difference in the nonlinear behavior of M/M_{max} observed at Site 2 between Stages 2 and 5 is assumed to be due to a combination of several factors, including: (1) the locations of the sensors relative to the load plate of the shakers and (2) changes in the soil caused by the intervening loading stages of the test regimen itself.

Due to the relatively large load plate of T-Rex, the entire sensor array at Site 2 fell within the "active Rankine zone" (Vesic, 1973) developed beneath the load plate, but only the shallowest sensors fell within the zone developed by Thumper's load plate (Figure 8.23). Additionally, disturbance could have affected several soil characteristics such as the cementation, structure, negative pore pressure distribution (suction), relative density, etc. There is a strong possibility that cementation bonds which were apparently intact at the time of the sinusoidal excitation tests in Stage 2 were partially destroyed by Stage 5 (see Figure 7.39). This alteration likely resulted in an effectively "different" soil being tested with T-Rex in Stage 5 than was tested in Stage 2 with Thumper.

Based on the results at Sites 1 and 2, the nonlinear stress-strain behavior of the constrained modulus is quite complex and appears to be a function of many factors, including the amount of overconsolidation and cementation in the soil and the locations of the sensors relative to the vibroseis load plate. Specifically, the measure of whether the compression waves generated by the vibroseis are fully or partially-constrained appears to depend on more than just how closely the steady-state, compression wave velocity agrees with the small-strain V_{Pv} from the downhole tests (e.g. Figure 9.2). Therefore, while the results of the tests at both Sites 1 and 2 indicate that the test procedure used in this study can be successfully used to investigate M, clearly more work is required in this area to fully quantify the response of the constrained modulus in the nonlinear strain range.

9.2.3 Evaluation of shear moduli in the nonlinear strain range

Shear moduli of the sandy silt at Site 2 in the linear- and nonlinear-strain ranges were evaluated from the steady-state horizontal excitation tests with T-Rex (Stage 6). In the steady-state horizontal excitation tests, no signal asymmetry was observed in the recorded voltage-time histories (Figures 8.25 to 8.28). Therefore, the S_{VH}-wave velocity between sensors was determined by fitting a single-frequency sinusoidal model to the

signal (similar to the method employed by Park (2010)). At depths below the vibroseis load plate greater than about 19 in. (48 cm), shear moduli were determined using the unit weight of the soil (100 pcf (1600 kg/m^3)) and the velocities of the S_{VH} waves between adjacent sensors. In this manner, the G and G/G_{max} values were successfully determined over a shear strain (γ) range from about 0.0004% to 0.006%, and the results are presented in the form of G – log γ and G/G_{max} – log γ relationships (see Figure 9.4).

In the steady-state horizontal excitation tests conducted at Site 2, neither Thumper nor T-Rex was capable of generating purely horizontal motion due to rocking/rotation of the shakers' load plates. In general, the amount of vertical motion (relative to the horizontal motion) was much higher when Thumper was used, and it is believed that this amount of vertical motion adversely affected evaluation of the G – log γ relationships

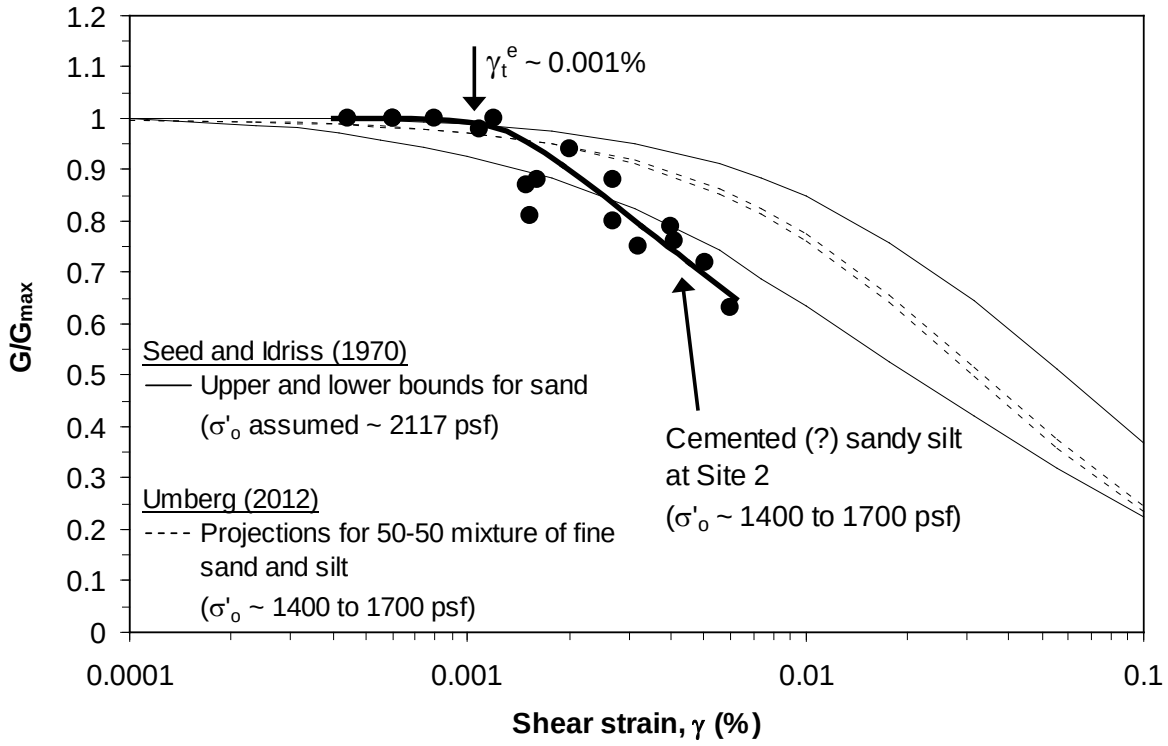

Figure 9.4. Comparison of G/G_{max} – log γ relationships for Site 2 with those proposed by Seed and Idriss (1970) and Umberg (2012)

using Thumper. The amount of relative vertical motion generated by T-Rex was much less and allowed determination of shear moduli over a wide range in shear strains (provided the shear strains are evaluated using a 4-node displacement-based method). The G/G_{max} – log γ relationship determined using T-Rex decreases with increasing shear strain and generally exhibits more nonlinearity than the curves for an uncemented sand (Seed and Idriss, 1970) and a sandy silt (Umberg, 2012), as shown in Figure 9.4. The more rapid decrease in G/G_{max} – log γ is representative of a lightly-cemented material. Similar results were reported by Park (2010) for a highly-cemented alluvium (see Figure 8.36).

As seen in Figure 9.4, the threshold shear strain at Site 2 is about 0.001%. This is essentially the same strain level as the threshold axial strain at which the M/M_{max} – log ε relationships determined in Stages 2 and 5 became nonlinear, as shown in Figure 9.5.

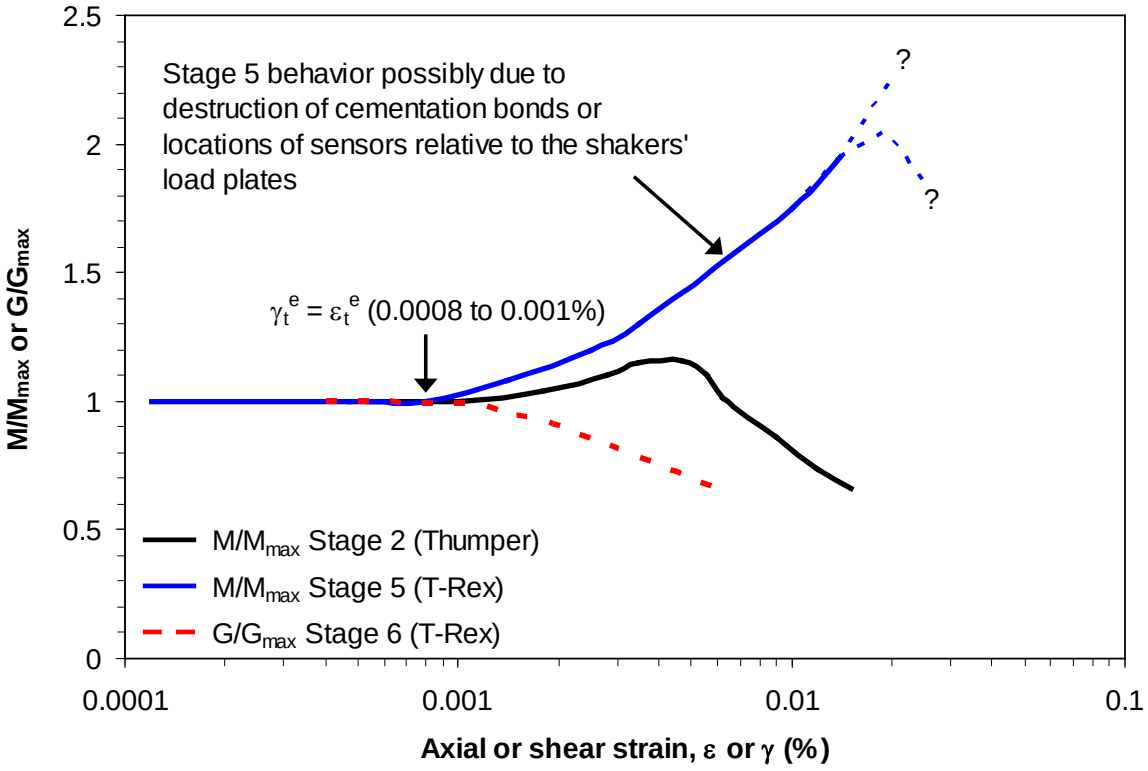

Figure 9.5. Average M/M_{max} – log ε and G/G_{max} – log γ relationships for Site 2

Additionally, as the strain level increases beyond about 0.007% strain, the M/M_{max} (in Stage 2) decreases with increasing strain at approximately the same rate as the G/G_{max} – log γ relationship.

9.3 RECOMMENDATIONS

The following recommendations are made to improve the quality of the current field test method and the resulting measurements.

1. A need exists for a better method to estimate the effective stresses in the field. In this study, the effective stresses were estimated by first determining the suction stress in the laboratory. Then, this value of suction stress was assumed to be constant. However, the suction stress in the field is unlikely to be constant at all locations and at all times. The errors associated with this assumption are unknown.

2. Since it stands to reason that the level of lateral constraint provided by the large load plate of T-Rex is higher than with Thumper, T-Rex is better suited for the generation and measurement of fully-constrained compression waves. Therefore, sinusoidal vertical excitations with T-Rex should probably be applied earlier in the staged loading sequence, i.e. before the use of Thumper (if Thumper is even used). In this manner, it can be determined whether the large increase in M/M_{max} with increasing axial strain observed in this study when using T-Rex is due to the breakdown of cementation (as assumed here) or is actually a function of the level of lateral constraint provided by T-Rex.

3. As noted in Chapter 5 and in Section 9.2, there is some evidence which suggests that the behavior of the M/M_{max} – log ε relationship is dependent on σ'_v. Since the load plates of the shakers were positioned directly on the ground surface in

this study, the range of σ'_v that could be applied with T-Rex was about the same as with Thumper. Therefore, to examine the behavior of M/M_{max} at higher confining pressures, T-Rex should probably be used in conjunction with another vertical shaker like "Raptor." These two shakers would phase together and be used to load a large rectangular concrete slab constructed at the site.

4. As noted in the conclusions in Section 9.2, the investigation of the linear and nonlinear shear moduli in this study with Thumper was generally less successful than in Park's (2010) study. One possible reason for this is that the load plates of the shakers were placed in direct contact with the native soil in both the vertical and horizontal sinusoidal excitation tests. While this arrangement is helpful in inducing more lateral constraint in the vertical excitation tests, this could actually be detrimental in the horizontal excitation tests since the contact between the load plates and the soil is questionable. Park (2010) conducted his horizontal sinusoidal excitation tests with the load plates of the shakers positioned on top of a cast-in-place concrete footing. The contact between the footing and the soil in this arrangement is undoubtedly better than in this study. Therefore, methods should be explored to increase the amount of contact between the vibroseis load plates and the soil.

5. The feasibility of using advanced analysis techniques should be explored. In this study, the cross-correlation technique was used to determine the P_V-wave velocity between sensors since the voltage-time histories in this case were often asymmetric. This asymmetric shape prevented the satisfactory fit of a single-frequency sinusoidal model to the signal. While the cross-correlation technique was successful and relatively fast, alternative analysis techniques could include: (1) the use of multi-frequency sinusoidal models in the time domain or (2) frequency domain filtering of the input signal to remove all frequencies in the signal except the driving frequency of the vibroseis.

6. As noted in Sections 8.2 and 8.3, the calculated P_V- and S_{VH}-wave velocities in the steady-state excitation tests were often either negative or infinite between the shallowest two sensors in the sensor array (midpoint depths between about 10 and 19 in. (25 and 48 cm) below the vibroseis' load plate). This problem was due to the voltage-time record of the first sensor either lagging or being in-phase with the record of the second sensor. This effect was generally the same regardless of the excitation frequency or vibroseis and was also noted at both Sites 1 and 2. This effect was not reported by Park (2010). It is possible that this phenomenon is a product of shaking directly on the ground surface (as done in this study) which does not occur when the vibroseis' load plate is positioned on top of a concrete footing (as done in Park's study). As such, the amount of nonlinearity induced in this upper layer could be large enough to cause the lagging noted in the shallowest sensor's time histories. It is also possible that the sensor cables were not buried deep enough and consequently came in contact with the load plate of the vibroseis. This observation should be more thoroughly investigated in future studies, and consideration should be given to deeper burial of the exiting portion of the sensor cables.

7. The horizontal motions created during vertical sinusoidal excitations should be more thoroughly investigated to better determine the extents of the lateral constraint provided by the vibroseis. This could be accomplished by constructing an embedded sensor array of greater horizontal dimensions than the load plate of the vibroseis. If the lateral constraint is indeed greater within a wedge of soil directly beneath the load plate (as assumed in this research), the horizontal motions should be less within this zone than the horizontal motions recorded by the sensors further from the centerline of the load plate.

APPENDIX A: SOIL PROFILE AT SITE 2

Following the test programs described in Chapter 6, a cased and grouted borehole was installed on September 28, 2011, at Site 2. This borehole was installed to a depth of 75 ft to allow future downhole seismic testing at this site. The boring log detailing the soil profile at this site is shown in Figure A.1.

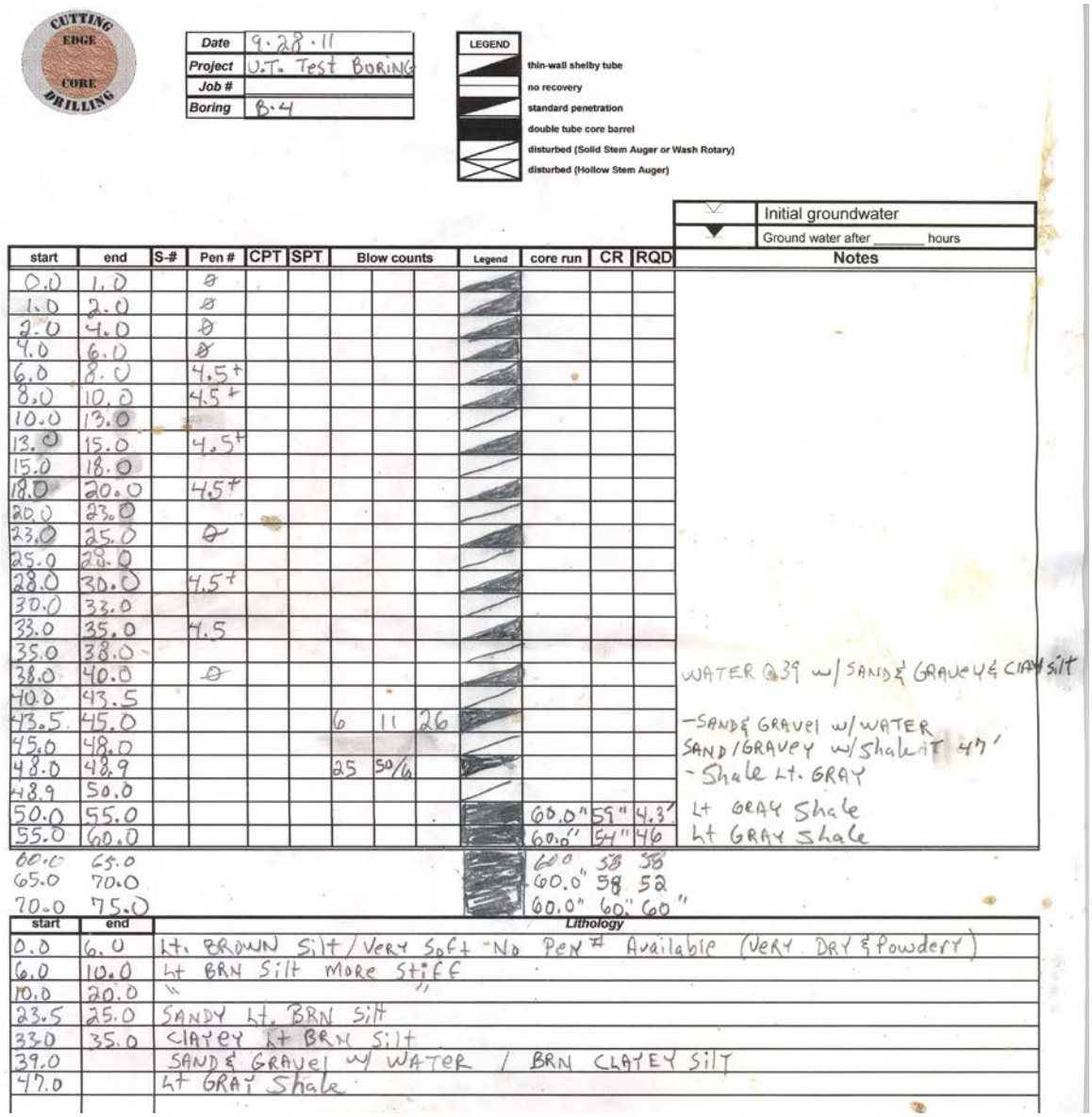

Figure A.1. Driller's log from the deep borehole installation at Site 2

APPENDIX B: TRIAXIAL TESTS ON REMOLDED SPECIMENS FROM SITE 2

Due to the extremely dry conditions at Site 2, an approximate method was used to estimate the suction stress in the field as described in Chapter 6. To use this method, some knowledge of the shear strength of the unsaturated soil was required. Therefore, laboratory triaxial strength tests were performed on remolded specimens taken from Site 2 at a depth of 2 ft (0.61 m).

The remolded specimens were compacted using the split-mold and drop hammer shown in Figure B.1. The split-mold had an inside diameter of 1.5 in. (3.8 cm) and a height of 3.0 in. (7.6 cm). The drop hammer consisted of a 2.2-lb (1.0-kg) weight dropped from a height of 11.6 in. (29.5 cm). Accordingly, the hammer delivered

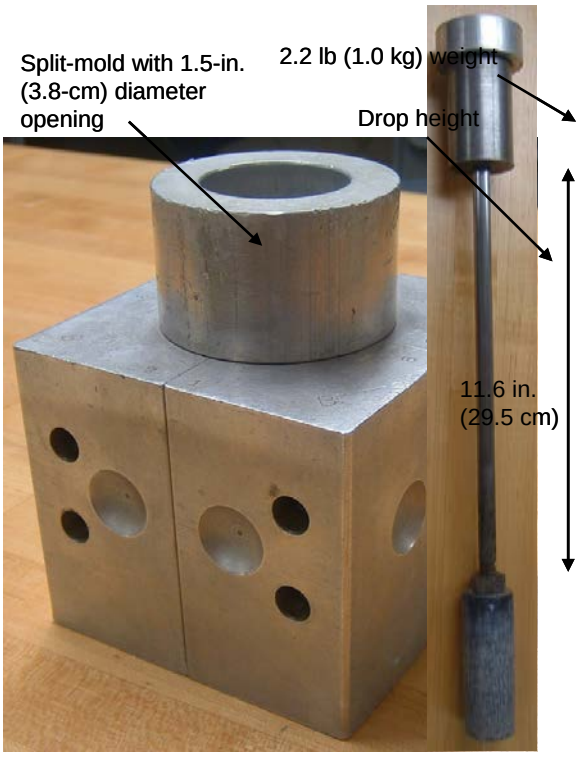

Figure B.1. Split-mold and drop hammer used to compact soil specimens

approximately 2.1 lb-ft (2.8 N-m) of energy to the soil with each blow. The diameter of the end of the hammer was slightly less than 3.0 in. (7.6 cm) to allow the hammer to fit inside the split-mold. Three soil specimens were compacted in the split-mold using an under-compaction technique consisting of six lifts with three hammer blows per lift. The average total unit weight and water content of the specimens was about 96.5 pcf (1546 kg/m^3) and 4.5%, respectively. The properties of the three specimens are summarized in Table B.1.

Table B.1. Properties of remolded specimens used in shear strength tests

Specimen ID	Volume (in^3)	Weight (g)	Water content (%)	Total unit weight (pcf)	Dry unit weight (pcf)
1	5.271	133.4	4.50	96.2	92.1
2	5.271	134.4	4.49	96.9	92.8
3	5.271	133.5	4.48	96.3	92.2

After the specimens were prepared, each was allowed to equilibrate overnight before being placed in the triaxial cell. The specimen was covered with a membrane, the cell was filled with water, and a confining pressure was applied to the specimen. In these tests, the confining pressures used were 5, 10, and 20 psi (34.5, 68.9, and 138.9 kPa). After the confining pressure was applied, the drainage valves were opened, and the specimen was again allowed to "equilibrate" under this confining pressure for one hour. After this time had passed, the drainage valves were closed, and the specimen was sheared undrained using a GeoJac load control module (shown in Figure B.2) at a rate of 0.13% strain per minute (0.0038 in/min or 0.097 mm/min). The load-strain plots for each of the three tests are shown in Figures B.3 to B.5, and the results of the tests are summarized in Table B.2. The Mohr's circles for each test and the resulting total stress failure envelope are shown in Figure B.6. The friction angle and cohesion determined for these unsaturated specimens was 37^o and 4 psi, respectively, as noted in Figure B.6.

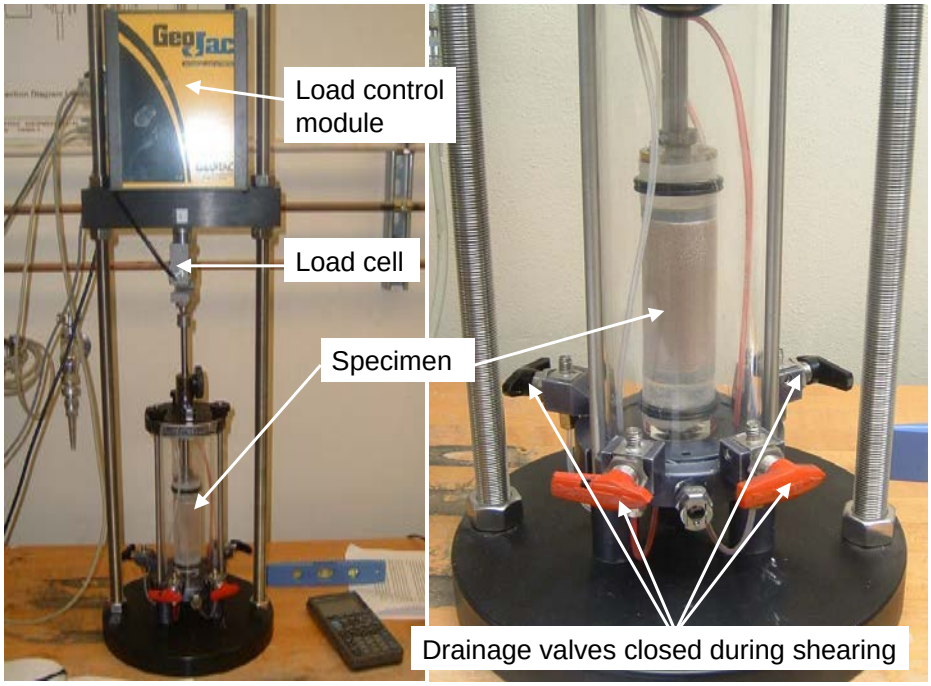

Figure B.2. Undrained triaxial test arrangement

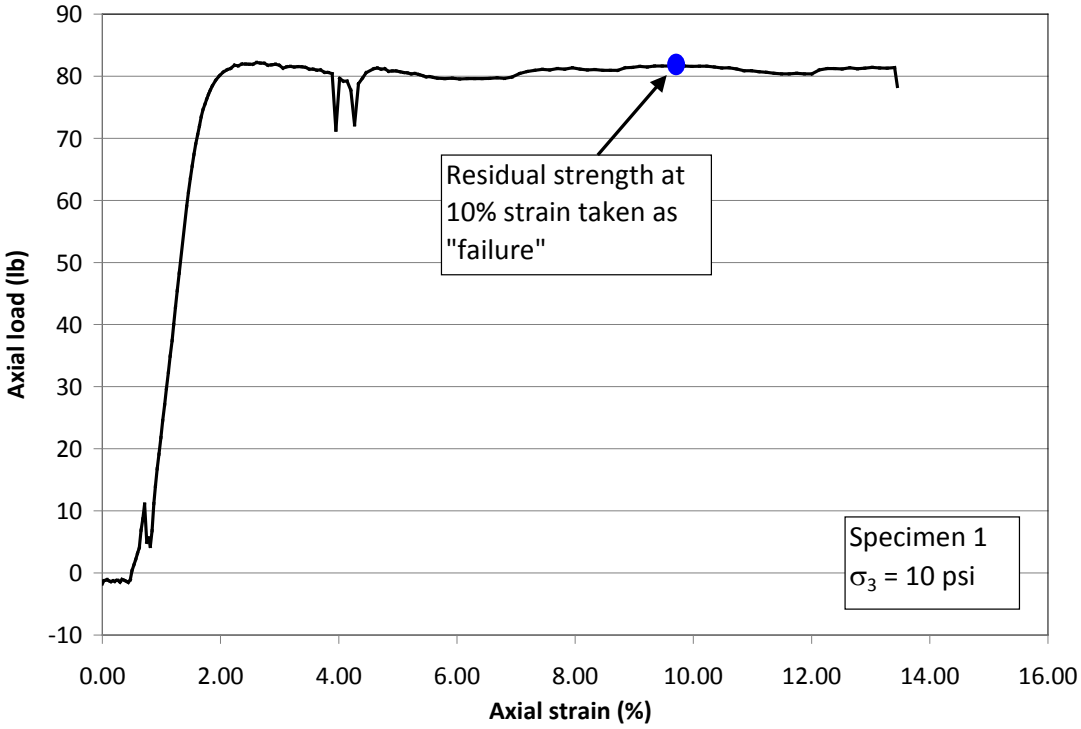

Figure B.3. Loading curve for undrained triaxial test at 10 psi confining pressure

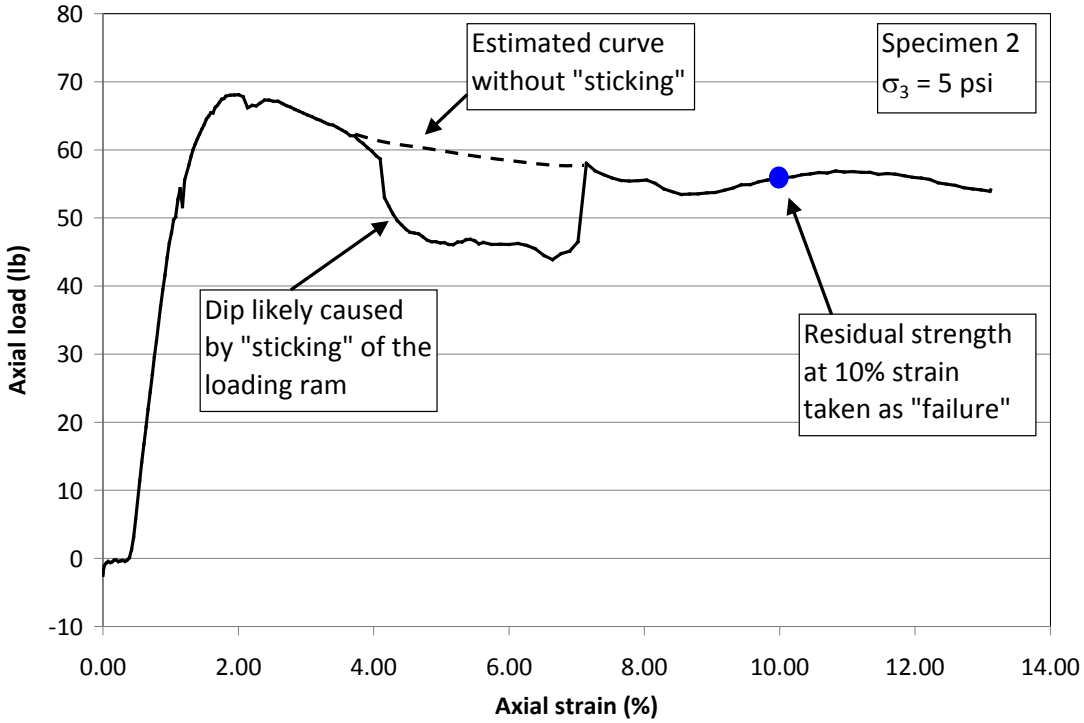

Figure B.4. Loading curve for undrained triaxial test at 5 psi confining pressure

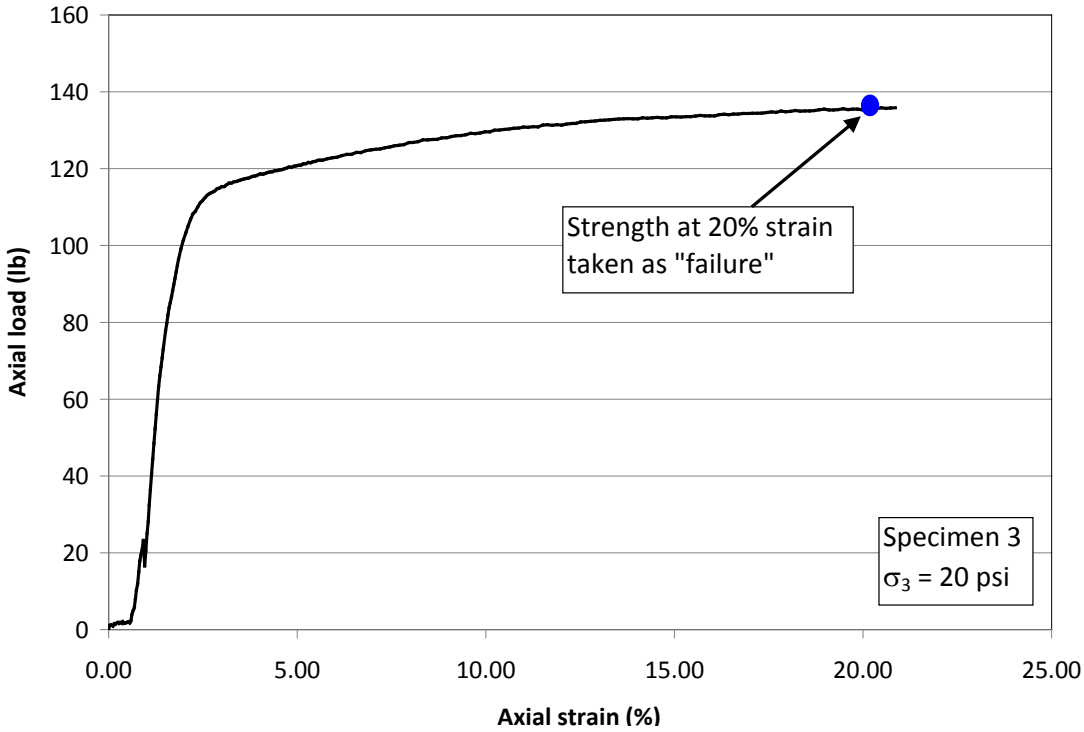

Figure B.5. Loading curve for undrained triaxial test at 20 psi confining pressure

Table B.2. Summary of undrained shear strength tests

Specimen	Minor principal stress, σ_3 (psi)	Major principal stress at failure, σ_{1f} (psi)	Shear stress, $\tau = (\sigma_{1f}-\sigma_3)/2$ (psi)
1	10	56.5	23.25
2	5	37.2	16.1
3	20	96.9	38.45

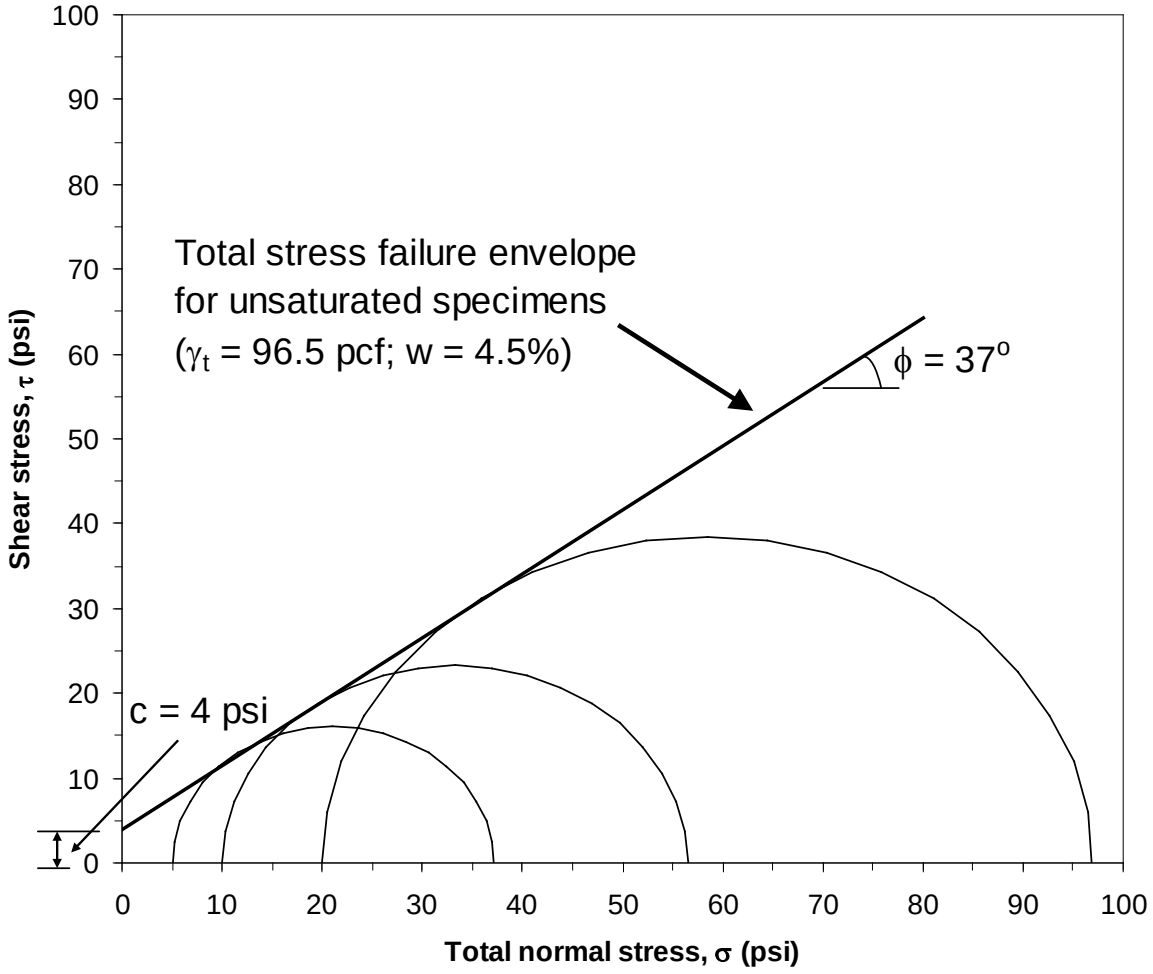

Figure B.6. Total stress failure envelope for remolded specimens from Site 2

APPENDIX C: RAW WAVEFORMS FROM VERTICAL STEADY-STATE EXCITATION TESTS AT SITE 2

As discussed in Chapters 6 and 8, vertical sinusoidal excitations were applied directly to the ground surface above an embedded sensor array at Site 2. Two nees@UTexas vibroseis trucks were used in the staged testing sequence at Site 2: Thumper in Stage 2 and T-Rex in Stage 5 (see Figure 8.1). This appendix provides the raw waveforms recorded by a representative number of sensors at several strain levels in these two stages. While the large volume of data recorded in these stages precludes the inclusion of all of the waveforms here, electronic copies of all data recorded in Stages 2 and 5 are maintained by the research group at The University of Texas at Austin and may be obtained by contacting the Geotechnical Engineering Center at (512) 471-4929.

Note that in the vertical excitation tests, the waveforms recorded by the vertical component of Sensor 11 were very weak compared to the other two sensors at the same depth (Sensors 6 and 2). The amplitude of the vertical response at Sensor 11 was about the same as the amplitudes of the two horizontal components. Therefore, the vertical component of Sensor 11 was assumed to be lost. Additionally, the center of the load plate of Thumper was not centered over the embedded sensor array in Stage 2, but was instead about 6 in. (15 cm) too far West. Accordingly, the Southeast sensor column was only about 2 in. (5 cm) from the edge of Thumper's load plate instead of the intended 9 in. (23 cm). Therefore, the data recorded in Stage 2 by the sensors in the Southeast column (Sensors 8, 7, 6, and 5) were not used in the analysis presented in Chapter 8.

Given the two issues noted in the preceding paragraph, only one complete sensor column (the North column; Sensors 4, 3, 2, and 1) provided good quality data in both Stages 2 and 5. Therefore, only the waveforms from these sensors are provided in this appendix. The waveforms from Stage 2 with Thumper are provided first (Figures C.1 to C.8), followed by the waveforms from Stage 5 with T-Rex (Figures C.9 to C.15).

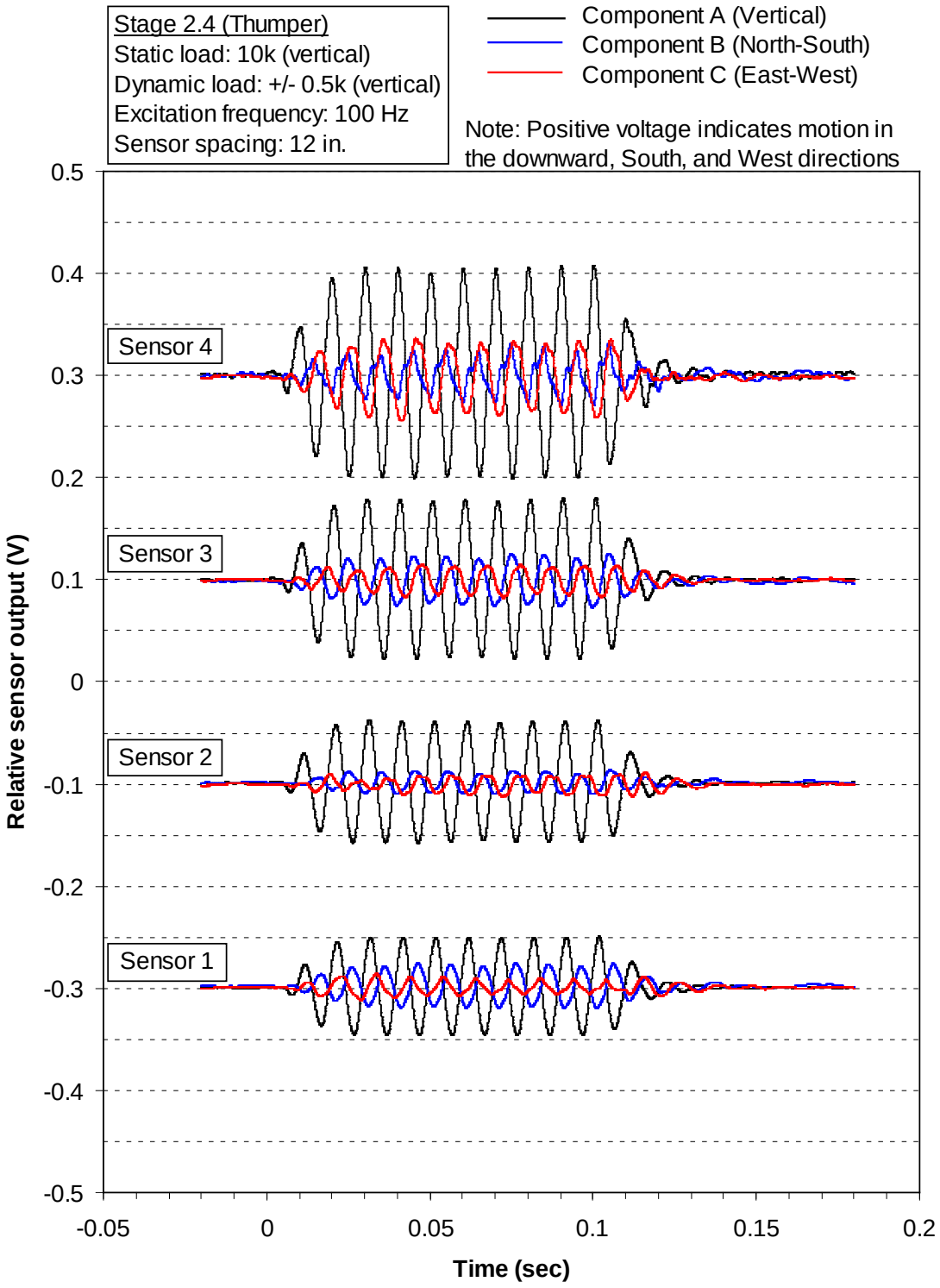

Figure C.1. Voltage-time histories of four sensors in the North column at Site 2 when subjected to a 100 Hz sinusoidal vertical excitation (+/- 0.5k) from Thumper in Stage 2.4

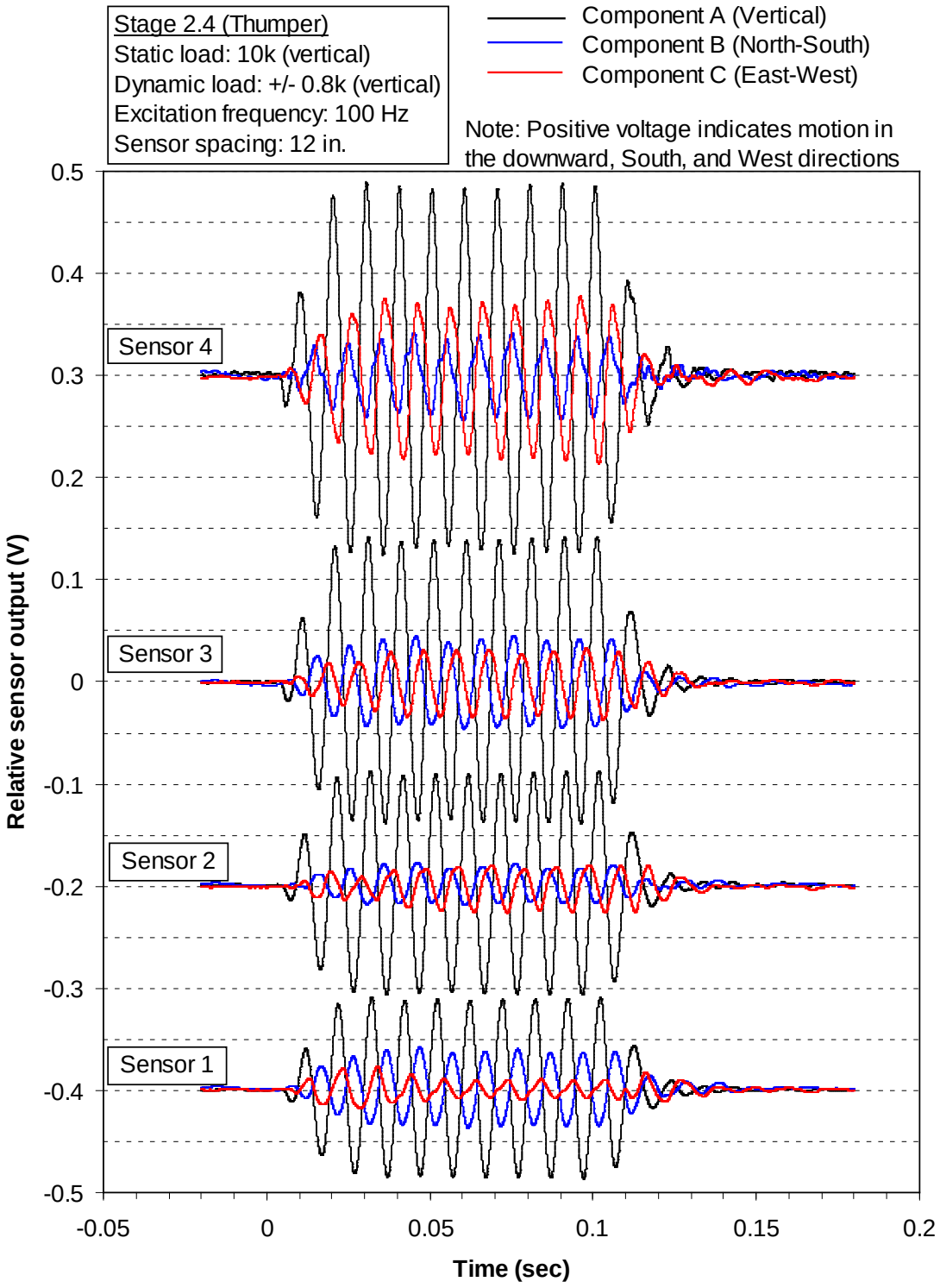

Figure C.2. Voltage-time histories of four sensors in the North column at Site 2 when subjected to a 100 Hz sinusoidal vertical excitation (+/- 0.8k) from Thumper in Stage 2.4

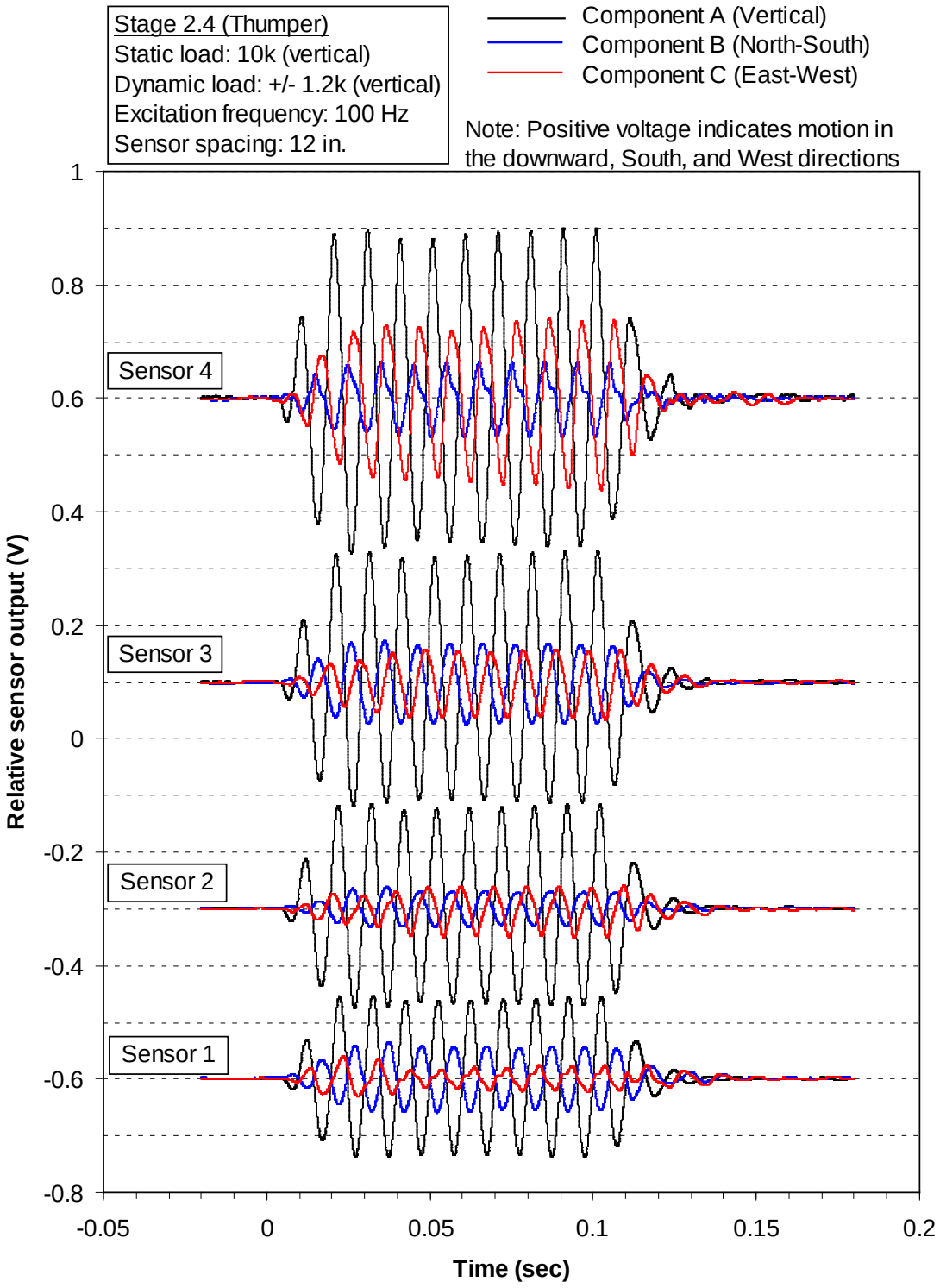

Figure C.3. Voltage-time histories of four sensors in the North column at Site 2 when subjected to a 100 Hz sinusoidal vertical excitation (+/- 1.2k) from Thumper in Stage 2.4

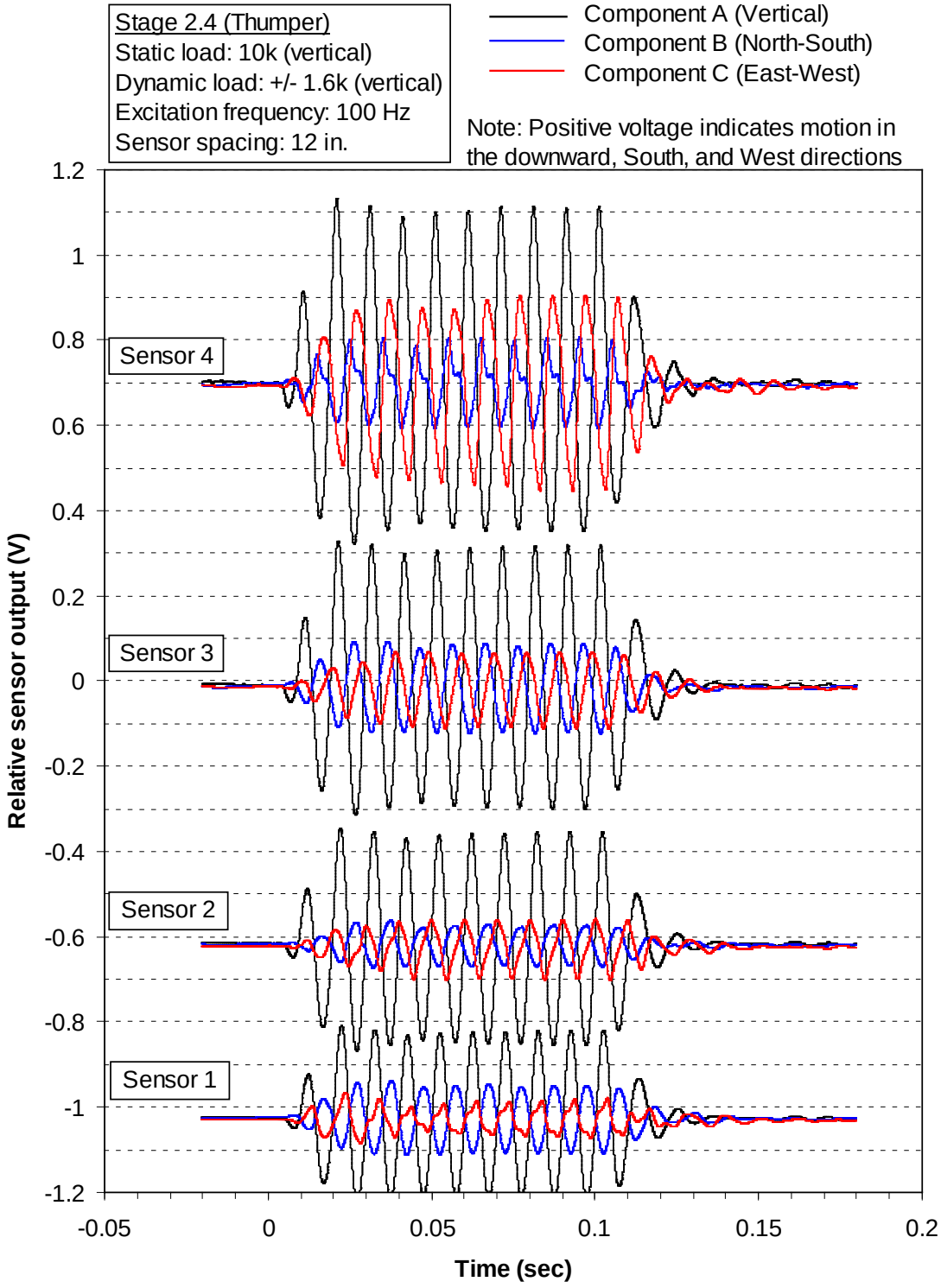

Figure C.4. Voltage-time histories of four sensors in the North column at Site 2 when subjected to a 100 Hz sinusoidal vertical excitation (+/- 1.6k) from Thumper in Stage 2.4

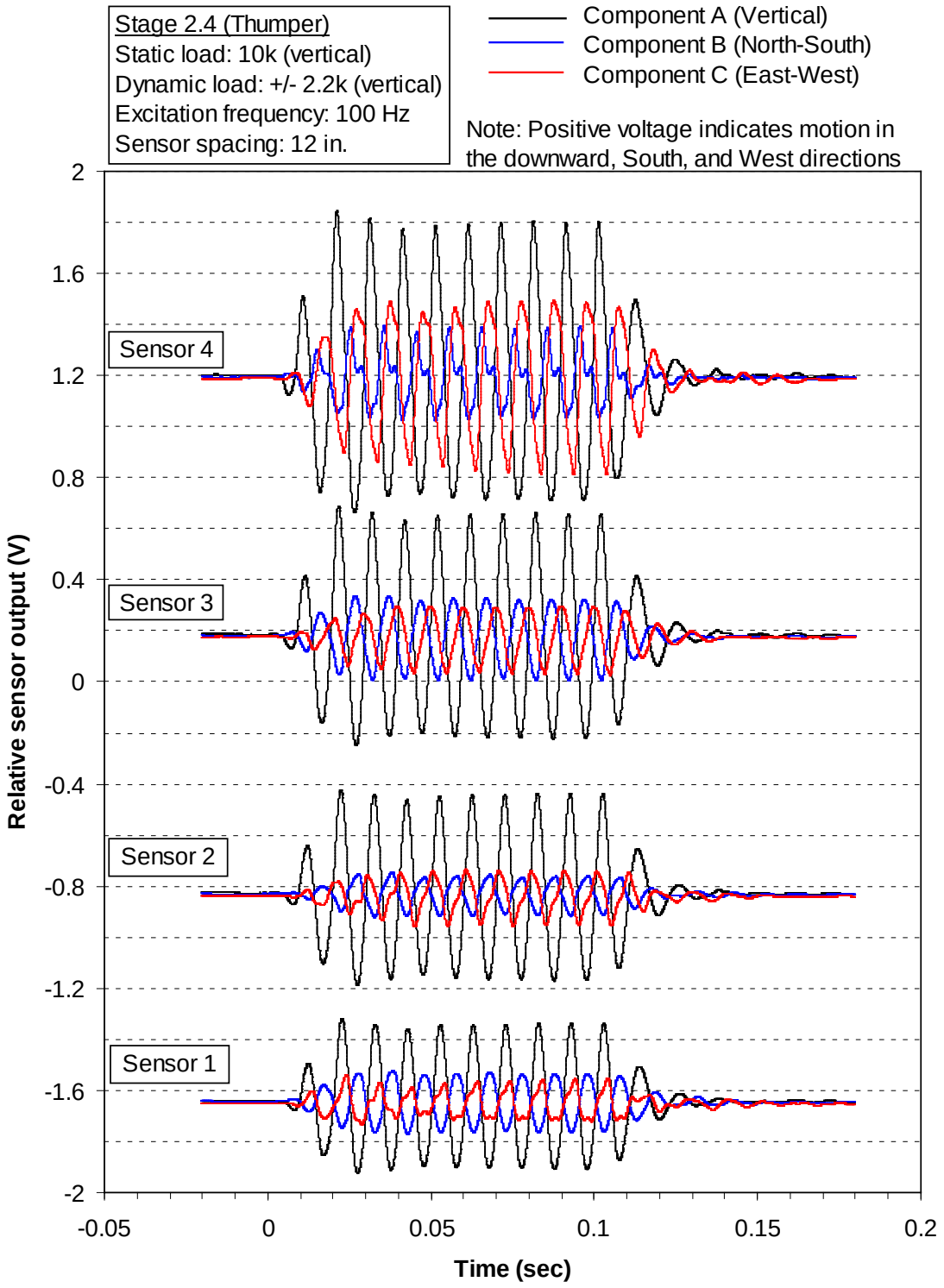

Figure C.5. Voltage-time histories of four sensors in the North column at Site 2 when subjected to a 100 Hz sinusoidal vertical excitation (+/- 2.2k) from Thumper in Stage 2.4

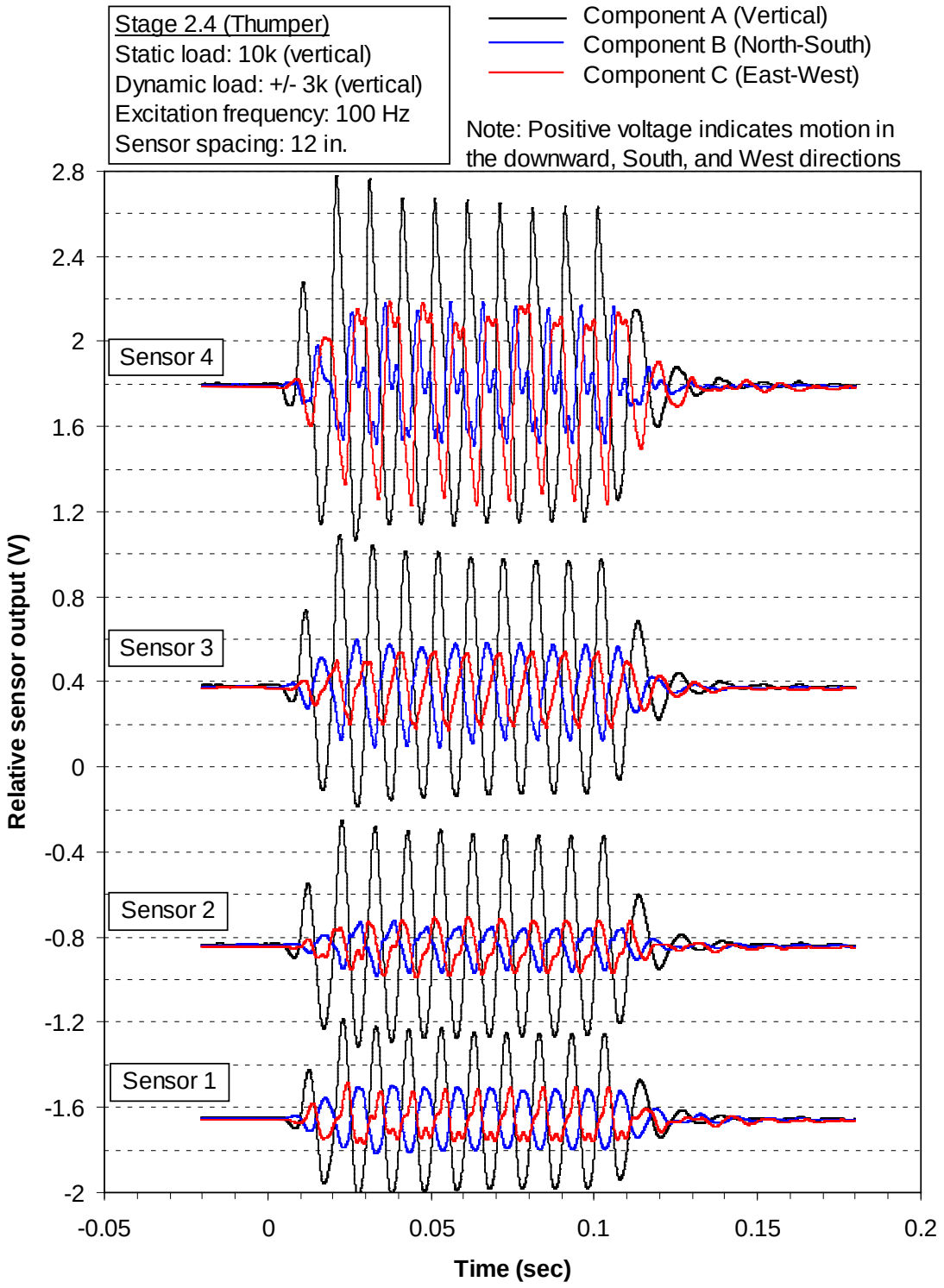

Figure C.6. Voltage-time histories of four sensors in the North column at Site 2 when subjected to a 100 Hz sinusoidal vertical excitation (+/- 3k) from Thumper in Stage 2.4

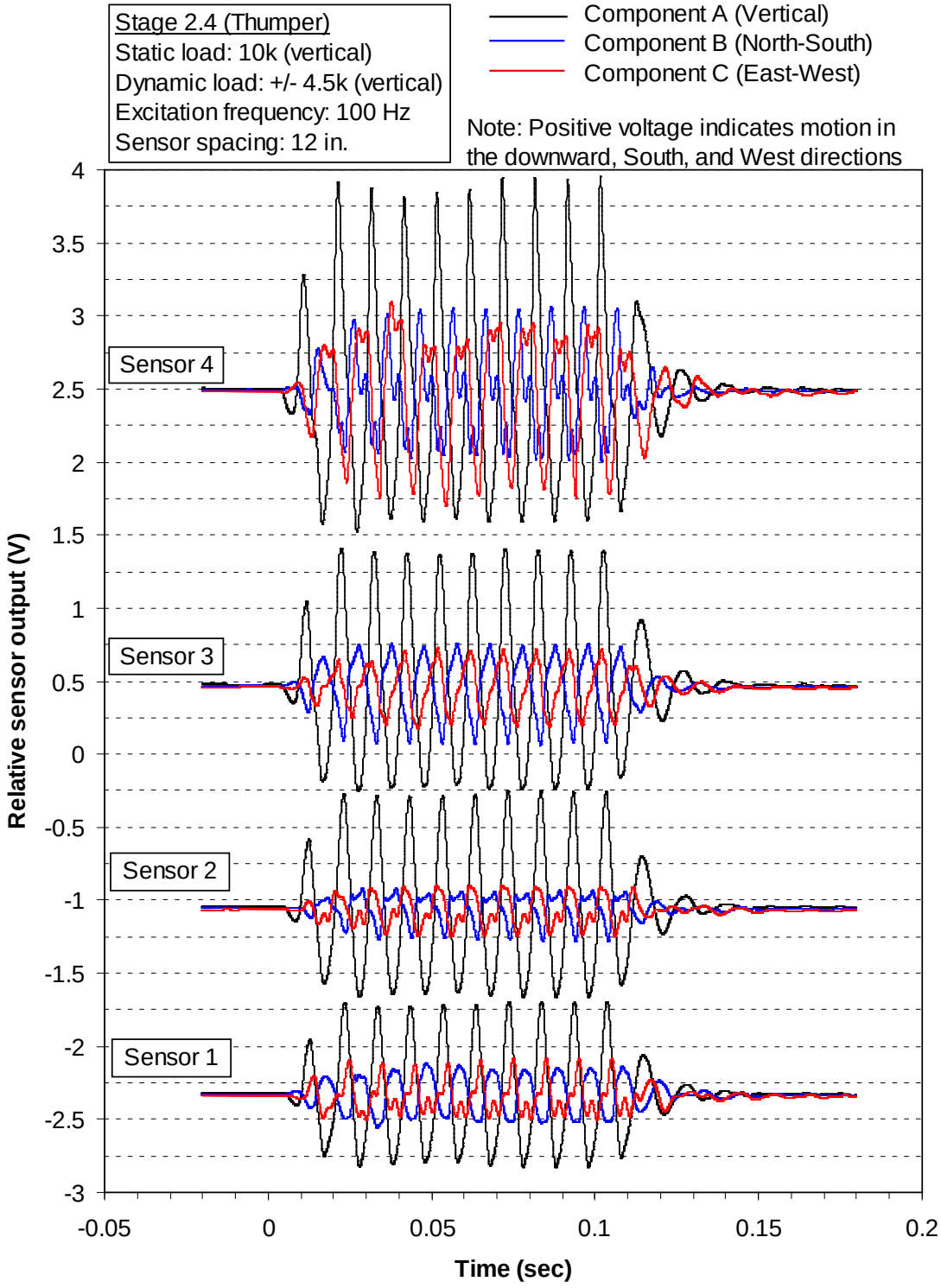

Figure C.7. Voltage-time histories of four sensors in the North column at Site 2 when subjected to a 100 Hz sinusoidal vertical excitation (+/- 4.5k) from Thumper in Stage 2.4

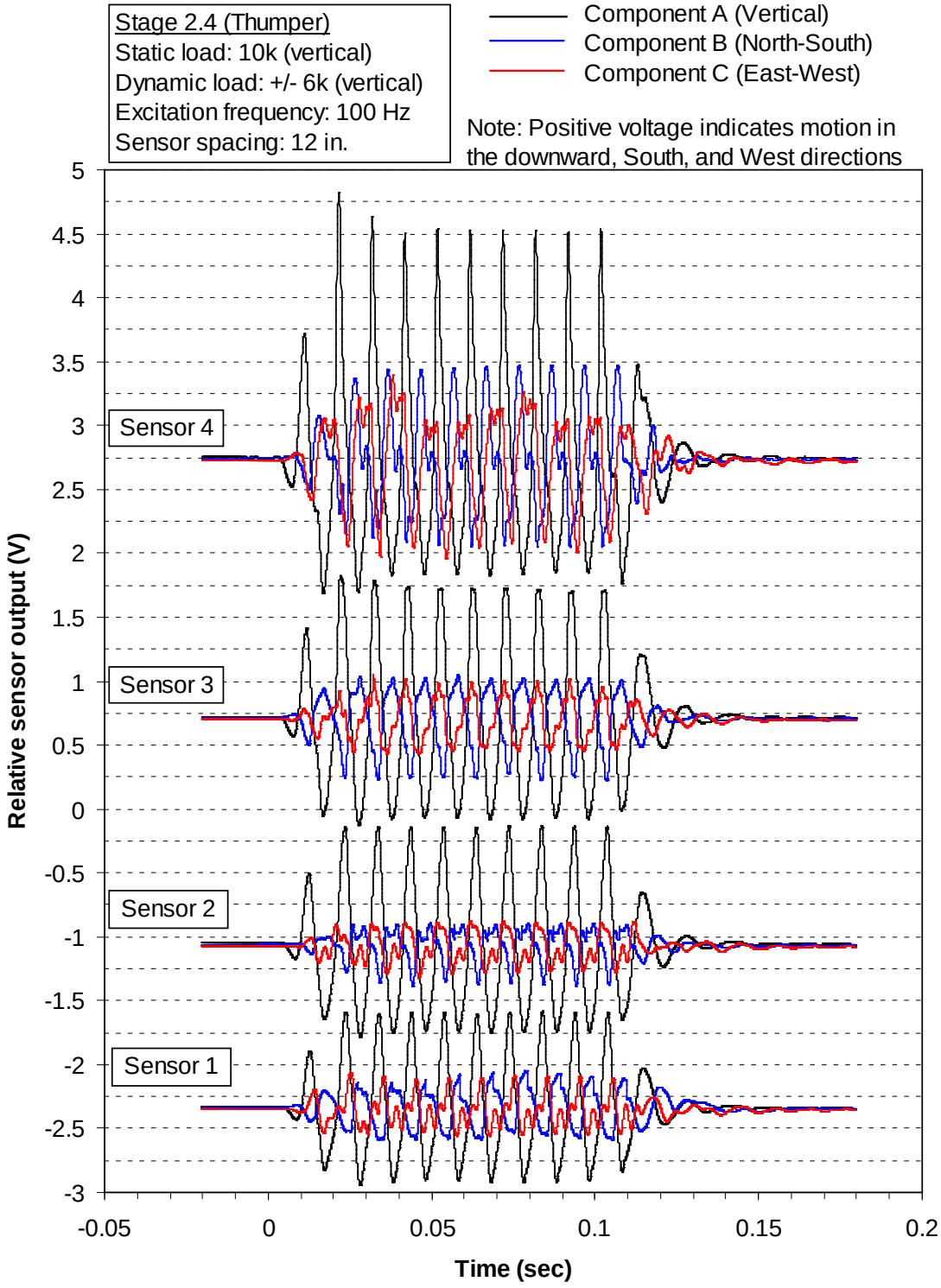

Figure C.8. Voltage-time histories of four sensors in the North column at Site 2 when subjected to a 100 Hz sinusoidal vertical excitation (+/- 6k) from Thumper in Stage 2.4

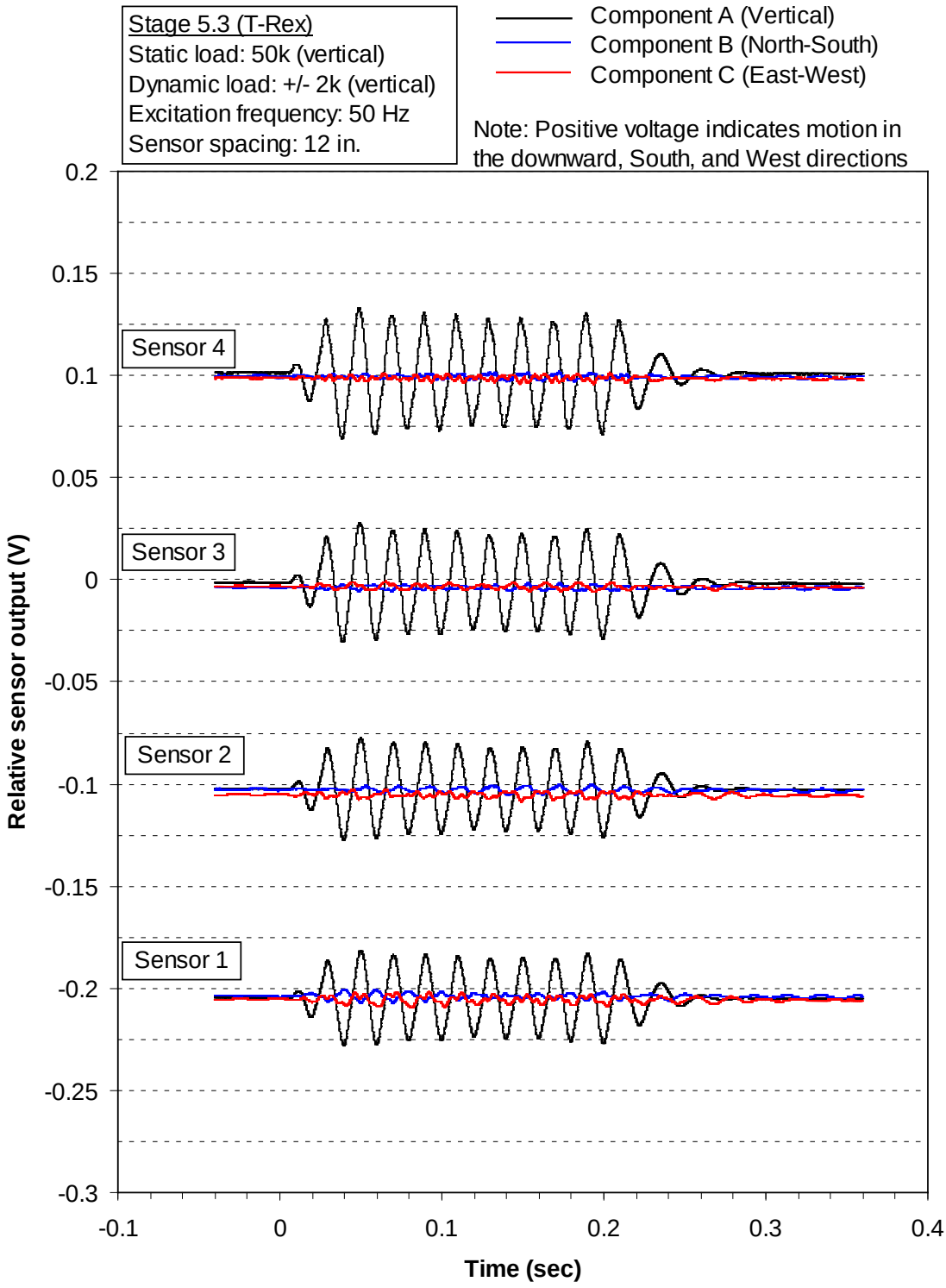

Figure C.9. Voltage-time histories from four sensors in the North column at Site 2 when subjected to a 50 Hz sinusoidal vertical excitation (+/- 2k) from T-Rex in Stage 5.3

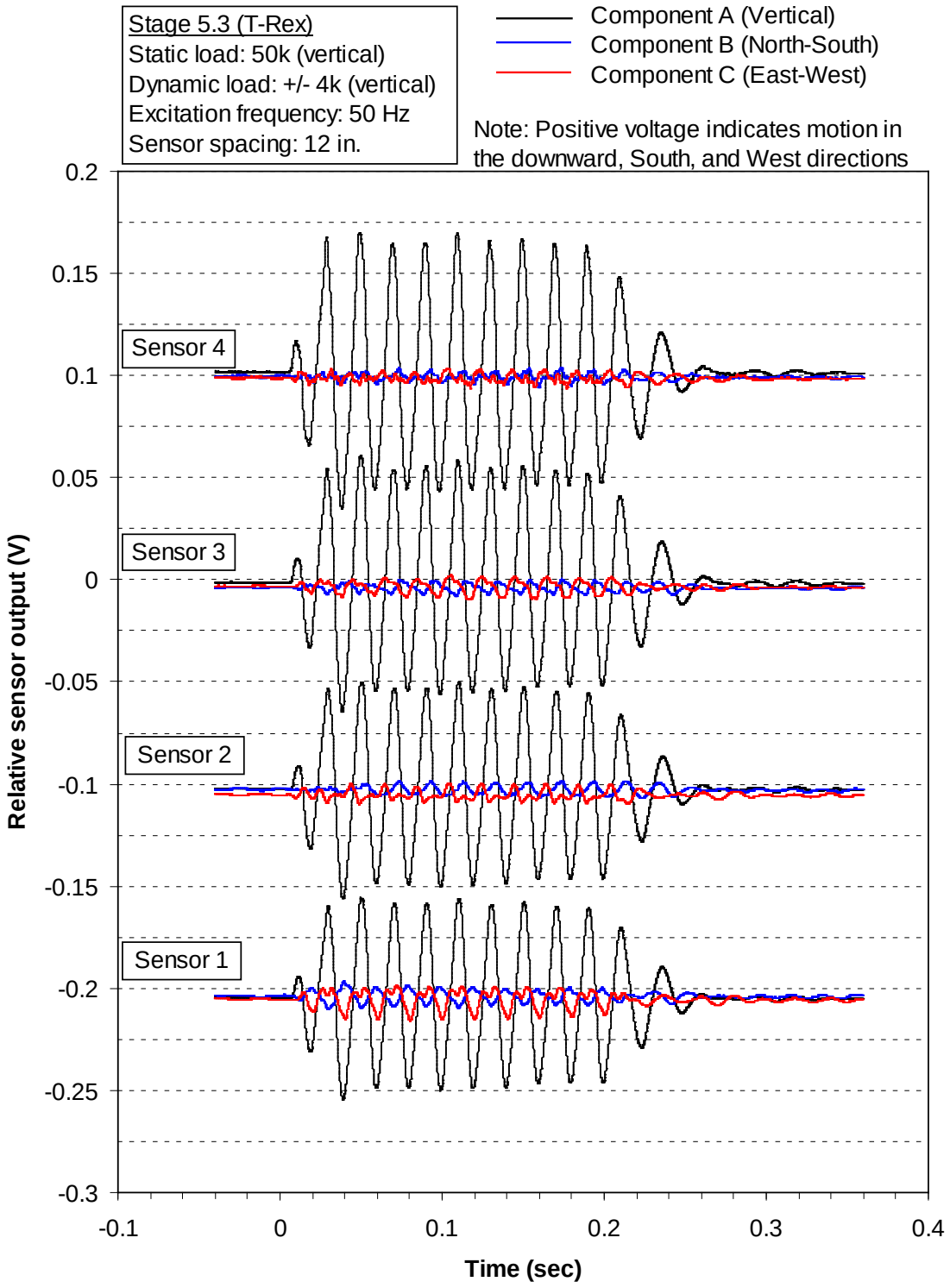

Figure C.10. Voltage-time histories of four sensors in the North column at Site 2 when subjected to a 50 Hz sinusoidal vertical excitation (+/- 4k) from T-Rex in Stage 5.3

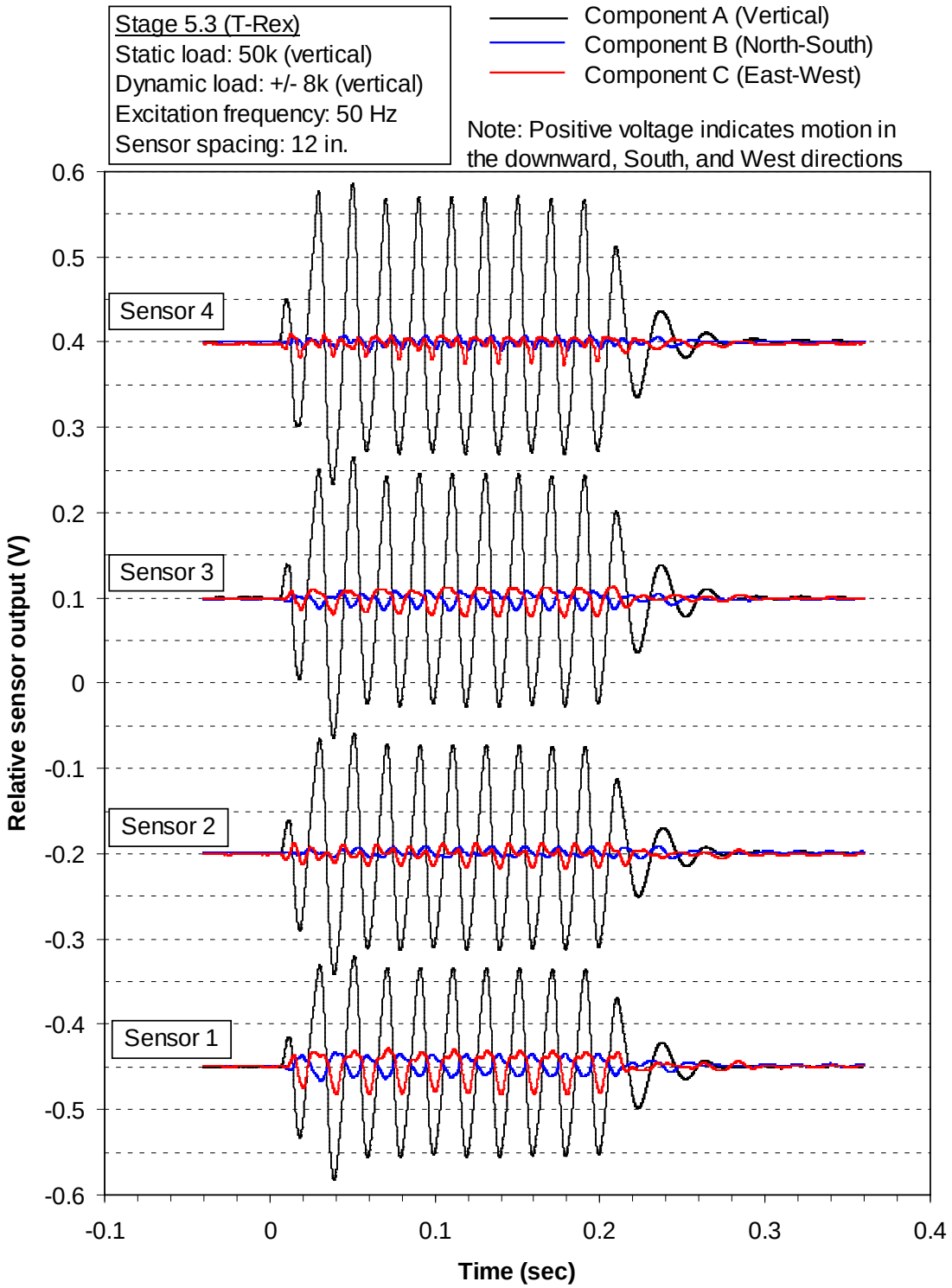

Figure C.11. Voltage-time histories of four sensors in the North column at Site 2 when subjected to a 50 Hz sinusoidal vertical excitation (+/- 8k) from T-Rex in Stage 5.3

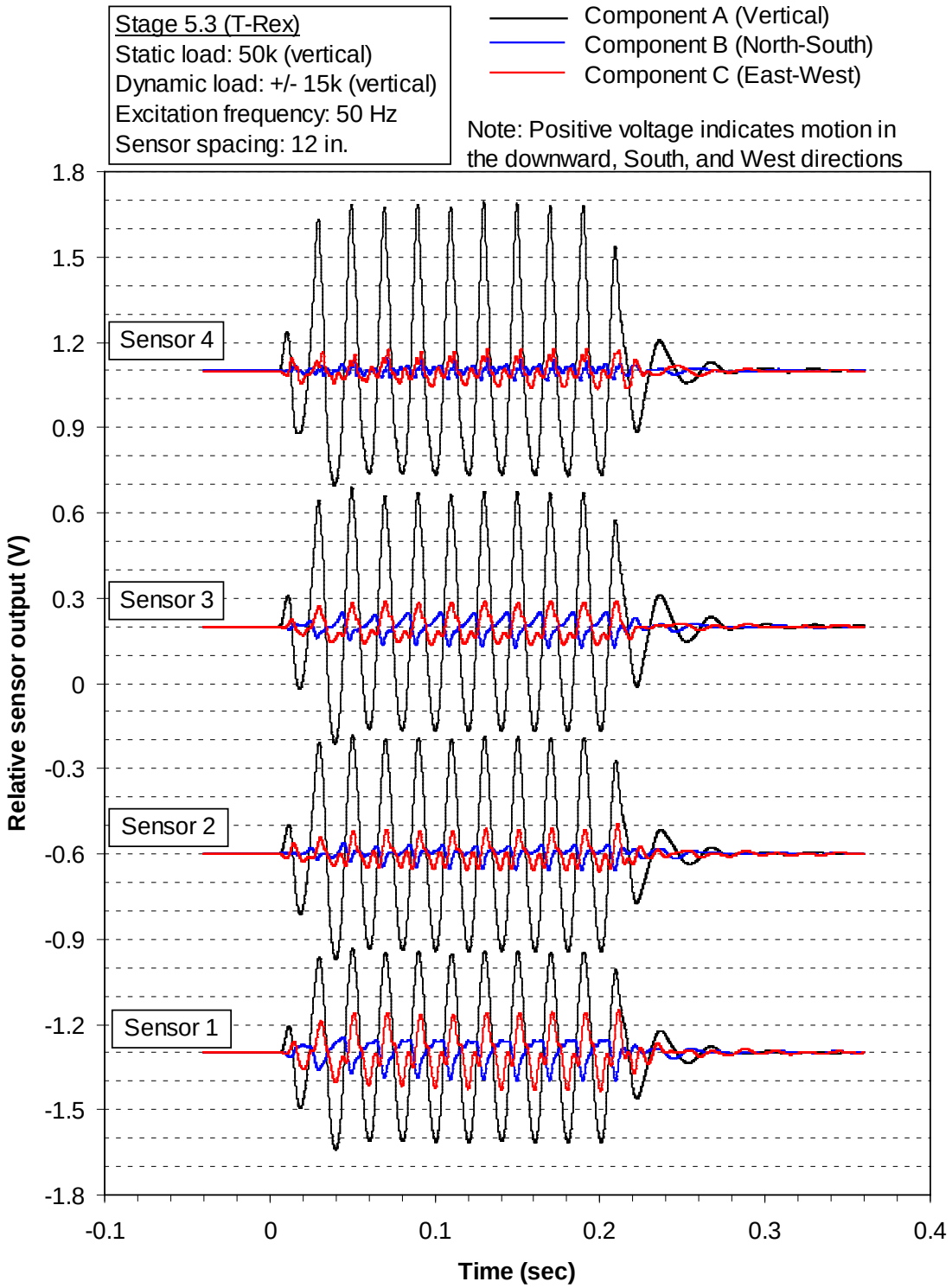

Figure C.12. Voltage-time histories of four sensors in the North column at Site 2 when subjected to a 50 Hz sinusoidal vertical excitation (+/- 15k) from T-Rex in Stage 5.3

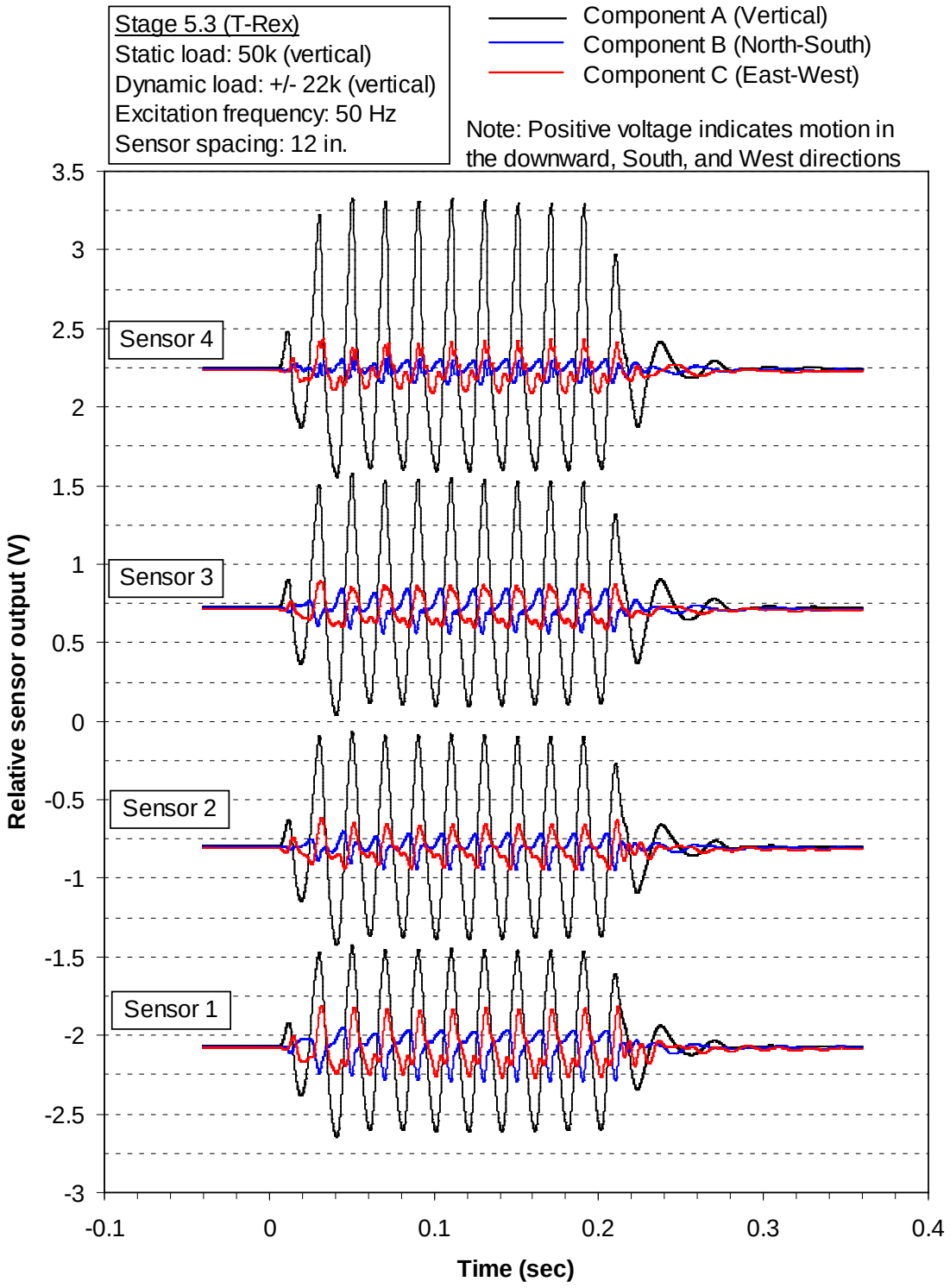

Figure C.13. Voltage-time histories of four sensors in the North column at Site 2 when subjected to a 50 Hz sinusoidal vertical excitation (+/- 22k) from T-Rex in Stage 5.3

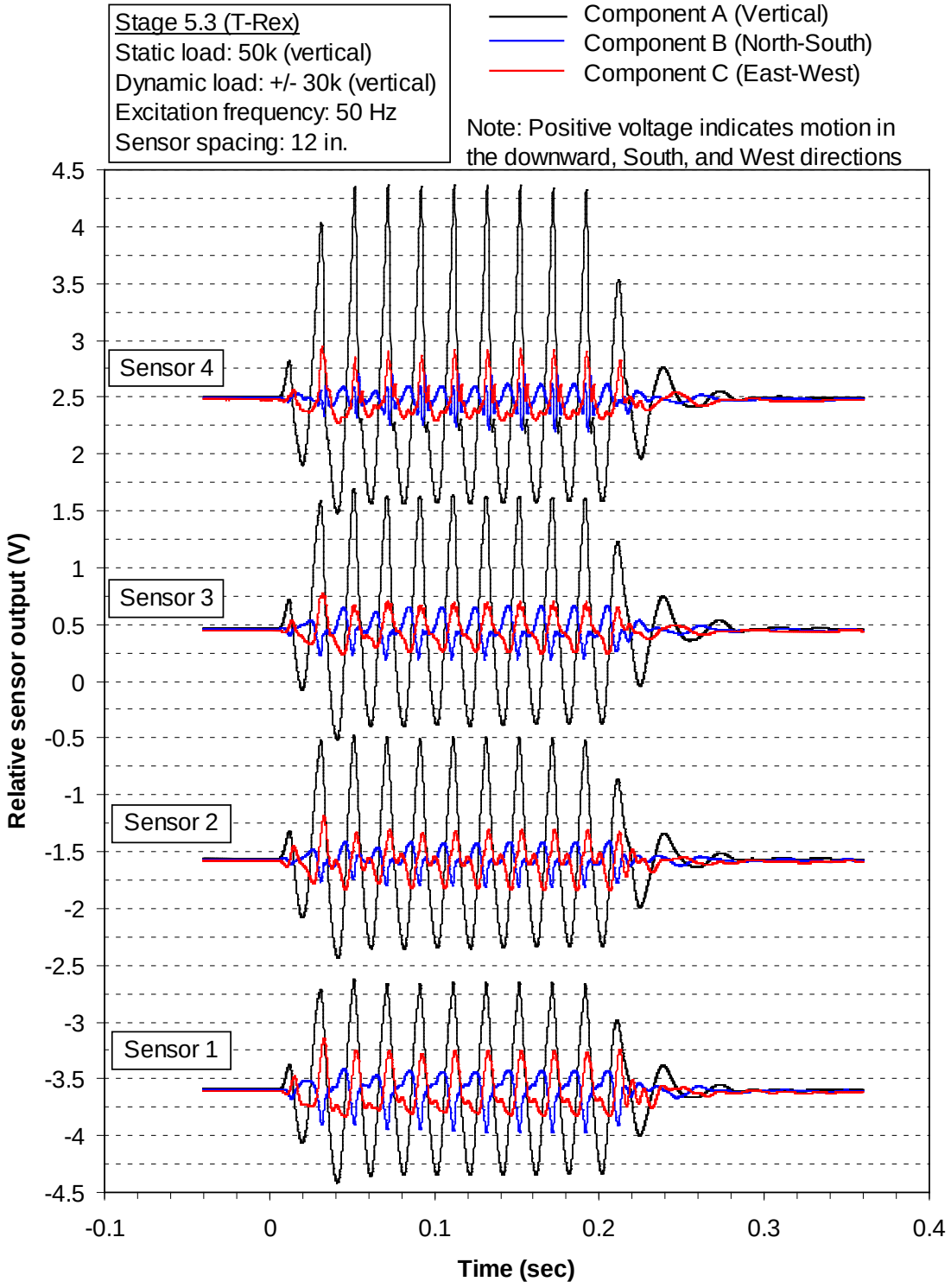

Figure C.14. Voltage-time histories of four sensors in the North column at Site 2 when subjected to a 50 Hz sinusoidal vertical excitation (+/- 30k) from T-Rex in Stage 5.3

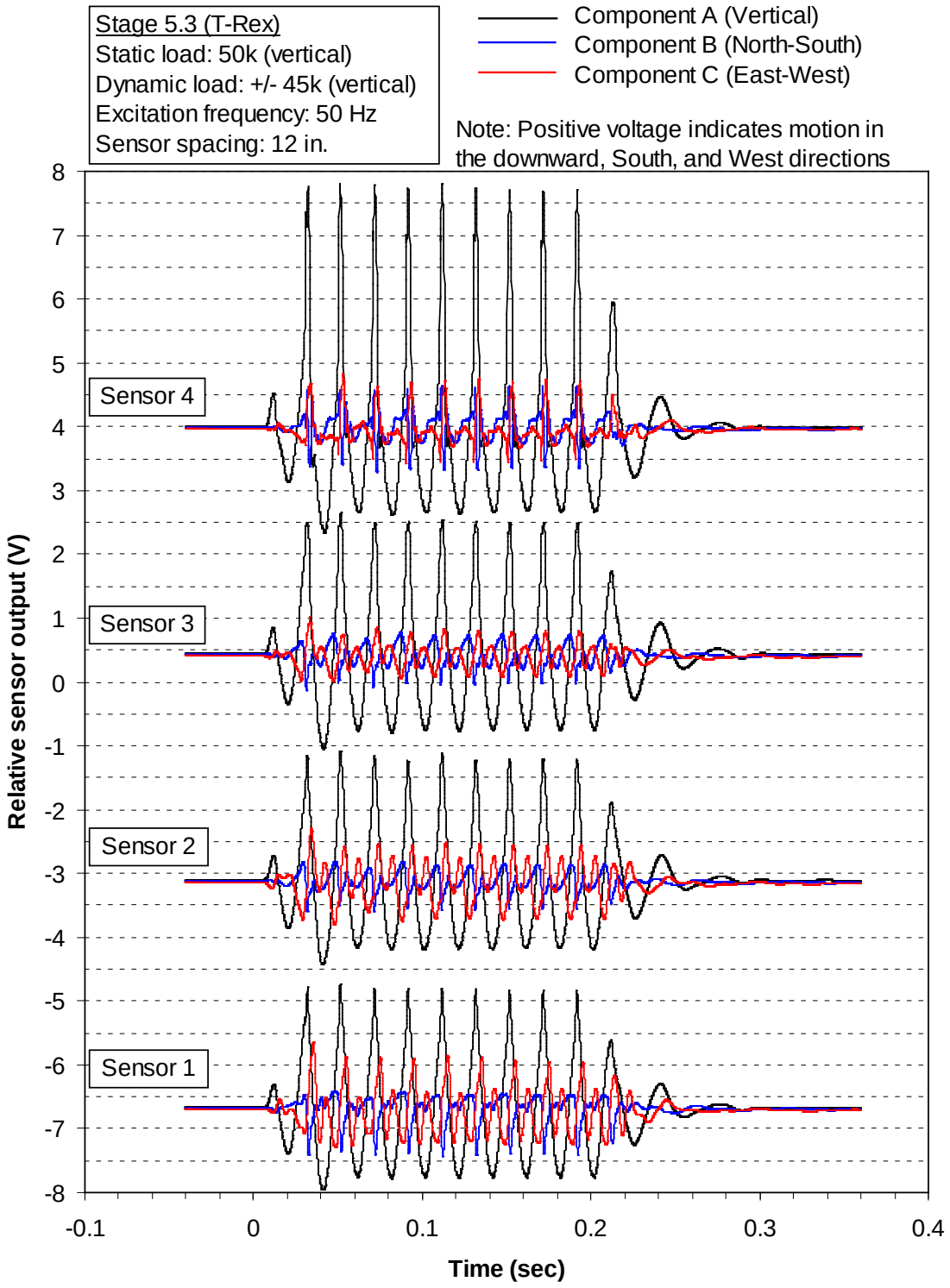

Figure C.15. Voltage-time histories of four sensors in the North column at Site 2 when subjected to a 50 Hz sinusoidal vertical excitation (+/- 45k) from T-Rex in Stage 5.3

APPENDIX D: RAW WAVEFORMS FROM HORIZONTAL STEADY-STATE EXCITATION TESTS AT SITE 2

As discussed in Chapters 6 and 8, horizontal sinusoidal excitations were applied directly to the ground surface above an embedded sensor array at Site 2. Two nees@UTexas vibroseis trucks were used in the staged testing sequence at Site 2: Thumper in Stage 3 and T-Rex in Stage 6 (see Figure 8.1). This appendix provides the raw waveforms recorded by a representative number of sensors at several strain levels in these two stages. While the large volume of data recorded in these stages precludes the inclusion of all of the waveforms here, electronic copies of all data recorded in Stages 3 and 6 are maintained by the research group at The University of Texas at Austin and may be obtained by contacting the Geotechnical Engineering Center at (512) 471-4929.

As discussed in Appendix C, only one complete sensor column (the North column; Sensors 4, 3, 2, and 1) provided good quality data in all the vertical excitation tests conducted in Stages 2 and 5. Therefore, to allow for a direct comparison of the nonlinear constrained and shear moduli at the same locations, only the waveforms from these same sensors in the horizontal excitation tests (Stages 3 and 6) are provided in this appendix. The waveforms from Stage 3 with Thumper are provided first (Figures D.1 to D.8), followed by the waveforms from Stage 6 with T-Rex (Figures D.9 to D.13).

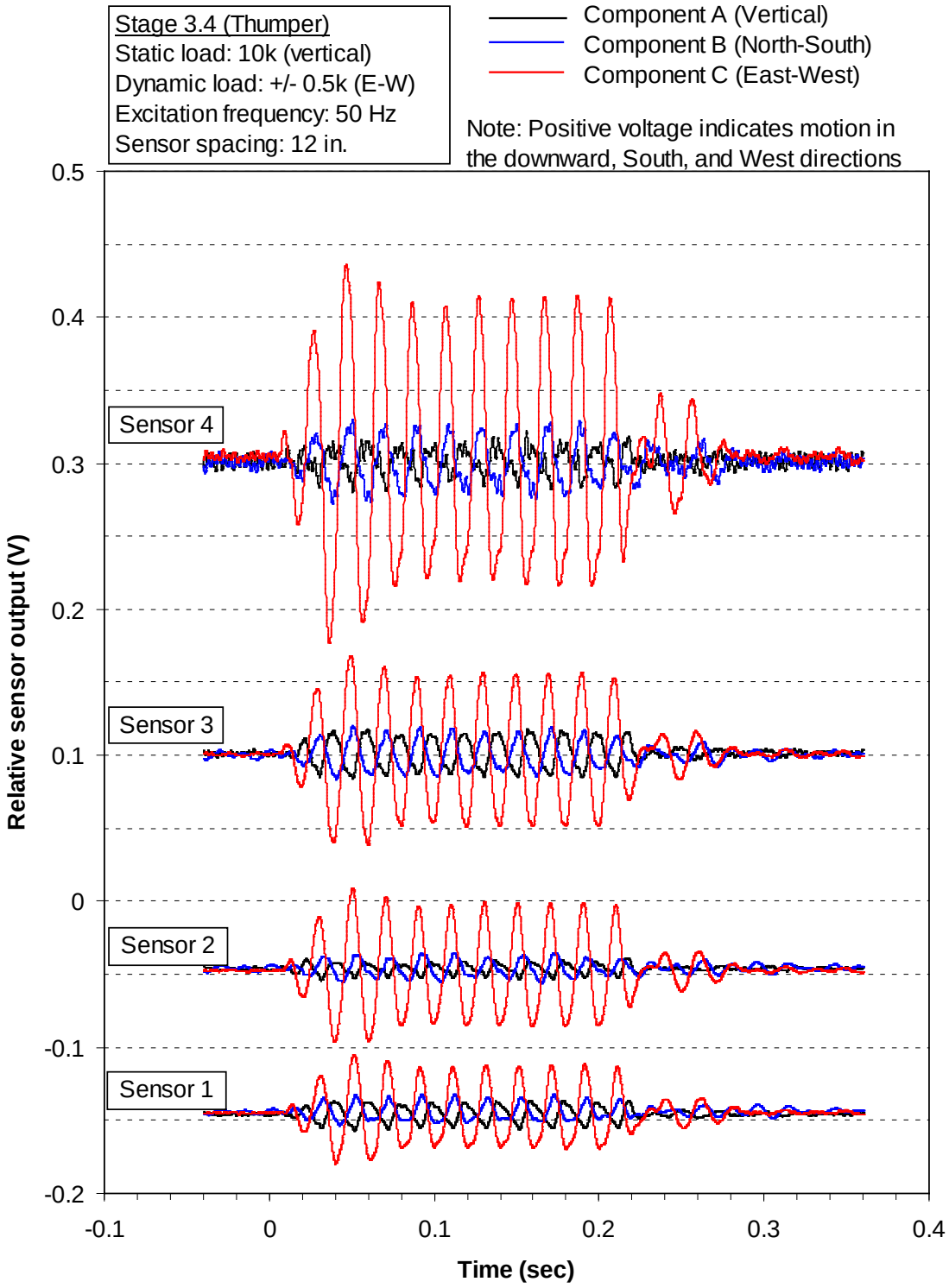

Figure D.1. Voltage-time histories of four sensors in the North column at Site 2 when subjected to a 50-Hz horizontal excitation (+/- 0.5k) from Thumper in Stage 3.4

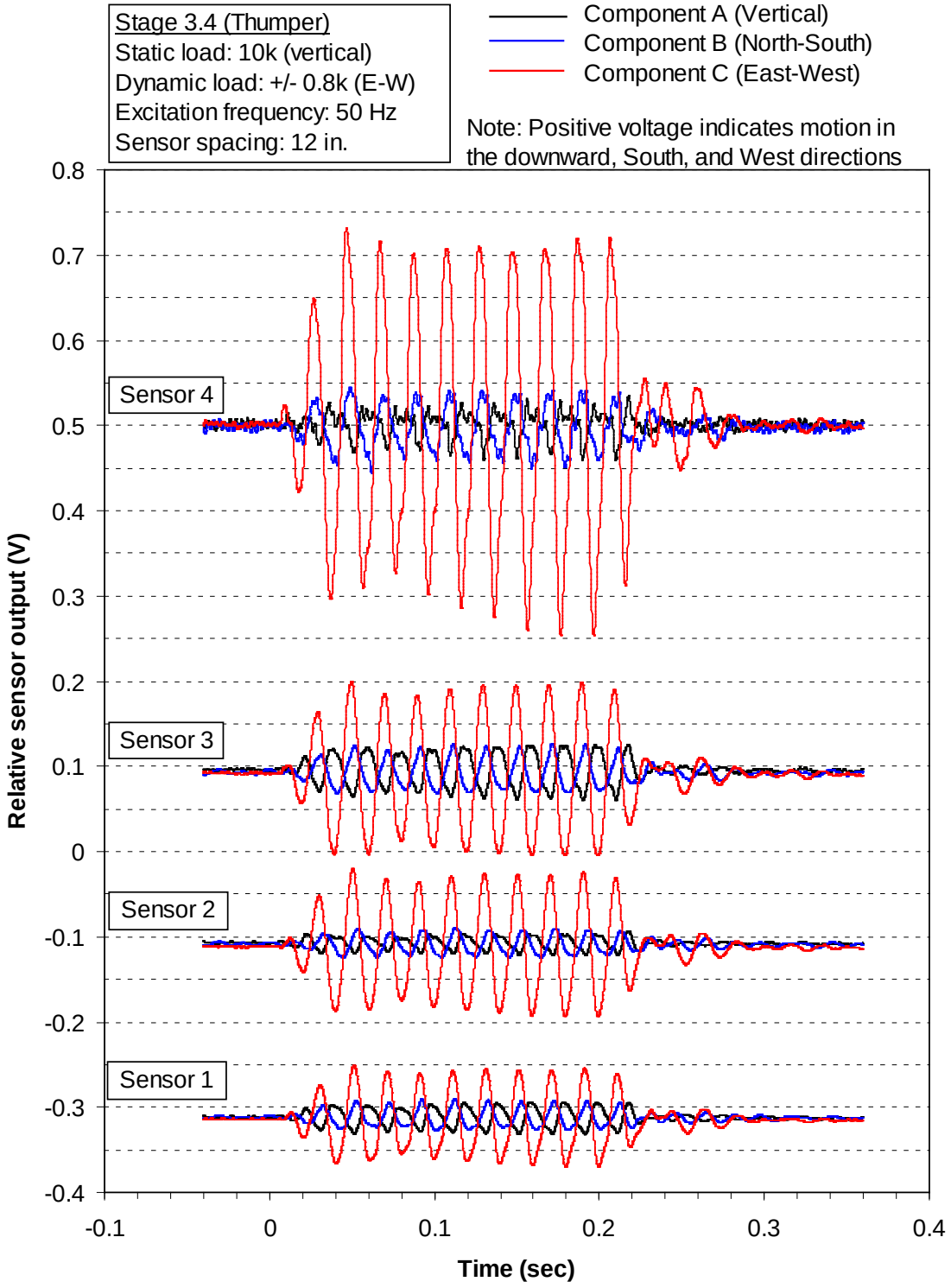

Figure D.2. Voltage-time histories of four sensors in the North column at Site 2 when subjected to a 50-Hz horizontal excitation (+/- 0.8k) from Thumper in Stage 3.4

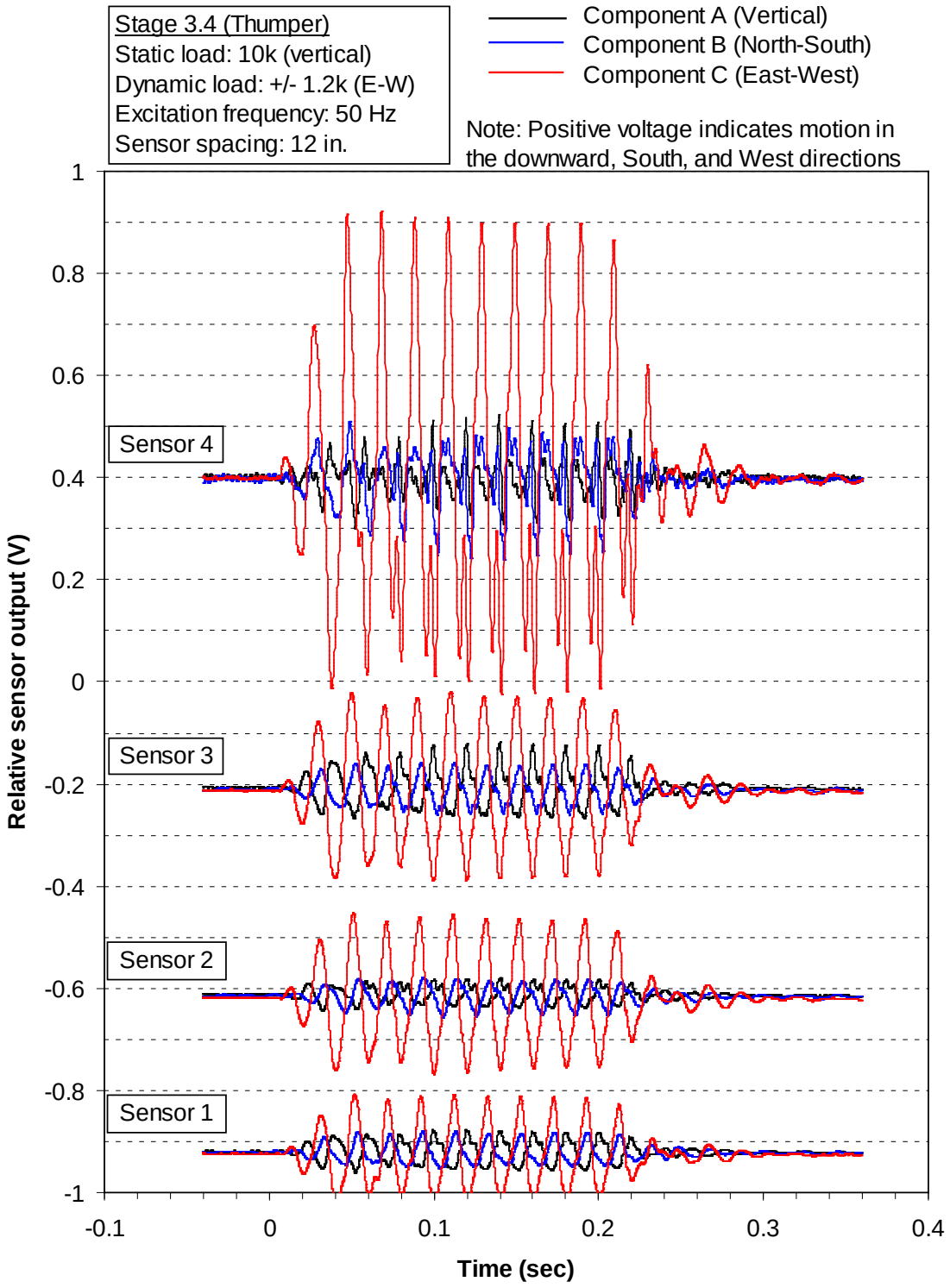

Figure D.3. Voltage-time histories of four sensors in the North column at Site 2 when subjected to a 50-Hz horizontal excitation (+/- 1.2k) from Thumper in Stage 3.4

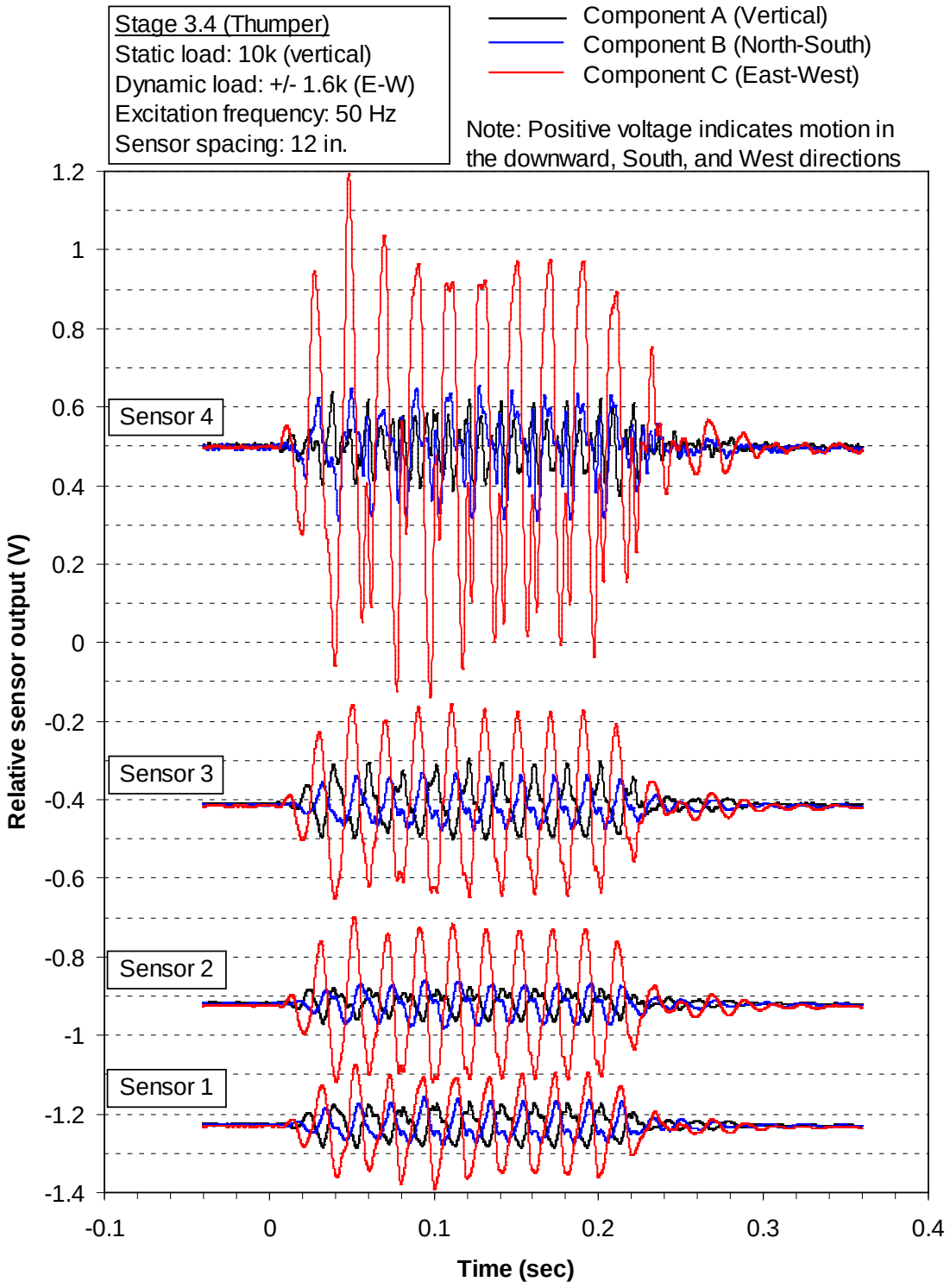

Figure D.4. Voltage-time histories of four sensors in the North column at Site 2 when subjected to a 50-Hz horizontal excitation (+/- 1.6k) from Thumper in Stage 3.4

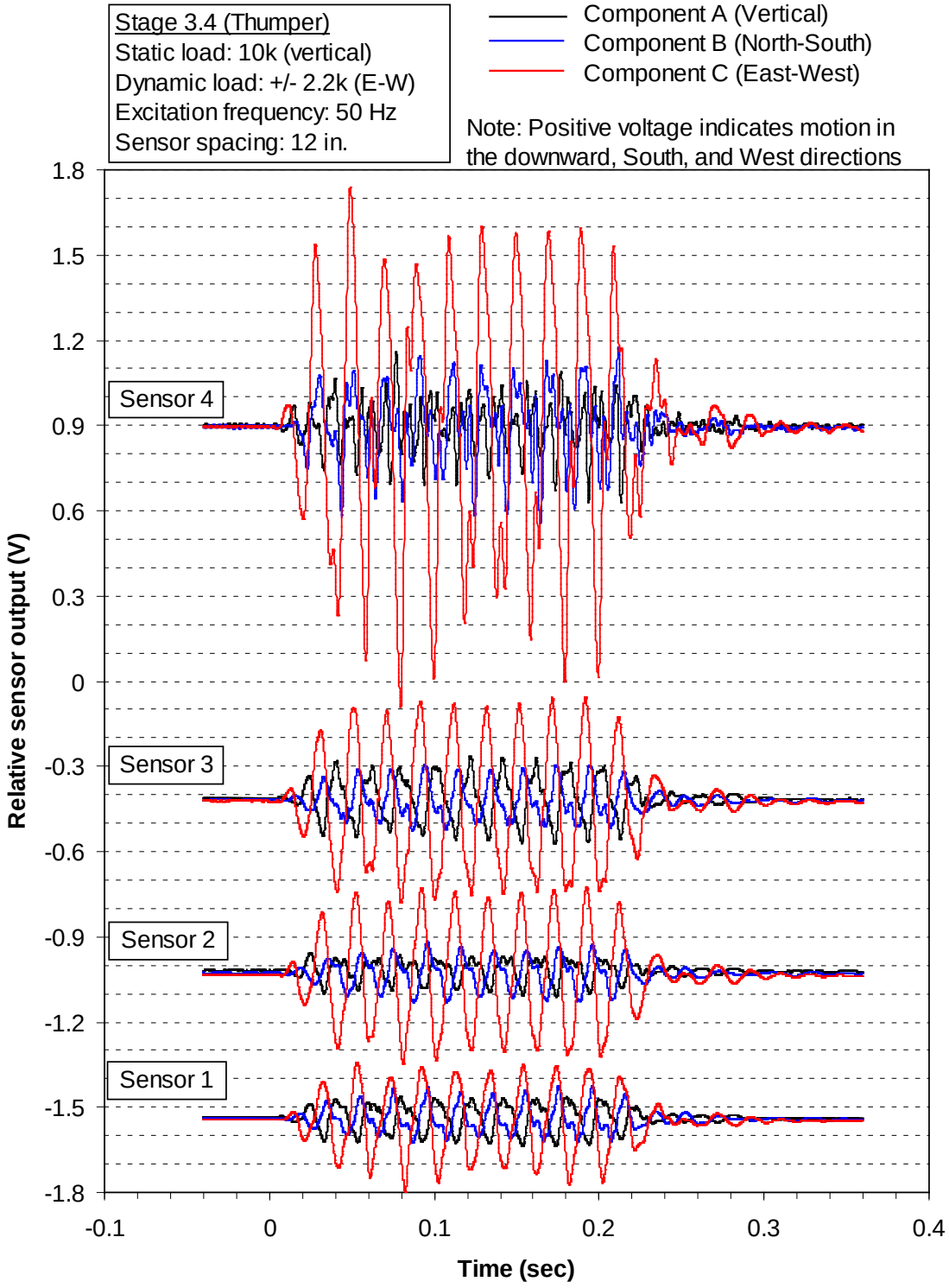

Figure D.5. Voltage-time histories of four sensors in the North column at Site 2 when subjected to a 50-Hz horizontal excitation (+/- 2.2k) from Thumper in Stage 3.4

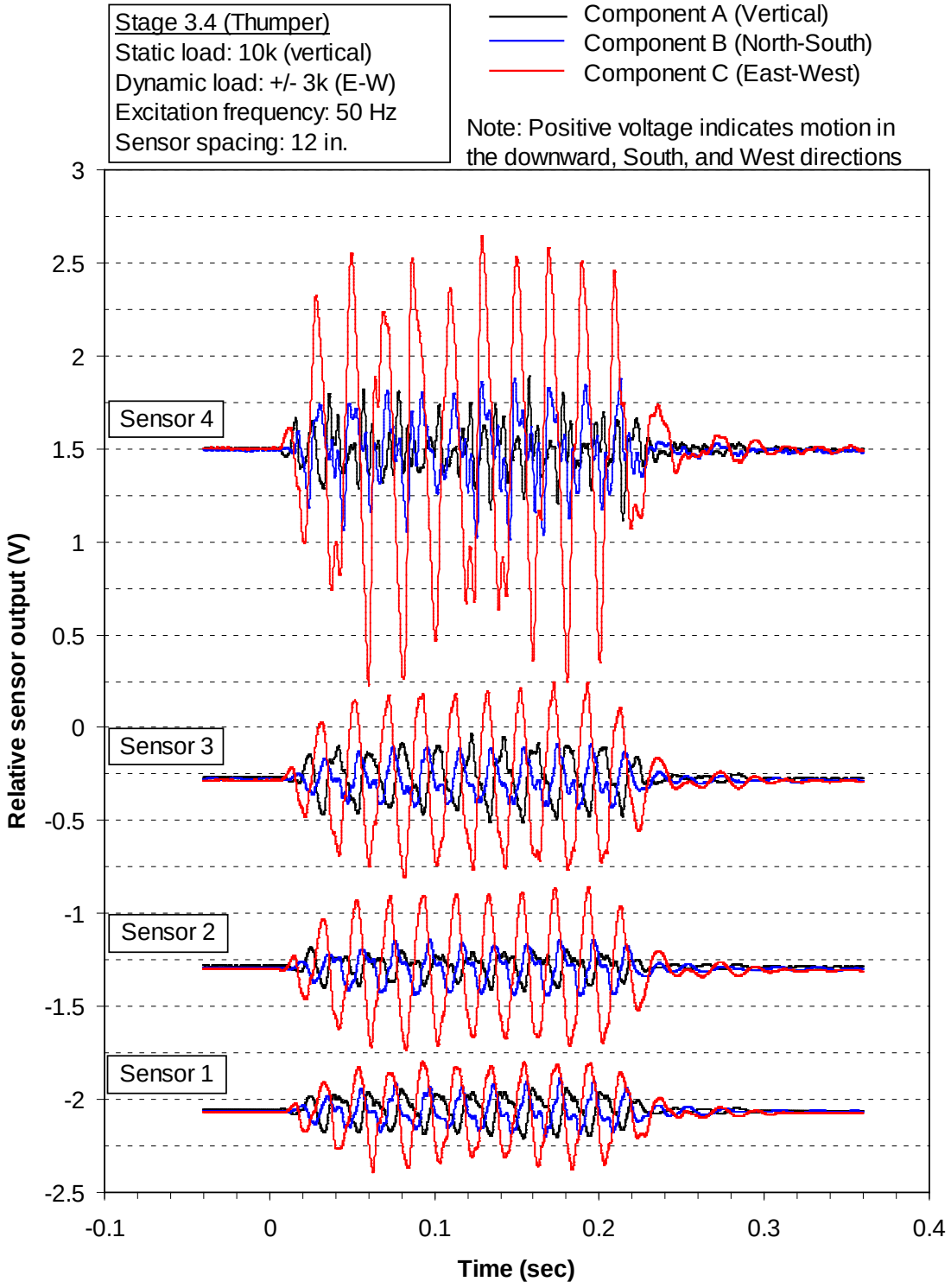

Figure D.6. Voltage-time histories of four sensors in the North column at Site 2 when subjected to a 50-Hz horizontal excitation (+/- 3k) from Thumper in Stage 3.4

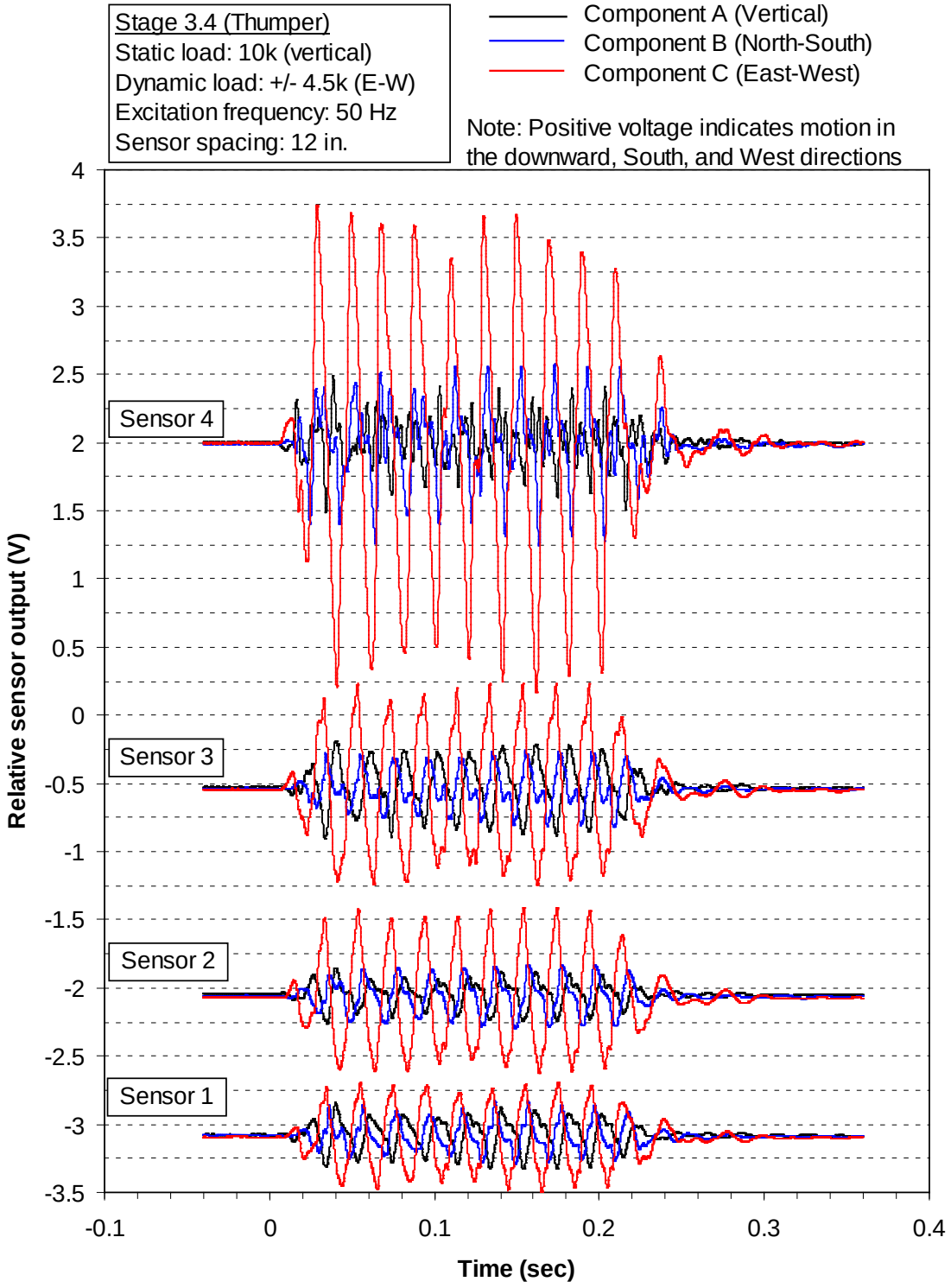

Figure D.7. Voltage-time histories of four sensors in the North column at Site 2 when subjected to a 50-Hz horizontal excitation (+/- 4.5k) from Thumper in Stage 3.4

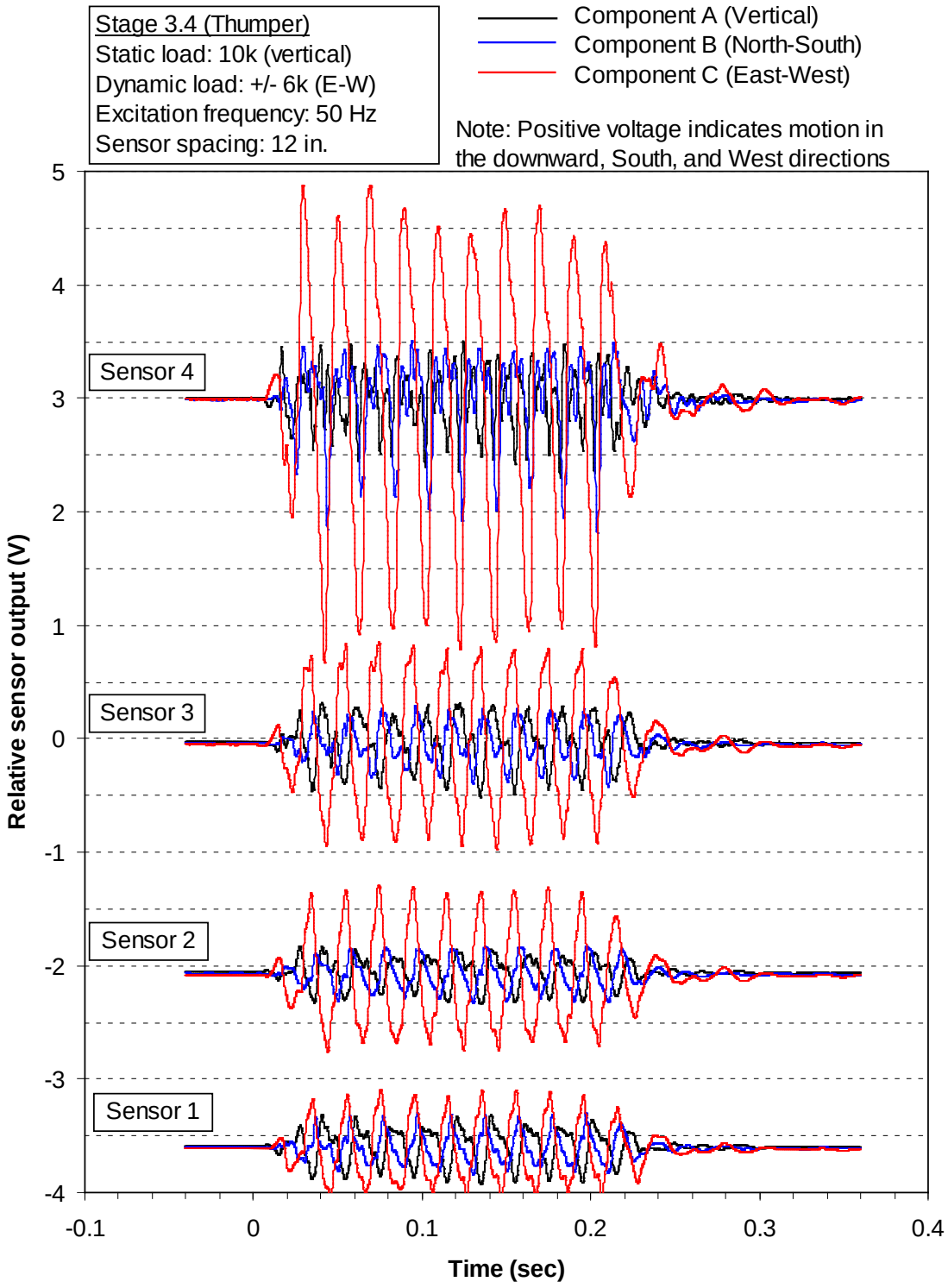

Figure D.8. Voltage-time histories of four sensors in the North column at Site 2 when subjected to a 50-Hz horizontal excitation (+/- 6k) from Thumper in Stage 3.4

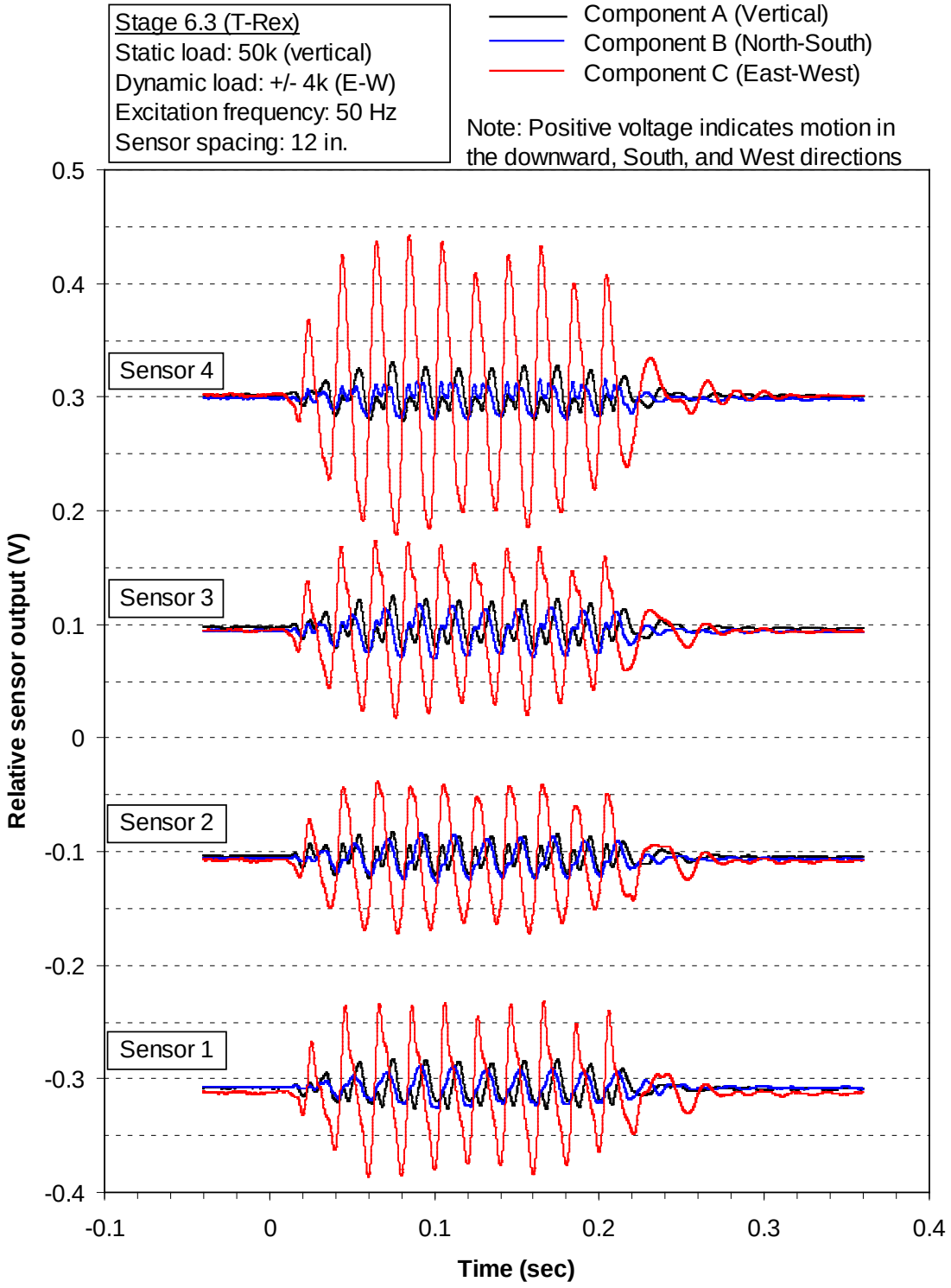

Figure D.9. Voltage-time histories of four sensors in the North column at Site 2 when subjected to a 50-Hz horizontal sinusoidal excitation (+/- 4k) from T-Rex in Stage 6.3

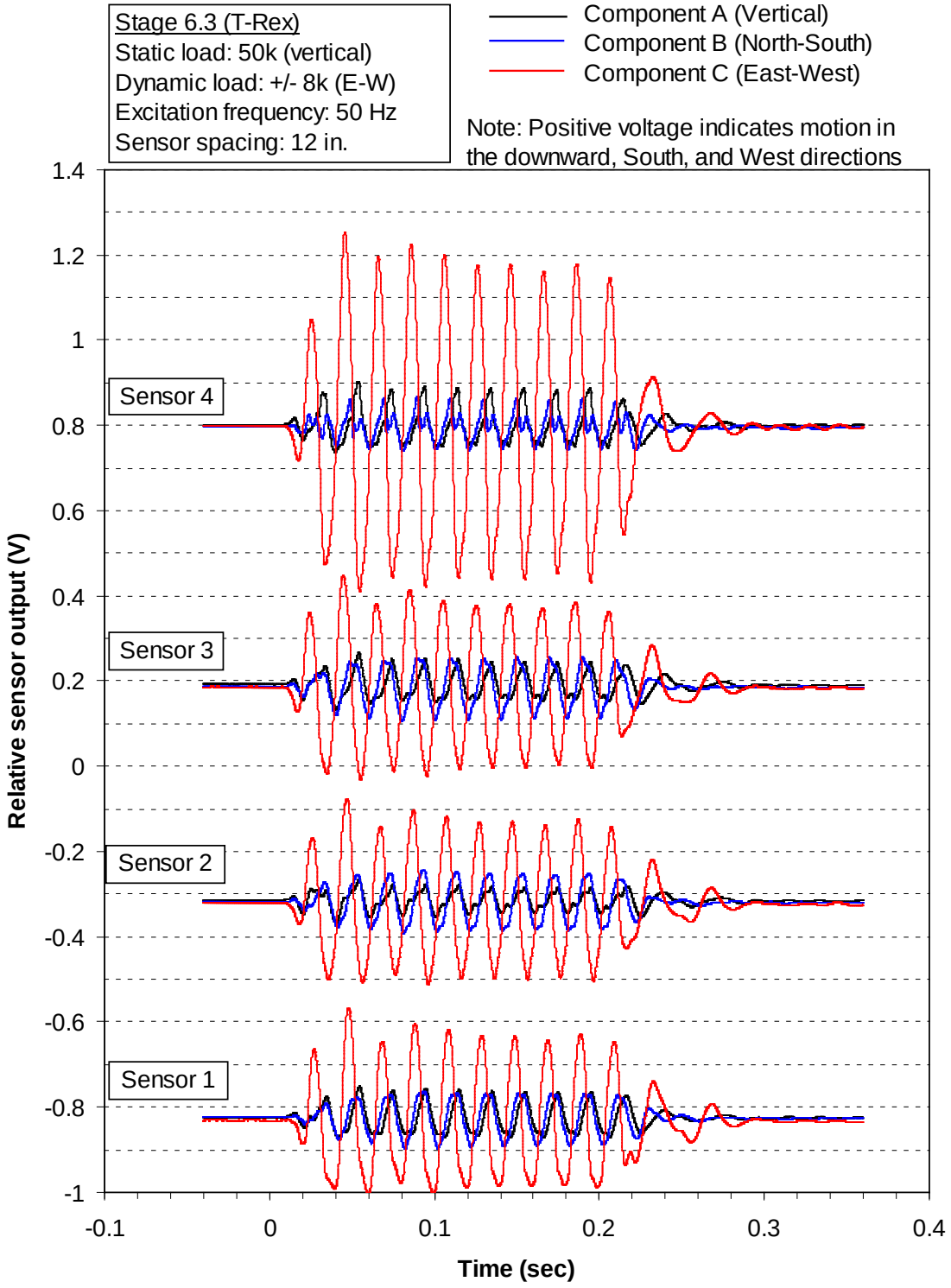

Figure D.10. Voltage-time histories of four sensors in the North column at Site 2 when subjected to a 50-Hz horizontal sinusoidal excitation (+/- 8k) from T-Rex in Stage 6.3

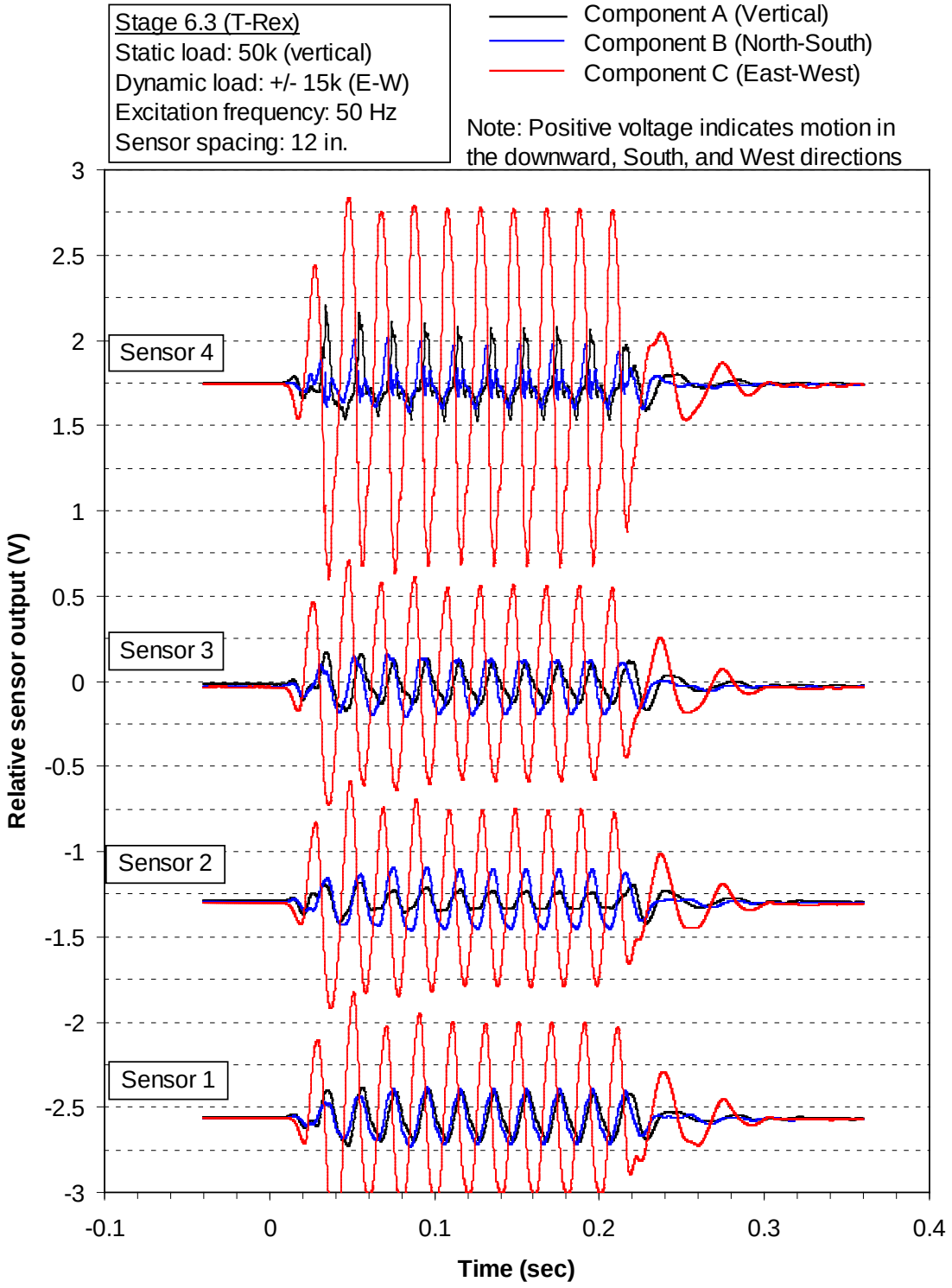

Figure D.11. Voltage-time histories of four sensors in the North column at Site 2 when subjected to a 50-Hz horizontal sinusoidal excitation (+/- 15k) from T-Rex in Stage 6.3

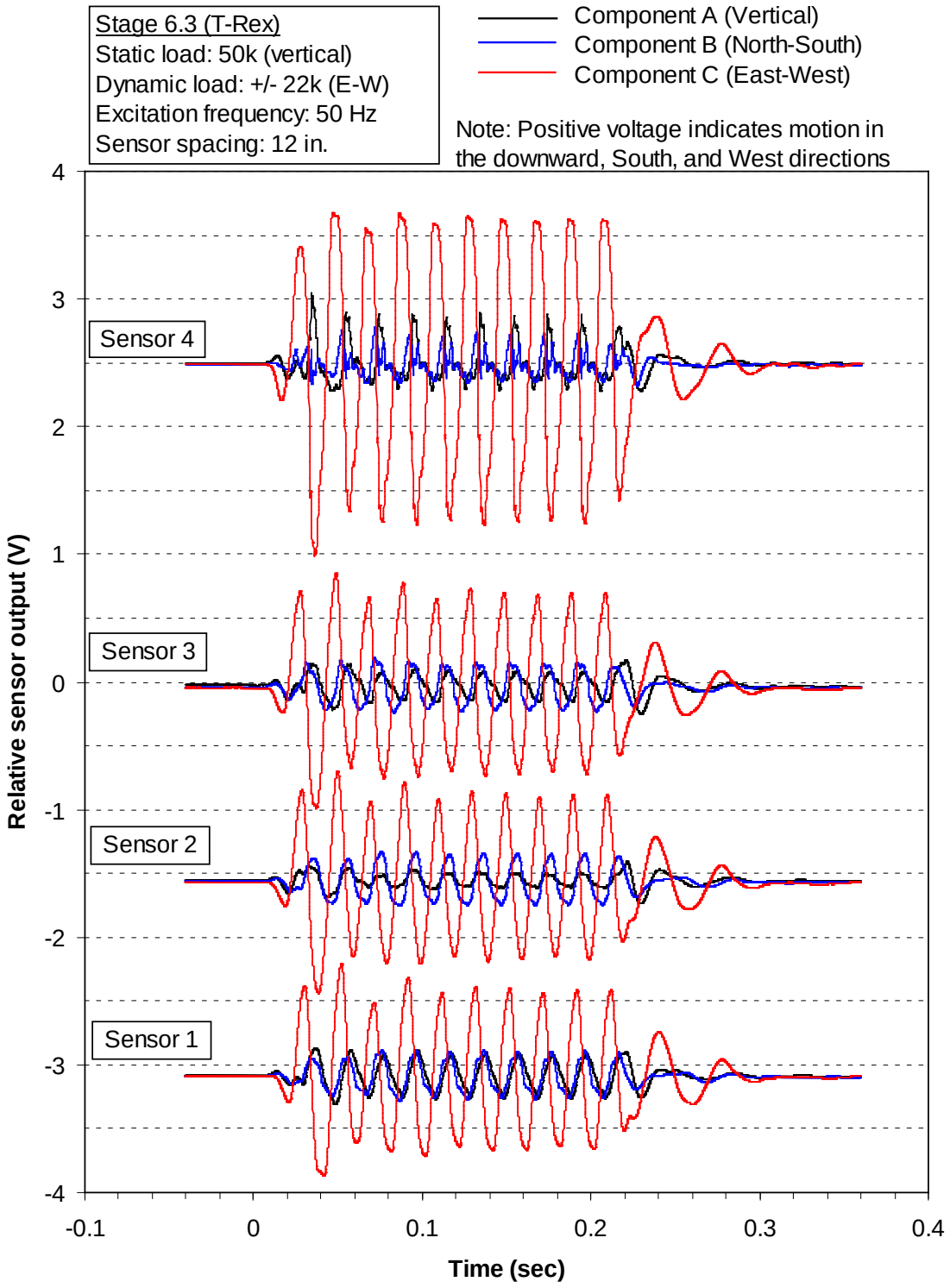

Figure D.12. Voltage-time histories of four sensors in the North column at Site 2 when subjected to a 50-Hz horizontal sinusoidal excitation (+/- 22k) from T-Rex in Stage 6.3

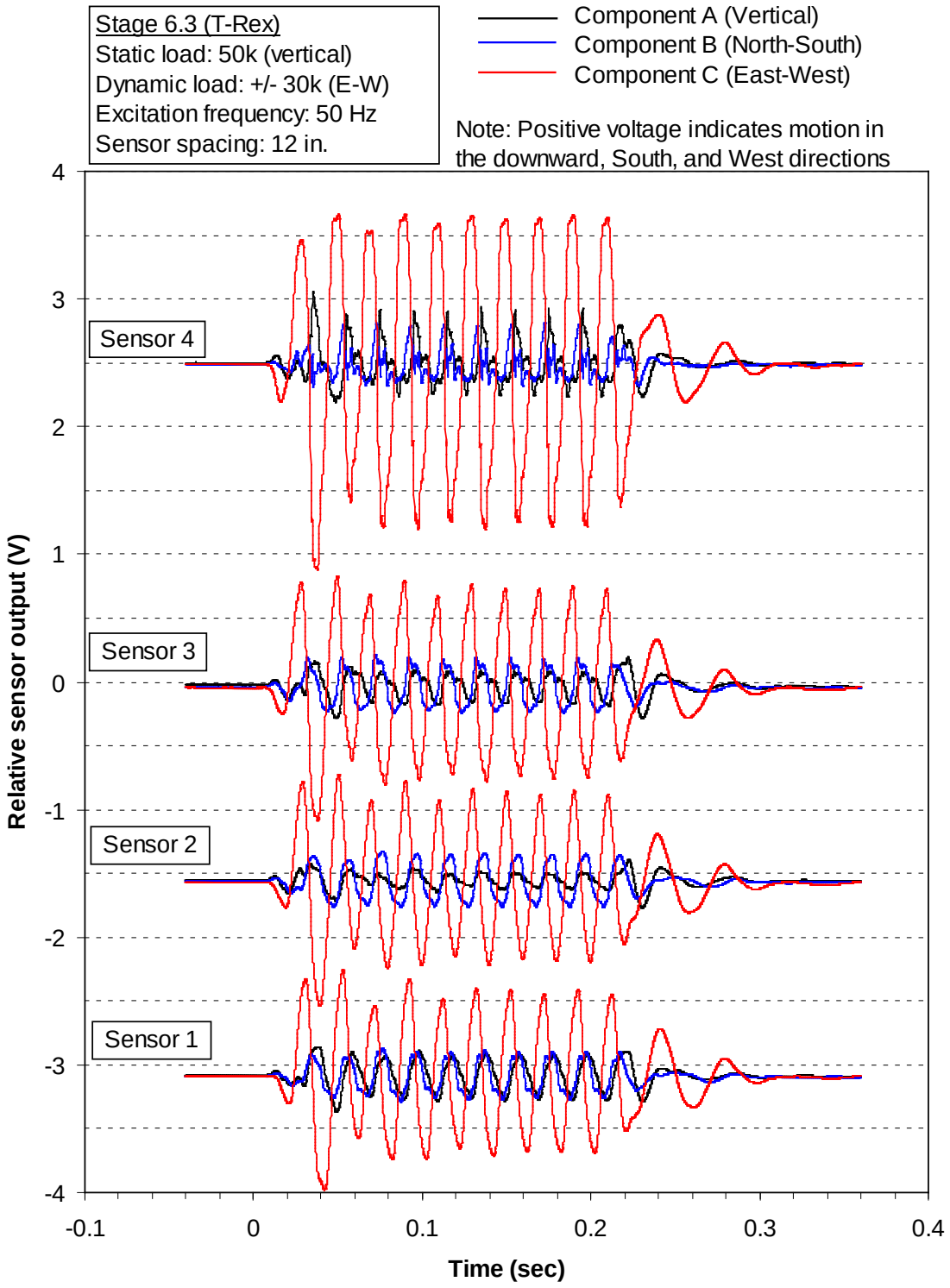

Figure D.13. Voltage-time histories of four sensors in the North column at Site 2 when subjected to a 50-Hz horizontal sinusoidal excitation (+/- 30k) from T-Rex in Stage 6.3

REFERENCES

ASTM D422, *Standard test method for particle-size analysis of soils*. Annual Book of ASTM Standards, 2000.

ASTM D2487, *Standard practice for classification of soils for engineering purposes (Unified Soil Classification System).* Annual Book of ASTM Standards, 2000.

ASTM D4318, *Standard test methods for liquid limit, plastic limit, and plasticity index of soils*. Annual Book of ASTM Standards, 2000.

Axtell, P.J., Stokoe, K.H., II, Rathje, E.M. and Chang, W.-J., (2002). *Development of methods to measure nonlinear properties and liquefaction characteristics of near surface soils*, Report No. GR02-4, Geotechnical Engineering Center, The University of Texas at Austin, USA.

Beresnev, I.A., Field, E.H., Abeele, K.V.D., and Johnson, P.A. (1998). Magnitude of nonlinear sediment response in Los Angeles basin during the 1994 Northridge, California, earthquake. *Bulletin of the Seismological Society of America.* **88:4**, 1079-1084.

Beresnev, I.A., Nightengale, A.M., and Silva, W.J. (2002). Properties of Vertical Ground Motions. *Bulletin of the Seismological Society of America.* **92:8**, 3152-3164.

Beresnev, I.A., and Wen, K.-L. (1995). P-wave amplification by near-surface deposits at different excitation levels. *Bulletin of the Seismological Society of America.* **85:5**, 1490-1494.

Beresnev, I.A., and Wen, K.-L. (1996a). The possibility of observing nonlinear path effect in earthquake-induced seismic wave propagation. *Bulletin of the Seismological Society of America.* **86:4**, 1028-1041.

Beresnev, I.A., and Wen, K.-L. (1996b). Nonlinear soil response – a reality? (a review). *Bulletin of the Seismological Society of America.* **86:6**, 1964-1978.

Chang, C. Y., Mok, C.M., and Tang, H.T. (1996). Interface of dynamic shear modulus from Lotung downhole data. *Journal of Geotechnical Engineering*, ASCE, **122:8**, 657-665.

Coduto, D.P. (1999). *Geotechnical Engineering: Principles and Practices*, Prentice-Hall, Upper Saddle River, NJ.

Darendeli, M.B. (2001). *Development of a new family of normalized modulus reduction and material damping curves*. PhD dissertation, The University of Texas at Austin, USA.

Electric Power Research Institute (EPRI) (1993). *Guidelines for determining design basis ground motions: method and guidelines for estimating earthquake ground motion in Eastern North America*, Report EPRI TR-102293, Vol. 1, Palo Alto, California.

Ghayamghamian, M.R., and Kawakami, H. (2000). On-site nonlinear hysteresis curves and dynamic soil properties. *Journal of Geotechnical Engineering*, ASCE, **126:6**, 543-555.

Hadala, P.F. (1973). *Effect of constitutive properties of earth media on outrunning ground shock from large explosions*, Technical Report S-73-6, U.S. Army Engineer Waterways Experiment Station, Vicksburg, Mississippi.

Hardin, B.O. (1978). The nature of stress-strain behavior for soils. *Earthquake Engineering and Soil Dynamics, Proceedings of the ASCE Geotechnical Engineering Division Specialty Conference*, Vol. 3, Pasadena, California, pp. 3-90.

Hardin, B.O., and Drnevich, V.P. (1972a). Shear modulus and damping in soils: measurement and parameter effects. *Journal of the Soil Mechanics and Foundations Division*, ASCE, **98:6**, 603-624.

Hardin, B.O., and Drnevich, V.P. (1972b). Shear modulus and damping in soils: design equations and curves. *Journal of the Soil Mechanics and Foundations Division*, ASCE, **98:7**, 667-692.

Kokusho, T., Aoyagi, T., and Wakunami, A. (2005). In situ soil-specific nonlinear properties back-calculated from vertical array records during the 1995 Kobe earthquake. *Journal of Geotechnical and Geoenvironmental Engineering*, ASCE, **131:12**, 1509-1521.

Kim, C. (2012). *Development of the Spectral-Analysis-of-Body-Waves (SABW) method for downhole seismic testing with boreholes or penetrometers.* PhD dissertation, The University of Texas at Austin, USA.

Kurtulus, A. (2006). *Field measurement of the linear and nonlinear shear moduli of soils using drilled shafts as dynamic cylindrical sources.* PhD dissertation, The University of Texas at Austin, USA.

LeBlanc, M.T., Stokoe, K.H., II, Branco, A.G., III, and Lee, R.C. (2012). Field determination of linear and nonlinear constrained moduli of soils using large mobile shakers. *15th World Conference on Earthquake Engineering*, Paper No. 3564, Lisbon, Portugal.

Lee, S.H. (1985). *Investigation of low-amplitude shear wave velocity in anisotropic material*. PhD dissertation, The University of Texas at Austin, USA.

Lu, N., and Likos, W.J. (2006). Suction stress characteristic curve for unsaturated soil. *Journal of Geotechnical and Geoenvironmental Engineering*, ASCE, **132:2**, 131-142.

Menq, F.-Y. (2003). *Dynamic properties of sandy and gravelly soils*. PhD dissertation, The University of Texas at Austin, USA.

Murphy, J.R., Davis, A.H., and Weaver, N.L. (1971). Amplification of seismic body waves by low-velocity surface layers. *Bulletin of the Seismological Society of America*. **61**, 109-145.

Park, K. (2010). *Field measurements of the linear and nonlinear shear moduli of cemented alluvium using dynamically loaded surface footings*. PhD dissertation, The University of Texas at Austin, USA.

Phillips, R.D. (2000). *Initial design and implementation of an in situ test measurement of nonlinear soil properties*. MS thesis, The University of Texas at Austin, USA.

Rathje, E.M., Chang, W-J., Stokoe, K.H., II, and Cox, B.R. (2004). Evaluation of ground strain from in situ dynamic testing. *13th World Conference on Earthquake Engineering*. Paper No. 3099, Vancouver, Canada.

Rathje, E.M., Phillips, R.D., Chang, W.J., and Stokoe, K.H., II. (2001). Evaluating nonlinear soil response in situ. *4th International Conference on Recent Advances in Geotechnical Earthquake Engineering and Soil Dynamics*, San Diego, California.

Richart, F.E., Jr., Hall, J.R., Jr., and Woods, R.D. (1970). *Vibration of Soils and Foundations*, Prentice-Hall, Upper Saddle River, NJ.

Seed, H.B., and Idriss, I.M. (1970). *Soil modulus and damping factors for dynamic response analysis*, Report No. EERC 70-10, Earthquake Engineering Research Center, University of California at Berkeley, USA.

Seed, H.B., Wong, R.T., Idriss, I.M., and Tokimatsu, K. (1986). Moduli and damping factors for dynamic analyses of cohesionless soils. *Journal of the Soil Mechanics and Foundations Division*, ASCE, **112:11**, 1016-1032.

Stokoe, K.H., II, Axtell, P.J., and Rathje, E.M. (2001). Development of an in situ method to measure nonlinear soil behavior. *3rd International Conference on Earthquake Resistant Engineering Structures*, Malaga, Spain, pp. 561-570.

Stokoe, K.H., II, Branco, A.G., III, and LeBlanc, M.T. (2011). *Preparation for field experiments using dynamic soil measurements to determine linear and nonlinear constrained and shear moduli of soils at Hornsby Bend, Austin, Texas*, Report No. GR11-04, Geotechnical Engineering Center, The University of Texas at Austin, USA.

Stokoe, K.H., II, Kurtulus, A., and Park, K. (2006). Development of field methods to evaluate the nonlinear shear and compression moduli of soil. *Earthquake Geotechnical Engineering Workshop*, University of Canterbury, Christchurch, New Zealand, 15 pgs.

Stokoe, K.H., II, Rathje, E.M., Wilson, C.R., Rosenblad, B.L., and Menq, F.Y. (2004). Development of the NEES large-scale mobile shakers and associated instrumentation for in situ evaluation of nonlinear characteristics and liquefaction resistance of soils. *13th World Conference on Earthquake Engineering.* Paper No. 535, Vancouver, Canada.

Umberg, D.R. (2012). *Dynamic properties of soils with non-plastic fines*. MS thesis, The University of Texas at Austin, USA.

Van Pelt, J.D. (2010). *Predicting Settlements of Shallow Foundations on Cohesionless, Granular Soil Using Dynamic Soil Measurements*. MS thesis, The University of Texas at Austin, USA.

Vesic, A.S. (1973). Analysis of ultimate loads of shallow foundations. *Journal of the Soil Mechanics and Foundations Division*, ASCE, **99:1**, 45-73.

Wen, K.-L. (1994). Non-linear soil response in ground motions. *Earthquake Engineering and Structural Dynamics*. **23:6**, 599-608.

Wen, K.-L., Beresnev, I.A., and Yeong, T.Y. (1994). Nonlinear soil amplification inferred from downhole strong seismic motion data. *Geophysical Research Letters*. **21:24**, 2625-2628.

Zalachoris, G. (2010). *Field Measurement of Linear and Nonlinear Shear Moduli of Solid Municipal Waste using a Dynamically Loaded Surface Footing*. MS thesis, The University of Texas at Austin, USA.

Zeghal, M., Elgamal, A.W., Tang, H.T., and Stepp, J.C. (1995). Lotung downhole array II: Evaluation of soil nonlinear properties. *Journal of Geotechnical Engineering*, ASCE, **121:4**, 363-378.